MINISTRY OF EDUCATION AND SCIENCE OF UKRAINE

East European Journal of Physics

No 4. 2020

2020

East European Journal of Physics

East European Journal of Physics

No 4. 2020

ORIGINAL PAPERS

East European Journal of Physics

No 4.   2020

POWER SPECTRA OF ULTRASONIC DOPPLER RESPONSE FROM BIOLOGICAL OBJECTS USING SYNTHETIC APERTURE TECHNIQUE

Iryna V. Sheina*, Olexander B. Kiselov, Evgen A. Barannik

Department of Medical Physics and Biomedical Nanotechnologies, V.N. Karazin Kharkiv National University
4, Svobody Sq., 61022, Kharkiv, Ukraine
*Corresponding Author: i.sheina@karazin.ua

The influence of dynamic change in the steering angle of incident and scattered wave beams on the spectra of the ultrasonic Doppler response is studied on the basis of the previously developed continuum model of ultrasound waves scattering in biological objects for the case, when the Doppler response signals are averaged over the period of changing the steering angle. A general expression is obtained, which combines the resultant spectrum of the power of the ultrasonic Doppler response signal from the region of interest, the spectral characteristics of the ultrasound scatterers movement, and the sensitivity function of the diagnostic synthetic aperture system. It is shown that, as compared to the Doppler response, which is a sequence of discrete values of the response signals from different steering angles, the use of averaging allows to reduce the width of the Doppler spectra without deterioration of their resolution. It is concluded that the achievement of better spatial resolution, when using the synthetic aperture method, is possible without deterioration of the spectral characteristics and, accordingly, of the accuracy of Doppler measurements of diagnostic parameters, which are determined during the ultrasound studies. The results obtained make it possible to optimize different Doppler techniques within the framework of the general synthetic aperture method.
KEYWORDS: ultrasound, Doppler spectra, synthetic aperture technique, continuum model of scattering, sensitivity function, dynamic focusing, response formation.

Currently, promising methods of ultrasound Doppler diagnostics of the state of the cardiovascular system and soft biological tissues are widely used, rapidly developing and being introduced into medical practice [1, 2]. Such methods include, in particular, spectral Doppler studies and Doppler color blood–flow mapping [3, 4], vector flow imaging [5, 6], tissue Doppler [7], vibro- and sonoelastography [8-11], etc. One of the major advantages of ultrasound methods, as compared to the other methods of medical diagnostics, is the possibility to obtain images in real time, what allows visualizing the dynamic structures in the human body. To provide a correct clinical interpretation [12] of the obtained data, ultrasound Doppler systems must meet certain requirements to the measurement accuracy.

In conventional Doppler ultrasound methods, to obtain an image, the diagnostic system utilizes an ultrasound transducer for sequential transmitting the ultrasonic pulses in the given direction, and for receiving the scattered waves [1, 12]. In this case, the entire sequence of emitted pulses is characterized by the same geometry of wave fronts and direction of their propagation. This approach has a number of disadvantages associated with limitations of the resolution, the ability to obtain a sufficient amount of data for accurate resolution of flows velocity, and the ability to focus, when radiating, only at one fixed depth.

The mentioned limitations can be removed by applying the synthetic aperture data acquisition technique. A distinctive feature of the synthetic aperture method is the use of wave fronts, in particular, flat [14, 15], differing as to the steering direction, with subsequent coherent compounding of the recorded ultrasonic responses [13, 16, 17]. The possibility to apply the synthetic aperture technique in medical ultrasound imaging is shown by many authors [6, 13, 18-20]. This method can be realized both in systems with a single-element transducer [21, 22], where the same element is used to transmit and receive ultrasound waves, and for systems with a multi-element transducer [17, 23, 24]. In particular, the synthetic aperture method for a circular aperture was investigated in [25].

Synthetic aperture technique is computationally intensive. Therefore, along with methods of reducing the number of computations [26], the synthetic aperture technique has received significant development with the advent of ultrasound scanners, which use parallel signal processing to produce image. [19, 27-30]. As a result of the introduction of multilinear data processing into ultrasound diagnostic systems, it became possible to visualize in-vivo blood flows using the synthetic aperture method, which, in comparison with the conventional Doppler techniques, allowed to improve spectral estimates [31], to determine the velocity vector [32], and to increase the sensitivity to slow velocity flows [33]. The methods of shear wave elastography [34, 35], estimation of local pulse wave velocity [36, 37], visualization of contrast agents [38] and of the brain activity [39] have been developed.

To date, the properties of B-images, obtained using the synthetic aperture technique, have been well studied. In particular, the dependence of the focusing quality on the number of different steering angles of plane waves has been established [40]. In [41], a technique for optimizing the parameters of plane wave radiation, which are essential for obtaining high-resolution images and estimating the velocity of both fast and slow flows, is proposed. The optimal

values of the parameters of the amount of radiation, the steering angle of the transmitted waves, and the size of the aperture are found, with the balance between the image quality and the frame rate taken into account. In [42] different effects, that influence the focusing in this synthetic aperture vector velocity estimation method, are investigated. They include the effect of phase errors in the emitted spherical waves, motion effects, and the effect of various interpolation methods in beam formation. Verification of the vector flow methods for laminar blood flows in the common carotid artery was carried out by comparing the parameters of peak systolic velocity and volumetric blood flow, obtained by independent methods such as Spectral Doppler [43-45] and magnetic resonance angiography [46]. In vivo the accuracy of plane wave vector flow imaging was investigated for the quantitative assessment of the laminar and turbulent flows dynamics [47], as well as for determining the volumetric flow rate and experimental measurement of errors in its determination, which were described earlier theoretically [48].

To date, the theoretical description of the influence of dynamic changes in the parameters and geometry of probing ultrasonic fields on the spectra of Doppler signals and, accordingly, on the assessment of the parameters of the biological objects motion is less developed. In this paper, to study the influence of dynamic change in time of the steering angle on the spectra of ultrasonic Doppler signals, we used a continuum model of ultrasonic waves scattering by inhomogeneities of density and compressibility [49-56]. Basing on this model with stationary probing fields, used in conventional Doppler techniques, practically important solutions were obtained for the power spectra of the Doppler response in the cases of uniform, correlated, vibrational [50] and uniformly accelerated [51, 52] motion of the ultrasound scatterers. These results are utilized, in particular, in ultrasound Doppler vibroelastography, spectral Doppler studies, Doppler color blood flow mapping and other applications. In [53], the spectral characteristics of Doppler response signals were theoretically investigated for the case, when ultrasonic probing was carried out using incident and reflected wave beams with the propagation direction, periodically changing in time.

In the present paper, we investigated the influence of dynamic change in the steering angle at transmitting and receiving the wave beams on the spectral characteristics of the sensitivity function of the probing system and the spectrum of the ultrasonic Doppler response in the case, when the Doppler response signals were averaged over the period of the change in the steering angle.

THEORETICAL MODEL

This theoretical study of the process of ultrasound scattering by blood and soft tissues is based on the assumption that these biological objects interact with the emitter field as if they are an isotropic continuous medium [54-56]. Within the framework of the continuum model, the scattering occurs on inhomogeneities of the density and compressibility of the medium, and the correlation function of the ultrasonic response signals can be represented as follows [50-52, 57-60]:

$$R(\tau) = k^4 \iint\limits_R e^{2i\vec{k}(\vec{r}_1 - \vec{r}_0)} \overline{G_p'^*(\vec{r}_0, t_0) G_p'(\vec{r}_1, t_1)} C(\vec{r}_1 - \vec{r}_0, \tau) d\vec{r}_0 d\vec{r}_1 , \qquad (1)$$

where $\vec{k}$ and $k = 2\pi / \lambda$ are the wave vector and the wave number of the ultrasonic transducer field in the plane wave approximation, respectively, λ is the wavelength, c is the velocity of ultrasonic waves in the medium, $G_p'(\vec{r}, t)$ is the complex function of the ultrasound system sensitivity distribution over the field, which is determined by the shape of the probing pulses, as well as by the amplitude and phase characteristics of the incident and reflected wave beams. The value $C(\vec{r}_1 - \vec{r}_0, \tau)$ is the correlation function, which describes the space-time characteristics of fluctuations in density and compressibility. In the case of stationary motion of the ultrasound scatterers after averaging over the statistical ensemble, this function depends only on the difference coordinate and the difference time $\tau = t_1 - t_0$.

Regardless of the method for determining the Doppler shift frequency and the spectral characteristics of Doppler signals, described in [61], when the synthetic aperture method is used, the sensitivity function also depends on time. The bar in the expression (1) means averaging over the initial moment of time t_0 since for a complete averaging of the autocorrelation function, it is necessary to take into account different initial steering angles at different t_0. Whereas for both stationary and non-stationary motion of ultrasound scatterers, the correlation function (1) turns out, in reality, to be a function of only the difference coordinate and the difference time.

The power spectrum of the Doppler signal is the Fourier transform of the correlation function

$$S(\omega) = \int R(\tau) e^{i\omega\tau} d\tau , \qquad (2)$$

at calculation of which it is necessary to take into account the explicit time dependence of the ultrasound system sensitivity function.

RESULTS AND DISSCUSSION

There are two possible ways of generating an ultrasonic Doppler signal using responses, obtained for different steering angles of a dynamically changing sensitivity function. In one of them, the Doppler response is a sequence of discrete values of the response signals for a sequence of different steering angles. In this case, the resultant power spectrum of the Doppler signal can be written as follows [53]:

$$S(\omega_k) = \frac{k^4}{(2\pi)^3} \sum_{j=-\infty}^{\infty} \int d\vec{q} \, C(\vec{q}, \omega_k - \omega_j) \left| G(\vec{q} + 2\vec{k}, \omega_j) \right|^2, \tag{3}$$

where $\omega_k = 2\pi k / T$ is the variable of the Fourier series expansion, and T is the period of the steering angles change. It is obvious, that in this case a change in the direction of the wave vector and the sensitivity function in time leads to the corresponding change in the Doppler angle ϑ between the wave vector and the direction of the motion velocity. As a result, even at a constant velocity of the ultrasound scatterers V, the measured speed $V \cos \vartheta$ also constantly increases or decreases, depending on whether the angle ϑ decreases or increases. This situation is physically equivalent to the accelerated movement of ultrasound scatterers, what leads to broadening of the Doppler signal spectrum, as shown in [52]. This circumstance is a disadvantage, as compared to the traditional methods of Doppler ultrasound probing.

The other method of generating an ultrasonic Doppler signal is that, at which the discrete values are obtained by summing the discrete values of the response signals for different steering angles over the entire period of changing the angles T. In the sense, such summation means averaging over the period T, taking into account of which the sensitivity function $G'_p(\vec{r}, t)$ is described by the expression

$$\overline{G'_p(\vec{r}, t)} = \int_{-T/2}^{T/2} G'_p(\vec{r}, t + t') dt'. \tag{4}$$

Substitution of formula (4) into (1) leads to the following expression for the autocorrelation function:

$$R(\tau) = k^4 \iint_R e^{2i\vec{k}(\vec{r}_1 - \vec{r}_0)} \overline{\int_{-T/2}^{T/2} G'^*_p(\vec{r}_0, t_0 + t) dt \int_{-T/2}^{T/2} G'_p(\vec{r}_1, t_1 + t') dt'} \cdot C(\vec{r}_1 - \vec{r}_0, \tau) d\vec{r}_0 d\vec{r}_1 \tag{5}$$

As in the derivation of equation (3), we assume that the registration of the ultrasonic Doppler response signals is performed within a finite time interval T. In the case of a periodic change in the sensitivity function, it is natural to use for this value, in particular, this period of change. In general, the periodic extension of the sensitivity functions and the correlation function of scattering fluctuations allows using their expansion in Fourier series:

$$G'^*_p(\vec{r}_0, t_0 + t') = \sum_{n=-\infty}^{\infty} e^{2\pi n(t_0 + t')/T} G'^*_p\left(\vec{r}_0, \frac{2\pi}{T} n\right),$$

$$G'_p(\vec{r}_1, t_1 + t') = \sum_{j=-\infty}^{\infty} e^{-2\pi j(t_1 + t')/T} G'_p\left(\vec{r}_1, \frac{2\pi}{T} j\right) = \sum_{j=-\infty}^{\infty} e^{-2\pi j(t' + t_0 + \tau)/T} G'_p\left(\vec{r}_1, \frac{2\pi}{T} j\right)$$

$$C(\vec{r}_1 - \vec{r}_0, \tau) = \frac{1}{(2\pi)^3} \int d\vec{q} \, e^{i\vec{q}(\vec{r}_1 - \vec{r}_0)} \sum_{m=-\infty}^{\infty} e^{-2\pi i m \tau / T} C\left(\vec{q}, \frac{2\pi}{T} m\right)$$

Here, the value $C(\vec{q}, 2\pi m / T)$ describes the spectral components of the correlation function of the space-time characteristics of fluctuations.

Substituting these expressions into formula (5), we obtain a general expression for the spectrum of the ultrasonic Doppler response, with the averaging over the period taken into account

$$S(\omega_k) = \sum_{n, j, m=-\infty}^{\infty} \frac{k^4}{(2\pi)^3} \int d\tau e^{i\omega_k \tau} \int d\vec{q} \iint_R d\vec{r}_1 d\vec{r}_0 e^{i(\vec{q} + 2\vec{k})(\vec{r}_1 - \vec{r}_0)} \times$$

$$\times \overline{\int_{-T/2}^{T/2} e^{2\pi i n(t_0+t)/T} G_p'^* \left(\vec{r}_0, \frac{2\pi}{T}n \right) dt \int_{-T/2}^{T/2} e^{-2\pi i j(t'+t_0+\tau)/T} G_p'\left(\vec{r}_1, \frac{2\pi}{T}j \right) dt' \cdot e^{-2\pi i m\tau/T} C\left(\vec{q}, \frac{2\pi}{T}m \right)}$$

For convenience, we rearrange the factors in the last expression as follows:

$$S(\omega_k) = \sum_{n,j,m=-\infty}^{\infty} \frac{k^4}{(2\pi)^3} \int d\tau e^{i\tau\left(\omega_k - \frac{2\pi j}{T} - \frac{2\pi m}{T} \right)} \int d\vec{q} \iint_R d\vec{r}_1 d\vec{r}_0 e^{i(\vec{q}+2\vec{k})(\vec{r}_1-\vec{r}_0)} \times$$

$$\times G_p'^*\left(\vec{r}_0, \frac{2\pi}{T}n \right) G_p'\left(\vec{r}_1, \frac{2\pi}{T}j \right) \int_{-T/2}^{T/2} e^{\frac{2\pi i n t}{T}} dt \int_{-T/2}^{T/2} e^{-\frac{2\pi i j t'}{T}} dt' \cdot \overline{e^{\frac{2\pi i t_0}{T}(n-j)}} C\left(\vec{q}, \frac{2\pi}{T}m \right) \tag{6}$$

Then calculating the average value over the initial moment of time leads to the Kronecker symbol

$$\overline{e^{\frac{2\pi i t_0}{T}(n-j)}} = \frac{1}{T} \int_{-T/2}^{T/2} e^{\frac{2\pi i t_0}{T}(n-j)} dt_0 = \delta_{n,j} \,,$$

what allows summing up over one of the indices in (6):

$$S(\omega_k) = \sum_{j,m=-\infty}^{\infty} \frac{k^4}{(2\pi)^3} \int d\tau e^{i\tau\left(\omega_k - \frac{2\pi j}{T} - \frac{2\pi m}{T} \right)} \int d\vec{q} \iint_R d\vec{r}_1 d\vec{r}_0 e^{i(\vec{q}+2\vec{k})(\vec{r}_1-\vec{r}_0)} \times$$

$$\times G_p'^*\left(\vec{r}_0, \frac{2\pi}{T}j \right) G_p'\left(\vec{r}_1, \frac{2\pi}{T}j \right) \int_{-T/2}^{T/2} e^{\frac{2\pi i j t}{T}} dt \int_{-T/2}^{T/2} e^{-\frac{2\pi i j t'}{T}} dt' \cdot C\left(\vec{q}, \frac{2\pi}{T}m \right)$$

Then, the integration over time leads to a similar outcome, as a result of which we find:

$$\int_{-T/2}^{T/2} e^{\frac{2\pi i j t}{T}} dt \int_{-T/2}^{T/2} e^{-\frac{2\pi i j t'}{T}} dt' = T^2 \cdot \delta_{j,0}$$

Given this, after summing over the index j, the expression for $S(\omega_k)$ takes the form:

$$S(\omega_k) = \sum_{m=-\infty}^{\infty} \frac{k^4}{(2\pi)^3} \cdot T^2 \int d\tau e^{i\tau\left(\omega_k - \frac{2\pi m}{T} \right)} \int d\vec{q} \iint_R d\vec{r}_1 d\vec{r}_0 e^{i(\vec{q}+2\vec{k})(\vec{r}_1-\vec{r}_0)} \cdot G_p'^*(\vec{r}_0,0) G_p'(\vec{r}_1,0) \cdot C\left(\vec{q}, \frac{2\pi}{T}m \right)$$

Besides,

$$\int d\tau e^{i\tau\left(\omega_k - \frac{2\pi m}{T} \right)} = \delta_{\omega_k,2\pi m/T} \,,$$

as a result of which we find

$$S(\omega_k) = \frac{k^4}{(2\pi)^3} T^2 \int d\vec{q} \iint_R d\vec{r}_1 d\vec{r}_0 e^{i(\vec{q}+2\vec{k})(\vec{r}_1-\vec{r}_0)} \cdot G_p'^*(\vec{r}_0,0) G_p'(\vec{r}_1,0) \cdot C(\vec{q},\omega_k).$$

By definition of the three-dimensional Fourier transform of the function, we have

$$\int_R d\vec{r} e^{i(\vec{q}+2\vec{k})\vec{r}} G_p'(\vec{r},0) = G(\vec{q}+2\vec{k},0).$$

Then, taking into account this Fourier transform, we obtain the final form of the power spectrum of the ultrasonic Doppler response signal in the considered case of averaging over the period T:

$$S(\omega_k) = \frac{k^4}{(2\pi)^3} T^2 \int d\vec{q}\, C(\vec{q}, \omega_k) \left| G(\vec{q} + 2\vec{k}, 0) \right|^2 . \qquad (7)$$

In contrast to the expression obtained in [52] and expression (3), formula (7) does not contain the frequency convolution of the correlation function of space-time fluctuations and the sensitivity function. This means that the width of the Doppler signal spectrum is narrower than that in the first version of the ultrasonic Doppler response signal generation. In this sense, formula (7) is similar to the integral expression for the power spectrum

$$S = \frac{k^4}{(2\pi)^3} \int d\vec{q}\, C(\vec{q}, \omega) \left| G(\vec{q} + 2\vec{k}) \right|^2 ,$$

which was obtained for stationary probing fields, used in conventional methods of Doppler probing [50]. In this case, sequential radiation in the given direction of ultrasonic pulses is used, which is characterized by the same spatial geometry of wave fronts and by the same direction of radiation. At the same time, the application of such techniques in practice has some disadvantages. The first of them is associated with a fixed focal length at transmitting, what worsens the spatial resolution, and the second one is caused by a long data acquisition time for imaging, thus, the attainable frame frequency is severely limited.

Coherent compounding of response signals in the synthetic aperture method provides high resolution for radiation in the entire range of depths. The resulting expression (7) shows that such an improvement in resolution can be achieved also with ultrasonic Doppler probing without deterioration of spectral characteristics and, in particular, the width of the spectrum of the ultrasonic Doppler response signals. The accuracy of measurement of the Doppler spectrum average frequency is discussed, as a rule [55, 62], proceeding from the known Nyquist limit and the Rao-Cramer inequality. Both of these criteria lead to the requirement for the minimum bandwidth of the Doppler signal. The results obtained make it possible to optimize specific Doppler and spectral-Doppler ultrasound medical diagnostic techniques, implemented by using the synthetic aperture technique.

CONCLUSIONS

To increase the efficiency of ultrasonic Doppler diagnostic methods, it is important to study the Doppler response spectra under the given area of interest, which directly affect the accuracy of estimation of the investigated parameters of the biological objects motions. Therefore, it is still relevant to study the influence of the factor of dynamic changes in the parameters and geometry of probing ultrasonic fields on the spectra of Doppler signals and, accordingly, on the estimates of the parameters of the biological objects motion.

This paper presents a general theory, which is suitable for describing the spectral characteristics of ultrasonic Doppler signals, using the up-to-date technique of dynamic focusing of the emitted ultrasonic beams by the synthetic aperture method. In accordance with this technique, each probing pulse of ultrasound waves is characterized by its own direction of propagation, and coherent compounding of ultrasonic response signals, received from a set of such probing pulses, is used for focusing the waves at transmitting and forming the image of a biological object. The influence of dynamic change in the angle of transmitting and receiving the wave beams on the spectral characteristics of the sensitivity function of the probing system and the spectrum of ultrasonic Doppler response, in the case, when the Doppler response signals are averaged over the period of the change in the steering angle of probing, are studied. A general expression is obtained, which connects the resultant power spectrum of the ultrasonic Doppler response signal, the spectral characteristics of the ultrasound scatterers movement, and the sensitivity function of the system. The results, obtained in this paper, show the difference between two possible strategies for collecting information while forming the Doppler signals, and can contribute to the improvement of various Doppler techniques within the framework of the general synthetic aperture method.

ORCID IDs
Iryna V. Sheina, https://orcid.org/0000-0002-0293-4849; **Olexander B. Kiselov,** https://orcid.org/0000-0002-7585-5180;
Evgen A. Barannik, https://orcid.org/0000-0002-3962-9960

REFERENCES
[1]   P.N.T. Wells, Phys. Med. Biol. **51**(13), R83-R98 (2006), https://doi.org/10.1088/0031-9155/51/13/R06.
[2]   P.R. Hoskins, K. Martin, and A. Thrush (eds.), *Diagnostic Ultrasound: Physics and Equipment*, 3rd ed. (CRC Press, Boca Raton, 2019), in https://doi.org/10.1201/9781138893603.
[3]   P.N.T. Wells, Eur. J. Ultrasound, **7**(1), 3-8 (1998), https://doi.org/10.1016/S0929-8266(98)00006-8.
[4]   D.H. Evans, Proc. Inst. Mech. Eng. H, **224**(2), 241-253 (2009), https://doi.org/10.1243/09544119JEIM599.

[5] J.A. Jensen, S.I. Nikolov, A.C.H. Yu, and D. Garcia, IEEE Trans. Ultrason. Ferroelectr. Freq. Contr. **63**(11), 1704-1721 (2016), http://doi.org/10.1109/TUFFC.2016.2600763.

[6] J.A. Jensen, S.I. Nikolov, A.C.H. Yuand, and D. Garcia, IEEE Trans. Ultrason. Ferroelectr. Freq. Contr. **63**(11), 1722-1732 (2016), http://doi.org/10.1109/TUFFC.2016.2598180.

[7] N. Pulkovski, P. Schenk, N.A. Maffiulettiand, and A.F. Mannion, Muscle & Nerve, **37**(5), 638–649 (2008), https://doi.org/10.1002/mus.20996.

[8] L. Gao, K.J. Parker, R.M. Lerner, and S.F. Levinson, Ultrasound Med. Biol. **22**(8), 959-977 (1996), https://doi.org/10.1016/S0301-5629(96)00120-2.

[9] J. Ophir, S.K. Alam, B.S. Garra, F. Kallel, E. Konofagou, T.A. Krouscop, C.R.B. Merritt, R. Righetti, R. Souchon, S. Srinivasan, and T. Varghese, J. Med. Ultrasonics, **29**(4), 155-171 (2002), https://doi.org/10.1007/BF02480847.

[10] P.N. Wells, and H.D. Liang, J. R. Soc. Interface, **8**(64), 1521-1549 (2011), https://doi.org/10.1098/rsif.2011.0054.

[11] K.J. Parker, M.M. Doyley, and D.J. Rubens, Phys. Med. Biol. **56**, R1-R29 (2011), https://doi.org/10.1088/0031-9155/56/1/R01.

[12] C.R. Hill, and J.C. Bamber, in: *Physical principles of medical ultrasonics*, edited by C.R. Hill, J.C. Bamber, G.R. ter Haar (John Wiley & Sons, West Sussex, 2004), pp. 255-302.

[13] J.A. Jensen, S.I. Nikolov, K.L. Gammelmarkand, and M.H. Pedersen, Ultrasonics, **44**(1), e5–e15 (2006), https://doi.org/10.1016/j.ultras.2006.07.017.

[14] M. Tanter, J. Bercoff, L. Sandrin, and M. Fink, IEEE Trans. Ultrason. Ferroelectr. Freq. Contr. **49**(10), 1363-1374 (2002), https://doi.org/10.1109/TUFFC.2002.1041078.

[15] J.Y. Lu, IEEE Trans. Ultrason. Ferroelec. Freq. Contr. **44**(4), 839–856 (1997), https://doi.org/10.1109/58.655200.

[16] S. Nikolov, *Synthetic aperture tissue and flow ultrasound imaging*, Ph.D. dissertation, Dept. Electr. Eng., Tech. Univ. Denmark, (Lyngby, Denmark, 2001).

[17] M. Karaman, P.C. Li, and M. O'Donnell, IEEE Trans. Ultrason. Ferroelec. Freq. Contr. **42**(3), 429–442 (1995), https://doi.org/10.1109/58.384453.

[18] M.H. Pedersen, K.L. Gammelmark, and J.A. Jensen, Ultrasound Med. Biol. **33**(1), 37-47 (2007), https://doi.org/10.1016/j.ultrasmedbio.2006.07.041.

[19] M. Tanter and M. Fink, IEEE Trans. Ultrason. Ferroelectr. Freq. Control. **61**(1), 102-119 (2014), https://doi.org/10.1109/TUFFC.2014.6689779.

[20] H. Yao *Synthetic Aperture Methods for Medical Ultrasonic Imaging*, Dept. Inform. Univ. Oslo, (University of Oslo, Oslo, 1997).

[21] D.K. Peterson, and G.S. Kino, IEEE Trans. Son. Ultrason. **31**(4), 337-351 (1984), https://doi.org/10.1109/T-SU.1984.31514.

[22] J.T. Ylitalo, and H. Ermert, IEEE Trans. Ultrason. Ferroelec. Freq. Contr. **41**(3), 333-339 (1994), https://doi.org/10.1109/58.285467.

[23] G.R. Lockwood, J.R. Talman, and S.S. Brunke, IEEE Trans. Ultrason. Ferroelec. Freq. Contr. **45**(4), 980-988 (1998), https://doi.org/10.1109/58.710573.

[24] C.R. Hazard, and G.R. Lockwood, IEEE Trans. Ultrason. Ferroelec. Freq. Contr. **46**(4), 972–980 (1999), https://doi.org/10.1109/58.775664.

[25] M. O'Donnell, and L.J. Thomas, IEEE Trans. Ultrason. Ferroelec. Freq. Contr. **39**(3), 366–380 (1992), https://doi.org/10.1109/58.143171.

[26] R. Moshavegh, J. Jensen, C.A. Villagómez-Hoyos, M.B. Stuart, M.C. Hemmsen, and J.A. Jensen, in: *Proceedings of SPIE Medical Imaging* (San Diego, California, United States, 2016), pp. 97900Z-97900Z-9, https://doi.org/10.1117/12.2216506.

[27] L. Sandrin, S. Catheline, M. Tanter, and M. Fink, in: *Acoustical Imaging*, edited by M. Halliwell, P. N. T. Wells (Springer, Boston, MA, 2002), pp. 485-492, https://doi.org/10.1007/0-306-47107-8_68.

[28] J. A.Jensen, O. Holm, L.J. Jerisen, H. Bendsen, S.I. Nikolov, B.G. Tomov, P. Munk, M. Hansen, K. Salomonsen, J. Hansen, K. Gormsen, H.M. Pedersen, and K.L. Gammelmark, IEEE Trans. Ultrason. Ferroelectr. Freq. Contr. **52(**5), 881-891 (2005), https://doi.org/10.1109/TUFFC.2005.1503974.

[29] J. Lu, J. Cheng, and J. Wang, IEEE Trans. Ultrason. Ferroelec. Freq. Contr. **53(**10), 1796–1812(2006), https://doi.org/10.1109/TUFFC.2006.112.

[30] P. Tortoli, L. Bassi, E. Boni, A. Dallai, F. Guidi, and S. Ricci, IEEE Trans. Ultrason. Ferroelec.Freq. Contr. **56(**10), 2207-2216 (2009), https://doi.org/10.1109/TUFFC.2009.1303.

[31] S.I. Nikolov, and J.A. Jensen, IEEE Trans. Ultrason. Ferroelec. Freq. Contr. **50**(7), 848-856 (2003), https://doi.org/10.1109/TUFFC.2003.1214504.

[32] J.A. Jensen, and N. Oddershede, IEEE Trans. Med. Imag. **25**(12), 1637-1644(2006), https://doi.org/10.1109/TMI.2006.883087.

[33] J. Bercoff, G. Montaldo, T. Loupas, D. Savery, F. Meziere, M. Fink, and M. Tanter, IEEE Trans. Ultrason. Ferroelec. Freq. Contr. **58**(1), 134-147 (2011), https://doi.org/10.1109/TUFFC.2011.1780.

[34] L. Sandrin, M. Tanter, S. Catheline, and M. Fink, IEEE Trans. Ultrason. Ferroelec. Freq. Contr. **49**(4), 426–435 (2002), https://doi.org/10.1109/58.996560.

[35] J. Bercoff , M. Tanter, and M. Fink, IEEE Trans. Ultrason. Ferroelec. Freq. Contr. **51**(4), 396–409 (2004), https://doi.org/10.1109/TUFFC.2004.1295425.

[36] H. Hasegawa, and H. Kanai, IEEE Trans. Ultrason. Ferroelec. Freq. Contr. **55**(12), 2626–2639 (2008), https://doi.org/10.1109/TUFFC.2008.978

[37] J. Vappou, J. Luo, and E.E. Konofagou, Am. J. Hypertens. **23**(4), 393–398 (2010),https://doi.org/10.1038/ajh.2009.272.

[38] O. Couture, M. Fink, and M. Tanter, IEEE Trans. Ultrason. Ferroelec.Freq. Contr. **59**(12), 2676–2683 (2012), https://doi.org/10.1109/TUFFC.2012.2508.

[39] E. Mace, G. Montaldo, I. Cohen, M. Baulac, M. Fink, and M. Tanter, Nature methods, **8**(8), 662–664 (2011), https://doi.org/10.1038/nmeth.1641.

[40] G. Montaldo, M. Tanter, J. Bercoff, N. Benech, and M. Fink, IEEE Trans. Ultrason. Ferroelectr. Freq. Contr. **56**(3), 489-506 (2009), https://doi.org/10.1109/TUFFC.2009.1067.

[41] J. Jensen, M.B. Stuart, and J.A. Jensen, IEEE Trans. Ultrason. Ferroelectr. Freq. Contr. **63**(11), 1922-1934 (2016), https://doi.org/10.1109/TUFFC.2016.2591980.

[42] N. Oddershedeand, and J.A. Jensen, IEEE Trans. Ultrason. Ferroelec. Freq. Contr. **54**(9), 1811-1825 (2007), https://doi.org/10.1109/TUFFC.2007.465.

[43] M.M. Pedersen, M.J. Pihl, P. Haugaard, J.M. Hansen, K.L. Hansen, M.B. Nielsen, and J.A. Jensen, Ultrasound Med. Biol. **38**(1), 145–151(2012), https://doi.org/10.1016/j.ultrasmedbio.2011.10.003.

[44] P. Tortoli, M. Lenge, D. Righi, G. Ciuti, H. Liebgott, and S. Ricci, Ultrasound Med. Biol. **41**(5), 1354-1362 (2015), https://doi.org/10.1016/j.ultrasmedbio.2015.01.008.

[45] I.K. Ekroll, T. Dahl, H. Torp, and L. Løvstakken, Ultrasound Med. Biol. **40**(7), 1629–1640 (2014), https://doi.org/10.1016/j.ultrasmedbio.2014.01.021.

[46] K.L. Hansen, J. Udesen, N. Oddershede, L. Henze, C. Thomsen, J.A. Jensen, and M.B. Nielsen, Ultrasonics, **49**(8), 659–667 (2009), https://doi.org/10.1016/j.ultras.2009.04.002.

[47] J. Jensen, M.S. Traberg, C.A. Villagómez Hoyos, J.B. Olesen, B. Tomov, R. Moshavegh, M.B. Stuart, C. Ewertsen, K.L. Hansen, M.B. Nielsen, and J.A. Jensen, in: *2017 IEEE International Ultrasonics Symposium (IUS)*, (IEEE, Washington, DC, 2017), pp. 1-4, https://doi.org/10.1109/ULTSYM.2017.8092535.

[48] J. Jensen, J.B. Olesen, M.B. Stuart, P.M. Hansen, M.B. Nielsen, and J.A. Jensen, Ultrasonics, **70**, 136-146 (2016), https://doi.org/10.1016/j.ultras.2016.04.023.

[49] E.A. Barannik, Ultrasonics, **39**(2), 311–317 (2001), https://doi.org/10.1016/S0041-624X(01)00059-2.

[50] I.V. Skresanova, and E.A. Barannik, Ultrasonics, **52**(5), 676-684 (2012), https://doi.org/10.1016/j.ultras.2012.01.014.

[51] E.A. Barannik, and O.S. Matchenko, East Eur. J. Phys. **2**(1), 36-40 (2015), https://doi.org/10.26565/2312-4334-2015-1-05. (in Russian)

[52] O.S. Matchenko, and E.A. Barannik, Acoust. Phys. **63**(5), 596-603 (2017), https://doi.org/10.1134/ S1063771017050086.

[53] E.A. Barannik, and O.S. Matchenko, East Eur. J. Phys. **3**(2) 61-64 (2016), https://doi.org/10.26565/2312-4334-2016-2-08. (in

[54] B.A.J. Angelsen, IEEE Trans. Biomed. Eng. **BME-27**(2), 61–67 (1980), https://doi.org/10.1109/TBME.1980.326708.

[55] P.J. Fish, in: *PhysicalPrinciplesofMedical Ultrasonics*, edited by C.R. Hill (EllisHorwood, Chichester, 1986), pp. 338-376.

[56] R.J. Dickinson, and D.K. Nassiri, in: *Physical principles of medical ultrasonics*, edited by C. R. Hill, J. C. Bamber, G. R. terHaar (John Wiley & Sons, West Sussex, 2004), p. 191–222.

[57] E.A. Barannik, Sov. Phys. Acoust. **38** (2), 237-244 (1992). (in Russian) http://www.akzh.ru/pdf/1992_2_237-244.pdf. (in Russian)

[58] E.A. Barannik, Acoust. Phys. **39** (5), 939-941 (1993). (in Russian), http://www.akzh.ru/pdf/1993_5_939-941.pdf. (in Russian)

[59] E.A. Barannik, Acoust. Phys. **40**(2), 212-214 (1994), http://www.akzh.ru/pdf/1994_2_212-214.pdf. (in Russian)

[60] E.A. Barannik, Acoust. Phys. **43**(4), 453–457 (1997),http://www.akzh.ru/pdf/1997_4_453-457.pdf. (in Russian)

[61] R.J. Eckersley, and J.C. Bamber, in: *Physical principles of medical ultrasonics*, edited by C.R. Hill, J.C. Bamber, G.R. ter Haar (John Wiley & Sons, West Sussex, 2004), p. 303-336.

[62] W. Gilson, and S. Orphanoudakis, in: *Proceedings of the Annual International Conference of the IEEE Engineering in Medicine and Biology Society* (IEEE, New Orleans, 1988), pp. 473-474, https://doi.org/10.1109/IEMBS.1988.94615.

СПЕКТРИ ПОТУЖНОСТІ УЛЬТРАЗВУКОВОГО ДОППЛЕРІВСЬКОГО ВІДГУКУ БІОЛОГІЧНИХ ОБ'ЄКТІВ ПРИ ЗАСТОСУВАННІ ТЕХНОЛОГІЇ СИНТЕЗОВАНОЇ АПЕРТУРИ

І.В. Шеіна*, О.Б. Кісельов, Є.О. Баранник

Кафедра медичної фізики та біомедичних нанотехнологій,Харківський національний університет імені В.Н. Каразіна
м. Свободи 4, Харків, 61022, Україна

На основі розвиненої раніше континуальної моделі розсіювання ультразвукових хвиль у біологічних об'єктах досліджено вплив динамічної зміни ракурсів випромінювання та прийому ультразвукових пучків хвиль на спектри ультразвукового допплерівського відгуку у випадку, коли проводиться усереднення сигналів допплерівського відгуку за періодом зміни кутів зондування. Здобуто загальний вираз, що пов'язує повний спектр потужності сигналу ультразвукового допплерівського відгуку з області інтересу, спектральні характеристики руху розсіювачів ультразвуку та функції чутливості діагностичної системи з синтезованою апертурою. Показано, що порівняно з допплерівським відгуком, який являє собою послідовність дискретних значень сигналів відгуку з різних ракурсів, застосування усереднення дає змогу зменшити ширину допплерівських спектрів без погіршення роздільної здатності. Зроблено висновок про те, що досягнення кращої роздільної здатності при застосування методу синтезованої апертури можливе без погіршення спектральних характеристик і, відповідно, точності допплерівських вимірювань діагностичних параметрів, що визначають в ході ультразвукових досліджень. Одержані результати дають змогу оптимізувати різні допплерівські техніки в межах загального методу синтезованої апертури.

КЛЮЧОВІ СЛОВА: ультразвук, допплерівський спектр, метод синтезованої апертури, континуальна модель розсіяння, функція чутливості, динамічне фокусування, формування відгуку

СПЕКТРЫ МОЩНОСТИ УЛЬТРАЗВУКОВОГО ДОППЛЕРОВСКОГО ОТКЛИКА БИОЛОГИЧЕСКИХ ОБЪЕКТОВ ПРИ ИСПОЛЬЗОВАНИИ ТЕХНОЛОГИИ СИНТЕЗИРОВАННОЙ АПЕРТУРЫ

И.В. Шеина, А.Б. Киселёв, Е.А. Баранник

Кафедра медицинской физики и биомедицинских нанотехнологий,
Харьковский национальный университет имени В.Н. Каразина
пл. Свободы 4, Харьков, 61022, Украина

На основании развитой ранее континуальной модели рассеяния ультразвуковых волн в биологических объектах изучено влияние динамического изменения ракурсов излучения и приёма пучков волн на спектры ультразвукового допплеровского отклика в случае, когда производится усреднение сигналов допплеровского отклика по периоду изменения углов

зондирования. Получено общее выражение, связывающее полный спектр мощности сигнала ультразвукового допплеровского отклика из области интереса, спектральные характеристики движения рассеивателей ультразвука и функции чувствительности диагностической системы с синтезированной апертурой. Показано, что по сравнению с допплеровским откликом, который представляет собой последовательность дискретных значений сигналов отклика с разных ракурсов, применение усреднения позволяет уменьшить ширину допплеровских спектров без ухудшения разрешающей способности. Сделан вывод о том, что достижение лучшей пространственной разрешающей способности при использовании метода синтезированной апертуры возможно без ухудшения спектральных характеристик и, соответственно, точности допплеровских измерений диагностических параметров, определяемых в ходе ультразвуковых исследований. Полученные результаты дают возможность оптимизировать разные допплеровские техники в рамках общего метода синтезированной апертуры.

КЛЮЧЕВЫЕ СЛОВА: ультразвук, допплеровский спектр, технология синтезированной апертуры, континуальная модель рассеяния, функция чувствительности, динамическое фокусирование, формирование отклика

PACS: 43.25.Yw

HEAT LOCALIZATION IN THE MEDIUM IN BLOW-UP REGIME

Nikolay G. Kokodii^{a,b,*}, Stanislav V. Pogorelov^b

^aV.N. Karazin Kharkiv National University, Kharkiv, Ukraine
^bNational University of Pharmacy, Kharkiv, Ukraine
Corresponding Author: kokodiyng@gmail.com, phone: +380-50-637-54-04
Received July 15, 2020; revised September 21, 2020; accepted October 14, 2020

The existence of the effect of heat metastable localization in the medium in the blow-up heating regime was experimentally proved. This is the regime in which the heating energy for a finite period of time tends to infinity. Previous theoretical studies have shown that in this case some regions, inside of which the temperature increases, may arise, while their size remains constant or decreases with time (heat localization regions). These regions exist as long as there is some energy input from the outside. An installation for the experimental study of the thermal blow-up regimes in a solid was developed. The object of research was an aluminum rod with a heater at its end. The temperature distribution along the rod was measured with thermocouples. The temperature of the rod end could vary according to the given law. Calibration of the installation was performed. The sensitivity of thermocouples was determined. The inertia of the heating and cooling process was estimated. The mathematical description of the thermal processes, occurring during the experiment, was made. The nonlinear equation of heat conduction for the rod was solved, with the heat exchange with the environment by convection and radiation taken into account. The thermal regime at the boundary, which is necessary to create the thermal structures, was determined. The temperature distribution in the rod in the blow-up regime and non-blow-up regime was measured. In the blow-up regime the heat front (the coordinate of the point with the temperature equal to half the maximum temperature) initially shifts from the heat source, and then in the opposite direction, and the size of the area under heating decreases. In the non-blow-up regime the size of the heated region increases all the time. The predicted effect was supposed to be used in installations for thermonuclear fusion where the target was heated by laser radiation pulses of a special shape. This effect can also be used for localized heating in cutting and welding, when the adjacent regions are not to get very hot, and in other similar situations.
KEY WORDS: heating, blow-up regime, heat structures, experiment

The blow-up regime is a system development regime, in which one or several parameters tend to infinity within a finite period of time. Real physical quantities, of course, do not reach infinite values, but they can increase sharply in a short time. The analysis of the blow-up regime shows that unbounded solutions manifest their characteristic properties before the infinite values are reached. This allows estimating the parameters of such a regime at the moments of time close to "disastrous".

The blow-up regimes exist both in physics and in the animate nature.

1. In the special theory of relativity it is indicated, that the increase in the particle mass, as the speed of its movement approaches the speed of light, occurs according to the hyperbolic law, that is, in the blow-up regime.

2. It is stated, that the population of the Earth is currently growing in the blow-up regime [1]. The investigations of the mathematical model of this process and comparison with graphs, plotted on the basis of historical data on the number of population in different epochs, were carried out in [2, 3]. They show the validity of this model.

3. The growth in the number of scientific publications and the growth in the number of research papers also take place in the blow-up regime. The articles have an autocatalytic effect. Each article facilitates writing the next one. And the more articles are published in a particular area, the easier it is to conduct subsequent researches in it.

4. There are thermal blow-up regimes. They were predicted by the team of A.A. Samarsky-S. P. Kurdyumov at the Keldysh Institute of Applied Mathematics RAS, Moscow, Russia. The theoretical studies have shown that under such regimes some new physical phenomena should arise, namely, localization of heat in certain areas of the body under heating and formation of heat structures, i.e. of regions with a high concentration of energy, which are sharply separated from the cold regions. The structures are self-sustained; they exist as long as there is an influx of energy from the external sources. This phenomenon is called "the effect of metastable heat localization" [4-7].

In these works the problem of heat propagation into a cold half-space, when the boundary was heated in the blow-up regime, was solved. In the one-dimensional case, the process of heat propagation is described by the nonlinear equation of heat conduction:

$$\frac{\partial}{\partial z}\left(a(T)\frac{\partial T}{\partial z}\right) - \frac{\partial T}{\partial t} = 0 \tag{1}$$

where T is temperature, $a(T) = k/c\rho$ is thermal diffusivity of the medium (it is emphasized that it depends on the temperature), k is heat conductivity factor, c is specific heat capacity, ρ is the medium density.

It has been found that if the temperature at the boundary of the medium with the coefficient of thermal diffusivity, which is growing with the temperature, increases, tending to infinity at approaching the finite moment of time, then there is no heat propagation deep into the medium during the time interval when the heat is supplied.

Let, $a(T) = a_0 T^\sigma$, where $\sigma > 0$, then the initial temperature of the medium is $T(z,0) = 0$.

At the boundary the temperature rises according to the law:

$$T(0,t) = \frac{T_0}{\left(t_f - t\right)^n},$$

where t_f is the time, called in these problems as "focusing time".

There are three heating regimes:

1. At $n > 1/\sigma$ (HS - regime) – the heat localization is absent. The heat propagates into the cold environment in the form of a wave with a growing half-width of the temperature front.

2. At $n = 1/\sigma$ (S - regime) the problem has the analytical solution:

$$T(z,t) = \begin{cases} T_0^{-1/\sigma} \left(1 - \frac{z}{z_F}\right)^{2/\sigma}, & 0 \le z \le z_F \\ 0, & z > z_F \end{cases}$$

(2)

where z_F is the depth of heating the matter by a thermal wave. The wave does not vary in time, although the amount of heat in the localization zone increases indefinitely. But the heat does not propagate further away into the medium.

3. At $n < 1/\sigma$ (LS - regime) the depth of heat penetration into the medium decreases with time, the wave front does not advance further, and the half-width of the front decreases.

Thus, the thermal effect of the boundary S - regime and LS – regime on the medium is localized.

In [7] the experiment conditions for the case, when the effect of heat localization could be observed, were formulated:

1. the presence of the blow-up heating regimes S or LS, when the amount of incoming heat increases in time drastically;

2. the medium thermal diffusivity grows as the temperature increases, what increases the influx of heat into the heated region and decreases the heat transfer to the cold region.

3. during the heating period the temperature at the boundary should increase by 10-30 times.

However, in [8] it was shown that the experiment conditions may not be so stringent. The effect of heat localization can also be observed in the media with the thermal diffusivity, which does not depend on the temperature. In this case there is no strict boundary for heat localization z_F. The coordinate of this point is constantly moving upward. But the half-width of the heat front remains constant or decreases in the process of exposure to heat. The temperature difference can be considerably less – by 5-6 times.

Further works on the study of the blow-up regimes were carried out in other directions; they were mainly associated with the analyses of these regimes in the nature and in human society. The investigations were devoted to connections of the emerging phenomena with synergetics, i.e. the science explaining the formation and self-organization of structures in open systems, which are far from the thermodynamic equilibrium [9]. These works were only of theoretical character.

The exception were studies of a new physical phenomenon – the T-layer effect – the occurrence of a stable zone in the plasma placed in a magnetic field with the stable zone temperature being higher than that of the rest of plasma. The phenomenon was discovered in 1965 by a team of scientists directed by A. N. Tikhonov and A. A. Samarsky at the Institute of Applied Mathematics of the USSR Academy of Sciences. The T-layer phenomenon plays an important role in theoretical and applied plasma physics (development of MHD generators, controlled thermonuclear fusion). The T-layer, like a piston moved by a magnetic field, allows controlling the behavior of low-temperature plasma and transforming its energy into optical radiation.

This phenomenon was experimentally investigated at the Institute of Theoretical and Applied Mechanics SB RAS (Novosibirsk) [10].

Several experimental works have appeared in recent years [11-16].

In work [16] were studied an insulator-metal transition (IMT) in vanadium dioxide films. Main features of the voltage-induced IMT in these systems can be understood within a theory of the blow-up overheating instability. In the blow-up regime, the IMT occurs locally even in uniform films: a narrow "hot" metallic channel occurs along the current direction. This was compared the obtained theoretical results with the experiments taken from literature [14, 15] and our own and find a good agreement between calculated and measured quantities.

Observed voltage-induced IMT is the local character of the transition nucleation. The IMT occurs within a narrow "hot" channel along the direction of the current flow, while the remaining sample is in the insulating "cold" phase. It was shown that this feature is an inherent property of the overheating instability in the geometry studied and does not require any additional suggestions about film homogeneity.

In all of these cases the blow-up regimen arises from the emergence of positive feedback between the current growth processes and the heating temperature, that there is a connection between the exit and the entrance of the system.

But in our work, studies have been carried out, when the heating regime of the system can be regulated completely regardless of the results of heating. There can be completely different cases - constant heating, slow mode without blow-up, rapid heating with or without blow-up. This is the first work to directly study of such processes.

EXPERIMENTAL SYSTEM

The block diagram of the experimental system is shown in Fig. 1. The target under heating is an aluminum rod 140 mm long with the end face of 10 x 14 mm. An electric heater is located at the end of the rod. he heating power can vary according to the given law. Ten copper-constantan thermocouples are placed along the rod at the distance of 10 mm from one another. The first thermocouple measures the temperature of the rod end. The signals from the thermocouples enter the indicator unit, where the temperature distribution in time at the control points is recorded.
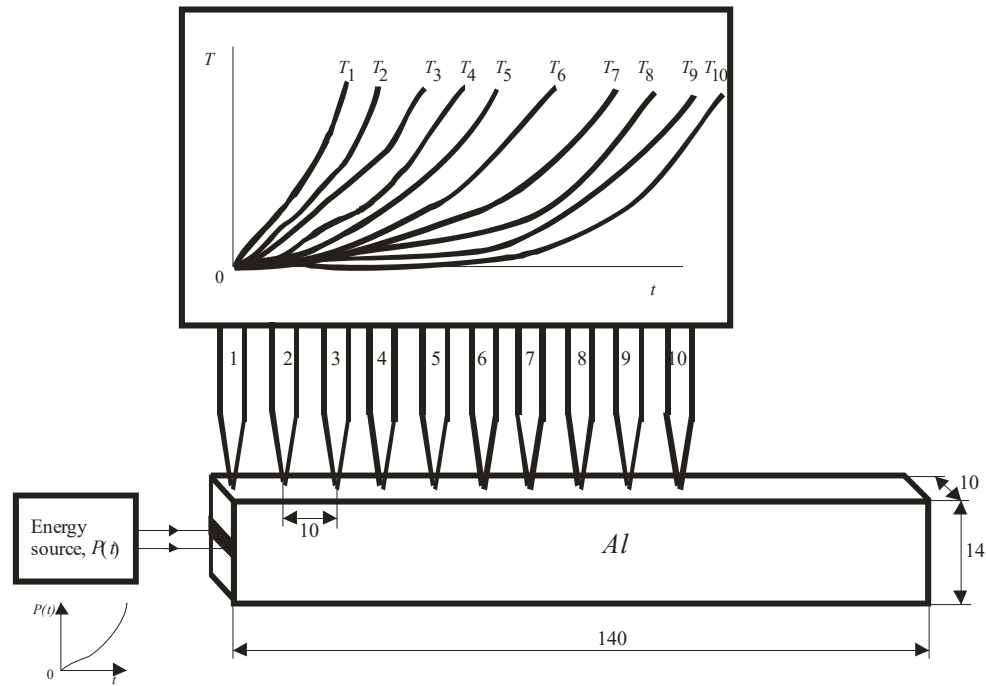
Figure 1. Experimental system

THERMOPHYSICAL PARAMETERS OF THE TARGET

To calculate the thermal conditions, it is necessary to know the target parameters: thermal conductivity k, specific heat capacity c, density ρ, thermal diffusivity a, coefficient of heat exchange with the environment α. The information about these values, except the heat exchange coefficient, was taken from reference books [17, 18]. Their values for the sample used in the experiment could differ from the tabulated values. However, this affects the values of the heating temperature, but not the nature of the thermal process.

Thermophysical parameters depend on the temperature. The linear approximation of the data for aluminum gives the following relations:

$$k(T) = 244 - 0.0486T, \text{ Вт/(м·град)}$$
$$c(T) = 878 + 0.528T, \text{ Дж/(кг·град)}$$
$$\rho(T) = 2710 - 0.218T, \text{кг/м}^3$$
$$a(T) = 10^{-4} - 5.18 \cdot 10^{-8} T, \text{ м}^2/\text{с}$$

(3)

In these formulas, T is the temperature in Celsius degrees.

The heat exchange coefficient depends on the shape of the object, its location in space (vertical, horizontal), surface treatment and other factors. To determine it an experiment was carried out.

It is known from the theory of heat transfer, that cooling of a heated body occurs according to the exponential law:

$$T(t) = T_0 \exp(-t / \tau) ,$$

(4)

where $\tau = mc/\alpha S$ is the thermal time constant, that is, the time, during which the temperature of the body at its cooling decreases by the factor of e, S is the body surface, m is its mass.

The analysis of the cooling curve (4) shoved the value of the thermal time constant being 380 s, the value of the heat exchange coefficient $\alpha = 14$ W/(m^2 · deg) at the temperature of 20° C, and the temperature dependence $\alpha(T)= 12+0.0136 T$, W/(m^2·deg).

THEORETICAL DESCRIPTION OF THE TARGET HEATING PROCESS

The thermal conductivity equation for the rod was used to describe the thermal processes in the target. The dependences of the thermophysical parameters on the temperature and heat removal into the environment from the lateral surface by convection and thermal radiation were taken into account. As long as the area of the ends is much

smaller than that of the lateral surface, heat removal from them can be ignored. In the presence of internal heat sources, the heat conduction equation has the following form [19]:

$$\frac{\partial^2 T(z,t)}{\partial z^2} - \frac{1}{a(T)}\frac{\partial T(z,t)}{\partial t} + \frac{A}{k(T)} = 0 \tag{5}$$

Here $A = \Delta P / \Delta V$ is the volume density of the heat energy transferred from the rod by convection and thermal radiation per unit of time to the environment.

The initial condition is:

$$T(z,0) = T_0, \tag{6}$$

where T_0 is the ambient temperature.

The boundary conditions:

$$T(0,t) = T(t), \qquad \frac{\partial T(L,t)}{\partial z} = 0 \tag{7}$$

They show that one end of the rod with length L ($z = 0$) gets heated according to the given law $T(t)$, and the heat exchange between the other end ($z = L$) and the environment is absent.

The power delivered to the environment by convection from the section of the rod with length Δz is described by Newton law for thermal processes

$$\Delta P_k = \alpha S (T - T_0) = 2\alpha(d+h)(T - T_0)\Delta z .$$

Here $S = 2(d+h)\Delta z$ is the section surface, d and h are the dimensions of the rod cross-section.

Therefore, for the convective heat exchange

$$A_k = \frac{\Delta P_k}{\Delta V} = \frac{2\alpha(d+h)}{dh}(T - T_0) . \tag{8}$$

At high heating temperatures, which occur in the blow-up regimes, the thermal radiation of the body should be taken into account. The radiation intensity I is described by Stefan-Boltzmann equation. With the non-zero ambient temperature taken into account, it has the following form:

$$I = \varepsilon\sigma\left[(T+273)^4 - (T_0+273)^4\right],$$

where ε is the absorption coefficient, σ is the Stefan-Boltzmann constant, T and T_0 are the temperature of the body and the environment, respectively, in Celsius degrees.

The power, radiated from the section of the rod with the length Δz, is

$$\Delta P_r = I S = 2(d+h)\varepsilon\sigma\left[(T+273)^4 - (T_0+273)^4\right]\Delta z .$$

Therefore, the volume density of the radiated power

$$A_r = \frac{\Delta P_r}{\Delta V} = \frac{2(d+h)\varepsilon\sigma}{dh}\left[(T+273)^4 - (T_0+273)^4\right] . \tag{9}$$

The heat total power transferred to the environment is the sum of the convective and radiated powers:

$$A = A_k + A_r .$$

Substitution of expressions (8) and (9) with the "minus" sign into formula (5) gives the following equation:

$$\frac{\partial^2 T}{\partial z^2} - \frac{2\alpha(d+h)}{kdh}(T - T_0) - \frac{2(d+h)\varepsilon\sigma}{kdh}\left[(T+273)^4 - (T_0+273)^4\right] - \frac{1}{a}\frac{\partial T}{\partial t} = 0 . \tag{10}$$

Equation (10) with the initial condition (6) and boundary conditions (7) was solved for two cases: the blow-up regime – *HS*, and the non-blow-up regime – *LS*.

In the non-blow-up regime the temperature of the rod end varies linearly:

$$T(t) = 5t + 20 . \tag{11}$$

In the blow-up regime the temperature law is set as hyperbolic:

$$T(t) = \frac{3 \cdot 10^8}{(158 - t)^{3.2}} . \tag{12}$$

The diagrams of these processes are shown in Fig. 2. The heating time is 100 s. The parameters of equations (11) and (12) were chosen, so that in both cases the temperature at the onset of the heating process would be about 20°, and at the end – about 600°.
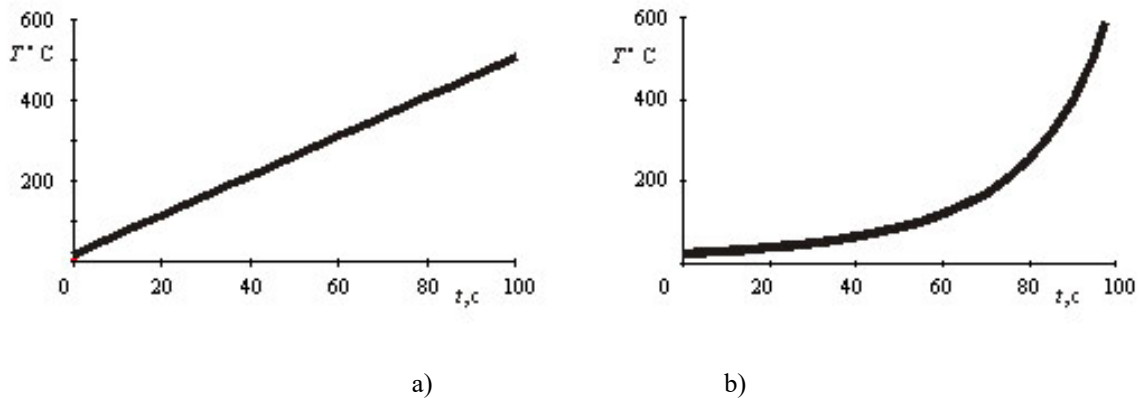
a)   b)
Figure 2. Variation of temperature at the boundary
a) *HS* (non-blow-up regime), b) *LS* (blow-up regime)

Fig. 3 shows the temperature distribution in the target at different moments of times. The dots indicate the width of the heat front at half the maximum temperature. In the non-blow-up regime (Fig. 3a) a constant expansion of the heated region occurs. In the blow-up regime (Fig. 3b) the heated area first increases and then decreases.

a)   б)
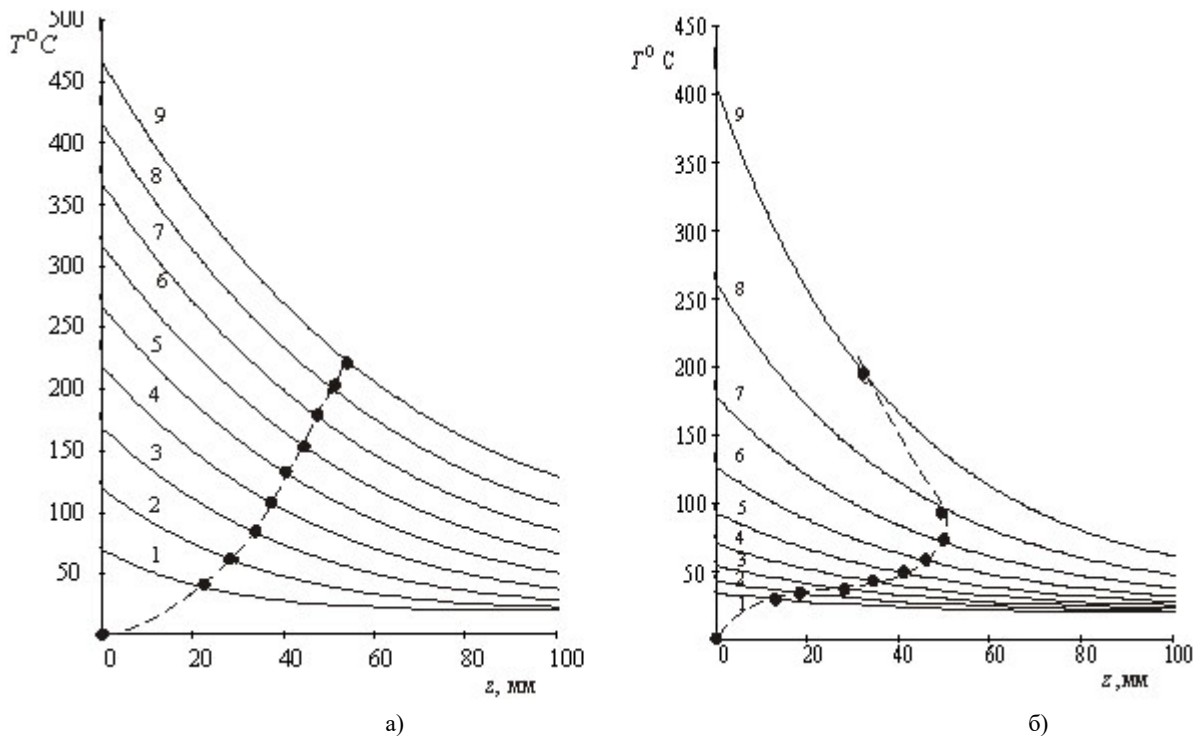
Figure 3. Heat propagation in the target (calculation)
a) in the non-blow-up regime , b) in the blow-up regime
$1 - t = 10$ s, $2 - t = 20$ s, $3 - t = 30$ s, $4 - t = 40$ s, $5 - t = 50$ s,
$6 - t = 60$ s, $7 - t = 70$ s, $8 - t = 80$ s, $9 - t = 90$ s.

EXPERIMENT
In the experiment, the target was heated by passing the electric current through the heater located at the end of the rod. The current varied in time, so that the temperature changed according to the law in the non-blow-up regime (11), and in the blow-up regime (12). The heating duration was 90 s.

Fig. 4 presents the results of the experiment, i.e. the measurements of the temperature distribution in the target.

a)   б)
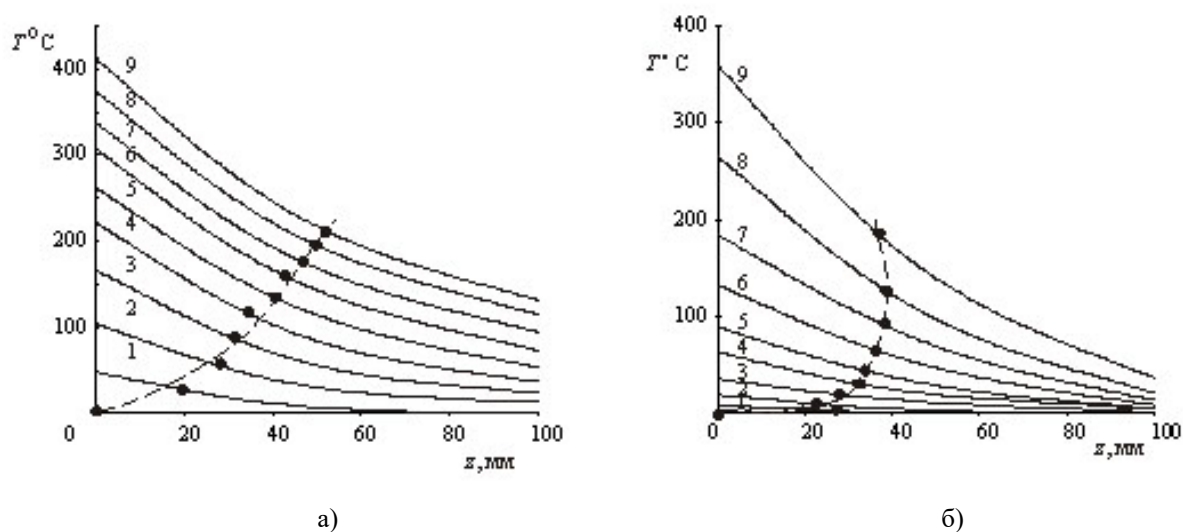
Figure 4. Heat propagation in the target (experiment)

a) in the non-blow-up regime, b) in the blow-up regime
$1 – t = 10$ s, $2 – t = 20$ s, $3 – t = 30$ s, $4 – t = 40$ s, $5 - t = 50$ s,
$6 - t = 60$ s, $7 - t = 70$ s, $8 – t = 80$ s, $9 - t = 90$ s.

The results of the experiment agree with those of the calculations. In the non-blow-up regime, the heat front moves along the rod, and the size of the heated region reaches the coordinate $z = 50$ mm. In the blow-up regime, the heat front reaches the coordinate $z = 40$ mm and then moves in the opposite direction.

The maximum heating temperature in both cases is approximately the same (350° - 400°), but the energy input in the blow-up regime is about 2 times lower than that in the non-blow-up regime.

CONCLUSION

1. The existence of the effect of heat metastable localization in blow-up regimes, predicted by A. A. Samarskii and S. Kurdyumov (Keldysh Institute of Applied Mathematics, RAS, Moscow, Russia), has been experimentally proved.

2. The maximum heating temperatures of the body in both regimes are approximately the same – about 400° C. But in the blow-up regime the energy input into the body is lower than that in the non-blow-up regime. This is due to the smaller size of the heated area. Thus, the way of strong local heating of the target at a lower input energy is shown. After the end of the process, the size of the heated area increases. But the maximum heating temperature at any point of the medium in the case of the blow-up regime is lower than that in the non-blow-up regime, since the input energy is lower.

3. The effect can be used, when strong local heating of a certain area of the body is required, while the adjacent areas are not to get very hot.

4. The investigations were carried out within the framework of the research work "Energy interaction of electromagnetic radiation with thin conducting fibres", state registration number 0119U002531, at the Department of Quantum Radiophysics of V.N. Karazin Kharkiv National University with participation of the Department of Biophysics and Information Technologies of the National University of Pharmacy.

ORCID IDs
Nikolay G. Kokodii, https://orcid.org/0000-0003-1325-4563; **Stanislav V. Pogorelov,** https://orcid.org/0000-0002-0189-8655

REFERENCES
[1] S.P. Kapitza, S.P. Kurdyumov, G.G. Malinetskiy, *Синергетика и прогнозы будущего* [*Synergetics and Forecasts of the Future*], (Nauka, Moscow, 2003), pp. 288. (in Russian)
[2] S.P. Kapitza, in: *World population growth as a scaling phenomenon and the population explosion. Climate change and energy policy*, edited by L. Rosen, and R. Glasser. (AIP, New York, 1992), pp. 241-248.
[3] S.P. Kapitza, World population growth. A world at the crossroads: new conflicts, new solutions, edited by J. Rotblat. (World Scientific, Singapore, 1994), pp. 198-217, https://doi.org/10.1142/9789814327008_0024.
[4] A.A. Samarsky, N.V. Zmitrenko, S.P. Kurdyumov, and A.P. Mikhailov, Доклады Академии Наук СССР [Reports of the USSR Academy of Sciences]. **233**(6), 1344-1347 (1975), http://www.mathnet.ru/links/0c91838b716a90926704d734c046bb31/dan39241.pdf. (in Russian)
[5] S.P. Kurdyumov, *Режимы с обострением* [*Peaking modes*]. (Физматлит, Москва, 2006), pp. 238. (in Russian)
[6] V.A. Kovalev, Сложные системы [Complex systems], **60**(3), 50 (2015), pp. 50. (in Russian)

[7] N.V. Zmitrenko, S.P. Kurdyumov, A.P. Mikhailov, and A.A. Samarskiy, Метастабильная локализация тепла в средах с нелинейной теплопроводностью и условия ее проявления в эксперименте [Metastable localization of heat in media with nonlinear heat conductivity and conditions for its manifestation in experiment], Preprint IPM AH SSSR, **103**, 103 (1977), (in Russian)

[8] V.A. Galaktionov, S.P. Kurdyumov, A.P. Mikhailov, and A.A. Samarskii, Действие граничных режимов с обострением на среду с постоянной теплопроводностью [Action of boundary regimes with sharpening on a medium with constant thermal conductivity], Preprint IPM AH SSSR, **28**, 76 (1979), (in Russian)

[9] E.N. Knyazeva, and S.P. Kurdyumov, *Основания синергетики. Режимы с обострением, самоорганизация, темпомиры* [*Foundations of Synergetics. Regimes with aggravation, self-organization, tempomir*], (Altateya, Sankt Petersburg, 2003), pp. 402. (in Russian)

[10] S.S. Katsnelson, A.M. Orishich, and G.A. Pozdnyakov, Прикладная механика и техническая физика [Applied Mechanics and Technical Physics], **44**(5), 23-29 (2003). (in Russian)

[11] A. Zimmers, L. Aigouy, M. Mortier, A. Sharoni, S. Wang, K.G. West, J.G. Ramirez, and I.K. Schuller, Phys. Rev. Lett. **110**, 056601 (2013), https://doi.org/10.1103/PhysRevLett.110.056601.

[12] J.G. Ramirez, R. Schmidt, A. Sharoni, M.E. Gomez, I.K. Schuller, and E.J. Patino, Appl. Phys. Lett. **102**, 063110 (2013), https://doi.org/10.1063/1.4792052.

[13] J. del Valle, Y. Kalcheim, J. Trastoy, A. Charnukha, D.N. Basov, and I.K. Schuller, Phys. Rev. Appl. **8**, 054041 (2017), https://doi.org/10.1103/PhysRevApplied.8.054041.

[14] A.L. Rakhmanov, V.S. Vysotsky, and N.V. Zmitrenko, IEEE Trans. Appl. Supercond. **13**, 1942-1945 (2003), https://doi.org/10.1109/TASC.2003.812971.

[15] V. Vysotsky, A. Rakhmanov, and N. Zmitrenko, Thermal stability of Bi-2223 wires, in *Research, Fabrication and Applications of Bi-2223 HTS Wires,* World Scientific Series in Applications of Superconductivity and Related Phenomena Vol. 1 (World Scientific, Singapore, 2015), pp. 105-122.

[16] V.I. Polozov, S.S. Maklakov, A.L. Rakhmanov, S.A. Maklakov, and V.N. Kisel, Phys. Rev. B, **101**, 214310 (2020), https://doi.org/10.1103/PhysRevB.101.214310.

[17] A. Misnar, *Теплопроводность твердых тел, жидкостей, газов и их композиций* [*Thermal conductivity of solids, liquids, gases and their compositions*]. (Mir, Moscow, 1968). pp. 464. (in Russian)

[18] I.K. Kikoin, editor, *Таблицы физических величин. Справочник* [*Tables of physical quantities. Handbook*]. (Atomizdat, Moscow, Москва, 1976). pp. 1008. (in Russian)

[19] A.V. Lykov, *Теория теплопроводности* [*Heat conduction theory*]. (Vysshchsya Shkola, Moscow, 1966). с. 600. (in Russian)

ЛОКАЛІЗАЦІЯ ТЕПЛА В СЕРЕДОВИЩІ В РЕЖИМІ З ЗАГОСТРЕННЯМ

М.Г. Кокодій[a,b], С.В. Погорєлов[b]
[a]Харківський національний університет імені В.Н. Каразіна, Харків, Україна
[b]Національний фармацевтичний університет, Харків, Україна

Експериментально доведено існування ефекту метастабільної локалізації тепла в середовищі в режимі нагрівання з загостренням. Це режим, при якому густина енергії нагрівання за кінечий проміжок часу росте до нескінченності. Раніше теоретичні дослідження показали, що при цьому можуть створюватись області, температура всередині яких зростає, а розмір залишається постійним або зменшується з часом (області локалізації тепла). Області існують, доки відбувається надходження енергії ззовні. Створена установка для експериментального вивчення теплових режимів з загостренням в твердому тілі. Об'єктом дослідження був алюмінієвий стрижень з нагрівачем на торці. Температура торця стрижня могла змінюватися за заданим законом. Розподіл температури вздовж стрижня вимірювався термопарами. Проведена калібровка установки. Визначена чутливість термопар. Оцінена інерційність процесу нагрівання і охолодження. Зроблено математичний опис теплових процесів, які протікають при проведенні експерименту. Розв'язане нелінійне рівняння теплопровідності для стрижня з урахуванням теплообміну з навколишнім середовищем конвекцією і випромінюванням. Визначено тепловий режим на границі, необхідний для створення теплових структур. Проведені вимірювання розподілу температури в стрижні в режимах з загостренням і без загострення. У режимі з загостренням тепловий фронт (координата точки з температурою, в два рази меншою максимальної температури) спочатку поширюється в сторону від місця нагрівання, а потім починає рухатися у зворотний бік, і розмір нагрітої області зменшується. У режимі без загострення розмір нагрітої області весь час збільшується. Ефект передбачалося використовувати в установках для здійснення термоядерного синтезу при нагріванні мішені імпульсами лазерного випромінювання спеціальної форми. Ефект також може бути використаний для локального нагрівання при різанні і зварюванні, коли сусідні області не повинні сильно нагріватися, і інших подібих випадках.

КЛЮЧОВІ СЛОВА: нагрівання, режим із загостренням, теплові структури, експеримент

ЛОКАЛИЗАЦИЯ ТЕПЛА В СРЕДЕ В РЕЖИМЕ С ОБОСТРЕНИЕМ

Н.Г. Кокодий[a,b], С.В. Погорелов[b]
[a]Харьковский национальный университет имени В.Н. Каразина, Харьков, Украина
[b]Национальный фармацевтический университет, Харьков, Украина

Экспериментально доказано существование эффекта метастабильной локализации тепла в среде в режиме нагрева с обострением. Это режим, при котором мощность энергии нагрева в течение конечного промежутка времени стремится к бесконечности. Ранее теоретические исследования показали, что при этом могут возникать области, внутри которых температура растет, а размер областей остается постоянным или уменьшается с течением времени (области локализации тепла). Области существуют, пока происходит поступление энергии извне. Создана установка для экспериментального изучения тепловых режимов с обострением в твердом теле. Объектом исследования был алюминиевый стержень с нагревателем на торце. Распределение температуры вдоль стержня измерялось термопарами. Температура торца стержня могла меняться по заданному закону. Проведена калибровка установки. Определена чувствительность термопар. Оценена

инерционность процесса нагрева и остывания. Сделано математическое описание тепловых процессов, протекающих при проведении эксперимента. Решено нелинейное уравнение теплопроводности для стержня с учетом теплообмена с окружающей средой конвекцией и излучением. Определен тепловой режим на границе, необходимый для создания тепловых структур. Проведены измерения распределения температуры в стержне в режимах с обострением и без обострения. В режиме с обострением тепловой фронт (координата точки с температурой, равной половине максимальной температуры) вначале двигается от источника тепла, а затем в обратную сторону, и размер нагреваемой области уменьшается. В режиме без обострения размер нагретой области все время увеличивается. Предсказанный эффект предполагалось использовать в установках для термоядерного синтеза при нагреве мишени импульсами лазерного излучения специальной формы. Эффект может быть также использован для локального нагрева при резании и сварке, когда соседние области не должны сильно нагреваться, и в других подобных случаях.
КЛЮЧЕВЫЕ СЛОВА: нагрев, режим с обострением, тепловые структуры, эксперимент

QUANTUM PHYSICS BASED ANALYTICAL MODELING OF DRAIN CURRENT OF SINGLE ELECTRON TRANSISTOR WITH ISLAND MADE OF ZIGZAG-TUNGSTEN DISULFIDE NANORIBBON

Milan K. Bera

Assistant Professor, Department of Physics, Maharishi Markandeshwar (Deemed to be University)
Mullana, Ambala, Haryana, India
Corresponding Author: m.k.bera@mmumullana.org

Among many emerging nanoelectronic devices, single-electron transistor (SET) is one of the frontier device architectures that can offer high operating speed at an ultra-low power consumption. It exploits controlled electron tunneling to amplify current and retains its scalability even on an atomic scale. A new island based SET device architecture is proposed which is made of monolayer tungsten disulfide nanoribbon (WS_2 NR) in zigzag pattern. The quantum physics based analytical model is developed in order to investigate the tunneling drain current flowing through the proposed WS_2 NR SET. It has been observed from the simulation study that the device current did not struggle in the coulomb blockade region whereas outside this region drain current value gradually decreases for longer nanoribbon likely due to formation of wider potential well in the island regime which helps to drop the rate of tunneling electrons.
KEYWORDS: Coulomb blockade, Nanoribbon, Single electron transistor, Tungsten Disulfide, Tunneling current

In digital integrated circuits, transistors operate in switching mode to change the desired logic voltage levels either 0 or 1. Downscaling of individual device size has been the driving force for improving the performance of ultra-large-scale integrated circuits (ULSIs) [1-2]. In this regard, Metal-oxides semiconductor field-effect transistors (MOSFETs) have been the most successful electronic devices for ULSI application. However, MOSFETs are now facing serious challenges to continue downscaling owing to its fundamental physical limitations in the deep-submicron regime. In this respect, single-electron transistors (SETs) are promising as emerging nanoscaled devices since these devices are scalable even on an atomic scale. Meanwhile, SET are able to control individual movement of electron. Therefore, if SETs are implemented in ULSI design, it will have the attributes of extremely high integration and low power consumption [2].

SET demonstrates unique switching characteristics utilizing quantum mechanically governed coulomb blockade and single electron tunneling phenomena mediated via island regime [3-5]. Furthermore, room temperature operation is the key for practical implementation of SET in ULSI. Although, the first experimentally demonstrated SET in 1987 was operable only at ultra-low temperature ranges (1.1-4.2 K), however, it was improved later on for room temperature operation by adopting silicon as island [6-7]. As soon as it was realized that the band structure and electrical properties of the island materials are the key for room-temperature operation, SET made of new island materials such as two-dimensional (2D) graphene have been demonstrated recently [8].

In this context, lower dimensional semiconductors particularly transition metal dichalcogenides (TMDs), as for example, MoS_2, $MoSe_2$, WSe_2, WS_2, WS_2 *etc.* possess additional benefits due to atomically smooth and dangling-bond free surface, charge carrier scattering or even thickness (hence bandgap) variation, thus, guarantees robust device performances at room temperature [9-10].

Therefore, in this study, a new island material made of monolayer tungsten disulfide (WS_2) nanoribbon in zigzag pattern is proposed in SET design. Quantum physics based analytical modelling of tunneling current has been developed in order to accurately predict the electrical performances of SET at room temperature via numerical simulations coded in Matlab and Mathematica.

MODELING AND SIMULATION OF SINGLE ELECTRON TRANSISTOR WITH ISLAND MADE OF MONOLAYER WS₂-NANORIBBON
Fundamentals of SET operation with island

Single-electron transistor is governed by quantum mechanical tunneling effect. A single electron transistor is simply constructed with an island sandwiched between two tunneling junctions formed at source and drain side. It is also connected through a capacitor into the gate electrode as shown in Figure 1a below. SET can also be seen as a confined box that has two separate junctions for the entrance and exit of a single electron. Now, according to the fundamentals of quantum mechanics, the electrical conduction of any tunnel junction purely depends on how effectively the barrier transmits the electronic waves. The electric current flow decreases exponentially with the barrier thickness.

As soon as an electron tunnels through the junction, the tunnel capacitance is charged with a single electronic charge and as a result tiny amount of potential is built up. This additional potential might be sufficient to prevent another electron to tunnel through the junction. In this scenario, the resistance of the tunnel junction rises consistently, thereby coulomb blockade condition arises which ultimately stops the flowing of current. When external bias is applied, the coulomb blockade situation overcomes then electrons resume tunneling one by one from source to the island, hence, adding excess

electrons to the island (see Figure 1b). A similar tunneling process will also occur from the island to the drain. Eventually, single electron transistor monitors the flow of electronic charge between source and drain with the assistance of gate electrode.
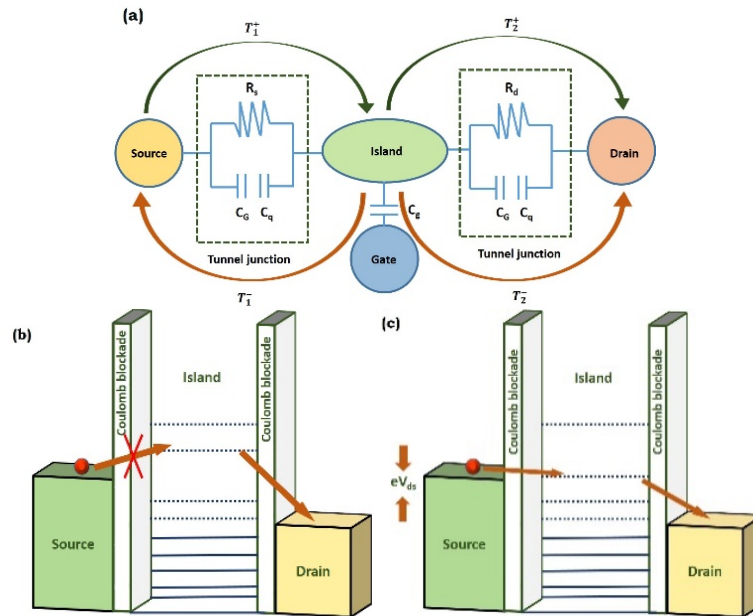
Figure 1. Schematic structure with equivalent circuit of single electron transistor, (b) Coulomb-blockade condition with zero current, (c) adequate drain-source bias voltage will assist to transfer of an electron across the barrier.

Basic structure of zigzag-WS₂-nanoribbon

Monolayer WS_2 nanoribbon can be patterned into two different forms, one in armchair and other in zig-zag shape. Zig-zag patterned WS_2 nanoribbon is composed of an inner layer of W metal atoms orderly positioned in triangular lattice. It is sandwiched between two layers of chalcogen sulfide (S) atoms positioned on the triangular lattice of interchanging hollow sites in a triangular prismatic style [11].
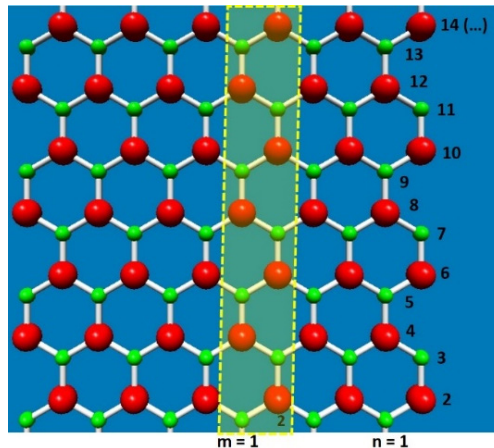
Figure 2. Top view of lattice structure of monolayer WS_2 in zig-zag pattern. Red and green spheres denote the metal (W) and chalcogenide (S) atoms, respectively. The shaded area indicates the unit cell in zig-zag pattern. The position of lattice sites are demarcated by coordinates (m, n).

The S-W-S layers are bonded by weak van der Waals forces. A schematic is shown in Figure 2. The unit cell described as (m, n) indices is illustrated by shaded rectangular area.

Modeling of tunneling current flowing through the proposed WS₂ NR SET

As per discussion in earlier section, a single electron transistor is made of source, gate, and drain electrodes along with an island which is located between source and drain but is not actually connected to them. It is shown schematically in Figure 3. The basic operation of SET is controlled by quantum tunneling of electrons to amplify the current values. As depicted in Figure 3, SET can be divided into three regions, corresponding to source, island and drain parts. The energy as a function of position alongside SET is also demonstrated. The proposed WS_2 NR island of length L can be assumed as a quantum well whose potential profile along the island is shown in Figure 3.

Now, following the fundamentals of quantum mechanics in solving Schrödinger equations, the electronic wave functions in various regions can be established as follows [03, 12]:

$$Reg - I: \psi_I = Ae^{k_I x} + Be^{-k_I x} \text{ but } \psi_I^* \psi_I \to 0 \text{ when } x \to -\infty, hence, B = 0 \tag{1}$$

$$Reg - II: \psi_{II} = Ce^{ik_{II}x} + De^{-ik_{II}x} \tag{2}$$

$$Reg - III: \psi_{III} = Ee^{k_{III}x} + Fe^{-k_{III}x} \text{ but } \psi_{III}^* \psi_{III} \to 0 \text{ when } x \to +\infty, hence, \varepsilon = 0 \tag{3}$$

where $k_I = k_{III} = \frac{\sqrt{2m_e^*\varepsilon}}{\hbar}$ and $k_{II} = \frac{\sqrt{2m_e^*(v_0-\varepsilon)}}{\hbar}$, $\varepsilon \,(<0)$ is the energy of electron, v_0 is potential well m_e^* is the effective mass of WS$_2$ NR, $\hbar$ is the reduced Planck's constant. The negative value indicates bound electronic energy states.
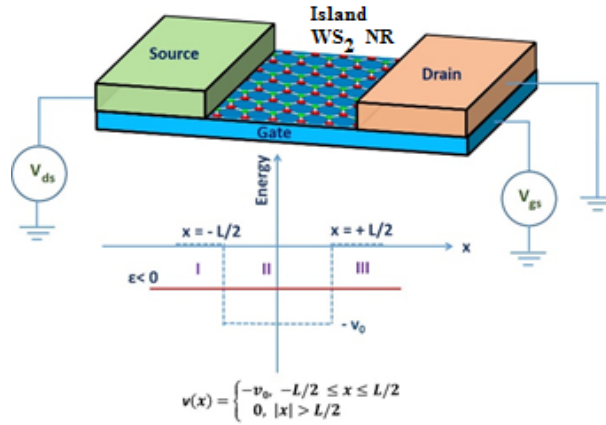
Figure 3. Schematic of proposed single electron transistor with island made of WS$_2$ nanoribbon. The biasing points at different electrodes as well as potential profile along the device are also shown.

Now, as per boundary conditions, the wave functions and its first derivatives must be continuous for the neighbouring regions at x = -L/2 and x = +L/2. Therefore, applying boundary conditions the above equations becomes:

$$Ae^{\frac{-k_I L}{2}} = Ce^{-\frac{ik_{II}L}{2}} + De^{\frac{ik_{II}L}{2}} \text{ at } x = -L/2, \ \psi_I = \psi_{II} \tag{4}$$

$$Ak_I e^{\frac{-k_I L}{2}} = Cik_{II}e^{-\frac{ik_{II}L}{2}} - Dik_{II}e^{\frac{ik_{II}L}{2}} \text{ at } x = -L/2, \ \frac{d\psi_I}{dx} = \frac{d\psi_{II}}{dx} \tag{5}$$

$$Ce^{\frac{ik_{II}L}{2}} + De^{\frac{-ik_{II}L}{2}} = Fe^{\frac{-k_{III}L}{2}} \text{ at } x = +L/2, \ \psi_{II} = \psi_{III} \tag{6}$$

$$Cik_{II}e^{\frac{ik_{II}L}{2}} - Dik_{II}e^{\frac{-ik_{II}L}{2}} = -Fk_{III}e^{\frac{-k_{III}L}{2}} \text{ at } x = +L/2, \ \frac{d\psi_{II}}{dx} = \frac{d\psi_{III}}{dx} \tag{7}$$

Next, the electron transmission coefficients in WS$_2$ NR SET can be calculated as follows:

$$T_{QWSNR}(\varepsilon) = \frac{(1+k_I^2)^2 k_{II}^2}{(\cos(Lk_{II})(-1+k_I^2)k_{II} - \sin(Lk_{II})k_I(1+k_{II}^2))^2} \tag{8}$$

The calculation details of the aforementioned equations can be found from Appendix.

Finally, the quantum current flowing through WS$_2$ NR SET can be easily estimated using Landauer formulae [03] as:

$$I_{QWSNR} = \frac{2e}{\hbar} \int \rho(n) T_{QWSNR}(\varepsilon)(f_{S \to D}(\varepsilon) - f_{D \to S}(\varepsilon)) d\varepsilon \tag{9}$$

where e is the electronic charge, $\rho(n)$ is the electron density, $f(E) = \frac{1}{\left(1+e^{\frac{(\varepsilon-\varepsilon_f)}{k_B T}}\right)}$ is the Fermi-Dirac distribution function, ε_f is the Fermi energy level, k_B is the Boltzmann constant and T is the temperature.

RESULTS AND DISCUSSION

The electrical characteristics of proposed WS$_2$ NR SET related to variation in nanoribbon length have been investigated. The simulation results are shown in Figure 4.

It is noteworthy that changes in WS$_2$ nanoribbon length does not have significant influences in the coulomb blockade region (*i.e.* nearby zero voltage). It can be farther evident from Figure 5 as the current value near zero bias does not struggle rather increases almost linearly. However, it has a direct impact on the SET current values particularly for applied bias (V_{ds}) outside the coulomb blockade regime. Meanwhile, the drain current, I_{ds} reduces moderately when nanoribbon lengths are varied from ~0.546 nm to ~2.002 nm. The physical phenomena of these behaviours could be interpreted as a consequence of formation of longer potential well in the island owing to increase in nanoribbon length.

Because of wider potential well formation between source-drain, the tunneling of electrons decreases, hence, the value of current drops significantly. The influence of operating temperatures on SET current flow have also been investigated. The temperature variation in I_{ds} *vs.* V_{ds} characteristics of WS$_2$ NR SET is shown in Figure 6. It can be easily seen from the figure that as temperature rises the tunneling current value increases mainly due to temperature dependent electron occupancy as per Fermi-Dirac distribution such that more electrons are available for tunneling. In addition, carrier freez-out effect may also affect the flow of current at lower temperature particularly at 4K [13].
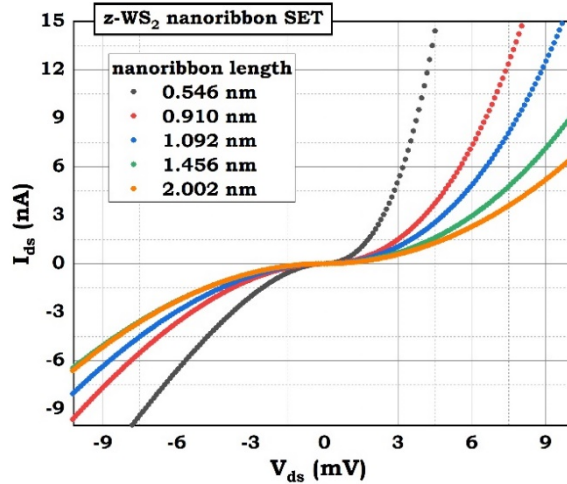
Figure 4. The simulated output characteristics (I_{ds} vs V_{ds}) of proposed zigzag-WS$_2$ NR SET with various nanoribbon length but keeping gate voltage constant at 1 mV.
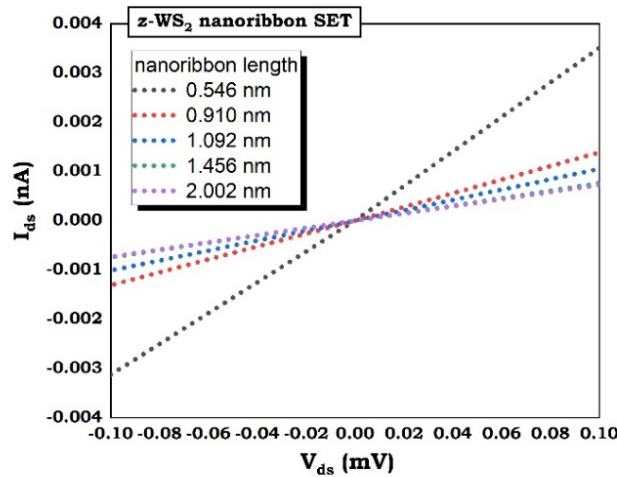
Figure 5. The simulated I_{ds} vs V_{ds} characteristics of zigzag-WS$_2$ NR SET with varying island length but keeping gate voltage constant at 1 mV.
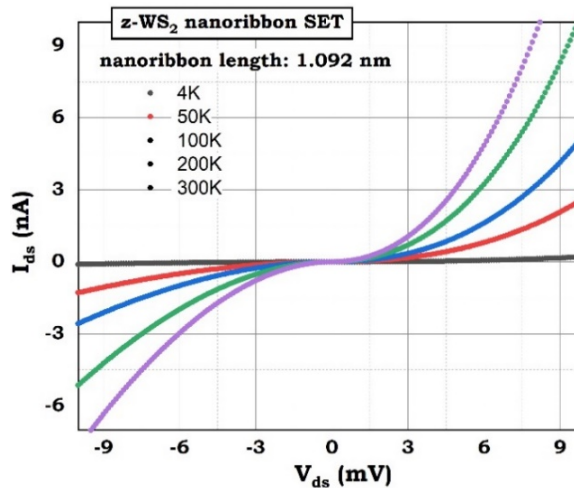
Figure 6. The output characteristics (I_{ds} *vs* V_{ds}) of armchair-WS$_2$ nanoribbon SET at room temperature (300 K) with varying gate voltage in the range of 1-9 mV.

On the other hand, in order to evaluate the gate controllability of the proposed single electron transistor, the simulations were performed on 1.341 nm long zigzag-WS$_2$ nanoribbon with applied gate voltage varies from 1-9 mV as can be seen from Figures 7.

Again, it can be noticed that there is no significant influence of coulomb blockade during applied gate bias, rather normal device characteristics have been observed.
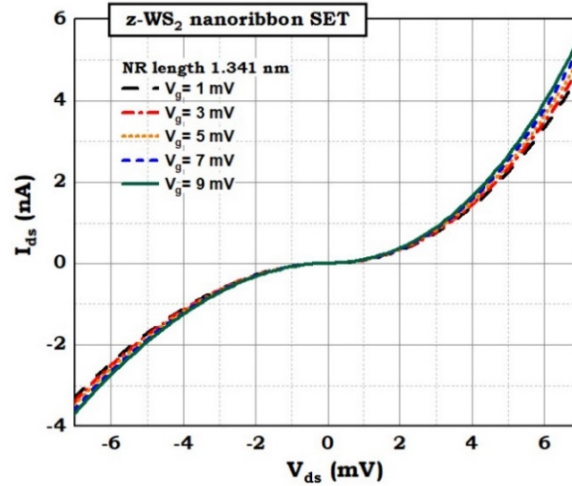
Figure 7. The gate control on the output characteristics (I_{ds} vs V_{ds}) of single electron transistor with WS$_2$ nanoribbon in zigzag pattern is shown.

CONCLUSIONS

In the present study, a new island material based on monolayer tungsten disulphide (WS$_2$) nanoribbon is proposed to design single electron transistor. Quantum physics based analytical model is developed to simulate the quantum current behaviour of proposed single electron transistor at room temperature. It has been observed that the variation of WS$_2$ nanoribbon length either does not have any significant influence on the coulomb blockade region. Instead, the values of SET current decreases slowly just outside of the coulomb blockade region presumably due to formation of longer potential well in the island, whereby deteriorating the rate of electron tunneling. In addition, variation in operating temperature from 4-300 K drastically improve the tunneling current mainly due to increase in electron occupancy so that more electrons can tunnel through. On the other hand, the gate controllability have also been investigated which exhibits reasonable device performances at room temperature without any trouble of coulomb blockade. Therefore, the proposed single electron transistor utilizing WS$_2$ nanoribbon in zigzag pattern as an island material might be potentially useful by embedding and integrating into advanced ULSI circuit design.

APPENDICES
Solution of Schrödinger equations with boundary conditions

Applying fundamentals of quantum mechanics, Schrödinger equations in all the regions of WS$_2$ NR SET can be established as follows [12]:

$$Reg-I: = \frac{-\hbar^2}{2m_e^*}\frac{d^2\psi_I}{dx^2} = \varepsilon\psi_I \ (where \ \varepsilon < 0 \ \& \ v(x) = 0) \tag{1}$$

$$Reg-II: = \frac{-\hbar^2}{2m_e^*}\frac{d^2\psi_{II}}{dx^2} + v(x)\psi_{II} = E\psi_{II} \ (where \ \varepsilon < 0 \ \& \ v(x) = -v_0) \tag{2}$$

$$Reg-III: = \frac{-\hbar^2}{2m_e^*}\frac{d^2\psi_{III}}{dx^2} = E\psi_{III} \ (where \ \varepsilon < 0 \ \& \ v(x) = 0) \tag{3}$$

The general solution of Schrödinger equation established in region-I (*i.e.* source side of SET) can be obtained as follows:

$$Reg-I: \psi_I = Ae^{k_Ix} + Be^{-k_Ix} \tag{4}$$

But according to basic postulates in quantum mechanics, the wave functions must be finite, continuous and single valued to form a wave packet, however, when $x \to -\infty$, $\psi_I^*\psi_I \to \infty$ that is the probability of finding the electron will be infinity, therefore, in order to have finite probability, $\psi_I^*\psi_I \to 0$ at $x \to -\infty$, which requires to set B = 0. Meanwhile, at region-II, (*i.e.* island side of SET), the solution becomes:

$$Reg-II: \psi_{II} = Ce^{ik_{II}x} + De^{-ik_{II}x} \tag{5}$$

Similarly, at region-III (*i.e.* drain side of SET), the solution of the Schrödinger equation can be easily obtained as follows:

$$Reg - III: \psi_{III} = Ee^{k_{III}x} + Fe^{-k_{IIi}x} \tag{6}$$

Again, $\psi_{III}^* \psi_{III} \to +\infty$ *when* $x \to +\infty$, hence, in order to have a finite probability of finding electrons in region-III, F must be zero. In the above equations, $k_I = k_{III} = \frac{\sqrt{2m_e^* \varepsilon}}{\hbar}$ *and* $k_{II} = \frac{\sqrt{2m_e^*(v_0 - \varepsilon)}}{\hbar}$, where ε (< 0) is the energy of electron, v_0 is potential well m_e^* is the effective mass of WS$_2$ NR, $\hbar = \frac{h}{2\pi}$ is the reduced Planck's constant.

Nevertheless, the wave functions must be continuous for any quantum mechanical system, thus, boundary conditions play important roles to unite the otherwise separated waves at the boundary region. Following boundary conditions, the wave functions and its first order derivatives must be continuous at the boundary of the neighbouring region which yields following equations:

$$Ae^{-k_I L/2} = Ce^{-ik_{II}L/2} + De^{ik_{II}L/2} \ (at \ x = -L/2, \ \psi_I = \psi_{II}) \tag{7}$$

$$Ak_1 e^{-k_I L/2} = Cik_{II}e^{-ik_{II}L/2} - Dik_{II}e^{ik_{II}L/2} \ (at \ x = -L/2, \ \tfrac{d\psi_I}{dx} = \tfrac{d\psi_{II}}{dx}) \tag{8}$$

$$Ce^{ik_{II}L/2} + De^{-ik_{II}L/2} = Fe^{-k_{III}L/2} \ (at \ x = +L/2, \ \psi_{II} = \psi_{III}) \tag{9}$$

$$Cik_{II}e^{ik_{II}L/2} - Dik_{II}e^{\frac{-ik_{II}L}{2}} = -Fk_{III}e^{\frac{-k_{III}L}{2}} \ (at \ x = +L/2, \ \tfrac{d\psi_{II}}{dx} = \tfrac{d\psi_{III}}{dx}) \tag{10}$$

Calculation of transmission coefficient

Now, the coefficients of the abovementioned equations from 7-10 can be obtained utilizing transfer matrix method [3,12]. From the x = -L/2 boundary condition, equations 7 & 8 can be written in matrix form as:

$$M_I \begin{pmatrix} A \\ B \end{pmatrix} = M_{II} \begin{pmatrix} C \\ D \end{pmatrix} \tag{11}$$

$$\therefore \begin{pmatrix} A \\ B \end{pmatrix} = M^I \begin{pmatrix} C \\ D \end{pmatrix}, where \ M^I = M_I^{-1} M_{II} \tag{12}$$

where $M_I = \begin{pmatrix} e^{-\frac{Lk_I}{2}} & 0 \\ k_I e^{-\frac{Lk_I}{2}} & 0 \end{pmatrix}$ and $M_{II} = \begin{pmatrix} e^{-\frac{iLk_{II}}{2}} & e^{\frac{iLk_{II}}{2}} \\ ik_{II}e^{-\frac{iLk_{II}}{2}} & -ik_{II}e^{\frac{iLk_{II}}{2}} \end{pmatrix}$ and M_I^{-1} is the inverse of M_I matrix.

In a similar way, continuity of $\psi(x)$ and $\frac{d\psi}{dx}$ at x = +L/2 gives the matrix equation as:

$$M_{III} \begin{pmatrix} C \\ D \end{pmatrix} = M_4 \begin{pmatrix} E \\ F \end{pmatrix} \tag{13}$$

$$\begin{pmatrix} C \\ D \end{pmatrix} = M^{II} \begin{pmatrix} E \\ F \end{pmatrix}, where \ M^{II} = M_{III}^{-1} M_{IV} \tag{14}$$

where $M_{III} = \begin{pmatrix} e^{\frac{iLk_{II}}{2}} & e^{-\frac{iLk_{II}}{2}} \\ ik_{II}e^{\frac{iLk_{II}}{2}} & -ik_{II}e^{-\frac{iLk_{II}}{2}} \end{pmatrix}$ and

$M_{IV} = \begin{pmatrix} 0 & e^{-\frac{Lk_I}{2}} \\ 0 & -k_I e^{-\frac{Lk_I}{2}} \end{pmatrix}$ and M_{III}^{-1} is the inverse of M_{III} matrix.

Combining Eqs. 11 and 13 gives an equation of the form:

$$\begin{pmatrix} A \\ B \end{pmatrix} = M \begin{pmatrix} E \\ F \end{pmatrix}, M = M^I M^{II} \tag{15}$$

where the 2x2 matrix is the product of two matrices of Eqs. 12 and 14. Then, the transmission coefficient can be obtained from the component of transfer matrix (M) as:

$$T_{QWSNR} = \left| \frac{1}{M_{12}} \right|^2 \tag{16}$$

The parameters used for the numerical simulation for WS$_2$ NR are listed in Table.

Table.

Parameters used in the modelling of tunneling current flowing through single electron transistor
with island made of WS$_2$ nanoribbon

Symbol	Parameters	Value [unit]
a	Lattice constant	3.153 (Å)
θ	Angle between W-S bond	0.71 (rad)
$z - m_e^*$	Effective mass of electron (armchair nanoribbon)	0.309 m$_0$ [a)]
$z - m_e^*$	Effective mass of electron (zigzag nanoribbon)	0.412 m$_0$ [a)]
T	Temperature	4-300 K
E$_g$	Band gap	1.55 eV
$\hbar$	Reduced Planck's constant	6.5821×10^{-16} eV.s
k_B	Boltzmann constant	8.6 x10^{-5} eV.K^{-1}

[a)] Electron rest mass

ORCID IDs

Milan K. Bera, https://orcid.org/0000-0002-2996-890X

REFERENCES

[1]   A.Lancaster, and M. Keswani, Integration, **60**, 204 (2018), https://doi.org/10.1016/j.vlsi.2017.09.008.
[2]   J. Gorss, (2018), https://go.nature.com/2Q4fQc5.
[3]   S. Datta, *Quantum Transport: Atom to Transistor* (Cambridge University Press, New York, 2005).
[4]   K. Goser, *Nanoelectronics and Nanosystems-From Transistors to Molecular and Quantum Devices*, (Springer, Berlin, Heidelberg, 2004).
[5]   D. Averin, and K. Likharev, *Mesoscopic phenomena in solids, 1st edn.* (North-Holland, Amsterdam, 1991).
[6]   T.A. Fulton, and G.J. Dolan, Phys. Rev. Lett. **59**, 109 (1987), https://doi.org/10.1103/PhysRevLett.59.109.
[7]   L. Zhung, L. Guo, and S.Y. Chou, Appl. Phys. Lett. **72**, 1205 (1998), https://doi.org/10.1063/1.121014.
[8]   C. Stampfer, E. Schurtenberger. F. Molitor, J. Güttinger, T. Ihn, and K. Ensslin, Nano Letters, **8**, 2378 (2008), https://doi.org/10.1021/nl801225h.
[9]   S. Manzeli, D. Ovchinnikov, D. Pasquier, O. Yazyev, and A. Kis, Nature Reviews Materials, **2**, 17033 (2017), https://doi.org/10.1038/natrevmats.2017.33.
[10] M.K. Bera, R. Kharb, N. Sharma, A.K. Sharma, R. Sehrawat, S.P. Pandey, R. Mittal, and D.K. Tyagi, Journal of Electronic Materials, **48**, 3504 (2019), https://doi.org/10.1007/s11664-019-07058-0.
[11] A.C Dias, F. Qu, D.L. Azevedo, and J. Fu, Phys. Rev. B, **98**, 075202 (2018), https://doi.org/10.1103/PhysRevB.98.075202.
[12] N. Zettili, *Quantum mechanics: concepts and applications. 2nd ed.* (Wiley & Sons, New York, 2009).
[13] S.M. Sze, and K.K. Ng, *Physics of Semiconductor Devices, 3rd ed.* (Wiley & Sons, New York, 2006).

КВАНТОВОМЕХАНІЧНЕ АНАЛІТИЧНЕ МОДЕЛЮВАННЯ СТРУМУ СТОКУ ОДНОЕЛЕКТРОННОГО ТРАНЗИСТОРА З ЗАТВОРОМ ІЗ ЗИГЗАГОПОДІБНОЇ НАНОСТРІЧКИ ДИСУЛЬФІДУ ВОЛЬФРАМУ

Мілан К. Бера
Доцент кафедри фізики Махаріші Маркандешвар (вважається університетом)
Муллана, Амбала, Хар'яна, Індія

Серед багатьох нових наноелектронних пристроїв одноелектронний транзистор (SET) є однією з граничних архітектур пристроїв, яка може запропонувати високу робочу швидкість при наднизькому енергоспоживанні. Він використовує контрольоване електронне тунелювання для посилення струму і зберігає свою масштабованість навіть в атомному масштабі. Запропоновано нову архітектуру пристрою SET на основі затвору, який виконаний з одношарової зигзагоподібної наностічки дисульфіду вольфраму (WS$_2$ NR). Аналітична модель, заснована на квантовомеханічному підході, розроблена для дослідження тунельного току стоку, що протікає через запропонований WS$_2$ NR SET. Із симуляційного дослідження було помічено, що струм пристрою не протікає у області кулонівської блокади, тоді як за межами цієї області значення струму стоку поступово зменшується для довших наностічок, ймовірно, через формування ширшого потенційного каналу у режимі затвору, що допомагає знизити швидкість тунельних електронів.

КЛЮЧОВІ СЛОВА: кулонівська блокада, наностічка, одноелектронний транзистор, дисульфід вольфраму, тунельний струм

КВАНТОВОМЕХАНИЧЕСКОЕ АНАЛИТИЧЕСКОЕ МОДЕЛИРОВАНИЕ ТОКА СТОКА ОДНОЭЛЕКТРОННОГО ТРАНЗИСТОРА С ЗАТВОРОМ ИЗ ЗИГЗАГООБРАЗНОЙ НАНОЛЕНТЫ ДИСУЛЬФИДА ВОЛЬФРАМА

Милан К. Бэра
Доцент кафедры физики Махариши Маркандешвар (считается университетом)
Муллана, Амбала, Харьяна, Индия

Среди многих новых наноэлектронных устройств одноэлектронный транзистор (SET) является одной из предельных архитектур устройств, которая может предложить высокую рабочую скорость при сверхнизком энергопотреблении. Он использует контролируемое электронное туннелирование для усиления тока и сохраняет свою масштабируемость даже в атомном масштабе. Предложена новая архитектура устройства SET на основе затвора, который выполнен из однослойной зигзагообразной наноленты дисульфида вольфрама (WS$_2$ NR). Аналитическая модель, основанная на квантово-механическом подходе, разработанная для исследования туннельного тока стока, протекающего через предложенный WS$_2$ NR SET. В модельных исследования было замечено, что ток устройства не протекает в области кулоновской блокады, тогда как за пределами этой области значение тока стока постепенно уменьшается для длинных нанолент, вероятно, через формирование более широкого потенциального канала в режиме затвора, что помогает снизить скорость туннельных электронов.

КЛЮЧЕВЫЕ СЛОВА: кулоновская блокада, нанолента, одноэлектронный транзистор, дисульфид вольфрама, туннельный ток

GAS-FILLED GAMMA-RADIATION DETECTOR BASED ON HIGH-PURITY XENON

Sergey Sokolov*, **Aleksey Pudov,** **Alexander Rybka,** **Vladimir Kutny,**
Alexander Abyzov, **Gennadiy Kholomyeyev,** **Serhii Melnikov**

National Scientific Center "Kharkiv Institute of Physics and Technology", Kharkiv, Ukraine
*Corresponding Author: sokolov@kipt.kharkov.ua
Received August 30, 2020; revised October 13, 2020; accepted October 15, 2020

This paper reports on the development, manufacturing and testing of proportional γ-ray detectors filled with gas mixtures based on high-purity xenon. To let the gas mixtures into the detector, a special installation was developed and manufactured, consisting of components designed to work with high-purity gases. The influence of the gas pressure, its composition (pure Xe or its mixture with H_2, CH_4), and the voltage at the anode on the spectrometric resolution and gas gain of the detectors was studied. The addition of H_2 or CH_4 to xenon is used to increase the charge carrier drift velocity. These additives also stabilize the gas mixture, i. e. decrease the probability of gas breakdown at high voltage between the detector electrodes. Gas xenon, as well as its mixtures, of research purity grade (99.9999%) have been used. Proportional γ-ray detectors based on xenon gas can operate in both counting and spectrometric modes. To study the characteristics of the detectors, we used standard sources of γ-radiation ^{241}Am, ^{137}Cs, ^{152}Eu, ^{133}Ba. The best energy resolution values to date were obtained for a detector filled with a gas mixture of Xe + 2.1% CH_4 at a pressure of 2.5 bar and an anode voltage of 2500 V; they were ~ 9.5% for an energy of 40 keV and ~ 5% for 120 keV. In the manufacturing of detectors intended for radiation monitoring and identification of radioactive materials, in particular in nuclear power, complex materials science problems have been solved. To increase the thermal and radiation resistance, all elements of the detector construction are made of materials that are weakly activated by ionizing radiation. In addition, the design of the detectors is completely free of glass elements and organic components. The detectors are designed to monitor technological processes and to work as part of radiation monitoring systems, including those at nuclear power plants.
KEY WORDS: detector, gamma radiation, count rate, spectrometry, xenon, gas gain

Gas-filled counters are well known and used to register alpha-, beta-particles, protons, gamma quanta, neutrons in various fields of fundamental and applied research. Proportional gamma-ray counters-spectrometers filled with xenon gas have a number of advantages: a wide range of operating temperatures, high sensitivity, long-term stability, and high radiation resistance. The unique combination of physical properties of xenon gas makes it very attractive as an active medium in radiation detectors: high stopping power, low Fano factor, mechanical and chemical stability, as well as low energy required to create an electron-ion pair. Xenon detectors, in particular, have proven themselves well in astronomical applications in space [1], where they operate in highly aggressive radiation and temperature regimes.

The specificity of using detectors for radiation monitoring and identification of radioactive materials, in particular in nuclear power, requires the solution of rather complex materials science problems: the choice of materials with low activation in intense fluxes of ionizing radiation, including neutrons, the rejection of the use of glass elements, the complete absence of organic components in the design of the detector, the provision of very low (at the picoampere level) leakage currents between the detector electrodes.

This paper presents the first results of a study of the counting and spectrometric characteristics of a proportional gamma radiation detector of a special design filled with pure Xe.

DETECTOR DESIGN

Be, Al, Mg and Ti [2] are the structural elements that are more suitable, in terms of their activation properties, in the manufacture of detectors designed to operate in intense fields of ionizing radiation. Considering the properties of nuclei, it is undesirable to use alloys containing Mn, Co and Ag in the design of detectors. The prevalence of stainless steel in the manufacturing of the detectors is determined by its manufacturability, corrosion and temperature resistance, despite its activation in neutron fluxes. When iron and nickel, the main components of stainless steel, capture a neutron, they form radioactive nuclides with a half-life of more than three years.

For the manufacture of anodes, molybdenum or tungsten is typically used, and tungsten is used for anode tensioning springs. Molybdenum powder and copper solder are the main components used in sintering metal elements with ceramics. Currently, mainly kovar or titanium is used in metal-glass and metal-ceramic insulators.

Fig. 1 shows the schematic of the design of the developed and manufactured detector. The detector body is a seamless thin wall pipe made of 12X18H10T steel (Ø25.5×0.3 mm, length 250 mm). The design includes a coaxial vacuum current feedthrough with a "guard ring" and a high-voltage connector, as well as protective insulators designed to reduce edge effects. The cylindrical design was selected as the one most used, however, there have been studies of alternative designs, i.e. in [3,4], which are potentially interesting.

The disadvantages of metal-glass insulators, which are usually used in gas-discharge counters, are the limited abrupt temperature changes to 45°C and the limited neutron flux density up to 10^7 $cm^{-2}s^{-1}$. In this detector, for the

manufacture of insulators, we used Macor ceramic glass manufactured by Corning Incorporated, USA. This new kind of glass-ceramic can be processed mechanically. The accuracy of machining is determined by the size of the mica crystals, the diameter of which is ~20 μm. The composition of the material is as follows: SiO_2 - 46%, MgO - 17%, Al_2O_3 - 16%, K_2O - 10%, B_2O_3 - 7%, F - 4%. Some mechanical, thermal and electrical properties of the ceramic are given in Table. 1.
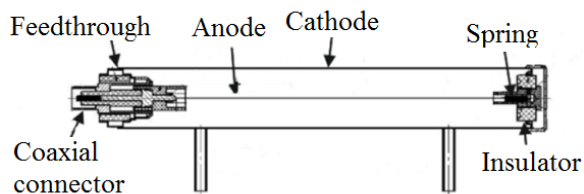
Figure 1. Detector design
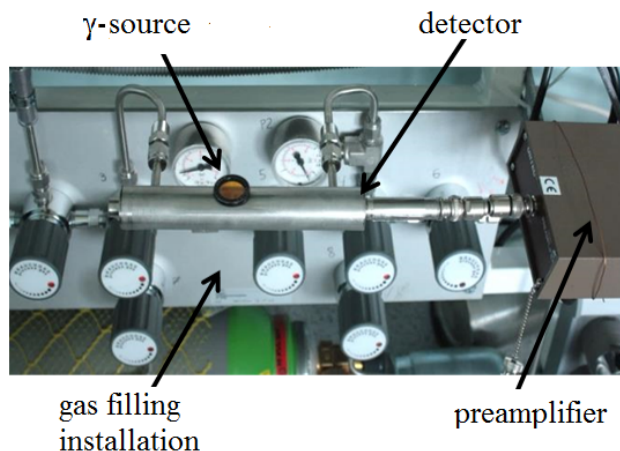
Figure 2. Installation for filling the detector with gas mixtures

Table 1.

Properties of glass-ceramics "MACOR"

Thermal expansion coefficient, 25 - 300ºC	$93 \cdot 10^{-7}/ºC$
Heat conductivity, 25ºC	1.46 Wt/m·ºC
Working temperature	800 ºC
Density	2.52 g/cm^3
Young's modulus, 25ºC	66.9 Gpa
Dielectric strength (for thickness 12 mm and 25°C)	62.4 kV/mm
Bulk resistance, 25°C	$>10^{16}$ Ohm·cm

The anode is a tungsten wire with a diameter of Ø60 μm, tensioned with a spring. Thus, the detector does not contain organic materials or glass.

To ensure the purity of the gas and prevent contaminants' release from the surface of the detector parts, various methods and cleaning technologies were used in the manufacture of all parts, and the detector as a whole. Sandblasting was carried out using aluminum oxide (Al_2O_3) particles with a size of 50 μm. We also used electrochemical polishing of the inner surface of steel pipes, electrochemical cleaning and polishing of thin tungsten wires, and final cleaning of the surface of all elements was carried out with dry ice CO_2. The detector was assembled by using laser welding. At various stages of cleaning and assembly, the control measurements of the resistance of the ceramic elements of the detector at high voltage were carried out.

To fill the detector with pure xenon and its mixtures, an installation was developed and manufactured, which used accessories from Spectron GCS GmbH (Fig. 2). Before filling, the detector, the valves and corresponding connecting tubes were evacuated and the detector was further degassed at an elevated temperature (~110ºC). The detector was filled with pure xenon or its mixture with H_2 (0.25%) or CH_4 (2.1%) to various pressures from 0.5 to 3 bar. These additives to xenon are used to increase the drift velocity of charge carriers [5] in gas, as well as to suppress secondary ionization processes. We used purified xenon gas, as well as purified xenon-hydrogen and xenon-methane gas mixtures of research grade purity (99.9999%). It was estimated that the gas in the detector had no more than 1 ppm contaminants. Table 2 shows the typical composition of impurities, in this case for the $Xe+H_2(0.25\%)$ gas mixture. The $Xe+CH_4(2.1\%)$ mixture has the same total amount of impurities and is assumed to have a similar impurity composition.

The counting and spectrometric characteristics of the detectors were investigated. A voltage bias from 100 to 2700 V was applied to the anode by using an Ortec 659 high-voltage power supply through an RC filter. The measurements were carried out by using an Ortec 142AH preamplifier, a 672 shaper amplifier, and a 927 ADC. The gain value was 100, the time constant of the shaping amplifier was 3 μs. The count rate and amplitude distributions of the detector signal were measured by using standard γ-sources [241]Am, ^{137}Cs, [152]Eu, [133]Ba.

Contaminants' composition in the gas mixture Xe+0.25%H$_2$.

% H$_2$	Contaminants, ppm. (not higher than)								
	Kr	O$_2$	N$_2$	Ar	C$_n$H$_m$	CO+CO$_2$	SF$_6$	S$_2$F$_6$	H$_2$O
0.25	0.1	0.1	0.2	-	0.1	0.1	0.1	0.1	0.1

RESULTS AND DISCUSSION

The dependence of the detector counting rate on the voltage measured for the γ-source ^{241}Am at different pressures of pure Xe or the xenon mixture Xe + 2.1% CH$_4$ is shown in Fig. 3. For all gas pressures in the detector, the counting rate of the detector begins to increase sharply when the voltage applied to the anode is above a certain threshold value. This threshold voltage shifts to higher values with increasing pressure in the detector. Thus, in practice, at higher pressure, a higher detector sensitivity is achieved, but higher voltage values are required.
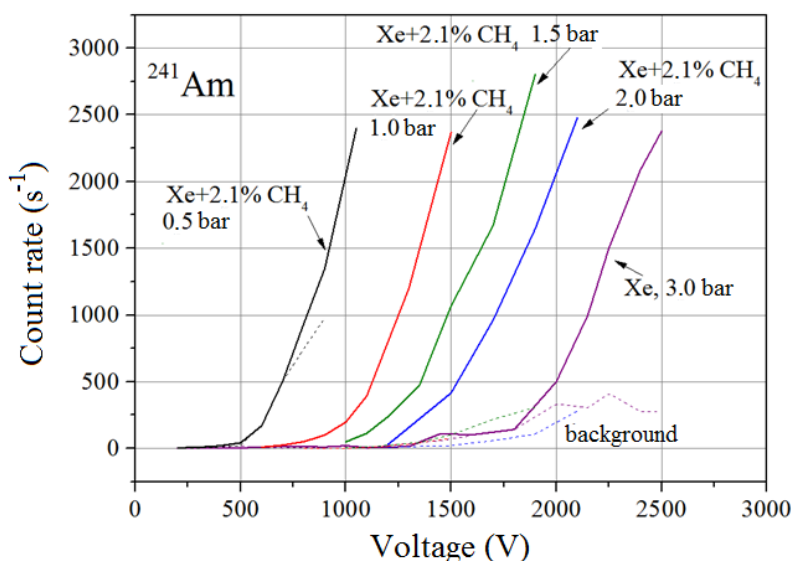
Figure 3. The count rate for ^{241}Am at different pressures of the gas mixture. Dashed lines represent the background measurements

The count rate measured as a function of the applied voltage for a detector filled with pure Xe up to a pressure of 1.5 bar is shown in Fig. 4. As can be seen, the number of counts in the background measurements is much lower than that in the measurements with the γ-source. Table 3 shows the signal-to-noise ratio values for the Xe+2.1%CH$_4$ mixture for the isotopes ^{241}Am, ^{133}Ba, ^{152}Eu at a pressure of 1.5 bar and anode voltage of 1900 and 2550 V.

Signal-to-noise ratio for the mixture Xe+2.1%CH$_4$ at 1.5 bar

Isotope	^{60}Am (59.5 keV)	^{133}Ba (80.9 keV)	^{152}Eu (121.8 keV)
Signal-to-noise ratio, 1900 V	8	11	16
Signal-to-noise ratio, 2550 V	25	34	50

With an increase in the pressure of the Xe+2.1%CH$_4$ mixture to 2.5 bar (Fig. 5), the look of the counting characteristics significantly differs depending on the type of the radiation source: the counting rate increases gradually with the anode voltage for ^{137}Cs, while for ^{241}Am it practically does not change at low voltage values, and above 1000 V begins to grow rapidly. This behavior corresponds to different energies of gamma rays emitted by these sources. Indeed, for ^{137}Cs, most of the detector signal is due to the broad spectrum of Compton scattered γ-quanta, since the quanta from the ^{137}Cs photopeak with an energy of 662 keV are not registered at such Xe pressures. On the other hand, ^{241}Am has several low-energy γ-lines (60 keV and below), and in the spectra of ^{241}Am, these lines (peaks) began to appear at voltages above 1000 V, therefore, the counting characteristic begins to increase significantly at these voltages.

Similar dependences were measured for the other mentioned gas mixtures and pressures, though it turned out that the addition of H$_2$ or CH$_4$ did not lead to significant changes in the counting characteristics of the detectors.

The examples of the measured amplitude distributions of the detector signal (spectra) are shown in Fig. 6. For comparison, the spectrum on the left shows a line obtained with an Ortec 419 precision pulse generator. As can be seen, the detector can register radiation with energies up to ~120 keV (^{152}Eu line). However, at a higher gas pressure in such detectors, it is possible to detect radiation with higher energies [6]. The energy resolution (from full width of a photopeak at the half-amplitude level, FWHM) of the detectors was determined from the photopeaks of different

γ-sources. For the detector filled with the Xe+2.1%CH$_4$ mixture at the pressure of 2.5 bar, and a voltage of 2500 V (Fig. 6), it ranged from ~9.5% for an energy of 40 keV to ~5% for 120 keV. Such values of the energy resolution of the detector are sufficient to identify a reasonable number of radioactive isotopes.
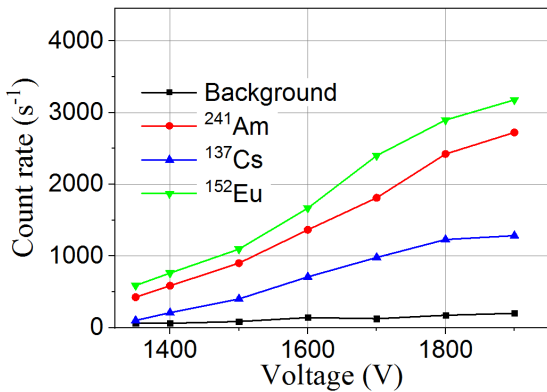
Figure 4. Voltage dependence of count rate for different isotopes, 1.5 bar, pure Xe
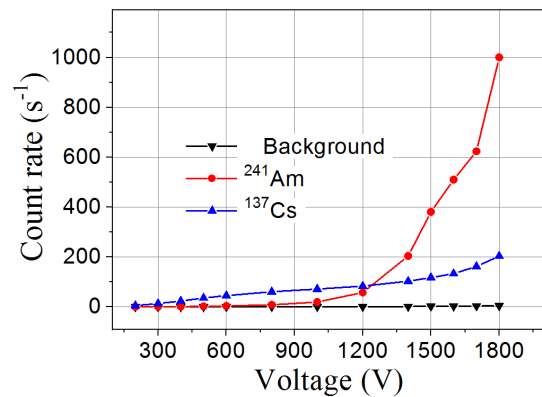
Figure 5. Voltage dependence of count rate for different isotopes, 2.5 bar, Xe + 2.1% CH$_4$
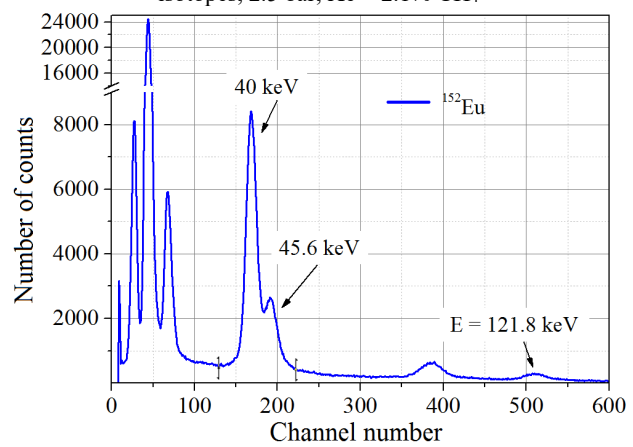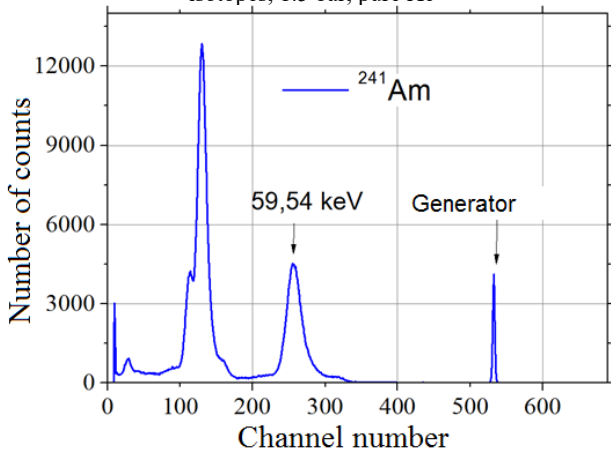
Figure 6. The measured spectra for ^{241}Am and ^{152}Eu, Xe+2.1% CH$_4$ mixture at 2.5 bar, and the anode voltage of 2500 V

The gas gain M is an important characteristic of a gas-filled detector operating in the proportional mode. For various values of pressure and composition of gas mixtures in the detector, it was determined by using the following formula [7]:

$$M = \frac{wVC_0}{Ae\epsilon_x},$$ (1)

where w is the average energy required to create one ion-electron pair in a gas mixture (21.5 eV for Xe), V is the pulse amplitude, C_0 is the detector capacitance (in our case, 20 pF), $A = 100$ is the amplifier gain, e is the electron charge, ϵ_x is the photon energy (for example 60 keV for ^{241}Am).
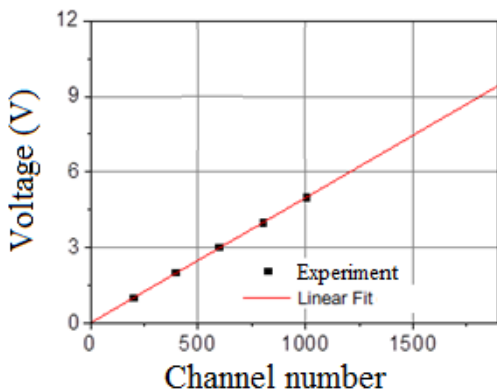
Figure 7. Dependence of the detector signal amplitude on the ADC channel number

Before determining the coefficient, the correspondence of the channel number of the measurement channel to the amplitude of the signal after the shaping amplifier was first carried out. The resulting dependence is linear (Fig. 7), with a linearity coefficient of 0.9999. Such a high degree of linearity indicates a high accuracy in determining the energy of spectral lines by the detector, which is necessary for the identification of radioactive isotopes.

The values of M depending on the applied voltage, calculated from the amplitude distributions for different values of pressure of the Xe+2.1%CH$_4$ mixture, are shown in Fig. 8. As can be seen, on a logarithmic scale, the dependence of the coefficient M on the applied voltage is nearly linear and shifts to the right with increasing gas pressure. Fig. 9 shows a comparison of the gas gain values for different gas compositions. As can be seen, the dependence of the gas gain on voltage is practically the same for the compositions of all mixtures, which were used.
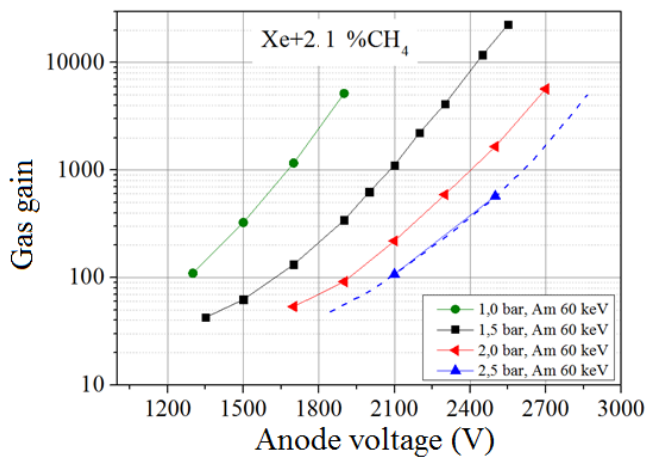
Figure 8. Gas gain versus anode voltage for Xe+2.1%CH4
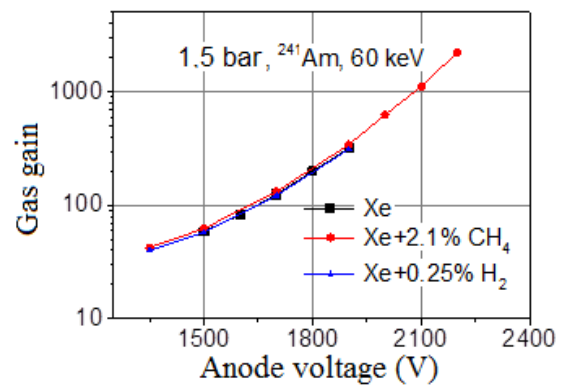
Figure 9. Gas gain as a function of the anode voltage at a pressure of 1.5 bar for clean Xe, Xe+2.1%CH4 and Xe+0.25%H2

Fig. 10 and Fig. 11 show the gas gain values calculated from the photopeaks of several different isotopes for pure Xe and a mixture of Xe + 2.1% CH4, respectively. As can be seen in both cases, the *M* values calculated using different gamma lines practically coincide. This behavior suggests that the gas gain does not depend on the number of charge carriers created during the primary ionization event, which corresponds to the proportional operating mode of the detector. The dependence of *M* on voltage in a significantly wider range was obtained for the mixture of Xe + 2.1% CH4, and it can be seen that for high voltages it is practically linear on a logarithmic scale (dashed line in Fig. 11). This behavior indicates that there is no effect of secondary ionization on the gas gain at the given applied voltages. The very fact that for the mixture of Xe + 2.1% CH4, in contrast to pure Xe, it was possible to carry out measurements at a much higher anode voltage indicates the stabilization of the gas mixture upon the introduction of additives such as methane, i.e. lowering the probability of gas breakdown.

The results obtained are in good agreement with the values of the gas gain obtained for similar compositions of mixtures [8]. Note also that, in the case of using a thinner anode [9] in the detector, lower voltage to achieve the same detector performance would be required.
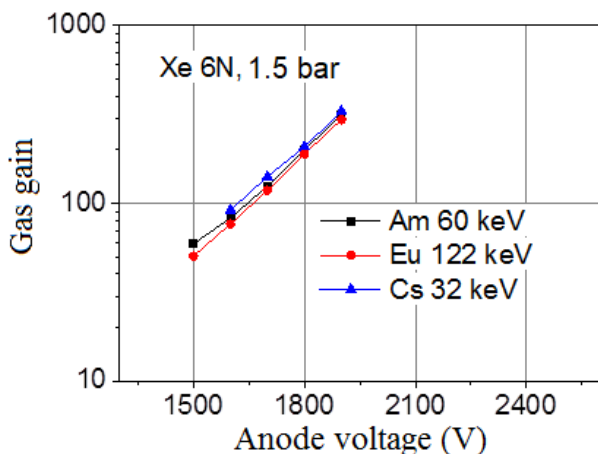
Figure 10. Gas gain for pure Xe at 1.5 bar, calculated for several gamma-ray energies
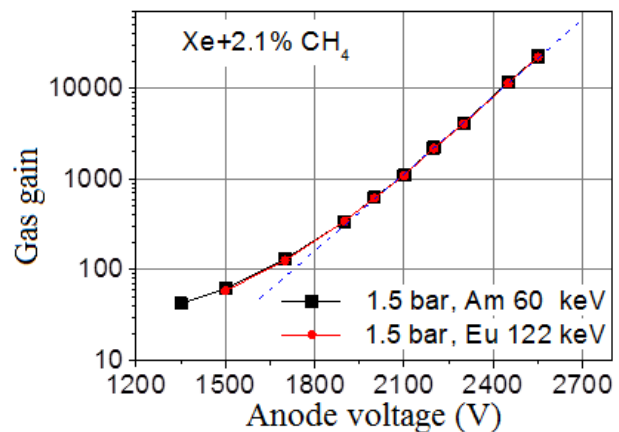
Figure 11. Gas gain for Xe + 2.1% CH4 mixture at 1.5 bar, calculated for several gamma-ray energies

CONCLUSIONS

Thus, the γ-radiation detectors filled with xenon, which have both high counting (dosimetric) and spectrometric properties have been developed, manufactured and tested. The detectors were made without using glass or organic materials. The influence of gas pressure, its composition (pure Xe or its mixture with H2, CH4), and the anode voltage on the spectral resolution and gas gain of the detectors was investigated. The detectors have shown sufficient operational characteristics, which will allow them to be used in various fields of application, including at nuclear power plants.

To improve the characteristics of the detector, it is planned to use a thinner anode (Ø≤30 μm), as well as to use ^{10}B in the detector design, which will lead to the possibility of using it as a neutron detector. It may also be promising to investigate the effect of mixtures of noble gases such as Xe and Ne in attempts to reduce the anode voltage due to a process of energy transfer between the two species, which produces extra electrons [10].

ORCID IDs

Sergey Sokolov, https://orcid.org/0000-0002-6134-905X; **Aleksey Pudov**, https://orcid.org/0000-0002-9499-379X
Alexander Rybka, https://orcid.org/0000-0003-4096-5539; **Vladimir Kutny**, https://orcid.org/0000-0001-8899-545X
Alexander Abyzov, https://orcid.org/0000-0002-1975-7586; **Gennadiy Kholomyeyev**, https://orcid.org/0000-0003-1779-9050
Serhii Melnikov, https://orcid.org/0000-0003-2494-1174

REFERENCES

[1] S.E. Ulin, K. F. Vlasik, A.M. Galper, V.M. Grachev, V.V. Dmitrenko, S.N. Zherebtsov, V.M. Kamaev, O.N. Kondakova, K.V. Krivova, D.V. Sokolov, and Z.M. Uteshev, in: *SPIE 3446, Hard X-Ray and Gamma-Ray Detector Physics and Applications Proceedings*, (IEEE, San Diego, 1998), https://doi.org/10.1117/12.312880.

[2] E.K. Malyshev, Yu.B. Zasadych, and S.A. Stabrovsky. Gas discharge detectors for monitoring nuclear reactors. (Energoatomizdat, Moscow, 1991). (in Russian)

[3] F.I.G.M. Borges, S.J.C. do Carmo, J.C.R. Mariquito, A.M.F. Trindade, and C.A.N. Conde, IEEE Transactions On Nuclear Science, **57**(4), 2205-2209 (2010), https://doi.org/10.1109/TNS.2010.2052930.

[4] A. Dastgheibi-Fard, and G. Geribier, (NEWS-G Collaboration), Nuclear Instruments and Methods in Physics Research A, **958**, 162390 (2020), https://doi.org/10.1016/j.nima.2019.162390.

[5] S.Ye. Ulin, *Gamma Spectrometers Based on Compressed Xenon (Development, Characterization, Applications),* (*Ph.D. thesis*), (Moscow State Institute of Engineering and Physics, Moscow, 1999).

[6] R.K. Sood, Z. Ye, and R.K. Manchanda, Nuclear Instruments and Methods in Physics Research A, 344, 384-393 (1994), https://doi.org/10.1016/0168-9002(94)90087-6.

[7] R.K. Manchanda, Z. Ye, and R.K. Sood, Ultra-high-pressure proportional counter Part I: Argon, Nuclear Instruments and Methods in Physics Research A, **292**, 373-385 (1990), https://doi.org/10.1016/0168-9002(90)90394-L.

[8] H. Sakurai, B.D. Ramsey, and M.C. Weisskopf, Nuclear Instruments and Methods in Physics Research A, 307, 504-511 (1991), https://doi.org/10.1016/0168-9002(91)90224-E.

[9] H. Sakurai, and B.D. Ramsey, Dependence of energy resolution on anode diameter in xenon proportional counters, Nuclear Instruments and Methods in Physics Research A, **313**, 155-161 (1992), https://doi.org/10.1016/0168-9002(92)90092-I.

[10] F.I.G.M. Borges, F.P. Santos, F. Amaro, T.H.V.T. Dias, J.F.C.A. Veloso, and C.A.N. Conde, in: *IEEE Transactions on Nuclear Science Proceedings*, (IEEE, Rome, 2004), https://doi.org/10.1109/NSSMIC.2004.1462248.

ГАЗОНАПОВНЕНИЙ ДЕТЕКТОР ГАММА-ВИПРОМІНЮВАННЯ НА ОСНОВІ ВИСОКОЧИСТОГО КСЕНОНУ

С. Соколов, А. Пудов, А. Рибка, В. Кутній, А. Абизов, Г. Холомєєв, С. Мельніков
Національний науковий центр «Харківський фізико-технічний інститут»
Харків, Україна

Газонаповнені детектори іонізуючого випромінення знайшли широке застосування для вимірювання ядерних та радіоактивних матеріалів, а також в медицині, астрономії, матеріалознавстві. Пропорційні детектори γ-випромінення на основі газу ксенону можуть працювати як в рахунковому, так і в спектрометричному режимах. Для використання цих детекторів для радіаційного контролю та ідентифікації радіоактивних матеріалів, зокрема в атомній енергетиці, потрібно вирішити досить складні матеріалознавчі завдання. Це вибір матеріалів з низькою активацією в інтенсивних потоках іонізуючого випромінення, в тому числі нейтронів, відмова від використання скляних елементів, повна відсутність органічних компонентів в конструкції детектора. У даній роботі повідомляється про розробку, виготовлення та випробування пропорційних детекторів гамма-випромінювання, наповнених газовими сумішами на основі особливо чистого ксенону. Для напуску в детектор газових сумішей була розроблена і виготовлена спеціальна установка складається з компонентів, призначених для роботи з особливо чистими газами. Досліджено вплив тиску газу, його складу (чистий Xe або його суміші з H_2, CH_4) і напруги на аноді на спектрометричне розрізнення і коефіцієнт газового посилення детекторів. Добавка H_2 або CH_4 до ксенону застосовується для підвищення швидкості дрейфу носіїв заряду. Ці добавки також призводять до стабілізації газової суміші, тобто зниження ймовірності газового пробою при високій напрузі між електродами детектора. Використовувався газ ксенон, а також його суміші дослідницької марки чистоти (99,9999%). Для дослідження рахункових і спектрометричних характеристик детектора в роботі використовувалися стандартні джерела γ-випромінення ^{241}Am, ^{137}Cs, ^{152}Eu, ^{133}Ba. Кращі, на даний момент, значення енергетичного розрізнення були отримані для детектора, наповненого газовою сумішшю Xe + 2,1% CH_4 при тиску 2,5 бар і напрузі на аноді 2500 В; вони склали ~ 9,5% для енергії 40 кеВ і ~ 5% для 120 кеВ. Для підвищення термічної і радіаційної стійкості, всі елементи конструкції детекторів виготовлені з матеріалів, що слабо активуються під дією іонізуючого випромінення. Детектори призначені для контролю технологічних процесів і для роботи в складі систем радіаційного контролю, в тому числі на AEC.

КЛЮЧОВІ СЛОВА: детектор, гамма-випромінення, швидкість відліку, спектрометрія, ксенон, газове підсилення

ГАЗОНАПОЛНЕННЫЙ ДЕТЕКТОР ГАММА-ИЗЛУЧЕНИЯ НА ОСНОВЕ ВЫСОКОЧИСТОГО КСЕНОНА

С. Соколов, А. Пудов, А. Рыбка, В. Кутний, А. Абызов, Г. Холомеев, С. Мельников
Национальный научный центр «Харьковский физико-технический институт»
Харьков, Украина

Газонаполненные детекторы ионизирующих излучений нашли широкое применение для измерения ядерных и радиоактивных материалов, а также в медицине, астрономии, материаловедении. Пропорциональные детекторы γ-излучения на основе газа ксенона могут работать как в счетном, так и в спектрометрическом режимах. Для применения этих

детекторов для радиационного контроля и идентификации радиоактивных материалов, в частности в атомной энергетике, требуется решить довольно сложные материаловедческие задачи. Это выбор материалов с низкой активацией в интенсивных потоках ионизирующих излучений, в том числе нейтронов, отказ от использования стеклянных элементов, полное отсутствие органических компонентов в конструкции детектора. В данной работе сообщается о разработке, изготовлении и испытании пропорциональных детекторов гамма-излучения, наполненных газовыми смесями на основе особо чистого ксенона. Для напуска в детектор газовых смесей была разработана и изготовлена специальная установка, состоящая из компонентов, предназначенных для работы с особо чистыми газами. Исследовано влияние давления газа, его состава (чистый Xe или его смеси с H_2, CH_4) и напряжения на аноде на спектрометрическое разрешение и коэффициент газового усиления детекторов. Добавка H_2 или CH_4 к ксенону применяется для повышения скорости дрейфа носителей заряда. Эти добавки также приводят к стабилизации газовой смеси, т.е. понижению вероятности газового пробоя при высоком напряжении между электродами детектора. Использовался газ ксенон, а также его смеси исследовательской марки чистоты (99,9999%). Для исследования счетных и спектрометрических характеристик детектора в работе использовались стандартные источники γ-излучения ^{241}Am, ^{137}Cs, ^{152}Eu, ^{133}Ba. Лучшие, на данный момент, значения энергетического разрешения были получены для детектора, наполненного газовой смесью Xe+2,1% CH_4 при давлении 2,5 бар и напряжении на аноде 2500 В; они составили $\sim 9,5\%$ для энергии 40 кэВ и $\sim 5\%$ для 120 кэВ. Для повышения термической и радиационной стойкости, все элементы конструкции детекторов изготовлены из материалов, слабо активируемых под действием ионизирующих излучений. Детекторы предназначены для контроля технологических процессов и для работы в составе систем радиационного контроля, в том числе на АЭС.

КЛЮЧЕВЫЕ СЛОВА: детектор, гамма-излучение, скорость счета, спектрометрия, ксенон, газовое усиление

ANGULAR DEPENDENCE OF IONOLUMINESCENCE FOR SILICA CASE

Sergiy Kononenko, Illia Mysiura, Vitaliy Zhurenko*,
Oleg Shyshkin, Oganes Kalantaryan
V.N. Karazin Kharkiv National University
4 Svobody Sq., Kharkov, 61022, Ukraine
*Corresponding Author: v.zhurenko@gmail.com

The paper deals with angular dependence of ionoluminescence from transparent glossy silica samples. We measured silica ionoluminescence spectra at wavelength range of 400–700 nm for different projectiles (H_1^+, H_2^+, He^+ 210 and 420 keV) and registered two most common intensive emission peaks (blue with a maximum at 456 nm and red one at 645 nm). To study luminescent angular dependence, the behavior of the blue peak maximum as a function of observation angle in the range of 0–70° was examined, namely, the indicatrix at the wavelength of 456 nm was found. The intensity corresponding to ionoluminescent indicatrices were found to be higher with respect to values from Lambertian angular distribution reaching approximately 20 % at large observation angles. We also calculated angular distribution of light above the sample surface taking into account refraction and reflection at the solid-ambient interface. The results obtained were in a good agreement with silica ionoluminescence experimental data for the average indicatrix curve. The latter indicates that the model assumption (luminescent light generated by fast ions within silica is unpolarized and isotropic) is correct. It was demonstrated that geometry of the experiment is very important, i.e., considering the light collected by the measuring system in a certain solid angle, one has to take into account that mutual arrangement of the sample and detector can distort angular distribution. The refraction at the border between a sample and vacuum (or air) strongly influences the luminescent light angular distribution.

KEY WORDS: SiO_2; spectroscopy; refraction; reflection, ions, radioluminescence, spectrum, indicatrix

Luminescent methods have been used for diagnostic purposes in various fields of science and technology recently. Their main advantage is high sensitivity to phase transitions, small concentrations of specific defects and impurities [1, 2]. These changes in crystal structure are easily diagnosed, since they become apparent by luminescent measurements of spectra with characteristic bands at certain wavelengths. These techniques of optical spectroscopy are well developed, and diagnostic tools are available and well-engineered.

Luminescent spectrum shape is sensitive to impurities, stresses, dislocations, nonstoichiometry and inclusions; therefore, systematic study requires qualitative control in sample preparation (see, for example [3]). In addition, many defects can combine together to minimize lattice stresses or electronic mismatches between dopants and lattice points. Luminescent methods enable to monitor the presence of an easily identifiable impurity, for example, a rare-earth metal ion, because there are characteristic emission spectra in this case. It should be noted that it is possible to detect the radiation associated with the defect under study in the spectrum despite the abundance of other defects [4–8].

The mentioned above reasons explain wide use of luminescent techniques not only by physicists [8, 9], but also by mineralogists and geologists, as well as by scientists of other specialties (see, for example [10, 11]). Recently, luminescence has been widely put into practice in medical applications, such as optical diagnostic methods of cancer of various types, diseases like caries, dose assessment technique for medical triage [12].

The features of luminescent technique applications for an analysis of various objects were scrupulously discussed (see, for example [13–14]). However, it should be noted that one aspect of luminescent research is poorly covered in publications, namely angular distribution of emitted light. An influence of observation angle on the light flux is more often taken into account in experiments with light emitting objects of limited geometry, such as nanorods, LEDs and various other radiating objects [15–17]. The experimental angular dependence study of the opal nanoscale spheres showed the influence indicatrix (dependence of light intensity on observation angle at certain wavelength) of the observation angle parameter on the measured spectra [18]. But, unfortunately, the reasons for the dependence were not discussed. In order to optimize operation of medical light devices some researchers dealt with the angular distribution of luminescent light from a point Lambert source [19]. It should be noted that they took into account the influence of the CCD cover glass. The results indicated a good agreement of the experimentally measured data with the Monte Carlo simulation of the emitted light angular distribution. Angular distributions of luminescence are also of great importance for X-rays screens in medical imaging detector applications [20]. The simulations and experimental measurements pointed out to a more directional angular distribution in comparison with the predicted Lambert's cosine distribution. The authors took into account absorption and scattering of light in matter in the calculations. When the light is generated inside a transparent extended bulk sample, the angular dependence of light radiation intensity under the surface can also appear due to the refractivity and transmittance on the boundary.

Optical measurements of luminescent radiation have some limitations associated with geometry of experiment (positioning and finite dimensions of registering detector). Light measurements are often carried out in a certain solid angle. Mutual arrangement of the sample being studied and the optics for analysis can define intensity variations of

luminescent signal. This paper is devoted to the dependence of luminescent intensity on observation angle for transparent polished samples on the example of silica.

EXPERIMENTAL SETUP

To study the angular characteristics of luminescence, we performed a series of experiments on the irradiation of silica by fast helium and hydrogen ions (both molecular and atomic species). The measurements were carried out at room temperature under vacuum conditions (residual gas pressure not less than 10^{-4} Pa) in the experimental setup, which is described in detail here [21]. We used the following bombarding projectiles: H_1^+ 210 and 420 keV, H_2^+ 420 keV and He^+ 420 keV. A beam of ions from the Van de Graaf accelerator passed through the diaphragm system and impinged the target at an angle of 30º (the angle is measured from the normal to the surface of the target). The beam diameter on the target was 1.5 mm. Luminescent radiation was detected by a spectrometric complex based on the grating monochromator. Light emitted at an observation angle β was collected by a light guide with an effective input aperture of 2 mm (in the plane of incidence). The light guide entrance slit was attached to the movable holder at a distance of 50 mm from the beam point on the target. It was possible to move the light guide in the plane of beam incidence along the circle with the center at the beam point on the target, thus observation angle could be changed from 0 to 70°. The beam axis, the normal to the target surface and the observation direction were in the same plane. The optical channel (light guide — focusing system — monochromator — photomultiplier) was calibrated by means of incandesce spectrometer lamp. We also measured ion beam current (wire probe diagnostics) simultaneously with the light signal registration. The samples were prepared from 1mm thick plane-parallel silica plate with finely polished surface.

EXPERIMENTAL RESULTS

As it is well-known silica showed bright ionoluminescence in the wavelength region 400–720 nm (visible light), due to intrinsic defects and impurities [22, 23]. In this spectral range, silica has two most common intensive emission peaks (blue with a maximum at 456 nm and red one at 645 nm). In our experiments we obtained the same two-band luminescent spectra with more intensive blue peak in comparison with red one. To study angular luminescent characteristics, we examined the behavior of the blue peak, namely, we studied the indicatrix at a wavelength of 456 nm. Figure 1 shows the generalized angular dependences of luminescence for several types of irradiating ions at low absorption doses (some experimental data were taken from our previous papers: H_1^+ 210 keV [21], He^+ 420 keV [24]). The spectral intensity $I(\beta)$ was normalized to $I(0°)$ value, i.e. $I_n(\beta) = I(\beta)/I(0°)$, where $I_n(\beta)$ is normalized intensity.

As we mentioned above Lambert's cosine law imposes that the luminous intensity $I(\beta)$ directed at an angle β, is given as $I(\beta)=I(0°)\cos\beta$ [25, 26]. Correspondingly, it is reasonable to replot the indicatrix normalized to cosβ (see Fig. 2). An additional curve corresponding to a Lambertian angular distribution is also shown for comparison purposes.

As it may be observed from Fig. 1–2: (1) sort of ion has no noticeable effect; (2) the shape of normalized indicatrices differs clearly from the shape of the Lambertian curve. Intensity values corresponding to ionoluminescent indicatrices were found to be higher with respect to values from Lambertian distribution. The difference was found to vary up to approximately 20 % at large observation angles. But Lambert's cosine law one should use only in diffusion solid-ambient surface case. In our experiments samples was polished and experimental distribution can't be explained by that law. Similar dependencies of the indicatrix were observed not only for the maximum of the blue band, but also for the maximum of the red band [27].
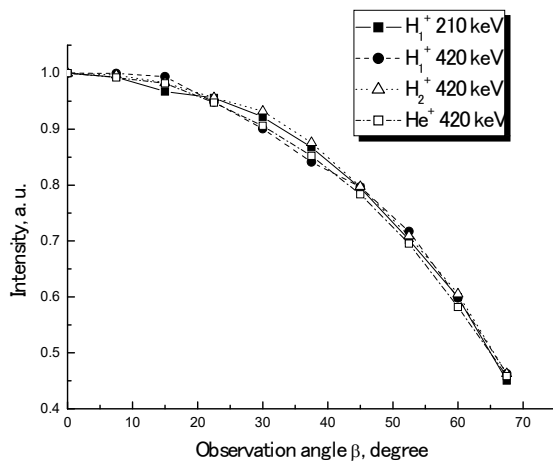
Figure 1. Angular dependences of ionoluminescent intensity for several types of irradiating ions (λ=456 nm)
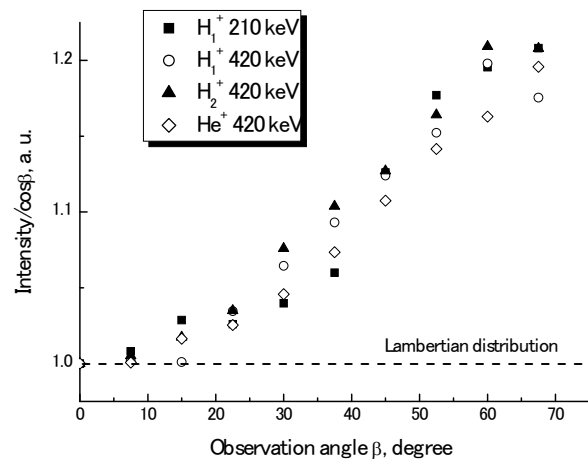
Figure 2. Ionoluminescent angular dependences normalized to cosβ

Angular dependence calculations

To understand the nature of the angular dependences of luminescence we considered the physical model that includes light refraction and reflection on solid-vacuum boundary. We formulated model's approximation based on analysis of the experimental condition and assumption about spatial distribution and polarization of the luminescent radiation in silica.

As the ions have been accelerated to energies of several hundred keV, the penetration depth reached several microns in silica [28]. The energetic projectiles provide intensive electronic excitation and induce light emission along their trajectories. Despite the fact that there is anisotropy associated with the ion beam, the photon emission is most likely not related to the projectile direction. The diameter of the beam spot on silica target was approximately 1.5 mm, while the distance between light detector (the light guide entrance slit) and silica target was equal 50 mm. So the luminescence is being observed at a distance large compared to the extent of the emitting zone. Taking into account the value of ion penetration depths in silica, we can assume the luminescent source to be point in our proposed model. Schematic representation for our model is presented on Fig. 3.

As far as detector moves in a plane perpendicular to the interface between media (the task is symmetrical with respect to azimuthal angle) the numerical problem is automatically reduced to 2D geometry. As one can see from Fig. 3 X-axis coincides with the separating surface and Y-axis is perpendicular to it and intersects the point source of luminescence.

The ray of the light emitted from the source at an angle α to the Y-axis is passing through the separating surface and refracts due to the difference between refraction indexes n_1 and n_2. We neglected absorption of luminescent light within the matter due to low extinction coefficient of silica in our wavelength range. Further the ray is traveling at an angle β to the Y-axis and enters the detector that moves in (X, Y) plane around the coordinate origin on a constant distance. The current angle position of the detector to the Y-axis is denoted by β.

To obtain relationship between angles of light generation inside a solid α and its further propagation in vacuum β we use well-known Snell's law (1)

$$n_2 \sin\alpha = n_1 \sin\beta \tag{1}$$

that binds the refractive indices with the angles of incidence and refraction.

In order to simulate transmittance distribution one should firstly recall Fresnel's equations [29] that describe the behavior of light pass the separating surface of two media with different refractive indices. The fraction of the intensity R_s of light reflected from the boundary for s-polarized case is given by

$$R_s = \left| \frac{n_2\cos\alpha - n_1\sqrt{1-\left(\frac{n_2}{n_1}\sin\alpha\right)^2}}{n_2\cos\alpha + n_1\sqrt{1-\left(\frac{n_2}{n_1}\sin\alpha\right)^2}} \right|^2 \tag{2}$$

and the intensity R_p of reflection for p-polarized case is

$$R_p = \left| \frac{n_2\sqrt{1-\left(\frac{n_2}{n_1}\sin\alpha\right)^2} - n_1\cos\alpha}{n_2\sqrt{1-\left(\frac{n_2}{n_1}\sin\alpha\right)^2} + n_1\cos\alpha} \right|^2 \tag{3}$$

Following the energy conservation law the corresponding transmittances T_s and T_p have the forms

$$T_s = 1 - R_s \tag{4}$$

And

$$T_p = 1 - R_p \tag{5}$$

When the light includes both s- and p-polarizations, for example if it is unpolarized, that means both polarizations are present as half to half. Then the transmittance reads as

$$T = 1 - \frac{1}{2}\left(R_s + R_p\right) \tag{6}$$

All the mentioned expressions where included in the numerical code and linked to the expression for angle dependencies (1) that allowed solving the problem of light transmittance at the interface between two media.

On Figure 4 one can see calculated transmittance versus the observation angle β dependence for several refractive index values (the data were normalized to the values at $\beta=0°$).
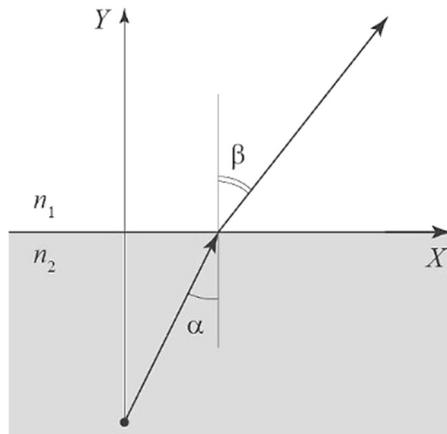
Figure 3. Schematic representation of light refraction at the interface between two mediums
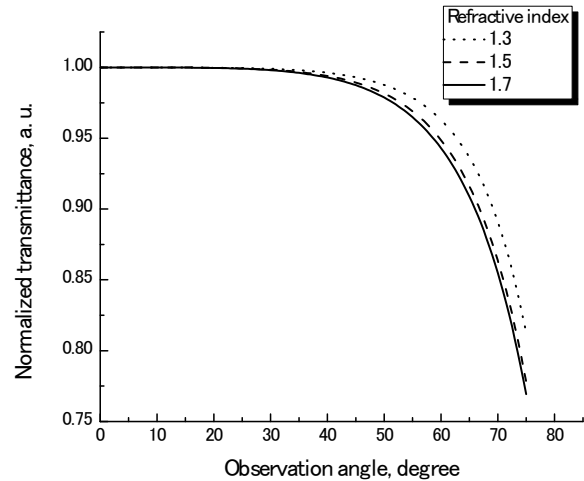
Figure 4. Normalized transmittance versus the detector angle position β for different refractive index n_2 values ($n_1=1$)

Let's consider our *2D* geometry experimental case (see Fig. 5). S is point luminescent source. The luminescent light power emitted in some angle range $\Delta\alpha$ from α_1 to α_2. It is evident that we registered light emission in the angle $\Delta\beta$, which is corresponding to the angle $\Delta\alpha$ inside the sample. So luminescent intensity of the light collected in small angle $\Delta\beta$ is proportional to value of $\Delta\alpha$. If $\Delta\beta$ is constant (which is most often realized in experiments), $\Delta\alpha$ will depend on β due to refractive law at the sample surface.

Snell's law defines the relationship between angles:

$$n_2 \sin\alpha_1 = n_1 \sin\beta_1 \tag{7}$$

$$n_2 \sin\alpha_2 = n_1 \sin\beta_2 \tag{8}$$
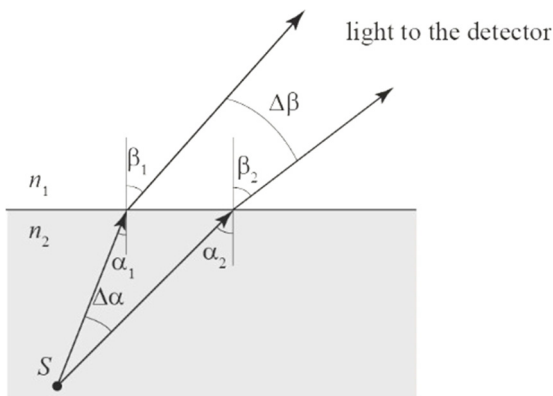
Figure 5. Luminescent light refraction at the interface between two mediums
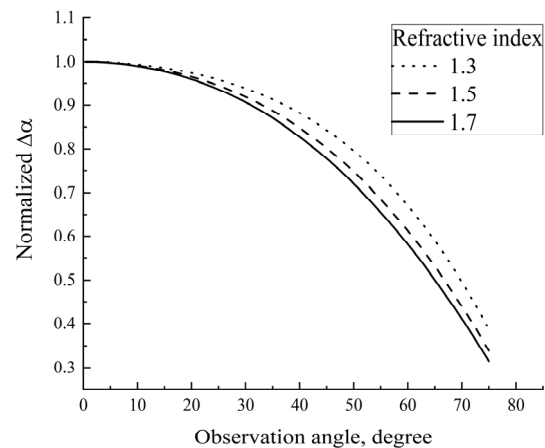
Figure 6. The normalized relation between $\Delta\alpha$ and the detector angle position for different refractive indices n_2 ($n_1=1$)

As we mentioned above, for our experimental geometry the light guide entrance slit had dimension of 2 mm and moved along a circle with a diameter of 50 mm. In our case constant angle $\Delta\beta$ during the indicatrix measurements has value $\approx2°$ (so we can consider this angle as small). It is possible to relate the detector angle position β and angles β_1, β_2:

$$\beta_2 = \beta + \frac{\Delta\beta}{2} \tag{9}$$

$$\beta_1 = \beta - \frac{\Delta\beta}{2} \tag{10}$$

Using expressions (7–10) it is possible to calculate $\Delta\alpha = \alpha_2 - \alpha_1$ depending on the detector angle position β. The dependence $\Delta\alpha=f(\beta)$ was calculated for three refractive indices (see Fig. 6).

As we pointed out earlier luminescent intensity of the light collected by the detector is proportional to value of Δβ, this nonlinear dependence $\Delta\alpha=f(\beta)$ predicts that registered luminescent intensity is changed at different observation directions. For example for n_2=1.5 normalized Δα changes from 1 (at β=0°) to 0.35 (at β=75°). It means that different detector positioning relative to the luminescent source leads to the intensity variations.

Validation of calculation model and discussion

Taking into account our previous calculations, indicatrix for the light leaving solid will be affected by the dependencies of the transmittance and reflectance. We calculated the normalized transmittance T and the normalized dependence Δα versus the detector angle position β for the silica case. The refractive index of silica at 456 nm is approximately 1.46 [30]. The result is analogical to one shown on Fig. 4 and Fig.6. Assume that light from point source is isotropic within silica and unpolarized light (*s*- and *p*-polarizations are present as half to half), then the indicatrix is constant for any angle α $(I(\alpha)=I_o)$. We calculated normaled functional dependence of the luminescent light collected by our detector on observation angle by multiplying the indicatrix within silica by the mentioned above relations $I(\beta)=I_0 \cdot T(\beta) \cdot \Delta\alpha(\beta)$ (see solid curve on Fig. 7). We also showed on Fig. 7 the average experimental indicatrix based on our data for different projectiles under study and Lambertian (to perform comparative analysis we normalized the data to $I(0°)$ values).

The results of calculated angular distribution are in good agreement with the experimental average indicatrix curve. This agreement confirms applicability of our model and initial assumption, that the light is initially unpolarized and emitted isotropically within silica.

We performed the calculations for our specific experiment. The reception path of the monochromator always limits the angular size of the region from which light is collected. In general, obtained results can be adapted for other cases. For that one has to vary Δβ and solid refractive index in equations. Moreover, two aspects must be taken into account. If there are other factors affecting the angular distribution (for example the presence of optical filters or etc.), then this can be taken into account in the indicatrix by multiplying by the corresponding dependence. Secondly, when you deal with substances with a strong dispersion in the wavelength range under study, not only the intensity but also the shape of the luminescence spectrum can change.
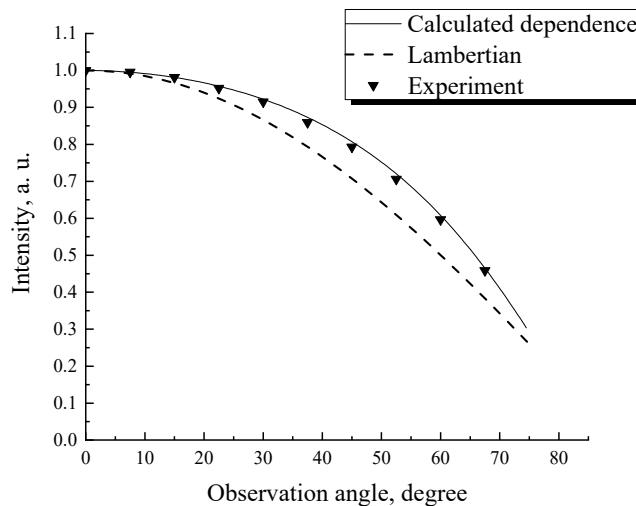
Figure 7. Normalized indicatrices of silica luminescent light: measured average angular dependence of light emission (squares), calculated angular distribution (solid curve), Lambert's cosine law (dashed curve).

CONCLUSION

The influence of the observation angle on the measured intensity of the luminescent radiation induced by ions from silica was shown. The functional angular dependence is significantly different from the well-known Lambert's law. The previously obtained experimental angular dependences of the silica ionoluminescence for several types and ion energies were the basis for the calculations performed. A good agreement between the experimental data and the calculated angular distribution was obtained.

The results obtained make it possible to draw the following conclusions:
a)   Luminescent light generated by fast ions within silica is unpolarized and isotropic.
b)   Geometry of the experiment is very important. Considering the light collected by the measuring system in a certain solid angle, one has to take into account that mutual arrangement of the sample and detector can distort angular distribution.

c) The refraction at the interface between the sample and vacuum (or air) strongly influences the luminescent light indicatrix.

The results are applicable for any glossy transparent materials.

ORCID IDs
Sergiy Kononenko, https://orcid.org/0000-0001-6060-2589; **Illia Mysiura**, https://orcid.org/0000-0002-1401-6412;
Vitaliy Zhurenko, https://orcid.org/0000-0002-4738-094X; **Oganes Kalantaryan,** https://orcid.org/0000-0002-5625-6908

REFERENCES
[1] P.D. Townsend, B. Yang, and Y. Wang, Revista Mexicana De Fisica S, **54**(2), 29-38 (2008), http://www.scielo.org.mx/pdf/rmf/v54s2/v54s2a5.pdf.
[2] O. Pen˜a-Rodrı´guez, D. Jime´nez-Rey, J. Manzano-Santamarı´a, J. Olivares, A. Muñoz, A. Rivera, and F. Agulló-López, Appl. Phys. Express **5**(1), 011101 (2012), https://doi.org/10.1143/APEX.5.011101.
[3] P.D. Townsend, M. Khanlary, and D.E. Hole, Surf. & Coat. Tech. **201**, 8160 (2007), https://doi.org/10.1016/j.surfcoat.2006.01.075.
[4] P.D. Townsend, and Y. Wang, Energy Proc. **41**, 64 (2013), https://doi.org/10.1016/j.egypro.2013.09.008.
[5] M.L. Crespillo, J.T. Graham, Y. Zhang, and W.J. Weber, J. Lumin. **172**, 208 (2016), https://doi.org/10.1016/j.jlumin.2015.12.016.
[6] D. Jimenez-Rey, O. Peña-Rodríguez, J. Manzano-Santamaría, J.Olivares, A.Muñoz-Martin, A.Rivera, and F.Agulló-López, Nucl. Instr. and Meth. Phys. Res. B, **286**, 282 (2012), https://doi.org/10.1016/j.nimb.2011.12.025.
[7] R. Skiba, I. Mysiura, O. Kalantaryan, V. Zhurenko, and S. Kononenko, East Eur. J. Phys. **4**, 93 (2018), https://doi.org/10.26565/2312-4334-2018-4-11.
[8] P.D. Townsend, Nucl. Instr. and Meth. Phys. Res. B, **286**, 35 (2012), https://doi.org/10.1016/j.nimb.2011.10.070.
[9] A. Finch, J. Garcia-Guinea, D. Hole, P.D. Townsend, and J.M. Hanchar, J. Phys. D: Appl. Phys. **37**, 2795 (2004), https://doi.org/10.1088/0022-3727/37/20/004.
[10] H. Calvo del Castillo, N. Deprez, T. Dupuis, F. Mathis, A. Deneckere, P. Vandenabeele, T. Calderón, and D. Strivay, Anal. Bioanal. Chem. **394**, 1043 (2009), https://doi.org/10.1007/s00216-009-2679-y.
[11] G. Valotto, A. Quaranta, E. Cattaruzza, F. Gonella, and G. Rampazzo, Spectrochem. Acta Part A: Mol. Biomol. Spectrosc. **95**, 533 (2012), https://doi.org/10.1016/j.saa.2012.04.045.
[12] R. De Witt, D.M.Klein, E.G. Yukihara, S.L. Simon, and S.W.S. McKeever, Health Phys. **98**(2), 432 (2010), https://doi.org/10.1097/01.HP.0000347997.57654.17.
[13] P.D. Townsend, and M.L. Crespillo, Phys. Proc. **66**, 345 (2015), https://doi.org/10.1016/j.phpro.2015.05.043.
[14] Y. Wang, and P.D. Townsend, J. Lumin. **142**, 202 (2013), https://doi.org/10.1016/j.jlumin.2013.03.052.
[15] N.C. Greenham, R.H. Friend, D.D.C. and Bradley, Adv. Mater. **6**(6), 491 (1994), https://doi.org/10.1002/adma.19940060612.
[16] F.A. Ponce, D.P. Bour, W. Götz, and P.J. Wright, Appl. Phys. Lett. **68**, 57 (1996), https://doi.org/10.1063/1.116756.
[17] D.C. Marra, E.S. Aydil, S.-J. Joo, E. Yoon, and V.I. Srdanov, Appl. Phys. Lett. **77**(21), 3346 (2000), https://doi.org/10.1063/1.1326837.
[18] A. N. Gruzintsev, Inorg. Mat. **51**(11), 1127 (2015) https://doi.org/10.1134/S0020168515110023.
[19] G.M. Haak, N.L. Christensen, and B.E. Hammer, Nucl. Instr. and Meth. Phys. Res. A, **390**, 191 (1997), https://doi.org/10.1016/S0168-9002(97)00355-0.
[20] I. Kandarakis, D. Cavouras, D. Nikolopoulos, A. Episkopakis, N. Kalivas, P. Liaparinos, I. Valais, G. Kagadis, K. Kourkoutas, I. Sianoudis, N. Dimitropoulos, C. Nomicos, and G. Panayiotakisc, App. Rad. Isot. **64**, 508 (2006), https://doi.org/10.1016/j.apradiso.2005.11.016.
[21] S. Kononenko, O. Kalantaryan, V. Muratov, and V. Zhurenko, Radiation Measurements, **42**, 751 (2007), https://doi.org/10.1016/j.radmeas.2007.02.061.
[22] P.J. Chandler, F. Jaque, and P.D. Townsend, Rad. Eff. **42**(1-2), 45 (1979), https://doi.org/10.1080/10420157908201735.
[23] R. Salh, in: *Crystalline Silicon - Properties and Uses* (InTech, 2011), pp. 135–172, http://dx.doi.org/10.5772/22607.
[24] V. Zhurenko, O. Kalantaryan, S. Kononenko, I. Mysiura, and E. Barannik, Nucl. Instr. Meth. Phys. Res**. B**, **407**, 5 (2017), https://doi.org/10.1016/j.nimb.2017.05.038.
[25] A.N. Matveev, *Optics* (Mir, Moscow, 2000).
[26] E.F. Zalewski, in: *Handbook of Optics*, edited by M. Bass (Mc Graw-Hill, New York, 1995).
[27] O. Kalantaryan, S. Kononenko, and V. Zhurenko, Func. Mat. **20**(4), 462 (2013), http://dx.doi.org/10.15407/fm20.04.462.
[28] J.F. Ziegler, M.D. Ziegler, and J.P. Biersack, Nucl. Instr. Meth. Phys. Res. B, **268**(11-12), 1818 (2010), https://doi.org/10.1016/j.nimb.2010.02.091.
[29] M. Born, and E. Wolf, *Principles of Optics* (Cambridge University Press, Cambridge, 2002).
[30] I.H. Malitson, J. Opt. Soc. Am. **55**(10), 1205 (1965), https://doi.org/10.1364/JOSA.55.001205.

КУТОВА ЗАЛЕЖНІСТЬ ЙОНОЛЮМІНЕСЦЕНЦІЇ ДЛЯ КВАРЦЕВОГО СКЛА

С. Кононенко, І. Мисюра, В. Журенко, О. Шишкін, О. Калантар'ян
Харківський Національний університет ім. В.Н. Каразіна
61022, Україна, м. Харків, пл. Свободи, 4

У статті розглядається кутова залежність йонолюмінесценції для прозорих полірованих зразків кварцового скла. Ми виміряли спектри йонолюмінесценцію кварцового скла в діапазоні довжин хвиль 400–700 нм для різних бомбардуючих йонів (H$_1^+$, H$_2^+$, He$^+$ 210 та 420 кеВ) та зареєстрували два відомих найпоширеніших піки інтенсивного випромінювання (синій з максимумом біля 456 нм та червоний — 645 нм). Для вивчення кутової залежності люмінесценції було досліджено поведінку максимуму синього піку як функцію кута спостереження в діапазоні 0–70°, а саме було знайдено індикатрису на довжині хвилі 456 нм. Встановлено, що інтенсивність, яка відповідає йонолюмінесцентним індикатрисам, вища значень,

характерних для кутового розподілу Ламберта, сягаючи значень перевищення приблизно 20 % для великих кутів спостереження. Ми також розрахували кутовий розподіл світла над поверхнею зразка з урахуванням заломлення та відбиття на поверхні твердого тіла. Отримані результати добре узгоджуються з експериментальними даними щодо йонолюмінесценції кварцового скла (H_1^+, H_2^+, He^+ 210 та 420 кеВ), а саме середньою індикатрисою. Останнє вказує на правильність модельного припущення (люмінесцентне світло, яке генерується швидкими іонами в кварцовому склі, є неполяризованим та ізотропним). Було продемонстровано, що геометрія експерименту дуже важлива, тобто, аналізуючи світло, яке збирає вимірювальна система під певним тілесним кутом, слід враховувати, що взаємне розташування зразка та детектора може вплинути на кутовий розподіл. Заломлення на межі розділу зразка та вакууму (або повітря) сильно впливає на кутовий розподіл люмінесцентного світла.

КЛЮЧОВІ СЛОВА: SiO_2, спектроскопія, заломлення, відбиття, йони, радіолюмінесценція, спектр, індикатриса

УГЛОВАЯ ЗАВИСИМОСТЬ ИОНОЛЮМИНЕСЦЕНЦИИ ДЛЯ КВАРЦЕВОГО СТЕКЛА

С. Кононенко, И. Мисюра, В. Журенко, А. Шишкин, О. Калатарьян

Харьковский национальный университет им. В. Н. Каразина

61022, Украина, г. Харьков, пл. Свободы, 4

В статье рассматривается угловая зависимость ионолюминесценции прозрачных полированных образцов кварцевого стекла. Мы измерили спектры ионолюминесценции кварцевого стекла в диапазоне длин волн 400–700 нм для различных бомбардирующих ионов (H_1^+, H_2^+, He^+ 210 и 420 кэВ) и зарегистрировали два известных распространенных пика интенсивного излучения (синий с максимумом около 456 нм и красный — 645 нм). Для изучения угловой зависимости люминесценции было исследовано поведение максимума синего пика как функцию угла наблюдения в диапазоне 0–70°, а, именно, была найдена индикатриса на длине волны 456 нм. Установлено, что интенсивность, которая соответствует ионолюминесцентным индикатрисам, выше значений, характерных для углового распределения Ламберта, достигая превышения примерно 20 % для больших углов наблюдения. Мы рассчитали угловое распределение света над поверхностью образца с учетом преломления и отражения на поверхности твердого тела. Полученные результаты хорошо согласуются с экспериментальными данными по ионолюминесценции кварцевого стекла (H_1^+, H_2^+, He^+ 210 и 420 кэВ), а, именно, средней индикатрисой. Последнее указывает на правильность модельного предположения (люминесцентный свет, генерируемый быстрыми ионами в кварцевом стекле, является неполяризованным и изотропным). Было продемонстрировано, что геометрия эксперимента очень важна, то есть, анализируя свет, который собирает измерительная система под определенным телесным углом, следует учитывать, что взаимное расположение образца и детектора может повлиять на угловое распределение. Преломление на границе между образцом и вакуумом (или воздухом) сильно влияет на угловое распределение люминесцентного света.

КЛЮЧЕВЫЕ СЛОВА: SiO_2, спектроскопия, преломление, отражение, ионы, радиолюминесценция, спектр, индикатрисса

STRUCTURAL, ELECTRONIC, MECHANICAL AND THERMAL PROPERTIES OF CoVZ (Z= Si, Ge, Sn, Pb) HALF-HEUSLER COMPOUNDS

Lalit Mohan[a], Sukhender[a], Sudesh Kumar[b], Shiv R. Bhardwaj[c], Ajay Singh Verma[a,*]

[a]Department of Physics, Banasthali Vidyapith, Banasthali 304022, India
[b]Department of Chemistry, Banasthali Vidyapith, Banasthali 304022, India
[c]Department of Physics, B. S.A. College, Mathura 282004, India
**Corresponding author: ajay_phy@rediffmail.com*
Received August 25, 2020; accepted September 15, 2020

Half-Heusler compounds pose unusual behavior because of their variable band gap and as well as both metallic and semi-metallic nature. These compounds can be used in different applications on the basis of band gap tenability. We have discussed the structural, electronic, elastic and magnetic properties of CoVZ (Z = Pb, Si, Sn, Ge) by using WIEN2k simulation code based on density functional theory (DFT). We have optimized the all-possible structural configuration of each compound and considered which optimized with lowest energy and lowest equilibrium volume. For determination of electronic exchange correlation energy, the generalized gradient approximation (GGA) is used in both platforms. We have also obtained the individual elastic constants, shear modulus, Young's moduli, B/G ratio and Poisson's ratio, which shows that these compounds are ductile except CoVGe shows little ductility. Debye temperatures are calculated by compression wave velocity, shear wave velocity and with their average value.
KEYWORDS: Half-Heusler compounds, structural properties, electronic properties, mechanical properties

The structure of Half Heusler compounds is a combination of rock salt and zinc blend type sublattices. This class of compounds can be represented as XYZ (Pb, Si, Sn, and Ge) type. Half-Heusler compounds, crystallize in the face-centered cubic having structurbericht designation C1b with the space group F-43 m [1]. These compounds can be viewed as Co and V form zinc blend sublattice arranged in a primitive cell at Wyckoff positions $(0, 0, 0)$ and $(\frac{1}{4}, \frac{1}{4}, \frac{1}{4})$ whereas NaCl sublattice is formed by V and Z at $(\frac{1}{2}, \frac{1}{2}, \frac{1}{2})$. We can also mention the ordering by interchanging above said Wyckoff positions, but the preferred atomic arrangements have a dependency on the size of involved atoms and the inter-atomic interaction between them [2-4]. Nevertheless, the size dependence on the transition metal configuration is the predominant influence over the inter-atomic interaction formed by the electronegativity of atoms. One can study the properties of such compounds simply by knowing the number of valence electrons per formula [5]. The properties of these XYZ compounds are highly dependent on the concentration of the number of valence electrons (n_v) in the primary cell, which predict the band structure and physical properties of the compounds [6].

The half Heusler compounds can be used to decrease electric power consumption by using them in photovoltaic devices. The most efficient way to do so is by transforming sunlight into electrical energy using semiconductor-based materials products. It is found that compounds with eight valence electrons are likely to be classic semi-conducting behaviors such as GaAs, Si. As with a K-shell, these valence electrons are tightly bound, as a result of which some gap separates the conduction and valence band. Similarly, the half Heusler compounds demonstrate the same behavior with the composition of the first, second and fifth group elements and can be used as traditional semiconductors to replace classical ones. The same behavior, however, is observed in compounds with 18 and 24 valence electrons.

In this study, we have 18 valence electrons compounds and it has been observed that this particular valence electrons count alloys shows the semiconducting behavior in both majority and minority spin states. The alloy's elastic constants are important mechanical properties, as well as correlated with other thermodynamic properties such as Debye temperature specific heat and heat of expansion. In addition, the elastic constants also provide useful information about the anisotropic bonding as well as mechanical stability. We have obtained the individual elastic constants, shear modulus, Young's moduli, B/G ratio and Poisson's ratio, which shows that these compounds are ductile [7,8]. The Debye temperatures obtained from the average sound velocity and have been discussed. In this paper, we have used the first-principles calculations to systematically examine structural, mechanical, electronic and magnetic stability to explore the potential properties of these compounds.

COMPUTATIONAL DETAIL

In order to explain the interaction between atomic core and valence electrons, the first principles calculations are made using the full potential linearized aungumated plane wave (FP-LAPW) method implemented in the WIEN2k simulation code [9,10]. The electronic wave function is extended keeping in mind the valance electrons. Generalized gradient approximation (GGA) is used at Perdew-Burke-Ernzerhof (PBE) to define the energy of exchange-correlation [11-13]. To optimize the geometry of the electronic structure; we have used the FP-LAPW method, which is the part of the spin-polarized density functional theory (SDFT). The value of l_{max} is taken as 4 to extend the spherical harmonics in the atomic sphere. In the central region, the charge density and the potential were developed as Fourier series

with a wave vector up to $G_{max} = 12$. The muffin-Tin radii of a particular atomic sphere as per the alloys studied and are listed in Table 1 [14]. The RK_{max} value are 6.68, 6.85, 6.84, 6.86 for CoVZ (Z= Si, Ge, Sn, Pb). Core states are considered relativistic and valence states are considered semi-relativistic, and the energy between these two states has been set -6.0 Ry. The SCF cycle are considered to be converged; when the energy difference and the integration of absolute charge density difference between subsequent iterations is less than 10^{-5} Ry and 0.001 Coulomb/formula unit respectively. Total numbers of K - point are kept 1000 for irreducible Brillouin zones in Wien2k. ElaStic_1.0 based on ab initio total-energy and/or stress calculations is used to calculate the full second-order elastic stiffness tensor for crystal structures. The maximum absolute value for Lagrangian strain is considered to be 0.5 with number of distorted strain structure are set to value 11.

Table 1.

For the prevention of overlapping spheres during the SCF process, the muffin-Tin radii of the specific atomic sphere for optimized lattice parameter of the individual alloy are shown.

Compounds Atom	CoVSi	CoVGe	CoVSn	CoVPb
Co	2.2	2.30	2.36	2.35
V	2.09	2.19	2.30	2.35
Z	1.82	2.19	2.36	2.47

RESULT AND DISCUSSION

The lattice constants were determined in the first step. The total energies are measured as a function of the lattice constant for the said compounds with a half-Heusler structure. The constants for the equilibrium lattice were obtained by minimizing the total energy.

Structural Properties

Half-Heusler compounds, crystallize in the face-centered cubic having structurbericht designation C1b with the space group F-43 m. These compounds can be viewed as V and Co form zinc blend sublattice arranged in a primitive cell at Wyckoff positions $(0, 0, 0)$ and $(\frac{1}{4},\frac{1}{4},\frac{1}{4})$; whereas NaCl sublattice is formed by V and Z at $(\frac{1}{2},\frac{1}{2},\frac{1}{2})$. Volume optimization has been performed for all possible arrangements of each compounds based on the Murnaghan equation of state. The volume vs. energy curves is shown in Figure1 and which has minimum energy and electronegativity order is to be considered [15-17].
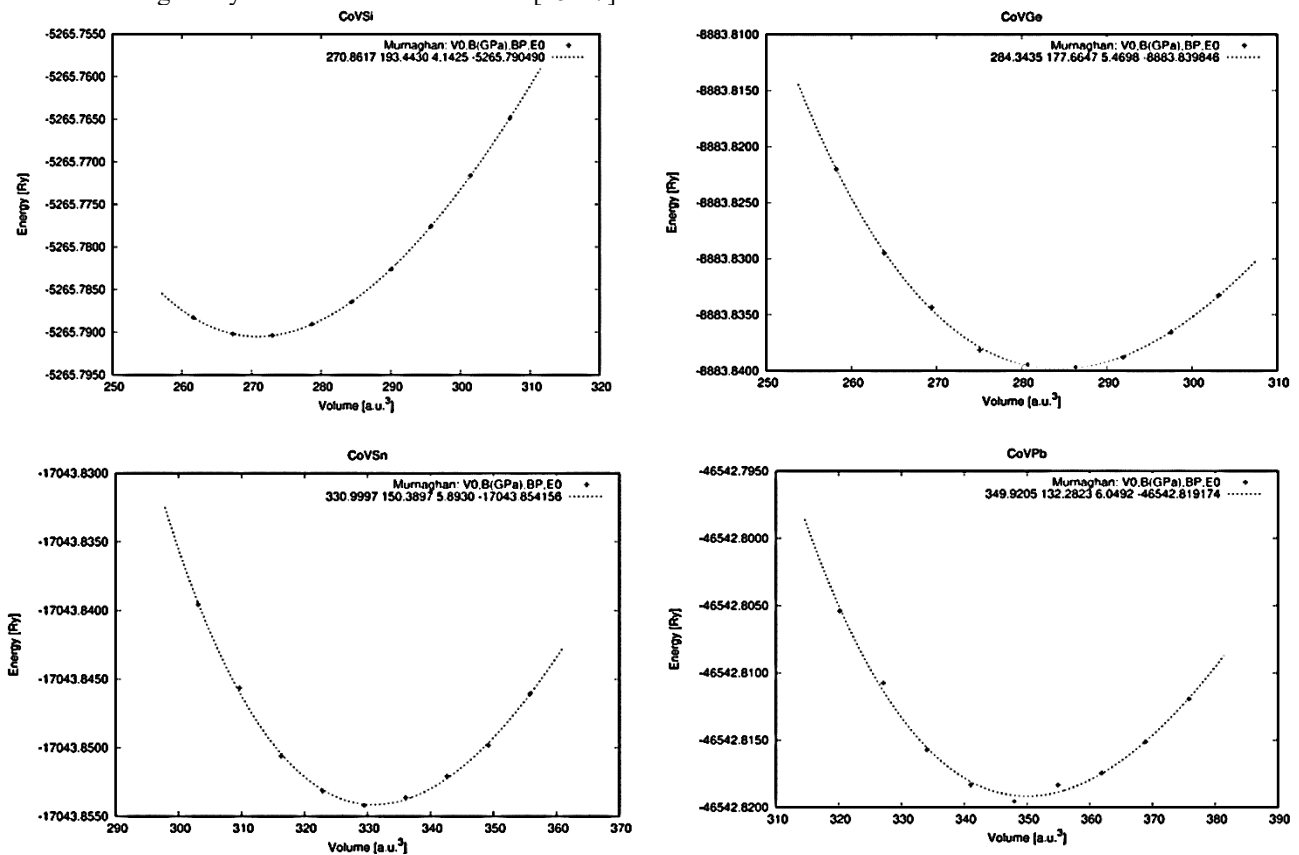
Figure 1. Total energy as a function of volume per formula unit corresponding to CoVSi, CoVGe, CoVSn and CoVPb alloys.

For the each arrangement electronegativity and energy for CoVPb are tabulated in Table 2.

Table 2.

We displayed the measured values of the equilibrium lattice constant a_0, equilibrium volume, the bulk modulus B (GPa), the bulk modulus pressure derivative and minimum energy during optimization.

	Co	**V**	**Pb**	**Energy (Ry)**	**Equilibrium Volume (a.u.³)**	**Band Gap (eV)**
Electronegativity	1.88	1.63	2.33			
Type a	$(\frac{1}{4},\frac{1}{4},\frac{1}{4})$	$(0, 0, 0)$	$(\frac{1}{2},\frac{1}{2},\frac{1}{2})$	-46542.82	349.97	0.69
Type b	$(\frac{1}{2},\frac{1}{2},\frac{1}{2})$	$(\frac{1}{4},\frac{1}{4},\frac{1}{4})$	$(0, 0, 0)$	-46542.73	389.50	0
Type c	$(0, 0, 0)$	$(\frac{1}{2},\frac{1}{2},\frac{1}{2})$	$(\frac{1}{4},\frac{1}{4},\frac{1}{4})$	-46542.67	415.20	0

Murnaghan's state equation [18] provides the total energy and pressure value as a function of volume and is described as:

$$E(V) = E_O + \left[\frac{BV}{B_P}\left(\frac{1}{(B_P - 1)}\left(\frac{V_O}{V}\right)^{B_P} + 1\right) - \frac{BV_O}{(B_P - 1)}\right]$$

$$P(V) = \frac{B}{B_P}\left\{\left(\frac{V_O}{V}\right)^{B_P} - 1\right\}$$

The structural parameters values have been presented in Table 3. To predict the electronic and magnetic properties of compounds, the optimized value of the lattice constant was used for the DOS, band structures and magnetic moment calculations.

Table 3.

Calculated values of the equilibrium lattice constant a_o, equilibrium volume, the bulk modulus B (GPa), the pressure derivative of bulk modulus B_P and minimum energy during optimization.

Compound	Lattice Parameter (A⁰)	Equilibrium Volume (V_0)	Bulk Modulus (GPa)	B_P	Energy
CoVSi	5.44	270.85	193.97	4.42	-5265.79
CoVGe	6.30	283.89	176.87	10.77	-8883.84
CoVSn	5.81	330.99	150.23	5.89	-17043.85
CoVPb	5.92	349.97	131.67	5.82	-46542.82

Electronic Properties

To get an in-depth analysis of the electronic structure for the CoVZ alloys (Z = Si, Ge, Sn, Pb), which have 18 valence electrons respectively, we first analysis their complete DOS configuration. Because the half-metallic band gap is an important factor in these materials partial DOS are also shown in Fig. 2 for all the four compounds.
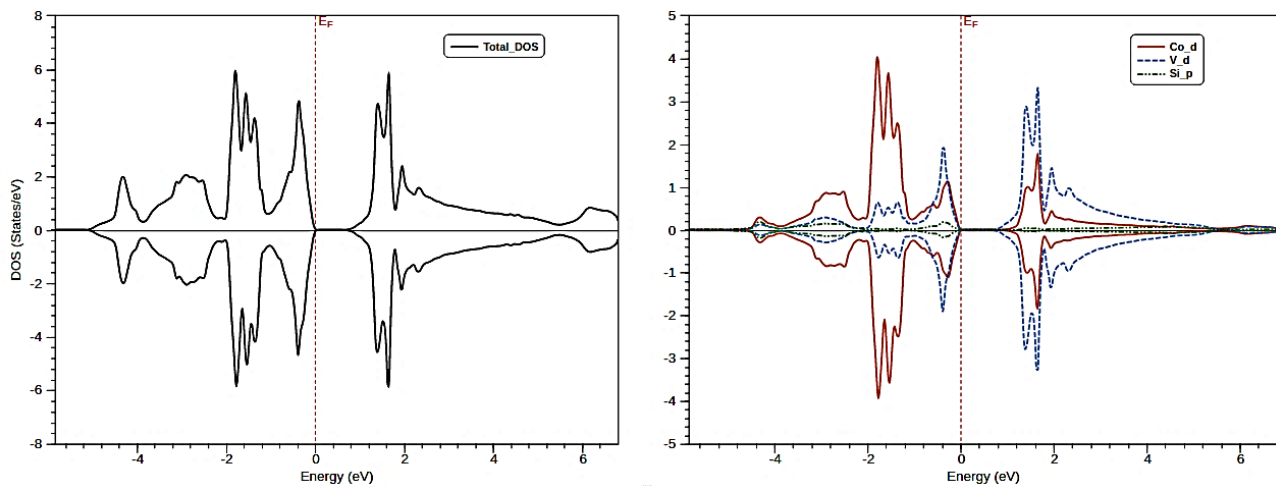
Figure 2. Total and atomic spin- density of states of all the compounds at their equilibrium lattice constant. Negative of DOS axis represents the minority spin (*Continued on next page*)
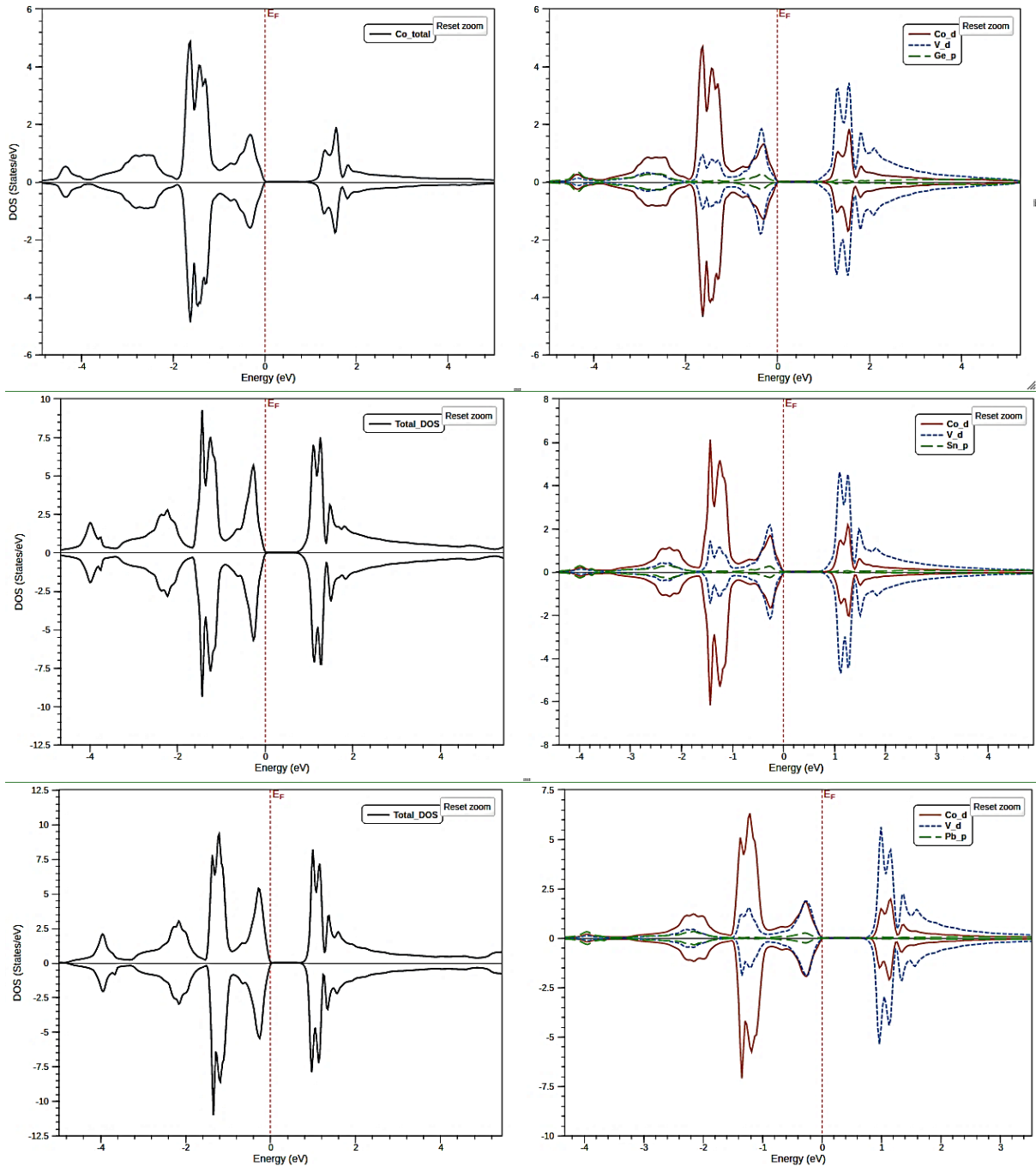
Figure 2. Total and atomic spin-density of states of all the compounds at their equilibrium lattice constant
Negative of DOS axis represents the minority spin

As illustrated in Fig. 2, their shapes are similar and the characters can be defined as follows: the low-energy component below -4.5eV, -3.7 eV, -4 eV, -3.5 eV is primarily the p states of the Si, Ge, Sn, Pb atom in the occupied valence states, which hybridize the Co atoms with and d electrons and decide the degree of occupation of the p – d orbitals. 3d metal atom states range from -0.5 to + 5.3eV, and hybridize with each other. CoVZ chemical bonding character can be studied from the density of State. It is evident from the partial densities of the figure below that the key mechanism of the chemical bond is the hybridization between the Co and V's d- states. Chemical bond has a covalent and ionic character at the same time, covalent since the d states of both transition elements are strongly hybridized and degenerate over much of their extension and ionic because the relative quantity of the 3d states of Co and V is different below and above Fermi point, the 3d states of V dominate.

To determine the band gap, we have also calculated the band structures of Half-Heusler compounds as shown in Figure 4. In the band structure of all half Heusler compounds, the valence band maximum (VBM) is at the W-point and the conduction band minimum (CBM) at the X-point. Thus, the band structure shows semiconducting behavior with an indirect energy gap. The origin of the gap is mainly attributed to the covalent hybridization between the d-states of the Co and V atoms, leading to the formation of bonding and anti-bonding bands with a gap in between [19].
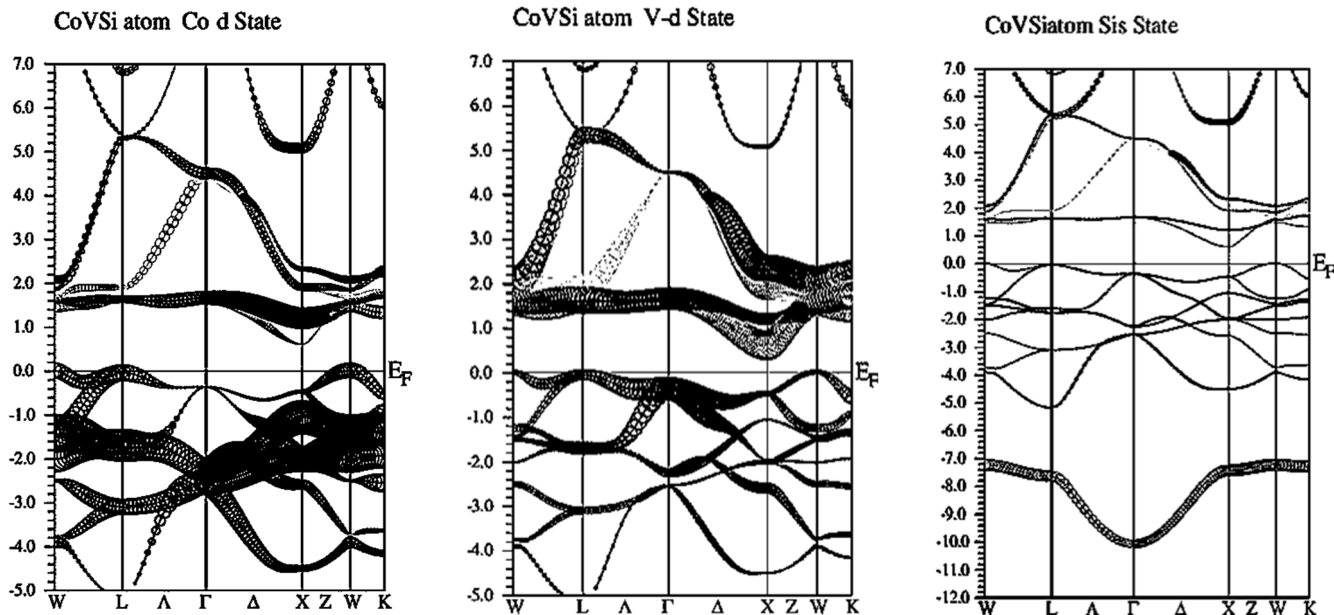
Figure 3. Orbital projected band structure of CoVSi for Co-d, V-d & Si-p states.

The orbital projected band structures (wide bands) of CoVSi as shown in Figure 3. The nearest V coordinating neighbors are 4 Co and 4 Si atoms. Analogous to the binaries, we have obtained in Figure 3 that the lowest bands below -5 eV are Si - p bands, separated by a pseudo gap from seven primarily V - d bands, which in turn are separated by an indirect gap from relatively wide Co-d bands. The relative positions of the Fe d and V d levels with respect to the Sb p levels are summarized in Table 4. The characteristic feature of all half-Heusler compounds is a d–d gap close to the Fermi level. All the states below this gap are occupied for the 18 valence electrons compounds; due to this the compound with 18 valence electrons doesn't have half metallic nature as shown by compounds with more than 18 valence electrons.

Table 4.

Indirect band gaps for hybridized d states and total energy band gaps

Compound	Co			V			E_g	Band Transition
	E_d	E_{eg}	E_{t2g}	E_d	E_{eg}	E_{t2g}		
CoVSi	0.44	0.45	0.61	0.23	0.28	0.56	0.59	W→X
CoVGe	0.51	0.53	0.71	0.28	0.29	0.64	0.69	L→X
CoVSn	0.45	0.5	0.64	0.21	0.57	0.55	0.66	L→X
CoVPb	0.47	0.48	0.71	0.16	0.28	0.49	0.69	L→X
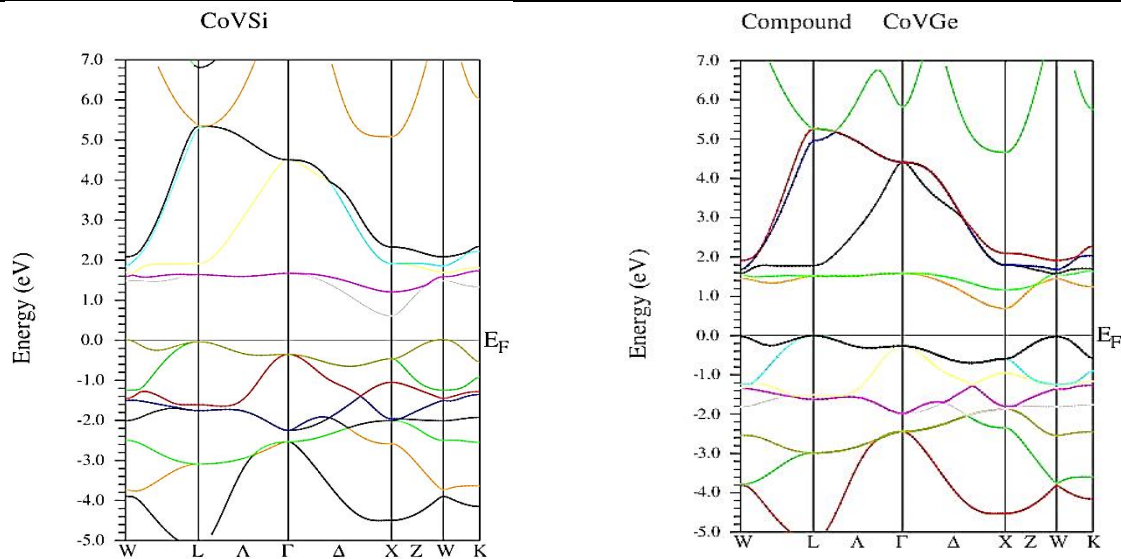
Figure 4. Band structure diagram of compounds corresponding to their equilibrium lattice constant.
(*Continued on next page*)
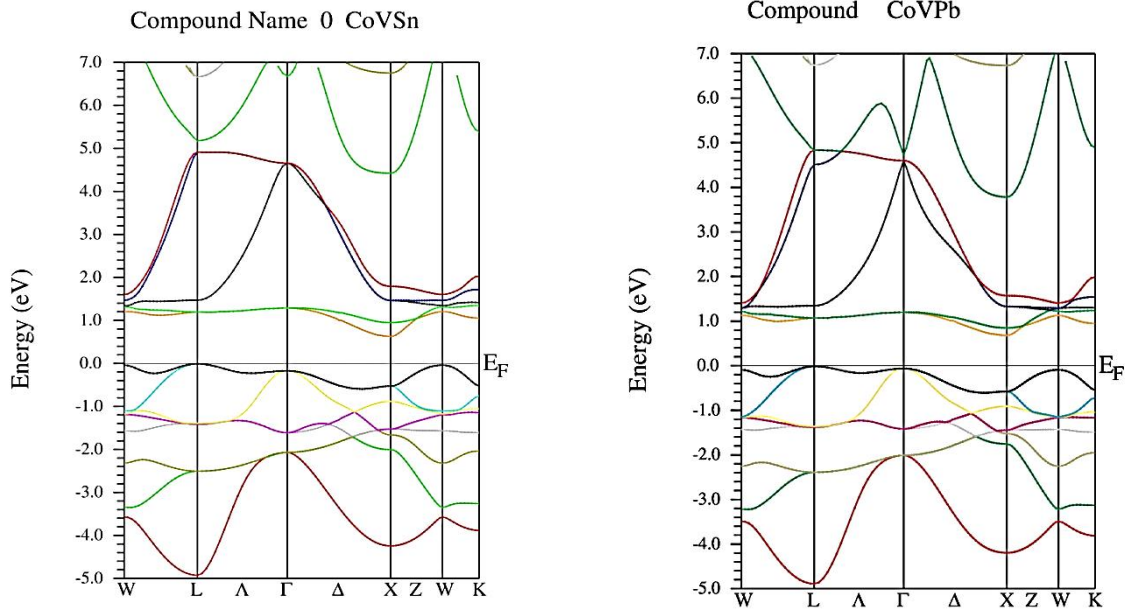
Compound Name 0 CoVSn

Compound   CoVPb

Figure 4. Band structure diagram of compounds corresponding to their equilibrium lattice constant.

Elastic properties

Hardness, stress and other structural deformations caused by pressure have been examined with the help of elastic constant. These constants play an important role in studying the Poisson ration effect, Young's modulus, Shear modulus, Debye temperature, and melting temperature of solid. They have three distinct elastic constants for cubic crystal namely C_{11}, C_{12} and C_{44}. Here the C_{ij} are the elastic constant tensors (in Voigt notation) resulting from the change in internal energy deformation [20,21]. The bulk modulus B defines the resistance of the solid to volume change and the shear modulus takes into account its resistance to shear deformation preserving volume.

Mechanical stability. Elastic structures play a significant role in the research and development of materials. Elastic tensors of any order are characterized by Taylor's expansion of the elastic energy or stress in terms of the applied strain. To define the dynamic and mechanical behavior of studied alloys there are three second – order elastic constants (SOEC) C_{11}, C_{12} and C_{44} need to be determined. According to Hooke's law, for cubic crystal structures, there are only three distinct elastic constants C_{11}, C_{12} and C_{44}. From the symmetry of the second – order elastic constant matrix in Voigt notation

$$C_{11}=C_{22}=C_{33}; \qquad\qquad C_{12}=C_{13}=C_{23}; \qquad\qquad C_{44}=C_{55}=C_{66}.$$

None of the eigen value of elastic constant matrix is zero confirms the stability of compound.
Apart from this condition, the stability criteria based on Born's theory given below [22]

$$C_{11}>0; \qquad C_{44}>0; \qquad C_{11}>|C_{12}|; \qquad\qquad (C_{11}+2C_{12})>0.$$

Computation of elastic properties. The elastic constants of the cubic crystals are assumed to be compatible with the above stability conditions, so studied XYZ compounds are mechanically stable. Different elastic properties based on SOEC's have shown in Table 5, 6 and 7 in Voigt, Reuss and Hill averaging scheme from elastic constants [23, 24]. The Shear constant C_S and elastic stiffness constant C_L are expressed in terms of SOECs as

$$C_S = \frac{C_{11}-C_{12}}{2}, \ \ C_L = \frac{C_{11}+C_{12}+2C_{44}}{2}$$

Bulk modulus (B), the measure of compressibility resistance have measured using the expression

$$B = \frac{C_{11} + 2C_{12}}{3}$$

The bulk modulus for a cubic structure is same for Voigt, Reuss and Hill averages [25].Shear modulus (G) is the deformation caused by force applied on any parallel face by keeping opposite face fixed by applying opposite forces,

$$G_V = \frac{C_{11}-C_{12}+3C_{44}}{5} \qquad \text{and} \qquad G_R = \frac{5C_{44}(C_{11}-C_{12})}{4C_{44}+3(C_{11}-C_{12})}$$

The Young's modulus (E) and Poisson's ratio (η) are calculated by the following relation [26]

$$E = \frac{9BG}{3B+G} \qquad \text{and} \qquad \eta= \frac{3B-E}{6B}$$

To quantify the anisotropy of these cubic crystals Zener's anisotropy index (A) can be calculated as

$$A = \frac{2C_{44}}{C_{11} - C_{12}}$$

The degree of elastic anisotropy (A*) has some practical importance. If A* has value zero or A=1 crystal represent elastic isotropy and A* gives relative magnitude of the actual elastic anisotropy possessed by crystal.

$$A^* = \frac{3(A-1)^2}{\{3(A-1)^2 + 25A\}}$$

Kleinman parameter (ζ) and Lame's coefficient (λ) for cubic crystals can be obtained as:

$$\zeta = \frac{C_{11} + 8C_{12}}{7C_{11} + 2C_{12}}; \qquad \lambda = C_{12} - \frac{A}{5}$$

Hardness of a material is determined by Vickers hardness factor (H$_V$) followed by relation [27]

$$H_V = 2[(K^2 G)^{0.585} - 3]$$

Where K is the Pugh ratio define as [28]; $K = \frac{B}{G}$

Table 5.
Elastic constants of CoVSi,CoVGe,CoVSn and CoVPb in the units of GPa.

Compounds	CoVSi	CoVGe	CoVSn	CoVPb
C$_{11}$	295.10	294.20	223.60	204.60
C$_{12}$	135.70	113.30	108.80	106.90
C$_{44}$	89.00	119.30	92.70	82.60

Table 6.
Voigt bulk modulus(B$_V$), shear modulus(G$_V$), Young modulus (Ev), Poisson ratio(η$_V$), Reuss bulk modulus(B$_R$), shear modulus(G$_R$), Young modulus (E$_H$), Poisson ratio(η$_V$), Hill bulk modulus(B$_H$), shear modulus(G$_H$), Young modulus (E$_H$), Poisson ratio(η$_H$) and B/G ratio calculated from ElaStic_1.0.

Compounds	CoVSi	CoVGe	CoVSn	CoVPb
B$_V$= B$_R$= B$_H$	188.84	173.60	147.07	139.47
G$_V$	85.25	107.78	78.58	69.09
G$_R$	85	105.83	74.39	64.72
G$_H$	85.13	106.81	76.48	66.90
E$_V$	222.30	267.91	200.11	177.89
E$_R$	221.73	263.87	190.96	168.14
E$_H$	222.02	265.89	195.55	173.04
η$_V$	0.30	0.24	0.27	0.29
η$_R$	0.30	0.25	0.28	0.30
η$_H$	0.30	0.24	0.28	0.29
B$_H$/G$_H$	2.22	1.63	1.92	2.09

Table 7.
Values of Zener anisotropy index (A), degree of elastic anisotropy in percentage (A*), Kleinman parameter (ζ), Lame's coefficient (λ), Pugh ratio (K) and Vickers hardness of material.

Compounds	CoVSi	CoVGe	CoVSn	CoVPb
A	1.12	1.32	1.62	1.69
A*(%)	0.15	0.92	2.75	3.27
ζ	0.59	0.53	0.61	0.64
λ	-0.05	-0.14	-0.13	-0.12
K	0.45	0.62	0.52	0.48
H$_V$	4.61	11.4	5.77	3.9

Thermodynamic Properties

Many physical properties of solids such that acoustic velocity, specific heat capacity, thermal expansion coefficient, elastic constants and melting temperature are related to Debye's temperature [29]. At low temperature, the vibrational excitation is induced solely by the acoustic vibrations, so that Debye temperature derived from elastic constants is the same as that determined by specific heat measurements. From the data of elastic properties of the materials, we have calculated the wave velocity V$_S$, longitudinal wave velocity V$_P$ and average wave velocity V$_m$ and obtained from Navier's equation given below listed in Table 8 [30, 31]

$$V_S = \left[\frac{G_H}{\rho}\right]^{\frac{1}{2}}; \quad V_P = \left[\frac{B_H + \frac{4}{3}G_H}{\rho}\right]^{\frac{1}{2}}; \quad V_m = \left[\frac{\frac{2}{V_S^3} + \frac{1}{V_P^3}}{3}\right]^{\frac{-1}{3}}$$

Another method to calculate Debye temperature is to estimate it from average elastic wave velocity V_m is represented as

$$\theta_D = \frac{\hbar}{k}\left[\frac{3n}{4\pi}\left(\frac{N\rho}{M}\right)\right]^{1/3}\nu_m$$

here h, K, N, n, M are plank's constant, Boltzmann's constant, Avogadro's number, number of atoms per formula unit, molecular mass per formula unit respectively, $\rho = M/V$ is the density of compound.

Table 8.

Thermodynamic parameters shear wave velocity (V_S), compression wave velocity (V_p), average wave velocity (V_m), molecular mass (M), crystal volume (V), density (ρ).

Compounds	CoVSi	CoVGe	CoVSn	CoVPb
M(g/mol)	137.96	182.51	228.58	317.07
V(a.u^3)	160.99	250.05	367.06	543.34
ρ(g/cc)	5.69	4.85	7.74	10.15
V_S	3867.99	4692.83	3143.43	2567.32
V_P	7289.48	8072	5672.40	4746.48
V_m	4322.68	5206.73	4787.94	4634.16
θ_D	565	588	586	556

SUMMARY AND CONCLUSIONS

In this paper, we have presented first-principles calculations on cubic CoVZ (Z = Pb, Si, Sn, Ge) half Heusler compounds including structural parameters, structural stability, band structure, density of state, elastic constants, Debye temperature and velocity of the acoustic wave in different directions. We have observed that for structure stabilities of these Heusler compounds, the electronegativity is an important factor to select the suitable structural arrangement. These compounds have indirect band gap and can be used in solar cell applications over the similar compounds obey Nowotny–Juza phase. Apart from this, these compounds also have useful aspects towards thermoelectric devices and topological insulators. Elastic properties of these compounds show that they have ductile nature except CoVGe, which is close to ductility. The Poisson ratio of CoVGe represent covalent character and others have metal character; which have predicted by their narrow band gaps. The hardness of materials can be compared by arranging them in decreasing order i.e. CoVGe>CoVSn>CoVSi>CoVPb. Debye's temperature is also calculated with the help of compressed, strained, average wave velocities.

ORCID IDs

Lalit Mohan, https://orcid.org/0000-0003-3323-8296; **Sukhender,** https://orcid.org/0000-0002-2149-5669
Sudesh Kumar, https://orcid.org/0000-0002-7507-4712; **Shiv R. Bhardwaj,** https://orcid.org/0000-0002-1895-158X
Ajay Singh Verma, https://orcid.org/0000-0001-8223-7658

REFERENCES:

[1] G.E Bacon, and J.S Plant, J. Phys. F: Metal. Phys. **1,** 524-532 (1971), https://doi.org/10.1088/0305-4608/1/4/325.
[2] A. Zakutayev, X. Zhang, A. Nagaraja, L. Yu, S. Lany, T. O. Mason, D. S. Ginley, and A. Zunger, J. Am. Chem. Soc. **135** (2013) 10048-10054, https://doi.org/10.1021/ja311599g.
[3] P. Villars, and L.D Calvert, *Pearson's handbook of crystallographic data for intermetallic phases*, (ASM International, Materials Park, OH, 1991).
[4] J. Nuss, and M. Jansen, Z. Anorg. Allg. Chem. **628**, 1152-1157 (2002), https://doi.org/10.1002/1521-3749(200206)628:5%3C1152::AID-ZAAC1152%3E3.0.CO;2-1.
[5] C. Felser, G. H Fecher, and B. Balke, Ang. Chem. Int. Ed. Engl. **46**, 668-699 **(**2007), https://doi.org/10.1002/anie.200601815.
[6] J. Pierre, R.V. Skolozdra, J. Tobola, S. Kaprzyk, C. Hordequin, M.A. Kouacou, I. Karla, R. Currat, and E. Leliévre-Berna, Properties on request in semi-Heusler phases, J. Alloys & Comp. **262**, 101-107 (1997), https://doi.org/10.1016/S0925-8388(97)00337-X.
[7] K. Chen, and L.R. Zhao, J. App. Phy. **93**, 2414 (2003), https://doi.org/10.1063/1.1540742.
[8] K. Chen, L.R. Zhao, J.S. Tse, and J.R. Rodgers, Phys. Lett. A. **31**, 400-403 (2004), https://dx.doi.org/10.1016/j.physleta.2004.09.034.
[9] P. Blaha, K. Schwarz, F. Tran, R. Laskowski, G.K.H Madsen, and D.L. Marks, J. Chem. Phys. **152**, 074101 (2020), https://doi.org/10.1063/1.5143061.
[10] K. Schwarz, P.G.K. Blaha, and H. Madsen, Comput. Phys. Commun. **147**, 71 (2002), http://sciold.ui.ac.ir/~sjalali/jalali/paper/LAPW/compu_phys_commu147_71_02.pdf.
[11] Z. Wu, and R.E. Cohen, Phys. Rev. B **73**, 235116 (2006), https://doi.org/10.1103/PhysRevB.73.235116.
[12] F. Tran, R. Laskowski, P. Blaha, and K Schwarz, Phys. Rev. B **75**, 115131 (2006), https://doi.org/10.1103/PhysRevB.75.115131.
[13] J. P Perdew, K Burke, and M Ernzerhof, Generalized gradient approximation made simple, Phys. Rev. Lett. **77**, 3865 (1996).

[14] B.M. Wong, and J.G. Cordaro, J. Phys. Chem. C **115**, 18333-18341 (2011), https://doi.org/10.1021/jp204849e.

[15] H.U. Schuster, H.W. Hinterkeuser, W. Schäfer, and G. Will, Z. Naturforsch. B, **31**, 1540-1541 (1976).

[16] H. Hohl, A. P. Ramirez, C. Goldmann, G. Ernst, B. Wolfling, and E. Bucher, J. Phys. Condens. Matter. **11**, 1697–1709 (1999), https://doi.org/10.1088/0953-8984/11/7/004.

[17] C.P. Sebastian, H. Eckert, S. Rayaprol, R.D. Hoffmann, and R. Pöttgen, Solid State Sciences, **8**(5), 560-566 (2006), https://doi.org/10.1016/j.solidstatesciences.2006.01.005.

[18] F.D. Murnaghan, Proc. Natl. Acad. Sci. **30**, 244–247 (1944), https://dx.doi.org/10.1073%2Fpnas.30.9.244.

[19] J. Toboła, and J. Pierre, J. Alloys and Comp. **296**, 243-252 (2000), https://doi.org/10.1016/S0925-8388(99)00549-6.

[20] M. Catti, Acta Cryst. A, **45**, 20-25 (1989), https://doi.org/10.1107/S0108767388008748.

[21] P. Dobson, Physics Bulletin, **36**, 506-506 (1985), https://doi.org/10.1088/0031-9112/36/12/027.

[22] M. Born, and K. Huang, Acta Cryst. **9**, 837-838 (1956), https://doi.org/10.1107/S0365110X56002370.

[23] W. Voigt, *Lehrbook der Kristallphysik*, (Teubner, Leipsig, 1928).

[24] I.R. Shein, and A.L. Ivanovskii, Scr. Mater. **59**, 1099-1102 (2008), https://doi.org/10.1016/j.scriptamat.2008.07.028.

[25] R. Hill, Proc. Phys. Soc. Lond. A, **65**, 349 (1952), https://doi.org/10.1088/0370-1298/65/5/307.

[26] A.M. Blanco, E. Francisco, and V. Luana, Comput. Phys. Commun. **158**, 57 (2004), https://doi.org/10.1016/j.comphy.2003.12.001.

[27] A.S. Verma, and S.R. Bhardwaj, J. Phys. Condens. Matter, **19**, 026213 (2006), https://doi.org/10.1088/0953-8984/19/2/026213.

[28] S.F. Pugh, Philos. Mag. **45**, 823 (1953), https://doi.org/10.1080/14786440808520496.

[29] E. Schreiber, O.L. Anderson, and N. Soga, *Elastic Constants and Their Measurements*, (McGraw-Hill, New York, 1973), pp. 196.

[30] T. Ichitsubo, H. Ogi, S. Nishimura, T. Seto, M. Hirao, and H. Inui, Phys. Rev. B, **66**, 052514 (2002), https://doi.org/10.1103/PhysRevB.66.052514.

[31] E. Franciso, M.A. Blanco, and G. Sanjurjo, Phys. Rev. B, **63**, 094107-094115 (2001), https://doi.org/10.1103/PhysRevB.63.094107.

СТРУКТУРНІ, ЕЛЕКТРОННІ, МЕХАНІЧНІ І ТЕПЛОВІ ВЛАСТИВОСТІ НАПІВХЕЙСЛЕРОВИХ СПОЛУК CoVZ (Z = Si, Ge, Sn, Pb)

Лаліт Мохан[a], Сукхендер[a], Судеш Кумар[b], Шив Р. Бхардвадж[c], Аджай Сингх Верма[a]
[a]Фізичний факультет, Банастхалі Відьяпітх, Банастхалі 304022, Індія
[b]Хімічний факультет, Банастхалі Відьяпітх, Банастхалі 304022, Індія
[c]Фізичний факультет, Коледж Б.С.А., Матхура 282004, Індія

Напівхейслерові сполуки демонструють незвичайну поведінку через їх змінну ширину забороненої зони, а також через їх металеву, і напівметалеву природу. Ці сполуки можуть використовуватися в різних застосуваннях залежно від ширини забороненої зони. Ми обговорили структурні, електронні, пружні і магнітні властивості CoVZ (Z = Pb, Si, Sn, Ge) використовуючи код моделювання WIEN2k, який заснований на теорії функціонала щільності (DFT). Ми оптимізували всю можливу структурну конфігурацію кожного з'єднання і розглянули, яка з них оптимізована з найменшою енергією і найменшим рівноважним об'ємом. Для визначення енергії кореляції електронного обміну в обох платформах використовується наближення узагальненого градієнта (GGA). Ми також отримали індивідуальні пружні постійні, модуль зсуву, модулі Юнга, відношення B/G і коефіцієнт Пуассона, які показують, що ці сполуки пластичні, за винятком сполук CoVGe, які показують низьку пластичність. Температури Дебая розраховані по швидкості хвилі стиснення, швидкості зсувної хвилі та їх середнього значення.

КЛЮЧОВІ СЛОВА: напівхейслерові сполуки, структурні властивості, електронні властивості, механічні властивості

СТРУКТУРНЫЕ, ЭЛЕКТРОННЫЕ, МЕХАНИЧЕСКИЕ И ТЕПЛОВЫЕ СВОЙСТВА ПОЛУХЕЙСЛЕРОВЫХ СОЕДИНЕНИЙ CoVZ (Z = Si, Ge, Sn, Pb)

Лалит Мохан[a], Сукхендер[a], Судеш Кумар[b], Шив Р. Бхардвадж[c], Аджай Сингх Верма[a]
[a]Физический факультет, Банастхали Видьяпитх, Банастхали 304022, Индия
[b]Химический факультет, Банастхали Видьяпитх, Банастхали 304022, Индия
[c]Физический факультет, Колледж Б.С.А., Матхура 282004, Индия

Полухейслеровы соединения демонстрируют необычное поведение из-за их переменной ширины запрещенной зоны, а также как металлической, так и полуметаллической природы. Эти соединения могут использоваться в различных приложениях в зависимости от ширины запрещенной зоны. Мы обсудили структурные, электронные, упругие и магнитные свойства CoVZ (Z = Pb, Si, Sn, Ge) с помощью кода моделирования WIEN2k, основанного на теории функционала плотности (DFT). Мы оптимизировали всю возможную структурную конфигурацию каждого соединения и рассмотрели, какая из них оптимизирована с наименьшей энергией и наименьшим равновесным объемом. Для определения энергии корреляции электронного обмена в обеих платформах используется приближение обобщенного градиента (GGA). Мы также получили индивидуальные упругие постоянные, модуль сдвига, модули Юнга, отношение B/G и коэффициент Пуассона, которые показывают, что эти соединения пластичны, за исключением CoVGe которые показывают низкую пластичность. Температуры Дебая рассчитаны по скорости волны сжатия, скорости волны сдвига и их среднему значению.

КЛЮЧЕВЫЕ СЛОВА: полухейслеровы соединения, структурные свойства, электронные свойства, механические свойства

ELECTRONIC, OPTICAL, ELASTIC AND MAGNETIC PROPERTIES OF CO₂VZ (Z= As, B, In, Sb) FULL HEUSLER COMPOUNDS

Sukhender[a], Lalit Mohan[a], Sudesh Kumar[b], Shiv R. Bhardwaj[c], Ajay Singh Verma[a],*

[a]Department of Physics, Banasthali Vidyapith, Banasthali 304022, India
[b]Department of Chemistry, Banasthali Vidyapith, Banasthali 304022, India
[c]Department of Physics, B. S.A. College, Mathura 282004, India
*Corresponding Author: ajay_phy@rediffmail.com
Received June 26, 2020; accepted October 2, 2020

Here in, we have investigated electronic, optical, elastic and magnetic properties of Co₂VZ (Z= As, B, In, Sb) full Heusler compounds by using two different computational methods. One is full potential linearized augmented plane wave (FP-LAPW) method as implemented in WIEN2k and second one is pseudo potential method as implemented in Atomistic Tool Kit-Virtual NanoLab (ATK-VNL). All these compounds show zero band gaps in majority spin channel in both computational codes and in minority-spin conduction band or valence band crosses the Fermi level. Magnetic moment calculated by these compounds Co₂VZ (Z= As, B, In, Sb) are 3.64 and 3.76, 2.00 and 1.97, 1.99 and 1.99, 3.96 and 3.82μ_B in WIEN2k and ATK-VNL simulation codes respectively. Optical properties of these compounds such as reflectivity, refractive index, excitation coefficient, absorption coefficient, optical conductivity and electron energy loss have been analyzed. Absorption coefficient and electron energy-loss function values are increases as we increase the value of energy. Absorption and reflection are inversely proportional to each other at same instant of time. Pugh's ratio B/G is greater than 1.75 for Co₂VZ (Z= B, In, Sb) compounds showing ductile in nature, but B/G value for Co₂VAs is less than 1.75, so this compound is brittle in nature. Values of Cauchy pressure ($C_P = C_{12} − C_{44}$) derived and these compounds Co₂VZ (Z= As, B, In, Sb) shows metallic nature.
KEYWORDS: band gap, Spintronics, magnetic moment, elastic constants

Half metallic ferromagnetism is those Heusler compounds, which shows zero band gap in spin up form representing metallic nature and a finite gap in spin down form exhibiting semiconducting nature [1-5]. Spin of electron is responsible for such type of dual nature of material and named as Spintronics. The materials which are metallic in majority spin and non-metallic in minority spin reveals 100% spin polarization at Fermi level [6-8]. Heusler alloys represent high magnetic moment and Curie temperature [9]. Due to such type of electronic and magnetic characteristics, half metallic ferromagnetic materials have wide application in Spintronics devices, such as magnetic tunneling junctions with tunnel magneto-resistance (TMR), magnetic sensors, spin torque oscillators (STO), non-volatile magnetic memory, spin light emitting diodes (LED) and so on. These devices increase the data processing speed and decrease the power consummation [10-15]. Ishida et al. [16] have put their results represent that the compounds Co₂MnZ (Z= Ge, Sn) are semi metals and showing 100% spin polarization. Shreder et al. [17] have studied the electronic, optical and magnetic properties of Fe₂TiAl, Fe₂Val and Fe₂CrAl. They observed radical conversion in band spectrum in domain of Fermi energy and when change Y= Ti, V, Al, there are significant changes in optical and electrical properties. Their results have good agreement with experimental results. Seema et al. [18] have studied the electronic, optical and magnetic properties of Co₂CrZ (Z= Al, Ga, Ge, Si). From their study, they have observed three types of disorders, namely DO₃, A₂ and B₂. In these disorders DO₃ and A₂ disorder leads decrease in the spin polarization and B₂ disorder retains the spin polarization at Fermi level. In this paper, we have performed the first principle calculation of the structural, electronic, optical, elastic and magnetic properties of Co₂VZ (Z= As, B, In, Sb) compounds, by using WIEN2k code and Atomistic Tool Kit-Virtual NanoLab (ATK-VNL) code within Generalized-gradient approximation (GGA) for exchange correlation functions.

COMPUTATIONAL DETAILS

We have performed by using full-potential linearized augmented plane wave (FP-LAPW) [19] executed by WIEN2k simulation code [20]. During optimization different parameters need to set, like $R_{mt}K_{max}$, k-point, lattice constant and optimized energy, Generalized-gradient approximation (GGA). Where R_{mt} denote plane wave smallest radius of muffin-tin sphere and K_{max} is used for elaboration of flat wave function by making maximum modulus of reciprocal lattice vector. Here $R_{mt} K_{max}$ (cutoff parameter), which is used for control the basis set size and we set 7.0 values for this. The energy between two states (core states are considered relativistically and valence states are considered as semi-relativistic) was set 6.0Ry. In first Brillouin zone, we fix 1000 k-points. This value of k-points is increased to 10000, when we calculate the optical properties of Heusler compounds. Angular momentum is used to expand the spherical harmonics in the atomic sphere taken as $l_{max} = 10$. In the central region the charge density and potential were elaborated with wave vector up to $G_{max}=10$. The value of energy convergence criterion was set to 0.0001Ry. For the each atom muffin tin sphere radii (R_{MT}) are tabulated in Table 1.

Muffin tin radius (R_{MT}) for Co_2VZ (Z= As, B, In, Sb).

R_{MT} (a.u.)	Compound			
	Co_2VAs	Co_2VB	Co_2VIn	Co_2VSb
Co	2.35	2.20	2.37	2.21
V	2.24	2.09	2.31	2.15
Z	2.24	1.82	2.37	2.21

A pseudo-potential method has been carried out in the framework of density functional theory is also apply for study of above physical fundamental properties of full Heusler alloys, used by a code Atomistic Tool Kit-Virtual NanoLab (ATK-VNL) [21]. Electronic and magnetic properties of Co_2VZ (Z= As, B, In, Sb) are calculated by using Pulay Mixer algorithm. Double-zeta (ζ) polarized basis set is applied for expanding the electron wave function and GGA (Generalized-gradient approximation) for exchange-correlation functional. When each atom achieves force convergence criteria 0.05 eV/Å; then we have obtained an optimized structure of a compound having maximum stress is 0.05 eV/Å^3. Maximum 200 numbers of steps are executed with a fix step size 0.2 Å for the optimization. Convergence is achieved by deciding mesh cutoff energy on the ground of convergence principle and for this computation 150 Ryd has been projected all over calculation as the most favorable after several convergence tests. Initial state has been selected up and down for spin polarization purpose in an atom. We used 10 x 10 x 10 Monkhorst-Pack k-mesh [22] for brillouin zone sampling to maintain balance between computational time and for accuracy results. Further, no any constrain in x, y and z directions are applied for structure optimization.

RESULTS AND DISCUSSIONS
Structural parameters

In this study, we have concentrated on the Full Heusler compounds with formula X_2YZ and having atomic composition 2:1:1. They are inter-metallic alloys formed by four penetrating FCC-lattices with atomic positions at X_1 (1/4, 1/4, 1/4), X_2 (3/4, 3/4, 3/4), Y (1/2, 1/2, 1/2) and Z (0, 0, 0). Where X and Y atoms are transition metal and Z is main group metal or semimetal. Their cubic lattice structure is of the $L2_1$ type having space group Fm-3m (no. 225) [23]. The equation of state given by Murnaghan [24] gives the value of total energy and pressure as a function of volume is stated as:

$$E(V) = E_O + \left[\frac{BV}{B_P} \left(\frac{1}{(B_P - 1)} \left(\frac{V_O}{V} \right)^{B_P} + 1 \right) - \frac{BV_O}{(B_P - 1)} \right]$$

$$P(V) = \frac{B}{B_P} \left\{ \left(\frac{V_O}{V} \right)^{B_P} - 1 \right\}$$

Pressure $(P) = -\frac{dE}{dV}$, $B_P = -V\frac{dP}{dV} = V\frac{d^2E}{dV^2}$

In the above equations E_0 is the minimum energy at T = 0K, B is the bulk modulus, B_P is the pressure derivative of the bulk modulus and V_o is the equilibrium volume. Structural optimization curves have been presented in figure 1. Comparison of lattice constants compiled from both the computational codes WIEN2k and ATK-VNL, revels the results that values of lattice constants of ATK-VNL are slightly greater than the lattice constants of WIEN2k. But in case of bulk modulus, there is a significant difference between the values generated by these computational codes. Bulk moduli of WIEN2k are slightly greater than the bulk modulus of ATK-VNL. The compound Co_2VSb have the lowest value of Pressure derivative while Co_2VIn have the highest value of Pressure derivative. Calculated values of the optimized lattice constant, equilibrium energy and pressure derivative have been presented in Table 2.

Lattice parameter, Bulk modulus, Equilibrium energy and Pressure derivative for Co_2VZ (Z= As, B, In, Sb).

Compound	Lattice Constants a_0 (Å)		Bulk modulus (GPa)		Equilibrium Energy (Ry)	Pressure derivative
	Calculated		Calculated			
	WIEN2k	ATK	WIEN2k	ATK		
Co_2VAs	5.814	5.794	170.66	182.91	-11994.720	4.193
Co_2VB	5.431	5.359	263.33	287.67	-7522.265	5.541
Co_2VIn	6.005	5.794	183.19	210.39	-19239.105	6.072
Co_2VSb	6.036	5.957	178.51	234.92	-20439.77	0.662
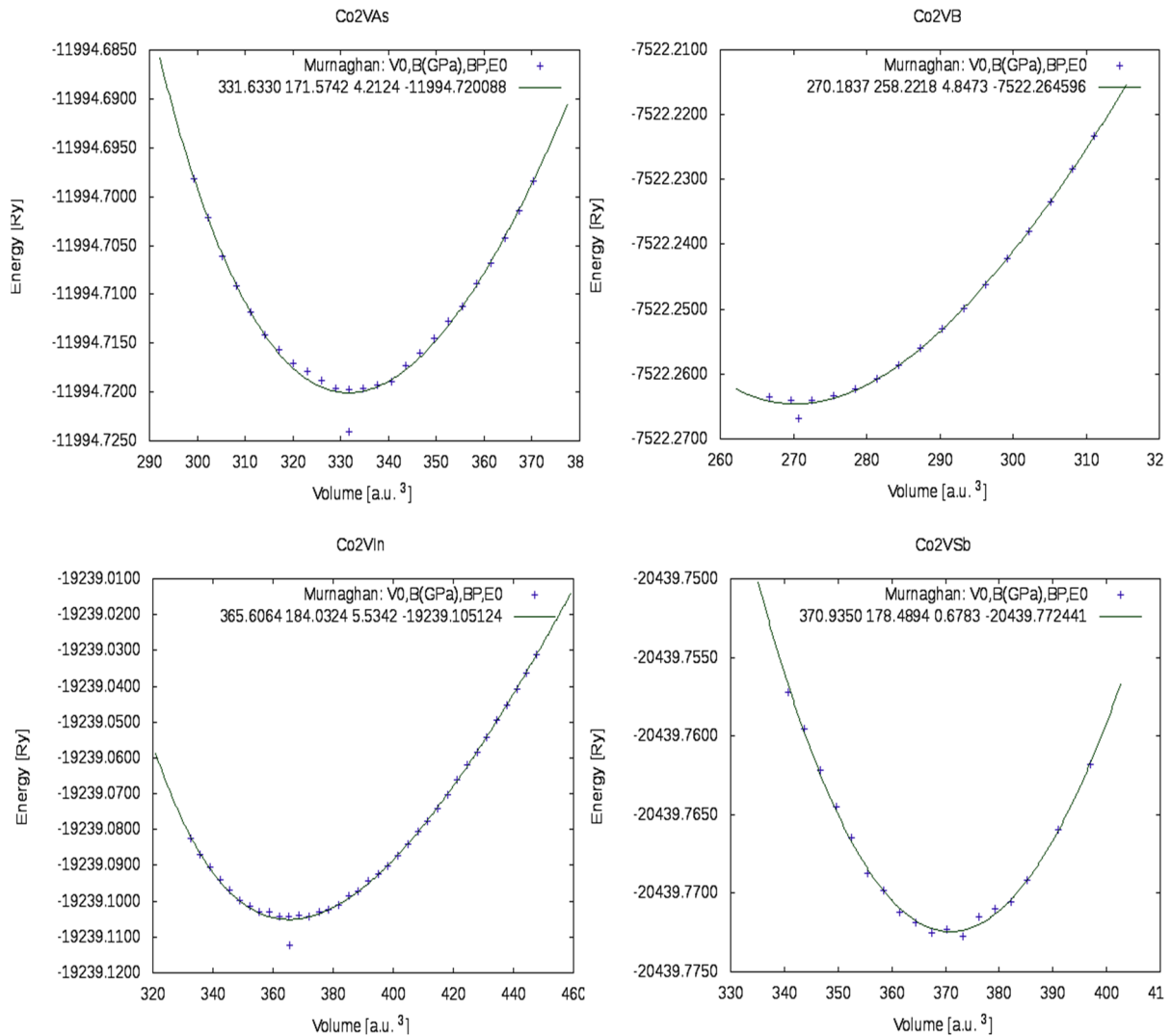
Figure 1. Volume optimization for the lattice parameters

Electronic and magnetic properties

Co-based Heusler alloys attracted researchers due to this trait half metallic ferromagnetic. Co-based Heusler alloys, which does not show any band gaps in up spin, are metallic by nature and down spin have a finite band gap and are semiconducting or insulating by nature. Then these Co-based materials are half metallic ferromagnetic showing 100% spin polarization at Fermi level. Now a day's Spintronics is a new growing field of research with numerous of applications. These materials have high Curie temperature and magnetic moment [25]. Due to such type of electronic and magnetic characteristics, half metallic ferromagnetic materials have wide application in Spintronics devices, such as magnetic tunneling junctions with tunnel magneto-resistance (TMR), magnetic sensors, spin torque oscillators (STO), non volatile magnetic memory, spin light emitting diodes (LED) and so on. These devices increase the data processing speed and decrease the power consummation. Different magneto-electronic and high processing devices are developed using the concept of Spintronics. These devices reduce electric power consummation and there is also decrease in heat dissipation. Spin polarized calculations of Co_2VZ (Z= As, B, In, Sb) compounds within Generalized-gradient approximation (GGA) have been carried out at the optimized lattice parameters. Value of spin polarization can be derived theoretically using the formula as given below.

$$P_n = \frac{n \uparrow - n \downarrow}{n \uparrow + n \downarrow}$$

If either $n_\uparrow = 0$ or $n_\downarrow = 0$, then $P_n = 1$ or -1. It means, if either up or down spin is existing then the spin polarization is 100%. These types of materials are known as half metals ferromagnetic. If the value of P_n is vanishes; then the materials are paramagnetic or anti-ferromagnetic even below the magnetic transition temperature. Study of energy gap from DOS and band structure of the compounds Co_2VZ (Z= As, B, In, Sb) shows that there are valence band extreme and conduction band extreme exists around the Fermi level. It is clear in minority spin that minima of conduction band crosses the Fermi level of compounds Co_2VZ (Z= As, B, Sb) and maxima of valence band touches the Fermi level of

compound. There does exist a significant band gap in WIEN2k code. The study of these graphs for those materials is near to half metallic. Both codes produce the same results with zero band gaps in majority spin representing the material is metallic. Graphical study of ATK-VNL also shows that the compounds Co₂VZ (Z= B, In, Sb) are near to half metallic, because their minima of conduction band crosses the Fermi level. But, the compound Co₂VAs is metallic in nature. The detailed results of band structures and density of states are shown in Figures 2-5.
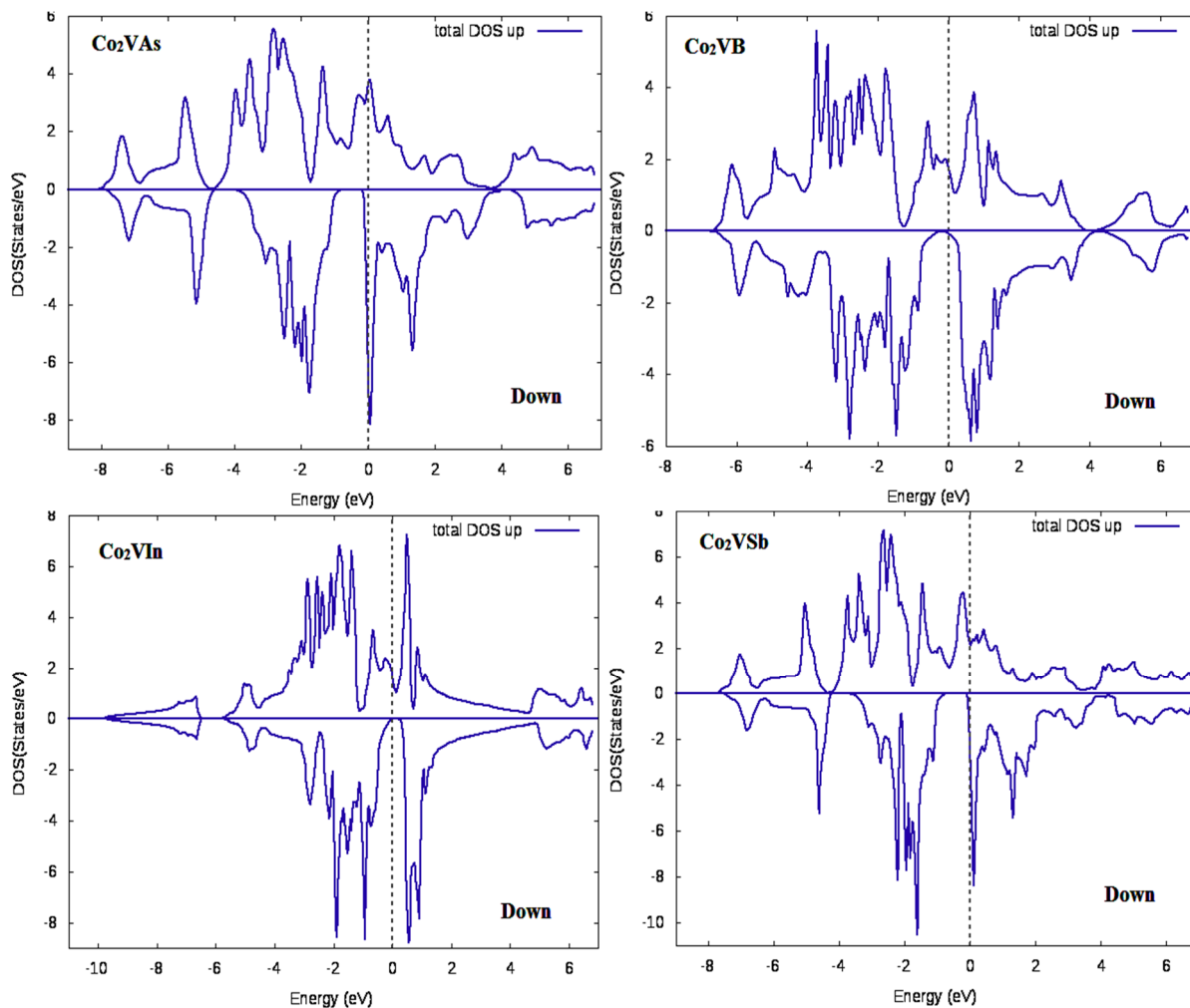
Figure 2. DOS of Co₂VZ (Z= As, B, In, Sb) using WIEN2K Code
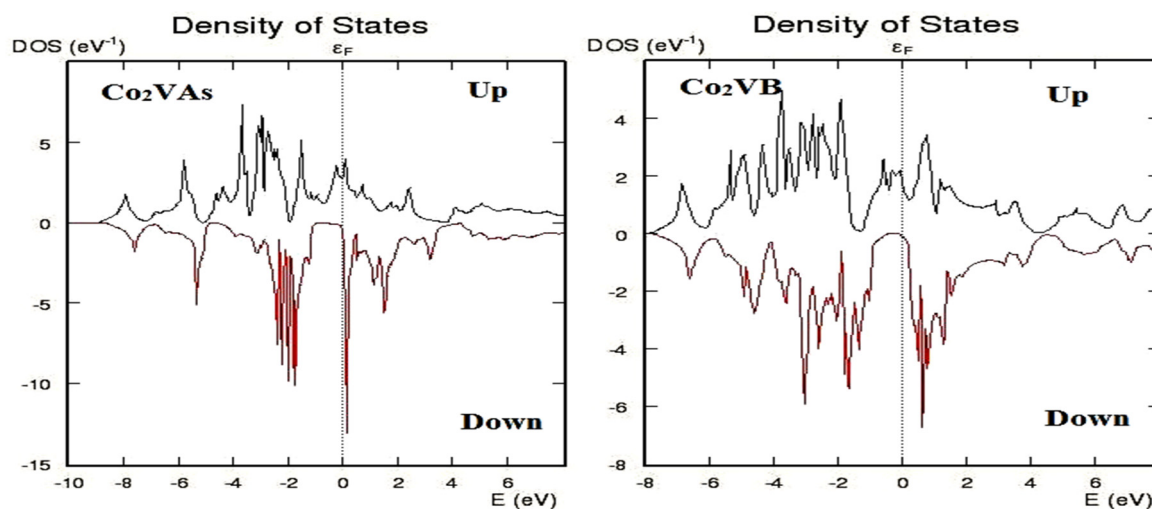
Figure 3. DOS of Co₂VZ (Z= As, B, In, Sb) using ATK-VNL Code

(Continued on next page)
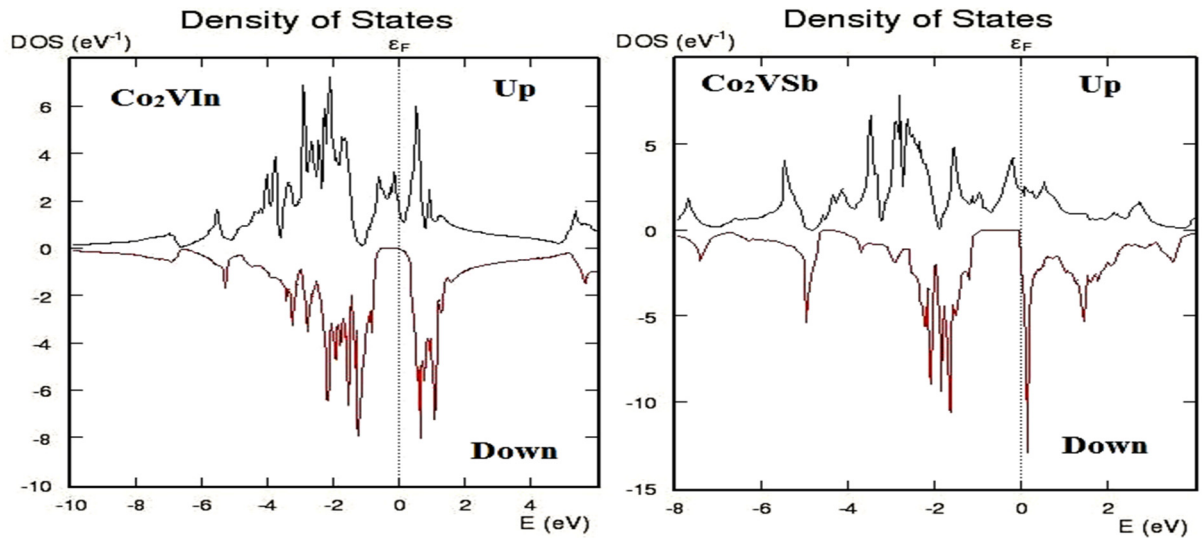
Figure 3. DOS of Co_2VZ (Z= As, B, In, Sb) using ATK-VNL Code.
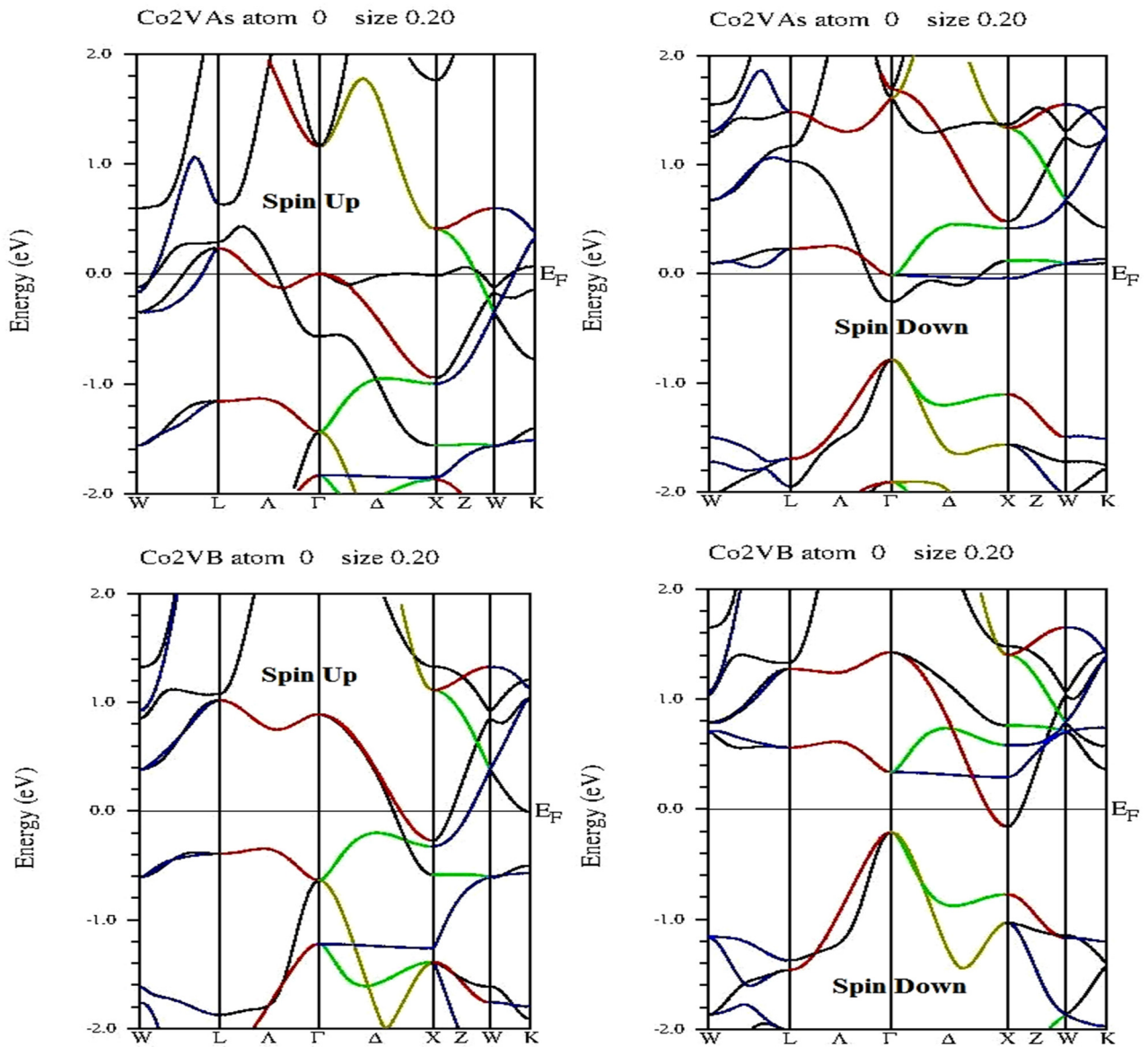
Figure 4. Band Structure of Co_2VZ (Z= As, B, In, Sb) using WIEN2K Code

(Continued on next page)
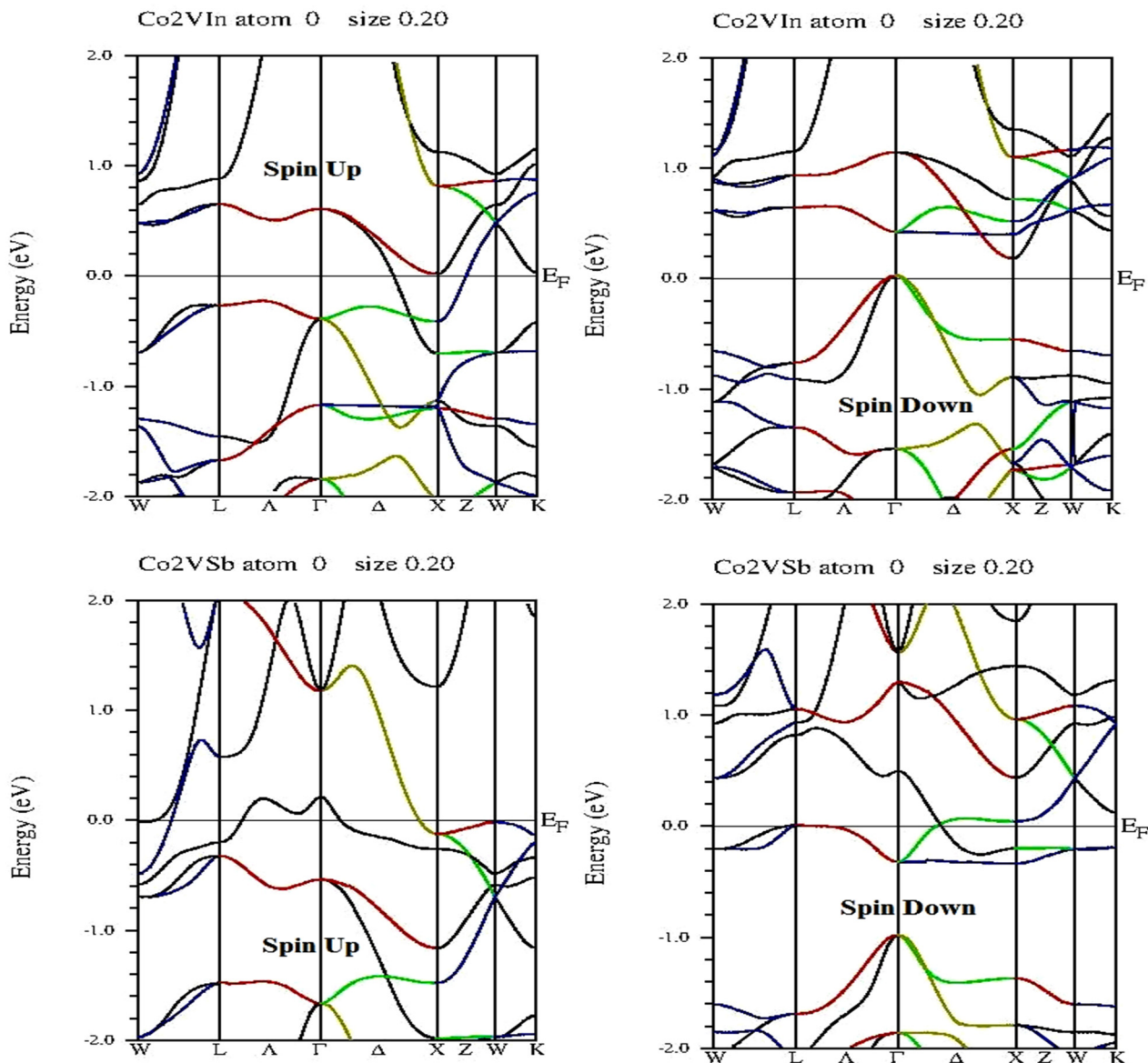
Figure 4. Band Structure of Co$_2$VZ (Z= As, B, In, Sb) using WIEN2K Code
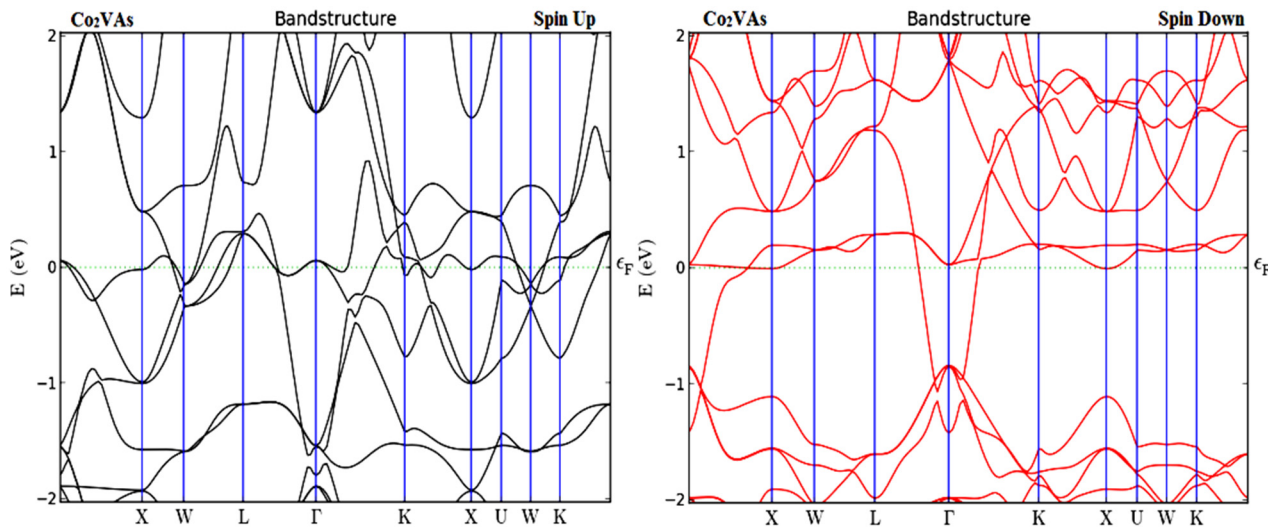
Figure 5. Band Structure of Co$_2$VZ (Z= As, B, In, Sb) using ATK-VNL Code

(Continued on next page)
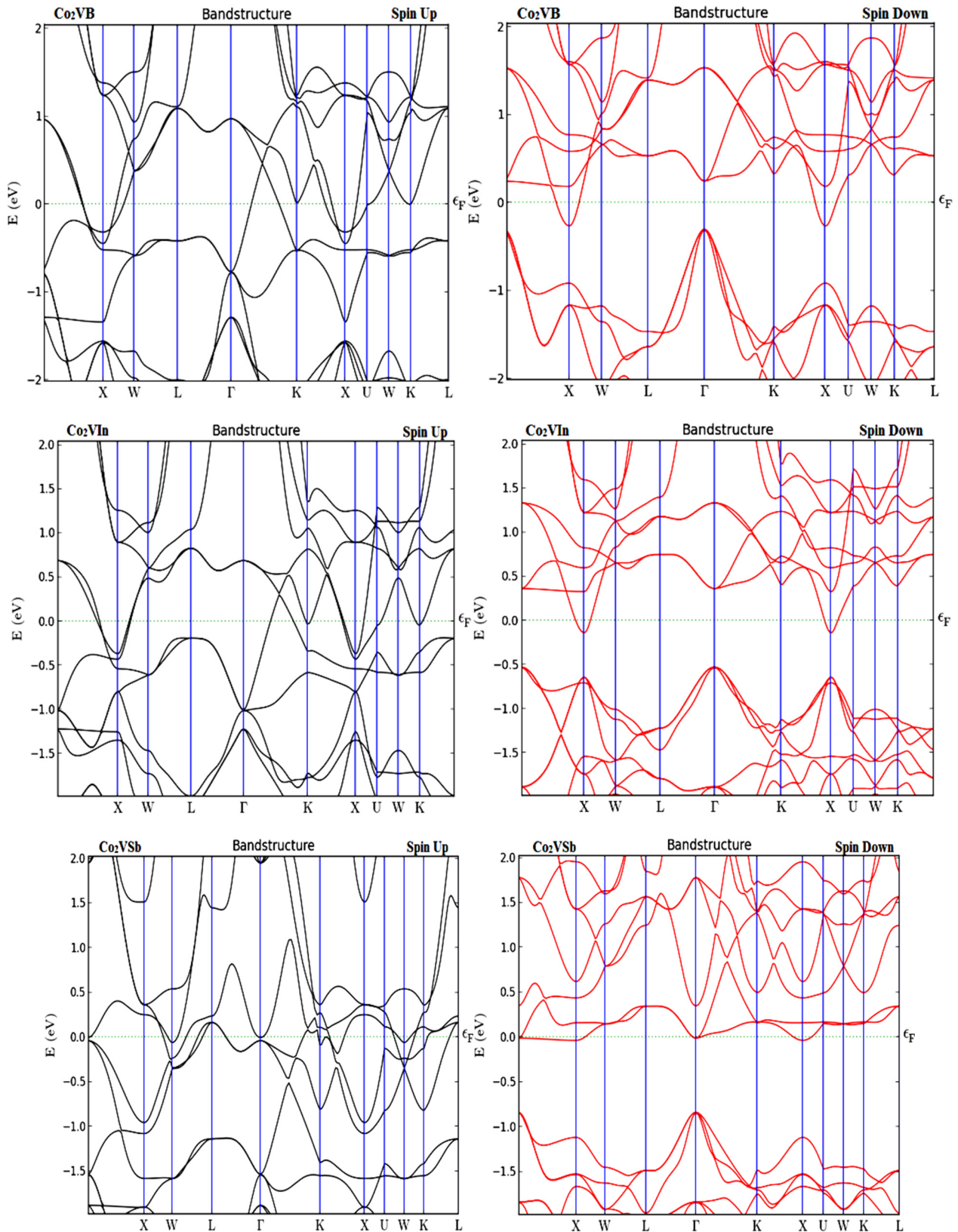
Figure 5. Band Structure of Co₂VZ (Z= As, B, In, Sb) using ATK-VNL Code

These magnetic moments and Curie temperature can be calculated by counting the total number of valence electron present in the compounds. Curie temperature is equal to the integral multiple of 175 K by the difference of total valence electron. In the same manner, magnetic moment per unit cell is equal to the difference between total numbers of valence electron. These theoretical results of magnetic moments are driven by Slater-Pauling rule [26]. Here, total number of valence electron of the compounds Co₂VZ (Z= As, B, In, Sb) are 28, 26, 26 and 28. According to the Slater-

Pauling rule their magnetic moments are 4, 2, 2 and 4 μ_B respectively and Curie temperature of these compounds Co_2VZ (Z= As, B, In, Sb) are 700, 350, 350 and 700 K respectively. We have summarized that these compounds have very good agreement with Slater-Pauling rule. The calculated results for magnetic moments for Co_2VZ (Z= As, B, In, Sb) obtained by full potential linearized augmented plane wave (FP-LAPW) method implemented in WIEN2k and pseudo-potentials method implemented in Atomistic Tool Kit-Virtual NanoLab (ATK-VNL) within Generalized-gradient approximation (GGA) for exchange and correlation functions and is tabulated in Table 3.

Table 3.

Total magnetic moments of the compounds Co_2VZ (Z= As, B, In, Sb).

Compound	Z_t	Magnetic moment (μ_B)		
		WIEN2k	ATK	Slater-Pauling (Z_t - 24)
Co_2VAs	28	3.64	3.76	4.00
Co_2VB	26	2.00	1.97	2.00
Co_2VIn	26	1.99	1.99	2.00
Co_2VSb	28	3.96	3.82	4.00

Optical properties

These optical properties are such as reflectivity, refractive index, excitation coefficient, absorption coefficient, optical conductivity and electron energy loss. The optical spectra for different optical properties are shown in Figure 6 (a-h).
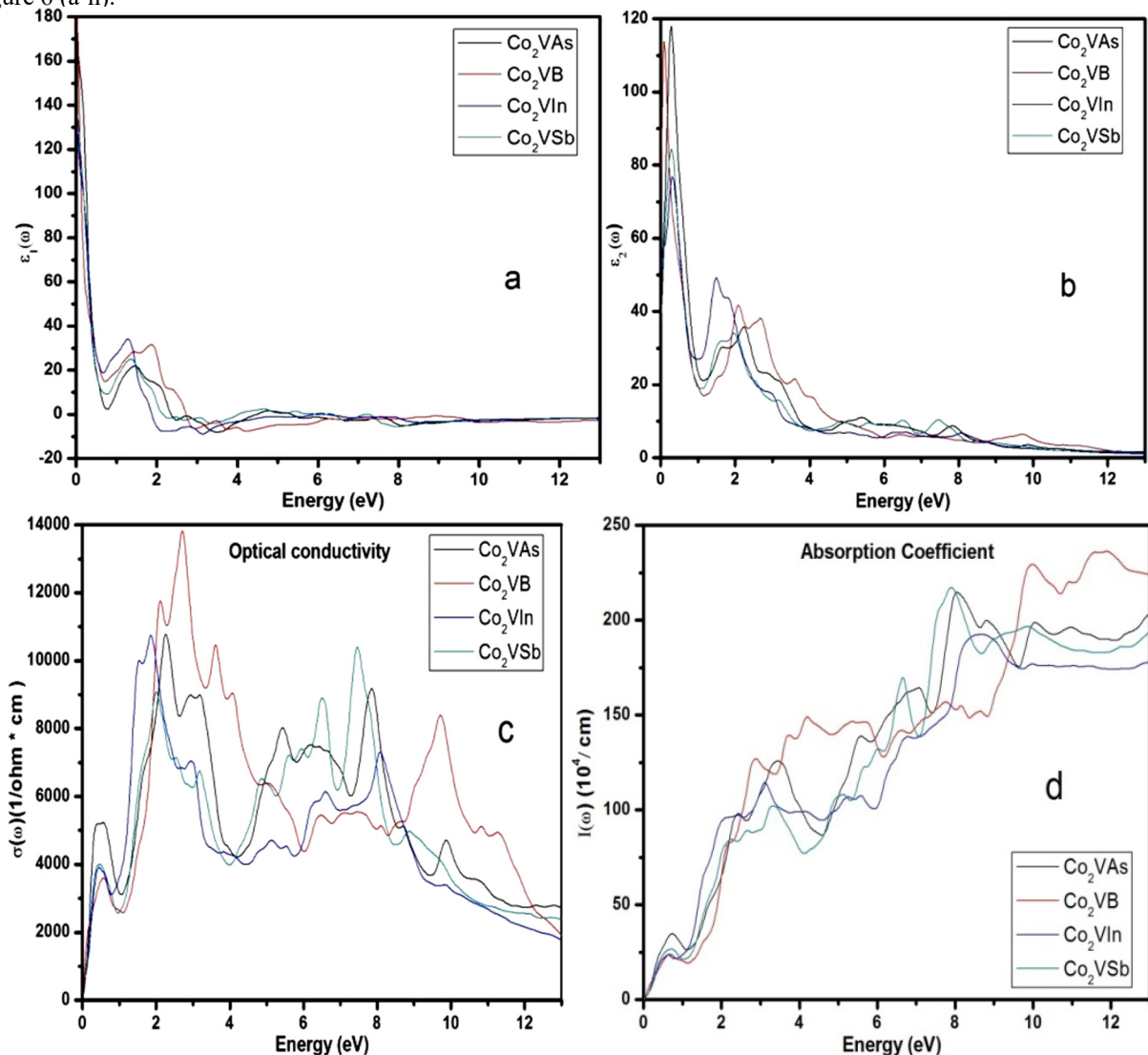
Figure 6. Calculated optical parameters (a) real part of dielectric function, (b) imaginary part of dielectric function, (c) optical conductivity, (d) absorption coefficient, (e) electron energy-loss function, (f) reflectivity, (g) refractive index and (h) extinction coefficient for Co_2VZ (Z= As, B, In, Sb).

(Continued on next page)
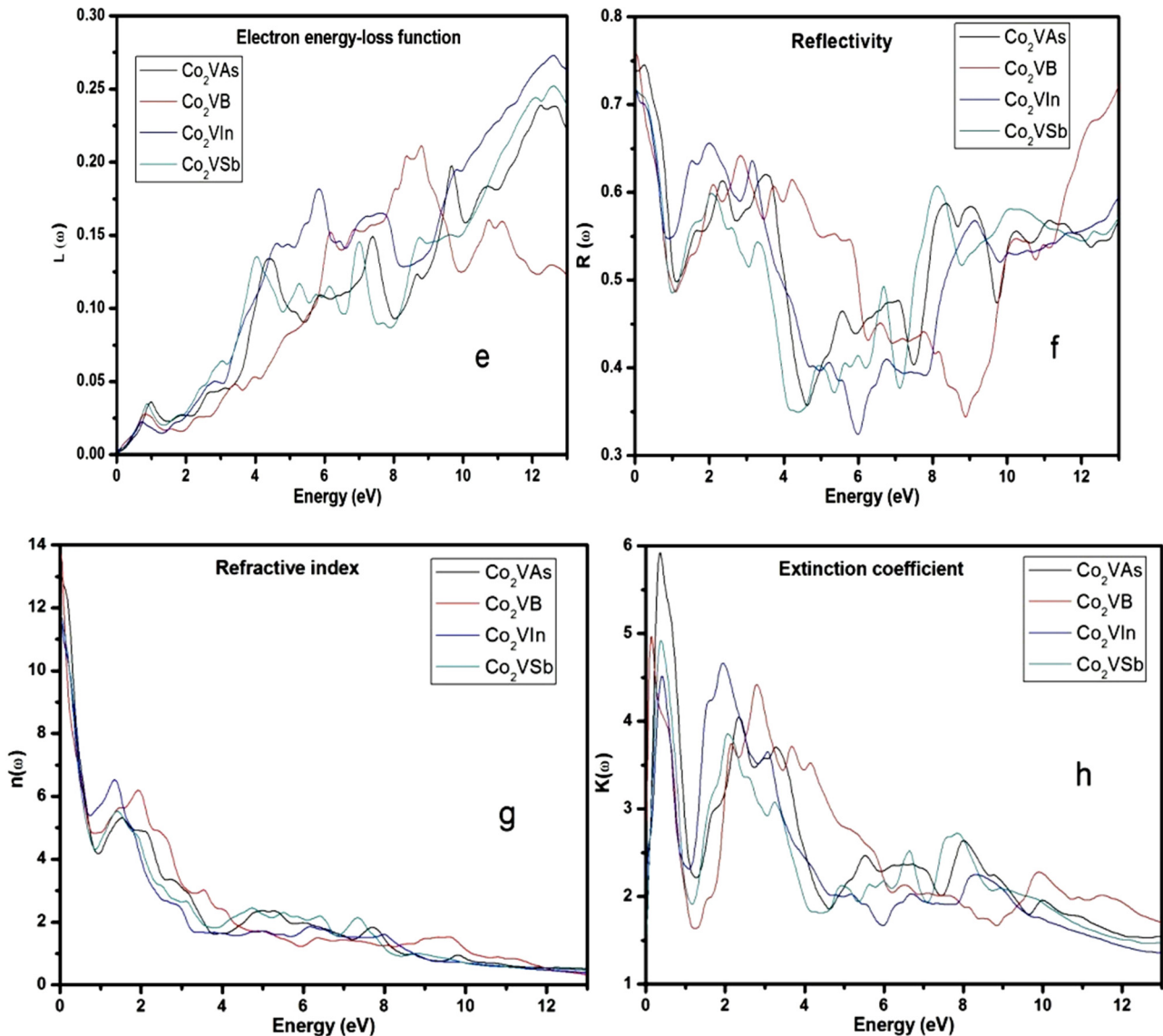
Figure 6. Calculated optical parameters (a) real part of dielectric function, (b) imaginary part of dielectric function, (c) optical conductivity, (d) absorption coefficient, (e) electron energy-loss function, (f) reflectivity, (g) refractive index and (h) extinction coefficient for Co_2VZ (Z= As, B, In, Sb).

From the Figure 6 (d-e), we have observed that along the increase of energy, values of absorption coefficient and electron energy-loss function are increases. The value of energy of fast moving particle is decreases or absorbed, when passes through a medium. Small wave vector optical response of material is described by complex dielectric function. This complex dielectric function can be written as $\varepsilon(m) = \varepsilon_1(m) + i\varepsilon_2(m)$. Where $\varepsilon_1(m)$ is the real part of complex dielectric function and ($\varepsilon_2(m)$) imaginary part of complex dielectric function. Which describe the polarization for material; when electric field is applied and gives the value of absorption in a material or loss of energy into the medium respectively [27-29]. The main peaks of imaginary part of dielectric function are obtained in infrared region from 0.08 to 0.30eV. After that, imaginary part of dielectric function decreases rapidly and some small peaks are observed near visible region. From figure 6 (a-b), we have obtained the zero frequency values of real ($\varepsilon_1(\omega)$) and imaginary part ($\varepsilon_2(\omega)$) of complex dielectric functions are 166.34 and 39.81, 180.54 and 78.45, 130.11 and 51.64, 136.16 and 37.02 for the compounds Co_2VZ (Z= As, B, In, Sb) respectively. Figure 6 (c), sharp peaks of optical conductivity are obtained in visible region and highest sharp peak is observed at 2.73eV by Co_2VB representing more conduction of electron as compared with other compounds. From figure 6 (f), we have determined the ability of material to reflect from material surface responding electromagnetic radiation. Zero frequency reflectivity values of the compounds Co_2VZ (Z= As, B, In, Sb) are 0.738, 0.756, 0.717 and 0.716 respectively. Reflection and absorption are inversely proportional to each other at the same instant of time. Plasma resonance corresponding frequency is known as plasma frequency at which sharp peaks are associated. Above the plasma frequency, material shows the dielectric behavior and below which the material shows metallic behavior. Refractive index has vast area of application such as dispersive power of prisms, focusing power of lenses, light guiding, and

critical angle for total internal reflection etc. Zero frequency value of refractive index from Figure 6 (g) for the compounds Co_2VZ (Z= As, B, In, Sb) were obtained as 12.98, 13.73, 11.62 and 11.77 respectively. Figure 6 (h) shows sharp peak of extinction coefficient infrared region and then some smaller peaks are obtained in visible region. Further, the values of extinction coefficient are decreases in the ultraviolet region.

Elastic properties

These constants provide information about structure stability, mechanical properties, bond indexes and anisropy of material. The cubic crystal must satisfy the traditional mechanical stability condition of elastic constant, which is as below [27].

$$C_{11} - C_{12} > 0, \; C_{11} > 0, \; C_{11} + 2C_{12} > 0, \; C_{44} > 0, \; C_{12} < B < C_{11}$$

Structural stability is necessary for any material, which is determined by anisotropic factor and denoted by 'A'. The material is anisotropic for the value of 'A' is other than one. A property of material which does not depend on the direction is known as isotropic. Anisotropic is related with reduced elastic constants as.

$$A = \frac{2C_{44}}{C_{11} - C_{12}}$$

Bond index can determine the Stiffness and flexibility of a material by using Cauchy pressure, which is expressed as $CP = C_{12} - C_{44}$. If the value of Cauchy pressure is positive, then the material is metallic and ductile nature in nature, otherwise material is nonmetallic and ductile in nature. Pugh's ratio B/G is used to determine the material is brittle or ductile. If the B/G ratio is less than 1.75 then material is brittle type otherwise it is ductile. Mechanical properties of the compounds are determined by Bulk modulus (B), young modulus (E), Shear modulus (G) and Poisson ratio (v) by Voigt-Reuss-Hill (VRH) averaging method [30]. Formulas for B, E, G and v by using elastic constant can be expressed as.

$$B = B_V = B_R = \frac{C_{11} + 2C_{12}}{3}$$

$$G = \frac{G_V + G_R}{2}$$

$$G_V = \frac{C_{11} - C_{12} + 3C_{44}}{5}$$

$$G_R = \frac{5C_{44}(C_{11} - C_{12})}{[4C_{44} + 3(C_{11} - C_{12})]}$$

(V = Voigt and R = Reuss)

Stiffness of material can be determined by Young modulus. This can be calculated in term of B and G.

$$E = \frac{9BG}{3B + G}$$

The value of Poisson ratio can be calculated with the help of B and G. The values of Poisson ratio lie between 0 - 0.5 for most of the material.

$$v = \frac{3B - 2G}{2(3B + G)}$$

Here, we have used Atomistic Tool Kit-Virtual NanoLab (ATK-VNL) package using Pseudo-potential method carried out in the framework of density functional theory (DFT). All the results carried out from this code are assembled in Table 4.

From the Table 4, we observe that traditional mechanical stability condition $C_{11} - C_{12} > 0$, $C_{11} > 0$, $C_{11} + 2C_{12} > 0$, $C_{44} > 0$, $C_{12} < B < C_{11}$ for the compounds Co_2VZ (Z= B, In, Sb) is satisfied but Co_2VAs compound does not show mechanical stability. Results of anisotropic constant 'A' are not equal to one for these compounds showing anisotropic in nature. Values of Poisson are lie between zeros to 0.5 except Co_2VAs. Table 4 revel the result that Pugh's ratio B/G is greater than 1.75 for Co_2VZ (Z= B, In, Sb) compounds showing ductile in nature; but B/G value for Co_2VAs is less than 1.75 and is brittle in nature. Values of Cauchy pressure ($C_P = C_{12} - C_{44}$) derived from the Table 4 and are positive for these compounds Co_2VZ (Z= As, B, In, Sb) and shows metallic nature.

Table 4.

Elastic constants and bulk modulus *B* (GPa), shear modulus *G* (GPa), Young's modulus *E* (GPa), *B/G* values, Poisson's ratio *v* and anisotropy factor *A* of Co_2VZ (Z= As, B, In, Sb) compounds.

Compound	Elastic constant			B (GPa)	G (GPa)	E (GPa)	B/G	v	A
	C_{11}	C_{12}	C_{44}						
Co_2VAs	150.56	199.08	104.21	182.91	-20.19	-76.14	-9.06	0.57	-4.30
Co_2VB	351.34	255.85	104.68	287.68	76.39	135.73	3.77	0.42	2.19
Co_2VIn	242.77	194.20	132.10	210.39	68.28	70.16	3.08	0.44	5.44
Co2VSb	251.04	226.86	112.70	234.92	49.24	35.66	4.77	0.47	9.32

SUMMARY AND CONCLUSIONS

First principle investigations are performed of full Heusler compounds Co_2VZ (Z= As, B, In, Sb). For it we calculate structural, electronic, optical, elastic and magnetic properties of these compounds by using first principle methods. Two computational codes are applied for above properties of Co_2VZ (Z= As, B, In, Sb) compounds. Results obtained by two computational codes are analyzed. First one is full potential linearized augmented plane wave (FP-LAPW) method implemented in WIEN2k and second one is pseudo- potentials method implemented in Atomistic Tool Kit-Virtual NanoLab (ATK-VNL) within Generalized-gradient approximation (GGA) for exchange and correlation function. Band structures in majority spin compounds have zero band gaps and in minority spin conduction or valence band crosses the Fermi level. Calculated magnetic moments per unit cell have good agreement with the Slater-Pauling behavior. Optical properties of these compounds named as reflectivity, refractive index, excitation coefficient, absorption coefficient, optical conductivity and electron energy loss have been observed. With the increase of energy, values of absorption coefficient and electron energy - loss function are increases. Results of elastic properties suggest that Co2VZ (Z= B, In, Sb) compounds are ductile in nature and Co_2VAs is brittle in nature. Compounds are metallic in nature.

ORCID IDs

Sukhender, https://orcid.org/0000-0002-2149-5669; **Lalit Mohan**, https://orcid.org/0000-0003-3323-8296
Sudesh Kumar, https://orcid.org/0000-0002-7507-4712; **Shiv R. Bhardwaj**, https://orcid.org/0000-0002-1895-158X
Ajay Singh Verma, https://orcid.org/0000-0001-8223-7658

REFERENCES

[1] Fr. Heusler, W. Starck, and E. Haupt, Verh. Deutsch. Phys. Ges. **5**(12), 220 (1903), https://archive.org/details/verhandlungende33unkngoog/page/n177/mode/2up.

[2] Fr. Heusler, and E. Take, Trans. Faraday Soc. **8**, 169-184 (1912), https://doi.org/10.1039/TF9120800169.

[3] R.A. De Groot, F.M. Muller, P.G. Van Engen, and K.H.J. Buschow, New class of materials: half-metallic ferrowmagnets, Phys. Rev. Lett. **50**, 2024-2027 (1983), https://doi.org/10.1103/PhysRevLett.50.2024.

[4] A. Aguayo, G. Murrieta, J. Magn. Magn. Mater. **323**, 3013-3017 (2011), https://doi.org/10.1016/j.jmmm.2011.06.038.

[5] M.I. Katsnelson, V.Y. Irkhin, L. Chioncel, A.I. Lichtenstein, and R.A. de Groot, Rev. Mod. Phys., **80**, 315-378 (2008), https://doi.org/10.1103/RevModPhys.80.315.

[6] S.A. Wolf, D.D. Awschalom, R.A. Buhrman, J.M. Daughton, S. von Molnar, M.L. Roukes, A.Y. Chtchelkanova, and D.M. Treger, Science, **294**, 1488-1495 (2001), https://doi/org/10.1126/science.1065389.

[7] I. Zutic, J. Fabian, and S. Das Sarma, Rev. Mod. Phys. **76**, 323-410 (2004), https://doi.org/10.1103/RevModPhys.76.323.

[8] C.M. Fang, G.A. Wijs, and R.A. de Groot, J. Appl. Phys. **91**, 8340-8344 (2002), https://doi.org/10.1063/1.1452238.

[9] S. Wurmehl, G. H. Fechel, H. C. Kandpal, V. Ksenofontov, C. Felser, and H. Lin, Appl. Phys. Lett. **88**, 032503 (2006), https://doi.org/10.1063/1.2166205.

[10] M. A. Tanaka, Y. Ishikawa, Y. Wada, S. Hori, A. Murata, S. Horii, Y. Yamanishi, K. Mibu, K. Kondou, T. Ono, and S. Kasai, J. Appl. Phys. **111**, 53902 (2012), https://doi.org/10.1063/1.3688324.

[11] L. Wollmann, S. Chadov, J. Kubler, and C. Felser, Phys. Rev. B, **90**, 214420 (2014), https://doi.org/10.1103/PhysRevB.90.214420.

[12] Z. Wen, T. Kubota, T. Yamamoto, and K. Takanashi, Sci. Rep. **5**, 18387 (2016), https://doi.org/10.1038/srep18387.

[13] X.P. Wei, J.B. Deng, G.Y. Mao, S.B. Chu, and X.R. Hu, Intermetallics, **29**, 86-91 (2012), https://doi.org/10.1016/j.intermet.2012.05.002.

[14] Z. Ren, Y. Liu, S. Li, X. Zhang, and H. Liu, **34**, 251-259 (2016), https://doi.org/10.1515/msp-2016-0043.

[15] S.N. Holmes, and M. Pepper, J. Supercond. **16**, 191-194 (2003), https://doi.org/10.1023/A:1023294314785.

[16] S. Ishida, S. Akazawa, Y. Kubo, and J. Ishida, J. Phys. F: Met. Phys. **12**, 1111 (1982), https://doi.org/10.1088/0305-4608/12/6/012.

[17] E. Shreder, S.V. Streltsov, A. Svyazhin, A. Makhnev, V.V. Marchenkov, A. Lukoyanov, and H.W. Weber, J. Phys.: Condens. Matter, **20**, 045212 (2008), https://doi.org/10.1088/0953-8984/20/04/045212.

[18] K. Seema, N.M. Umran, and R. Kumar, J. Supercond. Nov. Magn. **29**, 401-408 (2016), https://doi.org/10.1007/s10948-015-3271-7.

[19] J.P. Perdew, K. Burke, and M. Ernzerhof, Phys. Rev. Lett. **77**, 3865-3868 (1996), https://doi.org/10.1103/PhysRevLett.77.3865.

[20] P. Blaha, K. Schwarz, G.K.H. Madsen, D. Kvasnicka, and J. Luitz, in: *WIEN2k, An Augmented Plane Wave + Local Orbitals Program for Calculating Crystal Properties*, edited by K. Schwarz (Technical Universitatwien, Austria, (2001), ISBN 3-9501031-1-2.

[21] Synopsys, Inc., 690 East Middlefield Road, Mountain View, CA, 94043, Atomistix ToolKit-Virtual Nanolab (ATK-VNL), QuantumWise Simulator, Version. 2014.3 [Online]. Available: http://quantumwise.com/

[22] H.J. Monkhorst, and J.D. Pack, Phys. Rev. B, **13**, 5188-5192 (1976), https://doi.org/10.1103/PhysRevB.13.5188.

[23] N. Xing, Y. Gong, W. Zhang, J. Dong, and H. Li, Comput. Mater. Sci. **45**, 489-493 (2009), https://doi.org/10.1016/j.commatsci.2008.11.008.

[24] F.D. Murnaghan, Proc. Natl. Acad. Sci. USA. **30**, 244-247 (1944), https://dx.doi.org/10.1073%2Fpnas.30.9.244.

[25] C. Felser, G. Fecher, and B. Balke, Angewandte Chemie International Edition, **46**, 668-699 (2007), https://doi.org/10.1002/anie.200601815.

[26] Z.Y. Deng, and J.M. Zhang, Journal of Magnetism and Magnetic Materials, **397**, 120-124 (2016), https://doi.org/10.1016/j.jmmm.2015.08.089.

[27] T. Lantri, S. Bentata, B. Bouadjemi, W. Benstaali, B. Bouhafs, A. Abbad, and A. Zitouni, J. Magn. Magn. Mater. **419**, 74-83 (2016), https://doi.org/10.1016/j.jmmm.2016.06.012.

[28] S. Sharma, A.S. Verma, and V.K. Jindal, Mater. Res. Bull. **53**, 218-233 (2014), https://doi.org/10.1016/j.materresbull.2014.02.021.

[29] C.M.I. Okoye, J. Physics: Condensed Matter, **15**, 5945–5958 (2003), https://doi.org/10.1088/0953-8984/15/35/304.

[30] R. Hill, Proc. Phys. Soc. A, **65**, 349-354 (1952), https://doi.org/10.1088/0370-1298/65/5/307.

ЕЛЕКТРОННІ, ОПТИЧНІ, ПРУЖНІ ТА МАГНІТНІ ВЛАСТИВОСТІ ПОВНИХ ХЕЙСЛЕРОВИХ СПОЛУК CO₂VZ (Z = As, B, In, Sb)

Сухендер[a], Лаліт Мохан[a], Судеш Кумар[b], Шив Р. Бхардвадж[c], Аджай Сінгх Верма[a]

[a]Фізичний факультет, Банастхалі Від'япіт, Банастхалі 304022, Індія
[b]Хімічний факультет, Банастхалі Від'япіт, Банастхалі 304022, Індія
[c]Фізичний факультет, Коледж Б.С.А., Матхура 282004, Індія

За допомогою двох різних обчислювальних методів досліджені електронні, оптичні, еластичні та магнітні властивості сполук Хейслера Co₂VZ (Z = As, B, In, Sb). Один – це метод повного потенціалу лінеаризованої доповненої плоскої хвилі (FP-LAPW), реалізований у WIEN2k, а другий – метод псевдопотенціалу, реалізований в Atomistic Tool Kit-Virtual NanoLab (ATK VNL). Всі ці сполуки демонструють нульову ширину забороненої зони як в мажоритарному спіновому каналі в обох обчислювальних кодах, так і в зоні провідності з неосновним напрямком спіну, або зоні валентності, що перетинає рівень Фермі. Магнітний момент, розрахований для цих сполук Co₂VZ (Z = As, B, In, Sb), становить 3,64 та 3,76, 2,00 та 1,97, 1,99 та 1,99, 3,96 та 3,82 μв відповідно в модельних кодах WIEN2k та ATK-VNL. Проаналізовано оптичні властивості цих сполук, такі як відбивна здатність, показник заломлення, коефіцієнт збудження, коефіцієнт поглинання, оптична провідність та втрати енергії електронів. По мірі збільшення значення енергії коефіцієнт поглинання та значення функції втрат енергії електронами збільшуються. Поглинання і відбиття обернено пропорційні один одному в один і той же момент часу. Співвідношення П'ю – B/G перевищує 1,75 для сполук Co₂VZ (Z = B, In, Sb), які мають пластичну природу, але значення B/G для Co₂VA менше 1,75, отже ця сполука є крихкою за своєю природою. Отримано значення тиску Коші (CP = C12 - C44), що для сполук Co₂VZ (Z = As, B, In, Sb), показує їх металеву природу.

КЛЮЧОВІ СЛОВА: заборонена зона, спінтроніка, магнітний момент, пружні константи

ЭЛЕКТРОННЫЕ, ОПТИЧЕСКИЕ, УПРУГИЕ И МАГНИТНЫЕ СВОЙСТВА ПОЛНЫХ ХЕЙСЛЕРОВИХ СОЕДИНЕНИЙ CO₂VZ (Z = As, B, In, Sb)

Сухендер[a], Лалит Мохан[a], Судеш Кумар[b], Шив Г. Бхардвадж[c], Аджай Сингх Верма[a]

[a]Физический факультет, Банастхали Видьяпит, Банастхали 304022, Индия
[b]Химический факультет, Банастхали Видьяпит, Банастхали 304022, Индия
[c]Физический факультет, Колледж Б.С.А., Матхура 282004, Индия

С помощью двух различных вычислительных методов исследованы электронные, оптические, эластичные и магнитные свойства соединений Хейслера Co₂VZ (Z = As, B, In, Sb). Один – это метод полного потенциала линеаризированной дополненной плоской волны (FP-LAPW), реализованный в WIEN2k, второй – метод псевдопотенциала, реализованный в Atomistic Tool Kit-Virtual NanoLab (ATK VNL). Все эти соединения демонстрируют нулевую ширину запрещенной зоны как в мажоритарном спиновом канале в обоих вычислительных кодах, так и в зоне проводимости с неосновным направлением спина, или зоне валентности, пересекающий уровень Ферми. Магнитный момент, рассчитанный для этих соединений Co₂VZ (Z = As, B, In, Sb), составляет 3,64 и 3,76, 2,00 и 1,97, 1,99 и 1,99, 3,96 и 3 82 μв соответствии в модельных кодах WIEN2k и ATK-VNL. Проанализированы оптические свойства этих соединений, такие как отражательная способность, показатель преломления, коэффициент возбуждения, коэффициент поглощения, оптическая проводимость и потери энергии электронов. По мере увеличения значения энергии коэффициент поглощения и значение функции потерь энергии электронами увеличиваются. Поглощения и отражения обратно пропорциональны друг другу в один и тот же момент времени. Соотношение Пью – B/G превышает 1,75 для соединений Co₂VZ (Z = B, In, Sb), которые имеют пластическую природу, но значение B/G для Co₂VA менее 1,75, следовательно это соединение является хрупким по своей природе. Получено значение давления Коши (CP = C12 - C44), что для соединений Co₂VZ (Z = As, B, In, Sb), показывает их металлическую природу.

КЛЮЧЕВЫЕ СЛОВА: запрещенная зона, спинтроника, магнитный момент, упругие константы

DEPENDENCE OF INTERPHASE DISTRIBUTION COEFFICIENTS ON TEMPERATURE AND CONCENTRATION OF COMPONENTS IN DOUBLE METAL SYSTEMS

Alexey P. Shcherban*, Olga A. Datsenko

National Science Center "Kharkiv Institute of Physics and Technology"
1, Academichna str., 61108 Kharkiv, Ukraine
*Corresponding Author: shcherban@kipt.kharkov.ua
Received May 15, 2020; accepted October 13, 2020

In this work the computation of the equilibrium k_0 and limiting k_{0limB} distribution coefficients (DC) of the components according to the state diagrams of binary metal systems Mg–Ag, Ag–Mg, Al– Mg, Mg–Al, Ni–Ga, and Nb–Ge was achieved. These systems belong to systems with limited solubility and for them the approximating equations of the solidus and liquidus lines are obtained in the form of second-order polynomials in the temperature range from the melting point of the main component T_{MA} to the eutectic temperature T_{EA}. A mathematical analysis of the obtained equations for calculating DC is performed. For the first time by calculated and graphical methods the values of the limiting distribution coefficients k_{0limB} for such systems as Mg – Al, Mg – Ag, and Al – Mg were determined. The complete coincidence of the k_{0limB} values obtained by different methods is confirmed. For the Ag–Mg, Nb–Ge and Ni–Ga systems adjusted values of the limiting coefficient were obtained, which are in good agreement with the reference values. The dependences of the equilibrium distribution coefficients on temperature and concentration for the investigated systems are constructed. In the studied temperature range from T_{MA} to T_{EA}, a linear dependence of the distribution coefficients on temperature and concentration is observed.

KEY WORDS: equilibrium and limiting distribution coefficients, binary metal systems Mg–Ag, Ag–Mg, Al–Mg, Mg–Al, Ni–Ga, Nb–Ge

Crystallization from melt is an important process that most materials undergo during their manufacture, refining, and shaping. Directional crystallization is especially significant in the production of ultrapure materials, primarily in semiconductor technology. The most important parameter of the crystallization process for the targeted use of its refining action and the formation of solid solutions is the interphase distribution coefficient (DC).

The distribution coefficient characterizes the ratio of the concentration of components in various phases in thermodynamic equilibrium. By their physicochemical definition, DC differ for each concrete pair of a base - component. In this work, the distribution coefficient is used only to describe the concentration ratio at the liquid – solid interphase equilibrium, in this case it is determined by the concentration ratio in the solid and liquid phases. The general expression for equilibrium DC has the form of dependence: $k_0 = x_S / x_L$. In the following considerations, the existence of binary metal systems consisting of two components A - B is assumed.

The following distribution coefficients are considered in the literature [1-4]: effective DC k_B, equilibrium DC k_{0B} and limiting DC k_{0limB}. There are various both experimental and computational methods for determining the distribution coefficients. In turn, the choice of the determination method of DC depends on the nature of the solubility of the second component in the base: low solubility, limited and unlimited solubility. In [3], an analysis was made of the methods for determining distribution coefficients depending on the type of solubility of the second component in the base.

FORMULATION OF THE PROBLEM

The effective distribution coefficient k_B during directional crystallization is the ratio of the impurity concentration in the initial and final part of the ingot (zone melting, the Bridgman method), or the ratio of the impurity concentration in the ingot and the residue in the crucible (Czochralsky method). The k_B coefficient varies over a wide range from values less than $1 \cdot 10^{-3}$ to values greater than 10, which depends on the solidification conditions — crystallization rate and degree of mixing of the liquid. The k_B values determined in different experimental methods and conditions of directional crystallization cannot be compared with each other and cannot be operated on to construct any dependencies, correlations, etc. The k_B values can be used only for a rough estimate of the behavior of the components during crystallization. The k_B experimental values for a wide range of binary systems are given in [1].

The limiting distribution coefficient k_{0limB} is based on the value of the equilibrium distribution coefficient k_{0B} upon extrapolation of the content of the second component to zero concentration. The calculation methods for determining k_{0limB} depend on the type of solubility of the impurity in the base and are described in [3, 5, 6]. In these works, the calculated values of the limiting distribution coefficient are given for many systems with different solubilities of the components in the solid state. The temperature and concentration parameters were established there to achieve the limiting values of k_{0limB}: $x_{LB} < 0.1$ at. % and $\Delta T_{MA} < 1$ K. Below the specified parameters k_{0limB} is defined uniquely and assumes its constant value.

The equilibrium distribution coefficient of the impurity k_{0B} is equal to the ratio of the equilibrium concentrations of this component in two adjacent phases, and not concentrations in general. Although in practice, equilibrium

solidification is rarely achieved, because the rate of diffusion in the solid state is usually low; to estimate the distribution of the second component during crystallization of a substance from a melt, it is precisely the k_{0B} equilibrium DC that have the main practical value as a reference material.

In the reference literature, experimental and calculated values of k_{0B} are given [1, 6]. As a rule, these values are given for one concentration value of the second component, or even without indicating concentration. The equilibrium distribution coefficient k_{0B}, by definition, characterizes the ratio between the concentrations of components in two phases that are in equilibrium with each other under isothermal conditions. Based on the binary state diagram, the dependence of this coefficient on temperature and concentration is determined in general terms by the formula:

$$k_{0B}(T, x) = f(x_{SB}(T)/x_{LB}(T)). \tag{1}$$

Thus, the distribution coefficient can be considered as a function of temperature and concentration. If the liquidus and solidus lines of the state diagram (SD) are known with sufficient accuracy, then it is possible to determine the dependence of the equilibrium distribution coefficient functions on temperature and concentration for a fragment of the SD, for example, on the melting point of the main component to the singular points on the diagram (minimum point, maximum, eutectics, etc.). The literature data of the dependence of the equilibrium distribution coefficient k_{0B} on temperature and concentration for binary metal are very limited, therefore, research in this direction is of interest.

The aim of the work is to study the dependence of equilibrium distribution coefficients on temperature and concentration for individual metal systems with limited solubility of components in the solid α-phase.

CALCULATION METHOD

In this work, we studied the following binary metal systems: Mg – Ag, Ag – Mg, Al – Mg, Mg – Al, Ni – Ga, and Nb – Ge. The choice of these systems is due to the fact that they relate to systems with limited solubility and they were investigated for calculating such thermodynamic quantities as the partial dissolution enthalpy $\Delta\overline{H}_B^{\alpha}$, activity coefficients γ_B^{α}, and component activity a_B^{α} in these systems [7].

An analysis of the state diagrams of the explored systems [8] showed that their solidus and liquidus lines in the temperature range from the melting point of the pure component to the eutectic temperature are not linear and therefore k_{0B} is a function of temperature and concentration in this interval according to expression (1).

To calculate the dependence of the equilibrium DC k_{0B} on temperature and concentration, we used the method for determining the equilibrium distribution coefficients from binary state diagrams described in [6, 9]. This method consists in the mathematical expression of the shape of the solidus and liquidus lines of state diagrams in the form of second-order polynomials:

$$T_S = p_{SB}x_{SB}^{*2} + q_{SB}x_{SB}^{*} + T_{MA} \tag{2}$$

$$T_L = p_{LB}x_{LB}^{*2} + q_{SL}x_{LB}^{*} + T_{MA}, \tag{3}$$

where T_S and T_L – solidus and liquidus temperatures, T_{MA} – melting point of the main component A, x_{SB}^{*}, x_{LB}^{*} – molar fractions of component B in the solid and liquid phase, expressed in at.%, p_{SB}, q_{SB}, p_{LB}, q_{LB} - regression coefficients of approximating equations.

Since equilibrium DC is an isothermal concentration ratio x_S^{*}/x_L^{*}, equality have been observed

$$\Delta T_S = \Delta T_L = T_{MA} - T_S = T_{MA} - T_L = \Delta T_{MA}. \tag{4}$$

Considering condition (4), from expressions (1) and (2), it is possible write the equality:

$$p_{SB}x_{SB}^{*2} + q_{SB}x_{SB}^{*} = p_{LB}x_{LB}^{*2} + q_{LB}x_{LB}^{*}. \tag{5}$$

From this expression it is possible to derive the obvious expression k_{0B} as a function of the impurity concentration:

$$k_{0B}^{C} = \left(p_{LB}x_{LB}^{*} + q_{LB}\right)/\left(p_{SB}x_{SB}^{*} + q_{SB}\right). \tag{6}$$

In the same way, excluding concentration, it is possible to obtain an expression for the temperature dependence of the equilibrium distribution coefficient:

$$k_{0B}^{T} = \frac{p_{LB}\left(\pm\sqrt{q_{SB}^{2} - 4p_{SB}\Delta T_{MA}} - q_{SB}\right)}{p_{SB}\left(\pm\sqrt{q_{LB}^{2} - 4p_{LB}\Delta T_{MA}} - q_{LB}\right)}. \tag{7}$$

The degree of temperature influence is determined by the specific properties of the considered pair of substances. The regression coefficients p_{SB}, p_{LB}, q_{SB}, q_{LB} were determined by the least squares method using the pairs of values taken from the state diagrams: $T_{S(i)}$, $x_{SB(i)}$ and $T_{L(j)}$, $x_{LB(j)}$. It should be noted the scope of the regression equations (2) and (3). Their application is limited in the range from the melting temperature of the T_{MA} of the main component to the maximum temperature equal to the eutectic temperature $T_{max} = T_{EA}$.

As noted above, the limiting distribution coefficient k_{0limB} is determined by extrapolating the content of the second component to zero concentration $x_B \rightarrow 0$ or at $T \rightarrow T_{MA}$. This value can be obtained from formula (6) for $x_{LB}^{*} = x_{SB}^{*} = 0$.

$$k_{0\lim B} = q_{LB} / q_{SB}. \tag{8}$$

Table 1 shows the values of the regression coefficients of the approximating equations of the solidus and liquidus lines of the investigated systems and the temperature range of applicability of the equations, as well as the first calculated values of the limiting distribution coefficients k_{0limB} for such systems as Mg–Al, Mg–Ag, Al–Mg. For the Ag – Mg, Nb – Ge, and Ni – Ga systems, the refined values of the limiting coefficient were obtained, which are in good agreement with the reference values [6].

Table 1.

The values of the regression coefficients of the equations of the solidus and liquidus lines in the AB investigated systems, the temperature range of the equations applicability and k_{0limB} values

System	p_S	q_S	p_L	q_L	ΔT_{MA}, °C	κ_{0limB}	κ_{0limB} [6]
Ag - Mg	0,0394	-8,3938	-0,0458	-4,6347	202	0,55	0,56
Mg - Ag	13,8307	-92,5442	-0,2139	-6,5556	178	0,07	-
Mg - Al	0,0799	-18,8156	-0,0917	-4,2488	212	0,23	-
Al - Mg	0,3810	-17,8458	-0,0210	-4,7629	210	0,27	-
Nb - Ge	3,7895	-89,9375	-0,4615	-15,4285	569	0,17	0,3
Ni -Ga	0,2098	-15,9277	-0,1198	-4,2990	243	0,27	0,4

Figure 1 shows the dependences of the equilibrium distribution coefficients k_{0B}^{T} depending on the ΔT_{MA} constructed by expression (7) for Ag–Mg, Ni–Ga, Al–Mg, Mg–Al, Nb–Ge, Mg–Ag systems.
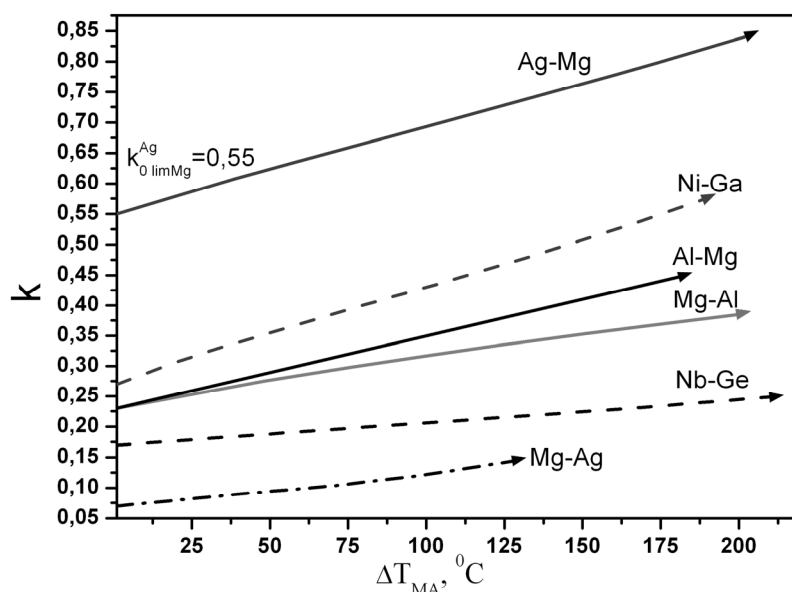
Figure 1. Dependences of equilibrium distribution coefficients on ΔT_{MA} for systems
Ag–Mg, Ni–Ga, Al–Mg, Mg–Al, Nb–Ge, Mg–Ag.

An analysis of the obtained dependences shows that for the investigated systems, a linear dependence k_{0B}^{T} from ΔT_{MA} is observed in the temperature range from the melting point of the main component T_{MA} to the eutectic temperature T_{EA}.

The nature of the concentration, as well as temperature, dependence of the equilibrium distribution coefficient is determined by the topology of the phase diagram drawing: the mutual disposition of the liquidus and solidus lines. To determine the concentration dependence of equilibrium DC k_{0B}^{C}, expression (6) is used. Table 2 shows the calculated values k_{0B}^{C} and k_{0B}^{T} in the investigated systems obtained from expressions (6) and (7) for the same ΔT_{MA} values. As can be seen from the table, either a complete coincidence of the obtained values is observed, or a slight deviation (<1%)

Table 2.

The calculated values of distribution coefficients k_{0B}^{C}, k_{0B}^{T} obtained for the same values ΔT_{MA}

Ag-Mg			Nb-Ge			Mg-Al		
k_{0B}^{C}	k_{0B}^{T}	ΔT_{MA}	k_{0B}^{C}	k_{0B}^{T}	ΔT_{MA}	k_{0B}^{C}	k_{0B}^{T}	ΔT_{MA}
0.61	0.608	38.93	0.203	0.207	90.756	0.252	0.252	23.97
0.635	0.635	57.93	0.231	0.236	168.55	0.275	0.275	48
0.662	0.664	78.93	0.231	0.236	168.55	0.298	0.298	75.7
0.703	0.703	106.93	0.269	0.269	248.93	0.353	0.353	150.16
0.748	0.745	136.93	0.299	0.298	313.756	0.386	0.385	200
Mg-Ag			Al-Mg			Ni-Ga		
k_{0B}^{C}	k_{0B}^{T}	ΔT_{MA}	k_{0B}^{C}	k_{0B}^{T}	ΔT_{MA}	k_{0B}^{C}	k_{0B}^{T}	ΔT_{MA}
0.089	0.09	41	0,29	0.293	42.322	0.306	0.306	19.776
0.103	0.104	71	0,302	0.304	58.822	0.393	0.393	75
0.12	0.121	99	0.345	0.345	109.572	0.482	0.482	134.27
0.146	0.145	129	0.364	0.364	127.452	0.532	0.531	164.45
0.195	0.21	157	0.384	0.387	146.452	0.573	0.573	188.388

From the obtained coinciding values k_{0B}^{T} and k_{0B}^{C} for the same ΔT_{MA} values (table 1), it is possible to conclude that the concentration dependence of the distribution coefficients will have, as well as the temperature, a linear dependence.

From the expressions (2) and (3) it follows that the distribution coefficient can be represented as:

$$k_{0B}^{A} = f(x_{L});\qquad(9)$$

$$k_{0B}^{A} = f(x_{S}).\qquad(10)$$

The extrapolation of these functions as $x_{B} \rightarrow 0$ allows us to determine the value of the limiting coefficient. Figure 2 shows the dependence curves $k_{0B}^{A} = f(x_{L}, x_{B})$ for the binary systems studied in this work. To build the concentration dependences, atomic percentages (at.%) of the components concentrations of the corresponding lines of liquidus and solidus were used.
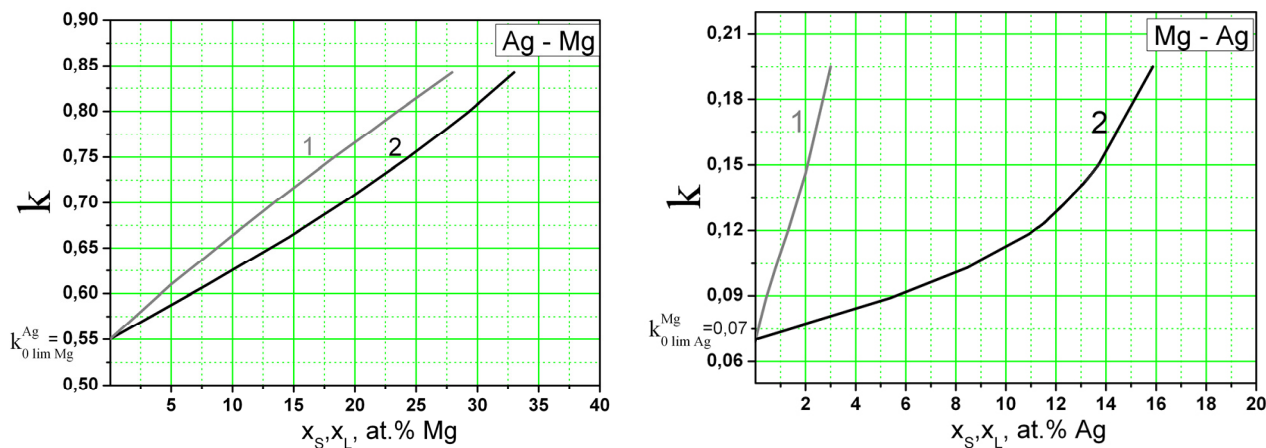
Figure 2. Dependences of equilibrium coefficients on the concentration of the second component in solid $k_{0B}^{A} = f(x_{S})$ - 1 and liquid $k_{0B}^{A} = f(x_{L})$ - 2 phases for binary systems Mg–Ag, Ag–Mg, Al–Mg, Mg–Al, Ni–Ga, Nb–Ge.

(Continued on next page)
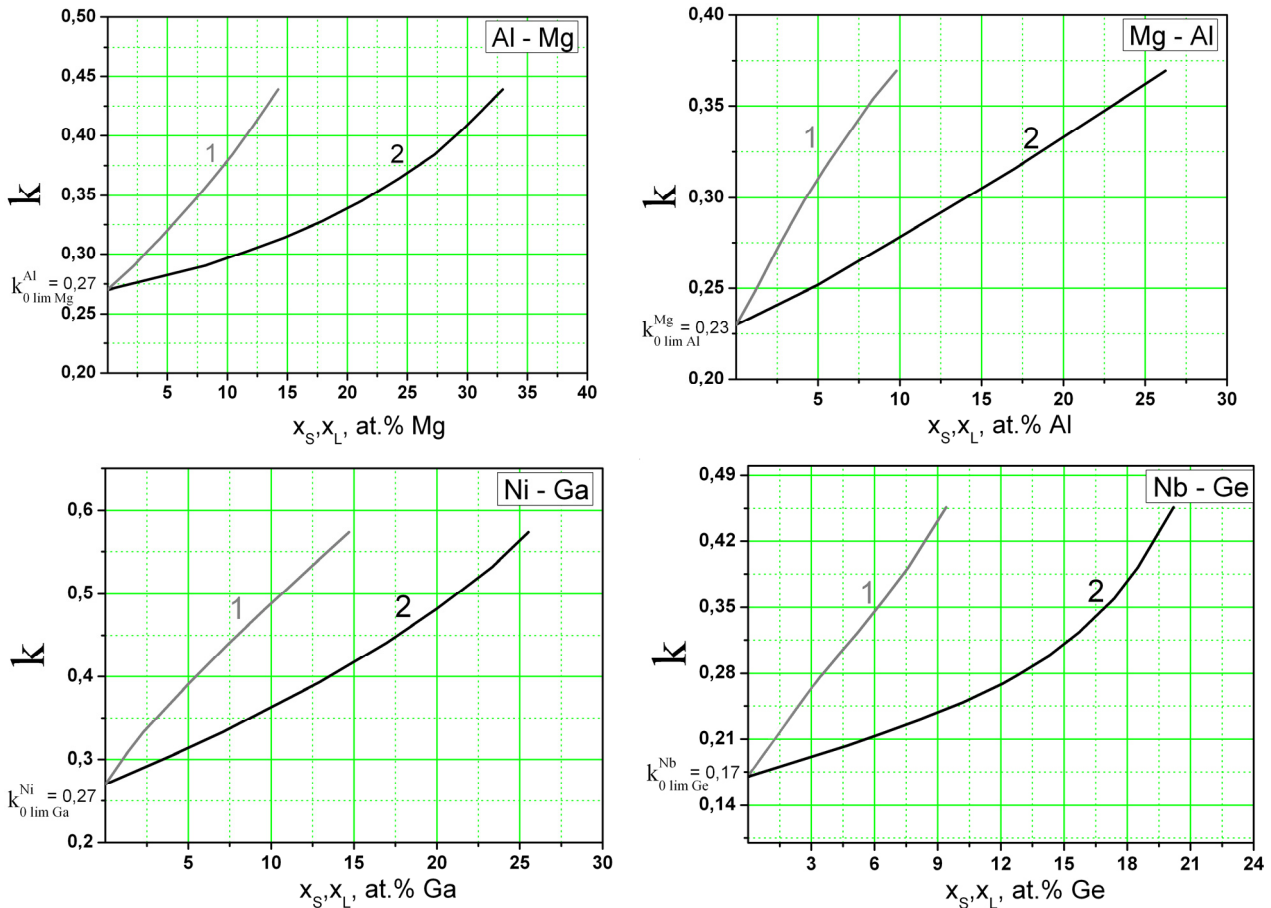
Figure 2. Dependences of equilibrium coefficients on the concentration of the second component in solid $k_{0B}^A = f(x_S)$ - 1 and liquid $k_{0B}^A = f(x_L)$ - 2 phases for binary systems Mg–Ag, Ag–Mg, Al–Mg, Mg–Al, Ni–Ga, Nb–Ge.

The curves have a different character depending on the curvature of the solidus and liquidus lines. However, they have a common intersection point as B → 0, which characterizes the limiting value $k_{0\lim B}^A$. The above calculations can be considered an additional graphical method for determining the limiting DC, and (or) use it to refine and verify the values of the limiting coefficients obtained by other methods.

CONCLUSIONS

By approximating the solidus and liquidus lines of the state diagrams in the form of second-order equations, the parameters for determining the equilibrium distribution coefficients in the Mg – Ag, Ag – Mg, Al – Mg, Mg – Al, Ni – Ga, Nb – Ge systems depending on the interfacial temperature equilibrium k_{0B}^T and concentration of components k_{0B}^C are obtained.

The dependences of the equilibrium distribution coefficients on temperature k_{0B}^T and concentration k_{0B}^C for the investigated systems are constructed. In the temperature range from the melting point of the main component of T_{MA} to the temperature of the eutectic T_{EA}, a linear dependence of k_{0B}^T and k_{0B}^C are observed.

By method of the analysis of binary state diagrams, the limiting distribution coefficients $k_{0\lim B}$ for such systems as Mg – Al, Mg – Ag, and Al – Mg were first determined. For the Ag – Mg, Nb – Ge, and Ni – Ga systems, refined values of the limiting coefficient were obtained, which are in good agreement with the reference values.

Based on the constructed dependences, the limiting distribution coefficients $k_{0\lim B}$ were obtained for the Mg – Ag, Ag – Mg, Al – Mg, Mg – Al, Ni – Ga, Nb – Ge systems, whose values coincide with the calculated values.

ORCID IDs
Alexey P. Shcherban, https://orcid.org/0000-0002-6004-0579; **Olga A. Datsenko,** https://orcid.org/0000-0002-5512-9878

REFERENCES
[1] L.A. Niselson, and A.G. Yaroshevsky, *Межфазные коэффициенты распределения* [*Interphase distribution coefficients*], (Nauka, Moscow, 1992), pp. 399. (in Russian)

[2] V. Pfann, *Зонная плавка* [*Zone melting*], (Metallurgizdat, Moscow, 1960), pp. 366. (in Russian)

[3] A.P. Scherban, Journal of V.N. Karazin Kharkiv National University. Series Nuclei, particles, fields, **946**(1), 75-80 (2011), http://nuclear.univer.kharkov.ua/lib/946_1(49)_11_p75-80.pdf. (in Russian)

[4] G.P. Kovtun, A.P. Shcherban, and O.A. Datsenko, *Коэффициенты распределения примесей в кадмии, цинке и теллуре при кристаллизационной очистке* [*The distribution coefficients of impurities in cadmium, zinc and tellurium during crystallization treatment*], Preprint, NSC KIPT, Kharkov, 2006), pp. 32. (in Russian)

[5] G.P. Kovtun, A.P. Scherban, and O.A. Datsenko, Problems of Atomic Science and Technology, Series "Vacuum, Pure Materials, Superconductors", **5**(13), 3-6 (2003). (in Russian)

[6] I. Barthel, E. Buring, K. Hein, and L. Kuharzh, *Кристаллизация из расплавов* [*Crystallization from melts*], Ref. ed. Translation from German, (Metallurgy, Moscow, 1987), pp. 320. (in Russian)

[7] A.P. Shcherban, and O.A. Datsenko, Problems of Atomic Science and Technology, Series "Vacuum, Pure Materials, Superconductors", **1**(125), 21-26 (2020).

[8] N.P. Lyakishev, *Диаграммы состояния Т.1* [*Phase diagrams Vol. 1*], (Mashinostroyeniye, Moscow, 1996), pp. 991; N.P. Lyakishev, *Диаграммы состояния Т.2* [*Phase diagrams Vol. 2*], (Mashinostroyeniye, Moscow, 1997), pp.1023; N.P. Lyakishev, *Диаграммы состояния Т.3* [*Phase diagrams Vol. 3*], (Mashinostroyeniye, Moscow, 2001), pp. 872. (in Russian)

[9] L. Kuchař, B. Wozniaková, and J. Drápala, Segregation behavior during the zone melting of refractory metals, Journal of Crystal Growth, **52**, 359–366 (1981), https://doi.org/10.1016/0022-0248(81)90219-0.

ЗАЛЕЖНІСТЬ МІЖФАЗНИХ КОЕФІЦІЄНТІВ РОЗПОДІЛУ ВІД ТЕМПЕРАТУРИ І КОНЦЕНТРАЦІЇ КОМПОНЕНТІВ У ПОДВІЙНИХ МЕТАЛЕВИХ СИСТЕМАХ

О.П. Щербань, О.А. Даценко

Національний науковий центр Харківський фізико-технічний інститут
вул. Академічна, 1, 61108, Харків, Україна

В роботі виконано розрахунок рівноважних k_0 і граничних k_{0limB} коефіцієнтів розподілення (КР) компонентів по діаграмах стану подвійних металевих систем Mg-Ag, Ag-Mg, Al-Mg, Mg-Al, Ni-Ga, Nb-Ge. Ці системи відносяться до систем з обмеженою розчинністю і для них отримані апроксимуючі рівняння ліній солідуса і ліквідуса у вигляді поліномів другого порядку в інтервалі температур від точки плавлення основного компонента T_{MA} до температури евтектики T_{EA}. Виконано математичний аналіз отриманих рівнянь для розрахунків КР. Розрахунковим і графічним методами вперше визначено значення граничних коефіцієнтів розподілу k_{0limB} для таких систем як Mg-Al, Mg-Ag, Al-Mg. Підтверджено повний збіг значень k_{0limB}, отриманих різними методами. Для систем Ag-Mg, Nb-Ge, Ni-Ga отримані уточнені величини граничних коефіцієнтом, які добре збігаються з довідковими значеннями. Побудовано залежності рівноважних коефіцієнтів розподілу від температури і концентрації для досліджуваних систем. У досліджуваному інтервалі температур від T_{MA} до T_{EA} спостерігається лінійна залежність коефіцієнтів розподілу від температури і концентрації.

КЛЮЧОВІ СЛОВА: рівноважні і граничні коефіцієнти розподілу, подвійні металеві системи, Mg-Ag, Ag-Mg, Al-Mg, Mg-Al, Ni-Ga, Nb-Ge

ЗАВИСИМОСТЬ МЕЖФАЗНЫХ КОЭФФИЦИЕНТОВ РАСПРЕДЕЛЕНИЯ ОТ ТЕМПЕРАТУРЫ И КОНЦЕНТРАЦИИ КОМПОНЕНТОВ В ДВОЙНЫХ МЕТАЛЛИЧЕСКИХ СИСТЕМАХ

А.П. Щербань, О.А. Даценко

Национальный Научный Центр Харьковский физико-технический институт
ул. Академическая, 1, 61108, Харьков, Украина

В работе выполнен расчет равновесных k_0 и предельных k_{0limB} коэффициентов распределения (КР) компонентов по диаграммам состояния двойных металлических систем Mg–Ag, Ag–Mg, Al–Mg, Mg–Al, Ni–Ga, Nb–Ge. Эти системы относятся к системам с ограниченной растворимостью и для них были получены аппроксимирующие уравнения линий солидуса и ликвидуса в виде полиномов второго порядка в интервале температур от точки плавления основного компонента T_{MA} до температуры эвтектики T_{EA}. Выполнен математический анализ полученных уравнений для расчетов КР. Расчетным и графическим методами впервые определены значения предельных коэффициентов распределения k_{0limB} для таких систем как Mg–Al, Mg–Ag, Al–Mg. Подтверждено полное совпадение значений k_{0limB}, полученных разными методами. Для систем Ag–Mg, Nb–Ge, Ni–Ga получены уточненные величины предельных коэффициентом, которые хорошо совпадают со справочными значениями. Построены зависимости равновесных коэффициентов распределения от температуры и концентрации для исследуемых систем. В исследуемом интервале температур от T_{MA} до T_{EA} наблюдается линейная зависимость коэффициентов распределения от температуры и концентрации.

КЛЮЧЕВЫЕ СЛОВА: равновесные и предельные коэффициенты распределения, двойные металлические системы, Mg-Ag, Ag–Mg, Al–Mg, Mg–Al, Ni–Ga, Nb–Ge

ELECTRONIC PROPERTIES OF BULK AND SINGLE-LAYER MOS$_2$ USING AB INITIO DFT: APPLICATION OF SPIN-ORBIT COUPLING (SOC) PARAMETERS

[iD]**Michael Gyan**[a,*], [iD]**Francis E. Botchway**[b,c], [iD]**Joseph Parbey**[a,b,c]

aSchool of Physics, University of Electronic Science and Technology of China, Chengdu 610054, China
bSchool of Material Science, University of Electronic Science and Technology of China, Chengdu 610054, China
cKoforidua, Technical University, Ghana
*Corresponding Author: mgyan173@gmail.com; phone: +8613228202349
Received September 2, 2020; accepted November 4, 2020

Two dimensional (2D) materials are currently gaining a lot of interest due to excellent properties that are different from their bulk structures. Single and few-layered of Transition metal dichalcogenides (TMDCs) have a bandgap that ranges between 1-2 eV, which is used for FET devices or any optoelectronic devices. Within TMDCs, a ton of consideration is focused on Molybdenum Disulfide (MoS2) because of its promising band gap-tuning and transition between direct to indirect bandgap properties relies upon its thickness. The density functional theory (DFT) calculations with different functionals and spin-orbit coupling (SOC) parameters were carried out to study the electronic properties of bulk and monolayer MoS$_2$. The addition of SOC brought about a noteworthy change in the profile of the band energy, explicitly the splitting of the valence band maximum (VBM) into two sub-bands. The indirect bandgap in bulk MoS$_2$ ranges from 1.17-1.71 eV and that of the monolayer bandgap was 1.6-1.71 eV. The calculated parameters were compared to the obtained experimental and theoretical results. The obtained density of states (DOS) can be used in explaining the nature of bandgap in both the bulk and monolayer MoS$_2$. These electronic characteristics are important for applications in material devices and energy-saving applications.
KEYWORDS: Electronic properties, Density functional theory, Spin-orbit coupling, Density of states, MoS$_2$, bandgap

One of the greatest discoveries in science is the successful flaking of graphene into a 2D sheet of carbon in 2004 by Novoselov et al [1]. Graphene exhibits excellent mechanical, electronic, and physical properties. It's unanticipated Zero bandgap limits its applications [2, 3]. The introduction of graphene has resulted in a great interest in other 2D materials such as phosphorene [4], silicone [5], TMDCs [6], and monochalcogenides [7, 8], creating huge attention in Nanoelectronic and optoelectronic devices [9-11]. From the various available 2D materials, 2D TMDCs exhibits superb physical properties like large bandgap which is needed in Photocatalytic water splitting [12,13].

Layered TMDCs materials are the best candidates for 2D materials because their bandgap lies between 1 to 2 eV [14]. Within the TMDCs, MoS$_2$ is the most sought for due to its industrial application starting from the use in lubricant [15], energy storage [16], photovoltaics [17], and catalyst [18]. Bulk MoS$_2$ is a semiconductor having an indirect bandgap of 1.23 eV, with its monolayer possessing a direct energy bandgap of 1.8 eV [19]. The electronic structure undergoes an excellent transition upon exfoliation from the bulk [1, 19-23]. Currently, field-effect transistor (FET) based on single-layer MoS$_2$ using HfO$_2$ as a gate insulator has been experimentally implemented [21]. These extraordinary properties have made monolayer MoS$_2$ an interesting material in optoelectronic devices and next-generation FET. Also, the transition from indirect to direct bandgap upon thinning shows excellent photoluminescence in 2D monolayer [24]. Albeit various brilliant investigations have been performed on the basic and electronic properties of MoS$_2$ [25-28]. The size-subordinate tunability of the electronic properties makes MoS$_2$ a novel material for nanoscale field-effect transistors and optical sensors [29-31]. However, as far as we could possibly know, the impact of SOC on both bulk and monolayer MoS$_2$ band structure has not been widely examined.

In this study, the band structure of bulk and monolayer MoS$_2$ were numerically investigated by the plane-wave based CASTEP, and local density approximation (LDA) and generalized gradient approximation (GGA) exchange-correlation functional were used. The influence of the spin-orbit coupling (SOC) effect on the electronic energy band structure of both monolayer and bulk MoS$_2$ has also been calculated in this study. Our results indicate that both bulk and monolayer MoS$_2$ materials are very good candidates for Opto- and spintronic device applications.

COMPUTATIONAL METHOD

First principle's calculation based on the pseudopotential plane-wave method [32] is executed in the Cambridge serial total energy package (CASTEP) [33]. This method has been used to study the electronic properties of monolayer GeI [34] and bulk and monolayer WSe$_2$. The generalized gradient approximations (GGA) of Perdew-Burke-Ernzerhof (PBE) and Local density approximations (LDA) functional [35, 36] including the spin-orbit coupling (SOC) [37] for exchange-correlation interactions. Furthermore, norm-conserving pseudopotential was used in the treatment of ion-electron exchange. The energy cut off for all calculations in this work was 700 eV, for both bulk and monolayer MoS$_2$, a k-points separation of 0.015/angstrom and SCF tolerance of 1.0×10^{-6} eV/atom were employed. The electronic minimizer was set to all bands/EDFT. Generally, the density mixing is the proposed choice for electronic minimizer, but to perform the calculation with SOC effect, the required electronic minimizer is set to all bands/EDFT in order to make a meaningful

comparism. The Monkhorst-Pack K-point was set to $7\times7\times7$ and $7\times7\times1$ for bulk and monolayer respectively. For monolayer MoS$_2$ case, we created 20 Å vacuum along Z axis in order to prevent any interaction between the layers. The pseudo atomic calculation performed for S: $3S^2, 3P^4$ and Mo: $4d^5, 5S^1$. The simulation of the band structure is performed in high symmetry direction $\Gamma - M - K - \Gamma$.

RESULTS
Structural parameters

Molybdenum disulfide has a hexagonal crystal structure linked to space group P 6_3/mmc (194). The structure is made up of the stacking of three atomic layers S-Mo-S layer. Monolayer MoS$_2$ has a single S-Mo-S layer as shown in Fig. 1b, whiles the bulk MoS$_2$ has a two-layer monolayer MoS$_2$ with one-layer Mo atoms place on top of the Sulphur atoms of the other layer, illustrated in Fig. 1b. From geometry optimization, the lattice constants for bulk MoS$_2$ are 3.192A in a and b axis and 12.478 in the c-axis. The monolayer slab was cleaved in 001 direction and a vacuum layer of 20A.
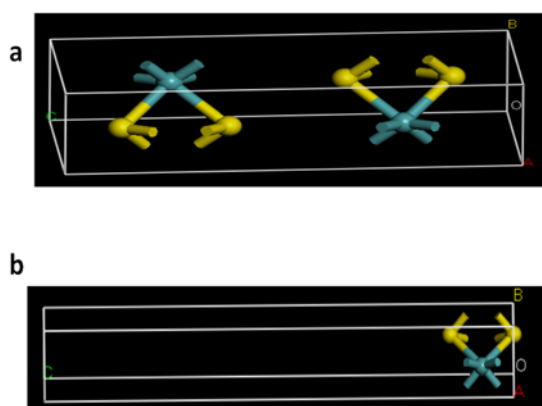
Figure 1. A ball and stick model of one-unit cell of the (a) bulk MoS$_2$ and (b) Monolayer MoS$_2$.
The blue atoms represent the Mo atoms, and the yellow atoms represent the S atoms.

Electronic properties and density of states

A series of calculations were performed on the bulk and monolayer MoS$_2$ with LDA CAPZ and GGA PBE functionals incorporated with or without SOC. The electronic band pattern of monolayer MoS$_2$ as shown in Fig. 2 has a direct bandgap situated at $K \rightarrow K$ of k point.
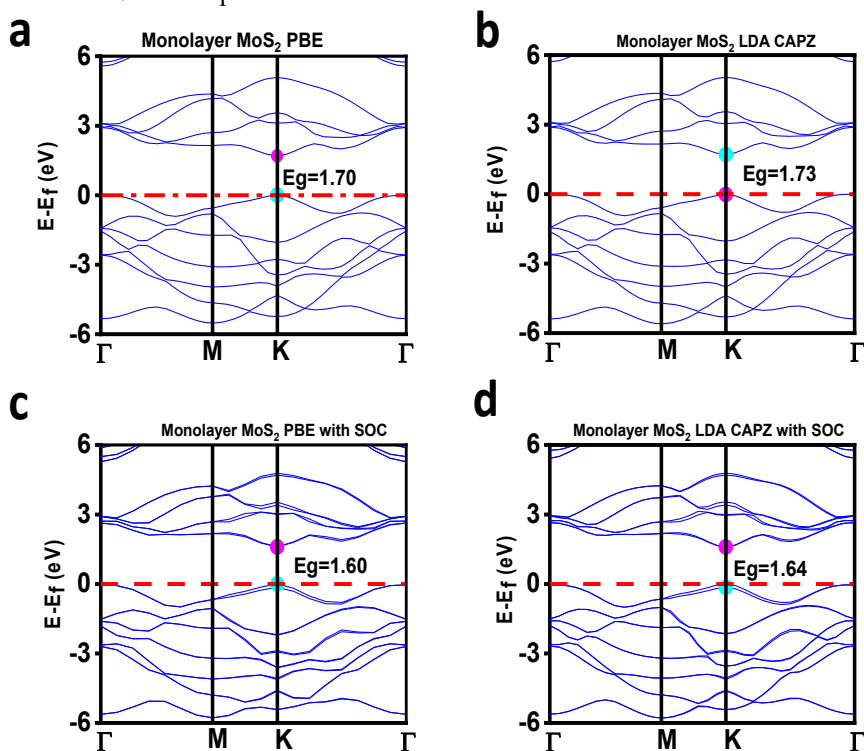
Figure 2. Band structure of (a)-monolayer MoS$_2$ PBE without SOC, (b)-Monolayer LDA CAPZ without SOC, (c)-Monolayer MoS$_2$ PBE with SOC, (d)-Monolayer MoS$_2$ LDA CAPZ with SOC

This transition in bandgap makes monolayer MoS$_2$ applicable to different devices. Interestingly, all the calculations either with or without SOC captures the direct bandgap feature for monolayer MoS$_2$. Also, the application of SOC for monolayer MoS$_2$ affects the band gap value. Furthermore, the valence band maximum and that of the conduction band both occur at high symmetric K point indicating a direct bandgap semiconductor as shown in Fig. 2(a-d) above. The bandgap value for monolayer MoS$_2$ ranges from 1.60 to 1.71eV. The experimental result indicates a slight shift from the theoretical result. The theoretical work gives a slight difference in bandgap than the experiment as illustrated in Table.

Table

Energy band gap (eV) and bandgap type for both Bulk and Monolayer

Functionals	Bulk MoS$_2$		Monolayer MoS$_2$	
	Indirect bandgap	Bandgap value	Direct bandgap	Bandgap value
GGA PBE no SOC	Yes	1.27	Yes	1.70
LDA CAPZ no SOC	Yes	1.23	Yes	1.73
GGA PBE SOC	Yes	1.22	Yes	1.60
LDA CAPZ SOC	Yes	1.17	Yes	1.64
EXP REF	Yes	1.23(ref [19]) 1.29(ref [27])	Yes	1.80 (ref [19])
THEOR REF	Yes	0.7(ref [38]) 1.05(ref [26]) 1.15(ref [39])	Yes	1.55 (ref [25,26]) 1.70 (ref [40]) 1.78 (ref [41]) 1.9 (ref [42])

From Fig. 2(a-d), the valence band maximum (VBM) and the conduction band minimum (CBM) lie below and above the Femi level respectively along with the K- symmetry. For the monolayer MoS$_2$, there is a reasonable band splitting as seen in Fig 2 (c) and (d), this band splitting is brought about by the utilization of SOC and can likewise help in the application of spintronic and valleytronics [43-47]. The band splitting is observed distinctly in the valence band (VB) of the high symmetry K-direction. This result is good agreement with previously reported literature [28, 43, 48].
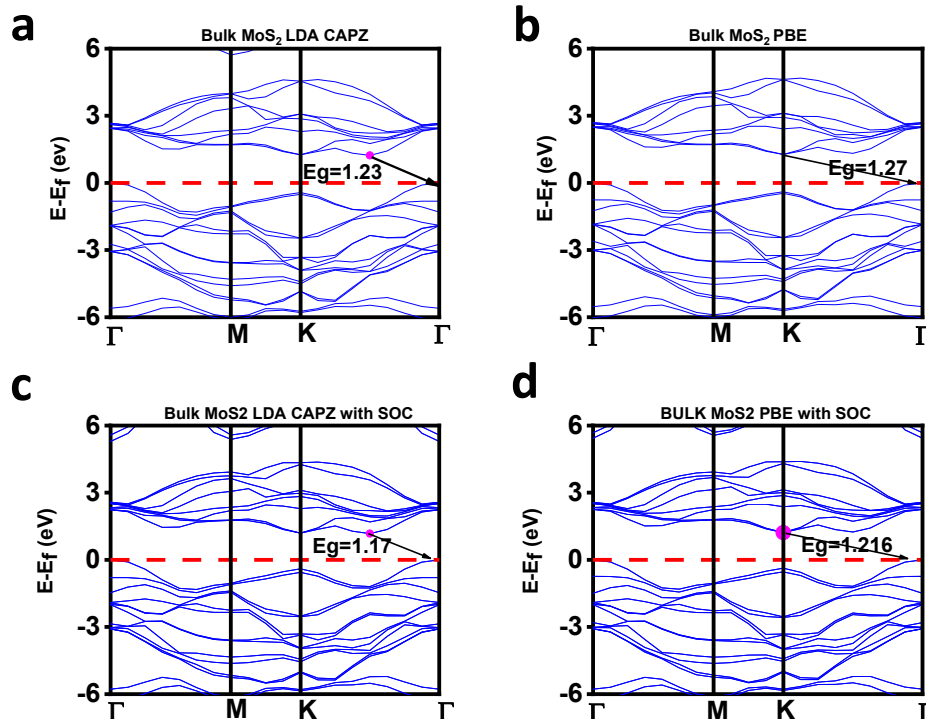
Figure 3. Band structure of (a) Bulk MoS$_2$ PBE without SOC (b) Bulk LDA CAPZ without SOC (c) Bulk MoS$_2$ PBE with SOC (d) Bulk MoS$_2$ LDA CAPZ with SOC

Fig. 3. (a)- (d) represents the band structure of bulk MoS$_2$ for PBE and LDA functionals. The band structure profiles obtained indicate an indirect semiconductor since the maxima of the valence band is situated at K Γ - path whiles that of the minimum of the conduction band is located at Γ -point. The obtained bandgap values range from 1.17-1.27 eV which is consistent with the experimental value [19, 27] shown in Table. From the obtained results of the electronic structures,

we realized that there are slight changes in the energy band with or without SOC. Also, it was observed that the bandgap value 0f the compound with SOC is smaller than the one without SOC. Fig. 3 (c) and (d) show a slight Valence band (VB) splitting on a high symmetry K direction. This splitting can be ascribed to the utilization of SOC [43, 49-53]. The SOC influences the valence band of the compound as appeared in Fig. 3(c,d).

Fig. 4. (a-d) represents the partial density of states of bulk and monolayer MoS_2 using two different functionals i.e. PBE and LDA. MoS_2 exhibits a neutral charge due to the presence of +4 in the valence of Mo and a charge of -2 for the S- atom. From Fig. 4(a-d), the partial density of states can be divided into three classes of states. For the first class, the density around -14eV is due to 3s orbital of S atom which is separated by a wide gap. The second class is the one below the Fermi level in which the contributing orbitals the 3p orbitals of S atom and 4d orbitals of Mo. This class possesses a strong hybridization. The third class is the one above the Fermi-level, here the contributing orbital is the 4d orbitals of Mo and is separated by the second class with a narrow gap. For both functionals, the bandgap occurs due to the 4d orbitals of Mo and 3p orbitals of S atoms in monolayer and bulk MoS_2.
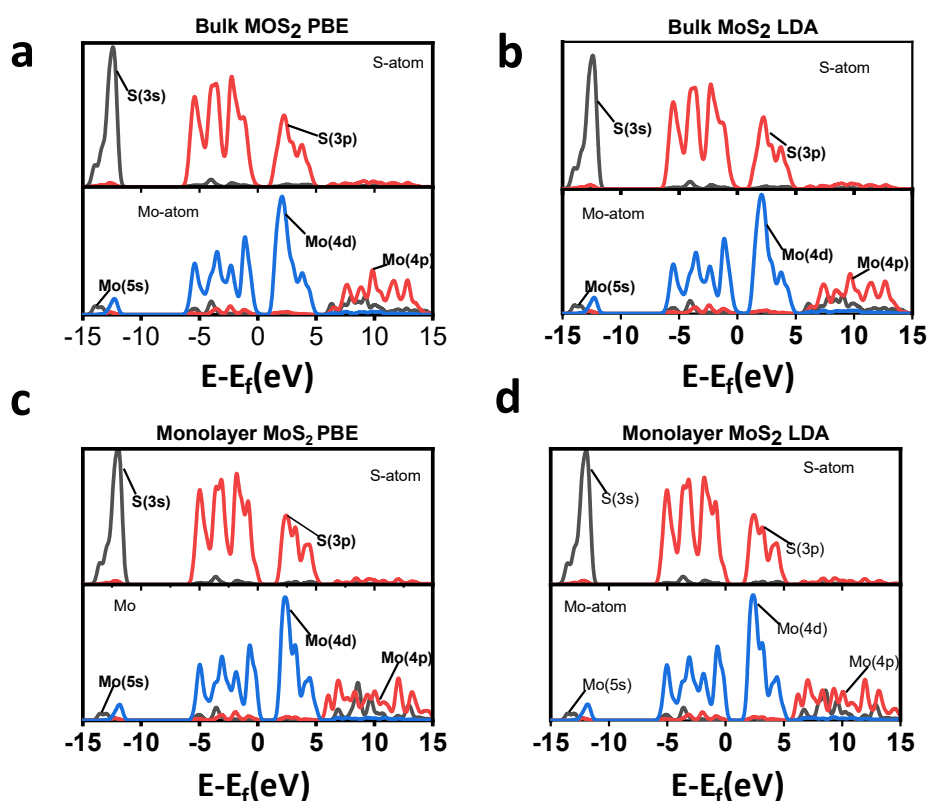
Figure 4. Partial density of states of (a) Bulk MoS_2 using PBE functional (b) Bulk MoS_2 using LDA (c) MoS_2 monolayer using PBE functional (d) MoS_2 monolayer using LDA

CONCLUSION

The electronic properties of bulk and monolayer MoS_2 have been studied using first-principle calculations based on the pseudopotential plane-wave method. Our results show that monolayer MoS_2 is a direct semiconductor whiles bulk MoS_2 has an indirect bandgap. Also, our calculations show that the bandgap of monolayer MoS_2 ranges from 1.6-1.73 eV whereas the bulk is 1.17-1.27 eV which is consistent with the available experimental and theoretical results. The electronic structure and density of states indicate many similarities between the monolayer and bulk MoS_2. The main contribution to the valence and conduction band are 4d states of Mo and 3p orbitals of s atom in both monolayer and bulk MoS_2. We have discovered that the incorporation of spin-orbit coupling influences the band structures and the splitting of degenerate valence band occurs on high symmetry K-point.

ORCID IDs
Michael Gyan, https://orcid.org/0000-0001-6337-2205; **Francis E. Botchway**, https://orcid.org/0000-0001-8327-4469;
Joseph Parbey, https://orcid.org/0000-0002-0277-0098

REFERENCES

[1]   K.S. Novoselov, D. Jiang, F. Schedin, T.J. Booth, V.V. Khotkevich, S.V. Morozov, and A.K. Geim, PNAS, **102**(30), 10451-10453 (2005), https://doi.org/10.1073/pnas.0502848102.

[2]   W. Choi, I. Lahiri, R. Seelaboyina, and Y.S. Kang, Critical Reviews in Solid State and Materials Sciences, **35**, 52-71 (2010), https://doi.org/10.1080/10408430903505036

[3]   M.J. Allen, V.C. Tung, and R.B. Kaner, Chemical Reviews, **110**(1), 132-145 (2010), https://doi.org/10.1021/cr900070d.

[4]   H. Liu, A.T. Neal, Z. Zhu, Z. Luo, X. Xu, D. Tománek, and P.D. Ye, ACS Nano. **8**(4), 4033-4041 (2014), https://doi.org/10.1021/nn501226z.

[5]   B. Lalmi, H. Oughaddou, H. Enriquez, A. Kara, S. Vizzini, B. Ealet, and B. Aufray, Applied Physics Letters, **97**(22), 223109 (2010), https://doi.org/10.1063/1.3524215.

[6]   Q.H. Wang, K. Kalantar-Zadeh, A. Kis, J.N. Coleman, and M.S. Strano, Nature Nanotechnology, **7**(11), 699-712 (2012), https://doi.org/10.1038/nnano.2012.193.

[7]   M. Safari, Z. Izadi, J. Jalilian, I. Ahmad, and S. Jalali-Asadabadi, Physics Letters A, **381**(6), 663-670 (2017), https://doi.org/10.1016/j.physleta.2016.11.040.

[8]   S. Das, J.A. Robinson, M. Dubey, H. Terrones, and M. Terrones, Annual Review of Materials Research, **45**(1), 1-27 (2015), https://doi.org/10.1146/annurev-matsci-070214-021034.

[9]   D.J. Late, B. Liu, H. Matte, C.N.R. Rao, and V.P. Dravid, Advanced Functional Materials, **22**(9), 1894-1905 (2012), https://doi.org/10.1002/adfm.201102913.

[10] C.V. Nguyen, N.N. Hieu, D. Muoi, C.A. Duque, E. Feddi, H.V. Nguyen, L.T.T. Phuong, B.D. Hoi, and H.V. Phuc, Journal of Applied Physics, 123(3), 034301 (2018), https://doi.org/10.1063/1.5009481.

[11] M.H. Fekri, R. Bazvand, M. Soleymani, and M.R. Mehr, International Journal of Nano Dimension, **11**(4), 346-354 (2020), http://www.ijnd.ir/article_675374_91ad4efdd80a983d0ba8492569c8e510.pdf.

[12] W. Zhang, Z. Huang, W. Zhang, and Y. Li, "Two-Dimensional Semiconductors with Possible High Room Temperature Mobility," Nano Research, **7**(12), 1731-1737 (2014), https://doi.org/10.1007/s12274-014-0532-x.

[13] M. Khaleghian, and F. Azarakhshi, International Journal of Nano Dimension, **10**(1), 105-113 (2019), http://www.ijnd.ir/article_661564_d54fcf021f466ebbe353d21c7a171061.pdf.

[14] J.A. Wilson, and A.D. Yoffe, Advances in Physics, **18**(73), 193-335 (1969), https://doi.org/10.1080/00018736900101307.

[15] Y. Kim, J.L. Huang, and C.M. Lieber, Applied Physics Letters, **59**(26), 3404-3406 (1991), https://doi.org/10.1063/1.105689.

[16] A.H. Reshak, and S. Auluck, Physical Review B, **68**, 125101 (2003), https://doi.org/10.1103/PhysRevB.68.125101.

[17] E. Fortin and W.M. Sears, Journal of Physics and Chemistry of Solids. **43**(9), 881-884 (1982), https://doi.org/10.1016/0022-3697(82)90037-3.

[18] K.H. Hu, X.G. Hu, and X.J. Sun, Applied Surface Science, **256**(8), 2517-2523 (2010), https://doi.org/10.1016/j.apsusc.2009.10.098.

[19] K.F. Mak, C. Lee, J. Hone, J. Shan, and T.F. Heinz, Physical Review Letters, **105**(13), 36805 (2010), https://doi.org/10.1103/PhysRevLett.105.136805.

[20] P. Joensen, R.F. Frindt, and S.R. Morrison, Materials Research Bulletin, **21**(4), 457-461 (1986), https://doi.org/10.1016/0025-5408(86)90011-5.

[21] B. Radisavljevic, A. Radenovic, J. Brivio, V. Giacometti, and A. Kis, Nature Nanotechnology, **6**, 147 (2011), https://doi.org/10.1038/nnano.2010.279.

[22] J.N. Coleman, M. Lotya, A. O'Neill, S.D. Bergin, P.J. King, U. Khan, K. Young, A. Gaucher, S. De, R.J. Smith, I.V. Shvets, S.K. Arora, G. Stanton, H.-Y. Kim, K. Lee, G.T. Kim, G.S. Duesberg, T. Hallam, J.J. Boland, J.J. Wang, J.F. Donegan, J.C. Grunlan, G. Moriarty, A. Shmeliov, R.J. Nicholls, J.M. Perkins, E.M. Grieveson, K. Theuwissen, D.W. McComb, P.D. Nellist, and V. Nicolosi, Science, **331**(6017), 568-571 (2011), https://doi.org/10.1126/science.1194975.

[23] D. Dey, and D. De, Int. J. Nano Dimens. **9**(2), 134-144 (2018), http://www.ijnd.ir/article_658988_772299c871dafd993e3f08bec602d2a1.pdf.

[24] J.K. Ellis, M.J. Lucero, and G.E. Scuseria, Applied Physics Letters, **99**(26), 261908 (2011), https://doi.org/10.1063/1.3672219.

[25] S. Ahmad, and S. Mukherjee, Graphene, **3**, 52-59 (2014), http://dx.doi.org/10.4236/graphene.2014.34008.

[26] A. Kumar, and P.K. Ahluwalia, Materials Chemistry and Physics, **135**(2), 755-761 (2012), https://doi.org/10.1016/j.matchemphys.2012.05.055.

[27] Th. Böker, R. Severin, A. Müller, C. Janowitz, R. Manzke, D. Voß, P. Krüger, A. Mazur, and J. Pollmann, Physical Review B, **64**, 235305 (2001), https://doi.org/10.1103/PhysRevB.64.235305

[28] D.P. Rai, T.V. Vu, A. Laref, Md.A. Hossain, E. Haque, S. Ahmad, R. Khenatag, and R.K. Thapah, RSC Advances, **10**(32), 18830-18840 (2020), https://doi.org/10.1039/D0RA02585B.

[29] F.J. Urbanos, A. Black, R. Bernardo-Gavito, A.L. Vázquez de Parga, R. Miranda, and D. Granados, Nanoscale, **11**(23), 11152-11158 (2019), https://doi.org/10.1039/c9nr02464f.

[30] Tung Pham, Guanghui Li, Elena Bekyarova, Mikhail E. Itkis, and Ashok Mulchandani, ACS Nano, **13**(3), 3196-3205 (2019), https://doi.org/10.1021/acsnano.8b08778.

[31] N. Goel, R. Kumar, and M. Kumar, *AIP Conference Proceedings*, **1942**(1), 050060 (2018), https://doi.org/10.1063/1.5028691.

[32] M.D. Segall, P.J.D. Lindan, M.J. Probert, C.J. Pickard, P.J. Hasnip, S.J. Clark, and M.C. Payne, Journal of Physics: Condensed Matter, **14**(11), 2717-2744 (2002), https://doi.org/10.1088/0953-8984/14/11/301.

[33] S.J. Clark, M.D. Segall, C.J. Pickard, P.J. Hasnip, M.I.J. Probert, K. Refson, and M.C. Payne, Zeitschrift für Kristallographie. 220(5-6), 567-570 (2005), https://doi.org/10.1524/zkri.220.5.567.65075.

[34] D.M. Hoat, T.V. Vu, M.M. Obeid, and H.R. Jappor, Chemical Physics, **527**, 110499 (2019), https://doi.org/10.1016/j.chemphys.2019.110499.

[35] J.P. Perdew, K. Burke, and M. Ernzerhof, Physical Review Letters, **77**(18), 3865-3868 (1996), https://doi.org/10.1103/PhysRevLett.77.3865.

[36] J.P. Perdew, K. Burke, and M. Ernzerhof, Phys. Rev. Lett. 77, 3865 (1996)]," Physical Review Letters, **78**(7), 1396-1396 (1997), https://doi.org/10.1103/PhysRevLett.77.3865.

[37] A.H. MacDonald, W.E. Picket, and D.D. Koelling, Journal of Physics C: Solid State Physics, **13**(14), 2675-2683 (1980), https://doi.org/10.1088/0022-3719/13/14/009.

[38] K. Kobayashi, and J. Yamauchi, Surface Science, **357-358**, 317-321 (1996), https://doi.org/10.1016/0039-6028(96)00173-2.

[39] L.F. Mattheiss, Physical Review Letters, **30**, 784-787 (1973), https://doi.org/10.1103/PhysRevLett.30.784.

[40] C. Ataca, and S. Ciraci, The Journal of Physical Chemistry C, **115**(27), 13303-13311 (2011), https://doi.org/10.1021/jp2000442.

[41] S. Lebègue, and O. Eriksson, Physical Review B, **79**(11), 115409 (2009), https://doi.org/10.1103/PhysRevB.79.115409.

[42] A. Kuc, N. Zibouche, and T. Heine, Physical Review B, **83**(24), 245213 (2011), https://doi.org/10.1103/PhysRevB.83.245213.

[43] Z.Y. Zhu, Y.C. Cheng, and U. Schwingenschlögl, Physical Review B, **84**(15), 153402 (2011), https://doi.org/10.1103/PhysRevB.84.153402.

[44] D. Xiao, G.-B. Liu, W. Feng, X. Xu, and W. Yao, Physical Review Letters, **108**(19), 196802 (2012), https://doi.org/10.1103/PhysRevLett.108.196802.

[45] H. Zeng, J. Dai, W. Yao, D. Xiao, and X. Cui, Nature Nanotechnology, **7**(8), 490-493 (2012), https://doi.org/10.1038/nnano.2012.95.

[46] M. Bieniek, L. Szulakowska, and P. Hawrylak, Physical Review B, **101**(3), 035401 (2020), https://doi.org/10.1103/PhysRevB.101.035401.

[47] Q. Chen, L. Liang, G. Potsi, P. Wan, J. Lu, T. Giousis, E. Thomou, D. Gournis, P. Rudolf, and J. Ye, Nano Letters, **19**(3), 1520-1526 (2019), https://doi.org/10.1021/acs.nanolett.8b04207.

[48] C.-H. Chang, X. Fan, S.-H. Lin, and J.-L. Kuo, Physical Review B, **88**(19), 195420 (2013), https://doi.org/10.1103/PhysRevB.88.195420.

[49] D.Y. Qiu, F.H. da Jornada, and S.G. Louie, Physical Review Letters, **111**(21), 216805 (2013), https://doi.org/10.1103/PhysRevLett.111.216805.

[50] A. Molina-Sánchez, D. Sangalli, K. Hummer, A. Marini, and L. Wirtz, Physical Review B, **88**(4), 045412 (2013), https://doi.org/10.1103/PhysRevB.88.045412.

[51] N. Alidoust, G. Bian, S.-Y. Xu, R. Sankar, M. Neupane, C. Liu, I. Belopolski, D.-X. Qu, J.D. Denlinger, F.-C. Chou, and M.Z. Hasan, Nature Communications, **5**, 4673 (2014), https://doi.org/10.1038/ncomms5673.

[52] X. Dou, K. Ding, D. Jiang, X. Fan, and B. Sun, ACS Nano. **10**(1), 1619-1624 (2016), https://doi.org/10.1021/acsnano.5b07273.

[53] N. Zibouche, A. Kuc, J. Musfeldt, and T. Heine, Annalen der Physik, **526**(9-10), 395-401 (2014), https://doi.org/10.1002/andp.201400137.

ПОЧАТКОВІ ДОСЛІДЖЕННЯ ЕЛЕКТРОННИХ ВЛАСТИВОСТЕЙ ОБ'ЄМНОГО ТА ОДНОШАРОВОГО MoS₂ З ВИКОРИСТАННЯМ ДПФ: ЗАСТОСУВАННЯ ПАРАМЕТРІВ СПІН-ОРБІТАЛЬНОГО ЗВ'ЯЗКУ (SOC)

Майкл Гайян[a], Френсіс Е. Ботвей[b,c], Джозеф Парбі[a,b,c]

[a]Китайська школа фізики Університету електронних наук і технологій Китаю, Ченду 610054, Китай
[b]Школа матеріалознавства, Китайський університет електронних наук і технологій, Ченду, 610054, Китай
[c]Кофорідва, Технічний університет, Гана

Двомірні (2D) матеріали в даний час викликають великий інтерес завдяки чудовим властивостям, що відрізняють їх від об'ємних структур. Одношарові та багатошарові дихалькогеніди перехідних металів (TMDC) мають ширину забороненої зони, яка коливається в межах 1-2 еВ, що використовується для пристроїв FET або будь-яких оптоелектронних пристроїв. У випадку TMDC розгляд зосереджено на дисульфіді молібдену (MoS₂) через перспективи регулювання забороненої зони, а перехід між властивостями прямих та непрямих переходів зони залежить від його товщини. Розрахунки теорії щільності функціонала (DFT) з різними функціоналами та параметрами спін-орбітальної зв'язку (SOC) проводились для вивчення електронних властивостей об'ємного та одношарового MoS₂. Додавання SOC спричинило помітну зміну профілю енергії зони, явно розділивши максимум валентної зони (VBM) на два діапазони. Зона з непрямими переходами об'ємного MoS₂ коливається в межах 1,17-1,71 еВ, а зона у випадку одного шару становить 1,6-1,71 еВ. Розраховані параметри порівнювали з отриманими експериментальними та теоретичними результатами. Отримана щільність станів (DOS) може бути використана для пояснення природи зони як в об'ємному, так і в одношаровому MoS₂. Ці електронні характеристики важливі для застосування в матеріальних пристроях та енергозберігаючих застосуваннях.

КЛЮЧОВІ СЛОВА: електронні властивості, теорія щільності функціонала, спін-орбітальний зв'язок, щільність станів, MoS₂, заборонена зона

ПЕРВОНАЧАЛЬНЫЕ ИССЛЕДОВАНИЯ ЭЛЕКТРОННЫХ СВОЙСТВ ОБЪЕМНОГО И ОДНОСЛОЙНОГО MoS₂ С ИСПОЛЬЗОВАНИЕМ ДПФ: ПРИМЕНЕНИЕ ПАРАМЕТРОВ СПИН-ОРБИТАЛЬНОЙ СВЯЗИ (SOC)

Майкл Гайян[a], Фрэнсис Э. Ботвей[b,c], Джозеф Парби[a,b,c]

[a]Китайська школа физики Университета электронных наук и технологий Китая, Чэнду 610054, Китай
[b]Школа материаловедения, Китайский университет электронных наук и технологий, Чэнду, 610054, Китай
[c]Кофоридва, Технический университет, Гана

Двухмерные (2D) материалы в настоящее время вызывают большой интерес благодаря замечательным свойствам, отличающих их от объемных структур. Однослойные и многослойные дихалькогениды переходных металлов (TMDC) имеют ширину запрещенной зоны, которая колеблется в пределах 1-2 эВ, что используется для устройств FET или любых оптоэлектронных устройств. В случае TMDC рассмотрение сосредоточено на дисульфиде молибдена (MoS₂) из-за перспективы регулирования запрещенной зоны, а переход между свойствами прямых и косвенных переходов зоны зависит от его толщины. Расчеты теории плотности функционала (DFT) с различным функционалом и параметрами спин-орбитальной связи (SOC) проводились для изучения электронных свойств объемного и однослойного MoS₂. Добавление SOC привело к заметному изменению профиля энергии зоны, явно разделив максимум валентной зоны (VBM) на два диапазона. Зона с косвенным переходами объемного MoS₂ колеблется в пределах 1,17-1,71 эВ, а зона в случае одного слоя составляет 1,6-1,71 эВ. Рассчитанные параметры сравнивали с полученными экспериментальными и теоретическими результатами. Полученная плотность состояний (DOS) может быть использована для объяснения природы зоны как в объемном, так и в однослойном MoS₂. Эти электронные характеристики важны для применения в материальных устройствах и энергосберегающих приложениях.

КЛЮЧЕВЫЕ СЛОВА: электронные свойства, теория плотности функционала, спин-орбитальная связь, плотность состояний, MoS₂, запрещенная зона

RESEARCH AND DEVELOPMENT OF NOVEL MATERIALS FOR ACCIDENT TOLERANT FUEL CLADDING OF NUCLEAR REACTORS

Kostiantyn V. Lobach[a],*, Oleksandr S. Kuprin[a], Sergiy Yu. Sayenko[a], Victor M. Voyevodin[a,b], Igor V. Kolodiy[a]

[a]National Science Center "Kharkiv Institute of Physics and Technology"
61108, Kharkiv, Ukraine
[b]V.N. Karazin National University, 61022, Kharkiv, Ukraine
*Corresponding Author: lobach0709@gmail.com

The paper describes the challenges and worldwide scientific studies aimed for the manufacturing of the fuel elements claddings tolerant to a loss of coolant accidents (Fukushima NPP, March 2011, Japan) for water-cooled reactors. The main research results obtained at NSC KIPT on the development of materials for fuel element claddings, tolerant to accidents with loss of coolant, are given. The structure and properties of the developed vacuum-arc chromium coatings were investigated. It is shown, that these coatings can be used as protective element for existing fuel claddings, made of zirconium alloys, in light-water reactors of the PWR and BWR types. Alloyed SiC-based ceramic was developed to replace zirconium-based fuel claddings. It has been established that doping of 0.5 wt% Cr into SiC leads to an increase in the ability to resist the formation of cracks (crack resistance) by 25 – 30%. The effect of Cr alloying on the corrosion resistance of SiC ceramics under conditions, simulating the medium of the first circuit of the VVER-1000 reactor, is analyzed. It was established that doping of even a small amount of Cr leads to a slowdown in corrosion processes in SiC ceramics. In order to create new material for fuel elements claddings Fe-Cr-Al-based alloys with the doping of alloying elements (Y, Zr and Mo) were also developed and studied. Obtained alloys showed high mechanical properties and resistance to high-temperature oxidation.
KEYWORDS: fuel elements cladding, corrosion, protective coatings, SiC/SiC composites, Fe-Cr-Al alloys

The term "ATFC" (Accident Tolerant Fuel Cladding) for water-cooled reactors came into use after the Fukushima NPP accident in March, 2011, in Japan. At that time, at a distance of 130 km from the coastal area of Japan the grade ≈ 9.0 earthquake took place, which caused the failure of NPP electric power lines, while the following earthquake wave flooded and put out of action emergency diesel generators, which were at lower levels of the NPP site. That resulted in the final and full NPP Station Blackout (SBO), and as a consequence, in the Loss-of-Coolant Accident [1]. Under this type of accidents, an intense heat generation continues in the nuclear reactor, accompanied with a temperature rise due the nuclear reactions in UO_2 fuel pellets. At about 950 $^{\circ}$C, the reaction between the zirconium fuel-element cladding and steam, known as the steam-zirconium reaction, begins

$$Zr + 2H_2O = ZrO_2 + 2H_2 + Q. \tag{1}$$

At a temperature of 1200 $^{\circ}$C, this reaction starts to develop rapidly with great heat liberation, thus becoming a self-sustaining reaction, and that leads to fuel cladding melting (Fig. 1) [2]. Concurrent with heat liberation, a great amount of hydrogen is also released (cf., ~ 0.5 l H_2 per one gram of reacting Zr), which is accumulated inside the reactor and the reactor block, this inevitably leading to dangerously explosive situation.
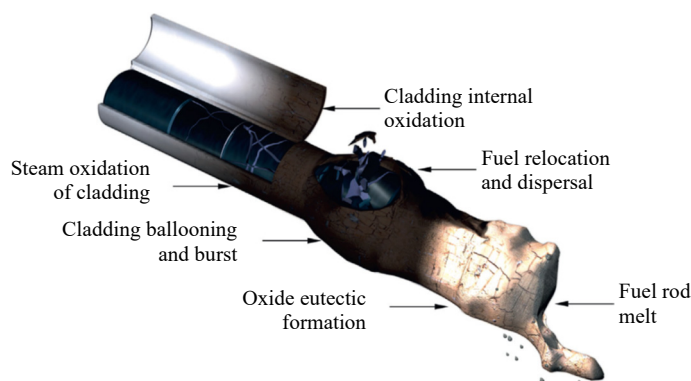
Figure 1. Evolution of a fuel rod under LOCA and SBO conditions [2]

To this date, it is common practice in the world to use for all water-cooled reactors the fuel claddings made of zirconium alloys (E110, M5, Zirlo, Zircaloy 4, etc.), and thus, the danger of hazardous consequences in case of loss-of-coolant accidents (LOCA) still remains. The creation of ATFCs should substantially improve the safe use of modern nuclear-power engineering.

Scientific studies into ATFC creation are carried out in different lines of research, and they differ in the term of their realization. The near-term technologies imply the application of protective coatings to the surfaces of existing zirconium-alloy claddings, whereas the mid-term technologies involve their complete replacement by claddings made from other materials such as metal alloys based on FeCrAl, Mo/FeCrAl, and SiC-base ceramic materials (Fig. 2 [3]).
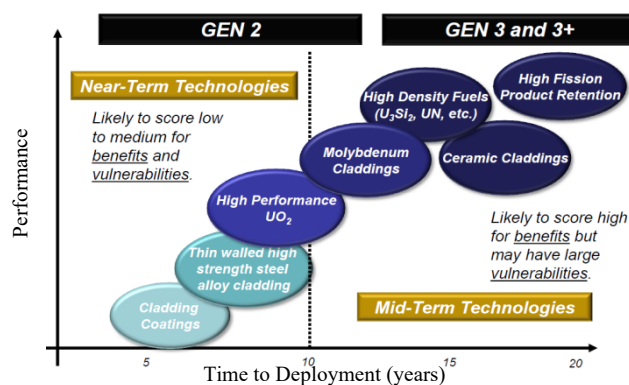
Figure 2. Development of ATF fuel [3]

All these studies are aimed at reducing the cooling load during the LOCA by decreasing the heat-release rate and the total volume of liberated heat (Q), which results from cladding oxidation under the action of high-temperature steam; that, in turn, reduces the rate of temperature rise. The slower increase of temperature retards the process of reaction (1) development, thereby providing some extra time for eliminating the accident and preventing its rapid development [4]. Therefore, the creation of ATFCs calls for the materials that show a considerably higher resistance to high-temperature steam oxidation than that of present-day zirconium claddings. Various R&D programs to solve the problem [5, 6] were initiated all over the world after the Fukushima accident. The undertaken studies have demonstrated that though the high-temperature steam is by far a more corrosive medium than dry O_2 [7], still to protect zirconium alloys, oxide films can be used. The films must be oxidation resistant in the high-temperature steam, and also, must be physically and chemically stable, serving as barriers, which restrict solid-phase diffusion between the base material and O, OH and H_2O. These properties are exhibited by three classes of protective films, namely, chromium oxide, alumina and silica [8].

Although zirconium oxide exhibits exceptional thermodynamic stability in the steam, however at T> 1100 °C it readily transmits oxygen, letting the base metal (zirconium) be unprotected. On the other hand, chromium oxide, aluminium oxide, and silicium oxide show acceptable stability in high-temperature steam; they can react with the steam and evaporate at higher temperatures [9-11], acting, though slowly, as efficient barriers for diffusion of reaction products (oxygen and hydrogen). The oxidation rate of these films is approximately two orders of magnitude lower. This reduction of oxidation rate directly leads to the decrease in the rate of heat/hydrogen generation in water-cooled reactors at LOCA-type accident.

The present paper offers a short survey of research data obtained at the NSC KIPT, concerned with two directions in creation of ATF claddings, being actively developed in various international programs.

COATINGS FOR FUEL CLADDINGS

The evident and developmental approach to creating the ATFC lies in applying protective coatings to the surface of zirconium-alloy claddings. It is expected that thin coatings will have the minimal effect on the thermomechanical behavior of Zr-based cladding [12], and have the potential to improve the cladding heat transfer characteristics. The coatings are required to have the maximal adhesion to the cladding material and to be chemically stable with the cladding when in normal service in water (T = 350 °C, P = 15 MPa) of the primary coolant circuit of the reactor, and also, they should protect the cladding against rapid oxidation under LOCA-type conditions. As mentioned above, chromium, aluminium and silicium oxides are the materials that are capable to show resistance to oxidation in the high-temperature steam. For this reason, any protective coating of the ATF cladding must include at least one of the elements: Cr, Al or Si. The protective coatings must have the radiation resistance as good as that of the zirconium cladding, on which they are deposited.

The experimental studies have demonstrated that among a wide range of protective coatings applied to zirconium alloys by different methods, it is the chromium coatings produced by the PVD method that show the best protective properties [13-14].

Among other PVD methods, the vacuum-arc method of coating deposition has an essential advantage, viz., a high degree of deposited material ionization, which is favorable for obtaining relatively thin (~10 to 20 μm) high-adhesive coatings without through pores. This method makes it possible to produce nanostructural multilayer coatings, including ceramic coatings, at the deposition temperature that does not exceed the finishing treatment temperature of zirconium-alloy claddings (~ 450 °C), thereby precluding the occurrence of structural changes in the made fuel elements, and also without sacrificing their mechanical properties at test temperatures of 20 and 350 °C [15-17].

Comprehensive studies are carried out at the NSC KIPT to develop and deposit protective vacuum-arc coatings onto fragments of zirconium-alloy fuel tubes, as well as to investigate their influence on the mechanical properties at different temperatures [15-17], oxidation resistance [18-20] and hydrogen saturation [21, 22]. Studies are also made to investigate the radiation resistance of chromium coatings [23].

The 10 μm thick multilayer Cr/CrN and Cr coatings, developed at NSC KIPT, substantially slow down the oxidation rate of zirconium alloys in both the air and water steam at a temperature of 1100 °C over a period of no less than 3600 s. The air-oxidation resistance of coatings on the E110 and Zr1Nb alloys at test temperatures ranging from 660 to 1100 °C is independent of the alloy type and phase transformations in zirconium. The high resistance of the developed coatings is determined by the formation of a dense chromium-oxide layer on their surfaces (Fig. 3) [18-20].

a   *b*
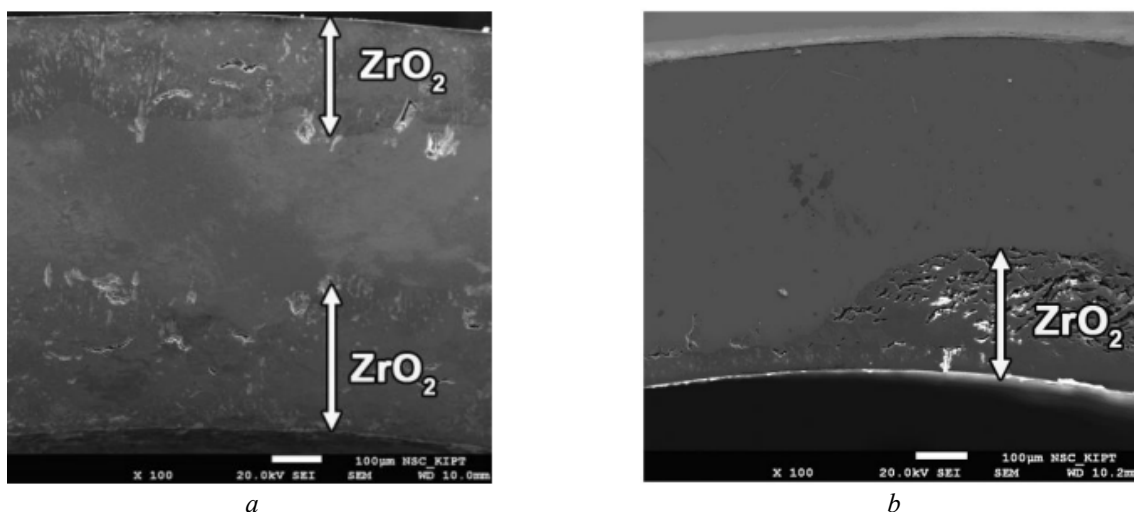
Figure 3. Electron microscope images of metallographic sections of E110 tubes after air oxidation at 1100 °C during 3600 s: a)uncoated, b) with protective Cr coating (10 μm) [20]

It has been established in Refs. [21, 22] that at the test temperatures ranging from 350 ° to 550 °C, and at test pressures of hydrogen (deuterium) between 0.01 and 0.8 Pa, the Cr and Cr/CrN coatings under study present a reliable barrier to hydrogen penetration, and protect zirconium from hydride accumulation.

The radiation resistance of chromium coatings was investigated by the TEM methods after their irradiation in the ESU-2 accelerator by 1.4 MeV Ar$^+$ ions at a temperature of 400 ° C in the dose range from 5 to 25 dpa [23]. The vacuum-arc chromium coatings in the output state show a sub-microcrystalline structure with an average grain size of ~ 250 nm. Inside the grains there are dislocations of density ~8×10^{14} m^{-2}. The electron-diffraction pattern of chromium coating shows textured maxima in the form of points, this being indicative of the oriented growth of some grains. Adjacent to the points, there are the maxima in the form of round brackets, which attest to the presence of grains of random orientation.
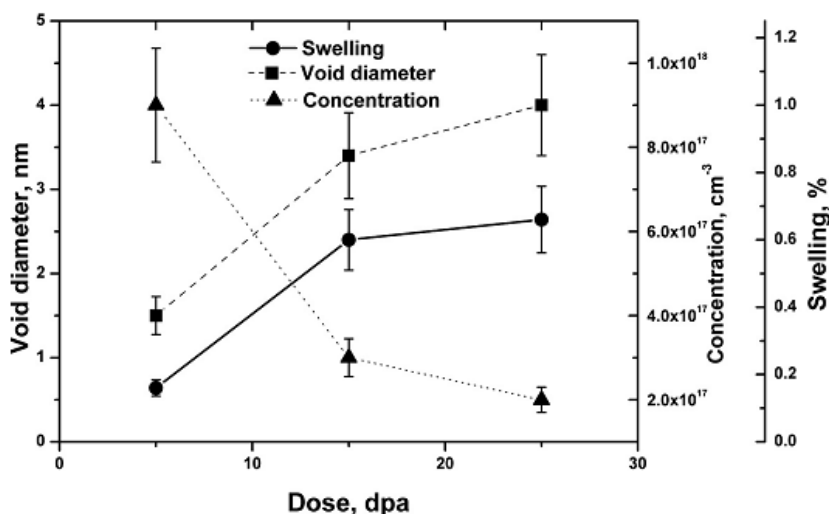
Figure 4. Dose dependence of average size, concentration of voids and swelling in irradiated Cr coatings [23]

Under exposure to a dose of 5 dpa, the radiative swelling of chromium coatings has been found to be ~ 0.16 %, and with a dose increase up to 25 dpa, it attains 0.66 % (Fig. 4), this pointing to a high radiation resistance of the developed chromium coatings.

The given research results demonstrate that the vacuum-arc chromium coatings can be used to provide corrosion and oxidation protection of zirconium-alloy claddings for water-cooled reactors of PWR and BWR types.

<div align="center">

SiC-BASED FUEL CLADDINGS

</div>

The SiC-based materials exhibit such attractive properties as high-temperature oxidation resistance [8], high-temperature chemical stability, strength and resistance to radiation damage, which make these materials most promising for applying as ATFC in water-cooled reactors. At present, the R&D world activities in production of SiC-based claddings are mainly performed in two separate directions using:

1. The Chemical Vapor Infiltration (CVI) method being the most common approach in the world to cladding production. The method includes the vapor-phase deposition of SiC onto SiC fibers that results in production of high-purity crystalline SiC composite showing a high radiation resistance but a relatively low density (porosity being 10 to 25 %) [24, 25].

2. The Nano-Infiltration and Transient Eutectic-phase (NITE) method, mainly used in Japan, involves the infiltration of SiC-fiber with β-SiC nanopowder with a further use of the hot pressing (HP) technique to produce the claddings made of SiC/SiC composite. The method ensures the production of high-density material with improved physical-mechanical properties [26, 27].

The NSC KIPT scientists are involved in the development of SiC-based materials using the high-speed hot pressing (HSHP) method [28], and also, in the studies into the influence of alloying additives on the mechanical characteristics of produced materials [29] and the SiC-based materials corrosion-resistance under hydrothermal conditions [30].

The studies in ref. [28] were aimed to establish optimum process parameters for producing the high-density SiC ceramics by the HSHP method. The method is based on passing directly the current through the press mold and the material sintered, and has an essential advantage over the HP method for the sintering rate (up to 400 °C/min.). Thus, during rapid heating, the process of sintering instantaneously passes through the low-temperature stage with usual dominance of the mechanisms of grain growth, and goes to the high-temperature stage, now with the dominance of densification mechanisms. Besides, the concentration of heat evolution on the particle surface causes the melting of surface layers and the destruction of oxide films with the result that chemical reactions get accelerated [31].

Figure 5 shows the cleavage structures of SiC ceramics produced at non-optimal/optimal process parameters of the HSHP method (Figs. 5a and 5b, respectively). It is found that the best physical-mechanical properties of SiC ceramics are attained at the sintering temperature T = 2050 °C , pressure P = 40 MPa and the holding-pressure time t = 30 min. The obtained ceramics exhibits a high density (up to 99.4 % of the theoretical value), the hardness 27.3 ± 0.5 GPa, and the monolithic and homogeneous structure with clear-cut grain boundaries and with the signs of brittle failure (Fig. 5b).

a   b
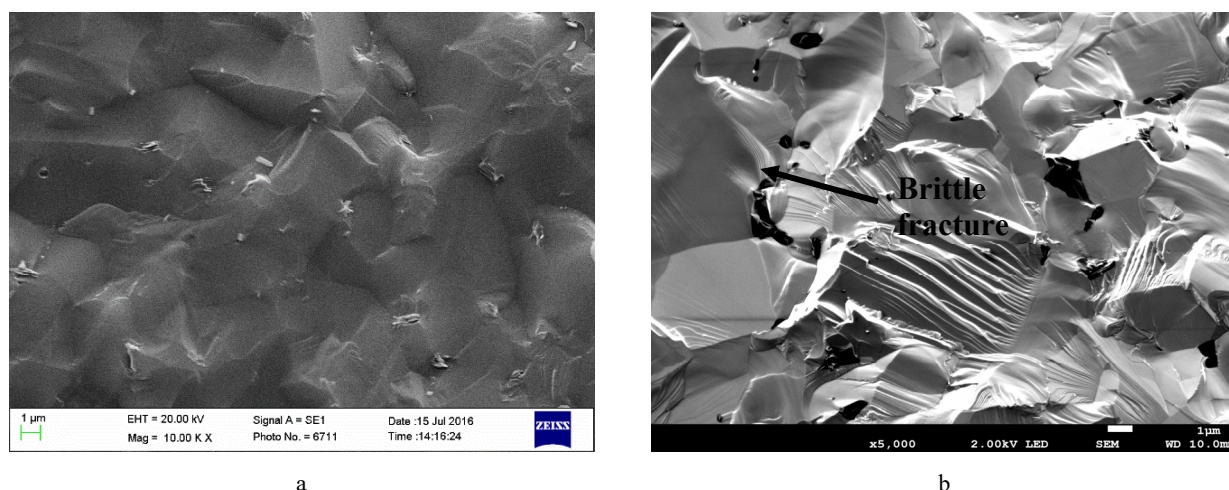
Figure 5. Microstructure of SiC ceramics cleavage: a – non-optimal parameters, b – optimal parameters of the HSHP method [29]

Paper [29] is concerned with the improvement of physical-mechanical properties of SiC through introduction of different alloying additives (Table 1).

<div align="right">

Table 1.

</div>

<div align="center">

Hardness and fracture toughness values of SiC

</div>

Samples	Density, g/cm^3	Open porosity, %	Hardness H$_v$, GPa	Crack growth resistance K$_{1c}$, MPa·m$^{1/2}$
SiC	3.19	0	27.3	4.3
SiC +Cr	3.16	0-1	28.0	6.2
SiC + Si	3.18	0-1	30.0	4.7

As is seen from the given data, at similar values of density, open porosity and hardness, the fracture toughness values have increased in the samples with Cr and Si additions. For example, the fracture toughness parameters increase from $K_{1c} = 4.3$ MPa·m$^{1/2}$ for the SiC ceramic samples up to $K_{1c} = 6.2$ MPa·m$^{1/2}$ for the SiC samples with Cr additions. Figure 6 demonstrates the influence of the Cr addition on the coefficient of fracture toughness. Thus, at the same load of 9.81 N, one can see that in the SiC sample with Cr additions (Fig. 6b) no noticeable cracks are observed, whereas in the pure SiC sample (Fig. 6a) the cracks do exist.

a   *b*
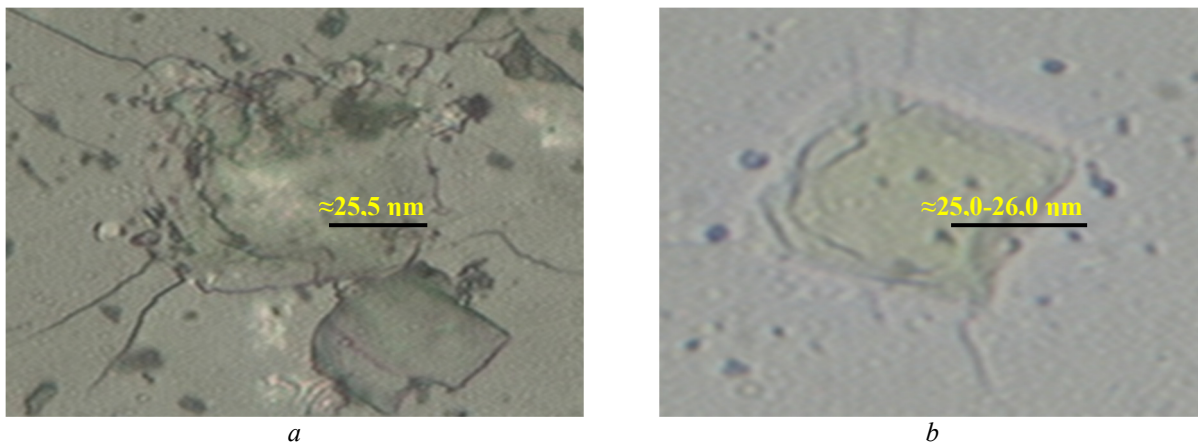
Figure 6. Effect of Cr on the coefficient of fracture toughness of SiC
a – pure SiC, b – SiC with Cr additions [30]

Obtained results may have a substantial effect on the production technology of SiC-matrix in SiC/SiC composites for manufacturing the fuel element claddings since there is a problem of manufacturing thin-walled tubes (claddings) from a brittle SiC ceramics, which has low values of the fracture toughness coefficient.

Experiments were made in [30] to investigate the behavior of SiC ceramics under hydrothermal conditions. It is known that in spite of corrosive resistance in a high-temperature steam, the SiC-based ceramics dissolves in high-temperature water, i.e., under conditions of non-emergency service in water-cooled reactors. The possibility was demonstrated to exist for the radionuclides to release from the nuclear fuel through the fuel element cladding to the coolant due to the occurrence of hydrothermal corrosion and microcracks [32]. The undertaken research suggests that for decreasing the rate of SiC dissolution under hydrothermal conditions, the methods should be developed for alloying of anticorrosive additives, and also, for use of corrosion-resistant coatings, or both methods in combination [33, 34].

As indicated above, the best corrosion-resistance data were obtained for the coatings based on Cr. This element is used in the development of metal alloys based on FeCrAl and Mo/FeCrFl, which exhibit high corrosion resistance [8]. Besides, Cr is used for improving the corrosion resistance in steels, e.g., the introduction of no less than 12 % Cr into the alloy drastically increases the corrosion resistance (stainless steel). Taking this into account, Cr was chosen in [30] as the main anticorrosion alloying additive.

Table 2 and the plots (Fig. 7) give the hydrothermal corrosion test data for the SiC samples (without/with Cr and Si additives) produced by the HSHP method at a water temperature of 350 °C and a pressure of 16.8 MPa. After 100 hours of holding time, the SiC samples with Cr additives exhibited the increase in mass per area of ~ 3.27 mg/dm^2. At that, the masses of SiC samples with and without additives get decreased. Then, the mass reduction is observed in the samples with Cr additions, too. However, as it can be seen from the plot (Fig. 6), the best corrosion resistance under hydrothermal test conditions was shown by the SiC ceramics with Cr additions.

Table 2.

Corrosion test results for SiC samples

Test duration (hours)	SiC + Cr, mg/dm^2	SiC, mg/dm^2	SiC + Si, mg/dm^2
0	0	0	0
100	3.27	-4.01	-2.74
350	-3.07	-7.27	-4.96
600	-5.42	-8.27	-7.20
1000	-8.49	-12.53	-10.66

Some teams of scientists who investigated the hydrothermal corrosion of silicon carbide [35, 36], have indicated that the following thermodynamic reactions may occur between SiC and water:

$$SiC + 2H_2O \rightarrow SiO_2 + CH_4; \tag{2}$$
$$SiC + 4H_2O \rightarrow SiO_2 + CO_2 + 4H_2 \tag{3}$$
$$SiC + 3H_2O \rightarrow SiO_2 + CO + 3H_2 \tag{4}$$
$$SiC + 2H_2O \rightarrow SiO_2 + C + 2H_2 \tag{5}$$
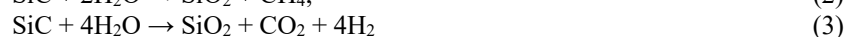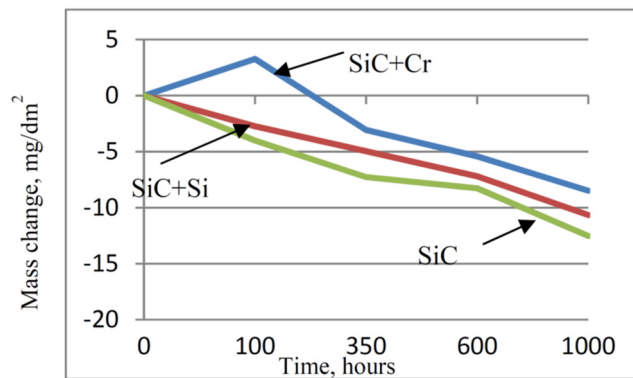
Figure 7. Results of corrosion tests of SiC samples [31]

As is obvious, by reactions (2) to (5), protective SiO_2 films are formed on the SiC surface. On this basis, the corrosion resistance difference can be explained by the formation of corrosion-resistant products (Cr_2O_3, and Cr_nC_x), which have a substantial effect on the capacity of SiO_2 films for passivation of sample surfaces.

Relying on the obtained data, it can be argued that the presence of even minor Cr additives content radically changes the behavior of the ceramics during oxidation, and leads to the formation of more corrosion-resistant protective SiO_2 films on the SiC sample surfaces with Cr additives, essentially reducing the corrosion under hydrothermal conditions.

FE-CR-AL-BASED ALLOYS AS A MATERIAL FOR FUEL CLADDINGS

Fe-Cr-Al based alloys are considered within the ATFC concept as one of the possible options for replacing traditional zirconium alloys for nuclear fuel claddings after the accident at the Japanese nuclear power plant Fukushima [8, 37]. These alloys have increased oxidation resistance (and, as consequence, reduced hydrogen accumulation) and higher strength compared to zirconium alloys, at least up to 1300 °C. A distinctive feature of Fe-Cr-Al based alloys is the formation of a thin protective alumina film during the high-temperature tests in water vapor [7] and high corrosion resistance during tests under conditions close to the normal operation, due to the formation of a spinel film from chromium and iron oxides [38]. In addition, the advantage of these alloys relative to the corrosion-resistant austenitic steels is the absence of nickel, the presence of which is undesirable in materials for thermal neutron reactors [39]. These alloys also satisfy the requirements for fuel cladding materials in terms of the complex of neutron-physical characteristics and radiation resistance [40, 41].

The study of the effect of alloying elements (Y, Mo and Zr) on the structure, heat resistance, physical and mechanical properties of alloys based on the Fe-Cr-Al system was carried out at NSC KIPT [42]. Six alloys (No. 1 – No. 6) were selected as materials for the study, two of which (No. 1 and No. 2) were industrial Kanthal alloys grade X23U5T: No. 1 - Kanthal alloy, grade X23U5T; No. 2 – Kanthal alloy after remelting; No. 3 – 72.5Fe-21Cr-6Al-0.5Y; No. 4 - 72Fe-21Cr-6Al-1Y; No. 5 – 70Fe-21Cr-6Al-1Y-2Mo; No. 6 – 63Fe-23Cr-9Al-1Y-2Mo-2Zr (all values are in wt %). XRD analysis showed that all alloys were single-phase (except the alloy No. 6) and consisted of a bcc phase (Fig.8a). It was established that molybdenum is uniformly distributed over the alloy, while yttrium is concentrated at grain boundaries and in oxide precipitations. Alloying Kanthal with 2%wt zirconium leads to the formation of a microstructure which consists of grains of the matrix bcc phase and intergranular eutectic "BCC matrix phase + FCC Laves phase $ZrFe_2$". The main amount of yttrium and zirconium is concentrated in the eutectic.
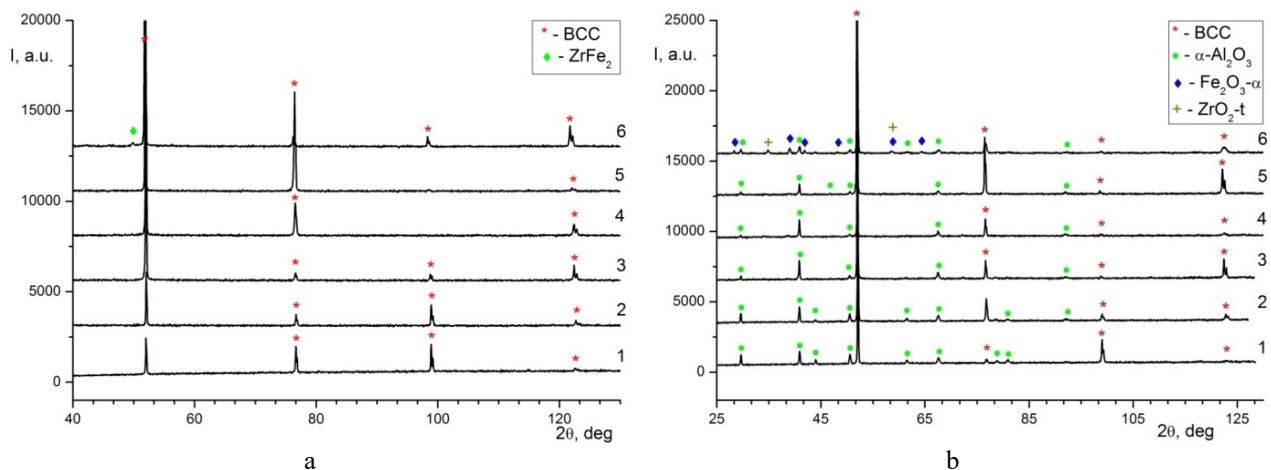
Figure 8. Diffraction patterns of Fe-Cr-Al alloys: a) initial state; b) after oxidation in air at T = 1300 °C for 3 hours

The effect of the alloys composition on their resistance to high-temperature oxidation was investigated by annealing in the furnace in air at temperature T = 1300 °C for 3 hours and atmospheric pressure. The results of this study are shown in Fig. 9.

All samples after high-temperature oxidation tests showed an increase in weight without shedding (peeling) with the formation of a dense dark-gray oxide film on the surface (Fig.10). The lowest mass gain (0.3 mg /cm^2) was observed in the samples doped with Y and Mo, and the highest (7.2 mg /cm^2) - in the samples doped with Y, Mo and Zr. Such different behavior of alloys during oxidation is associated with the formation of oxide layers of different phase composition on their surface. According to the X-ray diffraction analysis all samples consist of bcc matrix phase and alumina Al_2O_3-α (Fig.8b). Diffraction pattern of the alloy No. 6 (which shows the lowest stability) also revealed the presence of hematite Fe_2O_3-α and tetragonal zirconia ZrO_2-t in addition to the bcc phase and Al_2O_3-α. I.e., in this case, oxidation occurred not only of alloying elements but also of matrix elements.
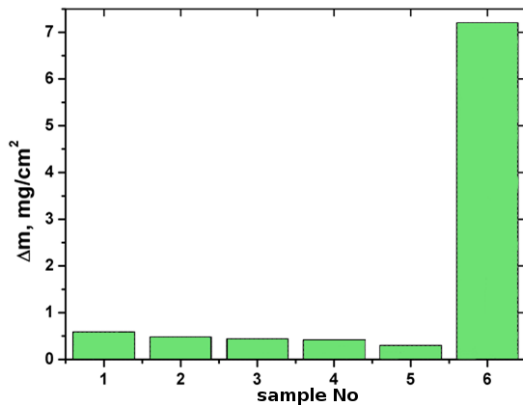
Figure 9. Mass gain of the Fe-Cr-Al samples after oxidation in air at T = 1300 °C for 3 hours
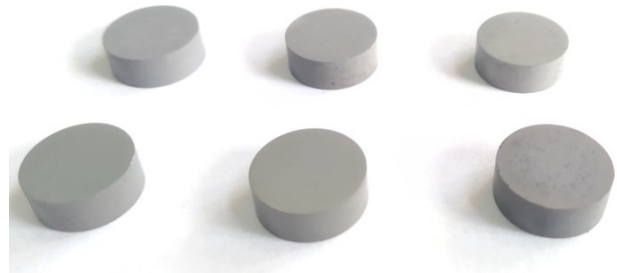
Figure 10. Appearance of the Fe-Cr-Al samples after high-temperature oxidation

Table 3 shows data on the mechanical properties of the investigated alloys. As it can be seen, alloying the Fe-Cr-Al alloys with various chemical elements affects their mechanical and wear-resistant properties. Parameters H/E and H^3/E^2 are used to assess the wear resistance and resistance of materials to plastic deformation, respectively [43, 44]. Nanohardness, Young's modulus, microhardness and compressive yield strength decrease for alloys alloyed only with Y (samples No. 3 and No. 4). Additional alloying with molybdenum (sample No. 5) leads to an increase in nanohardness and microhardness. Simultaneous alloying with Y, Mo and Zr (sample No. 6) increases all mechanical characteristics of the alloy, and the parameters H/E and H^3/E^2 are the highest among all the alloys under study.

Table 3.

Mechanical properties of the Fe-Cr-Al alloys (ρ – density, H – nanohardness, E – Young's modulus, H_μ^{200} – microhardness at load of 200 g, σ$_T$ – compressive yield strength, V$_S$ – cavitation failure rate)

Sample No	Mechanical properties							
	ρ, g/cm^3	H, GPa	E, GPa	H/E	H^3/E^2, GPa	H_μ^{200}, GPa	σ$_{Tc}$, kg/mm^2	V$_S$·10^2, mm^3/year
1	6.8	3.6	230.6	0.016	8.8·10^{-4}	2.35	60.2	9.7
2	7.13	3.7	218.7	0.017	1.1·10^{-3}	2.40	53.4	19.6
3	7.2	3.3	220.6	0.015	7.4·10^{-4}	2.22	44.2	18.8
4	6.82	3.4	217.5	0.016	8.3·10^{-4}	2.45	55.7	-
5	6.93	3.7	219.4	0.017	1.1·10^{-3}	2.51	54.5	27.3
6	6.56	4.9	215.6	0.023	2.5·10^{-3}	3.42	97.6	4.57

Since the strength characteristics of Fe-Cr-Al-based alloys are not worse than those of zirconium alloys, the most important characteristic for using these alloys as reactor material is their resistance to high-temperature oxidation. According to this alloy No. 5 (70Fe-21Cr-6Al-1Y-2Mo) is the most promising among the alloys under study.

CONCLUSIONS

The paper provides a brief overview of the main directions on the R&D of materials for fuel element claddings in the world and the research results on the development of materials for the ATFC at NSC KIPT:

- Developed chromium vacuum-arc coatings with a set of their properties can be used to provide protection against corrosion of fuel claddings made of zirconium alloys for water-cooled reactors of the PWR and BWR types and to prevent LOCA type accidents.

- Technical parameters for obtaining SiC ceramics by the VGP method with high physical and mechanical properties were optimized. It has been shown that alloying SiC ceramics with chromium leads to an increase in the crack resistance

coefficient (K_{1c}) by 25 – 30% and slows down corrosion processes under hydrothermal conditions corresponding to the normal operation of water-cooled reactors. Obtained SiC based ceramics can be used as a SiC matrix in SiC/SiC composites for the manufacturing of fuel element claddings.

- Experimental alloys based on Fe-Cr-Al alloyed with Y, Mo and Zr were developed, their structure, heat resistance, physical and mechanical properties were investigated. Studies have shown that these alloys can be a promising material for reactor fuel claddings to replace traditional zirconium alloys within the ATFC concept.

The results obtained at the NSC KIPT can be taken into account and applied to solve the problems of fuel claddings manufacturing for water-cooled reactors in the framework of the safe and sustainable development of nuclear energy in Ukraine.

ORCID IDs
Kostiantyn V. Lobach, https://orcid.org/0000-0002-9838-2259; **Oleksandr S. Kuprin,** https://orcid.org/0000-0003-4293-4197;
Sergiy Yu. Sayenko, https://orcid.org/0000-0002-2598-3598; **Victor M. Voyevodin,** https://orcid.org/0000-0003-2290-5313;
Igor V. Kolodiy, https://orcid.org/0000-0001-8598-9732

REFERENCES
[1] M. Holt, R.J. Campbell, and M.B. Nikitin, *Fukushima Nuclear Disaster*, (Congressional Research Service, 2012), pp. 12, https://fas.org/sgp/crs/nuke/R41694.pdf

[2] S.J. Zinklea, K.A.Terrani, J.C. Gehin, L.J. Ott, and L.L. Snead, Journal of Nuclear Materials, **448,** 374-379 (2014), https://doi.org/10.1016/j.jnucmat.2013.12.005.

[3] B.-S. Shannon, Nuclear News, **57**, 83-91 (2014), https://doi.org/10.2172/1122119.

[4] L.J. Ott, K.R. Robb, D. Wang, Journal of Nuclear Materials, **448**, 520-533 (2014), https://doi.org/10.1016/j.jnucmat.2013.09.052.

[5] F. Goldner, *Development Strategy for Advanced LWR Fuels with Enhanced Accident Tolerance*, (US Department of Energy, 2012), pp. 15, https://pdfs.semanticscholar.org/1b46/39a7109a0b27791662c802743c4798c0b44f.pdf.

[6] Y.-H. Koo, J.-H. Yang, J.-Y. Park, K.-S. Kim, H.-G. Kim, D.-J. Kim, Y.-I. Jung, and K.-W. Song, Nuclear technology, **186**(2), 295-304 (2014), https://doi.org/10.13182/NT13-89.

[7] B.A. Pint, K.A. Terrani, M.P. Brady, T. Cheng, and J.R. Keiser, Journal of Nuclear Materials, **440**, 420-427 (2013), https://doi.org/10.1016/j.jnucmat.2013.05.047.

[8] K.A. Terrani, Journal of Nuclear Materials, **501**, 13-30 (2018), https://doi.org/10.1016/j.jnucmat.2017.12.043.

[9] H.A. Mohd, and R. Othman, Advanced Materials Research**, 402,** 412-420 (2012), https://doi.org/10.4028/www.scientific.net/AMR.402.412.

[10] T. Amano, ECS Transactions, **25**, 3-19 (2010), https://doi.org/10.1149/1.3315791.

[11] E.J. Opila, J. Am. Ceram. Soc. **86**(8), 1238-1248 (2003), https://doi.org/10.1111/j.1151-2916.2003.tb03459.x.

[12] Y. Lee, J.I. Lee, and H.C. No, NET, **49**, 1031-1043 (2017), https://doi.org/10.1016/j.net.2017.03.012.

[13] C. Tang, M. Stueber, H.J. Seifert, and M. Steinbrueck, Corros. Rev. **35**, 141-165 (2017), https://doi.org/10.1515/corrrev-2017-0010.

[14] J. Bischoff, C. Delafoy, C. Vauglin, P. Barberis, C. Roubeyrie, D, Perche, D. Duthoo, F. Schuster, J.-C. Brachet, E.W. Schweitzer, and K. Nimishakavi, Nucl. Eng. Technol. **50**(2), 223-228 (2018), https://doi.org/10.1016/j.net.2017.12.004.

[15] V.A. Belous, P.N. V'jugov, A.S. Kuprin, S.A. Leonov, G.I. Nosov, V.D. Ovcharenko, L.S. Ozhigov, et al, PAST, **84**(2), 140-143 (2013), https://vant.kipt.kharkov.ua/ARTICLE/VANT_2013_2/article_2013_2_140.pdf. (in Russian)

[16] L.S. Ozhigov, V.A. Belous, V.I. Savchenko, G.I. Nosov, V.D. Ovcharenko, G.N. Tolmachova, A.S. Kuprin, and V.S. Goltvyanitsa, PAST, **108**(2), 168-172 (2017), https://vant.kipt.kharkov.ua/ARTICLE/VANT_2017_2/article_2017_2_168.pdf.

[17] P.I. Stoev, V.A. Belous, V.N. Voevodin, A.S. Kuprin, S.A. Leonov, V.D. Ovcharenko, M.A. Tihonovskij, V.M. Horoshih, PAST, **99**(5), 87-97 (2015), https://vant.kipt.kharkov.ua/ARTICLE/VANT_2015_5/article_2015_5_87r.pdf. (in Russian)

[18] A.S. Kuprin, V.A. Belous, V.N. Voyevodin, V.V. Bryk, R.L. Vasilenko, V.D. Ovcharenko, G.N. Tolmachova, P.N. V'ygov, PAST, **89**(1), 126-132 (2014), https://vant.kipt.kharkov.ua/ARTICLE/VANT_2014_1/article_2014_1_126.pdf.

[19] A.S. Kuprin, V.A. Belous, V.N. Voyevodin, V.V. Bryk, R.L. Vasilenko, V.D. Ovcharenko, E.N. Reshetnyak, G.N. Tolmachova, and P.N. V'yugov, Journal of Nuclear Materials, **465**, 400-406 (2015), https://doi.org/10.1016/j.jnucmat.2015.06.016.

[20] A.S. Kuprin, V.A. Belous, V.V. Bryk, R.L. Vasilenko, V.N. Voyevodin, V.D. Ovcharenko, G.N. Tolmachova, et al, PAST, **96**(2), 111-118 (2015), https://vant.kipt.kharkov.ua/ARTICLE/VANT_2015_2/article_2015_2_111.pdf.

[21] G.D. Tolstolutskaya, I.E. Kopanetz, V.V. Ruzhytskiy, V.A. Bilous, A.S. Kuprin, V.D. Ovcharenko, R.L. Vasilenko, and S.A. Leonov, PAST, 2015, **96**(2), 119-123 (2015), https://vant.kipt.kharkov.ua/ARTICLE/VANT_2015_2/article_2015_2_118.pdf.

[22] I.E. Kopanetz, G.D. Tolstolutskaya, A.V. Nikitin, V.A. Belous, A.S. Kuprin, V.D. Ovcharenko, and R.L. Vasilenko, PAST, **99**(5), 81-86 (2015), https://vant.kipt.kharkov.ua/ARTICLE/VANT_2015_5/article_2015_5_81.pdf.

[23] A.S. Kuprin, V.A. Belous, V.N. Voyevodin, R.L. Vasilenko, V.D. Ovcharenko, G.D.Tolstolutskaya, E. Kopanets, and V. Kolodiy, Journal of Nuclear Materials, **510**, 163-167 (2018), https://doi.org/10.1016/j.jnucmat.2018.07.063.

[24] Y. Katoh, K. Ozawa, C. Shih, T. Nozawa, R.J. Shinavski, A. Hasegawa, and L.L. Sneada, Journal of Nuclear Materials, **448**, 448-476 (2014), https://doi.org/10.1016/j.jnucmat.2013.06.040.

[25] O.A. Ageev, A.E. Beljaev, N.S. Boltovec, V.S. Kiselev, R.V. Konakova, A.A. Lebedev, V.V. Milenin, et al, *Карбид кремния: технология, свойства, применение [Silicon carbide: technology, properties, applications],* (Kharkiv, ISMA, 2010), pp. 532, http://isp.kiev.ua/images/Institute/lab33/Statti/SiCtechnologyPropertiesApplication.pdf. (In Russian)

[26] H.-W. Yu, P. Fitriani, S. Lee, J.-Y. Park, and D.-H. Yoon, Ceramics International, **41**(6), 7890-7896 (2015), https://doi.org/10.1016/j.ceramint.2015.02.127.

[27] Y. Katoh, A. Kohyama, T. Nozawa, and M. Sato, Journal of Nuclear Materials, **329-333**, 587-591 (2004), https://doi.org/10.1016/j.jnucmat.2004.04.157.

[28] V. Voyevodin, S. Sayenko, K. Lobach, R. Tarasov, A. Zykova, Ye. Svitlychnyi, A. Surkov, et al, PAST, **108**(2), 97-102 (2017), https://vant.kipt.kharkov.ua/ARTICLE/VANT_2017_2/article_2017_2_97.pdf.

[29] K. Lobach, Y. Kupriiyanova, I. Kolodiy, S. Sayenko, V. Shkuropatenko, V. Voyevodin, A. Zykova, et al, Functional Materials, **25**(3), 496-504 (2018), https://doi.org/10.15407/fm25.03.496.

[30] K.V. Lobach, S.Yu. Sayenko, V.A. Shkuropatenko, V.M. Voyevodin, H.V. Zykova, V.A. Zuyok, A.O. Bykov, et al, Materials Science, **55**(5), 672-682 (2020), https://doi.org/10.1007/s11003-020-00358-5.

[31] D.O. Moskovskikh, Ph.D. Thesis, *Получение субмикронного порошка карбида кремния и наноструктуированной керамики не его основе [Manufacturing of submicron silicon carbide powder and nanostructured ceramics on its basis],* National University of Science and Technology MISiS, 2015. (In Russian)

[32] S. Kondo, M. Lee, T. Hinoki, Y. Hyodo, and F. Kano, Journal of Nuclear Materials, **464**, 36-42 (2015), https://doi.org/10.1016/j.jnucmat.2015.04.034.

[33] V.A. Lavrenko, and Yu.G. Gogotsi, *Коррозия конструкторской керамики* [*Corrosion of engineering ceramics*], (Metallurgiya, Moscow, 1989), pp. 199. (In Russian)

[34] S.S. Raiman, P. Doyle, C. Ang, Y. Katoh, and K.A. Terrani, Corrosion, **75**(2), 217 (2019), https://doi.org/10.5006/2997.

[35] H. Hirayama, T. Kawakubo, A. Goto, and T. Kaneko, J. Am. Ceram. Soc. **72**, 2049-2053 (1989), https://doi.org/10.1111/j.1151-2916.1989.tb06029.x.

[36] E.J. Opila, N.S. Jacobson, D.L. Myers, E.H. Copland, The Journal of The Minerals, Metals & Materials Society, (TMS). **58**(1), 22-28 (2006), https://doi.org/10.1007/s11837-006-0063-3.

[37] Z. Duan, H. Yang, Y. Satoh, K. Murakami, S. Kano, Z. Zhao, J. Shen, and H. Abe, Nuclear Engineering and Design, **316**, 131-150 (2017), https://doi.org/10.1016/j.nucengdes.2017.02.031.

[38] K.A. Terrani, B.A. Pint, Y.-J. Kim , K.A. Unocic, Y. Yang, C.M. Silva, H.M. Meyer, and R.B. Rebak, Journal of Nuclear Materials, **479**, 36-47 (2016), https://doi.org/10.1016/j.jnucmat.2016.06.047.

[39] B.A. Pint, K.A. Terrani, Y. Yamamoto, and L.L. Snead, Metallurgical and Materials Transactions E, **2**, 190-196 (2015), https://doi.org/10.1007/s40553-015-0056-7.

[40] X. Wu, T. Kozlowski, and J.D. Hales, Annals of Nuclear Energy, **85**, 763-775 (2015), https://doi.org/10.1016/j.anucene.2015.06.032.

[41] K.G. Field, X. Hu, K.C. Littrell, Y. Yamamoto, and L.L. Snead, Journal of Nuclear Materials, **465**, 746 – 755 (2015), https://doi.org/10.1016/j.jnucmat.2015.06.023.

[42] I I.V. Kolodiy, V.A. Belous, M.A. Bortnitskaya, R.L. Vasilenko, V.N. Voyevodin, V.I. Kovalenko, A.S. Kuprin, et al, Functional materials, **27**(1), 79-86 (2020), https://doi.org/10.15407/fm27.01.79.

[43] A. Leyland, and A. Matthews, Wear, **246**, 1-11 (2000), https://doi.org/10.1016/S0043-1648(00)00488-9.

[44] J. Musil, F. Kunc, H. Zeman, and H. Polakova, Surf. Coat. Technol. **154**, 304-313 (2002), https://doi.org/10.1016/S0257-8972(01)01714-5.

ДОСЛІДЖЕННЯ І РОЗРОБКА НОВИХ МАТЕРІАЛІВ ДЛЯ ПАЛИВНИХ ЕЛЕМЕНТІВ ЯДЕРНИХ РЕАКТОРІВ, СТІЙКИХ ДО АВАРІЙНИХ СИТУАЦІЙ
К.В. Лобач[a], О.С. Купрін[a], С.Ю. Саєнко[a], В.М. Воєводін[a,b], І.В. Колодій[a]
[a]Національний науковий центр «Харківський фізико-технічний інститут», 61108, Харків, Україна
[b]Харківський національний університет імені В.Н. Каразіна, 61022, Харків, Україна

В роботі показані світові наукові напрями по створенню оболонок тепловиділяючих елементів (ТВЭЛ) стійких до аварій із втратою теплоносія (АЕС Фукусіма, Японія, березень 2011 р.) для водо-охолоджуваних реакторів. Наведені основні результати досліджень отриманих в ННЦ ХФТІ, щодо створення матеріалів для оболонок ТВЕЛ стійких до аварій із втратою теплоносія. Досліджені структура та властивості розроблених вакуумно-дугових хромових покриттів, які можуть бути використані для захисту існуючих паливних оболонок із цирконієвих сплавів для легководних реакторів типу PWR та BWR. Розроблена легована кераміка на основі SiC для заміни паливних оболонок із цирконієвих сплавів. Встановлено, що введення 0,5% Cr в SiC призводить до підвищення здатності чинити опір утворенню тріщин (тріщиностійкість) на 25 – 30%. Проаналізовано вплив Cr на корозійну стійкість SiC кераміки в умовах, що імітують середу 1-го контуру реактора ВВЕР-1000. Встановлено, що введення навіть невеликої кількості Cr призводить до уповільнення корозійних процесів в SiC кераміці. З метою створення нових металевих паливних оболонок також були розроблені та досліджені сплави на основі Fe-Cr-Al з добавкою легуючих елементів (Y, Zr та Mo). Показано високі механічні властивості та стійкість отриманих сплавів щодо високотемпературного окислення.
КЛЮЧОВІ СЛОВА: оболонка паливних елементів, корозія, захисні покриття, SiC/SiC композити, сплави Fe-Cr-Al

ИССЛЕДОВАНИЕ И РАЗРАБОТКА НОВЫХ МАТЕРИАЛОВ ДЛЯ ТОПЛИВНЫХ ЭЛЕМЕНТОВ ЯДЕРНЫХ РЕАКТОРОВ, СТОЙКИХ К АВАРИЙНЫМ СИТУАЦИЯМ
К.В. Лобач[a], А.С. Куприн[a], С.Ю. Саенко[a], В.Н. Воеводин[a,b], И.В. Колодий[a]
[a]Национальный научный центр «Харьковский физико-технический институт», 61108 Харьков, Украина
[b]Харьковский национальный университет имени В.Н. Каразина, 61022, Харьков, Украина

В работе показаны мировые научные направления по созданию оболочек тепловыделяющих элементов (ТВЭЛ) устойчивых к авариям с потерей теплоносителя (АЭС Фукусима, Япония, март 2011 года) для водо-охлаждаемых реакторов. Приведены основные результаты исследований, полученных в ННЦ ХФТИ, по созданию материалов для оболочек ТВЭЛ, устойчивых к авариям с потерей теплоносителя. Исследованы структура и свойства разработанных вакуумно-дуговых хромовых покрытий, которые могут быть использованы для защиты существующих топливных оболочек с циркониевых сплавов для легководных реакторов типа PWR и BWR. Разработанная легированная керамика на основе SiC для замены топливных оболочек с циркониевых сплавов. Установлено, что введение 0,5% Cr в SiC приводит к повышению способности сопротивляться образованию трещин (трещиностойкость) на 25 – 30%. Проанализировано влияние Cr на коррозионную стойкость SiC керамики в условиях, имитирующих среду 1-го контура реактора ВВЭР-1000. Установлено, что введение даже небольшого количества Cr приводит к замедлению коррозионных процессов в SiC керамике. С целью создания новых металлических топливных оболочек также были разработаны и исследованы сплавы на основе Fe-Cr-Al с добавкой легирующих элементов (Y, Zr и Mo). Показано высокие механические свойства и устойчивость полученных сплавов к высокотемпературному окислению.
КЛЮЧЕВЫЕ СЛОВА: оболочка топливных элементов, коррозия, защитные покрытия, SiC/SiC композиты, сплавы Fe-Cr-Al

INFLUENCE OF DIELECTRIC SCREENINGS ON PHONON FREQUENCIES AND ACOUSTIC PROPERTIES OF Pd-BASED BULK METALLIC GLASSES

ⓘ**R.R. Koireng[a,b]***, ⓘ**P.C. Agarwal[c]**, ⓘ**Alpana Gokhroo[a]**

[a]Samrat Prithviraj Chauhan Government College, Ajmer-305001, Rajasthan, India
[b]National Institute of Education NCERT, New Delhi-110016, India
[c]Regional Institute of Education NCERT, Bhubaneswar-751022, Odisha, India
*Corresponding Author: karenkrr@gmail.com
Received September 10, 2020; accepted October 15, 2020

The phonon dispersion curves for bulk metallic glasses (BMGs) $Pd_{40}Ni_{10}Cu_{30}P_{20}$ and $Pd_{64}Ni_{16}P_{20}$ are computed for the longitudinal and transverse phonon frequencies using the simple model given by Bhatia and Singh. Different dielectric screening functions are employed for the longitudinal mode. We obtain the values of the force constants β and δ calculated from the elastic constants of the material of the respective BMGs for computing the dispersion curves. The computed phonon dispersion curves show appropriate behaviour for both the longitudinal and transverse modes. The transverse sound velocity and the longitudinal sound velocities with various dielectric screenings are calculated in the long wavelength region from the computed dispersion curves for both the BMGs. The first peak position of the static structure factor is predicted from the dispersion curves. The values of sound velocities and the first peak of the static structure factor estimated from the computed dispersion curves show excellent agreement with the experimental values reported in literature for the BMGs under consideration and the results may be used for correlating other properties of the BMGs.

KEYWORDS: Bulk metallic glass, dispersion curves, dielectric screening, elastic properties

The advent of bulk metallic glasses (BMGs) has attracted a lot of interest due to its novel properties and applications in diverse technological areas [1–3]. Pd-based BMGs due to their unique mechanical and thermal properties have shown potential applications as electrode, jewelry and medical materials [4-5]. However, the understanding of phonon dynamics and atomic structure configuration are essential for understanding their mechanical and thermal properties [6-9]. The phonon dynamics of metallic glasses have been studied experimentally [10-11] using neutron scattering. Theoretically computed phonon frequencies have been investigated by many researchers [12-17] for correlating them with mechanical and thermal properties in a variety of metallic glasses. Three main theoretical approaches, namely Hubbard and Beeby [15], Takeno and Goda [16] and that of Bhatia and Singh [8] are widely used for computing phonon frequencies of metallic glasses.

In this paper, the phonon dispersion curves of $Pd_{40}Ni_{10}Cu_{30}P_{20}$ and $Pd_{64}Ni_{16}P_{20}$ BMGs are computed using the simple model given by Bhatia and Singh [8]. This model assumes a central force which is effective between the nearest neighbours and a volume dependent force. Bhatia and Singh [8] determine the values of force constants δ and β using the value of longitudinal and transverse sound velocities along with the calculated value of force constant κ_e. However, in the approach adopted by us, we fix the values of force constants δ and β used in the computation of dispersion curves by using the value of bulk modulus (B) and shear modulus (G) of the respective BMGs along with the calculated value of κ_e. This method of determining the values of δ and β from the elastic modulii of the BMGS for computing phonon frequencies using the simple model is applied for the first time for the $Pd_{40}Ni_{10}Cu_{30}P_{20}$ and $Pd_{64}Ni_{16}P_{20}$ BMGs. The dielectric screening due to conduction electrons in the long wavelength region of the phonon frequencies is quite significant. To study its effect on the phonon frequencies, various dielectric screening functions [13] namely, Bhatia and Singh (BS), Hartree (H), Hubbard (HB), Geldart and Vosko (GV), self-consistent screening due to Shaw (SCS) and Overhauser (OH) are employed for the longitudinal mode.

The longitudinal sound velocities (V_L) are computed for different dielectric screenings and the transverse sound velocity (V_T) is computed from the longitudinal and transverse dispersion curves respectively in the long wavelength region for both the $Pd_{40}Ni_{10}Cu_{30}P_{20}$ and $Pd_{64}Ni_{16}P_{20}$ BMGs. The first peak position of the static structure factor $S(q)$ denoted by q_p provides key structural information and elastic properties of amorphous materials [7]. The value of q_p is estimated from the dispersion curves, where it occurs around the first minimum of the longitudinal vibration mode [9].

THEORY

The details of this theory of the simple model employed are given by Bhatia and Singh [8] and others [12-13]. The equations for the longitudinal phonon frequencies (ω_L) and transverse phonon frequencies (ω_T) as given by Bhatia and Singh [8] can be written as

$$\omega_L^2 = \frac{2N}{\rho a^2}[\beta I_0 + \delta I_2] + \frac{\kappa_e K_{TF}^2 q^2 [G(qr_s)]^2}{\rho[q^2 + K_{TF}^2 \epsilon(q)]}, \tag{1}$$

and

$$\omega_T^2 = \frac{2N}{\rho a^2}\left[\left(\beta + \frac{1}{2}\delta\right)I_0 - \frac{1}{2}\delta I_2\right], \tag{2}$$

here q is the momentum wave vector; β, δ and κ_e are force constants. β and δ are defined in terms of the first and second derivatives of inter-atomic potential $W(r)$ at $r = a$, as

$$\beta = \frac{\rho a^2}{2M}\left[\frac{1}{r}\frac{dW(r)}{dr}\right]_{r=a}, \tag{3}$$

$$\delta = \frac{\rho a^3}{2M}\left[\frac{d}{dr}\left(\frac{1}{r}\frac{dW(r)}{dr}\right)\right]_{r=a}. \tag{4}$$

In equation (1), the relevant force constant κ_e due to the conduction electrons based on the Thomas–Fermi model can be written as

$$\kappa_e = 4\pi n_e n_i z e^2 / K_{TF}^2, \tag{5}$$

where e is the electron charge, n_i is the ionic density, $n_e = n_i z$ is mean electron density and z is the mean valence of the glassy system; $K_{TF}^2 = (4\,k_F/\pi a_0)$ is the Thomas-Fermi screening length with a_0 as the Bohr radius.

The $[G(qr_s)]^2$ in equation (1) is the shape factor to take into account the cancellation effects of kinetic and potential energies inside the core of the ions and is of the form

$$[G(qr_s)]^2 = \left[\frac{3(\sin(qr_s)-(qr_s)\cos(qr_s))}{(qr_s)^3}\right]^2, \tag{6}$$

where $r_s = [3/(4\pi n_i)]^{1/3}$ is the radius of the Wigner- Seitz sphere.

The term $\epsilon(q)$ in equation (1) is the dielectric screening function. We employ various dielectric screenings [13] namely Bhatia and Singh (BS), Hartree (H), Hubbard (HB), Geldart and Vosko (GV), self-consistent screening due to Shaw (SCS) and Overhauser (OH) in equation (1) to study the effect on phonon frequencies in the long wavelength region.

In equations (1) and (2), I_n can be written as [8]

$$I_n = \int_0^\pi \sin\theta \cos^n\theta \left[\sin^2\left(\frac{1}{2}qa\cos\theta\right)\right]d\theta, \tag{7}$$

so that with $x = qa$, I_0 and I_2 are respectively,

$$I_0(x) = 1 - \frac{\sin x}{x},$$

$$I_2(x) = \frac{1}{3} - \sin x\left[\frac{1}{x} - \frac{2}{x^3}\right] - \frac{2\cos x}{x^2},$$

for the limiting case $q \to 0$, equations (1) and (2) give the longitudinal and transverse sound velocities respectively, $V_L(0) = \omega_L/q$ and $V_T(0) = \omega_T/q$ as

$$\rho V_L^2(0) = N\left(\frac{1}{3}\beta + \frac{1}{5}\delta\right) + \kappa_e, \tag{8}$$

$$\rho V_T^2(0) = N\left(\frac{1}{3}\beta + \frac{1}{15}\delta\right). \tag{9}$$

In terms of the elastic moduli of the glassy material [8]

$$C_{11} = \rho V_L^2(0) = B + \frac{4}{3}G, \tag{10}$$

$$C_{44} = \rho V_T^2(0) = G. \tag{11}$$

The value of β and δ can be determined using equations (8), (9), (10) and (11). The sound velocities for both $Pd_{40}Ni_{10}Cu_{30}P_{20}$ and $Pd_{64}Ni_{16}P_{20}$ BMGs are estimated for the longitudinal mode (V_L) with different dielectric screenings and transverse mode (V_T) in the long wavelength region from the respective dispersion curves. The first peak of the static structure factor for both the BMGs is also estimated from the dispersion curves.

CALCULATIONS

For the $Pd_{40}Ni_{10}Cu_{30}P_{20}$ BMG, the experimental values of B, G and ρ [2] are $172.60\times10^9\,Nm^{-2}$, $35.50\times10^9\,Nm^{-2}$ and $9.259\times10^3\,kgm^{-3}$ respectively and for the $Pd_{64}Ni_{16}P_{20}$ BMG, the experimental values of B, G and ρ [2, 17] are taken as $172.00\times10^9\,Nm^{-2}$, $32.80\times10^9\,Nm^{-2}$ and $10.08\times10^3\,kgm^{-3}$ respectively. The values of n_i is calculated using the

relation $\rho = n_i M$ and found to be 7.57×10^{28} m^{-3} for Pd$_{40}$Ni$_{10}$Cu$_{30}$P$_{20}$ and 7.26×10^{28} m^{-3} for Pd$_{64}$Ni$_{16}$P$_{20}$. The two BMGs under consideration are of FCC structure and using the relation $a^3 n_i = \sqrt{2}$, gives $a = 2.65 \times 10^{-10}$ m and $a = 2.69 \times 10^{-10}$ m for Pd$_{40}$Ni$_{10}$Cu$_{30}$P$_{20}$ and Pd$_{64}$Ni$_{16}$P$_{20}$ respectively.

The value of κ_e calculated using equation (5) for Pd$_{40}$Ni$_{10}$Cu$_{30}$P$_{20}$ with $z = 1.90$ is 153.50×10^9 Nm^{-2} and for Pd$_{64}$Ni$_{16}$P$_{20}$ with $z = 2.20$ is 182.75×10^9 Nm^{-2}. Taking N=12 for FCC structure for both the BMGs Pd$_{40}$Ni$_{10}$Cu$_{30}$P$_{20}$ and Pd$_{64}$Ni$_{16}$P$_{20}$, the values of the respective force constants β and δ for both the BMGs are obtained by substituting the respective values of B, G and κ_e in equations (8), (9), (10) and (11). Hence all the input parameters for computing phonon dispersion curves for both the BMGs are known and are listed in Table 1.

Table 1.

Parameters used for computing phonon dispersion curves of Pd$_{40}$Ni$_{10}$Cu$_{30}$P$_{20}$ and Pd$_{64}$Ni$_{16}$P$_{20}$ BMGs.

	Pd$_{40}$Ni$_{10}$Cu$_{30}$P$_{20}$	Pd$_{64}$Ni$_{16}$P$_{20}$
$n_i (10^{28}$ m$^{-3})$	7.57	7.26
κ_e (10^9 Nm^{-2})	153.50	182.75
k_F (10^{10} m^{-1})	1.62	1.68
r_s (10^{-10} m)	1.47	1.49
K_{TF}^2 (10^{20} m^{-2})	3.90	4.04
β (10^9 Nm^{-2})	5.01	8.18
δ (10^9 Nm^{-2})	19.33	0.11
z	1.90	2.20

RESULTS AND DISCUSSION

The phonon dispersion curves computed for the BMGs Pd$_{40}$Ni$_{10}$Cu$_{30}$P$_{20}$ and Pd$_{64}$Ni$_{16}$P$_{20}$ using the simple model given by Bhatia and Singh [8] are shown in Figure 1a and 1b respectively. The phonon frequency curves for the longitudinal mode employing different dielectric screening functions, namely Bhatia and Singh (BS), Hartree (H), Hubbard (HB), Geldart and Vosko (GV), self-consistent screening due to Shaw (SCS) and Overhauser (OH) for the BMGs Pd$_{40}$Ni$_{10}$Cu$_{30}$P$_{20}$ and Pd$_{64}$Ni$_{16}$P$_{20}$ are obtained on the basis of equation (1). Similarly, the phonon frequency curves for the transverse mode (T) for the Pd$_{40}$Ni$_{10}$Cu$_{30}$P$_{20}$ and Pd$_{64}$Ni$_{16}$P$_{20}$ BMGs are obtained on the basis of equation (2) without dielectric screening. The dispersion curves for both the longitudinal mode (ω_L-q) as well as the transverse mode (ω_T-q) show linear dispersion curves in the long wavelength region and reproduce all the characteristic features as shown in Figure 1a and 1b.
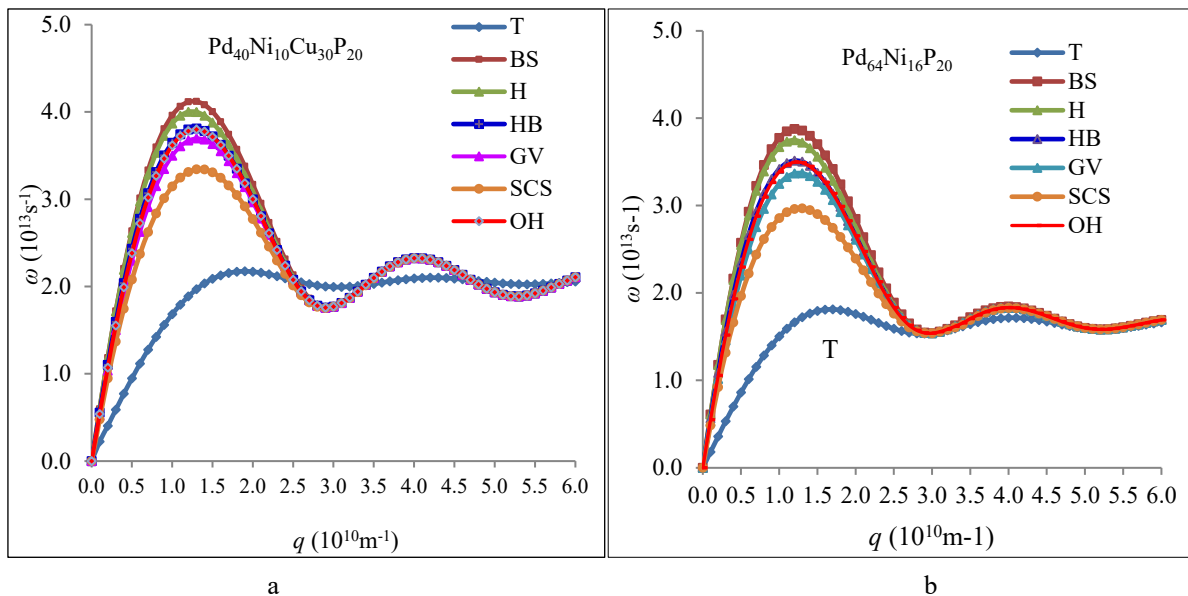
Figure 1. The transverse (T) phonon frequencies on the basis of equation (2) and longitudinal phonon frequencies due to dielectric screenings viz. BS, H, HB, GV, SCS and OH on the basis of equation (1) for the BMGs (a)Pd$_{40}$Ni$_{10}$Cu$_{30}$P$_{20}$ and (b) Pd$_{64}$Ni$_{16}$P$_{20}$

As seen in Figure 1a and 1b, the dielectric screening functions have significant effect in the long wavelength region of the ω_L-q dispersion curves for both the Pd$_{40}$Ni$_{10}$Cu$_{30}$P$_{20}$ and Pd$_{64}$Ni$_{16}$P$_{20}$ BMGs. The height of the first peak of the longitudinal vibrations mode depends on the type of dielectric screenings employed for computing the phonon frequencies. From the Figure 1a and 1b, it is evident that the difference in ω_L-q curves for different dielectric screenings

for both the BMGs increases with the wave number q and becomes more prominent at the first maxima and starts decreasing, and the curves converge at the q value corresponding to the first minima of ω_L-q curves.

The position of the first peak of the ω_L-q curves for the $Pd_{40}Ni_{10}Cu_{30}P_{20}$ BMG are found at $q = 1.3\times10^{10}$ m^{-1} for BS, HB, GV, SCS and OH, and at $q = 1.2\times10^{10}$ m^{-1} for H. In the case of $Pd_{64}Ni_{16}P_{20}$ BMG, the position of the first peak for ω_L-q curves are found at $q = 1.2\times10^{10}$ m^{-1} for BS, H, HB and OH, and at $q = 1.3\times10^{10}$ m^{-1} for GV and SCS. The first minima of the ω_L-q curves for $Pd_{40}Ni_{10}Cu_{30}P_{20}$ and $Pd_{64}Ni_{16}P_{20}$ are obtained at $q = 2.9\times10^{10}$ m^{-1} and $q = 3.0\times10^{10}$ m^{-1} respectively, independent of the dielectric screenings employed.

The first peak position of ω_T-q curves for $Pd_{40}Ni_{10}Cu_{30}P_{20}$ and $Pd_{64}Ni_{16}P_{20}$ are obtained at $q = 1.9\times10^{10}$ m^{-1} and $q = 1.7\times10^{10}$ m^{-1} respectively. For both the BMGs $Pd_{40}Ni_{10}Cu_{30}P_{20}$ and $Pd_{64}Ni_{16}P_{20}$, the first peak position for ω_T-q curves is at a higher q value than the first peak position of ω_L-q curves for all dielectric screenings. As expected, the ω_T-q dispersion curves for both the BMGs increases and attain peak value with the increase in wave number q and thereafter gets saturated around the first peak with a small variation.

In the long wavelength region ($q{\rightarrow}0$) of the dispersion curves, the sound velocities of the longitudinal and transverse modes are estimated for both the BMGs. The values of longitudinal velocities (V_L) computed from the longitudinal dispersion curves for different dielectric screenings and the transverse velocity (V_T) computed from the transverse dispersion curves for both the BMGs $Pd_{40}Ni_{10}Cu_{30}P_{20}$ and $Pd_{64}Ni_{16}P_{20}$ are listed in Table 2. The dielectric screenings have significant effect on the longitudinal sound velocity. The experimental values of the longitudinal sound velocity for $Pd_{40}Ni_{10}Cu_{30}P_{20}$ is 4.874×10^5 cms^{-1} [2] and for $Pd_{64}Ni_{16}P_{20}$ is 4.560 cms^{-1} [2,17]. The values of V_L computed from the dispersion curves for both the BMGs under consideration show closeness to the experimental value for the dielectric screening due to OH. The value of V_L computed from the dispersion curves due to OH screening is 4.839×10^5 cms^{-1} for $Pd_{40}Ni_{10}Cu_{30}P_{20}$ and 4.606×10^5 cms^{-1} for $Pd_{64}Ni_{16}P_{20}$. As shown in Table 2, the values of V_L computed for different dielectric screenings for both the BMGs are screening sensitive in the long wavelength region.

Table 2.

The transverse sound velocity (V_T) and longitudinal sound velocities (V_L) for different dielectric screenings for the BMGs $Pd_{40}Ni_{10}Cu_{30}P_{20}$ and $Pd_{64}Ni_{16}P_{20}$.

Dielectric screenings	$Pd_{40}Ni_{10}Cu_{30}P_{20}$		$Pd_{64}Ni_{16}P_{20}$	
	$V_L (10^5$ cms$^{-1})$	$V_T (10^5$ cms$^{-1})$	$V_L (10^5$ cms$^{-1})$	$V_T (10^5$ cms$^{-1})$
BS	5.358	1.827	5.181	1.735
H	5.313		5.133	
HB	4.949		4.722	
GV	4.664		4.405	
SCS	4.232		3.931	
OH	4.839		4.606	
Experimental	4.874[2]	1.959 [2]	4.560 [2,17]	1.790 [2,17]

The transverse sound velocity (V_T) computed from the slope of the dispersion curves in the elastic region for $Pd_{40}Ni_{10}Cu_{30}P_{20}$ is 1.827×10^5 cms^{-1} and for $Pd_{64}Ni_{16}P_{20}$ is 1.735×10^5 cms^{-1}. The experimental values of transverse sound velocities reported for $Pd_{40}Ni_{10}Cu_{30}P_{20}$ and $Pd_{64}Ni_{16}P_{20}$ are 1.959 cms^{-1} [2] and 1.790 cms^{-1} [2,17] respectively. Thus, the computed transverse sound velocities are very close to the experimental values reported for $Pd_{40}Ni_{10}Cu_{30}P_{20}$ and $Pd_{64}Ni_{16}P_{20}$.

From the ω_L-q curves of the BMGs under consideration, we estimate the first peak position (q_p) of the static structure factor $S(q)$. The first minimum of ω_L-q curves occurs around the same value of the wave number q where the first peak (q_p) of the static structure factor $S(q)$ occurs [9]. The position of the first minimum estimated from the ω_L-q curves for the BMGs $Pd_{40}Ni_{10}Cu_{30}P_{20}$ and $Pd_{64}Ni_{16}P_{20}$ occur at $q = 2.9\times10^{10}$ m^{-1} and $q = 3.0\times10^{10}$ m^{-1} respectively, independent of the dielectric screenings. The computed values of q_p for both the BMGs are given in Table 3. The experimental reported value of the first peak position q_p of the static structure factor for $Pd_{40}Ni_{10}Cu_{30}P_{20}$ is $q = 2.9\times10^{10}$ m^{-1} [7] (Table 3). However, no experimental data for the static structure factor of $Pd_{64}Ni_{16}P_{20}$ BMG is available, we estimate from the theoretical phonon dispersion curves to be at $q = 3.0\times10^{10}$ m^{-1}.

Table 3.

The position of the first peak (q_p) of static structure factor estimated from the dispersion curves of BMGs.

BMGs	q_p $(10^{10}$ m$^{-1})$
$Pd_{40}Ni_{10}Cu_{30}P_{20}$	2.9, 2.9 [7]
$Pd_{64}Ni_{16}P_{20}$	3.0

The computed values of q_p for both the BMGs are slightly less than $2k_F$, where k_F is calculated using the relation, $k_F = (3\pi^2 n_e)^{1/3}$. The calculated values of k_F are 1.62×10^{10} m^{-1} for $Pd_{40}Ni_{10}Cu_{30}P_{20}$ and 1.68×10^{10} m^{-1} for $Pd_{64}Ni_{16}P_{20}$ (Table I). The ratio of $2k_F/q_p$ is 1.12 for both the BMGs $Pd_{40}Ni_{10}Cu_{30}P_{20}$ and $Pd_{64}Ni_{16}P_{20}$. This is in agreement with the

stability of metallic glasses [18]**.** Since the peak position of the structure factor provides key structural information in understanding atomic network for amorphous materials, it is used for correlating with elastic properties of BMGs [7]. From the results obtained from the dispersion curves, we can infer that the value of q_p is not affected by the dielectric screening functions, though the dielectric screenings have a significant effect on the values of the longitudinal sound velocities for the BMGs.

CONCLUSION

We have computed the phonon dispersion curves for $Pd_{40}Ni_{10}Cu_{30}P_{20}$ and $Pd_{64}Ni_{16}P_{20}$ BMGs employing various dielectric screenings using the simple model by Bhatia and Singh. The force constants δ and β used in the computation of the phonon frequencies are determined using the experimental values of bulk modulus (*B*) and shear modulus (*G*) along with the calculated value of force constant κ_e of the BMGs under consideration for the first time. The computed dispersion curves reproduce the main characteristic of phonon frequencies of transverse and longitudinal modes. The values of the transverse and longitudinal velocities estimated from the dispersion curves show excellent agreement with the experimental values reported for both the BMGs. The position of the first peak of the static structure factor for both the BMGs are estimated from the dispersion curves and show excellent agreement with the available value reported in literature for $Pd_{40}Ni_{10}Cu_{30}P_{20}$. Since the experimental data for phonon frequencies are rare and the limitation of the experimental techniques for describing the micro-structure of metallic glasses, the approach presented in this paper using the Bhatia and Singh model can be employed for computing phonon frequencies. It is expected that appropriate theoretical computation of phonon dispersion curves will give insight in understanding the structural information and elastic properties of metallic glasses.

ORCID IDs
R.R. Koireng, https://orcid.org/0000-0003-3112-1078; **P.C. Agarwal,** https://orcid.org/0000-0002-1166-2611;
Alpana Gokhroo, https://orcid.org/0000-0002-5871-0983

REFERENCES
[1]   M. Telford, Materials Today, **7**, 36-43 (2004), https://doi.org/10.1016/S1369-7021(04)00124-5.
[2]   W.H. Wang, Progress in Materials Science, **57**, 487-656 (2012), https://doi.org/10.1016/j.pmatsci.2011.07.001.
[3]   M.M. Khan, A. Nemati, Z.U. Rahman, U.H. Shah, H. Asgar, and W. Haider, Critical Reviews in Solid State and Materials Science, **43**, 233-268 (2018), https://doi.org/10.1080/10408436.2017.1358149.
[4]   A. Inoue, Z. M. Wang, and W. Zhang, Reviews on Advanced Materials Science, **18**, 1-9 (2008), http://www.ipme.ru/e-journals/RAMS/no_11808/inoue.pdf.
[5]   L. Liu, A. Inoue, and T. Zhang, Materials, Transactions, **46**, 376-378 (2005), https://doi.org/10.2320/matertrans.46.376.
[6]   Y.Q. Cheng, and E. Ma, Progress in Materials Science, **56**, 379- 473 (2011), https://doi.org/10.1016/j.pmatsci.2010.12.002.
[7]   Y. Wu, H. Wang, Y. Cheng, X. Liu, X. Hui, T. Nieh, Y. Wang, and Z. Lu, Scientific Reports, **5**, 12137 (2015), https://doi.org/10.1038/srep12137.
[8]   A.B. Bhatia, and R.N. Singh, Physical Review B, **31**, 4751- 4758 (1985), https://doi.org/10.1103/PhysRevB.31.4751.
[9]   J. Hafner, Phyical Review B, **27**, 678- 695 (1983), https://doi.org/10.1103/PhysRevB.27.678.
[10] R. Babilas, D. Lukowiec, and L. Temleitner, Beilstein Journal of Nanotechnology, **8**, 1174-1182 (2017), https://doi.org/10.3762/bjnano.8.119.
[11] A. Gulenko, L.F. Chungong, J. Gao, I. Todd, A.C. Hannon, R.A. Martin, and J.K. Christie, Physical Chemistry Chemical Physics, **19**, 8504-8515 (2017), https://doi.org/10.1039/C6CP03261C.
[12] P.C. Agarwal, Physica B, **381**, 239-245 (2006), https://doi.org/10.1016/j.physb.2006.01.522.
[13] P.C. Agarwal, K.A. Aziz, and C.M. Kachhava, Acta Physica Hungarica, **72**, 183-192 (1992), https://doi.org/10.1007/BF03054162.
[14] A.M. Vora, and A.L. Gandhi, Armenian Journal of Physics, **12**, 289-294 (2019), http://ajp.asj-oa.am/1078/1/AMV_ALG_Armenian_Journal_of_Physics_pdf.pdf
[15] J. Hubbard, and J.L. Beeby, Journal of Physics C, **2**, 556-574 (1969), https://doi.org/10.1088/0022-3719/2/3/318.
[16] S. Takeno, and M. Goda, Progress of Theoretical Physics, **45**, 331-352 (1971), https://doi.org/10.1143/PTP.45.331.
[17] H.S. Chen, J.T. Krause, and E. Colemen, Journal of Non-Crystalline Solids, **18**, 157-171 (1975), https://doi.org/10.1016/0022-3093(75)90018-6.
[18] W.H. Wang, C. Dong, and C.H. Shek, Materials Science and Engineering: R: Reports **44**, 45-89 (2004), https://doi.org/10.1016/j.mser.2004.03.001.

ВПЛИВ ДІЕЛЕКТРИЧНОЇ ЕКРАНІЗАЦІЇ НА ФОНОННІ ЧАСТОТИ І АКУСТИЧНІ ВЛАСТИВОСТІ МЕТАЛІЧНИХ СТЕКОЛ НА ОСНОВІ Pd
Р.Р. Койренг[a,b], П.С. Агарвал[c], Альпана Гокру[a]
[a]Урядовий коледж Самрата Притвіраджа Чаухана, Аджмер-305001, Раджастан, Індія
[b]Національний інститут освіти (NCERT), Нью-Делі-110016, Індія
[c]Регіональний інститут освіти (NCERT), Бхубанешвар-751022, Одіша, Індія

Криві дисперсії фононів для об'ємних металевих стекол (ОМС) $Pd_{40}Ni_{10}Cu_{30}P_{20}$ та $Pd_{64}Ni_{16}P_{20}$ обчислюються для поздовжньої та поперечної частот фононів за допомогою простої моделі, наданої Бхатією та Сінгхом. Для поздовжнього режиму використовуються різні функції діелектричного екранування. Ми отримали значення силових констант β і δ, розрахованих з пружних констант матеріалу відповідних ОМС для обчислення кривих дисперсії. Обчислені криві дисперсії фононів демонструють належну поведінку як для поздовжньої, так і для поперечної мод. Поперечна швидкість звуку та

поздовжні швидкості звуку з різним діелектричним екрануванням обчислюються в області довжини довжини хвилі з обчислених кривих дисперсії для обох ОМС. Положення першого піка коефіцієнта статичної структури передбачено з дисперсійних кривих. Значення швидкостей звуку та перший пік коефіцієнта статичної структури, розраховані на основі обчислених дисперсійних кривих, показують чудову узгодженість з експериментальними значеннями, що наявні в літературі для розглянутих ОМС, і результати можуть бути використані для кореляції інших властивостей ОМС.
КЛЮЧОВІ СЛОВА: об'ємне металеве скло, дисперсійні криві, діелектричний екран, еластичні властивості

ВЛИЯНИЕ ДИЭЛЕКТРИЧЕСКОЙ ЭКРАНИРОВКИ НА ФОНОННЫЕ ЧАСТОТЫ И АКУСТИЧЕСКИЕ СВОЙСТВА МЕТАЛЛИЧЕСКИХ СТЕКОЛ НА ОСНОВЕ Pd

Р.Р. Койренг[a,b], П.С. Агарвал[c], Альпана Гокро Gokhroo[a]
[a]Урядовий колледж Самрат Притвираджа Чаухан, Аджмер-305001, Раджастан, Индия
[b]Национальний институт образования (NCERT), Нью-Дели-110016, Индия
[c]Региональний институт образования (NCERT), Бхубанешвар-751022, Одиши, Индия

Кривые дисперсии фононов для объемных металлических стекол (ОМС) $Pd_{40}Ni_{10}Cu_{30}P_{20}$ и $Pd_{64}Ni_{16}P_{20}$ исчисляются для продольной и поперечной частот фононов с помощью простой модели, предоставленной Бхатия и Сингхом. Для продольного режима используются различные функции диэлектрического экранирования. Мы получили значения силовых констант силы β и δ, рассчитанных по упругим константам материала соответствующих ОМС для вычисления кривых дисперсии. Вычисленные кривые дисперсии фононов демонстрируют надлежащее поведение как для продольной, так и для поперечной мод. Поперечная скорость звука и продольные скорости звука с разным диэлектрической экранированием исчисляются в области длины длины волны из вычисленных кривых дисперсии для обеих ОМС. Положение первого пика коэффициента статической структуры предсказано из дисперсионных кривых. Значения скоростей звука и первый пик коэффициента статической структуры, рассчитанные на основе вычисленных кривых дисперсии, показывают хорошее согласие с экспериментальными значениями, имеющиеся в литературе для рассматриваемых ОМС, и результаты могут быть использованы для корреляции других свойств ОМС.
КЛЮЧЕВЫЕ СЛОВА: объемное металлическое стекло, дисперсионные кривые, диэлектрический экран, эластичные свойства

SOLUBILITY OF CARBON, MANGANESE AND SILICON IN α-IRON OF Fe-Mn-Si-C ALLOYS

Natalia Filonenko[a,b,*], Alexander Babachenko[b], Ganna Kononenko[b], Ekaterina Domina[b]

aState Institution "Dnipropetrovsk Medical Academy of the Ministry of Health of Ukraine"
9, Vernadsky Str., Dnipro, 49044, Ukraine
bZ.I. Nekrasov Iron and Steel Institute of National Academy of Sciences of Ukraine
1, Akademika Starodubova Square, Dnipro, 49107, Ukraine
*Corresponding Author: natph2016@gmail.com

The study was performed on alloys with a carbon content of 0.37-0.57% (wt.), silicon 0.23-0.29% (wt.), manganese 0.7-0.86% (wt.), the rest – iron. To determine the phase composition of alloys used microstructural, microanalysis and X-ray analysis. In addition, the physical characteristics of the alloys studied in this paper were determined, such as alloy chemical dependence of extension and contraction ratio, impact toughness and hardness. The results obtained in this paper showed that the iron-based alloy with the content of carbon of 0.57 % (wt.), silicon of 0.28 % (wt.) and manganese of 0.86 % (wt.)) had the superior microstructure and physical properties. It was determined that after a number of crystallization and phase transformation the alloy phase structure includes two phases: α-iron and cement magnesium doping$Fe_{2.7}Mn_{0,3}C$. For the first time using the method quasi-chemistry received an expression of the free energy of a solid solution α-iron alloyed with silicon and magnesium, and determined the solubility limit of carbon, manganese and silicon. In δ-iron may dissolve to 0.09% (wt.) carbon, manganese up to 3.5% (wt.), silicon – 0.25% (wt.). The maximum content in α-iron can reach: carbon – 0.017% (wt.), manganese - 21% (wt.), silicon – 1.3% (wt.).

KEY WORDS: Fe-Mn-Si-C alloys, solubility limit of carbon, manganese, silicon in α-iron

As is known, there is currently a special interest in steels that have high strength and ductility. To increase the complex of mechanical properties in an economical way using alloying of alloys based on iron with manganese and silicon [1].

In the al loys of the Fe-Mn-Si-C system during the crystallization of the melt, the primary phase may be δ - iron with a carbon content of up to 0.2% (wt.), manganese up to 2% (wt.) and silicon up to 1% (wt.). During the crystallization of alloys of the Fe-Mn-Si-C system, successive transformations of peritectic were observed: L→L+δ→δ+γ→γ [2-5]. It is known that doping alloys based on iron with manganese and silicon has almost no effect on the temperature of point A_1 and shifts point S (eutectoid point on the equilibrium phase diagram of the Fe-C system) to a low carbon content, which leads to an increase in the volume fraction of perlite in the microstructure [6].

According to the results presented in [7-10], the solubility of carbon in ferrite is in the alloys of the Fe-C system - 0.095% (at.), Mn-C - 6% (at.), silicon Fe-Si - 10-18.5% (at.), Mn-Si – 18.5-10% (at.) in dependence from temperature. In the ternary system Fe-Mn-C are the solubility of carbon and manganese in α-iron at temperatures 505-971 K [4]. In this paper it is noted that at a temperature of 505 K the content of carbon in α-iron was $4 \cdot 10^{-9}$% (wt.), and manganese - 0.5% (wt.). The authors of [7] note that in the alloys of the Fe-Mn-Si-C system is the consistent formation of solid solutions, the carbon content of which is more than 0.08% (wt.). Thermodynamic databases (ThermoCalc, FactSage, MTDat, PANDAT, JMatPro, IDS and CALPHAD) are currently widely used in steel and alloy research, development of new materials and production technologies in the metallurgical industry, but the reliability of forecasts made with these programs is limited by the accuracy of thermodynamic data. Some experimental data, which are important for multicomponent systems, are quite old and insufficiently tested by modern experimental methods [11]. As is known, to predict the phase composition of alloys and phase transformations plays an important role solubility limit of the alloying elements in alloys.

The aim of this work was to determine the solubility limits of carbon, silicon and manganese in α-iron alloys of the Fe-Mn-Si-C system.

MATERIALS AND METHODS

Research carried out on alloys containing carbon 0.37-0.57% (wt.), silicon 0.23-0.29% (wt.), manganese 0.7-0.86% (wt.), the rest – iron. The smelting of alloys of the Fe-Mn-Si-C system was performed in a furnace in alundum crucibles in an argon atmosphere. The cooling rate of the alloys after casting was 10 K/s. Metallographic sections of Fe-Mn-Si-C alloys were made according to standard methods using diamond pastes. Chemical and spectral analysis were used to determine the chemical composition of the alloy [11]. The phase composition of the alloys was determined using an optical microscope "Neofot-21". The main results of micro-X-ray spectral analysis were obtained using an electron microscope JSM-6490 with a scanning attachment ASID-4D and energy-dispersive X-ray microanalyzer "LinkSystems 860" with software. X-ray diffraction analysis was performed on a DRON-3 diffractometer in monochromatized Fe-Kα radiation.

RESULTS AND DISCUSSION

The microstructure of the alloy with the carbon content of 0.37% (wt.), silicon 0.23% (wt.), manganese 0.86% (wt.) in the cast, state is represented by ferrite and perlite (Fig. 1a).
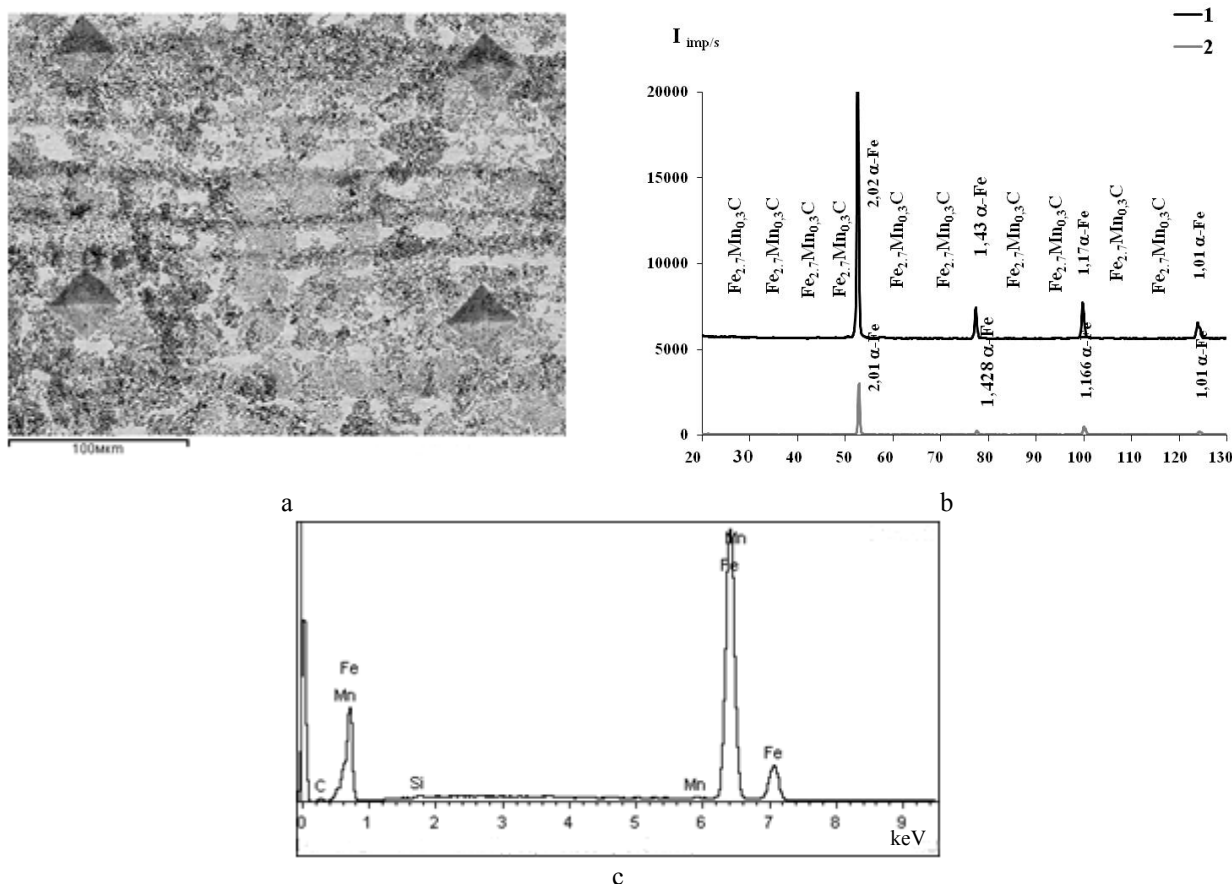
Figure 1. Alloy based on iron with a carbon content of 0.45% (wt.), silicon 0.23% (wt.), manganese 0.86% (wt.) in the cast state: a) microstructure, ×800, b) diffraction pattern (1 - α-iron of Fe-Mn-Si-C alloy, 2 - α-iron in Fe-C alloy), c) micro-X-ray spectral analysis curve

The results of X-ray analysis in this alloy were discovered only two phases – ferrite and carbide (Fig. 1b). Carbide, as a structural component of perlite, was presented in these alloys of the Fe-Mn-Si-C phase $Fe_{2.7}Mn_{0.3}C$. It should be noted that perlite has two colors after surface etching of the samples with sodium pirate – light and dark. In perlite light r color content of manganese – 0.37% (wt.), silicon – 0,38% (wt.). In perlite dark color high content of alloying elements: manganese – 0.79% (wt.), silicon – 0.41% (wt.). Thus, the results make it possible to assert that in alloys formed a reason region richest manganese and silicon.

On the diffraction pattern, the α-iron lines were shifted toward larger angles compared to pure α-iron. The obtained result can be explained by the fact that the ferrite is doped with manganese and silicon and the ferrite lattice parameter changes. According to the results of micro-X-ray spectral analysis in ferrite, the manganese content was 1.27% (wt.), silicon – 0.27% (wt.).

As Table shows, the characteristics of strength and hardness for all the alloys are high, and for the alloy containing carbon – 0.57% (wt.), silicon – 0.28% (wt.) and manganese – 0.86 % (wt.), plasticity and fracture toughness are higher as compared to those for the other alloys that are used in the manufacture of railway wheels.

Table.

Dependence of the extension andcontraction ratio, impact toughness and hardness on the chemical composition

Content of chemical elements in alloys, % (wt.)	Relative extension n, δ, %	Relative contractionψ, %	Impact toughness, KCU_{obed}, J/cm^2	Hardness, HB
C=0.37;Si=0.23; Mn=0.75	8	17	34	324
C=0.57; Si=0.28; Mn=0.86	11	25	40	341

A quasi-chemical method was used to determine the solubility of carbon, silicon, and manganese in the δ- and α-iron of Fe-Mn-Si-C alloys.

The structure of ferrite has a volume-centered lattice and belongs to the spatial group O_h^9 – Im3m with 8 atoms in the first coordination sphere [12]. Each atom of the BCC lattice has six tetrahedral and three octahedral pores. Of the six atoms surrounding the octahedral pore, two are closest to the others [14]. The arrangement of carbon atoms in the BCC lattice can be described as follows: the arrangement of carbon atoms in the octahedral pore, which have four nearest metal atoms at a distance of 2.02 Å, and two at a distance of 1,43 Å, each metal atom has 8 neighbors, which are located on distances of 2,48 Å from each other.

To obtain the calculated results of the solubility limit of carbon atoms in the ferrite lattice, a quasi-chemical method was used, taking in ti account data on the position of carbon in a solid solution of α-iron [13].

The interaction of Fe-Fe, Fe-C, Fe-Si, Fe-Mn and Fe-V atoms, where V is a vacancy can become side red as follows: the interaction energies of atomic pairs v_{FeFe}, v_{FeSi}, v_{FeV}, v_{FeC}, v_{MnV} and v_{MnC}. The results presented in [14-15] were used for numerical values of the interaction energy of pairs of atoms.

The free energy of ferrite can be determined by the formula: $F = E - kT \ln W$, where E is the internal energy of ferrite, W is the thermodynamic probability of the placement of atom is the nodes of the crystal lattice of ferrite, $k = 1,38 \cdot 10^{-23}$ J / K – Boltzmann constant, T – absolute temperature. Thus, the free energy of ferrite is determined as follows:

$$F = -8\left(N_{Fe}N_C v_{FeC} + N_{Mn}N_C v_{MnC} + N_{Si}N_C v_{SiC} + N_{Fe}N_V v_{FeV} + N_{Mn}N_V v_{MnV} + N_{Si}N_V v_{SiV}\right) -$$
$$-kT(8(N_{Fe} + N_{Mn} + N_{Si})(\ln(N_{Fe} + N_{Mn} + N_{Si}) - 1) -$$
$$-8N_{Fe}(\ln N_{Fe} - 1) - 8N_{Mn}(\ln N_{Mn} - 1) - 8N_{Si}(\ln N_{Si} - 1) +$$
$$+(N_C + N_V)(\ln(N_C + N_V) - 1) - N_C(\ln N_C - 1) - N_V(\ln N_V - 1)$$

To calculate the solubility of carbon in α-iron, wended it find the solution of the system of equations:

$$\frac{\partial F}{\partial N_C} = 0 , \ \frac{\partial F}{\partial N_V} = 0 , \ \frac{\partial F}{\partial N_{Si}} = 0 , \ \frac{\partial F}{\partial N_{Mn}} = 0 , \ \frac{\partial F}{\partial N_{Fe}} = 0 \tag{1}$$

The resulting system of equations (2) is transcendental. Usually the solution of such equations can be obtained graphically or numerically. But in the framework of this problem it is expedient to consider an asymptotic solution of the equations. For this we present the logarithm included in each of the equations of the system (1) in the form of Taylor series (this is acceptable in case of its convergence):

$$\frac{\partial F}{\partial N_C} = -8N_{Fe}v_{FeC} - 8N_{Mn}v_{MnC} - 8N_{Si}v_{SiC} - kT\left(\ln N_V + \sum_{n=1}^{\infty}\frac{(-1)^{n+1}}{n}\left[\frac{N_C^n}{N_V^n} - (N_C - 1)^n\right]\right) = 0$$

$$\frac{\partial F}{\partial N_V} = -8N_{Fe}v_{FeV} - 8N_{Mn}v_{MnV} - 8N_{Si}v_{SiV} - 8kT\left(\ln N_C + \sum_{n=1}^{\infty}\frac{(-1)^{n+1}}{n}\left[\frac{N_V^n}{N_C^n} - (N_V - 1)^n\right]\right) = 0$$

$$\frac{\partial F}{\partial N_{Fe}} = -8N_C v_{FeC} - 8N_V v_{FeV} - 8kT\left(\ln(N_{Mn} + N_{Si}) + \sum_{n=1}^{\infty}\frac{(-1)^{n+1}}{n}\left[\frac{N_{Fe}^n}{(N_{Mn} + N_{Si})^n} - (N_{Fe} - 1)^n\right]\right) = 0 \tag{2}$$

$$\frac{\partial F}{\partial N_{Mn}} = -8N_C v_{MnC} - 8N_V v_{MnV} - 8kT\left(\ln(N_{Fe} + N_{Si}) + \sum_{n=1}^{\infty}\frac{(-1)^{n+1}}{n}\left[\frac{N_{Mn}^n}{(N_{Fe} + N_{Si})^n} - (N_{Mn} - 1)^n\right]\right) = 0$$

$$\frac{\partial F}{\partial N_{Si}} = -8N_C v_{SiC} - 8N_V v_{SiV} - 8kT\left(\ln(N_{Mn} + N_{Fe}) + \sum_{n=1}^{\infty}\frac{(-1)^{n+1}}{n}\left[\frac{N_{Si}^n}{(N_{Mn} + N_{Fe})^n} - (N_{Si} - 1)^n\right]\right) = 0$$

To obtain an asymptotic estimate of system (2) solution it is sufficient to consider the first two terms of expansion in the logarithm expanding.

There sults of solving the system of equations showed that up to 0.09% (wt.) of carbon, manganese up to 3.5% (wt.), silicon – 0.25% (wt.) can be dissolved in δ-iron. The obtained result regarding the carbon content in δ-iron is consistent with the results of [16-17].

The maximum solubility of elements in α-iron is: carbon – 0.017% (wt.), manganese – 15% (wt.), silicon - 1.3% (wt.), which is consistent with the results presented in [3].

Thus, the maximum solubility of carbon, manganese and silicon in α-iron alloys of the Fe-Mn-Si-C system have lower numerical values compared it the insolubility in the corresponding binary systems. The obtained results can be explained by the fact that there placement of iron atoms by manganese and silicon atoms in the α-iron lattice ads it the deformation of the lattice, which affects the solubility of carbon [14].

CONCLUSION

The analysis phase composition in the studied alloys Fe-C-Mn-Si containing carbon 0.37-0.57% (wt.), silicon 0.23-29% (wt.), manganese 0.7-0.86 % (wt.), the rest - iron. It is determined that after crystallization and a number of phase transformations the microstructure of the alloy consists of α-iron and manganese-doped cementite $Fe_{2.7}Mn_{0.3}C$. In the structure of alloys the reason uneven distribution of alloying elements – there are areas of perlite enriched manganese and silicon. For the first time, depending on the free energy of a solid solution of α- and δ-iron doped with silicon and manganese, a quasi-chemical method was obtained and the solubility limits of carbon, manganese and silicon were determined. Up to 0.09% (wt.) of carbon, manganese up to 3.5% (wt.), silicon – 0.25% (wt.) can be dissolved in δ-iron. The maximum content in α-iron can reach carbon – 0.017% (wt.), manganese – 21% (wt.), silicon - 1.3% (wt.).

It was found that the maximum solubility of carbon, manganese and silicon in α-iron of Fe-Mn-Si-C alloys have lower numerical values compared it the insolubility in the corresponding binary systems.

ORCID IDs

Natalia Yu. Filonenko, https://orcid.org/0000-0003-1219-348X;
Alexander Babachenko, https://orcid.org/0000-0003-4710-0343;

REFERENCES

[1] Z. Zongy, and S. Rolf, Journal of Alloys and Compounds, **363**, 202 (2004), https://doi.org/10.1016/S0925-8388(03)00462-6.
[2] P. Presoly, G. Xia, P. Reisinger, and C. Bernhard, Berg Huettenmaenn Monatsh, **159,** 430 (2014), https://doi.org/10.1007/s00501-014-0306-5
[3] J. Miettinen, V.-V. Visuri, and T. Fabritius, *Thermodynamic description of the Fe–Al–Mn–Si–C system for modelling solidification of steels*, Acta Universitatis Ouluensis C Technica, **704**, (University of Oulu, Finland, 2019). pp. 242, http://jultika.oulu.fi/files/isbn9789526222516.pdf.
[4] D. Djurovic, B. Hallstedt, J. Appen, and R. Dronskowski, Calphad, **35**(4), 479 (2011). https://doi.org/10.1016/j.calphad.2011.08.002.
[5] W.S. Zheng, X.G. Lu, Y.L. He, and L. Li, J. Iron Steel Res. Int. **24,** 190 (2017), https://doi.org/10.1016/S1006-706X(17)30027-4
[6] P. Głowacz, M. Tenerowicz-Żaba, M. Sułowski, and J. Konstanty, International Journal "NDT Days", **II**(3), 300 (2019), https://www.bg-s-ndt.org/journal/vol2/JNDTD-v2-n3-a08.pdf.
[7] O.A. Bannykh, and M.E. Drytsa, *Диаграммы состояния двойных и многокомпонентных систем на основе железа* [*Phase Diagrams of Binary and multicomponent Systems based on of the iron: Handbook*] (Metallurgiya, Moscow, 1986), pp. 439. (in Russian)
[8] N.P. Lyakishev, *Диаграммы состояния двойных металлических систем: Справочник* [*Phase Diagrams of Binary Metal Systems: Handbook*], (Mashinostroenie, Moscow, 2001), pp. 498. (in Russian)
[9] E.G. Hoel, in: *Infacon VII*, (Trondheim, Norway, 1995), pp. 601, https://www.pyrometallurgy.co.za/InfaconVII/601-Hoel.pdf.
[10] I. Ohnuma, Sh. Abe, Sh. Shimenouchi, T. Omori, R. Kainuma, and K. Ishida, ISIJ International, **52**(4), 540 (2012). https://doi.org/10.2355/isijinternational.52.540.
[11] P. Presoly, J. Six, and C. Bernhard, Materials Science and Engineering, **119**, 012013-1 (2016). https://doi.org/10.1088/1757-899X/119/1/012013.
[12] S.V. Tverdokhlebova, Visnyk Dnipropetrovskogo nacionalnogo universytetu, serija Fizyka, Radioelektronika, **14**(12/1), 100-104 (2007), http://www.vdnu.narod.ru/v14/pdf/s26_14.pdf. (in Ukrainian)
[13] M.P. Shaskolskaya, *Кристаллография* [*Crystallography*], (Vyisshayashkola, Moscow, 1984), pp. 376. (in Russian)
[14] E. Vincent, C.S. Becquart, and C. Domain, Journal of Nuclear Materials, **351**, 88 (2006). https://doi.org/10.1016/j.jnucmat.2006.02.018.
[15] N.Yu. Filonenko, O.S. Baskevych, V.V. Soboliev, Naukovyi Visnyk Natsionalnoho Hirnychoho Universytetu, **4**, 74 (2012), http://nv.nmu.org.ua/index.php/ru/component/jdownloads/finish/34-04/528-2012-4-filonenko/0. (in Ukrainian)
[16] S.Y.P. Allain, S. Gaudez, G. Geandier, J.C. Hell, M. Gouné, F. Danoix, M. Soler, S. Aoued, and A. Poulon-Quintin, Mater. Sci. Eng. A, **710**, 245 (2018), https://doi.org/10.1016/j.msea.2017.10.105.
[17] Y.P. Sébastien, S. Aoued, A. Quintin-Poulon, M. Gouné, F. Danoix, J. Hell, M. Bouzat, and M. Soler, Materials, **11(**7), 1087 (2018), https://doi.org/10.3390/ma11071087

РОЗЧИННІСТЬ ВУГЛЕЦЮ, МАРГАНЦЮ ТА КРЕМНІЮ У α -ЗАЛІЗІ СПЛАВІВ СИСТЕМИ Fe-Mn-Si-C
Н.Ю. Філоненко[a,b], О.І. Бабаченко[b], Г.А. Кононенко[b], К.Г. Дьоміна[b]
[a]ДЗ «Дніпропетровська державна медична академія МОЗ України»
49044, Україна, м. Дніпро, вул. Володимира Вернадського, 9
[b]Інститут чорної металургії ім. З.І. Некрасова НАН України (ІЧМ НАНУ)
49107, Україна, м. Дніпро, пл. Ак. Стародубова К.Ф., 1

Дослідження проводили на сплавах з вмістом вуглецю 0,37-0,57 % (мас.), кремнію 0,23-0,29 % (мас.), марганцю 0,7-0,86 % (мас.), решта – залізо. Для визначення фазового складу сплавів використовували мікроструктурний, мікрорентгеноспектральний та рентгеноструктурний аналізи. В роботі були визначені фізичні характеристики сплавів, що досліджували в даній роботі, а саме, залежність відносного видовження, відносного звуження, ударної в'язкості та твердості

від хімічного складу сплаву. Отримані в даній роботі результати показали, що найкращі мікроструктурні та фізичні характеристики має сплав на основі заліза з вмістом вуглецю 0,57 % (мас.), кремнію 0,28 % (мас.), марганцю 0,88 % (мас.). Визначено, що після кристалізації та низки фазових перетворень фазовий склад сплаву представлений двома фазами: α-залізом та легованим марганцем цементитом $Fe_{2,7}Mn_{0,3}C$. Крім цього, в мікроструктурі сплаву існують ділянки фериту збагачені марганцем та кремнієм. Вперше з застосуванням квазіхімічного методу отримали залежність вільної енергії твердого розчину α-заліза, легованого кремнієм та марганцем, та визначили межу розчинності вуглецю, марганцю та кремнію. В δ-залізі може розчинятись до 0,09 % (мас.) вуглецю, марганцю до 3,5 % (мас.), кремнію – 0,25 % (мас.). Максимальний вміст в α-залізі може досягати: вуглецю – 0,017 % (мас.), марганцю – 21 % (мас.), кремнію – 1,3 % (мас.).
КЛЮЧОВІ СЛОВА: сплави Fe-Mn-Si-C, межа розчинності, вуглець, марганець, кремній, α-залізо

РАСТВОРИМОСТЬ УГЛЕРОДА, МАРГАНЦА И КРЕМНИЯ В α-ЖЕЛЕЗЕ СПЛАВОВ СИСТЕМЫ Fe-Mn-Si-C

Н.Ю. Филоненко[a,b], А.И. Бабаченко[b], А.А.Кононенко[b], К.Г. Дьомина[b]
[a]ГУ «Днепропетровская государственная медицинская академия МОЗ Украины»
49044, Украина, г. Днепр, ул. Владимира Вернадского, 9
[b]Институт черной металлургии им. З.И. Некрасова НАН Украины (ИЧМ НАНУ)
49107, Украина, г. Днепр, ул. Ак. Стародубова К.Ф., 1

Исследования проводились на сплавах с содержанием углерода 0,37-0,57 % (мас.), кремния 0,23-0,29 % (мас.), марганца 0,7-0,86 % (мас.), остальные - железо. Для определения фазового состава сплавов использовали микроструктурный, микрорентгеноспектральный и рентгеноструктурный анализы. В работе были определены физические характеристики сплавов, которые исследовали в данной работе, а именно, зависимость относительного удлинения, относительного сужения, ударной вязкости и твердости от химического состава сплава. Полученные в данной работе результаты показали, что лучшие микроструктурных и физические характеристики имеет сплав на основе железа с содержанием углерода 0,57 % (мас.), кремния 0,28 % (мас.), марганца 0,88 % (мас.). Определено, что после кристаллизации и ряда фазовых превращений фазовый состав сплава представлен двумя фазами: α-железом и легированным марганца цементитом $Fe_{2,7}Mn_{0,3}C$. Кроме этого, в микроструктуре сплава существуют участки феррита, обогащенные марганца и кремния. Впервые с применением квазихимического метода получили зависимость свободной энергии твердого раствора α-железа, легированного кремния и марганца, и определили границу растворимости углерода, марганца и кремния в нем. В δ-железе может растворяться до 0,09 % (мас.) углерода, марганца до 3,5 % (мас.), кремния - 0,25 % (мас.). Максимальное содержание в α-железе может достигать: карбона - 0,017 % (масс.), марганца – 21 % (масс.), кремния - 1,3 % (масс.).
КЛЮЧЕВЫЕ СЛОВА: сплавы Fe-Mn-Si-C, предел растворимости, углерод, марганец, кремний, α-железо

HYDRODYNAMIC KELVIN-VOIGT MODEL TRANSPORTATION SYSTEM

Oleh M. Pihnastyi[a],*, **Valery D. Khodusov[b],****

aNational Technical University "KhPI"
Kyrpychev str. 2, Kharkiv, Ukraine
bV.N. Karazin Kharkiv National University, Kharkiv, Ukraine
*Corresponding Author: pihnastyi@gmail.com, **E-mail: vkhodusov@ukr.net

The hydrodynamic Kelvin-Voigt model of production systems with a flow method of organizing production is considered. The main macro parameters of the state of the production line and the relationship between them are determined. The analysis of the main characteristics of models of elastic elements, which are used to analyze the occurrence of the dynamic stresses in a moving conveyor belt, is presented. A boundary value problem for elastic longitudinal vibrations in a conveyor belt with a moving material is formulated. It is assumed that the deformation of the conveyor belt element corresponds to the Kelvin-Voigt model and there is no sliding of the moving material on the belt. When determining the forces of resistance to motion acting on an element of the belt, the recommendations of DIN 22101: 2002-08 were used. The analysis of the Kelvin-Voigt model of the elastic element is carried out and the distinctive features of the model are demonstrated. The justification of the choice of the Kelvin-Voigt model of an elastic element for describing the process of occurrence of the longitudinal vibrations in a conveyor belt is given. The dependence of the non-uniform flow of material and the magnitude of tensions in the belt is estimated. An expression is written for the speed of propagation of disturbances along a moving conveyor belt with the material. The reasons for the acceleration and deceleration of the conveyor belt associated with the uneven supply of material at the entrance of the transport system are determined. The relationship between the speed of a conveyor belt and the mass of material along a section of the conveyor is demonstrated. It is shown that an increase in the power of the electric motor at the start and acceleration of the conveyor belt, as well as a decrease in power during the braking and stopping of the conveyor belt, is the cause of the appearance of dynamic stresses in it. The characteristic phases of the initial movement of the conveyor belt with the material are analyzed. The process of occurrence of dynamic tensions with the constant and variable acceleration of the conveyor belt for the phase of acceleration and deceleration of the conveyor belt is investigated. For the analysis, a dimensionless model of a conveyor line was used. An expression is obtained for static and dynamic tensions in the conveyor belt. The amplitude of oscillations of dynamic stresses and the characteristic time of damping of oscillations in a conveyor belt is estimated. A quadratic dependence of the speed of damping of a wave of dynamic tensions with an increase in the oscillation frequency is demonstrated. An inversely proportional dependence of the characteristic decay time of the generated dynamic tensions on the value of the viscosity coefficient of the composite material of the conveyor belt is shown.

KEY WORDS: hydrodynamic model of a transport system, two-moment description, Hooke model, balance equations, PDE production model

In article [1], the hydrodynamic Hooke's model of a transport system is considered, which was used to analyze the mechanism of the occurrence of longitudinal vibrations in a conveyor belt when material moves along a transportation route. To construct a model of the transport system, the equations of two-moment description (2) were used in the form [1, 2]:

$$\frac{\partial [\chi]_0(t,S)}{\partial t} + \frac{\partial [\chi]_1(t,S)}{\partial S} = \delta(S)\lambda(t), \qquad (1)$$

$$[\chi]_0(t,S)\frac{\partial \langle\mu\rangle}{\partial t} + [\chi]_1(t,S)\frac{\partial \langle\mu\rangle}{\partial S} = [\chi]_0(t,S)f(t,S), \qquad \langle\mu\rangle = \frac{[\chi]_1(t,S)}{[\chi]_0(t,S)}, \qquad (2)$$

where $[\chi]_0(t,S)$, $[\chi]_1(t,S)$ are respectively, the density of the material and the flow of material at the moment in time t at the point of the transport route, which is determined by the coordinate S, $S \in [0, S_d]$; S_d is the length of the transport route; $\lambda(t)$ is the intensity of material receipt at the entrance of the transport system at the point $S = 0$; $f(t,S)$ is the force that acts on the material per unit mass of the material and the belt [3]; $\delta(S)$ is Dirac delta function. We will assume that the specific density of the conveyor belt is constant and equal $[\chi]_{0C}$, the conveyor section is located horizontally, and the material does not crumble from the conveyor belt.

The force acting on the section dS of the density conveyor belt $[\chi]_{0C} = const$, on which the material with density $[\chi]_0(t,S)$ is located can be calculated as follows [1, Fig. 1]:

$$f(t,S)dm = R(t,S+dS) - R(t,S) - dF_W, \qquad dm = ([\chi]_0(t,S) + [\chi]_{0C})dS, \qquad (3)$$

$$R(S) = \sigma(t,S)Bh, \qquad (4)$$

where *dm* is the total mass acting on the belt; *B* is conveyor belt width; *h* is conveyor belt height; $\sigma(t,S)$ is conveyor belt tensions; F_W is sum of total resistances to belt movement [1]:

$$F_W = F_H + F_N + F_{St} + F_S. \qquad (5)$$

Descriptions of each component of the secondary resistance (5) are discussed in detail in [1]. Detailed information on the methods for calculating secondary resistances is given in [4].

Primary resistances F_H are related to the frictional resistance along the conveyor belt, with the exception of specific resistances. The primary resistances F_H, assuming a linear relationship between the resistances and the transported load, are determined by the expression

$$d\,F_H = dS \cdot f_C \cdot g_m \left([\chi]_{0R} + ([\chi]_0(t,S) + [\chi]_{0C})\cos\delta_C \right),$$

f_C is the coefficient of resistance to motion, which includes the rolling resistance of the driving rollers and the resistance of the belt being pressed; $g_m = 9.81\,(\text{m/sec}^2)$; $[\chi]_{0R}$ is linear load from rotating parts; δ_C is the angle of inclination of the section of the conveyor section. The force F_N, taking into account the influence on the movement of secondary resistances, can be expressed through the value of the primary resistance to movement F_H [4]:

$$F_N = (C-1)F_H, \quad C \approx 1.05.$$

The force F_{St}, characterizing the gradient resistance of the conveyor belt and transported material [4]

$$d\,F_{St} = dS \cdot \sin\delta_C \cdot g_m \left([\chi]_0(t,S) + [\chi]_{0C} \right)$$

for a horizontally located conveyor section ($\delta_C = 0$) not present.

The calculation of the force F_S, associated with special resistances in the transport system is determined by the design features of the transport system. For most conveyor-type transport systems, it is assumed

$$F_S \ll F_H.$$

Divide (3) by *dm*

$$f(t,S) = \frac{1}{([\chi]_0(t,S) + [\chi]_{0C})}\frac{\partial R(t,S)}{\partial S} - \frac{1}{([\chi]_0(t,S) + [\chi]_{0C})}\frac{\partial F_W}{\partial S}.$$

substituting the result into (2), we obtain an equation that, together with equation (1), determines the propagation of stress disturbances along the conveyor belt, taking into account the distribution of material along the transport route

$$\frac{\partial\langle\mu\rangle}{\partial t} + \langle\mu\rangle\frac{\partial\langle\mu\rangle}{\partial S} = \frac{1}{([\chi]_0(t,S) + [\chi]_{0C})}\frac{\partial R(t,S)}{\partial S} - \frac{1}{([\chi]_0(t,S) + [\chi]_{0C})}\frac{\partial F_W}{\partial S}. \qquad (6)$$

To solve the system of equations (1), (7), the relationship between the tensions and the relative deformation of the section of the conveyor belt must be known

$$\sigma(t,S) = f_\sigma(\varepsilon(t,S)).$$

This dependence is determined by the properties of the composite material from which the conveyor belt is made and is a model of an elastic element.

FORMULATION OF THE PROBLEM

The cost of transporting material from the place of extraction to the place of material processing reaches 20% of the total cost of mining material [5]. These costs can be significantly increased in the case of underloaded transport systems. This is especially important for long-distance transport systems [6, 7]. To reduce unit costs, systems are used to control the speed of the conveyor belt $\langle\mu\rangle$ and the value of the incoming flow $\lambda(t)$ to the input of a separate section from the accumulating bunker. The control of the parameters of the transport system changes the linear density of the material $[\chi]_0(t,S)$ along the transportation route. Control algorithms assume the operation of the conveyor section in the mode of acceleration or deceleration of the conveyor belt [8, 9]. This leads to the generation and propagation of tension disturbances along the conveyor belt [10]. If the maximum permissible tension value of the conveyor belt is

exceeded, such control modes destroy the transport system. The danger of such situations is relevant at the present time and requires a detailed analysis of the causes of disturbances for conveyor belts made of different materials.

MODEL OVERVIEW

The process of propagation of tension disturbances along the conveyor belt of the transport system largely depends on the properties of the material from which the conveyor belt is made. An overview of the models of elastic elements for materials of various properties is presented in [9]. The analysis of the main characteristics of elastic element models is presented: Hookean element, Newtonian element, Maxwell element, Kelvin element, Venant element, CDI geometric beam element and CDI five-element. The finite element method (FEM) is chosen to describe the transport system [11]. The calculation was carried out for the different start and stop modes of two operating transport systems with an elastic element of the CDI five-element composite model. The length of one of the conveyors was 9 km. The article [12] presents a comparative analysis of elastic element models: Vogit element and Maxwell element. A system of Lagrange equations was chosen to model the transport system. For the conveyor section, the calculation for speed, acceleration and tension in the belt for several modes of operation is performed. In [13], for the model of the elastic element Maxwell element and the model of the Winkler foundation transport system, a calculation was made for the speed of the conveyor belt. The article [14] presents the calculated "belt stretch curve" and "velocity curves" for the Kelvin-Voigt element model of the elastic element and the transport system model represented by the Lagrange system of equations. The article [15] analyzes the models of the elastic element Kelvin-Voigt element, the combination of Hooke and Kelvin-Voigt element, as well as the combination of two Kelvin-Voigt elements. The analysis of long-wave oscillations in the conveyor belt of the transport system for the Hooke element model and the analytical model of the transport system is presented in [1]. The mechanical properties of composite materials for the manufacture of a rubber conveyor belt with polyester and polyamide cartridges are given in [16]. The results of experimental studies of composite materials of a rubber conveyor belt with polyester and polyamide cartridges are presented. As a result of experimental studies, values were obtained for the tensile strength, elastic modulus, Poisson's ratio for new and operated rubber conveyor belts. Analysis of these indicators, which characterize the properties of a specific material of the conveyor belt, allows you to determine the model of the elastic element, and, accordingly, the type of dependence between the tension and the relative deformation.

CONVEYOR TYPE PRODUCTION LINE MODEL

In this paper, the Kelvin-Voigt element model will be used to analyze the arising stresses in the conveyor belt (Fig. 1):

$$\sigma(t,S) = E\varepsilon(t,S) + \eta \frac{d\varepsilon(t,S)}{dt}, \tag{7}$$

where E is the elastic modulus of the element; η is element viscosity.
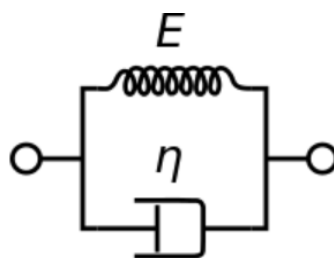
Figure 1. Kelvin-Voigt element

Equation (7) is used to calculate the normal tensions of an element. If the tension is constant $\sigma(t,S) = \sigma_0 = const$, then the equation has a solution

$$\varepsilon(t,S) = \frac{\sigma_0}{E}\left(1 - e^{-t/t_0}\right), \qquad t_0 = \frac{\eta}{E}.$$

At $t \gg t_0$, the limiting value for the element deformation is obtained:

$$\lim_{t \to \infty} \varepsilon(t,S) = \frac{\sigma_0}{E}.$$

At $\omega \ll \omega_\eta$, the limit transition to the model of an elastic element follows, in which the stress and strain can be calculated in accordance with Hooke's law:

$$\sigma(t,S) \approx E\varepsilon(t,S), \qquad E\varepsilon(t,S) >> \eta\omega\varepsilon(t,S), \qquad \frac{d\varepsilon(t,S)}{dt} \approx \omega\varepsilon(t,S), \qquad \frac{\eta}{E} = \frac{1}{\omega_\eta}.$$

The analysis of the arising deformations in accordance with Hooke's law was investigated in [1]. Substituting expression (7), which determines the relationship between stress and strain, into equation (6), we obtain

$$\frac{d\langle\mu\rangle}{dt} = \frac{BhE}{\left([\chi]_0(t,S) + [\chi]_{0C}\right)} \frac{\partial\varepsilon(t,S)}{\partial S} + \frac{Bh\eta}{\left([\chi]_0(t,S) + [\chi]_{0C}\right)} \frac{\partial^2\varepsilon(t,S)}{\partial t\partial S} - \frac{1}{\left([\chi]_0(t,S) + [\chi]_{0C}\right)} \frac{\partial F_W}{\partial S}. \qquad (8)$$

Let us introduce the absolute elongation of the conveyor belt $W(t,S)$ at the moment of time t for the technological position S. The ratio of the elongation $dW(t,S)$ of the element by the conveyor belt to the length of the segment dS is the relative deformation of the element

$$\varepsilon(t,S) = \frac{\partial W(t,S)}{\partial S}, \qquad \varepsilon(t,S) \approx 10^{-2}.$$

The speed of the conveyor belt $\langle\mu\rangle$, on which the material is located, consists of the speed of the belt in equilibrium μ_ψ and the oscillatory part of the belt speed $\frac{dW(t,S)}{dt}$:

$$\langle\mu\rangle = \mu_\psi + \frac{dW(t,S)}{dt}, \qquad \frac{dW(t,S)}{dt} = \frac{\partial W(t,S)}{\partial t} + \langle\mu\rangle\frac{\partial W(t,S)}{\partial S}.$$

Since the relative deformation of the element $\varepsilon(t,S)$ is small, then

$$\frac{dW(t,S)}{dt} = \frac{\partial W(t,S)}{\partial t} + \langle\mu\rangle\varepsilon(t,S) \approx \frac{\partial W(t,S)}{\partial t},$$

$$\left|\langle\mu\rangle\varepsilon(t,S)\right| << \left|\frac{\partial W(t,S)}{\partial t}\right|. \qquad (9)$$

For the relative deformation, represented in the form of a plane wave $W(t,S) \sim e^{i(\omega t - kS)}$, it follows

$$\langle\mu\rangle << \left|\frac{\omega}{k}\right| = \frac{1}{2\pi}\left|\lambda_k\omega\right| = \mu_{ph}, \qquad \frac{\partial W(t,S)}{\partial t} \sim \omega W(t,S), \qquad \varepsilon(t,S) = \frac{\partial W(t,S)}{\partial S} \sim kW(t,S),$$

where ω is the oscillation frequency; k is wave vector; λ_k is disturbance wavelength; μ_{ph} is the phase velocity of propagation of the disturbance wave, that is, the velocity of movement of a point with a constant phase of oscillatory motion in space, along a given direction. A negative value of the wave vector corresponds to the case of propagation of a backward wave. In this paper, we will consider perturbations whose propagation satisfies the condition (8). Assuming that for the case when the functions $W(t,S)$, $\langle\mu\rangle$ have a large gradient, the destruction of the conveyor belt occurs. Taking this into account, we write down the expression for the change in the speed of the belt, neglecting the values of higher orders of smallness

$$\frac{d\langle\mu\rangle}{dt} \cong \frac{d\mu_\psi}{dt} + \frac{\partial^2 W(t,S)}{\partial t^2},$$

where the order of smallness is given below:

$$\frac{\partial^2 W(t,S)}{\partial t\partial S} \sim \omega k W(t,S), \qquad \frac{\partial^2 W(t,S)}{\partial t^2} \sim \omega^2 W(t,S), \qquad \frac{\partial^2 W(t,S)}{\partial S^2} \sim k^2 W(t,S).$$

When the length of a segment dS of the transport route changes, the density changes $\left([\chi]_0(t,S) + [\chi]_{0C}\right)$. Let the length of the segment dS change and become equal $\left(dS + dW(t,S)\right)$, $dS >> dW(t,S)$. In this case, the linear density will change and become equal to $\left([\chi]_0(t,S) + [\chi]_{0C}\right) + \left(\Delta[\chi]_0(t,S) + \Delta[\chi]_{0C}\right)$. For a given segment of the transport route, we have

$$dS\left([\chi]_0(t,S) + [\chi]_{0C}\right) = \left(dS + dW(t,S)\right)\left([\chi]_0(t,S) + [\chi]_{0C}\right) + \left(\Delta[\chi]_0(t,S) + \Delta[\chi]_{0C}\right).$$

Neglecting a quantity of the second order of smallness $dW(t,S)\big(\Delta[\chi]_0(t,S) + \Delta[\chi]_{0C}\big)$, we obtain

$$0 \approx dS\big(\Delta[\chi]_0(t,S) + \Delta[\chi]_{0C}\big) + dW(t,S)\big([\chi]_0(t,S) + [\chi]_{0C}\big) \ ,$$

from where

$$\frac{\partial dW(t,S)}{\partial S} \approx -\frac{\Delta[\chi]_0(t,S) + \Delta[\chi]_{0C}}{[\chi]_0(t,S) + [\chi]_{0C}} \approx \varepsilon$$

and

$$\frac{BhE}{\big([\chi]_0(t,S) + [\chi]_{0C}\big)} \approx C_\psi{}^2(t,S)(1-\varepsilon), \qquad C_\psi{}^2(t,S) = \frac{BhE}{[\chi]_{0\psi}(t,S) + [\chi]_{0C}} \ .$$

The function $C_\psi{}^2(t,S)$ determines the speed of propagation of disturbances along the conveyor belt [8]. The local change in density as a result of stretching the belt does not significantly affect the propagation of stress disturbances along the conveyor belt. Thus, we represent equation (8) in the form

$$\frac{\partial^2 W(t,S)}{\partial t^2} = C_\psi{}^2(t,S)\frac{\partial^2 W(t,S)}{\partial S^2} + C_\psi{}^2(t,S)\frac{\eta}{E}\frac{\partial^3 W(t,S)}{\partial t \partial S^2} - \frac{C_\psi{}^2(t,S)}{BhE}\frac{\partial F_W}{\partial S} - f_\psi(t), \qquad (10)$$

where $f_\psi(t)$ is the acceleration of the conveyor belt for the steady state

$$\frac{d\mu_\psi}{dt} = f_\psi(t) \ .$$

For horizontal conveyor sections $\cos\delta_C = 1$, where

$$\frac{\partial F_W}{\partial S} = Cf_C g_m\big([\chi]_{0R} + \big([\chi]_0(t,S) + [\chi]_{0C}\big)\big).$$

The solution of the equation for the case

$$E\frac{\partial^2 W(t,S)}{\partial S^2} >> \eta\frac{\partial^3 W(t,S)}{\partial t \partial S^2}, \qquad \frac{E}{\eta} >> \omega$$

is presented in [1]. In this paper, we consider the case for which the relation $E/\eta \approx \omega$.

Let's assume that at the initial moment of time the linear density of the material is distributed along the transport route according to the law

$$[\chi]_0(0,S) \approx [\chi]_{0\psi}(0,S) = \mathrm{H}(S)\Psi(S), \qquad \mathrm{H}(S) = \begin{cases} 0, & S < 0, \\ 1, & S \ge 0, \end{cases} \qquad S \in [0; S_d].$$

Let us supplement the system of equations (10) with boundary conditions for the equation describing oscillatory processes in the transport system. The tensions $\sigma(t,0)$ and $\sigma(t,S_d)$ are determined by the tension forces of the conveyor belt T_1 and T_4 (Fig. 2).
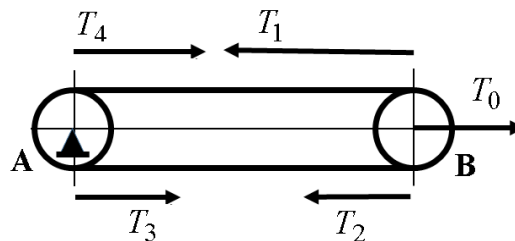
Figure 2. Conveyor belt tension diagram

Let us write the system of equations for the forces T_i, that determine the movement of the belt at the characteristic points of the horizontal conveyor section:

$$T_1 = T_2 \exp(k_b \alpha); \qquad T_3 = T_2 + F_{W\,(2-3)} + F_{\psi\,(2-3)}; \qquad T_4 = k_s T_3, \qquad T_1 = T_4 + F_{W\,(4-1)} + F_{\psi\,(4-1)}, \qquad (11)$$

$$F_{H\,(2-3)} = S_d \cdot f_C \cdot g_m \left([\chi]_{0R} + [\chi]_{0C}\right), \qquad F_{H\,(4-1)} = F_{H\,(2-3)} + f_C \cdot g_m \int_0^{S_d} [\chi]_0(t,S)dS, \quad \delta_C = 0,$$

$$F_{N\,(2-3)} = (C-1)F_{H\,(2-3)}, \qquad F_{N\,(4-1)} = (C-1)F_{H\,(4-1)},$$

$$F_{St\,(2-3)} = S_d \cdot \sin\delta_C \cdot g_m[\chi]_{0C} = 0, \qquad F_{St\,(4-1)} = F_{St\,(2-3)} + \sin\delta_C \cdot g_m \int_0^{S_d} [\chi]_0(t,S)dS = 0,$$

$$F_{\psi\,(2-3)} = f_\psi(t)[\chi]_{0C} S_d, \qquad F_{\psi\,(4-1)} = F_{\psi\,(2-3)} + f_\psi(t) \int_0^{S_d} [\chi]_0(t,S)dS,$$

$$F_W = F_H + F_N + F_{St} + F_S$$

where $F_{\psi\,(2-3)}, F_{\psi\,(4-1)}$ are forces associated with the acceleration or deceleration of the conveyor belt. We believe that the effects associated with a change in the angular speed of rotation of the drum are small due to the insignificant value of the moment of inertia of the rollers. The solution of the system of equations (11) makes it possible to determine the tractive effort for the transport conveyor for a steady motion:

$$T_1 = \left(k_s F_{W\,(2-3)} + k_s F_{\psi\,(2-3)} + F_{W\,(4-1)} + F_{\psi\,(4-1)}\right)\frac{\exp(k_b\alpha)}{\exp(k_b\alpha)-k_s}, \quad T_4 = T_1 - F_{W\,(4-1)} - F_{\psi\,(4-1)},$$

where k_b is the coefficient of adhesion between the drum and the belt; k_s is drum loss factor "A"; α is total belt wrap angle of drive drums. For steel drum without moisture is $k_b \approx 0.3$, $k_s \approx 1.03$ [17] and $\alpha = \pi$, we get $\exp(k_b\alpha) = 2.56$. In accordance with (9), the expression for the tension in the conveyor belt takes the form

$$\sigma(t,S) \approx E\frac{\partial W(t,S)}{\partial S} + \eta\frac{\partial^2 W(t,S)}{\partial t \partial S}.$$

At points $S = 0$, $S = S_d$, the conveyor belt is engaged with the drive and driven shafts of the conveyor section. In this regard, it can be assumed that

$$\left.\frac{d\varepsilon(t,S)}{dt}\right|_{S=0} = \left.\frac{\partial^2 W(t,S)}{\partial t\partial S}\right|_{S=0} = 0, \qquad \left.\frac{d\varepsilon(t,S)}{dt}\right|_{S=S_d} = \left.\frac{\partial^2 W(t,S)}{\partial t\partial S}\right|_{S=S_d} = 0. \qquad (12)$$

Taking into account the values of the acting forces T_1, T_4, let write down the boundary conditions

$$\sigma(t,S_d) = \frac{T_1}{Bh} = E\left.\frac{\partial W(t,S)}{\partial S}\right|_{S=S_d} + \eta\left.\frac{\partial^2 W(t,S)}{\partial t\partial S}\right|_{S=S_d} =$$

$$= \frac{1}{Bh}\left(k_s F_{W\,(2-3)} + k_s F_{\psi\,(2-3)} + F_{W\,(4-1)} + F_{\psi\,(4-1)}\right)\frac{\exp(k_b\alpha)}{\exp(k_b\alpha)-k_s},$$

$$\sigma(t,0) = \frac{T_4}{Bh} = E\left.\frac{\partial W(t,S)}{\partial S}\right|_{S=0} + \eta\left.\frac{\partial^2 W(t,S)}{\partial t\partial S}\right|_{S=0} = E\left.\frac{\partial W(t,S)}{\partial S}\right|_{S=S_d} - \frac{F_{W\,(4-1)} + F_{\psi\,(4-1)}}{Bh}.$$

Let us supplement the system of equations with initial conditions. Consider the mode of occurrence of oscillations, assuming that at the initial moment there were no oscillations

$$\left.\frac{\partial W(t,S)}{\partial t}\right|_{t=0} = 0.$$

The tension of the conveyor belt at the initial moment of time is determined by the initial distribution of material along the technological route $\Psi(S)$ and the acceleration of the conveyor belt $f_\psi(t)$. Then

$$\sigma(0,S) = \sigma(0,0) + F_{W\Psi\,(4-1)}(0,S) + F_{\psi\Psi\,(4-1)}(0,S),$$

$$F_{H\Psi\,(4-1)}(0,S) = f_C \cdot g_m \int_0^S \left([\chi]_{0R} + [\chi]_{0C} + \Psi(\zeta)\right)d\zeta, \quad F_{N\Psi\,(4-1)}(0,S) = (C-1)F_{H\Psi\,(4-1)}(t,S), \quad [\chi]_0(0,S) = \Psi(S)$$

$$F_{\psi\Psi\,(4-1)}(0,S) = f_\psi(0)\int_0^S \left([\chi]_{0R} + [\chi]_{0C} + \Psi(\zeta)\right)d\zeta, \quad F_{W\Psi\,(4-1)}(0,S) = F_{H\Psi\,(4-1)}(0,S) + F_{N\Psi\,(4-1)}(0,S).$$

Let us estimate the value of the acceleration of the conveyor belt $f_\psi(t)$. Asynchronous motors with phase rotor are usually installed on powerful belt conveyor sections. The acceleration and deceleration of the conveyor belt of a separate section occurs with the help of a rheostat, which sequentially changes the resistance in the rotor circuit. Simulation of starting up of the drive member of a mechanical system is given into [18]. The qualitative characteristic connecting the torque of the electric motor M_{eng} and the engine speed n_{eng} is shown in Fig.3 [19], where M_{eng0}, n_{eng0} is the rated torque of the electric motor and the rated engine speed. For the mode of acceleration and deceleration, the relative torque of the electric motor $\left(M_{eng}/M_{eng}0\right)$ fluctuates within insignificant limits with a change in the relative speed $\left(n_{eng}/n_{eng}0\right)$, (Fig.3). If the engine power N_{eng} is constant, the engine speed n_{eng} will fluctuate around the rated value n_{eng0}. Let us estimate the amplitude of the oscillation, which is associated with the uneven flow of material at the input of the conveyor section. We write the engine power through the traction force T_1, the radius of the drive shaft r and the rotation speed of the drive shaft:

$$N_{eng} = T_1 r \omega, \qquad \omega = 2\pi n_{eng}.$$

The change in force T_1 occurs due to uneven material receipt

$$\frac{dN_{eng}}{dt} = \frac{dT_1}{dt}r\omega + T_1 r\frac{d\omega}{dt} = \frac{dT_1}{dt}r\omega + T_1 f_\psi(t) = 0, \qquad f_\psi(t) = r\frac{d\omega}{dt}.$$

Assuming for steady motion $f_{\psi 0}(t) = 0$, the equation takes the following form

$$\frac{dM(t)}{dt}\omega \approx M(t)\frac{d\omega}{dt}, \qquad \frac{df_\psi(t)}{dt} << \frac{f_\psi(t)}{t_a} \qquad M(t) = \int_0^{S_d}\left([\chi]_{0C} + [\chi]_0(t,S)\right)dS,$$
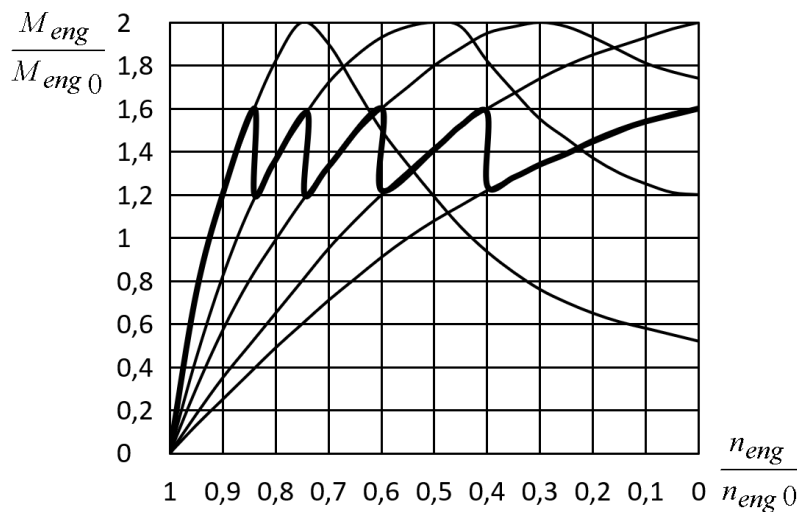
Figure 3. Mechanical characteristic of a phase rotor induction motor

where $M(t)$ is the total weight of the material with a belt for a separate conveyor section; t_a is the characteristic duration of the acceleration or deceleration mode. The maximum change in the mass of the material on the conveyor section occurs when the material arrives at the maximum intensity at the entrance of an empty conveyor line. In this

case, the mass of the belt without material is equal to $M(t) = [\chi]_{0C} S_d$, and the intensity of the incoming flow of material is $\lambda(t) \leq [\chi]_{0\,max} \omega r$. Then

$$\frac{d\omega}{dt} \approx -\omega \frac{1}{M(t)} \frac{dM(t)}{dt} \approx -\omega \frac{\lambda(t)}{M(t)} \approx -\omega \frac{[\chi]_{0\,max}}{[\chi]_{0C}} \frac{\omega r}{S_d},$$

Taking into account that

$$[\chi]_{0\,max} \sim [\chi]_{0C}, \qquad\qquad \frac{\omega r}{S_d} \sim \frac{1}{T_d},$$

follows

$$\frac{d\omega}{dt} \approx \frac{\omega}{T_d} << \frac{\omega}{t_a},$$

where T_d is the time it takes for the material to pass the transportation route. The inequality allows us to formulate an important result: the uneven flow of material at the entrance of the transport system does not accelerate or decelerate of the conveyor belt. Uneven material flow leads to the destruction of the conveyor belt as a result of shock loads [20].

DIMENSIONLESS MODEL OF CONVEYOR LINE

Let's introduce dimensionless designations [1, 21, 22]:

$$\tau = \frac{t}{T_d}, \quad \xi = \frac{S}{S_d}, \quad \theta_0(\tau,\xi) = \frac{[\chi]_0(t,S)}{[\chi]_{0max}}, \quad \psi(\xi) = \frac{\Psi(S)}{[\chi]_{0max}}, \quad \gamma(\tau) = \lambda(t)\frac{T_d}{S_d[\chi]_{0max}}, \quad g(\tau) = \mu_\psi(t)\frac{T_d}{S_d},$$

$$W_0(\tau,\xi) = \frac{W(t,S)}{W_{max}}, \qquad W_{max} = \frac{\sigma_b S_d}{E}, \qquad \theta_C = \frac{[\chi]_{0C}}{[\chi]_{0max}}, \quad \theta_R = \frac{[\chi]_{0R}}{[\chi]_{0max}}, \quad v_\eta = \frac{\eta}{ET_d},$$

$$v_b = \frac{Cf_C g_m([\chi]_{0max} + [\chi]_{0C})S_d}{\sigma_b Bh}, \qquad v_f = v_f(\tau) = \frac{([\chi]_{0max} + [\chi]_{0C})f_\psi(t)S_d}{\sigma_b Bh},$$

$$v_g^2 = \frac{BhE}{[\chi]_{0max} + [\chi]_{0C}}\left(\frac{T_d}{S_d}\right)^2, \qquad C_\psi^2(t,S) = \frac{BhE}{[\chi]_{0\psi}(t,S) + [\chi]_{0C}},$$

$$v_1^2 = v_g^2\frac{1+\theta_C}{\theta_C}, \qquad v_2^2 = v_g^2 v_b\left(1 + \frac{\theta_R}{\theta_C}\right), \qquad v_{2f} = v_f v_g^2 = v_f(\tau)v_g^2,$$

$$\alpha_{12} = \alpha_{12}(\tau) = v_b\frac{\theta_C}{1+\theta_C}\left(1 + \frac{\theta_R}{\theta_C}\right) + v_f(\tau)\frac{\theta_C}{1+\theta_C}, \quad \alpha_1 = \alpha_1(\tau) = K_{12}\alpha_{12}(\tau), \quad K_{12} = \frac{(k_s+1)\exp(k_b\alpha)}{\exp(k_b\alpha) - k_s},$$

where v_b determines the ratio of the resistance force $Cf_C g_m([\chi]_{0max} + [\chi]_{0C})S_d$ at maximum load $[\chi]_{0max}$ to the maximum permissible tension force, which ensures the belt break $\sigma_b Bh$; v_f is the ratio of the inertia force $([\chi]_{0max} + [\chi]_{0C})f_\psi(t)S_d$ at maximum load $[\chi]_{0max}$ and acceleration $f_\psi(t)$ to the maximum permissible tensile force, which ensures the belt break $\sigma_b Bh$; $v_g = C_\psi /(S_d / T_d)$ is the relative speed of wave propagation, which is defined as the ratio of the propagation speed of the disturbance wave C_ψ to the characteristic speed of the conveyor belt $a_{char} = (S_d / T_d)$. The forces $F_{W(2-3)}$, F_ψ $(2-3)$, $F_{W(4-1)}$, F_ψ $(4-1)$ taking into account dimensionless parameters can be written in the form:

$$\frac{F_{W(2-3)}}{\sigma_b Bh} = v_b\frac{\theta_C + \theta_R}{1+\theta_C}, \qquad\qquad \frac{F_\psi\ (2-3)}{\sigma_b Bh} = v_f(\tau)\frac{\theta_C}{1+\theta_C},$$

$$\frac{F_{W(4-1)}}{\sigma_b Bh} = v_b\frac{\theta_C + \theta_R}{1+\theta_C} + v_b\int_0^1\frac{\theta_0(\tau,\xi)}{1+\theta_C}d\xi, \qquad \frac{F_\psi\ (4-1)}{\sigma_b Bh} = v_f(\tau)\frac{\theta_C}{1+\theta_C} + v_f\int_0^1\frac{\theta_0(\tau,\xi)}{1+\theta_C}d\xi.$$

Then equation (10), which describes the oscillatory processes in the transport system, takes the dimensionless form

$$\frac{\partial^2 W_0(\tau,\xi)}{\partial \tau^2} = v_g^2 \frac{\partial^2 W_0(\tau,\xi)}{\partial \xi^2}\frac{1+\theta_C}{\theta_0(\tau,\xi)+\theta_C} + v_g^2 v_\eta \frac{\partial^3 W_0(\tau,\xi)}{\partial \xi^2 \partial \tau}\frac{1+\theta_C}{\theta_0(\tau,\xi)+\theta_C} - v_g^2 \frac{1+\theta_C}{\theta_C}\alpha_{12} +$$

$$+ v_g^2 v_b\left(\frac{\theta_R}{\theta_C} - \frac{\theta_R}{\theta_0(\tau,\xi)+\theta_C}\right), \tag{13}$$

with boundary conditions:

$$\left.\frac{\partial W_0(\tau,\xi)}{\partial \xi}\right|_{\xi=1} = \alpha_1 + \alpha_{12}\left(\frac{\exp(k_b\alpha)}{\exp(k_b\alpha)-k_s}\right)\int_0^1 \frac{\theta_0(\tau,\xi)}{\theta_C}d\xi - v_b\frac{\theta_R}{\theta_C}\left(\frac{\exp(k_b\alpha)}{\exp(k_b\alpha)-k_s}\right)\int_0^1 \frac{\theta_0(\tau,\xi)}{\theta_C}d\xi, \tag{14}$$

$$\left.\frac{\partial W_0(\tau,\xi)}{\partial \xi}\right|_{\xi=0} = \left.\frac{\partial W_0(\tau,\xi)}{\partial \xi}\right|_{\xi=1} - \frac{F_W(4-1)+F_\psi(4-1)}{\sigma_b Bh} =$$

$$= \alpha_1 + \alpha_{12}\left(\left(\frac{k_s}{\exp(k_b\alpha)-k_s}\right)\int_0^1 \frac{\theta_0(\tau,\xi)}{\theta_C}d\xi - 1\right) - v_b\frac{\theta_R}{\theta_C}\left(\frac{k_s}{\exp(k_b\alpha)-k_s}\right)\int_0^1 \frac{\theta_0(\tau,\xi)}{\theta_C}d\xi. \tag{15}$$

and initial conditions:

$$\left.\frac{\partial W_0(\tau,\xi)}{\partial t}\right|_{t=0} = 0, \tag{16}$$

$$\frac{\partial W_0(0,\xi)}{\partial \xi} = \left.\frac{\partial W_0(0,\xi)}{\partial \xi}\right|_{\xi=1} - v_b\int_\xi^1 \frac{\theta_C+\theta_R+\psi(\xi)}{1+\theta_C}d\xi - v_f(\tau)\int_\xi^1 \frac{\theta_C+\psi(\xi)}{1+\theta_C}d\xi\Bigg|_{\tau=0} =$$

$$= \alpha_1(0)+\alpha_{12}(0)\left(\left(\frac{k_s}{\exp(k_b\alpha)-k_s}\right)\int_0^1 \frac{\psi(\xi)}{\theta_C}d\xi - 1 + \xi + \int_0^\xi \frac{\psi(\xi)}{\theta_C}d\xi\right) - v_b\frac{\theta_R}{\theta_C}\left(\left(\frac{k_s}{\exp(k_b\alpha)-k_s}\right)\int_0^1 \frac{\psi(\xi)}{\theta_C}d\xi + \int_0^\xi \frac{\psi(\xi)}{\theta_C}d\xi\right) \tag{17}$$

ANALYSIS OF THE SOLUTION FOR LOW-LOADED CONVEYOR LINES

Let us consider a solution for the case of initial conveyor movement when the conveyor line is low loaded. The specific density of the material along such conveyor lines is low compared to the specific gravity of the conveyor belt

$$\theta_0(\tau,\xi) \ll \theta_C, \qquad \psi(\xi) = \theta_0(0,\xi) \ll \theta_C.$$

Taking into account this assumption, equation (13) takes the form

$$\frac{\partial^2 W_0(\tau,\xi)}{\partial \tau^2} = v_1^2 \frac{\partial^2 W_0(\tau,\xi)}{\partial \xi^2} + v_\eta v_1^2 \frac{\partial^3 W_0(\tau,\xi)}{\partial \xi^2 \partial \tau} - v_1^2 \alpha_{12}(\tau) \tag{18}$$

with boundary conditions:

$$\left.\frac{\partial W_0(t,\xi)}{\partial \xi}\right|_{\xi=1} = \alpha_1(\tau), \qquad \left.\frac{\partial W_0(\tau,\xi)}{\partial \xi}\right|_{\xi=0} = \alpha_1(\tau) - \alpha_{12}(\tau),$$

and initial conditions:

$$\left.\frac{\partial W_0(\tau,\xi)}{\partial t}\right|_{t=0} = 0, \qquad \frac{\partial W_0(0,\xi)}{\partial \xi} = \alpha_1(\tau) - \alpha_{12}(\tau)(1-\xi),$$

During the initial movement of the conveyor belt, three characteristic phases should be distinguished: a) the period of time of the initial start-up, when the conveyor belt from a state of rest turns into movement along the entire route; b) the phase of the formation of a static force, along the conveyor belt; c) the phase of acceleration of the conveyor belt to the rated speed. Let us dwell on the analysis of the last phase of the start of the conveyor belt. The phase of acceleration of the conveyor belt to the nominal speed is characterized by a quasi constant value of the traction torque (Fig.3), [19] and a quasi constant value of the acceleration of the elements of the conveyor belt. In this regard, the function $v_f(\tau)$

will be assumed to be slowly varying during the characteristic time of the acceleration process t_a.

Let us choose the solution to the equation in the form

$$W_0(\tau,\xi) = W_{00}(\tau,\xi) + W_{01}(\tau,\xi).$$

Let us represent a function $W_{01}(\tau,\xi)$ as

$$W_{01}(\tau,\xi) = A(\tau)\xi^2 + B(\tau)\xi + C_{01}.$$

where C_{01} is an unknown constant. We define the coefficients $A(\tau)$, $B(\tau)$ in such a way as to ensure the presence of boundary conditions for the function $W_{00}(\tau,\xi)$ in the form

$$\left.\frac{\partial W_{00}(\tau,\xi)}{\partial \xi}\right|_{\xi=1} = 0, \qquad \left.\frac{\partial W_{00}(t,\xi)}{\partial \xi}\right|_{\xi=0} = 0, \qquad \frac{\partial W_{00}(t,\xi)}{\partial \xi} = \frac{\partial W_0(t,\xi)}{\partial \xi} - \frac{\partial W_{01}(t,\xi)}{\partial \xi}.$$

This implies the conditions for determining the coefficients $A(\tau)$, $B(\tau)$

$$\left.\frac{\partial W_{00}(\tau,\xi)}{\partial \xi}\right|_{\xi=1} = \left.\frac{\partial W_0(\tau,\xi)}{\partial \xi}\right|_{\xi=1} - \left.\frac{\partial W_{01}(\tau,\xi)}{\partial \xi}\right|_{\xi=1} = \left(\alpha_1(\tau) - 2A(\tau)\xi - B(\tau)\right)\big|_{\xi=1} = \alpha_1(\tau) - 2A(\tau) - B(\tau) = 0,$$

$$\left.\frac{\partial W_{00}(\tau,\xi)}{\partial \xi}\right|_{\xi=0} = \left.\frac{\partial W_0(\tau,\xi)}{\partial \xi}\right|_{\xi=0} - \left.\frac{\partial W_{01}(\tau,\xi)}{\partial \xi}\right|_{\xi=0} = \left(\alpha_1(\tau) - \alpha_{21}(\tau) - 2A(\tau)\xi - B(\tau)\right)\big|_{\xi=0} = \alpha_1(\tau) - \alpha_{21}(\tau) - B(\tau) = 0.$$

From the solution of the system of equations it follows

$$A(\tau) = \frac{\alpha_{21}(\tau)}{2}, \qquad B(\tau) = \alpha_1(\tau) - \alpha_{12}(\tau),$$

$$W_0(\tau,\xi) = W_{00}(\tau,\xi) + \frac{\alpha_{12}(\tau)}{2}\xi^2 + \left(\alpha_1(\tau) - \alpha_{12}(\tau)\right)\xi + C_{01}.$$

Substitution $W_0(\tau,\xi)$ into (18), an equation for $W_{00}(\tau,\xi)$ is obtained

$$\frac{\partial^2 W_{00}(\tau,\xi)}{\partial \tau^2} = v_1^2 \frac{\partial^2 W_{00}(\tau,\xi)}{\partial \xi^2} + v_\eta v_1^2 \frac{\partial^3 W_{00}(\tau,\xi)}{\partial \xi^2 \partial \tau} - \frac{d^2\alpha_{12}(\tau)}{d\tau^2}\left(\frac{\xi^2}{2} - 1\right) - \frac{d^2\alpha_1(\tau)}{d\tau^2}\xi + v_\eta v_1^2 \frac{d\alpha_{12}(\tau)}{d\tau} \qquad (19)$$

with boundary conditions:

$$\left.\frac{\partial W_{00}(\tau,\xi)}{\partial \xi}\right|_{\xi=1} = 0, \qquad \left.\frac{\partial W_{00}(\tau,\xi)}{\partial \xi}\right|_{\xi=0} = 0$$

and initial conditions:

$$\left.\frac{\partial W_{00}(\tau,\xi)}{\partial \tau}\right|_{\tau=0} = -\left.\frac{d\alpha_{12}(\tau)}{d\tau}\right|_{\tau=0}\left(\frac{\xi^2}{2} - \xi\right) - \left.\frac{d\alpha_1(\tau)}{d\tau}\right|_{\tau=0}\xi, \qquad \frac{\partial W_{00}(0,\xi)}{\partial \xi} = 0.$$

a) the acceleration of the conveyor belt is absent or constant $v_f(\tau) = v_{f0} = const$.

If the acceleration value is constant or absent, then by definition $\alpha_{12}(\tau)$ it follows

$$\frac{d\alpha_{12}(\tau)}{d\tau} = 0, \qquad \frac{d^2\alpha_{12}(\tau)}{d\tau^2} = 0$$

and equations (19) take the form

$$\frac{\partial^2 W_{00}(\tau,\xi)}{\partial \tau^2} = v_1^2 \frac{\partial^2 W_{00}(\tau,\xi)}{\partial \xi^2} + v_\eta v_1^2 \frac{\partial^3 W_{00}(\tau,\xi)}{\partial \xi^2 \partial \tau}, \tag{20}$$

$$\left.\frac{\partial W_{00}(\tau,\xi)}{\partial \xi}\right|_{\xi=1} = 0, \qquad \left.\frac{\partial W_{00}(\tau,\xi)}{\partial \xi}\right|_{\xi=0} = 0,$$

$$\left.\frac{\partial W_{00}(\tau,\xi)}{\partial \tau}\right|_{\tau=0} = 0, \qquad \frac{\partial W_{00}(0,\xi)}{\partial \xi} = 0.$$

Let's represent the solution to the problem (20) in the view

$$W_{00}(\tau,\xi) = \sum_{n=0}^{\infty} T_n(\tau) X_n(\xi),$$

Using the boundary conditions for solving the problem, the solution is written as

$$W_{00}(\tau,\xi) = \sum_{n=0}^{\infty} T_n(\tau) \cos(\pi n \xi),$$

this implies

$$\frac{d^2 T_n(\tau)}{d\tau^2} + (\pi n)^2 v_\eta v_1^2 \frac{dT_n(\tau)}{d\tau} + (\pi n)^2 v_1^2 T_n(\tau) = 0.$$

Let us search a solution to the equation in the form $T_n(\tau) = \exp(p_n \tau)$. Substituting $T_n(\tau)$ into the original equation, carrying out the differentiation and after cancellation by $\exp(p_n \tau)$, the equation is obtained, that determines the parameter p_n

$$p_n^2 + 2\gamma_n p_n + \omega_n^2 = 0,$$

$$\gamma_n = \frac{v_\eta}{2}(\pi n v_1)^2 = \frac{v_\eta}{2}\omega_n^2, \qquad\qquad \omega_n^2 = (\pi n v_1)^2,$$

$$p_{n\ 1,2} = -\gamma_n \pm \sqrt{\gamma_n^2 - \omega_n^2}.$$

Of particular interest in the analysis of conveyor-type transport systems is the case $0 < \gamma_n < \omega_n$

$$p_{n\ 1,2} = -\gamma_n \pm i\omega_{pn}, \qquad \omega_{pn} = \sqrt{\omega_n^2 - \gamma_n^2}.$$

Let's represent the solution as

$$T_n(\tau) = C_{1n} \exp(p_{n1}\tau) + C_{2n} \exp(p_{n2}\tau),$$

and determine the constants of integration from the initial conditions

$$p_{n1} C_{1n} + p_{n2} C_{2n} = 0, \qquad\qquad C_{1n} + C_{2n} = 0.$$

Thus, if there is a constant acceleration of the conveyor belt under the considered boundary and initial conditions, there are no oscillations in the belt.

b) the acceleration of the conveyor belt is linearly dependent on time $v_f(\tau) = v_{f0} + v_{f1}\tau$.

With a linear dependence of acceleration on time

$$\frac{d\alpha_{12}(\tau)}{d\tau} = v_{f1}\frac{\theta_C}{1+\theta_C}, \qquad \frac{d^2\alpha_{12}(\tau)}{d\tau^2} = 0,$$

equation (19) takes the form

$$\frac{\partial^2 W_{00}(\tau,\xi)}{\partial \tau^2} = v_1^2 \frac{\partial^2 W_{00}(\tau,\xi)}{\partial \xi^2} + v_\eta v_1^2 \frac{\partial^3 W_{00}(\tau,\xi)}{\partial \xi^2 \partial \tau} + v_\eta v_1^2 v_{f1}\frac{\theta_C}{1+\theta_C}, \tag{21}$$

$$\left.\frac{\partial W_{00}(\tau,\xi)}{\partial \xi}\right|_{\xi=1}=0, \qquad\qquad\qquad \left.\frac{\partial W_{00}(\tau,\xi)}{\partial \xi}\right|_{\xi=0}=0,$$

$$\left.\frac{\partial W_{00}(\tau,\xi)}{\partial \tau}\right|_{\tau=0}=-v_{f1}\frac{\theta_C}{1+\theta_C}\left(\frac{\xi^2}{2}-\xi+K_{12}\xi\right), \qquad\qquad \frac{\partial W_{00}(0,\xi)}{\partial \xi}=0.$$

Let us search a solution to the problem in the form of an expansion in a Fourier series in ξ

$$W_{00}(\tau,\xi)=T_0(\tau)+\sum_{n=1}^{\infty}T_n(\tau)\cos(\pi n\xi),$$

considering τ as a parameter. To find $W_{00}(\tau,\xi)$ we define the functions $T_n(\tau)$. Let us write the initial conditions in the form of Fourier series:

$$\left.\frac{\partial W_{00}(\tau,\xi)}{\partial \tau}\right|_{\tau=0}=\frac{a_0}{2}+\sum_{n=1}^{\infty}a_n\cos(\pi n\xi), \qquad a_n=2\int_0^1\left.\frac{\partial W_{00}(\tau,\xi)}{\partial \tau}\right|_{\tau=0}\cos(\pi n\xi)d\xi.$$

Let's define the coefficients a_n

$$a_0=-2v_{f1}\frac{\theta_C}{1+\theta_C}\left(\frac{K_{12}}{2}-\frac{1}{3}\right), \qquad\qquad a_n-2v_{f1}\frac{\theta_C}{1+\theta_C}\left(\frac{1}{(\pi n)^2}+K_{12}\frac{(-1)^n-1}{(\pi n)^2}\right),$$

substitute the expected form of the solution $W_{00}(\tau,\xi)$ in (21)

$$\frac{d^2 T_0(\tau)}{d\tau^2}=v_\eta v_1{}^2 v_{f1}\frac{\theta_C}{1+\theta_C}, \qquad\qquad\qquad\qquad (22)$$

$$T_0(0)=0, \qquad\qquad \frac{dT_0(0)}{d\tau}=-v_{f1}\frac{\theta_C}{1+\theta_C}\left(\frac{K_{12}}{2}-\frac{1}{3}\right),$$

$$\frac{d^2 T_n(\tau)}{d\tau^2}+v_\eta v_1{}^2(\pi n)^2\frac{dT_n(\tau)}{d\tau}+v_1{}^2(\pi n)^2 T_n(\tau)=0, \qquad\qquad (23)$$

$$\frac{dT_n(0)}{d\tau}=-2v_{f1}\frac{\theta_C}{1+\theta_C}\left(\frac{1}{(\pi n)^2}+K_{12}\frac{(-1)^n-1}{(\pi n)^2}\right), \qquad\qquad T_n(0)=0.$$

The solution to equation (22) has the form

$$T_0(\tau)=v_{f1}\frac{\theta_C}{1+\theta_C}\left(v_\eta v_1{}^2\frac{\tau^2}{2}-\left(\frac{K_{12}}{2}-\frac{1}{3}\right)\tau\right). \qquad\qquad (24)$$

Let's search for the solution to equation (23) in the form $T_n(\tau)=\exp(p_n\tau)$. Substituting $T_n(\tau)$ into (23), differentiating and cancelling by $\exp(p_n\tau)$, we obtain the equation that determines the parameter p_n

$$p_n{}^2+2\gamma_n p_n+\omega_n{}^2=0,$$

$$\gamma_n=\frac{v_\eta}{2}(\pi n v_1)^2=\frac{v_\eta}{2}\omega_n{}^2, \qquad\qquad \omega_n{}^2=(\pi n v_1)^2.$$

Consider the form of the solution for the case $0<\gamma_n<\omega_n$

$$p_{n\,1,2}=-\gamma_n\pm i\omega_{pn}, \qquad \omega_{pn}=\sqrt{\omega_n{}^2-\gamma_n{}^2}.$$

The solution to the equation is searching as

$$T_n(\tau) = C_{1n}\exp(p_{n1}\tau) + C_{2n}\exp(p_{n2}\tau),$$

the integration constants are determined from the initial conditions

$$p_{n1}C_{1n} + p_{n2}C_{2n} = -2\nu_{f1}\frac{\theta_C}{1+\theta_C}\left(\frac{1}{(\pi n)^2} + K_{12}\frac{(-1)^n - 1}{(\pi n)^2}\right), \qquad C_{1n} + C_{2n} = 0.$$

wherefrom:

$$C_{1,2n} = \mp i\frac{\nu_{f1}}{\omega_{pn}}\frac{\theta_C}{1+\theta_C}\left(\frac{1}{(\pi n)^2} + K_{12}\frac{(-1)^n - 1}{(\pi n)^2}\right).$$

After simple transformations, the solution can be represented as

$$T_n(\tau) = e^{-\gamma_n\tau}\sin(\omega_{pn}\tau)\frac{\nu_{f1}}{\omega_{pn}}\frac{\theta_C}{(1+\theta_C)}\left(\frac{1}{(\pi n)^2} + K_{12}\frac{(-1)^n - 1}{(\pi n)^2}\right).$$

This allows us to write the solution for the equation (18). The obtained solution makes it possible to determine the voltage value in the conveyor belt along the transport route

$$\frac{\partial W_0(\tau,\xi)}{\partial \xi} = -\sum_{n=1}^{\infty} e^{-\gamma_n\tau}\sin(\omega_{pn}\tau)\frac{\nu_{f1}}{\omega_{pn}}\frac{\theta_C}{(1+\theta_C)}\left(\frac{1}{(\pi n)} + K_{12}\frac{(-1)^n - 1}{(\pi n)}\right)\sin(\pi n\xi) + \alpha_{12}(\tau)\xi + \alpha_1(\tau) - \alpha_{12}(\tau).$$

Over time, the amplitude of fluctuations in the magnitude of dynamic stresses decreases exponentially, so that after a time of the order of several $\tau_n \sim \dfrac{1}{\gamma_n}$, the oscillations completely damp out. The decay time of oscillations is inversely proportional to the square of the circular frequency of oscillations $\tau_n \sim \omega_n^{-2}$.

CONCLUSION

Changing the acceleration mode of the conveyor belt of the transport system is one of the sources of dynamic stresses along the conveyor belt. At the same time, the mechanical properties of composite materials that are used for the manufacture of conveyor belts have a significant effect on the occurrence of elastic vibrations and their propagation. The use of composite materials with mechanical properties corresponding to the Kelvin-Voigt model of an elastic element ensures damping of the resulting elastic vibrations. The paper investigates two modes of acceleration of the conveyor belt: constant acceleration mode and acceleration ramping over time. It has been demonstrated that the mode of movement of a conveyor belt with a linear change in the magnitude of acceleration in time is the cause of the occurrence of dynamic tensions. The damping rate of vibrations is proportional to the viscosity of the elastic element and the square of the vibration frequency in the transport system. The magnitude of the generated dynamic tensions is determined by the amplitudes of the oscillations of the first harmonics. During the characteristic time of change $\tau_1 \sim \gamma_1^{-1}$, the amplitude of oscillations for $n = 2$ will decrease by $e^4 \approx 0.5 \cdot 10^2$ times, for $n = 3$ will decrease by $e^9 \approx 10^4$ times. The system exhibits low-frequency oscillations of the first harmonics with a characteristic dimensionless time $\tau_n \sim \gamma_n^{-1}$ of variation of the oscillation amplitude and, therefore, the oscillation energy. The use of composite materials with a high value of the viscosity coefficient ensures attenuation of the arising dynamic stresses, which increases the reliability and durability of the functioning of transport systems.

ORCID-IDs

Oleh M. Pihnastyi, https://orcid.org/0000-0002-5424-9843; Valery D. Khodusov, https://orcid.org/0000-0003-1129-3462

REFERENCES

[1] O.M. Pihnastyi, and V.D. Khodusov, East European Journal of Physics, **1**, 121-136 (2020), https://doi.org/10.26565/2312-4334-2020-1-11.

[2] O.M. Pihnastyi, and V.D. Khodusov, Bulletin of the South Ural State University. Ser. Mathematical Modelling, Programming & Computer Software (Bulletin SUSUMMCS), **10**, 67-77 (2017), https://doi.org/10.14529/mmp170407.

[3] O.M. Pihnastyi, Scientific bulletin of National Mining University, **4**, 104–111 (2017), http://nbuv.gov.ua/UJRN/Nvngu_2017_4_18.

[4] DIN 22101:2002-08. Continous conveyors. Belt conveyors for loose bulk materials. Basics for calculation and dimensioning. [Normenausschuss Bergbau (FABERG), DIN Deutsches Institut für Normung e.v. Normenausschuss Maschinenbau (NAM)], (2002), pp.51.

[5] Ju. Razumnyj, A. Ruhlov, and A. Kozar, Mining Electromechanics and Automation, **76**, 24–28 (2006). https://docplayer.ru/64655888-Povyshenie-energoeffektivnosti-konveyernogo-transporta-ugolnyh-shaht.html

[6] M. Alspaugh, in: MINExpo-2004, (New York,Las Vegas, NV, USA, 2004), pp. 17-27 (2004), http://fliphtml5.com/pfyf/pccg/basic.

[7] SIMINE for conveyors. Siemens. (2020), https://new.siemens.com/global/en/markets/mining-industry/transport/conveyor-systems.html

[8] R. Pascual, V. Meruane, and G. Barrientos, in: X*XVI Iberian Latin-American Congress on Computational Methods in Engineering* (CILAMCE-2005, Santo, Brazil, 19th–21st October 2005), Paper CIL0620, (2005), pp. 1–15, http://citeseerx.ist.psu.edu/viewdoc/download?doi=10.1.1.494.34&rep=rep1&type=pdf

[9] L.K. Nordell, Z.P. Ciozda, Bulk Solids Handling, **4**(1), 99–104 (1984), http://www.ckit.co.za/secure/conveyor/papers/troughed/transient/transient-belt-stresses.htm

[10] X. Li. J. Pang, and Z. Kou, Shock and Vibration, **1**(1–6), 769309, (2015) http://downloads.hindawi.com/journals/sv/2015/769309.pdf

[11] T. Mathaba, and X. Xia, Energies, **8**(12), 13590–13608 (2015), https://doi.org/10.3390/en81212375

[12] G. Yang, Sensors and Transducers, **181**(10), 210–218 (2014), https://www.sensorsportal.com/HTML/DIGEST/P_2492.htm.

[13] Yan Lu, Fu-Yan Lin and Yu-Chao Wang, Journal of Theoretical and Applied Mechanics, **45**(3), 53–68 (2015), https://content.sciendo.com/view/journals/jtam/45/3/article-p53.xml

[14] Sanjay G. Sakharwade, Shubharata Nagpal, International Journal of Mathematical, Engineering and Management Sciences, **4**(5), 1169–1179 (2019), https://dx.doi.org/10.33889/IJMEMS.2019.4.5-092

[15] P. Kulinowski, Archives of Mining Sciences, **59**(1), 123–138 (2014), DOI 10.2478/amsc-2014-0009 https://journals.pan.pl/dlibra/show-content?id=93449&/simulation-method-of-designing-and-selecting-tensioning-systems-for-mining-belt-conveyors-kulinowski-piotr?language=en

[16] M. Manjgo, E. Piric, T. Vuherer, and M. Burzic, Annals of the Faculty of Engineering Hunedoara, **16**(1), 141–144 (2018). http://annals.fih.upt.ro/pdf-full/2018/ANNALS-2018-1-22.pdf

[17] V.V. Degtjarev, *Нормирование топливно-энергетических ресурсов и регулирование режимов энергопотребления* [*Rationing of fuel and energy resources and regulation of energy consumption modes*], (Nedra, Moscow, 1983), pp. 225, http://www.xn--80affsqimkl5h.xn--p1ai/_ld/7/735__-.pdf. (in Russian)

[18] S. Gramblička, R. Kohár, and M. Stopka, Procedia Engineering, **192**, 259-264 (2017). https://doi.org/10.1016/j.proeng.2017.06.045

[19] A.O. Spivakovsky and V.A. Dyachkov, *Транспортные машины* [*Transporting machines*], (Mechanical Engineering, Moscow, 1983), pp. 487. (in Russian)

[20] B. Karolewski, and D. Marasova, Maintenance and reliability, **16**(2), 229–235. (2014), http://www.ein.org.pl/sites/default/files/2014-02-09.pdf

[21] N.A. Azarenkov, O.M. Pihnastyi, and V.D. Khodusov, Reports of the National Academy of Sciences of Ukraine, **2**, 29-35 (2011), http://dspace.nbuv.gov.ua/handle/123456789/37227.

[22] O.M. Pihnastyi, Problems of Atomic science and technology, **3**, 322–325 (2007), http://dspace.nbuv.gov.ua/handle/123456789/111018.

ГІДРОДИНАМІЧНА KELVIN-VOIGT МОДЕЛЬ ТРАНСПОРТНОЇ СИСТЕМИ

О.М. Пігнастий[a], В.Д. Ходусов[b]
[a]Національний технічний університет «ХПІ», 61002
Україна, м. Харків, вул. Кирпичева, 2
[b]Харківський національний університет імені В.Н. Каразіна
61022, Україна, Харків, м. Свободи, 4

Розглянуто гідродинамічна Kelvin-Voigt модель виробничих систем з потоковим методом організації виробництва. Визначено основні макропараметри стану виробничої лінії і взаємозв'язку між ними. Представлений аналіз основних характеристик моделей пружних елементів, які використані для аналізу виникнення динамічних напружень в рухомій конвеєрній стрічці. Сформульовано крайову задачу для пружних поздовжніх коливань в конвеєрній стрічці з рухомим матеріалом. Передбачається, що деформація елемента стрічки конвеєра відповідає Kelvin-Voigt моделі і ковзання рухомого матеріалу по стрічці відсутній. При визначенні сил опору руху, діючих на одиничний елемент стрічки, використані рекомендації DIN 22101: 2002-08. Проведено аналіз Kelvin-Voigt моделі пружного елемента і продемонстровані відмінні риси моделі. Дано обґрунтування вибору Kelvin-Voigt моделі пружного елемента для опису процесу виникнення пружних поздовжніх коливань в конвеєрній стрічці. Оцінена залежність нерівномірного надходження потоку матеріалу і величини напружень в стрічці. Записано вираз для швидкості розповсюдження збурень вздовж рухається конвеєрної стрічки з матеріалом. Визначено причини прискорення і гальмування конвеєрної стрічки, пов'язані з нерівномірним надходженням матеріалу на вхід транспортної системи. Продемонстровано зв'язок між швидкістю руху конвеєрної стрічки і масою матеріалу уздовж секції конвеєра. Показано, що збільшення потужності електродвигуна при старті і прискоренні конвеєрної стрічки, а також зменшення потужності при гальмуванні і зупинці конвеєрної стрічки є причиною виникнення в ній динамічних напружень. Аналізуються характерні фази початкового руху конвеєрної стрічки з матеріалом. Досліджено процес виникнення динамічних напружень з постійним і змінним прискоренням конвеєрної стрічки для фази розгону і гальмування конвеєрної стрічки. Для

аналізу використана модель конвеєрної лінії в безрозмірному вигляді. Отримано вираз для статичних і динамічних напружень в конвеєрній стрічці. Оцінена амплітуда коливань динамічних напружень і характерний час загасання коливань в конвеєрній стрічці. Продемонстровано квадратична залежність швидкості загасання хвилі динамічних напружень зі збільшенням частоти коливання. Показана обернено пропорційна залежність характерного часу загасання виникли динамічних напружень від величини коефіцієнта в'язкості композиційного матеріалу конвеєрної стрічки.

КЛЮЧОВІ СЛОВА: гідродинамічна модель транспортної системи, двох моментне опис виробництва, Kelvin-Voigt модель, балансові рівняння, PDE-модель виробництва

ГИДРОДИНАМИЧЕСКАЯ KELVIN-VOIGT МОДЕЛЬ ТРАНСПОРТНОЙ СИСТЕМЫ

О.М. Пигнастый[a], В.Д. Ходусов[b]

[a]*Национальный технический университет «ХПИ»*
61002, Украина, г. Харьков, ул. Кирпичева, 2
[b]*Харьковский национальный университет имени В.Н. Каразина*
61022, Украина, Харьков, пл. Свободы, 4

Рассмотрена гидродинамическая Kelvin-Voigt модель производственных систем с потоковым методом организации производства. Определены основные макропараметры состояния производственной линии и взаимосвязи между ними. Представлен анализ основных характеристик моделей упругих элементов, которые использованы для анализа возникновения динамических напряжений в движущейся конвейерной ленте. Сформулирована краевая задача для упругих продольных колебаний в конвейерной ленте с движущимся материалом. Предполагается, что деформация элемента ленты конвейера соответствует Kelvin-Voigt модели и скольжение движущегося материала по ленте отсутствует. При определении сил сопротивления движению, действующих на единичный элемент ленты, использованы рекомендации DIN 22101: 2002-08. Проведен анализ Kelvin-Voigt модели упругого элемента и продемонстрированы отличительные особенности модели. Дано обоснование выбора Kelvin-Voigt модели упругого элемента для описания процесса возникновения упругих продольных колебаний в конвейерной ленте. Оценена зависимость неравномерного поступления потока материала и величины напряжений в ленте. Записано выражение для скорости распространения возмущений вдоль движущейся конвейерной ленты с материалом. Определены причины ускорения и торможения конвейерной ленты, связанные с неравномерным поступлением материала на вход транспортной системы. Продемонстрирована связь между скоростью движения конвейерной ленты и массой материала вдоль секции конвейера. Показано, что увеличение мощности электродвигателя при старте и ускорении конвейерной ленты, а также уменьшение мощности при торможении и остановке конвейерной ленты является причиной возникновения в ней динамических напряжений. Анализируются характерные фазы начального движения конвейерной ленты с материалом. Исследован процесс возникновения динамических напряжений с постоянным и переменным ускорением конвейерной ленты для фазы разгона и торможения конвейерной ленты. Для анализа использована модель конвейерной линии в безразмерном виде. Получено выражение для статических и динамических напряжений в конвейерной ленте. Оценена амплитуда колебаний динамических напряжений и характерное время затухания колебаний в конвейерной ленте. Продемонстрирована квадратичная зависимость скорости затухания волны динамических напряжений с увеличением частоты колебания. Показана обратно пропорциональная зависимость характерного времени затухания возникших динамических напряжений от величины коэффициента вязкости композиционного материала конвейерной ленты.

КЛЮЧЕВЫЕ СЛОВА: гидродинамическая модель транспортной системы, двух моментное описание производства, Kelvin-Voigt модель, балансовые уравнения, PDE-модель производства

VISCOSITY AND VORTEX FORMATION IN A LIQUID PLACED IN A ROTATING CYLINDRICAL VESSEL

Oksana L. Andrieieva[a,b,*], Leonid A. Bulavin[c], Igor N. Kudriavtsev[b],
Roman S. Sokolenko[a], Victor I. Tkachenko[a,b]

[a]National Science Center "Kharkiv Institute of Physics and Technology", Kharkiv
[b]V. N. Karazin Kharkiv National University, Kharkiv
[c]Taras Shevchenko National University of Kyiv, Kyiv
Corresponding Author: andreevaoksana@kipt.kharkov.ua, Phone +380-097-292-06-15
Received July 23, 2020; revised October 28, 2020; accepted November 5, 2020

The free fall of steel balls of different diameters in viscous liquids placed in a cylindrical vessel at rest or rotating at a constant rate as well as the vortex generation in a liquid rotating in a cylindrical vessel were experimentally studied. To solve the problem a test stand including a cylindrical glass vessel mounted on the axis of a governed-speed electric engine shaft, monitoring and measuring devices as part of a digital laser tachometer, a digital USB microscope and a laptop was developed to visualize the processes under study. Experimental dependences of the instantaneous velocity of the balls on the distance traveled by them were obtained. It has been demonstrated, that there is a transition mode of the ball velocity variation when it enters the liquid. The transition mode was characterized by a damped, periodic variation of instantaneous velocity depending on a distance. It has been found that at a certain distance traveled by the ball, the transition mode becomes stationary when the ball moves at a constant velocity. The dependence of the liquid viscosity on the vessel rotation frequency was studied in the stationary mode using the Stokes method. It has been demonstrated that the common behavior of such processes is decreasing the time of balls falling and, consequently, the coefficient of a liquid dynamic viscosity with increasing the rotation frequency of the vessel. A periodic variation in the coefficient of the dynamic viscosity depending on the frequency of the vessel rotation was found experimentally. It has been found experimentally that several threadlike spiral flows of a colored liquid are formed parallel to the axis of the cylinder, when the cylindrical vessel rotates. At that, the velocity of the downward drift of the colored liquid increases with increasing its rotation rate and it increases from the periphery to the center of the vessel.
KEYWORDS: liquid, cylindrical vessel, steady speed, viscosity, Stokes method, rotation, dynamic viscosity, vortex

One of the methods to determine the coefficient of a liquid dynamic viscosity is the Stokes method (SM). This method is based on application of the formula for the resistance force of a straight-line and uniform motion-of a ball in a viscous liquid, first obtained by Stokes [1]. Its essence consists in setting up an equation of balance of forces acting in a viscous liquid on a ball (gravity, Archimedes 'force and Stokes' force), from which the velocity of the ball stationary motion follows. In such reasoning, the effect of liquid vessel walls is not taken into account, since the diameter of the vessel exceeds significantly the diameter of the ball in the experiments. For SM applicability it is necessary to measure the viscosity in the area of uniform motion of the ball.

If the diameter of the ball is comparable to the diameter of the vessel, then the Stokes formula is not applicable and in order to determine the conditions for their stationary motion occurrence additional studies of the motion of balls in viscous liquid should be carried out. When a ball falls into a viscous liquid, two stages can be distinguished: the stage of the ball falling on the surface of the liquid and the stage of its uniform motion.

A large number of works are devoted to the study of the first stage (the ball fall on the liquid surface), among which one can name [2-5].

Fundamental experimental and theoretical calculations on the effect of solids on the water surface, which are of interest in ballistics for passing projectiles from air to water and in aeronautics - for landing seaplanes were carried out in [2]. The critical velocity of the impact of spheres on the water surface for formation of splashes, as well as the cone angle formed behind the impact object were experimentally investigated in [3].

Based on the theory of H. Wagner [6] in [4] the problem of fast immersion in water of a body of revolution with a vertical axis of symmetry is considered and the solution of the basic integral equation is obtained. As an example, a ball entry into water was studied, the resistance force of water acting on the ball was calculated and a comparison with the experimental data was made. The proposed description is applicable for small immersion depths not exceeding 0.035 ball diameter.

The effect of a solid object on a liquid surface is analyzed in [5]. Here, a numerical algorithm is proposed for modeling the entry of the solid object into the liquid medium taking into account the dynamics of the free surface of the liquid / gas interface. In this model taking into account, high viscosity of solid objects increases the accuracy of the results of the previous studies. The conclusions of the model are confirmed by comparing the experimental data of other researchers for the free fall of a circular disk and a sphere. The model is applicable for shallow immersion depths of objects in liquid.

The processes considered in [2-5] are transient and are not characterized by determination of a stationary motion velocity. Therefore, they cannot be used to determine the media viscosity by SM. As noted above, determination of stationary velocities of spheres motion in viscous liquid vessels is of interest for viscometry purposes based on SM.

The work [7] is devoted to this issue. It presents experimental data on the drug of cylindrical vessel walls to a sphere falling axially under the action of gravity in a viscous fluid. The data were obtained for 60 spheres of different diameters and densities, which moved in four cylinders of different diameters, and were filled with fifteen Newtonian fluids of different viscosities and densities. From the analysis of the results of more than 3000 measurements of spheres velocities it has been concluded that the wall effect is determined by two variables: the ratio of the sphere diameter to the diameter of the cylindrical vessel (d / D) and the Reynolds number R ($0.05 < R < 2 \times 10^4$) for the sphere. To describe the wall effect the authors of [7] determined the correction factors graphically in the form of the dependence of the ratio of the stationary velocity in the cylinder to the stationary velocity in an infinite mass of fluid (V / V_∞) on the Reynolds number at V_∞ for various ratios of diameters. It follows from the graph that the wall effect is maximal at low Reynolds numbers and large diameter ratios. For small diameter ratios (less than 0.1) the effect degree becomes insignificant at Reynolds numbers above 100.

In the later work on this issue [8] it is emphasized that experimental data on the motion of spheres were obtained in the twentieth century and are available in tabular form (see Historical Data [8]). Most of these data were obtained in experiments with small diameter cylindrical vessels, where the effect of a wall occurrence affects the results. The previously obtained analytical expressions for describing the dependence of the drag on the velocity of falling spheres were compared with this data set. Because of this comparison, two new descriptions of the stationary velocity of a sphere were proposed. One description is applicable for Reynolds numbers less than 2×10^5. The other is intended to predict the velocity of sphere falling with superior accuracy for Reynolds numbers less than 4000. This range of Reynolds numbers contains almost all applications of interest in environmental engineering.

When discussing issues related to determination of a stationary velocity of spheres motion, both in narrow and wide in diameter cylindrical vessels filled with a viscous liquid, one should be guided by the data of works [7, 8].

The case, when a vessel with a viscous liquid rotates at a constant speed and a sphere moves in it, has not been analyzed in the scientific literature as to the analysis of stationary velocity determination. The issue of such studies is of scientific and practical interest for environmental engineering, medicine, shipbuilding, and aircraft engineering.

Therefore, this article presents the results of an experimental study of the viscosity of a liquid placed in a rotating cylindrical vessel. In addition to the problem of determining the viscosity of a fluid rotating in a cylindrical vessel, the problem of vortex formation in it is also of interest.

The physics of rotating liquids has been studied beginning with the Rayleigh work [9]. Rayleigh's interest in this topic was caused by the need to describe the meteorological situation, which is very dependent on the dynamics of rotating volumes of liquid (cyclones and anticyclones). So, a need to have an accurate weather forecast for a fairly long term, based on the analysis of the dynamics of liquid rotating volumes, arose. In this work Rayleigh described the main features of liquid rotating volumes typical of cyclones and anticyclones. He formulated the law of conservation of the azimuthal moment of a rotating liquid. Besides, he deduced the stability criterion for an ideal liquid located between two rotating concentrically arranged cylinders.

The following rigorous studies of the stability of a rotating liquid heated from below are given in [10]. In particular, a number of experimental results on the study of the vortex formation in rotating and bottom-heated water and air [11] are presented here.

In the experiments the water was located in Pyrex glass cylinders with an outer diameter of 12 inches. Pyrex temperature-controlled electrically conductive heating plates were glued to the cylinder bottoms. Cylinders containing the water and the necessary accessories were placed on a support steel ring mounted on a vertical shaft. The steel ring was intended for alignment and other adjustments. The cylinder was driven using the shaft rotated by means of feed belts and an engine. Water layers of a depth of 2–17 cm and a rotation speed of up to 50 rpm were used in the experiments.

The temperature difference at two levels (one - near the upper and the other - near the lower surface of the liquid) was measured by copper - constantan wire thermocouples. The accuracy of the temperature measurement was ± 0.01°C and was sufficient to process the obtained results.

The experimental studies were of two types: visual and photographic performed using a rotoscope.

The experiments showed, that the liquid vortex motion in a rotating cylinder was observed when the rate of its bottom heating exceeded a certain value. The vortexes were visually observed in water, when a small amount of aluminum powder was dispersed above its surface. The motion of aluminum powder particles on the water surface was photographed using the time-lapse strip method and corresponded to a set of vortexes of approximately equal diameter (Fig. 1).

It follows from Fig. 1 that the traces of vortexes on the water surface are located generally near a concentric circle of a radius of about 2/3 of the cylinder radius.

The internal motion in the form of ascending vortexes is presented in Fig. 2. Such vortexes are detected when using a black ink placed initially in a thin layer at the vessel bottom. Apparently, the vorticity (see the definition below) of liquid individual volumes contributes towards accelerating the diffusion of ink and, as a consequence, its diffusion rises to the upper boundary of the liquid.

Based on the comparison of theoretical studies and experimental results it was concluded that they have quantitative and qualitative conformances. Hence, the authors concluded that the formation of vortexes in a cylinder

containing the water rotated and heated from below, when the boundaries are free above and solid below (as a whole - mixed boundary conditions), has a convective nature. They have determined that in a state of instability (vortex formation) the critical Rayleigh number is proportional to the Taylor number.
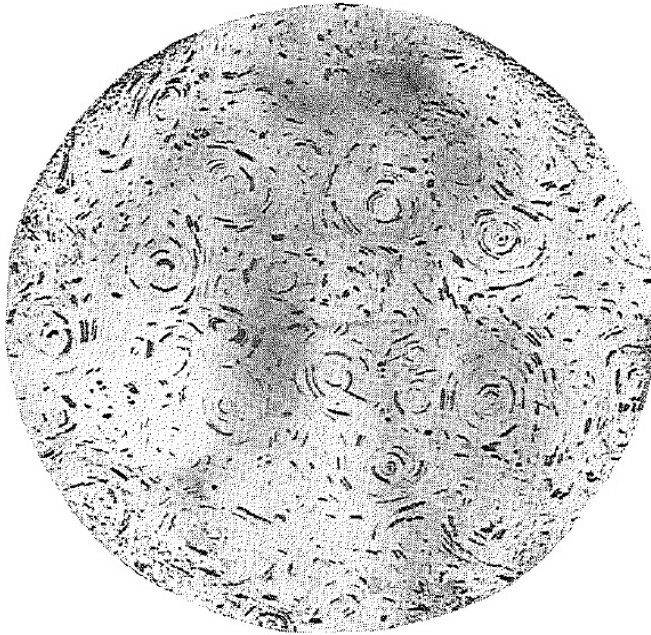

Figure 1. Convection cells which appear in water when in rotation and heated from below. The data to which the illustration refers are: depth 18 cm; difference in temperature 0.7°; rate of rotation 5.0 rev/min; Taylor number - 1.2×10^9 [10].

Figure 2. Side view of ink rising from the bottom of a cylinder of water in the ascending cores of cells. The data to which the illustration refers are: depth 18 cm; difference in temperature 0.5°; rate of rotation 10.9 rev/min; Taylor number - 5.5×10^9 [10].

The monograph of the famous English hydrodynamics H. Greenspan is devoted to issues of the theory of stability of a rotating liquid [12]. Such studies are used in the study of atmospheric and ocean currents on a rotating planet for weather forecasting. The author confirms the theoretical results by simple laboratory experiments using a flask rotated by a gramophone disc. The book presents the latest achievements at the time of its publication in the theory of non-stationary and non-linear motions, various oscillating (wave) processes and hydrodynamic stability.

Despite the wide topic area, the cases of vortex formation in a rotating cylinder filled with a liquid are not analyzed in [12], as described in [10].

However, it should be noted that the observed vortexes in [10, 11] do not have the structure of Benard convective cells [13], since the descending flows of ink-colored water are not found in the experiments. Besides, for the problem with mixed boundary conditions the local aspect number A_l (the ratio of the cell diameter to the depth of the water layer) is in the wide range $1.25 < A_l < 10.59$, which does not correspond to the value $A_l = 2.86$ obtained in [6 14].

These discrepancies indicate the possibility of another scenario for the formation of vortexes in a liquid located in a rotating cylinder.

It may be as follows.

A large number of ascending convective flows (termics) are generated in a rotating cylinder filled with water due to heating of the vessel bottom. The conditions for the formation of termics and their characteristic parameters are described in sufficient detail in [15]. The vortex generation place is determined by the spatial coincidence of one of the termics and the perturbation of the vertical interface of the azimuthal velocity along the cylinder radius. Such perturbations, due to the development of Kelvin – Helmholtz instability, form vortexes, which at the nonlinear stage form "cat eyes" represented in the album of liquid and gas flows [16].

Further, such vortexes leave their generation place like cyclonic and anticyclonic vortexes (rings) leave the Gulf Stream arrow as a result of meandering [17], and new ones appear at their place. At that, the rings located on opposite sides of the vertical interface of the azimuthal velocity have a different sign of vorticity $\vec{\omega}_\pm$ [18]:

$$\vec{\omega}_\pm = rot\left(\vec{V}_\pm\right) \tag{1}$$

where, $\vec{V}_\pm(\vec{r}) = \pm\frac{1}{2}\vec{\Omega}\times\vec{r}$ - mutually opposite rates of a simple liquid flow, $\vec{\Omega}$ - constant vector that determines the frequency of rotation of a fluid volume $\vec{\Omega}$, $\vec{r}$ - radius vector orthogonal to the axis of rotation.

The experimental data (images of the upper boundaries and the axial section) on the formation of vortexes in liquid media located in rotating vessels are presented in [10, 11]. It can be seen a large number of vortexes of almost the same size at the images. However, the temporal dynamics of the number of the appeared vortexes, their structure and rotation direction are not analyzed in these experimental data. Such an analysis would allow us to determine the physical nature of vortex generation, their internal structure and to describe the dynamics of their distribution in a liquid volume.

So, the objective of this work is experimental research of: free-falling velocity of steel balls in a cylindrical vessel containing a viscous liquid; viscosity of a liquid rotated at a constant rate in a cylindrical vessel; formation of vortexes in a liquid rotated in a cylindrical vessel at a constant rate.

EXPERIMENTAL FACILITIES

For research the test stand was developed and assembled (see Fig. 1, 2) [19]. This test stand includes: a cylindrical glass vessel (1) of a diameter of 28 mm mounted on the axis of the electric motor shaft the revolutions of which are continuously controlled using the appropriate driver. The stand has also monitoring and measuring devices: a digital laser tachometer HS2234 with an accuracy of rotation frequency measuring equal to 0.1 rpm (2); USB digital microscope (3) connected to a laptop to visualize the motion of balls and liquid that were recorded on video.

An electronic precision jewelry balance with an accuracy of 0.01 g and a power supply unit of a voltage of 12 V were used to ensure the stand operation.
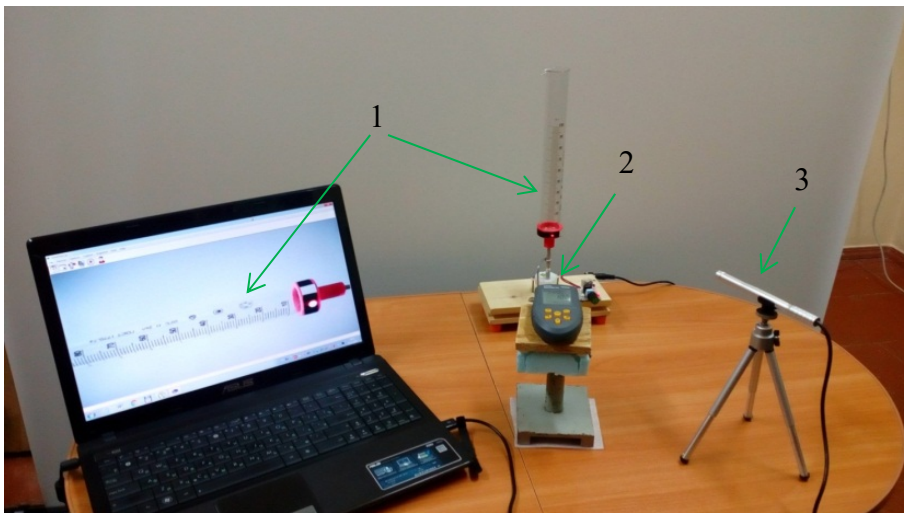

Figure 3. Measuring stand with the visualization system
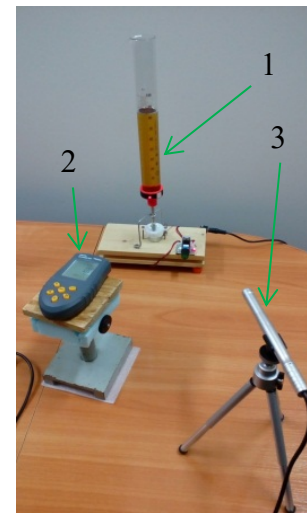
Figure 4. Fragment of the measuring bench

Engine oil of grade 10W40 and an aqueous solution of glycerol with glycerol concentration of 85% were used as a viscous liquid. Steel balls about 3 and 6 mm in diameter were used for viscosity measurement.

An experimental study of a free fall of steel balls in a cylindrical vessel containing a viscous liquid

Study of the free fall of steel balls in a cylindrical vessel filled with a viscous liquid is of interest in connection with a use of the SM for liquid viscosity measuring in this work. Inevitable errors associated both with the use of coaxial cylindrical vessels and freely falling balls in them arise at such viscosity measurements [20].

Study of the velocity dynamics of a steel ball during the transition from air to liquid is of independent interest.

In the experiments a steel ball with a diameter of 6 mm, mass of 0.94 g and a steel ball with a diameter of 3 mm and a mass of 0.126 g were dropped into the liquid. 10W40 grade engine oil with a volume of 90 ml and the aqueous solution of glycerol with glycerol concentration of 85 % were used as a liquid. The height of the liquid column in the cylinder was 150 mm. A special centering device in the form of a funnel was used to drop the ball; the funnel ended with a tube of a diameter slightly larger than the diameter of the ball and the axis of the tube and cylinder coincided. This device ensured the steel ball entering the oil along the axis of the cylinder at a specified drop height and eliminated the ball deviation from the cylinder axis in the oil. Such a ball motion in a viscous liquid corresponds to small Reynolds numbers ($\mathrm{Re} \ll 1000$) [21] realized in experiments.

The time of the ball fall was determined within a height range set by marks on the cylindrical flask (1).

The velocity of the balls when entering the liquid was 1.2 m/s. The balls were dropped from a height of 73 mm. The error in determining the velocity of the ball was 14 - 15%.

Graphs of ball velocity variation over the entire height of the liquid in the vessel are presented in Fig. 5. The zero mark corresponds in the height of the column to the free boundary of the liquid. Curves obtained by cubic spline interpolation in MathCAD.

Figure 5. Dependence of the instantaneous velocities of steel balls on the height of a viscous liquid
column h in a cylindrical vessel: □, ○ - oil; Δ - glycerol

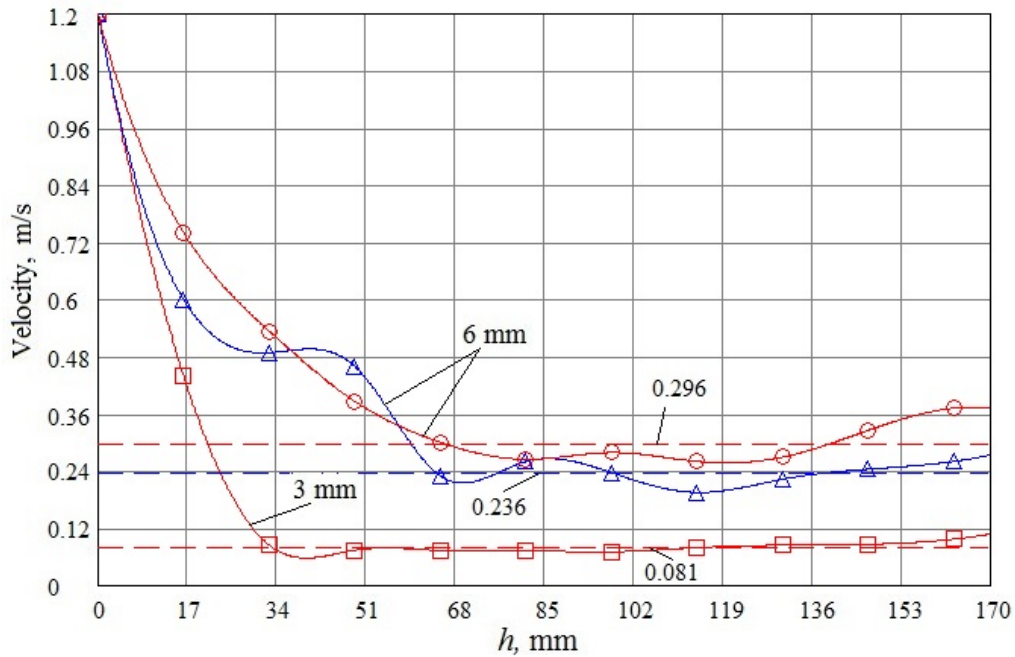Figure 5 shows the occurrence of a transition mode of the ball motion velocity characterized by its damped oscillations. It follows from the figure that the confidence interval for measuring viscosity by the SM, where the ball moves uniformly, starts from a depth of 7.5 cm. The average values of the velocity in this part of the trajectory are shown with a dotted line.

It should be noted that when considering the coincidence of the speed of motion of balls with diameters of 3 mm and 6 mm in oil at a finite interval of motion, it is necessary to take into account the measurement errors. In addition, the small, and not 4-times, according to the MS, the difference between these speeds is due to the screening of the cylinder wall [7].

It should be noted that the velocities of motion of balls with diameters of 3 mm and 6 mm in oil in the final interval of motion differ by approximately 3.75 times. A small deviation from the ratio of these velocities 4 - fold, which corresponds to the MS, due to measurement error, and shielding walls of the cylinder [7].

Based on the obtained result all subsequent measurements were carried out within the interval of uniform motion of steel balls.

The viscosity of a liquid located in a rotating cylindrical vessel

The experiments to study the viscosity of a liquid in a rotating cylindrical vessel were carried out using the SM [20]. The movement parameters of steel balls were analyzed at an interval of their uniform motion; they were determined experimentally in a series of preliminary experiments to study their free fall in a cylindrical vessel containing a viscous liquid. In the experiments, as noted above, the trajectory of the balls did not deviate from the axis of the cylinder. Besides, the vessel rotation did not lead to the ball rotation.

The viscosity coefficient of a rotating cylinder containing a liquid was determined by comparing the time of falling of a ball in a motionless liquid t_0 with the time of its falling t_Ω in a rotating in cylinder liquid. The relationship of these times obeys the ratio:

$$t_\Omega = t_0 \frac{\mu_\Omega}{\mu_0} \qquad (2)$$

were, μ_Ω and μ_0 - dynamic viscosity of a liquid with and without rotation, respectively.

Thus, knowing the ratio of the ball falling time in a rotating liquid to its falling time in a motionless liquid, the dynamic viscosity of a rotating liquid can be determined.

The experiments to determine the viscosity coefficient of a rotating liquid included a series of four measurements of the time of the ball falling in the liquid.

In the first series of experiments a steel ball with a diameter of 6 mm and a mass of 0.94 fell into the liquid. 10W40 grade engine oil of a volume of 90 ml and of the oil column height in the cylinder of 150 mm was used as a liquid. The ball was dropped by hand at a certain height above the oil level. The time of its falling was recorded within a height range set by marks on the cylindrical flask (1).

In the second series of experiments a steel ball with a diameter of 3 mm and a mass of 0.126 g was used. The other parameters of this series of experiments were the same as in the first series of experiments.

In the third series of experiments a special centering device was used, the purpose of which was described above. The other parameters of the third series of experiments were the same as in the second series.

In the fourth series of experiments the engine oil of 10W40 grade was replaced with a glycerol-water solution of 85% glycerol concentration. The other parameters of this series of experiments were the same as in the third series.

In the experiments a glass cylindrical flask with a diameter of 28 mm rotated with an angular rate, the value of which was set using the driver and varied within the range from 0 to 40 rpm. The steel ball was dropped from a certain height above the oil level. The time of its falling was within an interval of 150 mm in height, which was set by marks on a cylindrical flask (1). Then the obtained video sequences were processed using a computer. The time of ball motion in the liquid was determined by frame-by-frame analysis of the recorded video sequence at duration of one frame $\Delta t = 0.04$ s.

The results of measuring the dependence of the falling time of steel balls of different diameters on the rotation rate of a cylindrical vessel containing a viscous liquid are summarized in Table.

Table.

The dependence of the relative fall time t_Ω/t_0 of steel balls of different

diameters on the rotation rate of a cylindrical vessel containing a viscous liquid

Rotation frequency Ω, (rpm)	Steel ball diameter D, (cm).			
	Engine oil 10W40			Glycerol + water (85% of glycerol)
	1 series	2 series	3 series	4 series
	$D = 0.6^{\text{without c.d.)}}$	$D = 0.3^{\text{ without c.d.)}}$	$D = 0.3^{\text{with c.d.)}}$	$D = 0.3^{\text{ with c.d.)}}$
0	1	1	1	1
5	–	–	1.329	0.862
10	0.94	0.987	1.191	0.936
12.5	–	–	0.959	–
15	0.978	0.941	0.844	0.894
17.5	–	–	0.967	–
20	0.778	0.955	0.946	0.83
22.5	–	–	1.161	–
25	0.933	0.926	1.028	0.787
27.5	–	–	0.929	–
30	0.784	0.892	0.958	0.915
32.5	–	–	0.696	–
35	–	0.918	0.92	–
37.5	–	–	0.997	–
40	0.814	0.929	0.929	–

without c.d.) – without centering device
with c.d.) – with centering device

Discussion of the results of a study of the viscosity of a liquid located in a rotating cylindrical vessel

The results of measurements of the average time of balls falling into a viscous liquid depending on the rotation frequency of a cylindrical vessel are presented in Fig. 6.

As can be seen from Fig. 6, in the first series of experiments (marker □) the relative time of falling balls decreases on average with increasing the rotation frequency of a viscous liquid in a vessel. In this context the periodic minima are observed at multiple frequencies of 10, 20, and 30 rpm.

In the second series of experiments (marker Δ) poor oscillations of the time of balls motion are also observed at a general decrease of their falling time with increasing the vessel rotation frequency. The minima of the ball falling time at multiple frequencies of 15 and 30 rpm repeat the dynamics of previous experiments, but at high rotation frequencies.

In the 3rd and 4th series of experiments the resonance nature of the dependence of the balls falling time on the vessel rotation frequency is also observed.

In the 3rd series (marker ○) the minima of the ball falling time are near the values of 15 and 32 rpm.

In series 4 (marker ◊) such a resonant behavior of the ball falling time depending on the rotation frequency is poorly resolved, but can be detected.
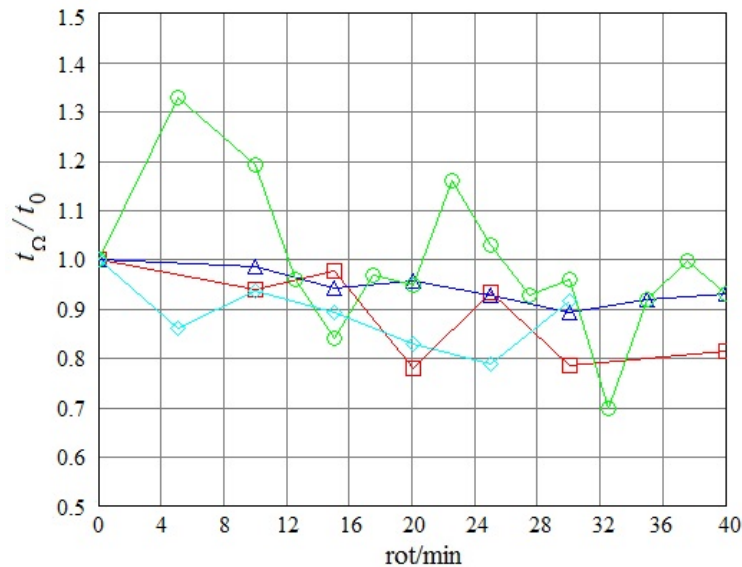
Figure 6. Dependence of the average relative time t_Ω / t_0 of balls falling upon the rotation

frequency of a cylindrical vessel containing a viscous liquid: □ – 1 series; Δ – 2 series;
○ - 3 series; ◊ – 4 series.

The general behavior in all series of experiments is decreasing the time of balls fall with increasing the vessel rotation frequency and the existence of a resonant dependence of the dynamic viscosity coefficient on the vessel rotation rate.

One of the possible explanations for the observed oscillations of the balls moving time is the occurrence of natural frequencies of oscillations in the liquid [12] or the occurrence of spatially periodic structures in the ball-oil-flask system [22].

An experimental study of vortex formation in a liquid, located in a rotating cylindrical vessel

In the experiments 10W40 grade oil painted with a small amount of bronze powder was fed from the top through a centering device until a thin surface layer of a colored liquid with a thickness of 3-4 mm was formed. A cylindrical vessel with a viscous liquid of a diameter of 28 mm and a height of 150 mm rotated with different angular rates from 5 to 40 rpm.

The following was found in the experiments.

In contrast to raising the black ink vortexes from the bottom of the vessel described in [10], in the experiments of the authors we studied the lowering of colored 10W40 engine oil from a thin surface layer.

The lowering began after 15 to 20 minutes of the vessel rotation. The colored liquid drifted in the vertical direction to the bottom of the vessel in the form of several separate vortexes of different lengths at low velocities compared with the liquid rotation rate. The generated vortexes had the form of threadlike curved spirals of colored oil parallel to the axis of the cylinder.

The type of vortices at the initial stage of their formation is shown in Fig. 7.
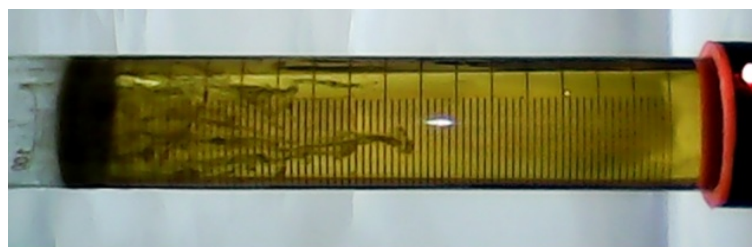
Figure 7. Generation of vortices of colored oil in a rotating cylindrical vessel.
The photo is reduced to horizontal view.

Analysis of the recorded video sequence using a digital microscope made it possible to determine the average velocities of the vertical drift of the powder particles. When the viscous liquid rotated at a rate of 15 rpm, the vertical drift velocity of the particles was 0.47 mm / s, 30 rpm - 0.50 mm / s, 40 rpm - 0.63 mm / s.

Analyzing the experimental results obtained in the work the following facts were found:
- several threadlike spiral flows of colored liquid parallel to the cylinder axis are formed during rotation;
- with increasing the liquid rotation rate, the downward drift velocity of the colored liquid also increases;

- the downward drift velocities of the colored threadlike flows in the rotating liquid increased from the periphery towards the center of the vessel.

Thus, the spatial structuration of flows corresponding to vortex formation in a viscous liquid was demonstrated experimentally in this section.

CONCLUSIONS

The results of the experimental study of free fall of steel balls in a viscous liquid, as well as the viscosity and the vortex formation in a liquid located in a rotating cylindrical vessel were presented in the paper.

The occurrence of a transitional mode of a ball velocity characterized by damped oscillations of the ball velocity after passing it through the upper boundary of the liquid was demonstrated. The confidence interval in the liquid column height was determined, where the SM for measuring the liquid viscosity can be used.

It has been experimentally shown that a general regularity of the process is a decrease in the time of balls falling with increasing the vessel rotation frequency.

The occurrence of the resonant dependence of the ball falling time and therefore the coefficient of the dynamic viscosity on the vessel rotation rate was also demonstrated. This dependence is expressed by periodic in rotation frequency variation of the dynamic viscosity coefficient against its general decreasing background.

Analyzing the experimental results obtained in the paper it has been found that several threadlike spiral flows of the colored liquid parallel to the axis of the cylinder are formed at the cylindrical vessel rotation. The velocity of the downward drift of the colored liquid increases with increasing its rotation rate and it increases from the periphery to the center of the vessel.

ORCID IDs

Oksana L. Andrieieva, https://orcid.org/0000-0001-9757-8519; **Leonid A. Bulavin**, https://orcid.org/0000-0002-8063-6441;
Igor N. Kudriavtsev, https://orcid.org/0000-0001-6677-9289; **R.S. Sokolenko**, https://orcid.org/0000-0001-6895-2006;
Victor I. Tkachenko, https://orcid.org/0000-0002-1108-5842

REFERENCES

[1] L.D. Landau, and E.M. Lifshits, *Теоретическая физика. Гидродинамика, Т.6,* [*Theoretical physics. Hydrodynamics, Vol.6,*] (Nauka, Moscow, 1986), pp. 736. (in Russian)
[2] E.G. Richardson, Proc. Phys. Soc. **61**(4), 352-367 (1948), https://doi.org/10.1088/0959-5309/61/4/308.
[3] M. Stephen, and Jr. Laverty, M.Sc. thesis, Massachusetts Institute of Technology, 2004, http://web.mit.edu/mhl/www/Impact%20Lab%20Page/Whole%20Thesis.pdf
[4] A.B. Lotov, Uchenyie zapiski TsAGI, **2**(4), 22-30 (1971). (in Russian).
[5] I. Mirzaii, and M. Passandideh-Fard, in: *19th Annual Conference on Mechanical Engineering-ISME-2011*, (The University of Birjand, Iran, 2011), pp. 1-4. https://www.researchgate.net/publication/307510320_The_Impact_of_a_Solid_Object_on_to_a_Liquid_Surface
[6] H. Wagner, Math. Mech. **12**, 193-215 (1932), http://dx.doi.org/10.1002/zamm.19320120402.
[7] V. Fidleris, and R.L. Whitmore, Br. J. Appl. Phys. **12**, 490-494 (1961), https://doi.org/10.1088/0508-3443/12/9/311.
[8] P.P. Brown, and D.F. Lawler, Journal of Environmental Engineering, **129**(3), 222-231 (2003), https://doi.org/10.1061/(ASCE)0733-9372(2003)129:3(222).
[9] Rayleigh Lord, Proc. Roy. Soc. London, Series A, **93**(648), pp. 148-154. Scientific papers, **6**, 447-453, (Cambridge University Press, 1917), pp. 254, https://www.jstor.org/stable/93794.
[10] S. Chandrasekhar, *Hydrodynamic and hydromagnetic stability,* (Oxford University Press, 1970), pp. 657. https://www.cambridge.org/core/journals/journal-of-fluid-mechanics/article/universal-stability-of-hydromagnetic-flows/826D62658D200A2DCE37F6006EE4390A
[11] Y. Nakagawa, and P. Frenzen, Tellus. **7**(1), 1-21 (1955), https://doi.org/10.3402/tellusa.v7i1.8773.
[12] H.P. Grinspen, *Теория вращающихся жидкостей* [*Rotating fluid theory*], (Gidrometeoizdat, Leningrad, 1975), pp. 321, https://www.twirpx.com/file/243427/. (in Russian)
[13] H. Bernard, Revue generale des Sciences, Pures et Appliques, **11**, 1261-1271 and 1309-1328 (1900).
[14] O.L. Patochkina, B.V. Borts, and V.I. Tkachenko, East Eur. J. Phys. **2**(1), 23-31 (2015). https://periodicals.karazin.ua/eejp/article/view/2810
[15] R. Skorer, *Аэрогидродинамика окружающей среды* [*Aero-hydrodynamics of the environment*], (Mir, Moscow, 1980), pp. 550. (in Russian)
[16] M. Van-Dajk, *Альбом течений жидкости и газа* [*Album of liquid and gas flows*], (Mir, Moscow, 1986), pp. 184. (in Russian)
[17] A.S. Monin, and G.M. Zhiharev, UFN, **160**(5), 1-47 (1990), https://doi.org/10.3367/UFNr.0160.199005a.0001. (in Russian)
[18] A.V. Tur, and V.V. Janovskij, *Гидродинамические вихревые структуры* [*Hydrodynamic vortex structures*], (Har'kov, NTK "Institut Monokristallov", 2012), pp. 294. (in Russian)
[19] O.L Andreeva, L.A. Bulavin, I.M. Kudrjavcev, R.S. Sokolenko, and V.I. Tkachenko, in: *International scientific and technical conference "Physical And Technical Problems Of Energy And Their Solutions 2019"*, (KhNU, Kharkiv, 2019), pp. 18-19, http://physics-energy.karazin.ua/resources/17c5203634424b2292944e8da8f6c686.pdf. (in Russian)
[20] F. Sherman, editor, *Эмульсии* [*Emulsions*], (Himija, Leningrad, 1972), pp. 448, https://www.studmed.ru/sherman-f-red-emulsii_1553621cafe.html. (in Russian)
[21] M.V. Krautsou, A.M. Krautsou, Izvestiâ vysših učebnyh zavedenij i ènergetičeskih ob″edinennij SNG. Ènergetika, **2**, 80–87 (2011), https://energy.bntu.by/jour/article/download/301/296 (in Russian)
[22] E.L. Koschmieder, *Benard Cell and Taylor Vortices*, (Cambridge University Press, 1993), pp. 337.

В'ЯЗКІСТЬ І ВИХРОУТВОРЕННЯ В РІДИНІ, ЩО ОБЕРТАЄТЬСЯ В ЦИЛІНДРИЧНІЙ ЄМНОСТІ

О.Л. Андрєєва[a,b], Л. А. Булавін[c], І. М. Кудрявцев[b], Р.С. Соколенко[a], В.І. Ткаченко[a,b]
[a]ННЦ "Харківський фізико-технічний інститут", Харків
[b]Харківський національний університет імені В.Н. Каразіна, Харків
[c]Київський національний університет імені Тараса Шевченка, Київ

Експериментально досліджено вільне падіння сталевих кульок різних діаметрів у в'язких рідинах, поміщених в циліндричну посудину, що покоїться або обертається з постійною швидкістю, а також вихроутворення рідини, що обертається в циліндричній посудині. Для дослідження цих питань розроблений експериментальний стенд, що складається з циліндричної скляної посудини, встановленої на осі валу електродвигуна з регульованими оборотами, контрольно-вимірювального обладнання в складі цифрового лазерного тахометра, цифрового USB-мікроскопа і ноутбука, для візуалізації досліджуваних процесів. Отримано експериментальні залежності миттєвої швидкості кульок від пройденої ними відстані. Показано наявність перехідного режиму зміни швидкості кульки при його вході в рідину. Перехідний режим характеризується загасаючою, періодичною змінною від відстані миттєвою швидкістю. Встановлено, що на певній пройденій кулькою відстані, перехідний режим переходить в стаціонарний, коли кулька рухається з постійною швидкістю. У стаціонарному режимі методом Стокса досліджена залежність в'язкості рідини від частоти обертання посудини. Показано, що загальною закономірністю таких процесів є зменшення часу падіння кульок, а, отже, коефіцієнту динамічної в'язкості рідини, з ростом частоти обертання посудини. Експериментально виявлено періодична зміна коефіцієнту динамічної в'язкості від частоти обертання посудини. Експериментально встановлено, що при обертанні циліндричної посудини утворюється кілька паралельних осі циліндра ниткоподібних спіральних потоків пофарбованої рідини. При цьому швидкість низхідного дрейфу пофарбованої рідини зростає зі збільшенням швидкості її обертання, а також вона збільшується від периферії до центру судини.

КЛЮЧОВІ СЛОВА: рідина, циліндрична ємність, постійна швидкість, в'язкість, метод Стокса, обертання, динамічна в'язкість, вихор

ВЯЗКОСТЬ И ВИХРЕОБРАЗОВАНИЕ В ЖИДКОСТИ, ВРАЩАЮЩЕЙСЯ В ЦИЛИНДРИЧЕСКОМ СОСУДЕ

О.Л. Андреева[a,b], Л.А. Булавин[c], И.Н. Кудрявцев[b], Р.С. Соколенко[a] В.И. Ткаченко[a,b]
[a]ННЦ "Харьковский физико – технический институт", Харьков
[b]Харьковский национальный университет имени В.Н. Каразина, Харьков
[c]Киевский национальный университет имени Тараса Шевченко, Киев

Экспериментально исследовано свободное падение стальных шариков разных диаметров в вязких жидкостях, помещенных в покоящийся или вращающийся с постоянной скоростью цилиндрический сосуд, а также вихреобразование во вращающейся в цилиндрическом сосуде жидкости. Для исследования этих вопросов разработан экспериментальный стенд, состоящий из цилиндрического стеклянного сосуда, установленного на оси вала электромотора с регулируемыми оборотами, контрольно-измерительного оборудования в составе цифрового лазерного тахометра, цифрового USB-микроскопа и ноутбука, для визуализации исследуемых процессов. Получены экспериментальные зависимости мгновенной скорости шариков от пройденного ими расстояния. Показано наличие переходного режима изменения скорости шарика при его входе в жидкость. Переходной режим характеризуется затухающим, периодическим изменением мгновенной скорости от расстояния. Установлено, что на определенном, пройденном шариком расстоянии, переходной режим переходит в стационарный, когда шарик движется с постоянной скоростью. В стационарном режиме методом Стокса исследована зависимость вязкости жидкости от частоты вращения сосуда. Показано, что общей закономерностью таких процессов является уменьшение времени падения шариков, а, следовательно, коэффициента динамической вязкости жидкости, с ростом частоты вращения сосуда. Экспериментально обнаружено периодическое изменение коэффициента динамической вязкости от частоты вращения сосуда. Экспериментально установлено, что при вращении цилиндрического сосуда образуется несколько параллельных оси цилиндра нитевидных спиральных потоков окрашенной жидкости. При этом скорость нисходящего дрейфа окрашенной жидкости возрастает с увеличением скорости ее вращения, а также она увеличивались от периферии к центру сосуда.

КЛЮЧЕВЫЕ СЛОВА: жидкость, цилиндрический сосуд, постоянная скорость, вязкость, метод Стокса, вращение, динамическая вязкость, вихри

EFFECT OF SURFACE PRE-TREATMENT ON ADHESIVE STRENGTH OF MULTI-COMPONENT VACUUM-ARC COATINGS

Serhiy V. Lytovchenko[a],*, Vyacheslav M. Beresnev[a], Serhiy A. Klymenko[b], Bohdan O. Mazilin[a], M.G. Kovaleva[c], Andrey S. Manohin[b], Denis V. Horokh[a], Igor V. Kolodiy[d], V.U. Novikov[c], Vyacheslav A. Stolbovoy[b,d], Irina V. Doshchechkina[e], Oleg V. Gluhov[f]

[a]*V.N. Karazin Kharkiv National University, Svobody Sq. 4, 61022, Kharkiv, Ukraine*
[b]*V.N. Bakul Institute of Superhard Materials of National Academy of Sciences of Ukraine, Avtozavodskaya St., 2, Kiev, Ukraine*
[c]*Belgorod State National Research University, Pobedy Square, 85, 308015, Belgorod, Russia*
[d]*National Scientific Center "KIPT" NAS of Ukraine, st. Academic, 1, 61108, Kharkiv, Ukraine.*
[e]*Kharkiv National Automobile and Highway University, 25, Ya. Mudryi St., 61200 Kharkiv, Ukraine*
[f]*Kharkiv National University of Radio Electronics, Nauki Ave. 14, 61166, Kharkiv, Ukraine*
*Corresponding Author: s.lytovchenko@karazin.ua

The results of investigations of multi-component nanostructured coatings of (TiAlSiY)N/CrN type are presented. The influence of different variants of substrate surface pretreatment on adhesive strength and hardness of coatings was studied. Pre-treatment of samples was carried out in plasma of two-stage gas discharge according to various technological schemes. Except for ion-plasma purification, some samples were pretreated with a sublayer of chromium within 5 minutes. The coatings were formed by a vacuum-arc deposition method at simultaneous spraying of two cathode targets. The first cathode is made of chromium, and the second cathode is made of multicomponent Ti - Al - Si - Y alloy obtained by vacuum-arc remelting of powder mixture of the mentioned elements. The coatings were deposited on polished stainless-steel substrates at negative 280 V bias potential. The geometry of the unit and its elements, as well as technological characteristics of the processes of evaporation-condensation were selected so that at a speed of rotation of samples 8 revolutions per minute the formation of the coating with a total thickness of about 9.0 microns occurred in approximately 60 minutes. The analysis of the composition of the coatings shows that the content of elements in the coating differs greatly from the content of elements in the sprayed cathodes. The X-ray diffractometry has shown that all deposition modes are characterized by the formation of phases with cubic (fcc) crystal lattice in both phase layers of multilayer coatings. In the layers formed at spraying of TiAlSiY alloy, a multi-element disordered solid solution (TiAlSiY)N with a crystal lattice of NaCl type and a lattice parameter of 0.4241 nm, as well as chromium mononitride CrN with a lattice parameter of 0.4161 nm, is determined. It has been established that preliminary formation of a chromium sublayer on the substrate leads to significant changes in adhesive strength of multi-component coatings compared to coatings without a sublayer.

KEYWORDS: multi-component nitride coatings, ionic treatment, surface preparation, adhesive strength, hardness

The analysis of publications on application of functional coatings testifies that the most important properties of wearproof protective coatings should include durability of adhesion of the coatings to a working surface, as well as their hardness [1 – 3]. It is these properties that determine the ability of coatings to resist external mechanical stresses leading to wear or other destruction. Recently, there has been an intensive development of various technological options for ion-plasma synthesis of multilayer coatings based on refractory metal nitrides [4, 5]. In these options, a targeted change in physical and mechanical properties of coatings is achieved by varying the structural and phase state of protective layers [6]. An essential improvement of performance properties can be achieved with a multi-layer architecture of coatings formed by a consistent or simultaneous use of ion-plasma sources with different evaporated materials, as well as with targeted management of physical and technological parameters of deposition [7].

Adhesion properties of coatings formed by PVD-technologies are determined by various factors: quality of substrate surface preparation, depth of substrate-coating mixing zone, efficiency of the chemical compounds formation in the transition zone, structural defects and stress state of the crystal lattice, segregation of gas impurities, etc. Ion bombardment during deposition has an ambiguous effect on each of the listed factors. Pre-bombardment of substrates with high energy gas ions immediately before coating activates their surface and promotes diffuse interaction at the coating-substrate boundary, but at the same time it also increases defects of the surface and subsurface area (up to 50 nm). The desired performance properties of coatings can be achieved only with the right choice and optimization of the entire process cycle, which includes both preliminary preparatory stages and stages of direct coating formation.

The purpose of this work is to study the influence of physical and technological parameters of multi-component coatings (TiAlSiY)N/CrN formation on the strength of adhesion to the substrate, as well as physical and mechanical properties of these coatings.

EXPERIMENTAL AND RESEARCH METHODS

The coatings were formed by a vacuum-arc deposition method at simultaneous spraying of two cathode targets. One cathode is made of chromium of X99H grade, and the second cathode is made of Ti - Al - Si - Y alloy obtained by

vacuum-arc remelting of powder mixture of the mentioned elements taken in the following quantities (at. %): Ti − 58.5; Al − 36, Si − 3, Y − 2.5. The coatings were deposited on the mechanically polished surface of 15 mm×15 mm×2.5 mm samples made of 12X18H9T steel. The working pressure of nitrogen during deposition (P_N) was 0.6 Pa. When forming coatings, the cathodes were placed in separate evaporators located on opposite walls of the vacuum chamber on one axis towards the center. In the center of the chamber there was a rotary device, on which samples were fixed in the normal direction to the axis. This device with samples during deposition rotated at a speed of 8 rpm. To obtain thicker coating layers, the rotary device was stopped at the corresponding cathode for a time sufficient to achieve the required thickness. The formation of the coating with a total thickness of about 9.0 microns was complete in approximately 60 minutes.

To clean the substrate surfaces before coating, they were pre-treated for 5 minutes in the plasma of a two-stage gas discharge [8] at different types (nitrogen or argon) and its pressure (P_N, P_{Ar}) in the chamber, the duration of cleaning when bombarding the substrate with chromium ions (t_{Cr}), at different values of the negative potential on the substrate (U_p). Some samples were previously deposited with a sublayer of Cr (+) for 5 minutes, the remaining samples were without a sublayer Cr (–). Specific modes of pre-treatment are given in Table 1.

A 4 series of samples were produced using various parameters of pre-treatment of sample surface (Table 1). In all experiments, the following parameters were kept constant: arc current I_a = 90 A, and focusing coil current I_f = 0.5 A.

The coatings on the samples of series 1-4 were formed within 60 minutes at a negative displacement potential on the substrate U_b = 280 V.

Table 1.

Modes of substrate surface pre-treatment and cleaning time

Series No.	P_N, P_{Ar}, Pa	cleaning time t_{Cr}, minutes	U_p, B	Cr: + / −
1	P_N = 0.3	30	-1000	+
2	P_N = 0.3	20	-1000	–
3	P_N = 0.3	20	-1000	+
4	P_{Ar} = 0.2	20	-500	+

Microscopic examination of coating surface was performed using a Nova NanoSEM 450 scanning electron microscope. The elemental composition of coatings was determined by the spectra of the characteristic X-ray radiation generated by the electron beam in the scanning electron microscope. The spectra were obtained with a EDAX PEGASUS energy-dispersion spectrometer installed in the microscope. The coatings thickness was measured using images of transverse grinding of samples with coatings obtained by raster electron microscopy.

The phase composition of coatings was determined by X-ray diffractometry on DRON-4 in Cu-K_α-radiation with graphite monochromator by the Bragg-Brentano method. The analysis of substructural characteristics (the size of coherent OCD scattering areas and the level of microstrain) was carried out using integral width of diffraction lines (the Williamson-Hall method).

Macrostresses in the samples were determined by the $\sin^2\psi$ method.

Microhardness of coatings was measured on a AFFRI DM-8 hardness tester by the micro-Vickers method at 50 g indenter load. Values obtained by averaging data on 10 injections are given for each sample type.

Adhesion/cohesion strength of coatings was determined by sclerometry using a Revetest scratch tester (CSM Instruments). The tests recorded changes in the coefficient of friction and acoustic emission at the growth of the scraping load, as well as recorded the main critical loads: L_{C1} - formation of the first chevron crack at the bottom and diagonal cracks at the scratch edges; L_{C2} - groups of chevron cracks at the scratch bottom; L_{C3} - local peeling of coating after formation of set of chevron cracks at the scratch bottom; L_{C4} - cohesive-adhesive destruction of coating; L_{C5} - plastic abrasion of coating to the substrate [9, 10]. Critical load L_{C5} leading to coating failure was taken as a criterion of adhesive strength. Two scratches were made on each sample to increase data reliability and reliability of results.

RESULTS AND DISCUSSION

The electron-microscopic research and analysis of the morphology of the substrate surface after the gas discharge treatment (Fig. 1a) and the coating surface (Fig. 1b) show that the surface is quite smooth, but both the defect level and the share/fraction of the droplet component on it are quite high.

The presence of the coating droplet fraction and cathode macroparticles on the surface is typical for the majority of condensates obtained from non-separated plasma flows by the vacuum-arc deposition method. In addition to the droplet component, there is a small number of macroparticles on the surface that locally distort the layered geometry of the coating.

The analysis of elemental composition of coatings (Fig. 2, Table 2) showed the presence of evaporable cathodes (Cr, Ti, Al, Si, Y) and nitrogen (reaction gas in the chamber during coating deposition) in all samples of the initial elements. The content of elements in the coating differs greatly from the content of elements in the sputtering cathodes. This is due to a significant difference in the partial pressures of the elements vaporized from the cathodes and the degree of their dispersion, as well as different characteristics of the interaction of the substrate surface with different plasma flow particles.

　　　　　　　　a　　　　　　　　　　　　　　　　　　　　　　　b
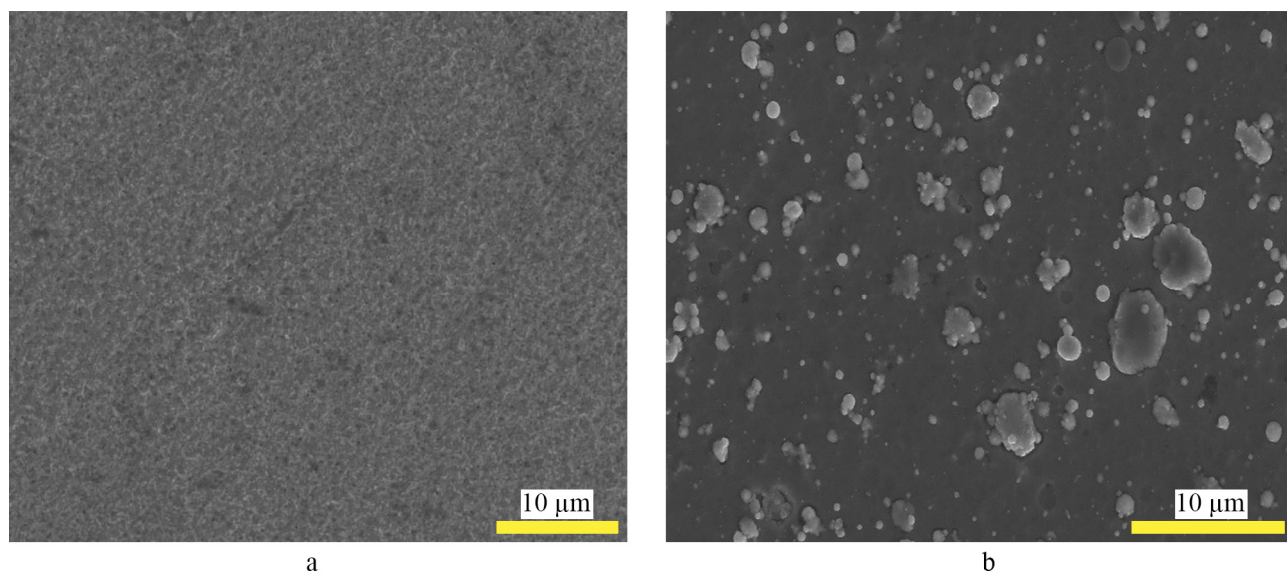
Figure 1. Surface morphology of sample series 1: a) after treatment in a gas discharge b) after coating formation
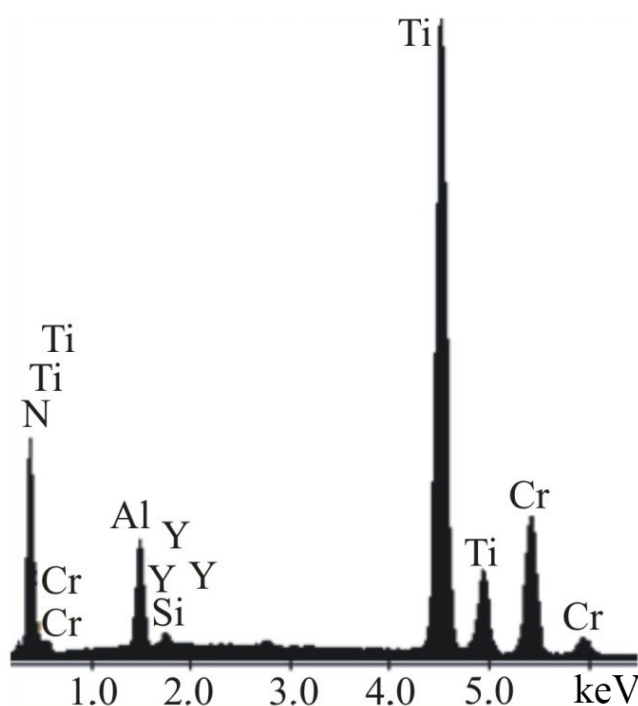
Figure 2. Section of energy dispersion spectrum of coatings

Table 2.

Elemental composition of coatings (TiAlSiY)N/CrN according to EDA data

Series No.	Contents of elements, at. %					
	N	Ti	Al	Cr	Si	Y
1	27.9	36.5	7.9	26.7	0.7	0.3
2	28.6	36.4	8.5	25.1	0.8	0.6
3	29.2	32.2	8.6	29.2	0.7	0.1
4	27.6	36.8	7.7	27.0	0.7	0.2

　　　The analysis of the results obtained for the elemental composition of coatings (see Table 2) shows that the element concentration in coatings substantially depends on the energy of the plasma flow particles.

　　　The analysis of diffraction spectra (Fig. 3) shows that formation of phases with cubic (GCC) crystal lattice in both layers of multilayer coatings is typical for the obtained coatings.
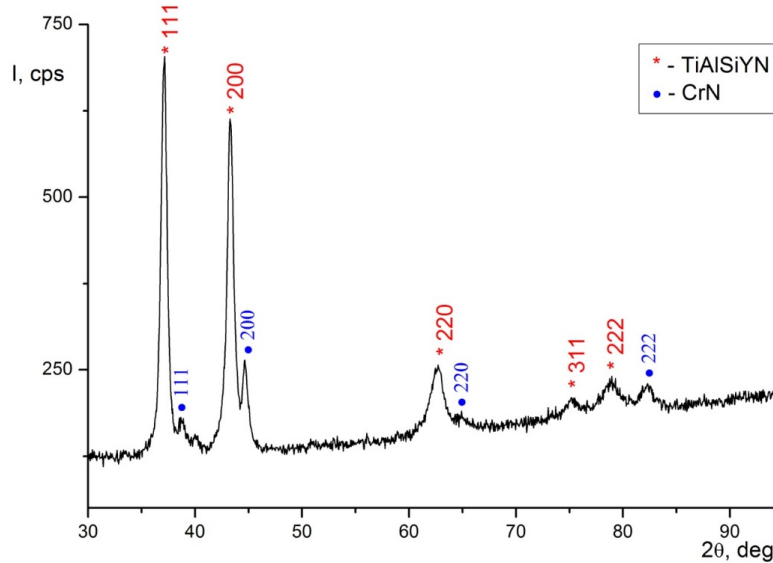
Figure 3. TiAlSiYN/CrN coating diffraction spectrum section

It should be noted that the formation of multielement GCC structures in nitride coatings is confirmed by many researchers [11, 12]. The analysis of publications suggests that for such materials, the formation of a single-phase solid solution of complex multi-element nitride phase is energetically more favourable than the formation of a number of separate coexisting simple nitrides.

According to the X-ray data in the nitride layers based on a TiAlSiY alloy, a disordered solid solution (TiAlSiY)N with a crystal lattice of the structural type NaCl and chromium mononitride CrN were registered. The analysis of X-ray line intensities points to the presence of a strong texture (111) in the multi-element CrN nitride and chromium nitride – the grains of these phases are mainly oriented in such a way that their crystallographic planes (111) are parallel to the sample surface. The lattice parameter of the nitride multi-component phase is 0.4241 nm. The macrostress level reaches $\sigma\varphi = -5.39$ GPa. The calculation of substructural properties of this phase shows that the size of OCD is 14.6 nm with a significant level of microstrain – up to $5.81 \cdot 10^{-3}$. The parameter of the CrN chromium mononitride lattice is 0.4161 nm, but the substructural properties of this phase could not be determined.

The determination of macrostresses was carried out along the main phase lines (TiAlSiY)N on the assumption that the diffraction lines intensity in the precision region was sufficient. The calculation was based on a number of assumptions. Firstly, since the values of Poisson's coefficient ν and Young's E modulus for the (TiAlSiY)N phase could not be found in reported scientific sources, these values for the phase TiAlN: $\nu = 0.25$ and $E = 378$ GPa [1] were used. Secondly, for textured samples, the anisotropy of the Young's modulus was not taken into account [13]. In this case, the similarity of structural states in the nitride interlayers based on the TiAlSiY alloy and nitrides of transition metals of Group VI (close ratio of the formed preferential orientations of crystallites in the interlayers) indicates the interrelation of the structures of the layers during their growth.

Hardness is known to be one of the most important mechanical properties. The results of microhardness measurements of coatings are given in Table 3.

Table 3.

Microhardness of coatings (TiAlSiY)N/CrN

Series No.	1	2	3	4
H_μ, GPa	36.5	30.0	31.1	34.4

However, apart from high hardness combined with sufficient viscosity, the material of nanocomposite coatings must have high adhesive strength.

The determination of the adhesion indices of coatings and analysis of the process of their destruction were carried out on the basis of data from scratch testing of samples in a mode of continuous linear increase in load on the indenter while its simultaneous linear movement on the sample surface. Fig. 4 presents diagrams of changes in amplitude of acoustic emission (the blue curve), friction coefficient (the red curve) and microphotographs of the surface of (TiAlSiY)N/CrN plasma coatings in samples of Series 1 and 2 at different stages of indenter loading (left pictures – at loading L_{C1}, right pictures – at loading L_{C5} respectively).

For the sample of Series 1 (see Table 1) the comparative analysis of structural features of a scratch allows to conclude that at loading less than 21.5 N (L_{C1}) the indenter leaves practically no traces on the coating. At high loads, both chevron cracks at the bottom of a scratch and diagonal cracks begin to appear. This is due to the presence of defects on the surface of the coating, as well as in the volume of vacuum-arc coating. When diagonal cracks close along the banks of a scratch, the detachment of individual scales is observed. The formation of such cracks is accompanied by

a monotonic increase in the friction coefficient up to 0.42. At 188.6 N (L_{C5}) load, the indenter reaches the substrate at the bottom of the scratch.

For the sample of Series 2, the level of L_{C1} was 21.7 N and L_{C5} – 150.1 N, respectively. The analysis of coating failure on this sample shows that the initial stage of failure is due to both surface and volume defects.

Interestingly, at the initial stages of loading (approximately to the value of L_{C1}) almost no acoustic emission signals are registered, although the adhesion of the indenter with the surface of the sample is growing. This confirms an increase in friction coefficient to the values of 0.3-0.36, which is close to a linear increase. With a further increase in the load on the indenter, signals of acoustic emission are registered, but their level and intensity is relatively small, which indicates the absence of active cracking in coatings.
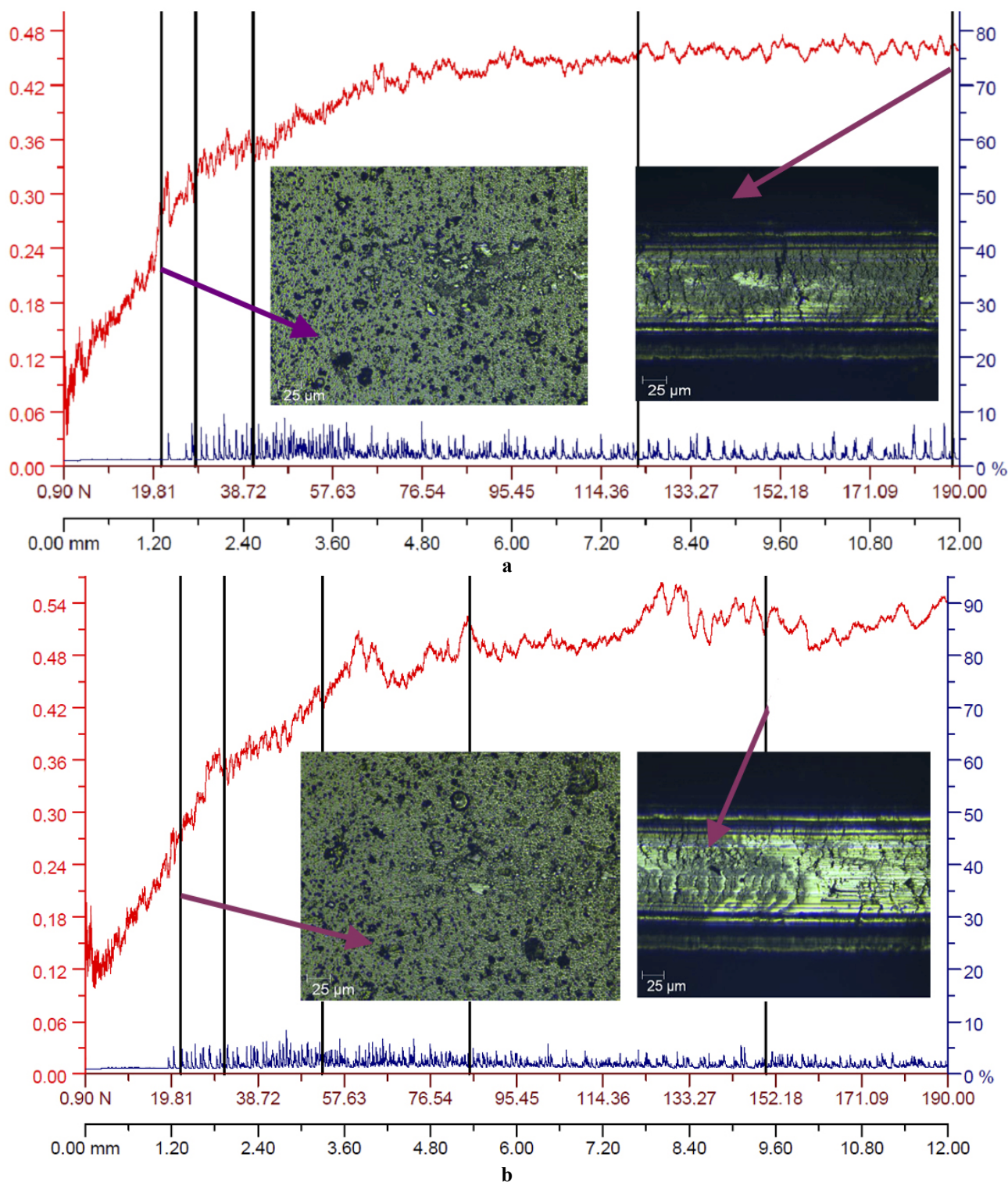

Figure 4. Scratch testing data of coatings (TiAlSiY)N/CrN obtained from straight-flow plasma beam
a – Series 1, loads 21.5 N (L_{C1}) and 188.6 N (L_{C5}); b – Series 2, loads 21.7 N (L_{C1}); 150.1 N (L_{C5})

Table 4.

Average values of critical loads at different stages of coating destruction (TiAlSiY)N/CrN

Series No.	Lc, N				
	1	2	3	4	5
1	21.5	28.6	40.9	122.0	188.6
2	21.7	41.3	52.8	85.1	150.1
3	21.8	27.5	44.5	69.8	180.9
4	22.9	28.2	39.0	78.8	186.4

The comparative analysis of coating destruction shows that the coatings wears out but do not peel off during scratching, i.e. they are destroyed by the cohesive mechanism associated with plastic deformation and formation of fatigue cracks in the coating material [13]. Differences in the adhesive strength of coatings are due to both mechanical interaction of the indent with the surface, which is influenced by the roughness of the contact surfaces, and physical and chemical interatomic interaction on the boundary of contacting bodies.

The analysis of sclerometry data confirms a positive effect of the chromium sublayer on the properties of coatings, which have a sufficiently high level of adhesive strength (Table 4) and an acceptable hardness (Table 3).

All obtained coatings have, on the one hand, a rather low coefficient of friction (maximum μ = 0.42 - 0.48 at high loads) determined by a low value of shear resistance. On the other hand, they have a sufficiently high hardness and strength of the surface layer, which determine resistance to mechanical destruction and wearing.

An essentially narrower spread in values of the coefficient of friction at loads > L_{C3} in the Series 1 coating with a chrome sublayer (Fig. 4, a) in comparison with similar properties of the Series 2 coating without a sublayer (Fig. 4, b) also confirms a positive influence of the chrome layer on the homogeneity and quality of the coating surface.

CONCLUSIONS

It is typical for all (TiAlSiY)N/CrN type coatings obtained by vacuum-arc deposition to have phases with cubic (GCC) crystal lattice formed in both layers of multilayer coatings. Compressive stresses $\sigma\varphi$ = - 5.39 GPa have been recorded in (TiAlSiY)N layers. The lattice parameter of this phase is 0.4241 nm, which slightly exceeds the lattice parameter of chromium mononitride CrN (0.4161 nm).

The coatings formed on substrates with pre-deposited chromium sublayer have higher hardness (H = 36.5 GPa) compared to similar samples without such a sublayer (H = 30.0 GPa). The presence of the chromium layer also contributes to the adhesion strength of (TiAlSiY)N/CrN coatings on substrates made of X18H10T steel. Critical values of fracture load for coatings with a chromium sublayer reach L_{C5} = 188.6 N, and without a chromium sublayer - L_{C5} = 150.1 N.

The obtained coatings have a relatively low of friction coefficient (at high loads μ_{max} = 0.42 - 0.48), high hardness and strength.

ORCID IDs
Serhiy V. Lytovchenko, https://orcid.org/0000-0002-3292-5468**;** **Vyacheslav M. Beresnev,** https://orcid.org/0000-0002-4623-3243**;**
Serhiy A. Klymenko, https://orcid.org/0000-0003-1464-3771**;** **Bohdan O. Mazilin,** https://orcid.org/0000-0003-1576-0590**;**
Andrey S. Manohin, https://orcid.org/0000-0003-1479-8482**;** **Denis V. Horokh,** https://orcid.org/0000-0002-6222-4574**;**
Igor V. Kolodiy, https://orcid.org/0000-0001-8598-9732**;** **Vyacheslav A. Stolbovoy,** https://orcid.org/0000-0001-7734-0642**;**
Irina V. Doshchechkina, https://orcid.org/0000-0002-6278-7780**;** **Oleg V. Gluhov,** https://orcid.org/0000-0003-2453-5504.

REFERENCES
[1] A. D. Pogrebnjak, O. M. Ivasishin, and V. M. Beresnev, Usp. Fiz. Met. **17**(1), 1-28 (2016), https://doi.org/10.15407/ufm.17.01.001.
[2] S.A. Glatz, C.M. Koller, H. Bolvardi, S. Kolozsvári, H. Riedl, and P.H. Mayrhofer, Surface & Coatings Technology **311**, 330-336 (2017), https://doi.org/10.1016/j.surfcoat.2017.01.001.
[3] M.M. Mamonova, V.V. Prudnikov, and I.A. Prudnikova, *Физика поверхности. Теоретические модели и экспериментальные методы* [*Surface physics. Theoretical models and experimental methods*], (Fizmatlit, Moscow, 2011), pp. 400. (in Russian).
[4] M. Naveed, A. Obrosov, A. Zak, W. Dudzinski, A. Volinsky, and S. Weiß, Metals, **6**, 265 (2016), https://doi.org/10.3390/met6110265.
[5] K.V. Smyrnova, A.D. Pogrebnjak, V.M. Beresnev, S.V. Litovchenko, S.O. Borba Pogrebnjak, A.S. Manokhin, S.A. Klimenko, B. Zhollybekov, A.I. Kupchishin, Ya.O. Kravchenko, and O.V. Bondar, Metals and Materials International, **24**(5), 1024-1035 (2018), https://doi.org/10.1007/s12540-018-0110-y.
[6] N. Koutná, P. Řehák, Z. Chen, M. Bartosik, M. Fallmann, M. Černý, Z. Zhang, M. Friák, M. Šob, P.H. Mayrhofer, and D. Holec, Scripta Materialia, **165**, 159-163 (2019), https://doi.org/10.1016/j.scriptamat.2019.02.021.
[7] I.I. Aksionov, A.A. Andreyev, V.A. Belous, V.Ye. Strel`nitskiy, and V.M. Khoroshikh, *Вакуумная дуга: источники плазмы, осаждение покрытий, поверхностное модифицирование* [*Vacuum arc: plasma sources, deposition of coatings, surface modification*], (Naukova dumka, Kiev, 2012), pp. 727. (in Russian).

[8] A.O. Andreev, V.M. Pavlenko, and Iu.O. Sysoiev, *Технологія машинобудування. Основи отримання вакуумно-дугових покриттів* [*Mechanical engineering technology. Basics of obtaining vacuum-arc coatings*], (KhAI Publishing House, Kharkiv, 2018), pp. 139-145. (in Ukrainian).

[9] J. Sekler, P.A. Steinmann, and H.E. Hintermann, Surface and Coatings Technology, **36**(1–2), 519-529 (1988), https://doi.org/10.1016/0257-8972(88)90179-X.

[10] J. Valli, Journal of Vacuum Science and Technology A, **4**(6), 3007-3014 (1986), https://doi.org/10.1116/1.573616.

[11] A.D. Pogrebnjak, A.A. Bagdasaryan, I.V. Yakushchenko, and V.M. Beresnev, Russian Chemical Reviews, **83**(11), 1027-1061 (2014), https://doi.org/10.1070/rcr4407.

[12] R. Chen, Z. Cai, J. Pu, Z. Lu, S. Chen, S. Zheng, and C. Zeng, Journal of Alloys and Compounds, **827**, 153836 (2020), https://doi.org/10.1016/j.jallcom.2020.153836.

[13] R. Radhika, and D. Arivuoli, Indian Journal of Physics, **87**(12), 1199-1206 (2013), https://doi.org/10.1007/s12648-013-0359-4.

[14] I.D. Ibatullin, *Кинетика усталостной повреждаемости и разрушения поверхностных слоев: монография* [*Kinetics of Fatigue Damage and Fracture of Surface Layers: Monograph*], (Samara, Samara Tech. Univ., 2008), pp. 387. (in Russian).

ВПЛИВ ПОПЕРЕДНЬОЇ ОБРОБКИ ПОВЕРХНІ НА АДГЕЗІЙНУ МІЦНІСТЬ БАГАТОКОМПОНЕНТНИХ ВАКУУМНО-ДУГОВИХ ПОКРИТТІВ

С.В. Литовченко[a], В.М. Береснєв[a], С.А. Кліменко[b], Б.О. Мазілін[a], М.Г. Ковалева[c], А.С. Манохін[b], Д.В. Горох[a], І.В. Колодій[d], В.Ю. Новіков[c], В.А. Столбовой[a,d], І.В. Дощечкіна[e], О.В. Глухов[f]

[a] *Харківський національний університет імені В.Н. Каразіна, майдан Свободи 4, 61022, м. Харків, Україна*

[b] *Інститут надтвердих матеріалів ім. В.М. Бакуля НАН України, вул. Автозаводська, 2, 04074, м. Київ, Україна*

[c] *Бєлгородський державний національний дослідницький університет, вул. Перемоги, 85, 308015, м. Бєлгород, Росія*

[d] *Національний науковий центр «Харківський фізико-технічний інститут», вул. Академічна, 1, 61108, м. Харків, Україна*

[e] *Харківський національний автомобільно-дорожній університет, вул. Ярослава Мудрого, 25, 61002, м. Харків, Україна*

[f] *Харківський національний університет радіоелектроніки, проспект Науки, 14, 61166, г. Харків, Україна*

Представлені результати досліджень багатокомпонентних наноструктурних покриттів типу (TiAlSiY)N/CrN. Вивчено вплив різних варіантів попередньої підготовки поверхні підкладинок на адгезійну міцність і твердість покриттів. Попередню обробку зразків проводили в плазмі двоступеневого газового розряду за різними технологічними схемами. Крім іонно-плазмового очищення на частину зразків попередньо протягом 5 хвилин напилювали підшар хрому. Покриття формували методом вакуумно-дугового осадження при одночасному розпиленні двох катодів-мішеней. Один катод виготовлений з хрому, а інший – з багатокомпонентного сплаву Ti – Al – Si – Y, отриманого вакуумно-дуговим переплавом суміші порошків зазначених елементів. Покриття осаджували на поліровані підкладинки з нержавіючої сталі при негативних потенціалах зміщення 280 В. Геометрія установки і її елементів, а також технологічні характеристики процесів випаровування-конденсації були підібрані так, що при швидкості обертання зразків 8 обертів за хвилину формування покриття загальною товщиною близько 9,0 мкм відбувалося приблизно за 60 хвилин. Аналіз елементного складу покриттів показав, що вміст елементів в покритті значно різниться порівняно з вмістом цих елементів у розпорошених катодах. Рентгенівська дифрактометрія показала, що для всіх режимів осадження характерним є утворення фаз з кубічними (ГЦК) кристалічними гратами в обох фазних прошарках багатошарових покриттів. У прошарках, сформованих при розпилюванні сплаву TiAlSiY, зафіксовано багатоелементний невпорядкований твердий розчин (TiAlSiY)N з кристалічними гратами структурного типу NaCl і параметром 0,4241 нм, а також мононітрид хрому CrN з параметром гратів 0,4161 нм. Встановлено, що попереднє формування підшару хрому на підкладинці призводить до суттєвої зміни адгезійної міцності багатокомпонентного покриття у порівнянні з покриттям без підшару.

КЛЮЧОВІ СЛОВА: багатокомпонентні нітридні покриття, іонна обробка, підготовка поверхні, адгезійна міцність, твердість

ВЛИЯНИЕ ПРЕДВАРИТЕЛЬНОЙ ОБРАБОТКИ ПОВЕРХНОСТИ НА АДГЕЗИОННУЮ ПРОЧНОСТЬ МНОГОКОМПОНЕНТНЫХ ВАКУУМНО-ДУГОВЫХ ПОКРЫТИЙ

С.В. Литовченко[a], В.М. Береснев[a], С.А. Клименко[b], Б.А. Мазилин[a], М.Г. Ковалева[c], А.С. Манохин[в], Д.В. Горох[a], И.В. Колодий[d], В.Ю. Новиков[c], В.А. Столбовой[a,d], И.В. Дощечкина[e], О.В. Глухов[f]

[a] *Харьковский национальный университет имени В.Н. Каразина, пл. Свободы, 4, 61022, г. Харьков, Украина*

[b] *Институт сверхтвердых материалов им. В.Н. Бакуля НАН Украины, ул Автозаводская, 2, 04074, г. Киев, Украина*

[c] *Белгородский государственный национальный исследовательский университет, ул. Победы, 85, 308015, г. Белгород, Россия*

[d] *Национальный научный центр «Харьковский физико-технический институт», ул. Академическая, 1, 61108, г. Харьков, Украина*

[e] *Харьковский национальный автомобильно-дорожный университет, ул. Ярослава Мудрого, 25, 61002, г. Харьков, Украина*

[f] *Харьковский национальный университет радиоэлектроники, проспект Науки, 14, 61166, г. Харьков, Украина*

Представлены результаты исследований многокомпонентных наноструктурных покрытий типа (TiAlSiY)N/CrN. Изучено влияние различных вариантов предварительной подготовки поверхности подложек на адгезионную прочность и твердость покрытий. Предварительную обработку образцов проводили в плазме двухступенчатого газового разряда по различным технологическим схемам. Кроме ионно-плазменной очистки на часть образцов предварительно в течение 5 минут напыляли подслой хрома. Покрытия формировались методом вакуумно-дугового осаждения при одновременном распылении двух катодов-мишеней. Один катод изготовлен из хрома, а другой – из многокомпонентного сплава Ti – Al – Si – Y, полученного вакуумно-дуговым переплавом смеси порошков указанных элементов. Покрытия осаждали на полированные подложки из нержавеющей стали при отрицательных потенциалах смещения 280 В. Геометрия установки и ее элементов, а также технологические характеристики процессов испарения – конденсации были подобраны так, что при скорости вращения образцов 8 оборотов в минуту формирование покрытия общей толщиной около 9,0 мкм происходило приблизительно за 60 минут. Анализ элементного состава покрытий показал, что содержание элементов в покрытии сильно отличается от содержания элементов в распыленных катодах. Рентгеновская дифрактометрия показала, что для всех режимов осаждения характерно образование фаз с кубической (ГЦК) кристаллической решеткой в обеих фазных прослойках многослойных

покрытий. В прослойках, сформированных при распылении сплава TiAlSiY, определяется многоэлементный неупорядоченный твердый раствор (TiAlSiY)N с кристаллической решеткой структурного типа NaCl и параметром решетки 0,4241 нм, а также мононитрид хрома CrN с параметром решетки 0,4161 нм. Установлено, что предварительное формирование подслоя хрома на подложке приводит к существенному изменению адгезионной прочности многокомпонентного покрытия по сравнению с покрытием без подслоя.

КЛЮЧЕВЫЕ СЛОВА: многокомпонентные нитридные покрытия, ионная обработка, подготовка поверхности, адгезионная прочность, твердость

INVESTIGATION OF THE EFFECT OF STRUCTURING METHODS ON THE CHANGE IN RESIDUL STRESSES IN POLYMER COMPOSITE MATERIAL

Hanna M. Cherkashina†, Vyacheslav L. Avramenko*, Oleh H. Karandashov††
National Technical University "Kharkiv Politechnic Institute"
Kirpichova str., 2, 61002, Kharkiv, Ukraine
*Corresponding Author: avramenko@kpi.kharkov.ua
†E-mail: annikcherkashina@gmail.com
††E-mail: nokturnok@gmail.com

The process of forming the cohesive strength of PCM is associated with a decrease in its volume. If there is no mechanical impact on the material, then this process is called shrinkage. Shrinkage occurs during cooling, when the solvent evaporates and during structuring. The free shrinkage of the PCM is hindered by its adhesive bond with the surface of the product, which is filled with a polymer compound, as a result of which more or less shrinkage stresses develop in the PCM over time. In addition to the latter in the PCM there are thermal internal stresses. Their occurrence is due to the combination of different materials in PCM, which differ significantly in the coefficients of thermal expansion. An effective way to reduce internal stresses is to add to the composition of PCM various fillers and plasticizers, what improves the relaxation properties of PCM. The aim of this work was to study the influence of different methods of structuring (polymerization), i.e. by convection and in the field of high frequency currents of epoxy, acrylic and epoxyacrylic PCM. The study of the emerging internal stresses, both shrinkage and temperature, was performed by the method of digital strain gauge, which allows not only to record the final level of residual stresses, but to monitor it in the process of structuring. The studies have shown that a more effective method of structuring is the process of structuring in the field of high-frequency current, which reduces residual stresses, increases the modulus of elasticity and forcing temperature of the studied compounds, what increases the strength and performance properties of PCM, and significantly reduces structuring time, providing uniform heating over the whole volume of PCM. It is recommended to use the obtained data in various industries related to the process of gluing and sealing both homogeneous and heterogeneous materials, as well as PCM products

KEYWORDS: internal stress, shrinkage, curing, high frequency current field, polymer composite material

Residual stresses arising in a polymer composite material (PCM) at curing (structuring), and the relaxation processes, occurring at the same time, affect the strength of PCM and often determine time variation in their operational and technological properties. The reasons for the residual stresses occurrence are: presence of temperature gradients, difference in the coefficients of thermal linear expansion of PCM components, manifestation of shrinkage, occurrence of microcracks, method and mode of curing, and some other factors [1-3].

The magnitude of the residual stresses and the rate of their development depend on the nature of the binder, and fillers, plasticizers and other components contained in it.

Besides, the temperature-time method of structuring or polymerization of PCM is extremely important for the residual stresses occurrence [4-5].

The occurrence of the residual stresses is caused by the incompleteness of relaxation processes in the PCM. Therefore, the problem of the occurrence and reduction of residual stresses is of great practical importance.

The purpose of this work is to study the level of the residual stresses in epoxy, acrylic and epoxy-acrylic compositions with different structuring methods applied: by convection heating and structuring in the field of high-frequency currents.

TEST METHODS

To prepare PCM the following materials were used: Epoxy oligomer of ED-20 grade, GOST 10587, dibutyl ester of phthalic acid (DBP) GOST 8728 was used as a plasticizer. Oligoester acrylate MGP-9 (Specification 6-01-450) was used as a modifying agent. Distilled polyethylene polyamine (PEPA) (Specification 6-02-594) was used as a curing agent. The content of the curing agent in the PCM made 10-15% of the oligomer weight. The low-level amine curing agent dicyanoethyldiethylenetriamine UP-0633 (Specification 6-05-1803) was used as a diluter.

AST-T plastic (Specification 64-2-226) was used as a binder for the acrylic composite materials. The curing time of the AST-T plastic at the temperature of 20 ± 0.5 °C ranges from 60 to 90 minutes.

Molybdenum disulfide (Specification 48-19-133), aluminum oxide (Interregional Specification 6-092046), and talc (Specification 2-036707) were used as dispersed fillers.

The content of the compositions investigated are shown in Table 1.

In the course of investigation, a comparative assessment of two methods of structuring (polymerization) – by convection, i.e. heating the compositions under study in the oven, and by curing these compositions in the field of high-frequency currents (HFC) was carried out. For this purpose, a high-frequency device HFD 2-2.5/81 was used, whose basic technical characteristics are given in Table 2.

Table 1.
Content of the compositions under study

Component	Amount, weight %											
	Composition											
	1	2	3	4	5	6	7	8	9	10	11	12
ED-20	100	100	100	100	100	100	100	100	100	100	100	100
PEPA	10	10		10	10	10	10	10	10	10	10	10
Dibutylphthalat		10			10	10	10	10			10	10
UP-0633			30	20								
MGP-9									20	20	20	20
AST-T												
CE-6												
MoS$_2$						20				20		
Talc							25				25	
Al$_2$O$_3$								30				30

Table 2.
Technical characteristics of the HFD 2-2.5/81 unit

Parameter name	Norm
Oscillatory power, kW	2.5±0.25
Operating frequency, MHz	81.36±0.8136
Rated supply voltage, V	380/220
Weight of the heated material, kg	0.25+0.6
Anode current, A	0.7+0.3
Grid current, A	0.2+0.3
Generating lamp filament voltage, V	6.0±0.3
Anode voltage, kV	5.0±0.25

Standard samples were made of the compositions under study by free pouring into open metal molds.

Combining all the components, included into the composition, was carried out in polyethylene containers, with pre-dosing them by weight or volumetric method. In case the samples were made on the bases of an epoxy oligomer, the polymer mass, which before its pouring was thoroughly stirred and evacuated for 10-15 minutes to remove air bubbles, then was poured into metal molds, pre-treated with an anti-adhesive composition (10% solution of HSR rubber in toluene). When pouring samples made of acrylic and mixed compositions, the combined components, polymer and monomer, were previously brought to swelling for 10-20 minutes to the state of the required viscosity, after which they were poured into the molds treated with the above-mentioned separable composition.

The PCM samples, based on epoxydiane oligomer, were structured by convection in an oven at 100 °C for 2 hours; the samples, based on acrylic oligomer, were cured at room temperature (20 ± 2) °C for 60-90 minutes.

When the PCM samples, based on an epoxy oligomer and acrylic polymer were cured in the field of HFC, they were cured in the optimal mode calculated according to a standard computer program.

RESEARCH METHODS

The physical and mechanical properties of epoxy and acrylic PCM specimens were determined by standard and laboratory methods, which are described in [6].

To measure stresses, the wire strain gauge method was used [7-9]. This method was used both to determine the residual stresses at various points of the compound and to measure the contact pressure.

To measure the contact pressure, a thin-walled metal cylinder was used, on whose inner surface wire strain gauges were bonded to measure axial and circumferential deformations, what allowed to control the uniformity of shrinkage deformations in the compounds. The cylinder with the bonded strain gauges was put into the mold. Then the model of the tested compounds was molded so that it formed a uniform layer of a given thickness around the cylinder and did not get inside the cylinder. In the course of curing the compound in the curing chamber, some residual stresses in the samples occur, which deform the cylinder. The cylinder deformation and, hence, the forces that caused it were determined by the magnitude of the change in the resistance of the strain gauges.

In the tested mold the metal cylinder relative deformation, caused by contact pressure, was determined by the formula for calculating the deformation of a thin-walled cylinder loaded with a uniformly distributed external load:

$$\varepsilon = \frac{P \cdot r}{E \cdot \Delta} \cdot \left(1 - \frac{\mu}{r}\right),$$

where: ε - relative circumferential deformation of the cylinder;

P - contact pressure of the compound, N/m^2;

E_{elast} - modulus of elasticity of the cylinder material, N/m^2;

Δ - cylinder wall thickness, mm;

r - cylinder mean radius, mm;

μ - Poisson's ratio.

To measure the contact pressure, the wire strain gauges of the FCL-15-200 type on a film base with the nominal grid resistance of 200 Ohm and the base of 15 mm, and the recommended AC bridge circuit with an electronic amplifier were used.

After the cylinder with the bonded strain gauges was prepared, it was installed into the mold with pre-lubricated lower end of the cylinder with a sealant to prevent compound leakage, and the mold was filled with PCM.

The contact pressure was calculated using the formula:

$P = 6.47\Delta R$

$\Delta R = (D_2 - D_1)$

where D_2 is the pressure of the unloaded cylinder;

D_1 - pressure of the loaded cylinder filled with compound;

6.47 - the coefficient for the cylinder.

The same method was used to determine the residual stresses in the compounds in the process of structuring (polymerization) in the HFC generator.

EXPERIMENTAL RESULTS AND THEIR DISCUSSION

The residual stresses, arising in a polymer material at curing, and the relaxation processes, which occur in this case, affect the PCM strength and so often determine the time variation of their operational properties. The reasons for the occurrence of residual stresses are: presence of temperature gradients, the difference in the coefficients of thermal expansion of PCM components, manifestation of shrinkage, occurrence of microcracks, method and mode of curing, and others [10-13].

The magnitude of the residual stresses and the rate of their development depend on the nature of the binder, on the fillers, plasticizers and other components introduced into it. Besides, the temperature-time regime of structuring or polymerization of PCMs is extremely important for the occurrence of the residual stresses [14-17]. The occurrence of residual stresses is caused by the incompleteness of relaxation processes in the PCM. Therefore, the problem of the occurrence and reduction of the residual stresses is of great practical importance [18-23].

The residual stresses in PCMs, cured in the field of high frequency current and by the method of convection heating, were investigated. The nature of structural transformations and the degree of the relaxation processes completion are significantly influenced by the method of curing. Thus, the use of HFC for the formation of PCM products allows to carry out uniform curing over the thickness of the material and to obtain PCM with a homogeneous ordered structure.

Figures 1, 2 present the kinetics of the residual stresses formation in the process of convection curing with a smooth rise in temperature for 2 hours, in the field of high frequency current – for 180 seconds.
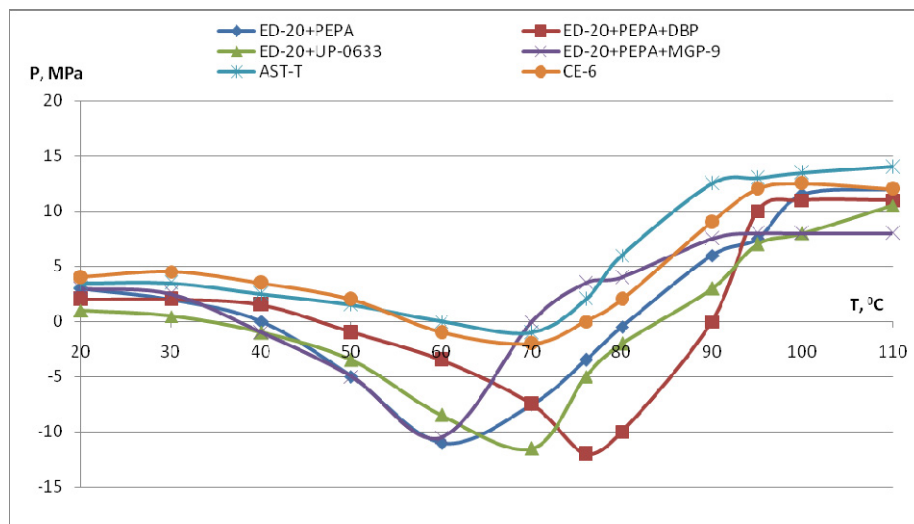
Figure 1. Kinetics of the residual stresses formation in the process of curing by the convection method

When the cured compound is heated, two competing processes occur: a decrease in the system viscosity, which causes a decrease in the residual stresses, and the cross-linking process. The residual stresses will decrease to the point of gel, after which the cross-linking process, which causes a uniform increase in the residual stresses, begins to prevail.

As the figures show, the gel point of epoxy compounds, cured by the convection method, occurs in the temperature range from 60 °C to 90 °C, subject to the compound composition. When the compounds are cured with a highly active curing agent PEPA, gelation occurs at a lower temperature, than when they are cured with a low-active curing agent UP-0633In the presence of the incompatible DBP plasticizer, the gelation process starts at the temperature 10 °C higher, than with the unplasticized compound. The residual stresses, after completion of the curing process for compounds cured in the HFC field, is 11-10 MPa lower than for those, cured by the convection method. With participation of the MGP-9 modifier, the temperature range of gelation is 42-31% narrower than that for the unplasticized compound, and is shifted towards lower temperatures by 18 °C. The gelation process in the compounds cured with UP-0633 starts, as it has been expected, at the highest temperature.

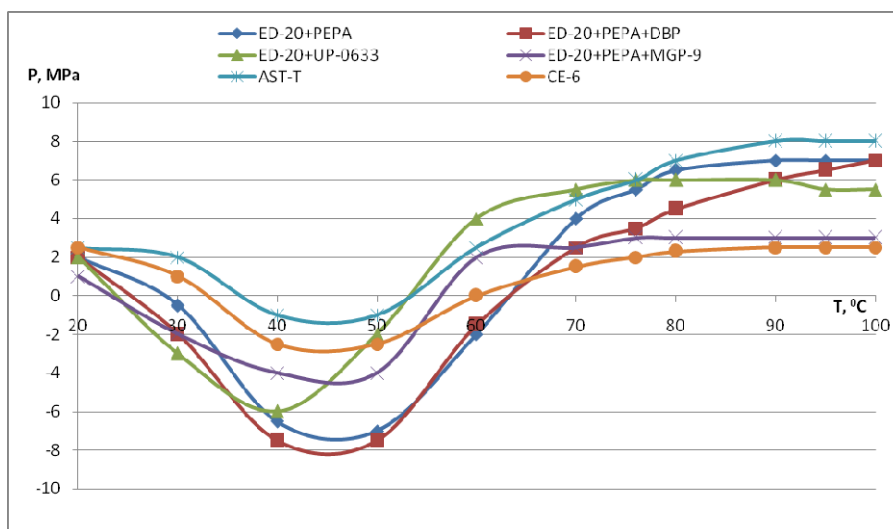**Figure 2.** Kinetics of the residual stresses formation in the process of curing in the field of high frequency current

The considered results show that almost all the compounds, based on oligomer of ED-20 grade, were cured under the optimum temperature conditions, which were close to T_g. The exception makes the compound with MGP-9, whose curing temperature and T_g are somewhat different, what is undesirable. In the course of curing in HFC, the gelation point for all the compounds occurs at lower temperatures, although the process itself proceeds in approximately the same temperature range as for the compounds cured by the convection method, but is shifted towards temperatures lower by 20-25 °C. This fact can be attributed to a more uniform distribution of the temperature field at PCM curing in the high frequency current. The residual stresses after the curing process completion, as can be seen from Table 3, for all the compounds without exception, cured in HFC field, are significantly lower than for those, cured by the convection method.

Table 3.

Characteristics of the epoxy compounds residual stresses change in the process of curing

Compound composition	σ_{init}, MPa	σ_{min}, MPA	σ_{max}, MPa	$\Delta\sigma_{1=}$ Σ_{init}-σ_{min}, MPa	$\Delta\sigma_{1=}$ Σ_{max}-σ_{min}, MPa	Gelation temperature, °C	Gelation completion temperature, °C
ED-20+PEPA	2.0/1.0	-3.8/-4.0	5.8/6.0	5.8/6.0	9.6/10.0	45/45	70/53
ED-20+ PEPA +Mo$_2$S	1.1/1.0	-3.2/-2.6	6.1/6.2	4.3/3.6	9.3/8.8	45/43	72/48
ED-20+ PEPA +talc	1.1/1.3	-3.5/-3.3	7.2/4.8	4.3/3.6	10.7/8.1	45/50	63/50
ED-20+ PEPA + Al$_2$O$_3$	0.8/1.1	-4.8/-1.5	4.8/3.4	5.6/2.6	9.6/4.9	45/43	63/53
ED-20+ PEPA+DBP	2.5/0.9	-4.8/-3.9	12.1/6.1	7.0/4.8	14.6/10.0	50/43	65/55
ED-20+ PEPA +DBP+ Mo$_2$S	2.8/0.5	-4.5/-5.0	9.9/5.3	7.4/5.5	14.5/10.3	55/46	70/54
ED-20+PEPA+DBP +talc	1.3/1.0	-5.1/-1.3	11.5/3.5	6.4/2.3	16.6/4.8	55/42	65/52
ED-20+PEPA+DBP+ Al$_2$O$_3$	1.4/0.9	-3.4/-3.3	8.1/2.5	4.8/4.2	11.5/5.8	60/43	70/43
ED-20+PEPA+MGP-9	0.5/0.9	-6.3/-8.0	9.2/5.9	6.8/8.9	15.2/13.9	50/42	78/55

Compound composition	σ_{init}, MPa	σ_{min}, MPA	σ_{max}, MPa	$\Delta\sigma_{1=}$ $\Sigma_{init}-\sigma_{min}$, MPa	$\Delta\sigma_{1=}$ $\Sigma_{max}-\sigma_{min}$, MPa	Gelation temperature, °C	Gelation completion temperature, °C
ED-20+ PEPA + MGP-9+Mo$_2$S	1.0/0.8	-6.2/-6.1	7.8/6.8	7.2/6.9	14.0/12.8	45/42	68/65
ED-20+ PEPA + MGP-9+talc	1.3/1.1	-4.9/-3.9	11.2/5.6	6.2/4.0	16.1/9.5	53/45	79/75
ED-20+ PEPA + MGP-9+ Al$_2$O$_3$	1.8/1.0	-3.8/-3.8	6.0/4.6	5.6/4.8	9.8/8.4	70/45	85/60
ED-20+UP-0633	1.2/1.2	-9.3/-10.0	6.5/4.3	10.5/11.2	15.8/14.3	51/40	72/65
ED-20+UP-0633+Mo$_2$S	1.3/1.0	-11.0/-6.3	5.6/2.9	12.3/7.2	15.6/9.2	48/45	63/63
ED-20+UP-0633+talc	1.1/1.1	-12.2/-10.5	7.1/9.0	13.3/11.6	19.3/16.5	68/49	65/70
ED-20+UP-0633+Al$_2$O$_3$	1.2/0.8	-5.5/-7.0	4.2/2.4	6.7/7.8	9.7/9.4	59/52	85/70

For acrylic compositions (Figure 1, 2), cured both by the convection method and in the field of HFC, a slightly different nature of the residual stresses formation in the process of curing is observed. The residual stresses transition to the negative region for AST-T and CE-6 is 0.5 MPA and 0.6 MPA at convection heating, and 1.0 MPa and 1.9 MPa in the HFC field, respectively. For epoxy polymers, the residual stresses range from 5.5 MPa to 9.2 MPa. This indicates, that the segmental mobility of the acrylic polymers is limited as compared to the epoxy PCMs. This fact is confirmed by the dynamic mechanical characteristics, from which it can be seen, that the value of the modulus G` in the glassy state is 1.11-1.61% higher, than that of epoxy compounds, cured by PEPA. The glass transition temperature difference is 25 °C. The residual stresses of epoxyacrylic composition CE-6, cured by the convection method, are higher than those of epoxy PCMs, and when cured in high-frequency current, the residual stresses decrease and make 2.2 MPa. Thus, the residual stresses magnitude depends on the rate of relaxation processes, which, in turn, is determined by the degree of curing and the polymer structure, the presence and nature of the plasticizer, and the conditions for the formation of a three-dimensional polymer lattice.

Subsequently, the following fillers were introduced into the investigated binders: aluminum oxide, molybdenum disulfide, and talc. In the filled PCMs, the value of the residual stresses depends on the size and concentration of the filler particles, on the differences in the physical properties of the polymer and filler, and on their interaction. The role of relaxation phenomena in the presence of the fillers, which affect the strength of PCM and often determine the time variations in their performance properties, should be especially emphasized. This is caused by the fact, that the residual stresses are formed in PCM due to the shrinkage of the polymer during its structuring, and due to the external impacts.

As Table 3 shows, the fillers have an ambiguous effect on the residual stresses in the epoxy compounds with PEPA, cured by the convection method. In PCM with aluminum oxide they decrease by 15%, while in PCM with talc, on the contrary, they grow to 23%. The fillers did not significantly affect the nature of the kinetics of the curing process. When the compounds were cured in HFC, the fillers had a more significant effect on the relaxation processes during crosslinking, as well as in the cured state. This especially becomes apparent, when aluminum oxide is used in the compounds, in which the residual stresses decreased by 45%. The width of the α-relaxation transition became 18% narrower, although the temperature of the gelation point remained unchanged. When the compound was cured in HFC, in contrast to the convection method, Talc also had a positive effect on the value of the residual stresses, although less noticeable than that of aluminum oxide. In general, the value of the residual stresses in the solid-state compounds, cured in the field of high-frequency current, is 50-60% lower, than that at the convection method of curing. The area of gelation shifted towards the temperatures lower by 20-25 °C.

In general, all the compounds, cured with PEPA in the presence of DBP, both with fillers and without them, when using the convection method of curing, have higher residual stresses, than the same compounds without a plasticizer. When considering the effect of the filler, it can be seen, that in PCMs the aluminum oxide has a significant positive effect on the nature of the formation and the magnitude of residual stresses; the residual stresses have decreased by 30%. Other fillers reduced the residual stresses, but less significantly, namely, molybdenum disulfide by 25%, and talc by 15%.

For compounds with MGP-9, as well as for those with DBP, the aluminum oxide had the maximum effect on the value of residual stresses. The residual stresses decreased by 11%, and $\Delta\sigma_2$ for the compounds, cured by the convection method, made 9.8 MPa, and for those, cured in HFC, it was 8.4 MPa, what testified to a high degree of the compound homogenization. Talc had the effect on the residual stresses formation process itself. This process proceeds in a narrower temperature range, although the residual stresses slightly increased as compared to the process with the unfilled composition, but the character of the curve slope indicates, that in the process of further structuring their value decreased, what was confirmed by further investigations.

In the course of structuring in the HFC field, the residual stresses in compounds 1 and 3 are close in value, and the width of the gelation region is narrower for the compounds with fillers, what confirms positive contribution of the fillers

in the process of structuring. After the gelation process completion, the filled compounds, cured with UP-0633 by the convection method, have residual stresses at approximately the same level as the compounds, cured with PEPA containing DBP and MGP-9. For all the compounds, structured in the field of high frequency current, the value of residual stresses is 40-50% lower. When the convection structuring method is used, the inhibitory effect of the fillers on the curing process and on the formation of a three-dimensional structure is observed. In HFC field this influence is ignored. It should be noted, that aluminum oxide behaves similarly both at the convection heating and when exposed to HFC field. Molybdenum disulfide and talc do not change their effect. All mentioned above is illustrated by diagrams (Figure 3-6).

Figure 3. The effect of the filler on the kinetics of residual stresses formation in the process of structuring

Figure 4. The effect of the filler on the kinetics of residual stresses formation in the process of structuring
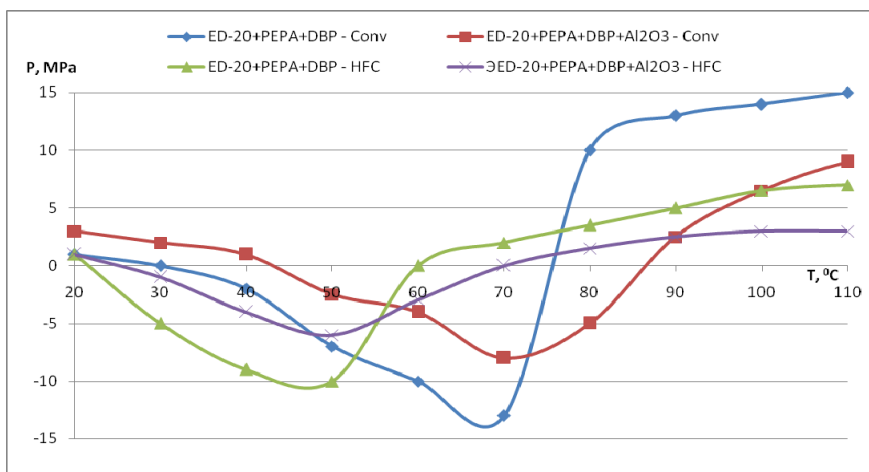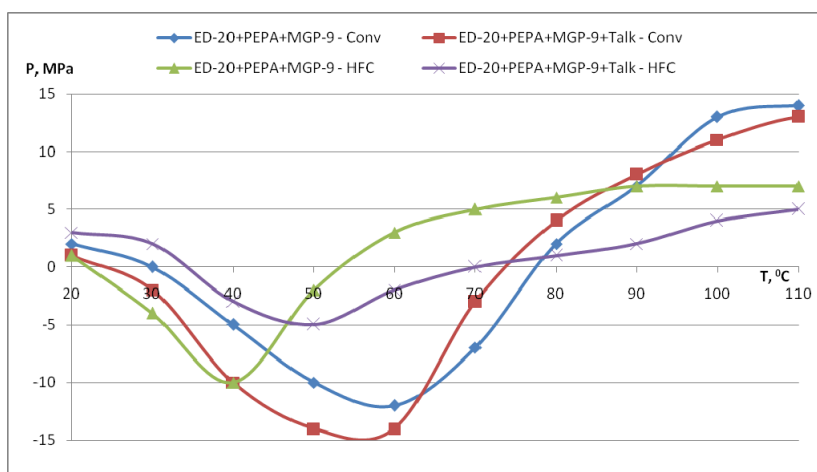

Figure 5. The effect of the filler on the kinetics of residual stresses formation in the process of structuring

Figure 6. The effect of the filler on the kinetics of residual stresses formation in the process of structuring
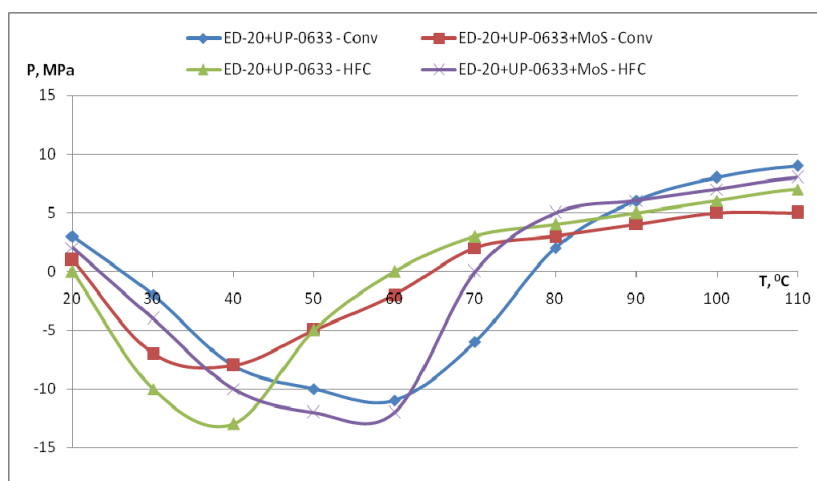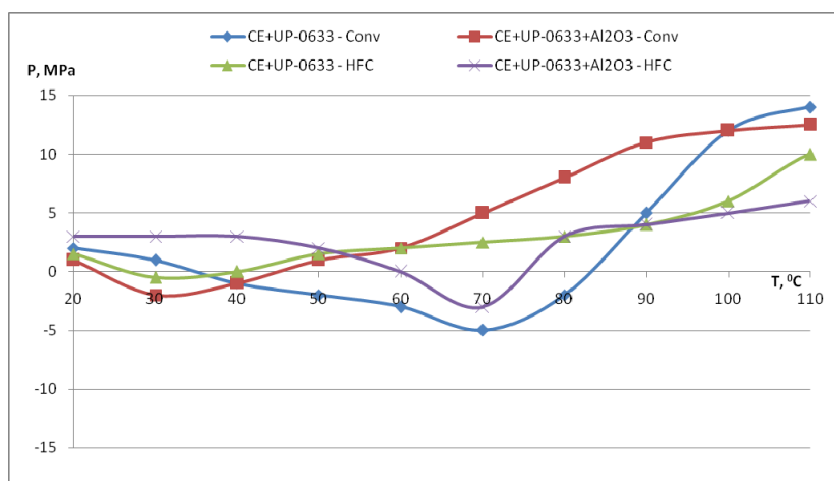
For CE-6 compound, cured by the convection method and in HFC field, the best of the tested fillers is aluminum oxide, which reduces the residual stresses by 43% and 51%, respectively (Fig.6)

Thus, it is shown that HFC has a positive effect on the curing process and on the formation of residual stresses, both in unfilled and filled compounds. As a result, the performance properties of PCM, structured in the field of HFC, are characterized by a higher level and higher stability as compared to the properties of PCM, cured by the convection method [24-25].

CONCLUSIONS

1. A complex of researches on the effect of methods for structuring (polymerization) of epoxy, acrylic and epoxyacrylic PCMs on the value of residual stresses, occurring in PCM during structuring by two different methods, i.e. convection heating and structuring in the field of high-frequency current, was carried out.

2. It is shown, that structuring in the field of high-frequency current can significantly reduce the level of residual stresses, what has a positive effect on the strength properties of the material and the degree of curing.

3. It has been established, that the HFC electric field has the same effect on the properties of the compounds under study, irrespective of the polymer chemical nature, what is, apparently, due to the distribution of the electron density of epoxy and acrylic polymers.

4. The nature of the relaxation processes in PCM, which are structured in the field of HFC, has been studied. An increase in the dynamic modulus of elasticity and glass transition temperature for a number of PCMs, as compared to the PCMs structured by the convection method, has been determinedThe increase in the dynamic modulus of elasticity and glass transition temperature is associated with an increase in the frequency of the spatial lattice and, as a consequence, an increase of the intermolecular interactionIn this case, the level of the residual stresses in PCM, structured in the HFC field, is lower as compared to the convection method, what allows to recommend this method for formation of sealing and adhesive joints, due to the achievement of a stable complex of strength, plasticity, and performance properties.

ORCID IDs

Vyacheslav L. Avramenko, https://orcid.org/0000-0002-6968-1321;
Oleh H. Karandashov, https://orcid.org/0000-0002-3192-6944

REFERENCES

[1]   Y. Abou Msallem, F. Jacquemin, N. Boyard, A. Poitou, D. Delaunay, and S. Chatel, Composites part a: applied science and manufacturing, **41**(1), 108-115 (2010), https://doi.org/10.1016/j.compositesa.2009.09.025.
[2]   Y. Zhao, T. Zheng, K. Yang, X. Wang, and Y. He, in: *IEEE International Conference on High Voltage Engineering and Application (ICHVE)*, (IEEE, Athens, 2018), pp. 1–4, https://doi.org/10.1109/ICHVE.2018.8641913.
[3]   D. Abliz, J. Zhang, L. Steuernagel, and L. Xie, Journal Polymers and Polymer Composites, **21**(6), 341-348 (2013), https://doi.org/10.1177/096739111302100602.
[4]   Y. Chen, and G. Malysheva, in: *IOP Conference Series: Materials Science and Engineering*, **683**, 012065 (IOP Publishing, 2019), https://doi.org/10.1088/1757-899X/683/1/012065.
[5]   S. Lu, C, Zhao, L, Zhang, D, Chen, D. Chen, X. Wang, and K. Ma, RSC Advances, **39**(8), 22078-22085 (2018), https://doi.org/10.1039/C8RA03445A.
[6]   L.P. Podgornaya, G.M. Черкашина, and B.B. Lebedev, *Теорія та методи дослідження і випробування пластмас, клеїв та герметиків. Навчальний посібник* [*Theory and methods of research and testing of plastics, adhesives and sealants. Tutorial*], (LLC "Pidruchnyk", NTU "KhPI", Kharkiv, 2012), pp. 266.
[7]   A.R. Plepys, and R.J. Farnis, Polymer, **31**(10), 1932-1936 (1990), https://doi.org/10.1016/0032-3861(90)90019-U.

[8] V. Popovici, D. Gârleanu, G. Gârleanu, and M. Iliescu. In: *Proceedings of the 3rd WSEAS international conference on Finite differences - finite elements - finite volumes - boundary elements*, edited by M. Grigoriu, V.M. Mladenov, C.A. Bulucea, O.I. Martin, and N.E. Mastorakis, (WSEAS, Wisconsin, US, 2010), pp. 78–81.

[9] M. Harsch, J. Karger-Kocsis, and F. Herzog, Journals Macromolecular Materials and Engineering, **292**(4), 474-483 2007, https://doi.org/10.1002/mame.200600432.

[10] A. Singh, Nucl. Instrum. Meth. B, **185**, 50-54 (2001), https://doi.org/10.1016/S0168-583X(01)00753-4.

[11] C. Decker, Macromol. Rapid Comm. **23**, 1067–1093 (2003), https://doi.org/10.1002/marc.200290014.

[12] D. Beziers, P. Perilleux, and Y. Grenie, Radiat. Phys. Chem. **48**, 171–177 (1996), https://doi.org/10.1016/0969-806X(95)00420-3.

[13] C. Saunders, V. Lopata, J. Barnard, and T. Stepanik, Radiat. Phys. Chem. **57**, 441–445 (2000), https://doi.org/10.1016/S0969-806X(99)00411-9.

[14] A.A. Silva, R. Stein, D. Campos, T. Indrusiak, G. Soares, and G.M.O. Barra. Front. Mater. **6**, 156 (2019), https://doi.org/10.3389/fmats.2019.00156.

[15] G. Tao, and Z. Xia, International Journal of Fatigue, **29**(12), 2180-2190 (2007), https://doi.org/10.1016/j.ijfatigue.2006.12.009.

[16] L. Pupure, S. Saseendran, J. Varna, and M. Basso, Journal of composite materials, **52**(24), 3277-3288 (2018). https://doi.org/10.1177/0021998318764275.

[17] S. Paul, M. Motalab, Md.A. Zobayer, and Md.J. Hossain. Strain rate and curing condition effects on the stress–strain behaviour of e epoxy adhesive materials. Journal of Adhesion Science and Technology, **31**(16), 1782-1795 (2017), https://doi.org/10.1080/01694243.2017.1283109.

[18] M.B. Prime, Journals Fatigue and Fracture of Engineering Materials and Structures, **22**(3), 195-204 (1999), https://doi.org/10.1046/j.1460-2695.1999.00155.x.

[19] B. Winiarski, and P.J. Withers, Journal of Strain Analysis for Engineering Design. **50**(7), 412-425 (2015), https://doi.org/10.1177/0309324715590957.

[20] G.S. Schajer, J. Eng. Mater. Technol. **103**(2), 157-163 (1981), https://doi.org/10.1115/1.3224988.

[21] M.M. Shokrieh, and A.R.G. Mohammad in: *Residual Stresses in Composite Materials*, edited by M.M. Shokrieh, (Woodhead Puplishing, 2014), pp. 3-14, https://doi.org/10.1533/9780857098597.1.3.

[22] P. Salagnac, P. Dutournié, and P. Glouannec, AIChE Journal, **50**(12), 3149-3159 (2004), https://doi.org/10.1002/aic.10224.

[23] M.M. Reboredo, and A. Vazquez, Curing of thermosetting polymers by an external fluid. Polymer Engineering and Science, 35(19), 1521-1526 (1995), https://doi.org/10.1002/pen.760351905.

[24] S. Liu, Y. Li, Y. Shen, and Y. Lu, The International Journal of Advanced Manufacturing Technology, **103**, 3479–3493 (2019), https://doi.org/10.1007/s00170-019-03707-0.

[25] I. Fotiou, A. Baltopoulos, A. Vavouliotis, and V. Kostopoulos, Journal of Applied Polymer science. **129**(5) 2754-2764 (2013), https://doi.org/10.1002/app.39003

ДОСЛІДЖЕННЯ ВПЛИВУ СПОСОБІВ СТРУКТУРУВАННЯ НА ЗМІНУ ЗАЛИШКОВИХ НАПРУГ В ПОЛІМЕРНИХ КОМПОЗИЦІЙНИХ МАТЕРІАЛАХ

Г.М. Черкашина, В.Л. Авраменко, О.Г. Карандашов
Національний технічний університет «Харківський політехнічний інститут»
вул. Кирпичова, 2, 61002, Харків, Україна

Процес формування когеційної міцності ПКМ пов'язаний зі зменшенням його об'єму. Якщо при цьому відсутні механічний вплив на матеріал, то такий процес називають усадкою. Усадка має місце при охолоджені, при випаровуванні розчинника і в процесі структурування. Вільній усадці ПКМ перешкоджає його адгезійний зв'язок з поверхнею виробу, що заливається полімерним компаундом, в результаті чого в ПКМ з часом розвивається більш або менш усадкові напруження. Крім останніх, в ПКМ мають місце термічні внутрішні напруги. Їх виникнення обумовлено поєднанням різних матеріалів в ПКМ, які значно відрізняються коефіцієнтами термічного розширення. Ефективним засобом для зниження внутрішніх напруг є додавання до складу ПКМ різних наповнювачів і пластифікаторів, що покращує релаксаційні властивості ПКМ. Метою даної роботи було дослідження впливу різних методів структурування (полімеризації) – конвекційного і в полі струмів високої частоти епоксидних, акрилових та епоксіакрилових ПКМ. Дослідження виникаючих внутрішніх напруг, як усадочних, так і температурних проводили методом цифрової тензометрії, яка дозволяє не тільки фіксувати кінцевий рівень залишкових напруг, але підслідувати його в процесі структурування. Проведеними дослідженнями встановлено, що більш ефективним методом структурування є процес структурування в полі струму високої частоти, який сприяє зниженню рівня залишкових напруг, підвищенню модулю пружності і температури силування досліджених компаундів, що сприяє підвищенню комплексу міцносних та експлуатаційних властивостей ПКМ, а також значно скорочує час структурування, забезпечуючи рівномірний нагрів по всьому об'єму ПКМ. Отримані дані рекомендовано використовувати в різних галузях, які пов'язані з процесом склеювання та герметизації, як однорідних, так і різнорідних матеріалів, а також виробів з ПКМ.
КЛЮЧОВІ СЛОВА: внутрішнє напруження, усадка, структурування, поле струмів високої частоти, полімерний композиційний матеріал

ИССЛЕДОВАНИЕ ВЛИЯНИЯ СПОСОБОВ СТРУКТУРИРОВАНИЯ НА ИЗМЕНЕНИЕ ОСТАТОЧНЫХ НАПРЯЖЕНИЙ В ПОЛИМЕРНЫХ КОМПОЗИЦИОННЫХ МАТЕРИАЛАХ

А.Н. Черкашина, В.Л. Авраменко, О.Г. Карандашов
Национальный технический университет «Харьковский политехнический институт»
Ул. Кирпичова, 2, 61002, Харьков, Украина

Процесс формирования когезионной прочности ПКМ связан с уменьшением его объема. Если при этом отсутствуют механическое воздействие на материал, то такой процесс называют усадкой. Усадка имеет место при охлаждении, при испарении растворителя и в процессе структурирования. Свободной усадке ПКМ препятствует его адгезионная связь с поверхностью изделия, которая заливается полимерным компаундом, в результате чего в ПКМ со временем развивается более или менее усадочные напряжения. Кроме последних, в ПКМ имеют место термические внутренние напряжения. Их

возникновение обусловлено сочетанием различных материалов в ПКМ, которые значительно отличаются коэффициентами термического расширения. Эффективным средством для снижения внутренних напряжений является добавление в состав ПКМ различных наполнителей и пластификаторов, что улучшает релаксационные свойства ПКМ. Целью данной работы было исследование влияния различных методов структурирования (полимеризации) - конвекционного и в поле токов высокой частоты эпоксидных, акриловых и епоксиакрилових ПКМ. Исследование возникающих внутренних напряжений, как усадочных, так и температурных проводили методом цифровой тензометрии, которая позволяет не только фиксировать конечный уровень остаточных напряжений, но отслеживать его в процессе структурирования. Проведенными исследованиями установлено, что более эффективным методом структурирования является процесс структурирования в поле ТВЧ, который способствует снижению уровня остаточных напряжений, повышению модуля упругости и температуры принуждения исследованных компаундов, что способствует повышению комплекса прочностных и эксплуатационных свойств ПКМ, а также значительно сокращает время структурирования, обеспечивая равномерный нагрев по всему объему ПКМ. Полученные данные рекомендуется использовать в различных отраслях, связанных с процессом склеивания и герметизации, как однородных, так и разнородных материалов, а также изделий из ПКМ.

КЛЮЧЕВЫЕ СЛОВА: внутреннее напряжение, усадка, структурирование, поле токов высокой частоты, полимерный композиционный материал

AUTONOMOUS NEUTRON FACILITY FOR DETECTING FISSILE NUCLEAR MATERIALS

Eduard L. Kuplennikov*,　Mykola I. Ayzatsky,　Alexander N. Vodin,　Olexii S. Deiev,　Stanislav N. Olejnik,　Iryna S. Timchenko,　Sergii S. Kandybei, Alexander S. Kachan, Larisa P. Korda, Yurii N. Solodovnikov

NSC «Kharkov Institute of Physics and Technology», Kharkov, 61108, Akademicheskay 1, Ukraine
*Corresponding Author: kupl@kipt.kharkov.ua

The prospect of creating an autonomous neutron facility for the detection of fissile nuclear materials in samples, including those in confined volume, is discussed. It is proposed to obtain a reference field of thermal neutrons on the basis of a polyethylene moderator ball and a portable fast neutrons source, developed at NRC "Accelerator" NSC KIPT based of a continuous electrostatic accelerator of deuterons. The developed source of thermal neutrons is planned to be used to activate small objects and goods in order to identify substances prohibited for movement containing to find ^{233}U, ^{235}U and ^{239}Pu in their composition. The prompt finding of fissile elements will indicate about an attempt to transport them illegally. A more thorough inspection can be carried out using special equipment after the detention of suspicious goods, citizens or vehicles. The possibility of detecting prompt fission neutrons is considered not only in the traditional way using a polyethylene moderator and proportional ^{3}He detector, but also without application of any moderator using oxide or semiconductor scintillators. For detection fissile materials the method based on using the high-energy part of the γ-spectrum of fission fragments (greater than 4900 keV), as well, as the approach applied in the passive non-destructive analysis by the γ-line with E_γ = 185.7 keV from ^{235}U, are substantiated. It is shown that the proposed facility for the detection of fissile nuclear materials is able to determine the presence of isotopes ^{233}U, ^{235}U and ^{239}Pu in tested objects and goods with the using non-destructive testing method.

KEY WORDS: fissile nuclear materials, non-destructive analysis, neutron source, moderator, thermal neutrons, fission fragments, prompt neutrons

　　　　Виявлення ядерних матеріалів, що діляться, у виробах і вантажах є найважливішим, фактором системи обліку і контролю ядерних матеріалів, безпеки ядерно-енергетичних установок, нерозповсюдження ядерних технологій, припинення обороту елементів поділу у випадку їх несанкціонованого транспортування і т. д. В якості заборонених до перетину кордонів матеріалів слід виділити два основних види: вибухові речовини і елементи поділу. У зв'язку з цим, світовою спільнотою на міжнародному та регіональному рівнях прийнято низку правових актів і одним з них є, зокрема, «конвенція про захист ядерних матеріалів» (1980 рік). Найбільш привабливим з точки зору терористів є ^{239}Pu, оскільки мінімальна маса кулі з «чистого» металу, що забезпечує протікання самопідтримуваної ланцюгової реакції поділу з ^{9}Be відбивачем товщиною 32 см, усього 2,47 кг [1]. «Чистий» означає (90 - 95)% ^{239}Pu, (1 - 7)% ^{240}Pu, вміст інших елементів не перевищує десятих часток відсотка. Для порівняння аналогічна величина для ^{235}U з 93,5% збагаченням і з BeO відбивачем ~ 8,9 кг [2].

　　　　Існуючі ядерно-фізичні методи неруйнівного контролю, що спрямовані на виявлення та визначення кількості ядер поділу у зразках, включаючи вироби зі складним гетерогенним складом, наприклад, ТВС, їх збагачення і т.д., досить різноманітні. Знайдено цілий ряд рішень цієї задачі і одним з них є активація вантажу тепловими нейтронами (ТН), з подальшою реєстрацією та аналізом продуктів реакції. При взаємодії з ТН стратегічно важливі ядра ^{233,235}U, ^{239}Pu діляться, випромінюючи уламки поділу, миттєві нейтрони і γ-кванти (за час ~ 10^{-14} і ~ 10^{-9} с, відповідно), запізнілі нейтрони, β-частинки, антинейтрино. Число запізнілих нейтронів, як правило, становить ~ 1% від числа миттєвих. Вони випромінюються зупиненими продуктами поділу після попереднього β$^-$-розпаду за час від сотень мілісекунд до ~ 60 с і енергією (0,25 - 0,62) МеВ. Що стосується γ-квантів, то в середньому на однин акт поділу утворюються від 7 до 10 фотонів, а їх енергія близька 1 МеВ. Середня кількість нейтронів, що утворюються в одному акті вимушеного поділу (ν) при енергії взаємодіючих частинок 0,025 еВ дорівнює для ^{233}U – 2,48, ^{235}U – 2,42 і ^{239}Pu – 2,86. При енергії вище 0,025 еВ величина ν зростає. Енергетичні спектри розглянутих ядер близькі один до одного [3,4], є суцільними, і добре описуються виразом $N(T) = (\varepsilon)^{1/2} \times \exp(-E/T)$, де E – кінетична енергія нейтронів, T = 1,31, 1,29, 1,33 МеВ, відповідно. Спектри простягаються від 0,01 до 10 МеВ. Зустрічаються енергії до 18 МеВ, але їх дуже мало. Максимум енергетичного розподілу знаходиться при енергії ~ 0,7 МеВ. Середня енергія нейтронів поділу близько 2 МеВ. Миттєві нейтрони випромінюються уламками поділу рівноімовірно в усіх напрямках.

　　　　Утворені в результаті реакції вторинні частинки, реєструються відповідними детекторами, аналізуються, даючи відповідь, наявні чи відсутні в досліджуваному зразку заборонені ізотопи, їх маса, збагачення і т. д. Очевидно, що метод вимушеного поділу вимагає наявності досить потужного потоку ТН. Таке джерело на базі поліетиленової кулі-сповільнювача і медичного генератора швидких нейтронів був нами запропонований в роботі [5].

Метою цієї роботи є обговорення можливості створення автономної установки для знаходження ядерних елементів поділу у зразках, в тому числі і таких, що знаходяться в замкнутих об'ємах. Створення такого пристрою вимагає ретельного попереднього розгляду, відповідних аналітичних розрахунків, економічного обгрунтування і т. д. Тому основні зусилля першого етапу роботи планується направити на:

1. обгрунтування за допомогою сучасного програмного забезпечення застосування тих чи інших конструктивних елементів, їх розмірів, розташування в просторі та ін.;
2. визначення переліку необхідних приладів і обладнання;
3. розробку і створення опорного нейтронного поля;
4. проведення технічних і організаційних заходів, спрямованих на безпеку обслуговуючого персоналу під час роботи з нейтронним джерелом і матеріалами, що діляться;
5. монтаж стенду для наладки, тестування і підготовки конструкції для введення в експлуатацію.

Відразу ж відзначимо, що в роботі не розглядається можливість знаходження кількості матеріалів, що діляться, визначення ізотопного складу, збагачення і т. д. У принципі, це подальша перспектива другого етапу досліджень.

ДЖЕРЕЛО ОПОРНОГО ПОЛЯ ТЕПЛОВИХ НЕЙТРОНІВ

При розробці детекторів нейтронного потоку однією з основних проблем є тестування і калібрування приладів, що використовуються. У лабораторній практиці найбільш доступними і широко використовуваними пристроями для градуювання і вивчення характеристик детекторів є конструкції на базі опорних полів радіонуклідних джерел. Це пов'язано з тим, що при розміщенні випромінювачів у різних уповільнюючих середовищах, можна сформувати опорні поля випромінювання з різними характеристиками. В якості сповільнювача використовують водневомісне середовище, як правило, поліетилен (ПЕ) через відповідні механічні, хімічні та інші властивості, а також зручності при експлуатації. Номенклатура таких джерел широка. Їх параметри залежать від виду використаного радіоізотопу, розміру активної зони, конструкції, використаних матеріалів і т. д. Найчастіше перевага віддається двом типам опорних полів, які створюються на базі атестованих випромінювачів ^{252}Cf [6] або ^{239}Pu-Be [7]. Обидва джерела мають суцільний спектр і високий рівень γ-фону.
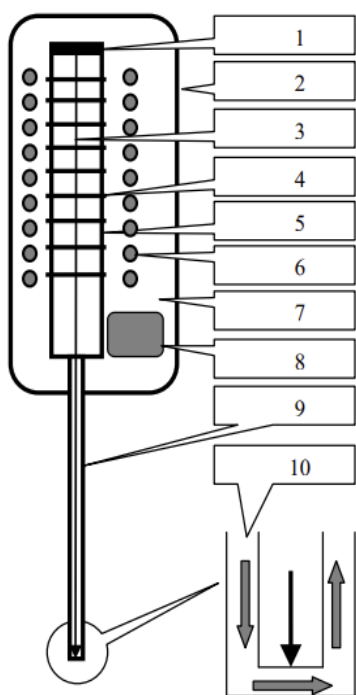

Рис. 1. Блок-схема ПВН. 1 - джерело дейтронів; 2 – кожух; 3 – дейтрони; 4 - прискорювальні електроди; 5 - вакуумная трубка; 6 - градиєнтні кільця; 7 - елегаз; 8 – вакуумний насос; 9 - іонопровід; 10 - вода

У даній роботі пропонується, з використанням досвіду [6-7], створити опорне поле ТН на основі ПЕ кулі-сповільнювача і портативного випромінювача нейтронів (ПВН) НДК «Прискорювач» ННЦ ХФТІ, розробленого на основі електростатичного прискорювача дейтронів [8-9]. На рис. 1 показана блок-схема ПВН.

Принцип роботи установки наступний. Прискорені дейтрони електростатичного прискорювача направляються у вузький іонопровід, пройшовши який, частинки фокусуються на ^{9}Be мішені розміром 10×10 мм. Довжина трубки для прискорення $\leq 0,6$ м. Нейтрони генеруються в результаті реакції $^{2}H + ^{9}Be \rightarrow ^{10}B + n$. Очікуваний потік нейтронів $\sim 10^{9}$ н·с$^{-1}$ у кут 4π з середньою енергією $\sim 2,5$ МеВ. Перевагою даної конструкції (у порівнянні з [6,7] і подібними аналогами) є відсутність потужного, стаціонарного джерела випромінювання. Нейтрони генеруються тільки під час санкціонованого включення ПВН. Крім того, використання ^{252}Cf і ^{239}Pu-Be випромінювачів коштує значно дорожче, ніж робота запропонованого приладу. Додаткова зручність полягає в тому, що опромінення доброякісних і злоякісних новоутворень (як це припускали автори [8-9]) або, наприклад, різних вантажів і виробів можна проводити або швидкими нейтронами (ШН) Ве-випромінювача ПВН, або тепловим полем того ж джерела, розташованого у центрі ПЕ сповільнювача. Отже, конструкція може застосовуватися не тільки для лікування онкологічних захворювань, але й при необхідності для опромінення ручної поклажі пасажирів аеропортів, поштових відправлень, виробів і вантажів з метою знаходження в їхньому складі ядерних матеріалів [10].

Заради справедливості відзначимо, що нейтрони для визначення ядер урану і плутонію в радіоактивних відходах використовувалися в ННЦ ХФТІ, починаючи з 2000-х (див., зокрема, роботу [11]). З цією метою застосовувався лінійний прискорювач електронів ЛПЕ-300. Енергія електронів 20 МеВ, середній струм 2 мА, частота 50 Гц, інтенсивність нейтронів $\sim 10^{12}$ н·с$^{-1}$.

В експерименті [11] у матриці з 10 кг піску розміщувалися зразки ^{238}U з 2% збагаченням ^{235}U. За час експозиції 600 с було виявлено мінімальну кількість ^{235}U – 0.012 г, що відповідало концентрації $1,2 \cdot 10^{-6}$ г·г$^{-1}$. Порівняння показує, що генератор на основі ПВН, є значно легшим, простішим, дешевшим, ніж складний, громіздкий, прив'язаний до наукового центру ЛПЕ-300, але, в той же час, має інтенсивність потоку приблизно на три порядки менше, що не дозволяє проводити дослідження певного класу.

ПОШУК ЯДЕРНИХ МАТЕРІАЛІВ

Під час митного огляду, перш за все, важливий сам факт негайного виявлення нелегального транспортування елементів поділу. Більш ретельна інспекція може бути проведена із застосуванням спеціального обладнання після затримання підозрілих громадян або транспорту. В роботі [10] показано, що існує реальна можливість знаходження ядерних матеріалів, якщо використовувати сповільнювачі з вмістом водню і імпульсні нейтронні генератори з виходом $(10^7 - 10^8)$ н·с$^{-1}$. Вміст ^{235}U і ^{239}Pu масою $(5 - 10)$ г можна визначити з ймовірністю 99,9% за $(5 - 7)$ с роботи. При цьому доглядові комплекси, які використовуються для запобігання обігу елементів поділу мають відповідати таким основним умовам [10]:

1. вихід нейтронного джерела визначається радіаційною обстановкою в обслуговуваних приміщеннях і не повинен перевищувати $(10^7 - 10^8)$ н·с$^{-1}$;
2. джерело випромінювання повинно вимикатися в перервах між циклами робіт;
3. не повинно бути радіоактивного забруднення приміщення навіть при повному руйнуванні джерела;
4. простота конструкції, малі розміри радіаційного захисту і порівняно низька вартість;
5. прийнятний час експлуатації без заміни джерела нейтронного випромінювання.

У перерахованих умовах роботи радіаційної небезпеки, пов'язаної з активацією досліджуваних предметів, немає. Лише поблизу зовнішньої поверхні установки існує зона розміром не більше 0,5 м, де рівень опромінення персоналу може перевищити граничні дози. Однак у цій зоні забезпечується автоматичне переміщення вантажу.

У багажній камері існує деякий нерівномірний розподіл щільності потоку ТН, обумовлений положенням джерела відносно об'єму, що інспектується. Але градієнт поля, в крайньому випадку, в разі імпульсного випромінювача, малий [10]. Як видно, описані вище вимоги для успішного визначення матеріалів, що діляться, повністю відповідають режимам роботи ПВН.

Пропонований експеримент являє собою послідовний ряд процедур. Джерело ШН нейтронів ПВН з інтенсивністю 10^9 н·с$^{-1}$ розміщується в центрі ПЕ кулі. Вихідний потік, уповільнених до теплових енергій нейтронів, направляється на досліджуваний об'єкт. При наявності в об'ємі ядер поділу відбувається їх взаємодія з ТН, у результаті чого вони розвалюються. Реакція супроводжується випромінюванням вторинних продуктів поділу.

На практиці моніторинг ТН, у більшості випадків проводиться пропорційними ^{3}Не-лічильниками, заповненими сумішшю $(95 - 97)$% ^{3}He і Ar. Детектори витримують опромінення до $\sim 10^{13}$ н·см$^{-2}$ і реєструють відносно слабкі потоки в присутності γ-фону ≤ 1 Р/год. Достатньо великий обсяг детектора, забезпечує хорошу ефективність взаємодії ТН з ^{3}Не. Окрім того, за робочим діапазоном енергій, простоті конструкції, дешевизні, і пригніченням γ-квантів, лічильник перевершує інші моделі. У таблиці 1 показана імовірність взаємодії ТН і фотонів з матеріалами лічильника [12]. Видно, що має місце сильне пригнічення γ-квантів з енергією ~ 1 МеВ.

Таблиця 1.

Імовірність взаємодії нейтронів і γ-квантів у пропорційному ^{3}Не-лічильнику

Тип материалу детектора	Імовірність взаємодії	
	Теплові нейтрони	Фотони з енергією 1 МеВ
^{3}Не у трубці діаметром 2,5 см і тиском 2 атм	0,77	0,0001

Іноді, надмірно велика кількість γ-квантів небажана для того чи іншого дослідження, що вимагає застосування захисного екрана. Як правило, це свинець. При опроміненні детектора нейтронами поділу з енергією 1 МеВ у присутності γ-випромінювання з енергією 1 МеВ захист зі свинцю товщиною 5 см, поглинає $\sim 0,1$% нейтронів і 90% γ-квантів [12].

У випадку реєстрації ШН, їх попередньо термалізують до теплових енергій. На практиці було виявлено, що застосування сповільнювача збільшує габарити і вагу блоку детектування, а також знижує ефективність реєстрації нейтронів до 10% [13-14]. Один з перших ефективних лічильників ШН був розроблений у 1947 р. Це була довга камера, заповнена газом BF$_3$ з 96% збагаченням, і парафіновий сповільнювач. Ефективність реєстрації нейтронів практично не залежала від їх енергії в області 10 кеВ – 3 МеВ. У численних аналогах, створених у подальшому, діапазон енергії, що реєструється, мав обмеження ≤ 10 МеВ. Значно пізніше T.W. Bonner із співробітниками запропонував систему [15], засновану на використанні сповільнювачів нейтронів сферичної форми і чутливого детектора, розміщеного у центрі. Устаткування дозволяє проводити вимірювання полів у діапазоні енергій від теплових до багатьох ГеВ.

Зрозуміло, що з усієї кількості частинок, що виникають в результаті реакції поділу, в детектор потрапляє лише частина, пропорційна $S·ε·R^{-2}$, де S – площа детектора, $ε$ – ефективність рахування детектора, R - відстань до детектора. Тому, для підвищення ефективності реєстрації нейтронів бажано створити «лінійку детекторів», що утворюють замкнену систему навколо вимірювальної камери. У даному випадку на першому етапі найпростішої «лінійкою» можуть слугувати три довгих металевих пропорційних ^{3}He-лічильника СНМ-66. Діаметр 25,5 мм, довжина 601,5 мм, робоча напруга 1600 В, ефективність до ТН 80% [16]. Даний детектор і його параметри обрані в якості прикладу з урахуванням середнього розміру ручної поклажі, дозволеної для провезення в авіалайнерах, 55×40×20 см (по довжині, ширині, висоті) або 115 см у сумі по трьом вимірам [17].

Описані вище газонаповнені детектори розроблені в 60-х роках і до теперішнього часу їх характеристики іноді не відповідають висунутим вимогам. Нещодавно для контролю нейтронного потоку пройшли атестацію нові детектори на основі оксидних і напівпровідникових сцинтиляторів [14,18] виробництва Харківського інституту сцинтиляційних матеріалів НАН України.

РЕЄСТРАЦІЯ НЕЙТРОНІВ ТВЕРДОТІЛЬНИМИ ЛІЧИЛЬНИКАМИ

Дослідження останнього десятиліття, показали, що детектори на базі оксидних і напівпровідникових сцинтиляторів реєструють теплові і швидкі нейтрони не гірше інших лічильників, що мають застосування в науці і техніці. Використання, наприклад, датчика нейтронного випромінювання на основі кристала $CdWO_4$ або CWO показало, що він з успіхом замінює дорогі ^{3}He пропорційні лічильники [18]. Експериментально доведено можливість реєстрації ТН і ШН неорганічними сцинтиляторами з високим $Z_{ефф}$ з ефективністю ~ (40 - 50)%, що в кілька разів вище, ніж у детекторах, що традиційно використовуються. Крім того, за рядом параметрів, таких як габарити, вага, дешевизна, навіть перевершують їх. Найбільш імовірним механізмом ефективної реєстрації нейтронів вважається реакція непружного розсіяння (n,n′γ). Недоліком сцинтиляторів є те, що вони крім нейтронів активно реєструють γ-випромінювання. На рис. 2 наведена блок-схема пристрою, яким користувалися у всіх проведених експериментах [14]. Позначення: 1 – ^{239}Pu-Be; 2 – кристал; 3 – ФЕП R1306; 4 – і 5 – поглинач ТН GdO у вигляді циліндра діаметром 40 мм і кришки товщиною $d = 10$ мм; 6 – і 7 – свинець $d = 40$ і 4 мм, відповідно.

Ефективність реєстрації (ЕР) швидких нейтронів визначалася методом внутрішнього рахування γ-квантів, що з'являються в сцинтиляторі з реакції (n,n′γ), які мають енергію (10 – 300) кеВ. Оцінка ефективності та чутливості проведена за допомогою ^{239}Pu-Be джерела (0,1 - 10,7) МеВ і системи детектування сцинтилятор - ФЕП, яка реєструвала фотони в різних енергетичних діапазонах. Крім того, вимірювання γ-спектрів розсіяних нейтронів, проводилися з випромінювачем ^{252}Cf і блоком реєстрації сцинтилятор - лавинний фотодіод ЛФД S 8664-55 Hamamatsu. Ефективність реєстрації ШН для CWO 10×10×10 мм^3 в енергетичному діапазоні (70 - 800) кеВ 28%.
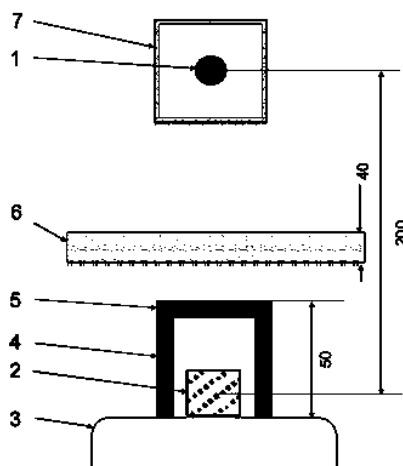

Рис. 2. Блок-схема установки

Спектри γ-випромінювання, здобуті при взаємодії ШН з різними типами сцинтиляторів розміром 10×10×10 мм, показують, що ЕР швидких нейтронів мало відрізняються для сцинтиляторів одного і того ж розміру. Області енергій переважної реєстрації γ-квантів приблизно однакові для всіх досліджених зразків. У той же час чутливість детекторів пропорційна геометричним розмірам. Результати вимірювань ЕР [14] ШН і ТН сцинтиляторами CWO, DGO, GSO, ZnWO, ZnSe, LiI(Eu) та ін. в області енергій (10 - 300) кеВ проілюстровані в таблиці 2. Наведені величини узгоджуються з даними, які відомі з літератури [19]. Наведені вище параметри оксидних і напівпровідникових сцинтиляторів з високим ефективним зарядом $Z_{ефф}$ ~ (33 - 75) і реєстрацією γ-випромінювання в енергетичному вікні (10 - 300) кеВ, підходять для детектування миттєвих нейтронів вимушеного поділу ядер.

Відзначимо, що в експериментах γ-спектрометри вимірювали як повну швидкість рахування, тобто для всього діапазону енергій, так і незалежно по чотирьом енергетичним вікнам: 30 - 300, 300 - 1000, 1000 – 1300, 1300 – 3000 кеВ. Це давало можливість підвищити чутливість системи при знаходженні конкретних джерел випромінювання, а також визначити тип ізотопу по ідентифікації вікна, де сталося виявлення (у випадку наявності одного типу ізотопу).

Таблиця 2.

Ефективність реєстрації, %

Сцинтилятор	ZnSe	NaJ	LiJ	CsJ	GSO	ZnWO	CWO	DGO	LiJ (реакція Li(n,α)T)
$Z_{ефф}$	33	51	52	54	59	61	66	75	52
ШН	43	18	25	20	46	54	42	48	0.66
ТН	0	30	90	0	65	44	67	34	93

ВИЯВЛЕННЯ ^{235}U І ^{239}Pu ЗА ДОПОМОГОЮ γ-ВИПРОМІНЮВАННЯ ПРИ $E_γ$ > 4900 кеВ

Як відомо, продукти поділу крім нейтронів випромінюють також фотони, за допомогою яких можна визначити ізотопи поділу. Автори [20] запропонували використовувати для виявлення ^{235}U і ^{239}Pu високоенергетичну частину γ-спектра більше 4900 кеВ. У цьому випадку γ-випромінювання супутніх елементів не заважає аналізу. Висока енергія γ-квантів дає змогу обстежити масивні зразки, застосувати фільтрацію низькоенергетичного випромінювання. Особливості пропонованого підходу роблять його привабливим при розвідці родовищ урану, знаходження ізотопів поділу в закритих об'ємах, визначення відносного вмісту ^{235}U і ^{239}Pu у відпрацьованих і свіжих ТВЕЛ-ах і т.д. Для аналітичних вимірювань можуть бути використані реактор, нейтронний генератор, радіоізотопні джерела ^{252}Cf і ^{239}PuBe.
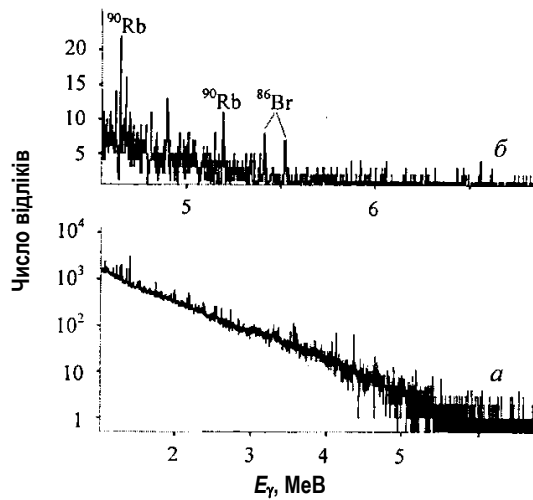

Рис. 3. γ-Спектр продуктів поділу ^{235}U

Слід зазначити, що фотони, які виникають при взаємодії запізнілих нейтронів зразка, ні в якому разі не є в пропонованому методі перешкодою. Їх реєстрація тільки підвищує ефективність методу. Для детектування γ-випромінювання крім напівпровідникового германієвого детектора (HPGe) з високим енергетичним розрізненням підходить і γ-спектрометр з кристалом NaI(Tl), який оснащений захистом від низькоенергетичного γ-випромінювання і нейтронів. При цьому особливу увагу слід звернути на коректний вибір нижньої межі використовуваного γ-спектра, щоб виключити можливий внесок ліній ^{49}Ca (4738 кеВ) і ^{88}Rb (4742 і 4853 кеВ) близьких до енергії 4900 кеВ. На рис. 3 наведено детальний γ-спектр продуктів поділу ^{235}U, виміряний HPGe-детектором на нейтронному пучку IP-8. Вимірювання проведено для діапазону 1000 - 6700 (а), 4550 - 6850 кеВ (б). Оптимальний режим роботи: 120 с опромінення, 60 с витримка і 120 с вимірювання.

Можливості визначення відносного вмісту ^{235}U і ^{239}Pu пов'язані з різним виходом деяких продуктів поділу. Зокрема, для чітко виражених у спектрі на рис. 3 піків ^{86}Br і ^{90}Rb виходи відрізняються в 3 рази. Не виключено, що ще більш перспективним може виявитися виділення із спектру ліній нижче 5 МеВ. Так, інтенсивність γ-ліній ^{106}Tc 2789 і 3186 кеВ на акт поділу ^{239}Pu у 10 разів вище, ніж при поділі ^{235}U.

СПОНТАННИЙ ПОДІЛ ^{235}U і ^{239}Pu

Визначення параметрів уранового зразка, засноване на вимірюванні природного γ-випромінювання ^{235}U, є широко використовуваним методом неруйнівного аналізу. Знаходження ядер урану і визначення ступеня його збагачення засновано на реєстрації одиночної γ-лінії 185,7 кеВ. Попередньо випромінювання пропускають через фільтр і коліматор. Фільтр поглинає γ-кванти в області енергій нижче 185,7 кеВ, а за допомогою коліматора встановлюється площа видимої детектором поверхні. γ-Лінія 185,7 кеВ утворюється з імовірністю (57,5±0.9)%. Її питома інтенсивність ~ 4,3·10^4 с$^{-1}$·г$^{-1}$ [12]. При віддаленні зразка від детектора у відсутності коліматора ефективність реєстрації буде зменшуватися за законом близьким до $1/r^2$, де r – радіус детектора.
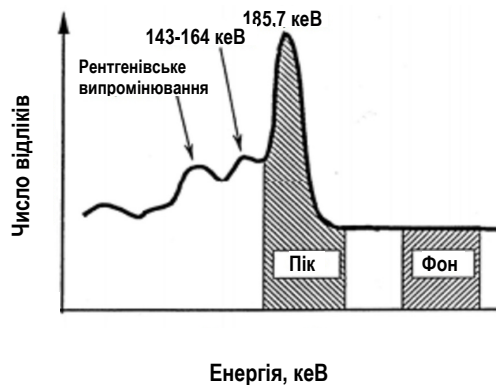

Рис. 4. γ-спектр ^{235}U, виміряний NaI(Tl)-детектором

У той же час його використання дозволяє зменшити залежність від цього фактору, але не усуває її повністю. Чим менше діаметр пропускного отвору, тим ближче реальна геометрія до ідеальної, тим менший вплив ефекту $1/r^2$.

Якщо урановий зразок досить великий, то в його глибині γ-кванти повністю поглинаються і не дають ніякого вкладу на поверхні. Тобто, зі збільшенням товщини потік γ-променів на поверхні досягає рівноважного значення, яке практично не залежить від фізичної форми зразка. Для чистих уранових сумішей це значення пропорційне величині збагачення. Фотони бажано реєструвати напівпровідниковими HPGe-детектором. Висока енергетична роздільна здатність дозволяє повністю відокремити пік 185,7 кеВ від сусідніх максимумів. Між ними з'являються рівні ділянки фону, що полегшує задачу визначення площі фотопіка і швидкості рахування. Однак можна отримувати дані, застосовуючи сцинтиляційний γ-спектрометр на основі монокристала NaI(Tl). Спектр γ-випромінювання ^{235}U, виміряний NaI(Tl)-детектором, показаний на рис. 4. Видно, що наявність у

γ-спектрі окремого піка при енергії 185,7 кеВ вказує на присутність у досліджуваному об'ємі ^{235}U. Швидкість рахування в діапазоні навколо піку залежить не тільки від концентрації ^{235}U у зразку. Фотопік розташований на досить великій підкладці, яка представляє континуум спектра комптонівських електронів. Для калібрування системи детектування потрібен відповідний еталон – атестований урановий зразок. Точність аналізу залежить від ступеня збагачення і становить (1 - 5)% при вимірюванні за допомогою NaI(Tl)-детектора і (0,1 - 1)% для HPGe-детектора. Головний недолік методу вимірювання збагачення, заснованого на дослідженні лінії 175,7 кеВ – необхідність калібрування системи реєстрації для кожного нового контейнера зі зразком урану. Насправді існує три енергетичних діапазони в спектрі γ-випромінювання, які можна вибрати для визначення збагачення урану. Це 53 - 68, 84 - 130 і 185 - 1001 кеВ. Усі наведені діапазони включені до відповідних програмних кодів для розрахунку збагачення урану.

На результати аналізу за описаною схемою (фільтр, коліматор) можуть вплинути два фактори. Це неврахована при обчисленнях геометрія експерименту та інтерференція з іншими піками. Ще одна систематична похибка, що виникає при визначенні збагачення, це інтерференція γ-ліній 185,7 кеВ від ^{235}U і 186 кеВ продуктів поділу ^{238}U. При хорошій роздільній здатності внесок від цього піка в досліджуваний фотопік 185,7 кеВ для природного урану складає всього 0,1% і стає дуже незначним при збільшенні збагачення. Відповідно для сильно збіднених зразків внесок від випромінювання ^{238}U слід враховувати.
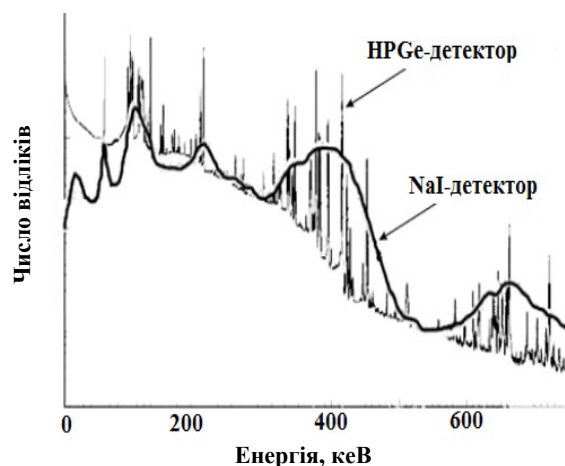
Таблиця 3.

Спектральні області ^{239}Pu

Спектральні області, кеВ	^{239}Pu	
	E_γ, кеВ	Інтенсивність, квант·с$^{-1}$·г
40 - 60	51,63	6,19·10^5
90 - 105	98,78	2,80·10^4
120 - 450	129,3	1,44·10^5
	203,5	1,28·10^4
	345,0	1,28·10^4
	375,0	3,60·10^4
	413,7	3,42·10^4
450 - 800	646,0	3,42·10^2
	717,7	6,29·10^1

Рис. 5. γ-Спектр ^{239}Pu, виміряний NaI(Tl)- і HPGe-детекторами

Що стосується плутонію, то метод неруйнівного аналізу ізотопного складу матеріалів, що містять плутоній (більшість зразків плутонію містять ^{238}Pu, ^{239}Pu, ^{240}Pu, ^{241}Pu і ^{242}Pu), є найбільш розробленим методом і не вимагає калібрування за допомогою еталонів [2,12]. У розрахунках використовуються відомі значення фундаментальних фізичних констант і внутрішні калібрування. Цей підхід дозволяє проводити вимірювання ізотопного складу в зразках різних розмірів, форми, фізичного і хімічного складу всередині контейнерів з невідомими розмірами і хімічним вмістом. На рис. 5 наведений γ-спектр ^{239}Pu з 93% збагаченням, виміряний HPGe- і NaI(Tl)-детекторами. Як видно з рисунка, плутоній не має одиночних, інтенсивних γ-ліній у спектрі, що помітно відрізняються від інших. Тому для ізотопних вимірювань використовуються відомі спектральні області, які наведені в таблиці 3. Принципові підходи, які використовуються для визначення збагачення урану, також можуть бути застосовані і для знаходження ізотопного складу плутонію. Хоча є і ряд відмінностей. У даний час, для визначення ізотопного складу урану і плутонію найчастіше використовуються математичні коди, розроблені в Лос-Аламоській лабораторії (США). Це коди MGA (MGAU для визначення збагачення урану) і FRAM [12].

ВИСНОВКИ

Обговорюється перспектива створення автономної установки НДК «Прискорювач» ННЦ ХФТІ для виявлення ядерних матеріалів, що діляться, у виробах і вантажах, у тому числі і тих, що знаходяться в замкнутих об'ємах. Розглянуто різні варіанти аналізу, що включають опромінення досліджуваних зразків опорним полем теплових нейтронів; реєстрацію миттєвих нейтронів поділу не тільки традиційним способом за допомогою поліетиленового сповільнювача і пропорційного ^{3}He-детектора, а також без сповільнювача, застосовуючи оксидні або напівпровідникові сцинтилятори, що прямим чином перетворюють енергію випромінювання в електричний сигнал; підходи, які використовують високоенергетичну частину γ-спектра уламків поділу більше 4900 кеВ, а також метод, що застосовано в пасивному неруйнівному аналізі ^{235}U, який

заснований на вимірюванні та аналізі γ-лінії з енергією 185,7 кеВ. Показано, що запропонована установка здатна визначити присутність найбільш важливих ядерних матеріалів у досліджуваних виробах, поштових відправленнях, багажі пасажирів і т. д.

ORCID IDs
Eduard L. Kuplennikov, https://orcid.org/0000-0001-9102-3459; **Mykola I. Ayzatsky,** https://orcid.org/0000-0003-4706-9614;
Alexander N. Vodin, https://orcid.org/0000-0002-3774-1051; **Olexii S. Deiev,** https://orcid.org/0000-0003-4565-9039;
Stanislav N. Olejnik, https://orcid.org/0000-0003-0300-0658; **Iryna S. Timchenko**, https://orcid.org/0000-0003-2917-5026;
Sergii S. Kandybei, https://orcid.org/0000-0003-3598-0427

REFERENCES
[1]   M. Gaisinsky, and J. Adlov, *Радиохимический словарь элементов* [*Radiochemical Dictionary of Elements*], (Atomizdat, Moscow, 1968), pp. 255. (in Russian)

[2]   I.N. Beckman, *Ядерное оружие* [*Nuclear Weapons*], (MGU, Moscow, 2010), pp. 21. (in Russian), www.profbeckman.narod.ru/Uran.files/Glava15.pdf. (in Russian)

[3]   S.G. Plachkova, in: *Физические основы работы ядерных реакторов,* [*Physical bases of operation of nuclear reactors*], (Energetika, Kyiv, 2013). (in Russian)

[4]   I.N. Beckman, *Ядерная Физика. Курс лекций* [*Nuclear physics. Lecture course*], (MGU, Moscow, 2010), pp. 511. (in Russian)

[5]   V. Krasilnikov, and E. Kuplennikov, Danish Scientific Journal. http://www.danish-science.org/wp-content/uploads/2020/02/DSJ_32_1.pdf.

[6]   E.A. Belogorlov, G.I. Britvich, G.I. Krupny, V.N. Lebedev, V.S. Lukanin, A.V. Makagonov, V.N. Peleshko, and Ya.N. Blooming, *Методические вопросы применения многошарового спектрометра Боннера в радиационных исследованиях* [*Methodological issues of using the Bonner multi-ball spectrometer in radiation research*], (PREPRINT IFVE 85-3, Serpukhov, 1985), pp. 22. (in Russian)

[7]   Yu.V. Mokrov, and S.V Morozova, Pisma v ECHAYA, **11**(2), 219-232 (2014), (in Russian), http://www1.jinr.ru/Pepan_letters/panl_2014_2/10_mok.pdf

[8]   A.N. Dovbnya, V.A. Tsymbal, A.F. Stoyanov, D.Y. Shahov, and I.N. Zaytsev, Problems of atomic science and technology. Series: "Nucl. Phys. Invest.", **3**(103), 84-86 (2016), https://vant.kipt.kharkov.ua/ARTICLE/VANT_2016_3/article_2016_3_84.pdf.

[9]   A.F. Stoyanov, A.N. Dovbnya, and V.A. Tsymbal, Problems of atomic science and technology. Series: "Nucl. Phys. Invest.", **6**(112), 172-174 (2017), https://vant.kipt.kharkov.ua/ARTICLE/VANT_2017_6/article_2017_6_172.pdf.

[10] V.L. Romodanov, V.V. Afanasyev, A.G. Belevitin, V.K. Sakharov, and A.A. Ignatov, Atomnaya Energiya, **101**(2)**,** 125-130 (2006), (in Russian), http://elib.biblioatom.ru/text/atomnaya-energiya_t101-2_2006/go,0/.

[11] V.V. Kirichenko, L.A. Makarenko, and V.I. Noga, Problems of atomic science and technology. Series "Nucl. Phys. Invest.", **2**(41), 111-115 (2003), https://vant.kipt.kharkov.ua/ARTICLE/VANT_2003_2/article_2003_2_111.pdf.

[12] V.I. Boyko, and M.E. Silaev, *Методы и приборы для измерения ядерных и других радиоактивных материалов* [*Methods and instruments for measuring nuclear and other radioactive materials*], (MNTTs, Moscow, 2011), pp. 356. (in Russian)

[13] A.Yu. Buki, and S.A. Kalenik, Journal of Kharkov National University. Series: "Nuclei, Particle, Fields", **2**(54), 110-113 (2012), (in Russian), https://periodicals.karazin.ua/eejp/article/view/13828/13019.

[14] V.D. Ryzhikov, *Международная конференция ИСМА НАН Украины «Разработка сцинтилляционных детекторов и создание устройств на их основе»* [*International Conference ISMA NAS of Ukraine "Development of scintillation detectors and creation of devices based on them"*], (KHISM, Kherkov, 2012) pp. 1-35. (in Russian), www.2012.ismart.kharkov.ua/presentations/23/23_11-00_Ryzhikov.pdf.

[15] R.L. Blamblett, R.J. Ewing, and T.W. Bonner, Nuclear instrument and methods, **9**, 1-12 (1960), https://doi.org/10.1016/0029-554X(60)90043-4.

[16] M.L. Baranochnikov, *Приемники и детекторы излучений. Справочник* [*Radiation receivers and detectors. Reference Book*], (DMK Press, Moscow, 2012), pp. 640. (in Russian)

[17] A. Zakharova, *Как правильно перевозить ручную кладь в самолете. Размер и вес ручной клади* [How to properly transport hand luggage on the plane. Size and weight of carry-on baggage], (Skyscanner, Moscow, 2019), pp. 2-3. (in Russian), https://www.skyscanner.ru/news/pravila-provoza-ruchnoi-kladi.

[18] V.D. Ryzhikov, B.V. Grynyov, G.M. Onishchenko, L.A. Piven, O.K. Lysetska, L.L. Nagornata, I.M. Zenya, and A.Y. Berezhnoy, Telecommunications and Radio Engineering, **71**(18), 1665-1686 (2012), https://doi.org/10.1615/TelecomRadEng.v71.i18.50.

[19] M. Anelli, G. Battistoni, S. Bertolucci, C. Bini, P. Branchini, C. Curceanu, G. De Zorzi, A. Di Domenico, B. Di Micco, A. Ferrarie, P. Gauzz, S. Giovannella, F. Happacher, M. Iliescu, M. Martini, S. Miscetti, F. Nguyen, A. Passeri, A. Prokofiev, P. Sala, B. Siascia, and F. Sirghi, Nuclear instrument and methods, **A580**, 368-372 (2007), https://doi.org/10.1016/j.nima.2007.08.005.

[20] A.M. Demidov, L.I. Govor and I.V. Mikhailov, Atomnaya Energiya, **98**(5), 365-370 (2005), (in Russian), http://elib.biblioatom.ru/text/atomnaya-energiya_t98-5_2005/go,0/.

АВТОНОМНА НЕЙТРОННА УСТАНОВКА ДЛЯ ВИЯВЛЕННЯ ЯДЕРНИХ МАТЕРІАЛІВ, ЩО ДІЛЯТЬСЯ
Е.Л. Купленніков, М.І. Айзацький, О.М. Водін, О.С. Деєв, С.М. Олійник, І.С. Тімченко,
С.С. Кандибей, О.С. Качан, Л.П. Корда, Ю.М. Солодовніков
ННЦ «Харківський фізико-технічний інститут»,
61108, Харків, Академічна 1

Обговорюється перспектива створення автономної нейтронної установки для виявлення ядерних матеріалів, що діляться, у зразках, у тому числі і в тих, що знаходяться у замкнутих об'ємах. Пропонується на основі поліетиленового шара-сповільнювача і портативного джерела швидких нейтронів, розробленого в НДК «Прискорювач» ННЦ ХФТІ на базі

електростатичного прискорювача дейтронів безперервної дії, отримати опорне поле теплових нейтронів. Отримане джерело теплових нейтронів планується використовувати для активації невеликих виробів і вантажів з метою виявлення в їхньому складі заборонених для переміщення речовин, що містять ^{233}U, ^{235}U і ^{239}Pu. Оперативне знаходження елементів поділу буде свідчити про спробу їх нелегального транспортування. Більш ретельна інспекція може бути проведена із застосуванням спеціального обладнання після затримання підозрілих вантажів, громадян або транспорту. Розглянута можливість реєстрації миттєвих нейтронів не тільки традиційним способом за допомогою поліетиленового сповільнювача і пропорційного ^{3}He детектора, але і без використання будь-якого сповільнювача, використовуючи оксидні або напівпровідникові сцинтилятори. Для виявлення матеріалів, що діляться, обґрунтовано метод використання високоенергетичної частини γ-спектру уламків поділу (більше 4900 кеВ), а також підхід, що застосовується у пасивному неруйнівному аналізі ^{235}U за γ-лінією з $E_γ = 185{,}7$ кеВ. Доведено, що запропонована установка для виявлення ядерних матеріалів, що діляться, здатна за допомогою методу неруйнівного контролю визначити присутність ізотопів ^{233}U, ^{235}U і ^{239}Pu у досліджуваних виробах і вантажах.

КЛЮЧОВІ СЛОВА: ядерні матеріали, що діляться, неруйнівний аналіз, джерело нейтронів, сповільнювач, теплові нейтрони, уламки поділу, миттєві нейтрони

АВТОНОМНАЯ НЕЙТРОННАЯ УСТАНОВКА ДЛЯ ОБНАРУЖЕНИЯ ДЕЛЯЩИХСЯ ЯДЕРНЫХ МАТЕРИАЛОВ

Э.Л. Купленников, Н.И. Айзацкий, А.Н. Водин, А.С. Деев, С.Н. Олейник, И.С. Тимченко,
С.С. Кандыбей, А.С. Качан, Л.П. Корда, Ю.Н. Солодовников

ННЦ «Харьковский физико-технический институт»,
61108, Харьков, Академическая 1

Обсуждается перспектива создания автономной нейтронной установки для выявления делящихся ядерных материалов в образцах, в том числе и находящихся в замкнутых объемах. Предлагается на основе полиэтиленового шара-замедлителя и портативного источника быстрых нейтронов, разработанного в НИК «Ускоритель» ННЦ ХФТИ на базе электростатического ускорителя дейтронов непрерывного действия, получить опорное поле тепловых нейтронов. Полученный источник тепловых нейтронов планируется использовать для активации небольших изделий и грузов с целью выявления в их составе запрещенных к перемещению веществ, содержащих ^{233}U, ^{235}U и ^{239}Pu. Оперативное нахождение делящихся элементов будет свидетельствовать о попытке их нелегальной транспортировки. Более тщательная инспекция может быть проведена с применением специального оборудования после задержания подозрительных грузов, граждан или транспорта. Рассмотрена возможность регистрации мгновенных нейтронов деления не только традиционным способом с помощью полиэтиленового замедлителя и пропорционального ^{3}He-детектора, но и без применения какого-либо замедлителя, используя оксидные или полупроводниковые сцинтилляторы. Для обнаружения делящихся материалов обоснован метод использования высокоэнергетической части γ-спектра осколков деления (больше 4900 кэВ), а также подход, применяемый в пассивном неразрушающем анализе ^{235}U по γ-линии с $E_γ = 185{,}7$ кэВ. Показано, что предложенная установка для выявления делящихся ядерных материалов способна с помощью метода неразрушающего контроля определить присутствие изотопов ^{233}U, ^{235}U и ^{239}Pu в исследуемых изделиях и грузах.

КЛЮЧЕВЫЕ СЛОВА: ядерные делящиеся материалы, неразрушающий анализ, источник нейтронов, замедлитель, тепловые нейтроны, осколки деления, мгновенные нейтроны

REGULARITIES OF LOW-TEMPERATURE DEFORMATION AND FRACTURE OF POLYIMIDE FILMS OF KAPTON H TYPE OF DIFFERENT THICKNESS

Viktory A. Lototskaya[a],*, Leonid F. Yakovenko[a], Evgeniy N. Aleksenko[a], Vyacheslav V. Abraimov[b], Wen Zhu Shao[b]

[a]B. Verkin Institute for Low Temperature Physics and Engineering of National Academy of Science of Ukraine
Avenue Nauky, 47, Kharkov, 61103, Ukraine
Corresponding Author: lototskaya@ilt.kharkov.ua
[b]Harbin Institute of Technology
Harbin, the People's Republic of China
Received October 5, 2020; last revised November 3, 2020; accepted November 6, 2020

The mechanical characteristics (limit of forced elasticity σ_{forc}, rupture stress σ_r, relative deformation to rupture ε_r) of polyimide films of kapton H type under uniaxial tension conditions along the direction of drawing in the temperature range (4.2-293 K), deformation rates (10^{-5} - 10^{-3} s^{-1}) and film thicknesses (25, 75 and 125 μm) were investigated. It is discovered, that the forced-elastic state remains for all films up to 4.2 K of all strain rates - $\sigma_{fors} < \sigma_r$. In this case, the reserve of elasticity significantly depends on the thickness of the film with a decrease in temperature. A sharp decrease in ε_r occurs in films: 125 μm thick - at 77 K, 75 μm thick - at 4.2 K. Two variants of deformation curves are possible in a 25 μm thick film at 4.2 K: with a short nonlinear stage or with a long one proceeding jumpily. The working surface of the samples that have undergone jump deformation is covered with a deformation relief, partially representing a delayed highly elastic deformation. The σ_{fors} limit is most sensitive to the strain rate. The nature of the strain rate sensitivity $\sigma_{fors}(\dot{\varepsilon})$ depends on the temperature and film thickness. The change to the opposite in the character of $\sigma_{fors}(\dot{\varepsilon})$ and $\sigma_r(\dot{\varepsilon})$ with a decrease in temperature to 4.2 K in 75 and 125 thick films was found for a first time. Change in the character of $\sigma_{fors}(\dot{\varepsilon})$ is not observed in 25 μm thick film which retains the maximum reserve of elasticity at 4.2 K.

KEYWORDS: polyimides, low temperatures, limit of forced elasticity, rupture stress, deformation

　　　　The study of the mechanical and structural properties of polyimides has been going on for decades, and the results of these studies in the field of normal and elevated temperatures are given in numerous articles, monographs and reference books. Since the end of the XX century, the widespread use of polymers of this class in cryogenics, astronautics and nuclear power began. Interest in the study of their properties has shifted to the area of low temperatures and the effect of radiation factors. It is known that most polymers, including polyimides, become embrittled below room temperature and, especially, the temperature of liquid nitrogen (77 K) [1, 2]. Only polypyromellitimide films (such as kapton H and PM) retain some deformability up to the temperature of liquid helium (4.2 K) [3,4] and are used (as thermal control coatings and screen-vacuum thermal insulation) in devices operating under extreme conditions. The films of this type are up to ~100 μm thick are most widely used.

　　　　The compliance of their mechanical properties with the required performance characteristics is one of the criteria for their applicability. These are, first of all, strength and deformability at different strain rates in a wide temperature range of 4.2-300 K. It is important to establish how the film thickness affects these characteristics at helium temperatures, where the elasticity of the films decreases. Another important aspect, already from the point of view of the physics of polymers, is the study of their ability to create a highly oriented structure at low temperatures, the establishment of the physical mechanisms of film shape change under these conditions, since these questions are still open.

　　　　In this work, we continued the study of the mechanical properties of polyimide films of the kapton H type, begun in [5], in wider ranges: temperatures (4.2-293 K), strain rates (10^{-5}-10^{-3} s^{-1}) and film thicknesses (25-125 microns).

MATERIAL AND METHOD OF RESEARCH

　　　　The objects of study were samples of thermoplastic film of aromatic polyimide – poly-4,4'-diphenylene oxide pyromellitimide, manufactured by PRC (People's Republic of China). Polyimide films kapton H (manufactured in the USA) and PM (manufactured in the Russian Federation) are their well-studied analogs. The thickness of the films was δ = 25, 75, and 125 μm.

　　　　The structure of films with a thickness of 75 and 125 μm in the initial state and after deformation to rupture at 293 and 77 K was previously investigated in [6] by X-ray diffraction analysis for reflection from the sample plane. Both films were found to be in an amorphous state upon delivery. A higher degree of ordering and a noticeable unevenness in the distribution of the density of the substance over the thickness was found in the initial film with a thickness of 125 μm. The change in the degree of ordering was observed only in a film with a thickness of 125 μm after deformation to rupture (i.e., into the stage of irreversible deformations). The formation of regions with long-range order occurred in it both after deformation at 293 K and at 77 K, which is in good agreement with the results of [7].Although in the film with δ= 75 μm, the contribution of irreversible deformation at 293 K was greater than in the film with δ= 125 μm.

The structure of a film with 25 μm thickness has not been studied. However, films with this type of monomer of small thickness (<70 μm), as a rule, are amorphous, according to the data which obtained by other authors in [1,7-9].

Two-blade samples according to State Standard 11262 (Fig. 1) with the tension axis along the direction of the film drawing were using a special die. The sample was fixed in testing machine with special clamping grippers, which gripped and pressed rollers with blades of non-working surfaces of the sample wrapped around them.
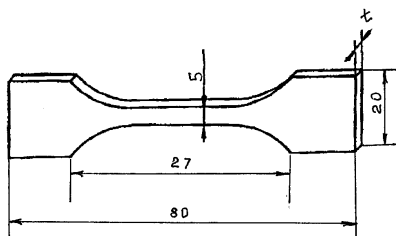

Figure. 1. The shape of the tensile test sample.

The samples deformation under uniaxial tension was performed using FPZ-100/1 tensile testing machine with a low-temperature unit, designed and created in the Institute for Low Temperature Physics and Engineering [10]. Film samples with a thickness of 25 μm were tested at three temperatures of 293, 77 and 4.2 K and three active rod moving speed $V_{def.}$= 0,085; 0,85 and 7,6 mm/min, and, correspondingly, with the strain rate $\dot{\varepsilon}$ =7·10⁻⁵, 7·10⁻⁴ and 6·10⁻³ s⁻¹ ($\dot{\varepsilon}$ =$V_{def.}$/L_o, where L_o is the initial working length of the sample). Film samples of 75 and 125 μm were tested at three temperatures with deformation rate $\dot{\varepsilon}$ = 7·10⁻⁵ s⁻¹ and with all rate $\dot{\varepsilon}$ at T=4,2 K. Data of investigations for films with a thickness of 75 and 125 microns with strain rates $\dot{\varepsilon}$ =7·10⁻⁴ and 6·10⁻³ s⁻¹ at 293 and 77 K were received earlier [5].

In the process of deformation a tensile diagram was recorded in the coordinates "load P-elongation ΔL", from which the following mechanical characteristics were determined: the apparent limit of forced elasticity, corresponding to the stress, at which the highly elastic deformation is 1% (according to State Standard 14236), $\sigma_{forc.}$ = $P_{1\%}$/S_o; rupture stress of the sample σ_r = P_r/S_o, where S_o is the initial cross section of the sample; relative deformation to rupture ε_r = ΔL_r/L_o, where ΔL_r elongation corresponding to the moment of the sample rupture, and L_o – value of the original working length of the sample.

Elongation to rupture ΔL_r can include same contributions: reversible (elastic) elongation ΔL_{elast}, associated with the unrelaxed elastic modulus of the polymer, elongation $\Delta L_{high\ el.1}$, due to highly elastic deformation reversible at the test temperature, elongation $\Delta L_{high\ el.2}$, due to delayed high elastic deformation, and elongation $\Delta L_{irrevers}$, corresponding to irreversible deformation that does not disappear upon heating up to the melting temperature T_m. The types of contributions may vary depending on the test temperature. The procedure for their determination is described in detail in [5]. In this work, we do not give the values of the contributions, but, the deformed to rupture films were annealed at 623 K (350°C) for 2 hours in air as in [5], to determine the presence of the contribution of irreversible deformation and the total value of highly elastic deformation ($\varepsilon_{high\ el.1}$ + $\varepsilon_{high\ el.2}$).

Before the low-temperature test, the sample in the deforming device was held in a cryostat with a refrigerant for at least 30 min.

All mechanical characteristics are presented below as average values based on the results of tests of 4 - 10 samples, depending on the magnitude of the spread of values under the given test conditions.

Fractures of the samples were studied using an optical microscope МБС-9.

RESULTS OF EXPERIMENTS

Deformation curves. Fig. 2 a,b shows typical curves "stress (σ)-deformation (ε)" of polyimide film samples of different thickness at temperatures 293, 77 and 4,2 K for the limiting deformation rates in this experiment – 7·10⁻⁵ s⁻¹ (Fig. 2a) and 6·10⁻³ s⁻¹ (Fig. 2b). It can be seen that, the tension diagrams for films with a thickness of 75 and 125 μm at all temperatures exhibit two stages: a linear stage associated with elastic deformation and a nonlinear stage including the contributions of highly elastic deformation (reversible with removal of the load and delayed) and at 293 K containing the contribution of irreversible deformation [5]. The first elastic linear stage occupies most of the deformation curves of samples of these films at temperature of 4.2 K. In this case, a stress jump is observed at a short nonlinear stage on the curves of some samples of films with a thickness of 75 μm at all deformation rates.

Curves (σ–ε) of films of 25 μm at temperatures of 293 and 77 K have three stages: linear elastic and two nonlinear. The slope coefficient dσ/dε is higher in the last third stage than in the second nonlinear stage. Samples of a thin film at 4.2 K at all test rates exhibit two different types of deformation curves: 1) 2-stage curves (σ – ε) similar to the other two films with a very short second nonlinear stage, monotonic or containing one or two jump of stress (Fig. 2, curves 1a), 2) curves with a noticeable (up to ε~35%) nonlinear stage of deformation proceeding jumpily (Fig. 2, curves 1b). Curves (σ – ε) are three-stage at the lowest strain rate $\dot{\varepsilon}$ = 7·10⁻⁵ s⁻¹ - the nonlinear range has two stages with different slope coefficients, as at higher temperatures.

Temperature influence on mechanical properties. Figure 3 shows the temperature dependences of the average values of mechanical characteristics: the limit of forced elasticity σ_{forc} (Fig. 3a, d), rupture stress σ_r (Fig. 3b, e) and relative deformation before rupture ε_r (Fig. 3c, f) of films of different thicknesses at two limiting strain rates, $\dot{\varepsilon}$ =7·10⁻⁵ s⁻¹ (Fig. 3 a,b,c) and $\dot{\varepsilon}$ =6·10⁻³ s⁻¹ (Fig. 3 e,f,g).
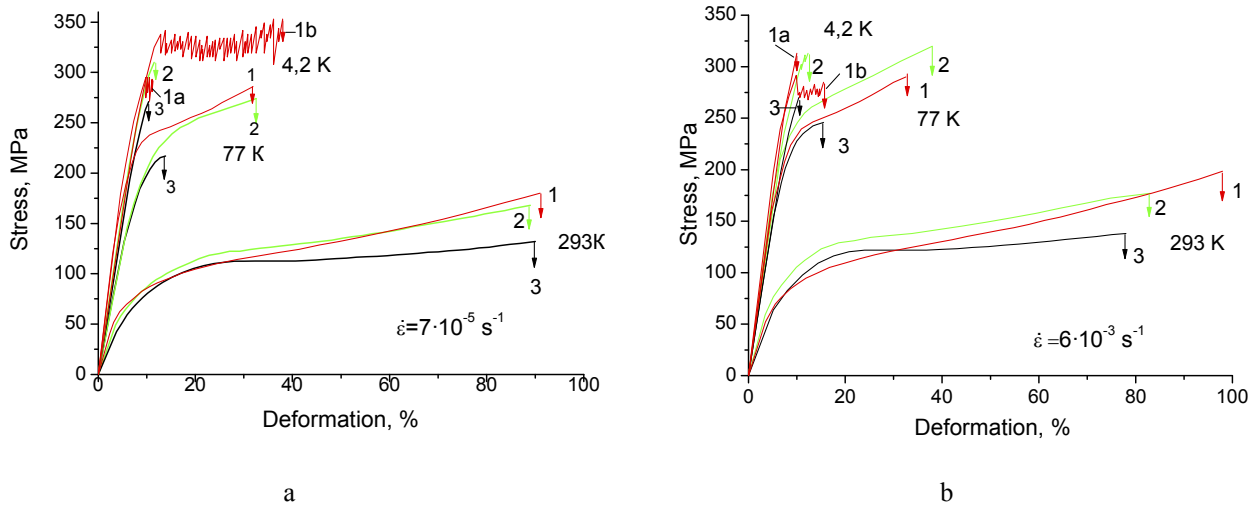
a   b

Figure. 2. The typical deformation curves of films of 25 μm (curves 1, 1a,b), 75 μm (curves 2) and 125 μm (curves 3) at interval temperatures 4,2-293 K and deformation rates: a) - $\dot{\varepsilon}$ =7·10⁻⁵ s⁻¹ , б) - $\dot{\varepsilon}$ =6·10⁻³ s⁻¹

a   b   c
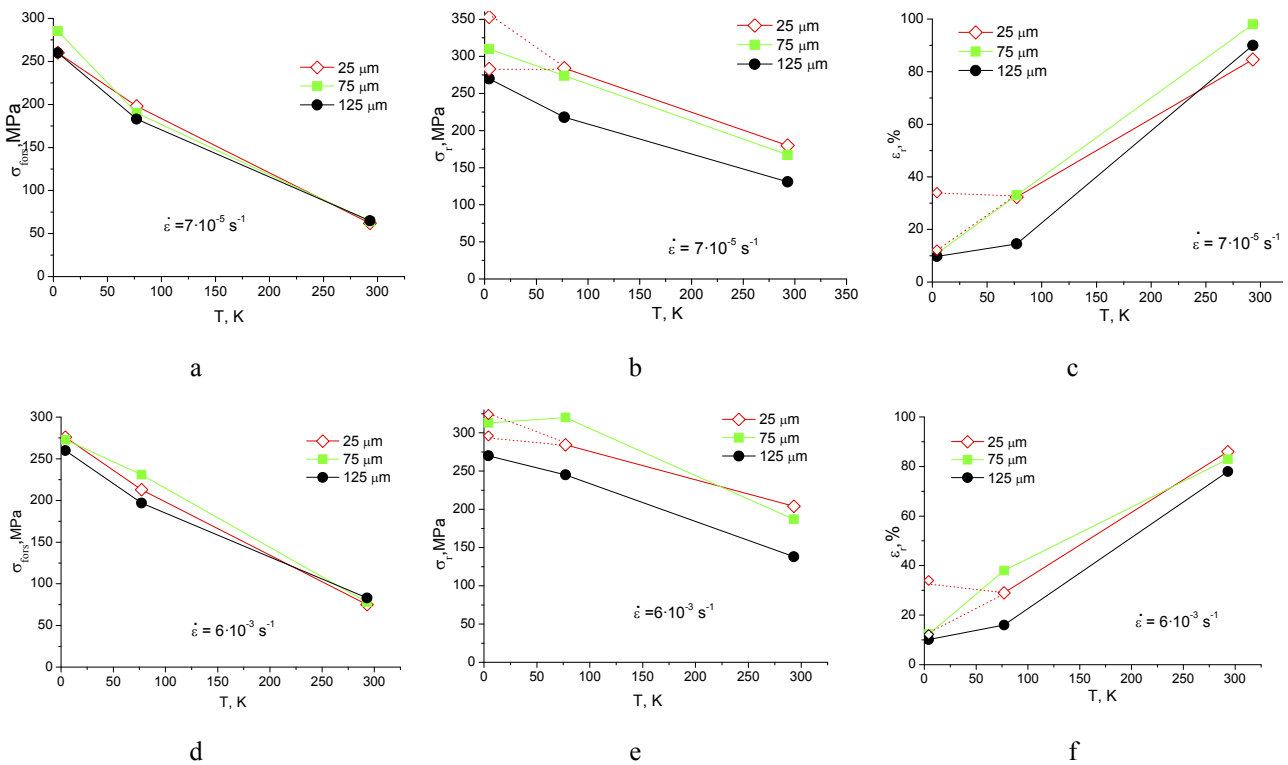
d   e   f

Figure. 3. Temperature dependences of the mechanical characteristics of polyimide films in the temperature range 4,2-293 K at strain rates $\dot{\varepsilon}$ =7·10⁻⁵ s⁻¹ (a,b,c) and $\dot{\varepsilon}$ =6·10⁻³ s⁻¹ (d,e,f): a, d - forced elasticity limit, b,e- rupture stress; c,f – relative deformation to rupture

Figure 4 shows the limits of the scatter of the values of mechanical characteristics $\pm(\Delta\sigma_{forc}/\sigma_{forc},\%, \Delta\sigma_r/\sigma_r,\%$ and $\Delta\varepsilon_r/\varepsilon_r,\%)$ under these conditions. The scatter of the measured characteristics in films of 75 and 125 μm is significantly lower than in a film of 25 μm, and changes with decreasing temperature are also much less. The spread in the values of the characteristics of a 25 μm film sharply increases with decreasing temperature, especially for the values of deformation to rupture ε_r. As shown in Fig. 2, for samples of a film with a thickness of 25 μm at 4.2 K, two types of curves are observed, and for ε_r it is possible to distinguish, as it were, two average values and two values of the scatter (Fig. 4c, d) for each type of curves. For rupture stress, two predominant average values can also be distinguished, but in this case there is no clear correspondence - higher strength values and higher deformation, or vice versa. Although at a strain rate of $\dot{\varepsilon}$ =7·10⁻⁵ s⁻¹ the samples which show curves of type 1b (Fig. 2, T = 4.2 K) have predominantly higher

values, and at $\dot{\varepsilon}$ =6•10^{-3} s^{-1} - lower. In this regard, two limiting values are shown in Fig. 3 for the rupture stress and relative deformation to rupture of the 25 μm film at 4.2 K instead of the average values of the characteristics.

Figure 3 shows, that the values of the forced elasticity limit $\sigma_{fors.}$ of the films strongly depend on temperature and only slightly depend on the thickness. The limit $\sigma_{fors.}$ with decreasing temperature from room temperature to 4.2 K increases in films of all thicknesses by more than 4 times at a minimum strain rate of $7 \cdot 10^{-5}$ s^{-1} and by 3.2 - 3.4 times at a maximum rate of $6 \cdot 10^{-3}$ s^{-1}. The magnitude of the rupture stress $\sigma_{fr.}$ in all films with a decrease in temperature to 4.2 K grows much more slowly – by 1.7-2 times. Even at 4.2 K, at all deformation rates, there is a certain reserve of elasticity – the ratio $\sigma_{fors.}/\sigma_r < 1$ and is equal to ~0.94, 0.9 and 0.8, respectively, for films with δ=125, 75 and 25 μm. The rupture stress σ_r depends on the film thickness much more strongly than the limit $\sigma_{fors.}$. Thus, a thick film (δ = 125 μm) has the lowest values σ_r (20 - 30% lower than the values σ_r of the average film) in the entire temperature range at all strain rates. The magnitude σ_r of the films 75 μm and 25 μm differ significantly less. The maximum difference is observed at low temperatures and reaches 10-17%, and depending on the strain rate, either the values σ_r of the thinnest film ($\dot{\varepsilon}$ = $7 \cdot 10^{-5}$ s^{-1}) or the average ($\dot{\varepsilon}$ = $6 \cdot 10^{-3}$ s^{-1}) are higher, which is associated, as will be shown below, with the different strain rate sensitivities of the films of these thicknesses.
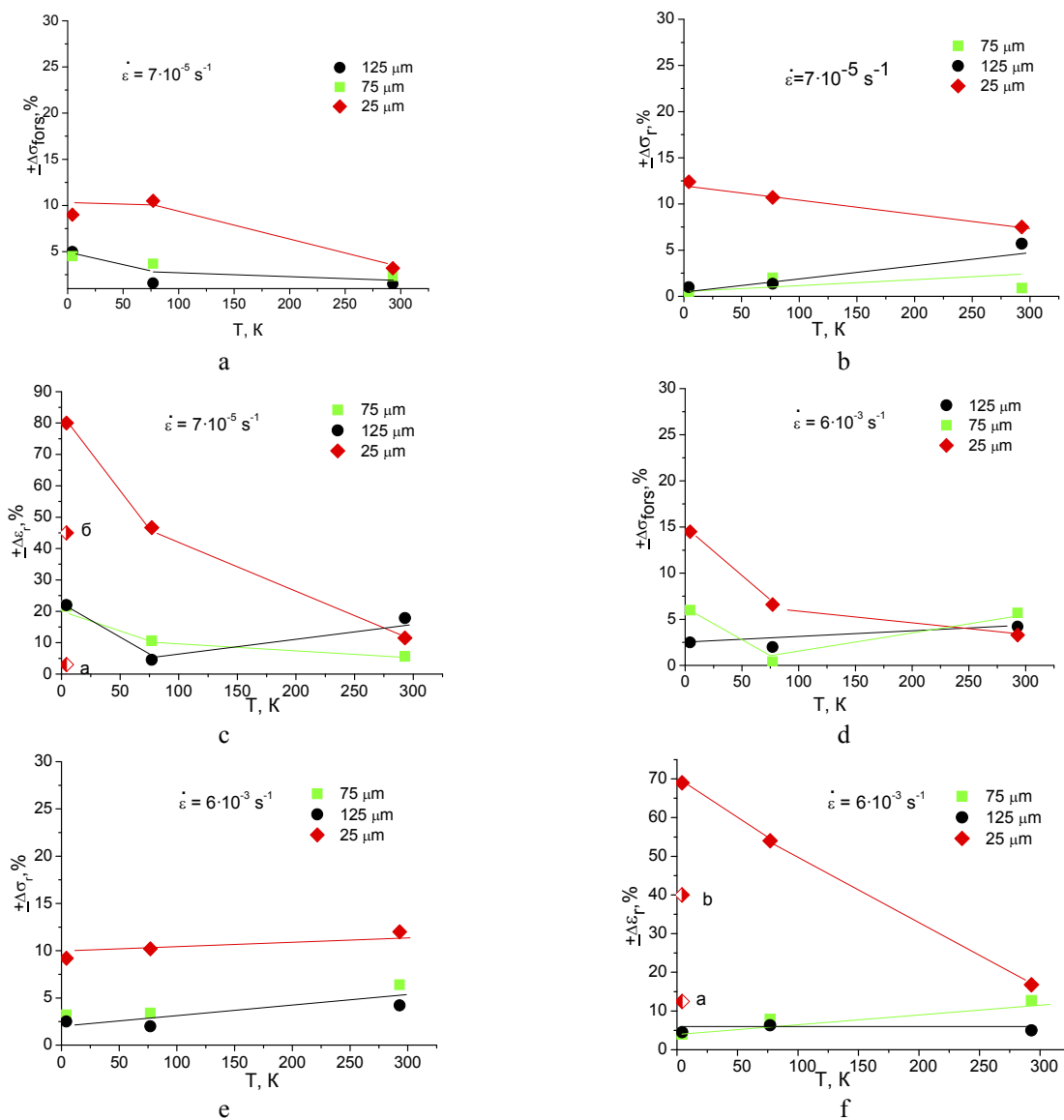

Figure. 4. Temperature dependences of the spread in the values of the mechanical characteristics of polyimide films in the temperature range 4,2-293 K at strain rates $\dot{\varepsilon}$ =$7 \cdot 10^{-5}$ s^{-1} (a,b,c) and $\dot{\varepsilon}$ =$6 \cdot 10^{-3}$ s^{-1} (d,e,f): a, d – error in measuring forced elasticity limit, b,e- rupture stress; c,f – relative deformation to rupture (points a and b correspond to the values $\pm\Delta\varepsilon_r/\varepsilon_r$ for curves of type a and b for samples of a film with a thickness of 25 μm at 4.2 K in Fig. 2)

The temperature dependences of the deformation before rupture (Fig.3 c, f) indicate that a film with a thickness of 125 μm sharply decreases its elasticity already in the range of T=77 K, and a film of 75 μm - in the range of 4.2 K.

However, the level of highly elastic deformation even in a film 125 μm at 4.2 K remains at a level of not less than 2.5% at all strain rates. In the thinnest film of 25 μm at 4.2 K, the samples have two average values: the values ε_r: magnitudes ε_r of some of the samples practically coincide with the values ε_r of thick films, and some of the samples demonstrate elasticity, as at 77 K.

Strain rate influence. The dependences of the average values of the mechanical characteristics of the films on the strain rate at temperatures of 293, 77, and 4.2 K are shown in Fig.5a-c.
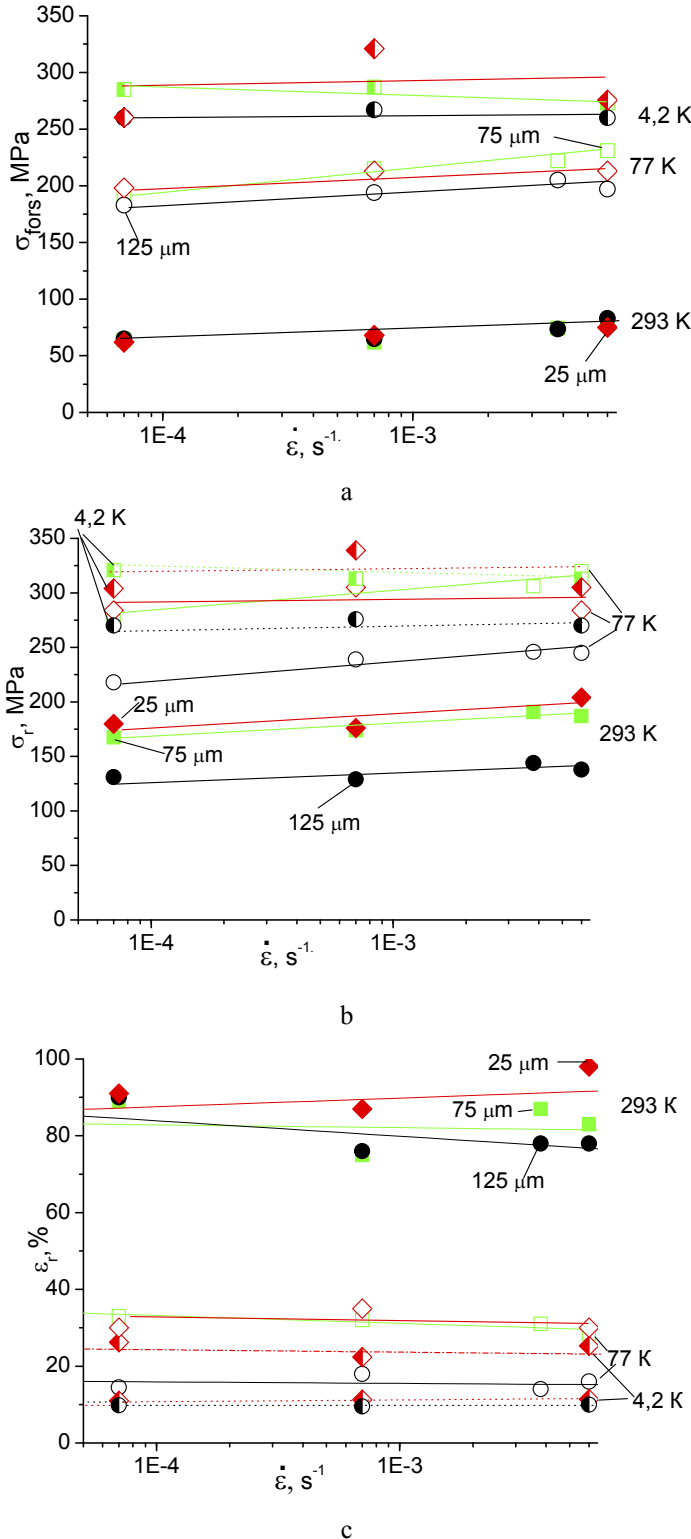

a

b

c

Let us consider the dependence of the forced elasticity limit of films on the strain rate $\sigma_{fors.}(\dot{\varepsilon})$. Fig. 5a shows that at room temperature the values σ_{fors} of all films practically coincide in the entire range of strain rates and grow weakly with increasing $\dot{\varepsilon}$, which is in good agreement with the data obtained on polymer films earlier [2]. As noted in [5], limit σ_{fors} in thicker films increases with strain rate $\dot{\varepsilon}$ at 77 K (especially in a film with δ= 75 μm). The slope of the dependence $\sigma_{fors.}(\dot{\varepsilon})$ of the thinnest film remains the same as at 293 K and, accordingly, the values of limit $\sigma_{fors.}$ at strain rate $\dot{\varepsilon}$ =6·10⁻³ s⁻¹ are lower than the $\sigma_{fors.}$ values of the average film thickness.

At 4.2 K, the limit $\sigma_{fors.}$ of a thinnest film practically ceases to depend on deformation rate $\dot{\varepsilon}$, while for thicker films an inverse relationship is observed — an increase in the limit $\sigma_{fors.}$ with decreasing rate $\dot{\varepsilon}$. Such a rate dependence $\sigma_{fors.}(\dot{\varepsilon})$ at T = 4.2 K was observed for the first time. Dependencies $\sigma_r(\dot{\varepsilon})$ behave in a similar way (Fig.5b). It should be noted that the values of rupture stress σ_r at 4.2 K for all three films at the highest strain rate of $\dot{\varepsilon}$ =6·10⁻³ s⁻¹ are close to those at 77 K. In this regard, in order to better distinguish the dependences of $\sigma_{fr.}(\dot{\varepsilon})$ at 77 K and 4,2 K, the latter for clarity in Fig. 5b are shown by a dotted line. For the same purpose, the dependences of $\sigma_r(\dot{\varepsilon})$ at 4.2 K in Fig. 5c are also represented by dotted lines.

The relative deformation before rupture ε_r for all films (except for the 125 μm film at 4.2 K), taking into account the large scatter of values, can be considered practically independent of the strain rate at all test temperatures. It should only be noted that the values of ε_r at temperatures of a sharp decrease in elasticity practically coincide for all films. Namely, for samples of a film with a thickness of 125 μm, the ε_r values practically coincide at temperatures of 77 and 4.2 K. At 4.2 K, the ε_r values coincide for all samples of films with a thickness of 75 and 125 μm and samples of a film with 25 μm, having a deformation curve of the type 1a (Fig. 2). In samples of a thinnest film with deformation curves of type 1b (Fig. 2), the ε_r values at 4.2 K at all strain rates are close to those at 77 K.

Fracture of films. In fig. 6 (a-i) and 7 (a-i) show photographs of the fracture zones of

Figure 5. Dependences of the forced elasticity limit (a), rupture stress (b) and relative deformation before rupture (c) of polyimide films on the rate at 4.2, 77, and 293 K.

samples of different thicknesses, deformed at temperatures of investigation and limiting deformation rates. Figures 6i and 7i show the fracture zones of film samples with a thickness of 25 μm, which at 4.2 K had the character of curves (σ – ε), similar to that of thicker films (type 1a, Fig. 2).Figures 8a-d show the surface relief of thin film specimens, which found noticeable jump-like deformation at 4.2 K.

Figure 6. Surfaces of samples with a thickness 25 (a, d, g), 75 (b, e, h) and 125 μm (c, f, i) in the fracture zone at temperatures of 293 (a, b.c), 77 (d, e, f) and 4.2 K (g, h, i) at a strain rate $\dot{\varepsilon}$ =7·10⁻⁵ s⁻¹
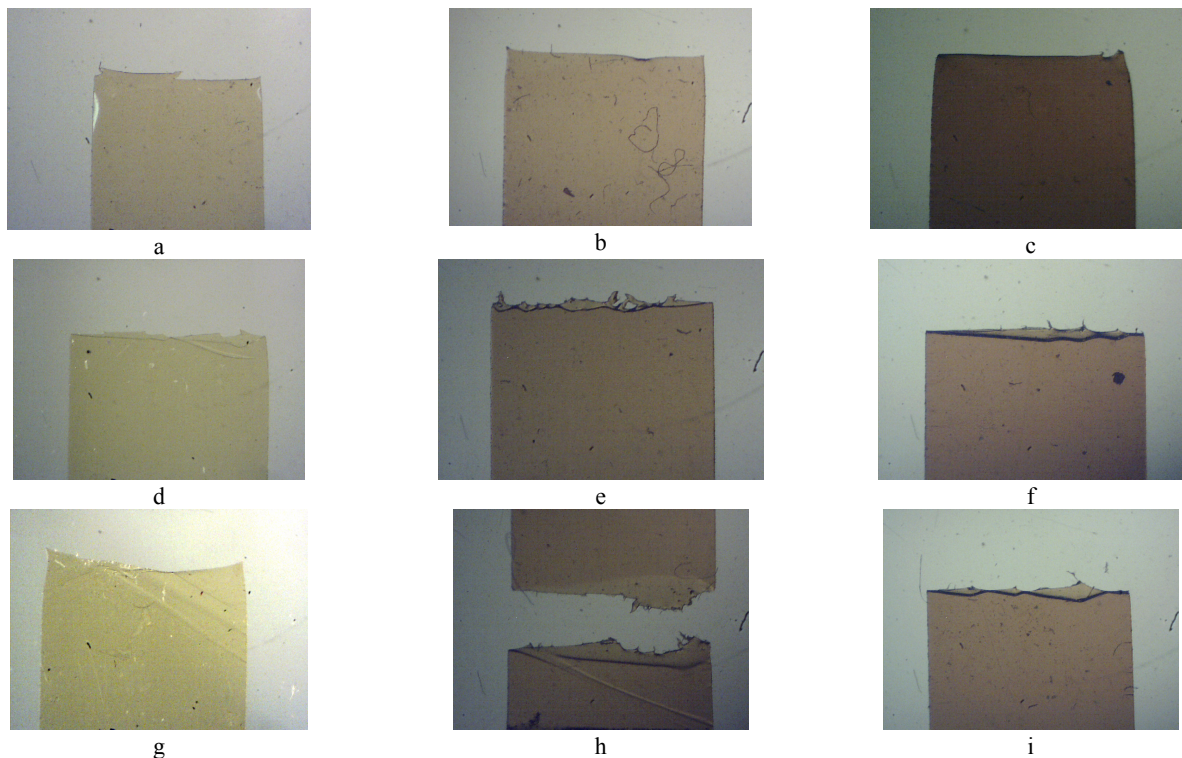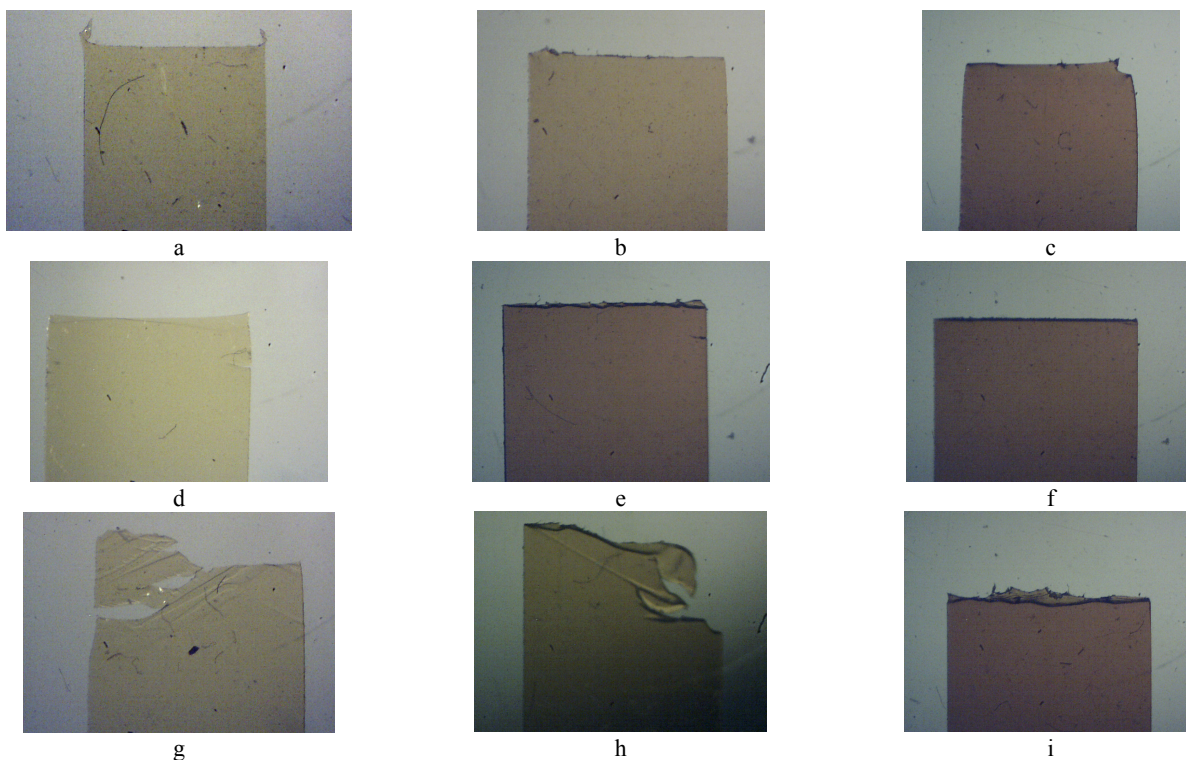

Figure 7. Surfaces of samples with a thickness 25 (a, d, g), 75 (b, e, h) and 125 μm (c, f, i) in the fracture zone at temperatures of 293 (a, b.c), 77 (d, e, f) and 4.2 K (g, h, i) at a strain rate $\dot{\varepsilon}$ =6·10⁻³ s⁻¹

Figures 6 and 7 show that the fracture of the films occurs by tearing off perpendicular to the tensile axis of the sample at temperatures of 293 and 77 K. Weak necks in the plane of the film, which are absent in thickness, were found on the fractures of all films at room temperature. Up to a temperature of 4.2 K, the neck is retained only in a film with a thickness of 25 μm. Ties and shear zones parallel to the separation zone (apparently, the tear zones of a part of the fibers) appear in films with a thickness of 75 and 125 μm at 77 and 4.2 K. The length of the tension bars extended from the zone of tear at 77 K decreases with an increase in the strain rate $\dot{\varepsilon}$, especially in a film with a thickness of 125 μm.

The shape of the 125 μm film surface in the fracture zone, which is characteristic at 77 K, remains at the temperature of liquid helium. Shear bands at an angle of 60 ° to the tension axis associated with the fracture zone appear in addition to tension bars at a low strain rate in the thinnest film of 25 μm at 77 K. At a strain rate of $\dot{\varepsilon} = 6 \cdot 10^{-3}$ s^{-1}, tension bars and shear bands in it are absent and well the neck is visible in the plane of the film.

Shear bands at an angle of 60 ° to the tension axis associated with the fracture zone are observed at 4.2 K in films of small and medium thickness at all strain rates. Cracks appear in them at a high strain rate. Shear bands are observed only near a fracture in films with a thickness of 25 μm with a small elongation to rupture. This deformation relief in films of both thicknesses is irreversible and is retained after annealing destroyed samples at 350°C for 2 hours. Shear bands, oriented in two directions at an angle of 60 ° to the tension axis, extend over the entire working part of the sample in films with a thickness of 25 μm with a noticeable nonlinear stage (Fig.8a and b). The number of shear bands agrees well with the number of jumps on the deformation curves. Part of this relief disappears after annealing the destroyed samples at 350 ° C for 2 hours. (Fig.8c and d).
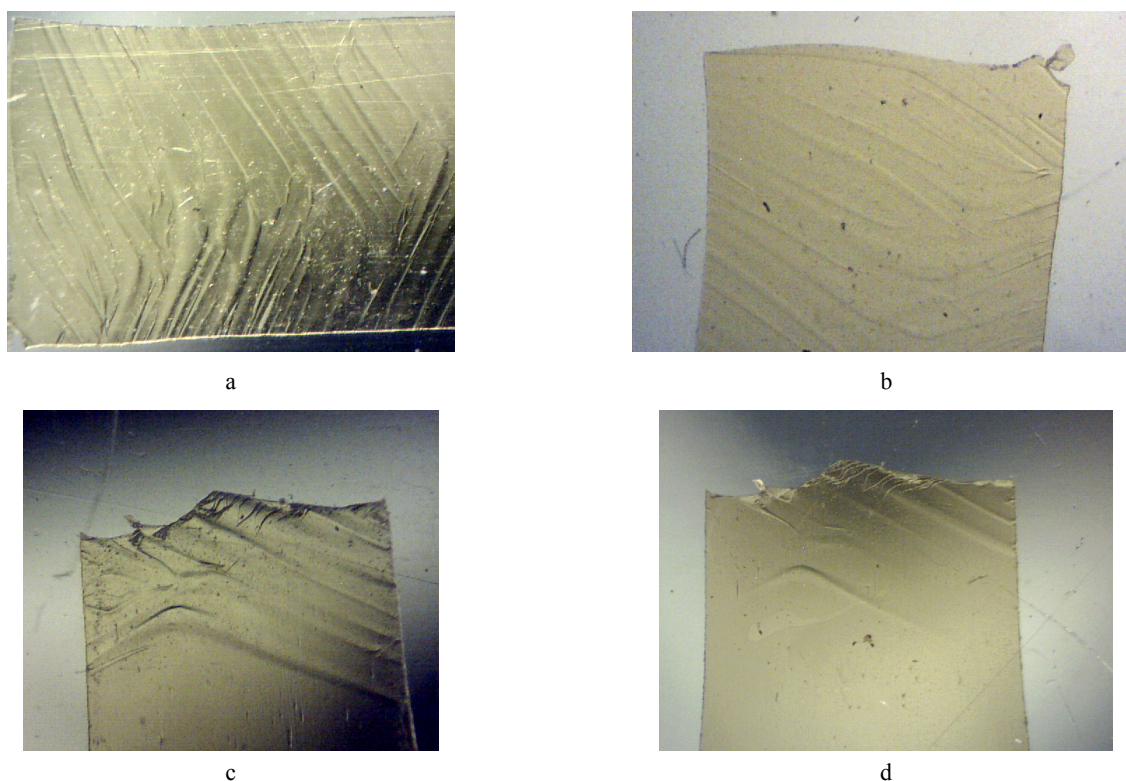

| a | b |
| c | d |

Figure 8. Surfaces of the working part of 25 μm thick specimens deformed to rupture at 4.2 K at strain rates $\dot{\varepsilon}$: 7·10^{-5} s^{-1} (a, c) and 6·10^{-3} s^{-1} (b) after warming up to room temperature (a-c) and annealing at 350°C for 2 hours. (d)

DISCUSSION OF INVESTIGATION RESULTS

The deformation curves of the studied amorphous films do not show a maximum upon transition to the forced elastic state, while the films have high limits of forced elasticity and strength. This is typical for pre-stretched, oriented amorphous polymers [2]. The X-ray method can detect such a texture only when shooting at the end of the film, perpendicular to the axis of the broach in the technological process. According to the available data of X-ray diffraction analysis [6], obtained during recording by reflection from the film plane, it was found that the initial films have different degrees of ordering and density. In the case of linear polymer molecules, this may mean that the polymer chains have different angles of disorientation along the tensile axis in films of different thicknesses. A film with a thickness of 125 μm has the highest ordering in the initial state. Long-range order is formed in it after deformation at both 293 K and 77 K.

Despite the larger contribution of irreversible deformation, long-range order was not detected in the thinner film (75 μm). However, the ordering processes in this and even more disoriented film with a thickness of 25 are seemed to

Regularities of Low-Temperature Deformation and Fracture of Polyimide Films...

151
EEJP. 4 (2020)

proceed more intensively. The appearance on the deformation curves of a 25-μm-thick film of the second nonlinear stage with a higher hardening coefficient, which is observed in some samples even at 4.2 K, indicates this. This allows us to assume the possibility of orientation in this film under the action of an external force not only of individual segments of molecules, but also the orientation of molecules as a whole and even bundles of molecules along the tensile direction at the second nonlinear stage. But these processes are also more reversible when unloading due to the smaller thickness. In films deformed at low temperatures, these processes are also reversible upon heating to room temperature.

Irreversible deformation that develops at the last stages of deformation is associated not only with shear deformation without violating the integrity (orientation), but also with the processes of material destruction - the formation of microcavities, microcracks and their growth in the oriented material. This is especially evident at low temperatures, where deformation begins to proceed partially localized already at 77 K and completely at 4.2 K. The appearance at 77 K of a relief in the form of shear bands observed on the surfaces of deformed samples of the thinnest film (25 μm) near the fracture, and in thicker films - directly in the fracture zone indicates this. Cracks are also clearly visible on the surface of shear bands at 4.2 K. The retention of shear bands after annealing in films deformed at 77 K and the formation of cracks in them at 4.2 K indicates that the main process of the formation of localization zones is precisely the processes of destruction - the formation of microdefects and the development of microcracks, which become macroscopic at 4.2 K.

Despite the significant reduction in elasticity and the appearance of cracks in the shear bands from the point of view of the ratio of the values of the forced elasticity limit and the rupture stress ($\sigma_{fors} < \sigma_r$) at these strain rates, the brittleness temperature T_{br} is not yet reached in any of the films even at 4.2K. However, the appearance of strain rate sensitivities $\varepsilon_r(\dot{\varepsilon})$ in films with a thickness of 75 and 125 μm at 4.2 K with a slope opposite to that at 77 K indicates that the achievement of T_{br} is possible at higher strain rates. Although there is a weak margin of orientational elasticity in these films at 4.2 K, the main process occurring at the nonlinear stage of deformation is the formation and growth of microcracks according to the microstructures of fractures.

The ability to orient the segments of polymer molecules without cracking in the places of localization of deformation is retained in a film 25 μm thick at 4.2 K. This is evidenced by the disappearance of a part of the relief during subsequent annealing (Fig.8c, d), the presence of a neck in the fracture zone (Fig. 6g and 7g) and the smallest ratio σ_{fors}/σ_r. However, the competition between the course of orientation processes without and with the formation of cracks is strong. As a result, some specimens with a more favorable arrangement of molecular chains exhibit high elasticity values, while in others, cracking immediately develops with destruction of the specimen.

The limit σ_{fors} determines the stress at which the forced elastic deformation begins to develop steadily, i.e. processes of rearrangement of segments of polymer molecules occur. When the external force changes, they lag behind the equilibrium ones, i.e. have a relaxing nature. According to the developed relaxation theory, σ_{fors} depends on the deformation rate of the material and increases with an increase in the latter, which was observed in various polymers [2] and by us at 293 and 77 K. A change in the film thickness and a change in the structure, which are observed with a change in the thickness of the initial films, in the room temperature area does not lead to a change in the slope of the $\sigma_{fors}(\dot{\varepsilon})$ dependence for films of different thicknesses, or to a change in the σ_{fors} values.

The difference in the thickness and in the initial degree of ordering of the structure of the films leads with a decrease in temperature to 77 K to different values of the slopes of the dependences $\sigma_{fors}(\dot{\varepsilon})$. However, an increase in σ_{fors} with an increase in $\dot{\varepsilon}$ occurs for all films. It can be assumed that microfracture processes begin to operate at all deformation rates simultaneously with entropic orientational processes in a film with δ=125 μm, which sharply decreases its elasticity already at 77 K. As a result, no significant growth of σ_{fors} occurs with increasing speed. The processes of orientation of segments of polymer molecules continue to remain primary in the film with δ=75 μm at all strain rates. The critical relaxation time τ (the onset of the development of highly elastic deformation) can be achieved at a lower temperature with an increase in the strain rate at significantly higher stresses σ_{fors}. And the processes of orientation in a film with δ=25 μm, which has the lowest density and the most amorphous structure, are the least complicated and the slope of the $\sigma_{fors}(\dot{\varepsilon})$ dependence is similar to that at T = 293 K.

The processes of orientation of both molecular segments and microfracture seem to turn on almost simultaneously when the σ_{fors} limit is reached at 4.2 K in thicker films (75 and 125 μm). Moreover, the higher the rate of deformation, the earlier the processes of microfracture start. As a result, the dependences $\sigma_{fors}(\dot{\varepsilon})$ and $\sigma_r(\dot{\varepsilon})$ have a reverse course - a decrease in the values of σ_{fors} and σ_r with an increase in the strain rate. A noticeable change in the slope of the deformation rate dependences of the strength properties is not found in a film with δ=25 μm, which retains sufficient elasticity at 4.2 K. This allows us to assume the preservation of the mechanisms of shape change, characteristic at room temperature, up to 4.2 K, but their flow is localized along the working part of the sample.

CONCLUSION

1. The characteristics of strength (forced elasticity limit σ_{fors} and rupture stress σ_r) and deformability (relative deformation before fracture ε) of three polyimide films of the kapton H type (made in China) of different thickness

(25, 75 and 125 μm) in the temperature range 4.2 -293 K and strain rates 10^{-5}-10^{-3} s^{-1}. The significant hardening of the films with a decrease in temperature to 4.2 K was discovered.

2. It was found that the deformation curves of films with a thickness of 75 and 125 μm have two stages at all temperatures and strain rates: linear and nonlinear. On the (σ-ε) curves of a 25-μm-thick film at 293 and 77 K, three stages are observed: a linear and two nonlinear ones with different hardening coefficients, and at 4.2 K, two types of curves are observed - with a small and large stage of nonlinear deformation proceeding jumpily.

3. It has been established that the brittleness temperature T_{br} is not reached ($\sigma_{fors}<\sigma_r$) for films of all thicknesses at investigation temperatures and strain rates. The minimum elasticity level for all films is similar, and the temperature at which it is reached depends on the film thickness. It occurs for a film with a thickness of 125 μm at 77 K, for a film with a thickness of 75 μm and samples of a 25 μm film with a short nonlinear stage - at 4.2 K.

4. Necks in the fractures of the film samples in the plane of the film, the presence of which depends on the thickness and temperature were found. Necks are observed in all films at all strain rates at room temperature. With a decrease in temperature, only in thinnest film samples.

5. For the first time, a deformation relief in the form of shear bands associated with the localization of deformation at low temperatures was observed. The presence of a relief, the temperature of its appearance and the area of the working part of the sample occupied by it depend on the thickness of the film. The relief at a small film thickness can be caused by two different processes: irreversible processes of formation and development of cracks and reversible processes of orientation of segments of polymer molecules.

6. For the first time, it has been established that the strain rate sensitivity of the strength properties depends on the film thickness both in magnitude and in character at low temperatures. It was found that the character of the rate sensitivity of the σ_{fors} and σ_{fors} limits changes to the opposite at 4.2 K in more ordered thick films (75 and 125 μm) and that the character of the $\sigma_{fors}(\dot{\varepsilon})$ and $\sigma_r(\dot{\varepsilon})$ dependences remains up to 4.2 K in the most amorphous thin film (25 μm).

ORCID IDs
Viktory A. Lototskaya, https://orcid.org/0000-0001-8766-3154; **Leonid F. Yakovenko**, https://orcid.org/0000-0003-0001-5571;
Evgeniy N. Aleksenko, https://orcid.org/0000-0002-6505-0426

СПИСОК ЛИТЕРАТУРЫ
[1] M.I. Bessonov, M.M. Koton, V.V. Kudryavtsev, and l.A. Layus, *Полііміди – клас термостійких полімерів [Polyimides – class of heat-resistant polymers]*, (Nauka, Leningrad, 1984), pp. 328. (in Russian).

[2] G.M. Bartenev, and Yu.S. Zuev, *Міцність та руйнування високоеластичних матеріалів [Strength and rupture of highly elastic materials]*, (Himiyu, Moscow, 1964), pp. 335. (in Russian)

[3] V.V. Abraimov, N.N. Agashkova, L. Bone, I.V. Budnyak, N.I. Velichko, A.V. Krevsun, V.I. Kostenko, F. Lura, and A.M. Markus, Kosm. nauka tehnol. **1**(1), 57-68 (1995), https://doi.org/10.15407/knit1995.01.057. (in Russian).

[4] V.P. Soldatov, G.I. Kirichenko, V.V. Abraimov, I.S. Braude, and V.G. Geidarov, Low Temperature Physics, **42**, 817 (2016), https://doi.org/10.1063/1.4963917.

[5] V.A. Lototskaya, L.F. Yakovenko, E.N. Aleksenko, V.V. Abraimov, and Wen Zhu Shao, East. Eur. J. Phys. **4,** 44-52 **(**2017), https://doi.org/10.26565/2312-4334-2017-2-06.

[6] V.G. Geidarov, I.S. Braude, N.N. Gal'tsov, Yu.M. Pohribnaya, V.A. Lototskaya, and N.A. Aksenova, Structural Studies of Polyimide Films. Size Effect, Nano Studies, **19**, 11-14 (2019) http://dspace.nplg.gov.ge/bitstream/1234/312051/1/Nano_Studies_2019_N19.pdf.).

[7] Ye.G. Lur'e, L.G. Kazaryan, E.L. Uchastkina,V.V. Kovriga, K.N. Vlasova, M.L. Dobrokhotova, L.N. Yemel'yanova, Polymer Science U.S.S.R. 13(3), 685-692 (1971), https://doi.org/10.1016/0032-3950(71)90033-5.

[8] E.G. Lur'e, and V.V. Kovriga, Polymer Mechanics, **13**, 496–501 (1977), https://doi.org/10.1007/BF00859325.

[9] V.P. Pshenitsyna, L.G. Kazaryan, Ye.G. Lur'ye, M.L. Lebedinskaya, and V.V. Kovriga, The spectroscopic study of polyimide film deformations, Polymer Science U.S.S.R. 14(3), 702-707 1972, https://doi.org/10.1016/0032-3950(72)90242-0.)

[10] L.M. Volikova, and V.K. Chernetskiy, in: *Прикладне кріогенне і вакуумне матеріалознавство [Applied cryogenic and vacuum material science]*, (Naukova dumka, Kyiv, 1991), pp. 137-143. (in Russian)

ЗАКОНОМІРНОСТІ НИЗЬКОТЕМПЕРАТУРНОЇ ДЕФОРМАЦІЇ ПОЛІІМІДНИХ ПЛІВОК ТИПУ KAPTON H РІЗНОЇ ТОВЩИНИ

В.О. Лотоцька[a], Л.Ф. Яковенко[a], Є.М. Алексенко[a], В.В. Абраімов[b], Вень Чжу Шао[b]
[a]Фізико-технічний інститут низьких температур ім. Б.І. Вєркіна Національної академії наук України
пр. Науки, 47, м. Харків, 61103, Україна
[b]Харбінський Політехнічний інститут, м. Харбін, КНР

Досліджено механічні характеристики поліімідних плівок (границя вимушеної еластичності $\sigma_в$, напруга руйнування σ_p, відносна деформація до руйнування ε_p) типу kapton H (виробництва КНР) в умовах одноосьового розтягу вздовж напрямку витяжки в диапазоні температур (4,2-293 K), швидкостей деформації (10^{-5} – 10^{-3} с$^{-1}$) та товщін плівки (25, 75 й 125 мкм). Виявлено, що аж до 4,2 K при всіх швидкостях деформації у всіх плівок зберігається вимушено-еластичний стан - $\sigma_в<\sigma_p$.

При цьому запас еластичності при зниженні температури істотно залежить від товщини плівки. Різке зниження ε_p відбувається в плівках: товщиною 125 мкм - при 77 К, товщиною 75 мкм - при 4,2 К. У плівці товщиною 25 мкм при 4,2 К можливі два варіанти деформаційних кривих - з короткою нелінійної або з довгою стадією, що протікає стрибкоподібно. Робоча поверхня зразків, що зазнали стрибкоподібну деформацію, покрита деформаційним рельєфом, який частково представляє затриману високоеластичну деформацію. Границя $\sigma_в$ найбільш чутлива до швидкості деформації. Характер швидкісний чутливості $\sigma_в(\dot\varepsilon)$ залежить від температури і товщини плівки. Вперше виявлено зміна характеру $\sigma_в(\dot\varepsilon)$ на протилежний в плівках товщиною 75 і 125 мкм при зниженні температури до 4,2 К. У плівці товщиною 25 мкм, що зберігає максимальний запас еластичності при 4,2 К, зміни характеру $\sigma_в(\dot\varepsilon)$не спостерігається.

КЛЮЧОВІ СЛОВА: полііміди, низькі температури, границя змушеної еластичності, напруга руйнування, деформація

ЗАКОНОМЕРНОСТИ НИЗКОТЕМПЕРАТУРНОЙ ДЕФОРМАЦИИ И РАЗРУШЕНИЯ ПОЛИИМИДНЫХ ПЛЕНОК ТИПА KAPTON H РАЗЛИЧНОЙ ТОЛЩИНЫ

В.А. Лотоцкая[a], Л.Ф. Яковенко[a], Е.Н. Алексенко[a], В.В. Абраимов[b], Вень Чжу Шао[b]

[a]*Физико-технический институт низких температур им. Б.И. Веркина Национальной академии наук Украины пр. Науки, 47, г. Харьков, 61103, Украина*

[b]*Харбинский Политехнический институт, г. Харбин, КНР*

Исследованы механические характеристики (предел вынужденной эластичности $\sigma_в$, напряжение разрушения σ_p, относительная деформация до разрушения ε_p) полиимидных пленок типа kapton H (производства КНР) в условиях одноосного растяжения вдоль направления вытяжки в диапазоне температур (4,2-293 К), скоростей деформации (10^{-5} - 10^{-3} с$^{-1}$) и толщин пленки (25, 75 и 125 мкм). Обнаружено, что вплоть до 4,2 К при всех скоростях деформации у всех пленок сохраняется вынужденно-эластическое состояние - $\sigma_в<\sigma_p$. При этом запас эластичности при снижении температуры существенно зависит от толщины пленки. Резкое снижение ε_p происходит в пленках: толщиной 125 мкм при 77 К, толщиной 75 мкм – при 4,2 К. В пленке толщиной 25 мкм при 4,2 К возможно два варианта деформационных кривых - с короткой нелинейной или с длинной стадией, протекающей скачкообразно. Рабочая поверхность образцов, претерпевших скачкообразную деформацию, покрыта деформационным рельефом, частично представляющим задержанную высокоэластичную деформацию. Предел $\sigma_в$ наиболее чувствителен к скорости деформации. Характер скоростной чувствительности $\sigma_в(\dot\varepsilon)$ зависит от температуры и толщины пленки. Впервые обнаружено изменение характера $\sigma_в(\dot\varepsilon)$ и $\sigma_p(\dot\varepsilon)$ на противоположный в пленках толщиной 75 и 125 мкм при понижении температуры до 4,2 К. В пленке толщиной 25 мкм, сохраняющей максимальный запас эластичности при 4,2 К, изменения характера $\sigma_в(\dot\varepsilon)$ не наблюдается.

КЛЮЧЕВЫЕ СЛОВА: полиимиды, низкие температуры, предел вынужденной эластичности, напряжение разрушения, деформация

154

OPTICAL AND ELECTRICAL PROPERTIES OF GRAPHITE THIN FILMS PREPARED BY DIFFERENT METHODS

Mykhailo M. Solovan[a,*], H.M. Yamrozyk[a], Viktor V. Brus[b], Pavlo D. Maryanchuk[a]
[a]Yuriy Fedkovych Chernivtsi National University, st. Kotsyubyns'kogo 2, 58012, Chernivtsi, Ukraine
[b]Nazarbayev University, 53 Kabanbay Batyr, 010000, Nur-Sultan City, Kazakhstan
Corresponding Author: m.solovan@chnu.edu.ua

The paper reports on the structural, optical and electrical properties of graphite thin films prepared by two methods: the vacuum-free method "Pencil-on-semiconductor" and via the electron beam evaporation such studies are of great importance for the further development of high-efficiency devices based on heterojunctions for electronics and optoelectronics. Graphite thin films prepared by the non-vacuum method has annealed at a temperature of 920K.The transmission spectra of the investigated graphite films and the electrical properties of these thin films were measured at T = 300 K. The value of the height of potential barriers E_b at the grain boundaries and the temperature dependence of the electrical conductivity in the range $ln(\sigma \cdot T^{1/2}) = f(10^3/T)$ were determined, It is established that the height of the potential barrier at the grain boundaries for the drawn graphite films is E_b = 0.03 eV, for annealed E_b = 0.01 eV and for the graphite films deposited by the electron beam evaporation E_b = 0.04 eV, ie for annealed film the barrier height is the smallest. It is shown that graphite films deposited by the electron beam evaporation reveals the highest transmittance (T550 ≈ 60 %), and the transmission of drawn films is the lowest, annealing leads to its increase. The minimum values of transmission at a wavelength λ = 250 nm are due to the scattering of light at the defects that are formed at the grain boundaries. Annealed graphite films have been found to possess the best structural perfection because they have the lowest resistivity compared to non-annealed films and electron-beam films and have the lowest barrier height. Simultaneous increase of transmission in the whole spectral range, increase of specific electrical conductivity and decrease of potential barrier at grain boundaries of the annealed drawn graphite film clearly indicate ordering of drawn graphite flakes transferred onto a new substrate, which led to the reduction of light scattering and the improvement of charge transport due to the larger area of overlap between graphite flakes.
KEY WORDS: "pencil-on-semiconductor", annealing, thin films, graphite, grain boundaries

В останні роки невпинно збільшується інтерес науковців до методів отримання тонких вуглецевих шарів. Вуглець – це унікальний елемент, який відрізняється від інших елементів здатністю утворювати кристалічні структури із різним типом зв`язку [1-3]. Серед усіх відомих форм вуглецю тонкі плівки графіту займають важливе місце завдяки своїм особливостям [4,5]. Можливість застосування тонких плівок графіту для виготовлення різних приладів електроніки та оптоелектроніки обумовлена їх унікальними властивостями: хорошою електропровідністю, високою рухливістю носіїв заряду при кімнатній температурі, прозорістю, хорошими механічними властивостями [1,2].

Вакуумні методи напилення тонких плівок графіту потребують використання інертних газів і є досить складними для напилення плівок. Тому в останні роки науковців почали більше цікавити безвакуумні методи отримання тонких плівок, найдешевшим з яких для виготовлення плівок графіту виявився метод «олівець-на-напівпровіднику» [3]. Незважаючи на недолік даного методу, який полягає у необхідності грубої механічної або хімічної обробки поверхні підкладки для формування її шорсткості (необхідної для рисування плівки олівцем), запропонований метод має низьку вартість та є екологічно безпечним.

Плівки графіту вже успішно використовуються для створення гетероструктур типу діодів Шотткі, які можна використовувати в якості фотодіодів та детекторів ультрафіолетового випромінювання [6,7]. Підвищення ефективності таких фотоприймачів безпосередньо пов'язано з підвищенням якості вихідних матеріалів для створення гетероструктур та розумінням їх фізичних властивостей.

Мало робіт присвячено результатам комплексних експериментальних досліджень оптичних та електричних властивостей плівок графіту отриманих різними методами. Але такі дослідження мають велике значення для подальшої розробки високоефективних приладів на основі гетеропереходів для електроніки і оптоелектроніки [8,9].

В даній роботі проводяться дослідження структурних, оптичних та електричних властивостей тонких плівок графіту, виготовлених нами методом «олівець-на-напівпровіднику», а потім відпалених для покращення їх параметрів, та методом електронно-променевого випаровування для порівняння.

ЕКСПЕРИМЕНТАЛЬНА ЧАСТИНА

Тонкі плівки графіту виготовлені безвакуумним методом «олівець-на-напівпровіднику» та методом електронно-променевого випаровування. Відповідно до методу «олівець-на-напівпровіднику» [3] одна з поверхонь свіжосколотої монокристалічної соляної підкладки (NaCl) механічно шліфувалася до шорсткості R_a = 0,2 мкм, R_z=0,23 мкм та R_{max}=1,1 мкм. Однорідну графітову плівку рисували на підготовленій поверхні соляної підкладки за допомогою чистого графітового стержня (1 мм у діаметрі) при постійній силі притискання в 1 Н. Далі зразок обережно розміщували на поверхні дистильованої води плівкою графіту зверху. Соляна

підкладка повністю розчинялася за певний час і отримували нарисовану тонку плівку графіту, яка плавала на поверхні води. Плаваючу намальовану плівку графіту переносили на кварцову підкладку типорозміром 10×10×0,5 мм. Після перенесення плівку висушували у потоці гарячого повітря (350 К) для видалення залишків води та формування якісного оптичного контакту з гладкою поверхнею підкладки. Відпал отриманих тонких плівок графіту проводили протягом 5 годин при температурі 920 К у вакуумі в електропечі СНОЛ 15/1300 з мікропроцесорним регулятором температури типу RT26-S765. Товщина нарисованих плівок становила 150 нм (товщину вимірювали за допомогою Мікроінтерферометра МИИ-4).

Також було напилено плівку графіту на кварцову підкладку розміром 10×10×0,5 мм методом електронно-променевого випаровування в універсальній вакуумній установці Leybold-Heraeus L560 із спресованих таблеток порошку графіту за температури підкладок 920 К. Потужність випаровуча становила 40 % від максимального значення. Час напилення тривав 1–2 хв. Сформовані таблетки графіту розміщували в мідному тиглі з водяним охолодженням і поступово прогрівали електронним променем у вакуумній камері, яка відкачувалася турбомолекулярним насосом до вакууму $5 \cdot 10^{-5}$ мбар. Щоб запобігти випаровуванню забруднень з поверхні на початковому етапі підігріву таблеток заслінка між тиглем і підкладками була закрита. Товщина напилених плівок становила 30 нм.

Варто відзначити, що температура відпалу і температура напилення тонких плівок графіту методом електронно-променевого випаровування обиралася однаковою (920 К) для порівняння. Відповідно, до наших попередніх досліджень, це оптимальна температура для отримання полікристалічних плівок графіту.

Потужність електронного променю, товщину та швидкість напилення плівки контролювали за допомогою контролера напилення тонких плівок INFICON XTC. Перед напиленням таблетки графіту підігрівали, для запобігання інтенсивному газуванню порошку графіту у разі його різкого нагрівання. Температуру підкладок контролювали системою термопар у вакуумній камері і задавали за допомогою контролера на панелі управління.

Дослідження морфології поверхні тонких плівок графіту проводили за допомогою електронного скануючого електронного мікроскопа (СЕМ) Hitachi S-4100.

Спектри раманівського розсіювання вимірювали за допомогою раманівського мікроскопа LabRAM при довжині хвилі лазерного випромінювання 632,82 нм.

Спектри пропускання напилених та відпалених тонких плівок графіту вимірювали за допомогою спектрофотометра СФ-2000. Експериментальні точки знімалися в області довжин хвиль 200 – 1200 нм з кроком 1 нм.

Вимірювання температурної залежності електричного опору досліджуваних тонких плівок графіту проведені шляхом вимірювання струму, який проходив через зразок при прикладеній напрузі у 10 В. Контроль температури зразка здійснювали за допомогою мідь-константанової термопари. Нагрівання зразка здійснювали електричною пічкою, яка живилася від джерела стабілізованої напруги. Для підтримки постійної температури зразка використовувався терморегулятор.

РЕЗУЛЬТАТИ ТА ОБГОВОРЕННЯ
Структурні властивості тонких плівок графіту

На рис. 1. показано СЕМ зображення поверхні і поперечного перерізу двох тонких плівок графіту, а саме: нарисованої плівки графіту та відпаленої при 920 К та отриманої методом електронно-променевого випаровування при температурі підкладки 920 К.
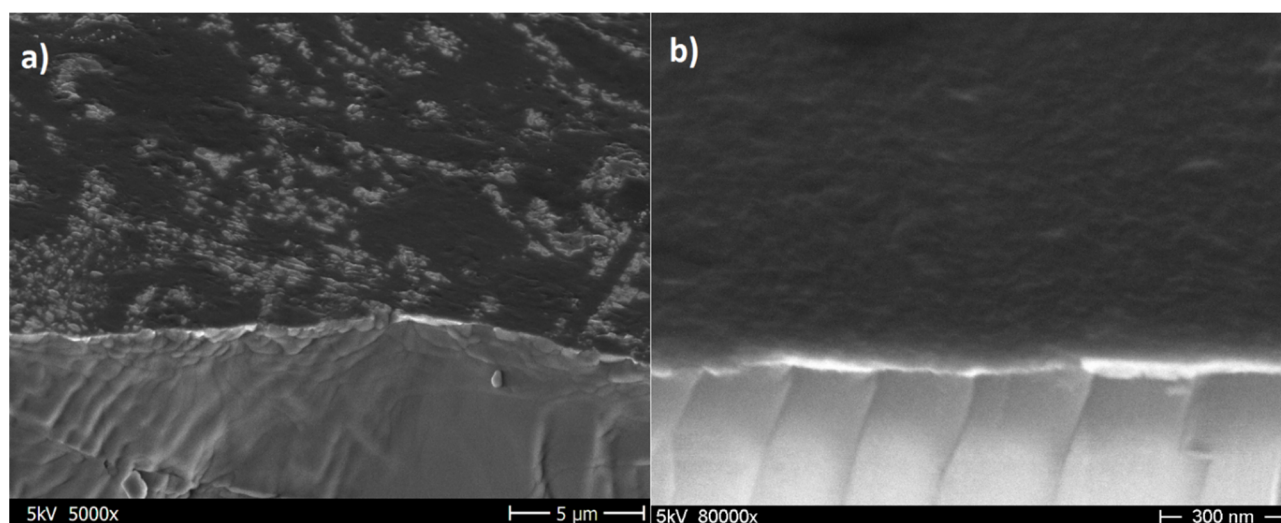

Рис. 1. СЕМ-зображення тонких плівок графіту виготовлених різними методами
а) - нарисована плівка графіту, б) - плівка виготовлена методом електронно-променевого випаровування.

Поверхня нарисованої плівки графіту має видимі отвори (рис. 1а), що є небажаним при виготовленні високоякісних електричних контактів, а поверхня тонкої плівки виготовленої методом електронно-променевого випаровування (рис. 1б) гладка і без видимих отворів, що має вирішальне значення для створення якісних і стабільних електронних приладів з високим коефіцієнтом випрямлення та високою фоточутливістю. Товщина досліджуваної тонкої плівки становила близько 30 нм, що добре узгоджується з даними, отриманими за допомогою контролера осадження INFICON XTC.

Спектри раманівського розсіювання для поверхні тонких плівок графіту отриманих двома різними методами наведено на рис. 2. Відомо, що в однофононних раманівських спектрах досконалих монокристалів графіту спостерігається одна вузька лінія G при 1580 см$^{-1}$, відповідальними за яку є симетричні E_{2g} коливання розтягування – стискування sp^2-зв'язків C–C в 6-атомних ароматичних графенових шарах [10].
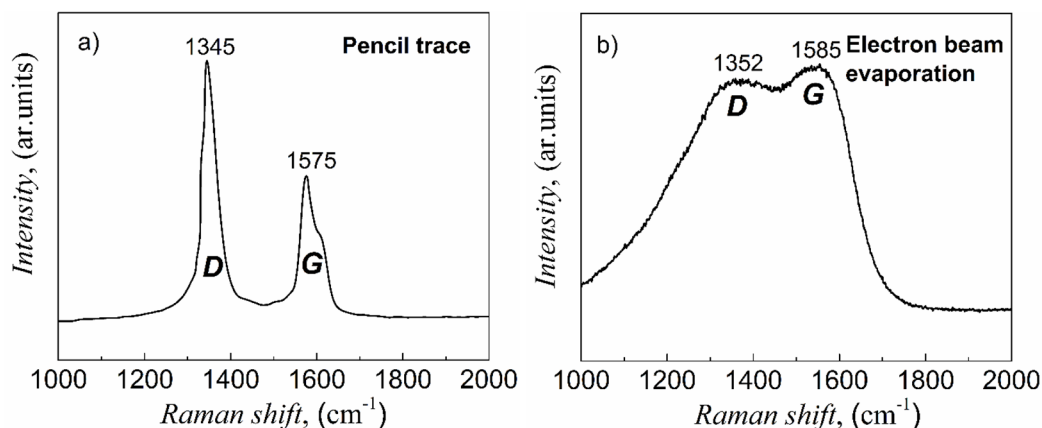

Рис. 2. Раманівські спектри тонких плівок графіту виготовлених різними методами
а) - нарисована плівка графіту, б) - плівка виготовлена методом електронно-променевого випаровування

При дробленні монокристалів графіту до мікро- або нанокристалітів у нанокристалах графіту виявляються можливими раманівські переходи за участю фононів в околі точки K зони Бріллюена, внаслідок чого в спектрах поблизу 1350 см$^{-1}$ з'являється відома смуга D [10], тому смуга D може служити індикатором присутності у вуглецевій структурі графітоподібних кластерів [11].

На відміну від смуги D смуга G спостерігається при будь-якій організації зв'язків вуглецю, включаючи всі можливі кільця і ланцюги, в тому числі і розупорядковані.

Варто відмітити, що G смуга на спектрах раманівського розсіювання (рис. 2) для нарисованих плівок графіту та для плівок отриманих електронно-променевим випаровуванням корелює з раманівським спектром високоорієнтованого піролітичного графіту [12], а яскраво виражена D смуга, походить від невпорядкованої структури нарисованих олівцем графітових плівок, які були відпалені при 920 К (рис. 2а) та плівок отриманих електронно променевим випаровуванням (рис. 2б). Наявність більш розмитих піків на спектрах раманівського розсіювання для плівки отриманої методом електронно променевого випаровування (рис. 2б) свідчить про те, що тонка плівка отримана таким методом є полікристалічною і володіє меншим розміром зерен в порівнянні з нарисованою плівкою.
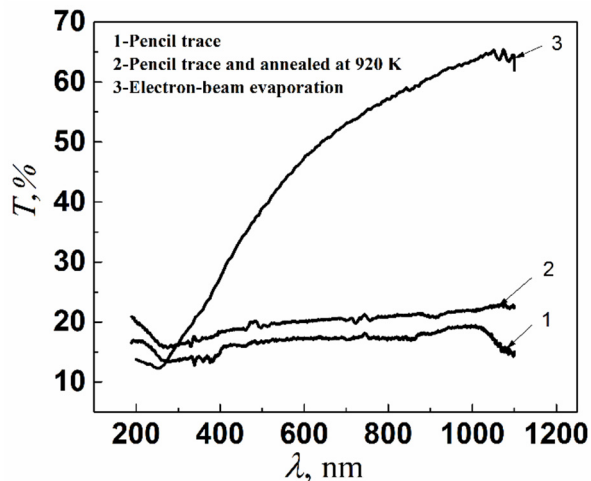
Оптичні властивості тонких плівок графіту

На рис. 3 зображено спектри пропускання тонких плівок графіту, для трьох графітових плівок, які були виготовлені двома методами: "олівець-на-напівпровіднику" та методом електронно-променевого випаровування, після чого одна з нарисованих плівок була відпалена при температурі 920 К.

З рисунка бачимо, що відпал призвів до зростання пропускання. Це обумовлено покращенням структурної досконалості плівок в процесі відпалу. Пропускання для тонких плівок отриманих методом електронно-променевого випаровування є найвищим в порівнянні з нарисованими плівками, що обумовлено їх найменшою товщиною ($d_{ел-про}$=30 нм, $d_{нарисована}$ = 150 нм). Мінімальні значення пропускання при 250 нм пояснюються розсіюванням світла на дефектах, які утворюються на границях зерен [13].

Рис. 3. Спектри пропускання тонких плівок графіту, виготовлених різними методами

Електричні властивості тонких плівок графіту

Результати вимірювання температурної залежності електричного опору досліджуваних тонких плівок графіту представлені на рисунку 4а показали, що опір зменшується при зростанні температури, що вказує на напівпровідниковий тип провідності.
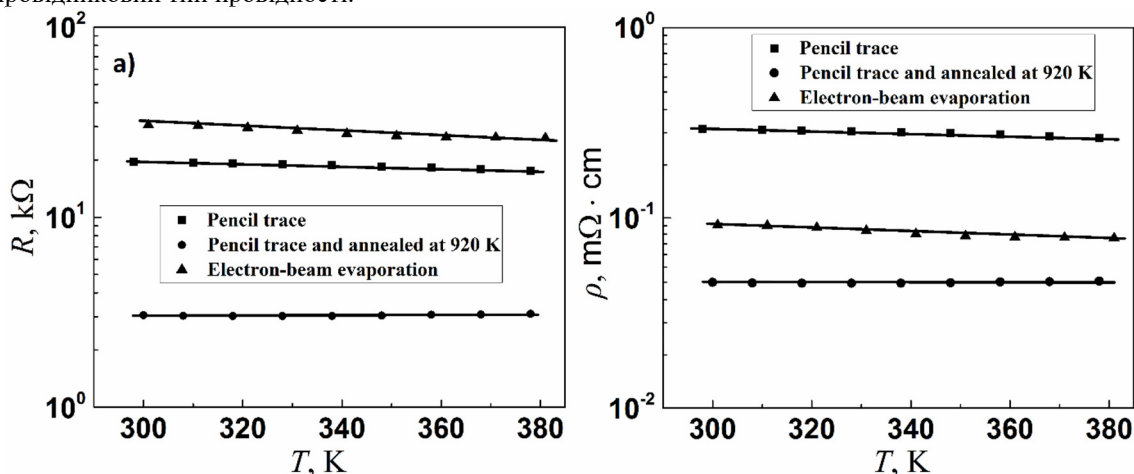

Рис. 4. Температурні залежності опору тонких плівок графіту виготовлених різними методами
а) – електричного опору, б) – питомого опору

Із залежності питомого опору від температури показаної на рисунку 4,б видно, що нарисовані плівки графіту володіють вищим питомим опором ніж плівки отримані електронно-променевим випаровуванням, але відпал нарисованих плівок графіту привів до зменшення питомого опору, що відбулося через покращення їх структурної досконалості, а як наслідок отримали найменші значення питомого опору.

Відомо, що границі зерен у графіті і графітоподібних матеріалах суттєво впливають на фізичні властивості матеріалу [14]. Електричне поле зарядів на границі зерен утворює енергетичні бар'єри E_b для руху носіїв заряду. Між кристалітами утворюються області товщиною δ, які збіднені на основні носії заряду.

Сумарний струм крізь полікристалічний матеріал визначається як провідністю зерен[15], так і механізмом переходу носіїв заряду з одного кристаліта в інший[16-18], тобто провідністю міжзеренних границь. Провідність зерен суттєво більша за провідність границь. Через це при вивченні руху носіїв заряду у полікристалічних плівках в першу чергу слід розглядати провідність областей між кристалітами[19,20]. Провідність полікристалічних плівок σ з врахуванням енергетичних бар'єрів на межі зерен, описується виразом:

$$\sigma = \frac{Lq^2 n}{\sqrt{2\pi m^* kT}} \exp\left(-\frac{qV_b}{kT}\right), \tag{1}$$

де L – середній розмір кристалітів; m^* - ефективна маса носіїв заряду; n – концентрація носіїв заряду всередині кристаліта; $qV_b = E_b$ – висота потенціального бар'єра на границі зерен.

Для визначення висоти потенціальних бар'єрів E_b на границях зерен у графітизованих тонких плівках вуглецю була використана температурна залежність електропровідності у діапазоні 300 K < T < 380 K побудована у напівлогарифмічних координатах $ln(\sigma \cdot T^{1/2}) = f(10^3/T)$ (рис. 6.)
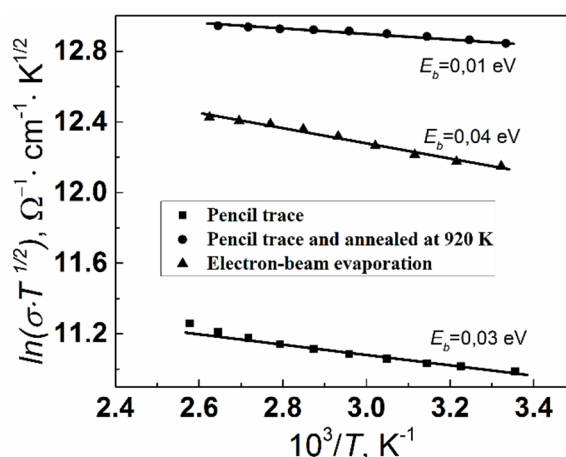

Рис. 6. Температурні залежності електропровідності плівок графіту, отриманих різними методами

Висота потенціального бар'єра на границях зерен для нарисованих плівок графіту становить E_b = 0,03 еВ, для відпаленої E_b = 0,01 еВ та для тонких плівок графіту виготовлених електронно-променевим випаровуванням E_b = 0,04 еВ. Видно, що для відпаленої плівки висота потенціального бар`єра є найменшою.

ВИСНОВКИ

Досліджено структурні властивості двох тонких плівок графіту, а саме: нарисованої плівки графіту та відпаленої при 920 К та отриманої методом електронно-променевого випаровування при температурі підкладки 920 К. Згідно результатів СЕМ структурно досконаліші плівки графіту отримані електронно-променевим осадженням, а наявність більш розмитих піків на спектрах раманівського розсіювання для плівки, отриманої методом електронно-променевого випаровування, свідчить про те, що тонка плівка отримана таким методом є полікристалічною і володіє меншим розміром зерен в порівнянні з нарисованою плівкою.

Досліджено вплив відпалу на нарисовані плівки графіту: їх оптичні та електричні властивості до і після термообробки.

Показано, що плівки графіту отримані методом електронно-променевого випаровування володіють найвищим пропусканням ($T_{550} \approx 60$ %), а пропускання нарисованих плівок є найменшим, відпал приводить до його зростання. Мінімальні значення пропускання при довжині хвилі λ = 250 нм обумовлені розсіюванням світла на дефектах, які утворюються на границях зерен.

Встановлено, що тонкі плівки графіту володіють стрибковою провідністю з енергетичними бар'єрами для невідпаленої E_b = 0,03 еВ, для відпаленої E_b = 0,01 еВ та для виготовленої електронно-променевим методом E_b = 0,04 еВ.

Встановлено, що відпалені плівки графіту володіють найкращою структурною досконалістю оскільки вони мають найменший питомий опір, в порівнянні з невідпаленими плівками та плівками отриманими електронно-променевим методом та володіють найменшою висотою потенціального бар'єра. Одночасне збільшення пропускання у всьому спектральному діапазоні, підвищення питомої електричної провідності та пониження потенціального бар'єра на границях кристалітів відпаленої нарисованої плівки графіту чітко свідчить про упорядкування нарисованих пластівців графіту, перенесених на нову підкладку, що привело до зменшення розсіювання світла та покращення умов струмопереносу між пластівцями графіту за рахунок більшої площі перекриття між ними.

Встановлено, що відпалені плівки графіту не поступаються електричними властивостями, а є навіть кращими від плівок напилених методом електронно-променевого випаровування. Метод «олівець-на-напівпровіднику» є більш екологічним і дешевшим, тому виготовлення тонких плівок графіту даним методом є актуальним.

ORCID IDs

Mykhailo M. Solovan, https://orcid.org/0000-0002-1077-5702; **Viktor V. Brus,** https://orcid.org/0000-0002-8839-124X, **Pavlo D. Maryanchuk,** https://orcid.org/0000-0002-5523-4280

СПИСОК ЛІТЕРАТУРИ

[1] E. Rollings, G.-H. Gweon, S.Y. Zhou, B.S. Mun, J.L. McChesney, B.S. Hussain, A.V. Fedorov, P.N. First, W.A. de Heer, and A. Lanzara, J. Phys. Chem. Sol. **67**, 2172 (2006), https://doi.org/10.1016/j.jpcs.2006.05.010.
[2] S. Tongay, T. Schumann, X. Miao, B.R. Appleton, and A.F. Hebard, Carbon, **49**, 2033 (2011), https://doi.org/10.1016/j.carbon.2011.01.029.
[3] V.V. Brus, and P.D. Maryanchuk, Carbon, **78**, 613-616 (2014), https://doi.org/10.1016/j.carbon.2014.07.021.
[4] M. Murakami, A. Tatami, and M. Tachibana, Carbon. **145**, 23-30 (2019), https://doi.org/10.1016/j.carbon.2018.12.057.
[5] Q. Zheng, P.V. Braun, and D. G. Cahill, Adv. Mater. Interfaces. **3,** 1600234 (2016), https://doi.org/10.1002/admi.201600234.
[6] V.V. Brus and P.D. Maryanchuk, Applied Physics Letters, **104**, 173501 (2014), https://doi.org/10.1063/1.4872467.
[7] M.M. Solovan, H.P. Parkhomenko, and P.D. Marianchuk, Journal of Physical Studies, **23**, 4801 (2019), https://doi.org/10.30970/jps.23.4801.
[8] S.M. Sze, and K. Kwok, *Physics of Semiconductor Devices*, (Wiley, New Jersey, 2007), pp. 832.
[9] B.L. Sharma, and R.K. Purohit, *Semiconductor hetero-junctions,* (Pergamon, 1974).
[10] A.C. Ferrari, and J. Robertson, Phys. Rev. B, **61,** 14095 (2000), https://doi.org/10.1103/PhysRevB.61.14095.
[11] É.A. Smorgonskaya, and V.I. Ivanov-Omskii, Semiconductors, **39**, 934 (2005), https://doi.org/10.1134/1.2010688.
[12] T. Kaplas, and P. Kuzhir, Nanoscale Res. Lett. **11,** 54 (2016), https://doi.org/10.1186/s11671-016-1283-2.
[13] V.V. Brus, M. Gluba, J. Rappich, F. Lang, P.D. Maryanchuk, and N.H. Nickel, ACS Applied Materials and Interfaces. **10,** 4737 (2018), https://doi.org/10.1021/acsami.7b17491.
[14] V.V. Brus, M. Ilashchuk, I. Orletskyi, M. Solovan, G. Parkhomenko, I.S. Babichuk, N. Schopp, G.O. Andrushchak, A. Ostovyi, and P. D Maryanchuk, Nanotechnology, **31**, 505706 (2020) https://doi.org/10.1088/1361-6528/abb5d4.
[15] G. Lormand, Journal de Physique Colloques, **43** (C6), C6-283 (1982), https://doi.org/10.1051/jphyscol:1982625.
[16] A. Tschöpe, and R. Birringer, Journal of Electroceramics, **7**, 169 (2001), https://doi.org/10.1023/A:1014483028210.
[17] V.H. Nguyen, U. Gottlieb, A. Valla, D. Muñoz, D. Belleta, and D. Muñoz-Rojas, Mater. Horiz. **5**, 715 (2018), https://doi.org/10.1039/C8MH00402A.
[18] H.-S. Kim, S.D. Kang, Y. Tang, R. Hanus, and G.J. Snyder, Mater. Horiz. **3**, 234 (2016), https://doi.org/10.1039/C5MH00299K.
[19] C.H. Seager, and G.E. Pike, Appl. Phys. Lett. **40**, 471 (1982).
[20] P. Forsyth, R. King, G. Metcalfe, and B. Chalmers, Nature, **158,** 875 (1946), https://doi.org/10.1038/158875a0.

ОПТИЧНІ І ЕЛЕКТРИЧНІ ВЛАСТИВОСТІ ТОНКИХ ПЛІВОК ГРАФІТУ ОТРИМАНИХ РІЗНИМИ МЕТОДАМИ

М.М. Солован[a], Г.М. Ямрозик[a], В.В Брус[b], П.Д. Мар'янчук[a]

[a]Чернівецький національний університет імені Юрія Федьковича
вул. Коцюбинського 2, 58012 Чернівці, Україна
[b]Університет імені Назарбаева, 53, Қабанбай батир, 010000, Нур-Султан, Казахстан

У роботі представлено результати досліджень структурних, оптичних і електричних властивостей тонких плівок графіту виготовлених двома методами, а саме: безвакуумним методом «Олівець-на-напівпровіднику» та методом електронно-променевого випаровування, такі дослідження мають велике значення для подальшої розробки високоефективних приладів на основі гетеропереходів для електроніки і оптоелектроніки. Виготовлені безвакуумним методом тонкі плівки графіту були відпалені при температурі 920 К. Виміряні спектри пропускання досліджуваних графітових плівок при Т = 300 К та електричні властивості тонких плівок, визначено значення висоти потенціальних бар'єрів E_b на границях зерен, для цього була використана температурна залежність електропровідності у діапазоні 300 К < T < 380 К побудована у координатах $ln(\sigma \cdot T^{1/2}) = f(10^3/T)$. Встановлено, що висота бар'єра на границях зерен для нарисованих плівок графіту становить $E_b = 0,03$ еВ, відпаленої - $E_b = 0,01$ еВ та для тонких плівок графіту виготовлених електронно-променевим випаровуванням $E_b = 0,04$ еВ, тобто для відпаленої плівки висота потенціального бар'єра є найменшою. Показано, що плівки графіту отримані методом електронно-променевого випаровування володіють найвищим пропусканням (T550 ≈ 60 %), а пропускання нарисованих плівок є найменшим, відпал призводить до його зростання. Мінімальні значення пропускання при довжині хвилі λ=250нм обумовлені розсіюванням світла на дефектах, які утворюються на границях зерен. Встановлено, що відпалені плівки графіту володіють найкращою структурною досконалістю оскільки вони мають найменший питомий опір, в порівнянні з невідпаленими плівками та плівками отриманими електронно-променевим методом та володіють найменшою висотою потенціального бар'єра. Одночасне збільшення пропускання у всьому спектральному діапазоні, підвищення питомої електричної провідності та зниження потенціального бар'єру на границях кристалітів відпаленої нарисованої плівки графіту чітко свідчить про упорядкування нарисованих пластівців графіту, перенесених на нову підкладку, що привело до зменшення розсіювання світла та покращення умов струмопереносу між пластівцями графіту за рахунок більшої площі перекриття між ними.

КЛЮЧОВІ СЛОВА: «олівець-на-напівпровіднику», відпал, тонкі плівки, графіт, границі зерен

ОПТИЧЕСКИЕ И ЭЛЕКТРИЧЕСКИЕ СВОЙСТВА ТОНКИХ ПЛЕНОК ГРАФИТА ПОЛУЧЕНЫХ РАЗНЫМИ МЕТОДАМИ

М.Н. Солован[a], Г.Н. Ямрозык[a], В.В. Брус[b], П.Д. Марьянчук[a]

[a]Черновицкий национальный университет имени Юрия Федьковича
ул. Коцюбинского 2, 58012 Черновцы, Украина
[b]Университет имени Назарбаева, 53, Қабанбай батыр, 010000, Нур-Султан, Казахстан

В работе представлены результаты исследований структурных, оптических и электрических свойств тонких пленок графита изготовленных двумя методами: а именно безвакуумным методом «карандаш-на-полупроводнике» и методом электронно-лучевого испарения, такие исследования имеют большое значение для дальнейшей разработки высокоэффективных приборов на основе гетеропереходов для электроники и оптоэлектроники. Полученные безвакуумным методом тонкие пленки графита были отожжены при температуре 920 К. Измерены спектры пропускания исследуемых графитовых пленок при Т = 300 К и электрические свойства тонких пленок, определено значение высоты потенциальных барьеров E_b на границах зерен, для этого была использована температурная зависимость электропроводности в диапазоне 300 К < Т <380 К построенная в координатах $ln(\sigma \cdot T^{1/2}) = f(10^3/T)$. Установлено, что высота барьера на границах зерен нарисованной пленки графита составляет $E_b = 0,03$ еВ, для отожженной $E_b = 0,01$ еВ и для тонких пленок графита изготовленных электронно-лучевым испарением $E_b = 0,04$ еВ, то есть для отожженной пленки высота потенциального барьера является наименьшей. Показано, что пленки графита, полученные методом электронно-лучевого испарения, обладают высоким пропусканием (T550 ≈ 60 %), а пропускание нарисованных пленок является наименьшим, отжиг приводит к его росту. Минимальные значения пропускания при длине волны λ = 250 нм обусловлены рассеянием света на дефектах, которые образуются на границах зерен. Установлено, что отожженные пленки графита обладают лучшим структурным совершенством поскольку они имеют наименьшее удельное сопротивление, по сравнению с не отожжёнными пленками и пленками, полученными электронно-лучевым методом, и обладают наименьшей высотой потенциального барьера. Одновременное увеличение пропускания во всем спектральном диапазоне, повышение удельной электрической проводимости и понижение потенциального барьера на границах кристаллитов отожженной нарисованной пленки графита четко свидетельствует об упорядочении нарисованных хлопьев графита, перенесенных на новую подложку, что привело к уменьшению рассеяния света и улучшению условий токопереноса между хлопьями графита за счет большей площади перекрытия между ними.

КЛЮЧЕВЫЕ СЛОВА: «карандаш-на-полупроводнике», отжиг, тонкие пленки, графит, границы зерен

RESEARCH AND SELECTION OF PROSPECTIVE MATERIALS FOR ACTIVATION DOSIMETRY OF INTENSE BREMSSTRAHLUNG RADIATION

Olexii S. Deiev, Roman M. Dronov, Valentyn A. Shevchenko, Boris I. Shramenko*

National Science Center "Kharkov Institute of Physics and Technology" Kharkiv, Ukraine
Corresponding Author: bshram@kipt.kharkov.ua

Radiation technologies based on the use of powerful electron beams and gamma radiation are closely related to the need for dosimetry of these beams. Dosimetry based on the use of the inelastic gamma-ray scattering reaction on a number of nuclei with the formation of isomers with different half-lives and energies of radiation quanta is very successful for these purposes. An example of this application in dosimetry is the ^{115}In $(\gamma,\gamma')^{115m}$In reaction, which results in the formation of the ^{115m}In isomer, having a gamma line with an energy of 336.24 keV and a half-life of 4.5 hours. There was a successful application of this technique in dosimetry in solving certain practical problems (irradiation complexes based on ^{60}Co source- cobalt "guns"). In this work, it is shown that the use of In detectors for dosimetry of gamma-radiation with a wide energy spectrum (bremsstrahlung) is associated with significant uncertainty in measuring the equivalent dose of the gamma spectrum with an upper limit of 10 MeV. This uncertainty is due to the relatively high threshold of the aforementioned reaction of 1.08 MeV. The quantitative contribution to the total radiation flux of the region of the gamma spectrum below the threshold (γ,γ') of the reaction on the In nucleus was determined and it was shown that, depending on the direction of radiation, there is an systematic error in measuring the equivalent dose, reaching 20-60%. Investigated and proposed for use alternative materials detectors, allowing reducing the systematic error in measuring the equivalent dose to 2-3%, which is quite acceptable for practical use.

KEYWORDS: linear electron accelerator, gamma-radiation, (γ,γ') reaction, isomer, dosimetry

ОБГРУНТУВАННЯ НЕОБХІДНОСТІ ПОШУКУ НОВИХ МАТЕРІАЛІВ, ПЕРСПЕКТИВНИХ ДЛЯ ДОЗИМЕТРІЇ ГАММА-ВИПРОМІНЮВАННЯ ВЕЛИКОЇ ІНТЕНСИВНОСТИ

Використання мішені з індію (In) для дозиметрії гамма-випромінювання по «наведеній» активності ізомеру ^{115m}In, що утворюється в реакції ^{115}In $(\gamma,\gamma')^{115m}$In описано, наприклад, в роботах [1,2], де такий метод дозиметрії був застосований для моніторингу гамма-випромінювання джерел на основі ізотопу ^{60}Co (кобальтових гармат) промислового застосування. Така методика була застосована для дозиметрії інтенсивних потоків гальмівного випромінювання більш високої енергії: 10-70 МеВ. В роботах [3,4] показано, що чутливість методу є практично постійною в області енергій 10-70 МеВ, що надзвичайно важливо. Визначено дозиметричний ресурс In детекторів (по тепловому навантаженню), що дорівнює $\approx 10^7$ Гр, який при використанні додаткового охолодження може бути збільшений на 1-2 порядки. Таким чином, на додаток до даних робіт [5,6], показана можливість використання детекторів з In для дозиметрії інтенсивних потоків гамма-квантів в області енергій до 70 МеВ.

З огляду на те, що енергія збудження ізомерного рівня ^{115m}In дорівнює 1,08 МеВ (поріг (γ,γ') реакції), проведено аналіз кількісного внеску ділянки спектра в інтервалі енергій 0-1,08 МеВ в загальний потік гамма-випромінювання з верхньою межею діапазону 10 МеВ. Для цього використано код *GEANT4*, *PhysicsList G4LowEnergy* і розраховані спектри гальмівних гамма-квантів і електронів для різних тілесних кутів реєстрації, на основі спектрів розраховані дозові характеристики гамма-випромінювання з верхньою межею діапазону 10 МеВ. Розрахунки виконані для гальмівної мішені з танталу (Ta), товщиною 2,4 мм і енергії електронів 10 МеВ (розподіл електронів - нормальний, FWHM=0,8 МеВ, діаметр пучка 2 мм, що близько до реальних умов на прискорювачі ЛУЕ -10).

Конвертер з Ta розташований у центрі сфери і показаний на Рис.1. Гальмівні кванти реєструються системою сферичних детекторів, відповідно до геометричної схеми, яка показана на Рис. 1б. Більш детально методика розрахунків в *GEANT4* описана в [5].

Послідовність розрахунків потоків гальмівного випромінювання у залежності від кута вильоту (реєстрації) була наступною:

- поверхня сфери ділиться на сектори, кутова ширина яких відповідає кроку 0,1 радіан. ($\pm$0,05 радіан або $\pm$2,86°);

- в центрі сфери знаходиться конвертор (радіатор) з Ta розмірами 5×5×2,4 мм;

- в кожному кутовому секторі підраховується число гамма-квантів $N_{0-1,08}$ в інтервалі енергій 0-1,08 МеВ та загальна кількість гамма-квантів N_{total} в інтервалі енергій 0-10 МеВ.

- розраховується відношення $N_{0-1,08}$ / N_{total} для різних кутів випромінювання.

В результаті математичного моделювання в *GEANT4* отримані спектри гальмівного випромінювання для конвертора Ta 5×5×2,4 мм і енергії електронів E_e =10 МеВ. (Рис. 2).
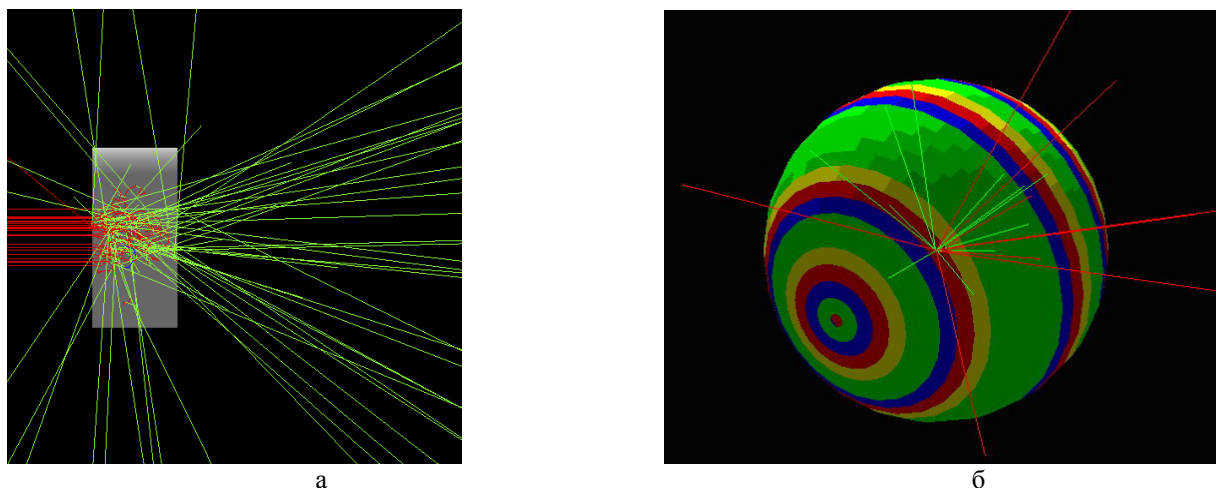
Рис. 1. Конвертер з Ta - а, розташування сферичних детекторів, що реєструють виліт електронів (червоні лінії) і гамма-квантів (зелені лінії) - б. Крок по куту 0,1 радіан
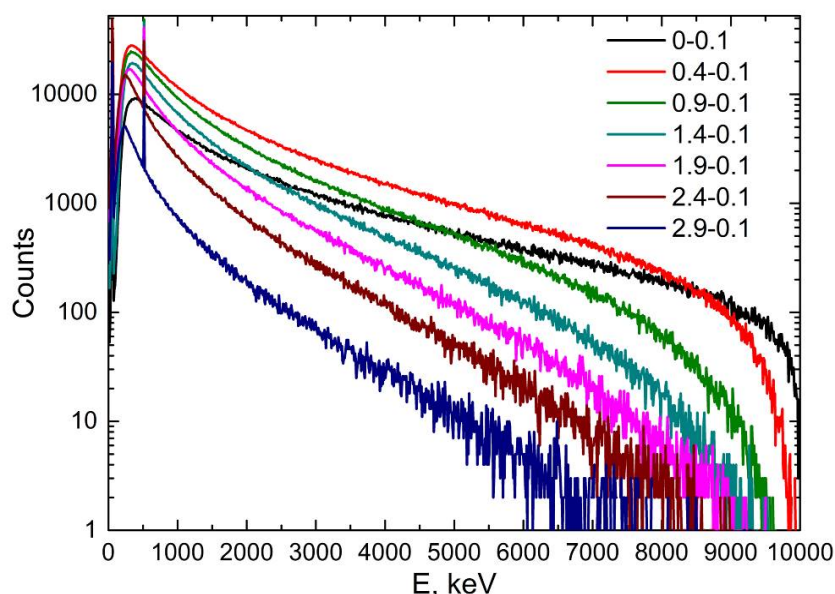

Рис. 2. Спектри гальмівних гамма-квантів для різних інтервалів кутів випромінювання (в радіанах).
Ta 5×5×2,4 мм, E_e =10 МеВ.

Як видно з Рис. 2, спектр гальмівного випромінювання істотно залежить від тілесного кута випромінювання (реєстрації). Загальна інтенсивність гальмівних спектрів різко падає зі збільшенням кута. Високоенергетична частина спектра в міру збільшення кута випромінювання зменшується значніше, ніж низькоенергетична частина. Наступним кроком було обчислення співвідношення $N_{0-1.08}$ / N_{total} для різних кутів випромінювання. Чисельні відношення кількості гамма-квантів в інтервалі енергій від 0 до1,08 МеВ – $N_{0-1,08}$ до повного числа квантів в інтервалі енергій від 0 до10 МеВ – N_{total} для різних кутів випромінювання з інтервалом 0,1 рад подані в Таблиці 1.

Таблиця 1.
Співвідношення кількості гамма-квантів $N_{0-1,08}$ в інтервалі енергій від 0 до 1,08 МеВ до повного числа квантів N_{total} для різних кутів випромінювання з інтервалом 0,1 рад. Ta 5×5×2,4 мм, E_e =10 МеВ.

Кут середини смуги, рад	Кут середини смуги, град.	$N_{0-1,08}$ / N_{total}
0,05	2,86	0,463
0,15	8,59	0,486
0,25	14,32	0,509
0,35	20,05	0,531
0,45	25,78	0,550
0,55	31,51	0,567
0,65	37,24	0,583

Кут середини смуги, рад	Кут середини смуги, град.	N $_{0-1,08}$ / N$_{total}$
0,75	42,97	0,597
0,85	48,70	0,607
0,95	54,43	0,616
1,05	60,16	0,624
1,15	65,89	0,632
1,25	71,62	0,639
1,35	77,35	0,647
1,45	83,08	0,653
1,55	88,81	0,658
1,65	94,54	0,672
1,75	100,27	0,690
1,85	106,00	0,707
1,95	111,73	0,727
2,05	117,46	0,745
2,15	123,19	0,762
2,25	128,92	0,776
2,35	134,65	0,790
2,45	140,38	0,800
2,55	146,11	0,810
2,65	151,84	0,818
2,75	157,57	0,823
2,85	163,30	0,828
2,95	169,03	0,831
3,05	174,76	0,833

Дані Табл. 1 показані у вигляді графіка на Рис. 3. Повна похибка розрахункових величин не перевищує 2% і змінюється від 0,2% до 2% зі збільшенням кута реєстрації від 0 до 180^0.
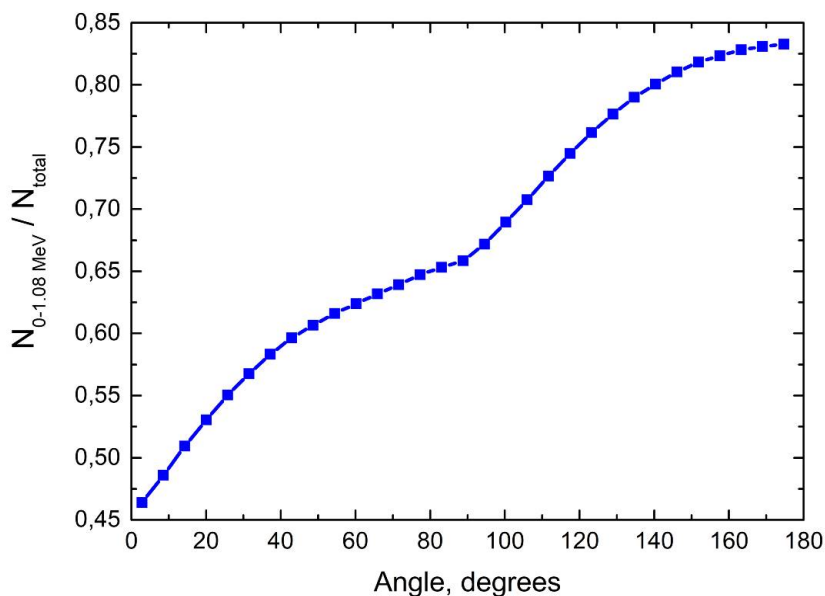

Рис. 3. Співвідношення кількості гальмівних квантів N $_{0-1,08}$ /N$_{total}$ для різних кутів випромінювання (в градусах)
Ta 5×5×2,4 мм, E$_e$ =10 MeB.

Характерний прогин під кутом 90 градусів вказує на той факт, що під цим кутом мішень поглинає частину низькоенергетичних квантів, зменшуючи співвідношення числа гальмівних квантів. Істотним фактом є те, що низькоенергетичне випромінювання в інтервалі 0-1,08 MeB становить значну частку в загальному випромінюванні гамма-квантів, починаючи від значення близько 0,48 для кута 10 градусів, досягаючи величини 0,83 для кута 175 градусів.

В кінцевому підсумку нас цікавить інформація про дози, обумовлені гамма-квантами, і похибки у вимірюванні дози, які пов'язані з використанням детекторів з In. Для цього використані дані про «дозові коефіцієнти гамма-квантів», взяті з роботи [6], які наведені в Табл.2.

Таблиця 2.

Питомі максимальні еквівалентні дози і еквівалентні дози для гамма-квантів різних енергій

E_γ, кеВ	Питома максимальна еквівалентна доза h_M; Зв×см²/фотон	Коефіцієнт якості; k	Еквівалентна доза; h_M×k; Зв×см²/фотон
5	6,50E-09	2,6	1,69E-08
10	1,30E-09	1,8	2,34E-09
20	2,60E-10	1,4	3,64E-10
30	1,10E-10	1,5	1,65E-10
50	5,20E-11	1,7	8,84E-11
100	7,20E-11	1,5	1,08E-10
200	1,20E-10	1,2	1,44E-10
500	2,60E-10	1,1	2,86E-10
1000	4,80E-10	1,0	4,80E-10
2000	8,30E-10	1,0	8,30E-10
5000	1,60E-09	1,0	1,60E-09
10000	2,90E-09	1,0	2,90E-09

Використовуючи дані Табл. 2, визначена залежність співвідношення дози для гамма-квантів в інтервалі 0-1,08 МеВ до повної дози в інтервалі 0-10 МеВ для всіх кутів випромінювання. Ці дані представлені в Табл. 3.

Таблиця 3.

Еквівалентні дози для різних енергетичних інтервалів і їх співвідношення в залежності від кута випромінювання для In

Кут середини смуги; рад	Доза $_{0-1,08\,МеВ}$; Зв×см²/фотон	Доза $_{0-10\,МеВ}$; Зв×см²/фотон	Доза $_{0-1,08\,МеВ}$/Доза $_{0-10\,МеВ}$
0,05	0,020	0,098	0,198
0,15	0,040	0,187	0,213
0,25	0,049	0,210	0,231
0,35	0,053	0,213	0,248
0,45	0,055	0,206	0,266
0,55	0,055	0,194	0,283
0,65	0,054	0,181	0,299
0,75	0,052	0,167	0,314
0,85	0,050	0,152	0,327
0,95	0,047	0,138	0,340
1,05	0,044	0,127	0,351
1,15	0,042	0,116	0,361
1,25	0,040	0,107	0,371
1,35	0,037	0,098	0,382
1,45	0,035	0,089	0,390
1,55	0,032	0,081	0,397
1,65	0,031	0,075	0,413
1,75	0,030	0,069	0,434
1,85	0,029	0,065	0,454
1,95	0,029	0,061	0,476
2,05	0,028	0,056	0,497
2,15	0,027	0,052	0,519
2,25	0,026	0,048	0,538
2,35	0,024	0,043	0,555
2,45	0,022	0,038	0,569
2,55	0,019	0,033	0,584
2,65	0,016	0,027	0,596
2,75	0,013	0,022	0,601
2,85	0,010	0,016	0,609
2,95	0,007	0,011	0,614
3,05	0,003	0,005	0,618

На Рис. 4. показані результати розрахунків співвідношення дози для гамма-квантів в інтервалі 0-1,08 МеВ до повної дози в інтервалі 0-10 МеВ в графічному вигляді.
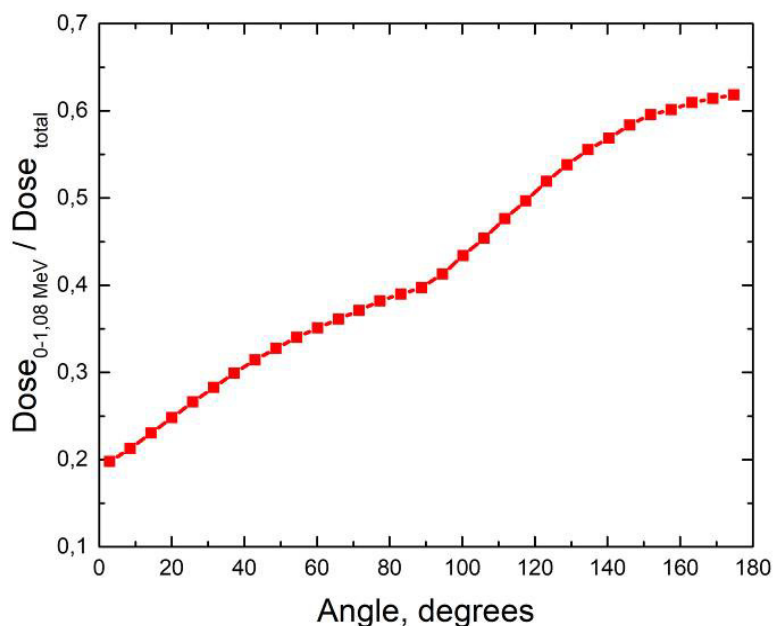

Рис. 4 Кутова залежність співвідношення еквівалентної дози низькоенергетичного гамма-випромінювання в інтервалі 0-1,08 МеВ до повної дози гамма-випромінювання в інтервалі 0-10 МеВ для зразка In. Ta 5×5×2,4 мм, Е_e =10 МеВ.

Аналізуючи дані, наведені в Табл. 3 і на Рис. 4 приходимо до висновку, що частка еквівалентної дози низькоенергетичного випромінювання в інтервалі 0-1,08 МеВ вносить значний вклад в загальну дозу у всьому інтервалі тілесних кутів випромінювання гамма-квантів з максимальною енергією 10 МеВ - від 20 до 60%. Це, фактично, визначає систематичну похибку вимірювань дози за допомогою детекторів на основі In. Очевидно, що при використанні гамма-випромінювання з верхньою межею, що дорівнює кільком десяткам МеВ, невизначеність, обумовлена внеском інтервалу 0-1,08 МеВ, буде зменшуватися в міру збільшення верхньої межі діапазону, тобто для ситуацій, що мають місце в роботах [3, 4].

Збільшення верхньої межі діапазону пом'якшує ситуацію з невизначеністю при вимірюванні абсолютної поглиненої дози, але не знімає цю проблему повністю. Таким чином, використання детекторів на основі In для визначення абсолютних значень еквівалентної дози гамма-квантів з максимальною енергією 10 МеВ пов'язано з погрішностями від 20 до 60%, хоча вимірювання відносних значень поглиненої дози цілком правомірні.

Виходом з цієї ситуації може бути пошук і використання таких активаційних детекторів, енергії збудження ізомерних рівнів яких, мають більш низькі значення в порівнянні з рівнем 1,08 МеВ ізомера ^{115m}In, що дозволить забезпечити вимірювання дози випромінювання з меншою похибкою. Пошуку таких можливостей присвячені подальші дослідження.

ВИБІР ПЕРСПЕКТИВНИХ МАТЕРІАЛІВ ДЛЯ АКТИВАЦІЙНОЇДОЗИМЕТРІЇ ГАЛЬМІВНОГО ВИПРОМІНЮВАННЯ ВЕЛИКОЇ ІНТЕНСИВНОСТІ

При виборі нових матеріалів для активаційної дозиметрії гальмівного випромінювання головними критеріями були фізичні характеристики матеріалів і характеристики розпаду ізотопів , що утворюються.

Серед фізичних характеристик нових матеріалів, перш за все, необхідні:
- термостійкість;
- стійкість до високої потужності дози;
- висока максимальна доза.

Серед характеристик розпаду ізотопів що утворюються слід враховувати:
- мінімальне накопичення довгоживучих нуклідів;
- мінімальне значення енергії збудження ізомерного рівня;
- відносно короткий період напіврозпаду ізомера;
- високе значення перерізу (γ,γ') реакції

В результаті ретельного відбору матеріалів-претендентів нашу увагу, перш за все, було зосереджено на матеріалах з низьким порогом збудження ізомерних станів ядер. Вони перераховані в Табл. 4.

Як видно з Табл. 4, до переліку ізомерів-претендентів були віднесені: ^{111m}Cd, ^{117m}Sn, ^{135m}Ba, ^{180m}Hf. Були проведені експерименти з напрацювання очікуваних ізомерів за допомогою опромінення обраних зразків

матеріалів пучком гальмівного випромінювання прискорювача ЛУЕ-10. Опромінення всіх зразків проводилося в стандартній геометрії опромінення з наступним режимом:
- енергія електронів E_0 = 11,5 МеВ,
- тривалість експозиції 1,3 години,
- доза опромінення 4,8 кГр.

Таблиця 4.

Можливі реакції в перспективних мішенях

Цільовий ізотоп	Реакція	Поріг реакції, МеэВ	Усереднений перетин, мбарн
^{111}Cd	^{112}Cd (24%) $(\gamma,n)^{111}$Cd	9,80	100-120
	^{110}Cd (12,5%) $(n,\gamma)^{111}$Cd	-	250
^{111m}Cd	^{111}Cd (12,8%) $(\gamma,\gamma')^{111m}$Cd	0,40	-
^{115}Cd	^{116}Cd (7,5%) $(\gamma,n)^{115}$Cd	8,70	-
	^{114}Cd (28,7%) $(n,\gamma)^{115}$Cd	-	160 – швидкі нейтрони; ≈350 – теплові нейтрони
^{117m}Sn	^{118}Sn (24,2%) $(\gamma,n)^{117m}$Sn	9,65	≈150
	^{116}Sn (18,7%) $(n,\gamma)^{117m}$Sn	-	≤ 90
	^{117}Sn (7,3%) $(\gamma,\gamma')^{117m}$Sn	0,32	-
^{135m}Ba	^{135}Ba (6,5%) $(\gamma,\gamma')^{135m}$Ba	0,30	-
	^{136}Ba (7,8%) (γ,n) ^{135m}Ba	>9,00	-
^{180m}Hf	^{180}Hf (29%) (γ,γ') ^{180m}Hf	1,10	-
^{182m}Hf	^{186}W (29%) $(\gamma,\alpha)^{182m}$Hf	1,00	-

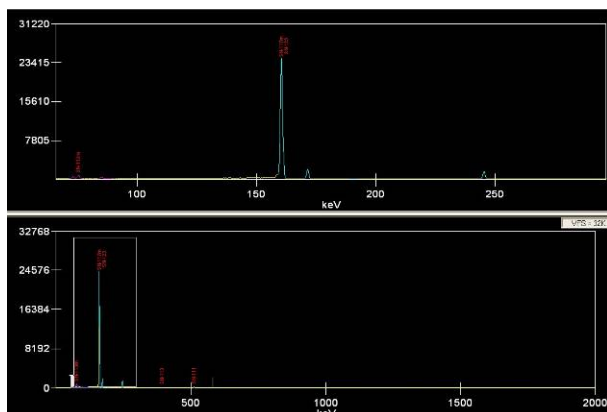Гамма-спектри опромінених зразків матеріалів наведені, відповідно, на Рис.5. - Рис.8.

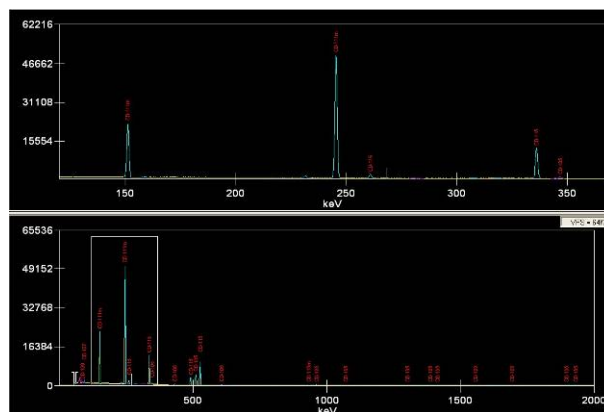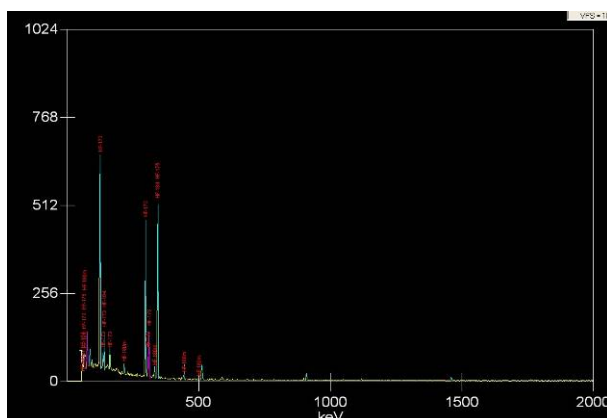Рис. 5. Спектр опроміненого зразка Sn

Рис 6. Спектр опроміненого зразка Cd

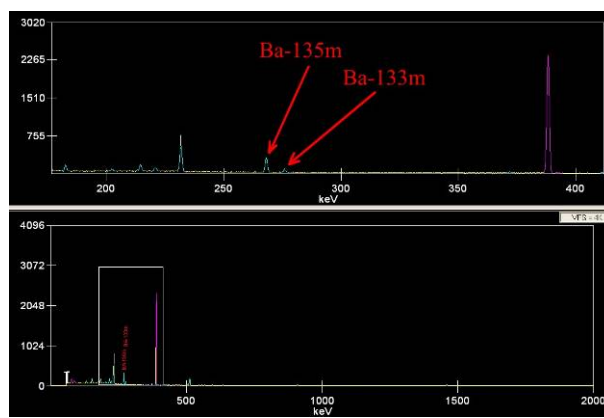**Рис. 7**. Спектр опроміненого зразка Hf

Рис. 8. Спектр опроміненого зразка Ba

Вимірювання активності цільових і домішкових ізотопів в опромінених зразках виконано за допомогою спектрометричного комплексу CANBERRA [5]. Узагальнені дані цільових і домішкових ізотопів в перспективних мішенях зведені в Табл. 5.

Активність цільових і домішкових ізотопів в перспективних мішенях

Ізотоп	Період напіврозпаду, $T_{1/2}$	Гамма-лінія, кеВ	Активність, кБк/г	Невизначеність вимірювань, кБк/г
^{111m}**Cd**	49 хв	245	<u>243,000</u>	1,600
^{105}Cd	55 хв	961	60,000	5,000
^{115}Cd	53 год	527	45,000	12,000
^{115m}Cd	44,5 дня	933	6,000	2,000
^{113m}Sn	21,4 хв	77,4	2,000	0,700
^{117}**Sn**	13,6 днів	158	<u>33,800</u>	1,200
^{123m}Sn	129 днів	1088	< 1,000	-
^{123}Sn	40 хв	160	< 1,000	-
^{133m}Ba	38,9 год	280	2,230	0,200
^{135m}**Ba**	28,7 год	270	<u>14,600</u>	0,700
^{173}Hf	23,6 год	123	1,300	0,900
^{175}Hf	70 днів	343	2,600	0,090
^{180m}**Hf**	5,5 год	332	<u>0,135</u>	0,016
^{184}Hf	4,1 год	139; 345	0,580	0,068

Отримані результати з наведеної активності досліджуваних зразків після опромінення пучком гальмівного випромінювання (як видно з табл. 5), вказують на те, що за час опромінення зразків, найменшу активність має ізомер ^{180m}Hf. З огляду також на той факт, що ізомер ^{180m}Hf має порівняно високий поріг збудження (1,1 МеВ) - це дає підстави для виключення його з переліку перспективних ізотопів для активаційної дозиметрії.

Таким чином, в якості нових перспективних дозиметричних детекторів можуть бути використані наступні матеріали: Cd, Sn, Ba. При опроміненні цих матеріалів гамма-квантами збуджуються ізомери з найбільш прийнятними для вимірювання і використання характеристиками - ^{111m}Cd; ^{117m}Sn; ^{135m}Ba. Доречно порівняти кутові залежності дозових відношень перспективних ізомерів з ізомером ^{115m}In. Таке порівняння демонструє Рис. 9.
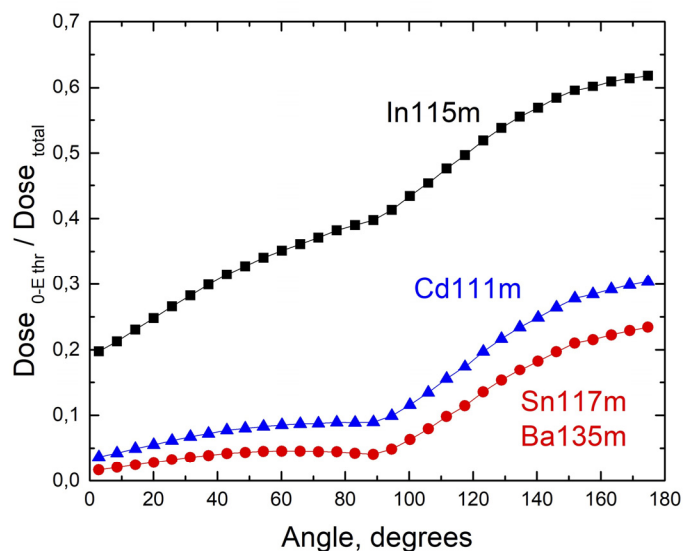

Рис. 9. Порівняння кутової залежності співвідношення еквівалентної дози низькоенергетичного гамма-випромінювання (від нуля до порога реакції) до повної дози в інтервалі 0-10 МеВ для різних ізомерів:
(0-1,08 МеВ - ^{115m}In); (0-0,4 МеВ - ^{111m}Cd); (0-0,32 МеВ - ^{117m}Sn); (0-0,3 МеВ - ^{135m}Ba).

З Рис. 9 видно, що використання в якості дозиметричних детекторів Cd, Sn або Ba дозволяє істотно знизити похибку у вимірюванні еквівалентної дози гамма-випромінювання в порівнянні з детектором з In для всіх кутів вильоту гамма-випромінювання. Наприклад, якщо при детектуванні гамма-випромінювання, спрямованого «вперед», похибка у вимірі дози детектором In становить 20%, то для детекторів Sn і Ba, така похибка становить 2%, а для детектора Cd – 3%. Таким чином, значення систематичних помилок у вимірі еквівалентної дози гамма-випромінювання детекторами Cd, Sn і Ba до 10 разів менше, ніж для детекторів з In, отже, вони більш прийнятні для практичного використання в якості нових, перспективних активаційних дозиметричних детекторів.

ВИСНОВКИ

1. В результаті проведених досліджень характеристик матеріалу In, у якості дозиметричного детектора, отримані кількісні оцінки внеску інтенсивності низькоенергетичної частини гамма-випромінювання (в інтервалі енергій 0-1,08 МеВ) в повну інтенсивність випромінювання з верхньою межею 10 МеВ.

2. Показано, що використання для дозиметрії детекторів In пов'язано зі значними систематичними невизначеностями при вимірюванні еквівалентної дози гамма-випромінювання з верхньою межею 10 МеВ, які досягають 20-60% (в залежності від кута випромінювання).

3. Проведено аналіз фізичних характеристик різних матеріалів і характеристик можливих ізомерних станів ядер, які придатні в якості перспективних детекторів для дозиметрії потоків гамма-випромінювання високої інтенсивності.

4. На основі експериментальних даних про величину активності, отриману після опромінення обраних для дослідження зразків пучками гальмівного випромінювання лінійного прискорювача ЛУЕ-10, зроблено вибір матеріалів-детекторів, найбільш придатних для активаційної дозиметрії гамма-випромінювання.

5. Показано, що в якості дозиметричних детекторів, найбільш придатними матеріалами є: Cd, Sn і Ba, при опроміненні яких збуджуються відповідні ізомери з прийнятними для вимірювань характеристиками: ^{111m}Cd; ^{117m}Sn; ^{135m}Ba.

6. Використання в якості дозиметричних активаційних детекторів Cd, Sn і Ba дозволяє знизити систематичну помилку в вимірі еквівалентної дози гамма-випромінювання до 2-3%. Так як період напіврозпаду ізомеру ^{111m}Cd (49 хвилин), є найбільш відповідним для вимірювань в порівнянні з періодами напіврозпаду ізомерів ^{117m}Sn; ^{135m}Ba, можна зробити висновок про те, що матеріал Cd є найбільш прийнятним для практичного використання в якості активаційного дозиметричного детектора.

ORCID IDs
Olexii S. Deiev, https://orcid.org/0000-0003-4565-9039; **Roman N. Dronov**, https://orcid.org/0000-0002-1824-835X,
Boris I. Shramenko, https://orcid.org/0000-0003-4583-6963

СПИСОК ЛІТЕРАТУРИ
[1] Jiunn-Hsing Chao, Pin-Chieh Hsu, and Hong-Ming Liu, Applied Radiation and Isotopes, **55**, 549-556 (2001), https://doi.org/10.1016/S0969-8043(01)00076-8.
[2] A. Murataka, S. Endo, Y. Kojima, and K. Shizuma, J. Radiat. Res. **51**(2), 197-203 (2010), https://doi.org/10.1269/jrr.09083.
[3] V.I. Nikiforov, A.Eh. Tenishev, A.V. Torgovkin, V.L. Uvarov, V.A. Shevchenko, I.N. Shlyahov, and B.I. Shramenko, Problems of Atomic Science and Technology, **4**(80), 181-184, (2012), https://vant.kipt.kharkov.ua/ARTICLE/VANT_2012_4/article_2012_4_181.pdf. (In Russian).
[4] Ju.V. Rogov, V.A. Shevchenko, I.N. Shlyakhov, B.I. Shramenko, A.Eh. Tenishev, A.V. Torgovkin, V.L. Uvarov, and V.F. Zhiglo, Problems of Atomic Science and Technology, **6**(100), 120-124 (2015), https://vant.kipt.kharkov.ua/ARTICLE/VANT_2015_6/article_2015_6_120.pdf.
[5] J.H. Chao, and A.C. Chiang, Radiation Measurements, **45**(9), 1024-1033 (2010), https://doi.org/10.1016/j.radmeas.2010.08.012.
[6] A.A. Lychagin, E.V. Koryakina, and S.E. Ulyanenko, Meditsinskaya Fizika, **3**, 15-23 (2015), http://medphys.amphr.ru/_private/DB/67_15.pdf. (in Russian)
[7] A.N. Dovbnya, O.S. Deyev, V.A. Kushnir, V.S. Malyshevsky, T.V. Malykhina,V.V. Mitrochenko, S.A. Perezhogin, A.V. Torgovkin, G.V. Fomin, and B.I. Shramenko, Problems of Atomic Science and Technology, **6**(88), 192-195, (2013), https://vant.kipt.kharkov.ua/ARTICLE/VANT_2013_6/article_2013_6_192.pdf.
[8] *Нормы радиационной безопасности НРБ-76/87 [Radiation safety standards NRB-76/87]*, (Energoizdat, Moscow, 1988).

ДОСЛІДЖЕННЯ ТА ВИБІР ПЕРСПЕКТИВНИХ МАТЕРІАЛІВ ДЛЯ АКТИВАЦІЙНОЇ ДОЗИМЕТРІЇ ГАЛЬМІВНОГО ВИПРОМІНЮВАННЯ ВЕЛИКОЇ ІНТЕНСИВНОСТІ

О.С. Деєв, Р.М. Дронов, В.А. Шевченко, Б.І. Шраменко
Національний Науковий Центр «Харківський фізико-технічний інститут»
1 вул. Академічна, м. Харків Україна 61108

Радіаційні технології, засновані на застосуванні потужних пучків електронів та гамма-випромінювання тісно пов'язані з необхідністю дозиметрії цих пучків. Вельми успішною для цих цілей є дозиметрія, заснована на використанні реакції непружного розсіювання гамма-квантів на цілому ряді ядер з утворенням ізомерів з різними періодами напіврозпаду і енергіями квантів випромінювання. Прикладом такого застосування в дозиметрії є реакція ^{115}In $(\gamma,\gamma')^{115m}In$ в результаті якої утворюється ізомер ^{115m}In, що має гамма-лінію з енергією 336,24 кеВ і період напіврозпаду 4,5 годин. Мало місце успішне застосування цієї методики в дозиметрії при вирішенні певних практичних завдань (опромінювальні комплекси на основі джерел ^{60}Co - кобальтові «гармати»). У даній роботі показано, що використання детекторів з In для дозиметрії гамма-випромінювання з широким енергетичним спектром (гальмівне випромінювання) пов'язане зі значною невизначеністю при вимірюванні еквівалентної дози гамма-спектра з верхньою межею 10 МеВ. Така невизначеність обумовлена відносно високим порогом вищезгаданої реакції -1,08 МеВ. В даній роботі визначено кількісний вклад у повний потік випромінювання ділянки гамма-спектра нижче порогу (γ,γ') реакції на ядрі In та показано, що в залежності від напрямку випромінювання має місце систематична похибка при вимірюванні еквівалентної дози, що досягає 20-60%. Досліджено та

запропоновано для використання альтернативні матеріали - детектори, що дозволяють зменшити систематичну похибку при вимірі еквівалентної дози до 2-3%, що є цілком прийнятним для практичного застосування.

КЛЮЧОВІ СЛОВА: лінійний прискорювач електронів, гамма-випромінювання, (γ,γ') реакція, ізомер, дозиметрія

ИССЛЕДОВАНИЯ И ВЫБОР ПЕРСПЕКТИВНЫХ МАТЕРИАЛОВ ДЛЯ АКТИВАЦИОННОЙ ДОЗИМЕТРИИ ТОРМОЗНОГО ИЗЛУЧЕНИЯ БОЛЬШОЙ ИНТЕНСИВНОСТИ

О.С. Деев, Р.М. Дронов, В.А. Шевченко, Б.И. Шраменко

Национальный Научный Центр «Харьковский физико-технический институт»

1 ул. Академическая, Харьков Украина 61108

Радиационные технологии, основанные на применении мощных пучков электронов и гамма-излучения, тесно связаны с необходимостью дозиметрии этих пучков. Весьма успешной для этих целей является дозиметрия, основанная на использовании реакции неупругого рассеяния гамма-квантов на целом ряде ядер с образованием изомеров с различными периодами полураспада и энергиями квантов излучения. Примером такого применения в дозиметрии является реакция ^{115}In (γ,γ')^{115m}In в результате которой образуется изомер ^{115m}In, имеющий гамма-линию с энергией 336,24 кэВ и период полураспада 4,5 часа. Имело место успешное применение этой методики в дозиметрии при решении определенных практических задач (облучательные комплексы на основе источников ^{60}Co – кобальтовые «пушки»). В настоящей работе показано, что использование детекторов из In для дозиметрии гамма-излучения с широким энергетическим спектром (тормозное излучение) сопряжено со значительной систематической ошибкой в измерении эквивалентной дозы гамма-спектра с верхней границей 10 МэВ. Такая неопределенность обусловлена относительно высоким порогом вышеупомянутой реакции -1,08 МэВ. В работе определен количественный вклад в полный поток излучения участка гамма-спектра ниже порога (γ,γ') реакции на ядре In. Показано, что в зависимости от направления излучения имеет место систематическая ошибка в измерении эквивалентной дозы, достигающая 20-60%. Исследованы и предложены для использования альтернативные материалы – детекторы, позволяющие уменьшить систематическую ошибку в измерении эквивалентной дозы до 2-3%, что является вполне приемлемым для практического применения.

КЛЮЧЕВЫЕ СЛОВА: линейный ускоритель электронов, гамма-излучение, (γ,γ') реакция, изомер, дозиметрия

INSTRUCTIONS FOR PREPARING MANUSCRIPT IN EAST EUROPEAN JOURNAL OF PHYSICS

Nikita F. Author[a,*], Peter V. Co-author(s)[b,†]
[a]Affiliation of first author
[b]Affiliation of second author (if different from first Authors)
*Corresponding Author: corresponding_authors@mail.com, [a]ORCID ID
[†]E-mail: co_authors@mail.com, [b]ORCID ID
Received October 25, 2020; revised November 25, 2020 accepted December 5, 2020

Each paper must begin with an abstract. The abstract should be typed in the same manner as the body text (see below). Please note that these Instructions are typed just like the manuscripts should be. The abstract must have at least **1800 phonetic symbols**, supplying general information about the achievements, and objectives of the paper, experimental technique, methods applied, significant results and conclusions. Page layout: the text should be printed on the paper **A4** format, at least **5 pages**, with margins of: **Top - 3, Bottom, Left and Right - 2 cm**. The abstract should be presented in English (only for foreign authors), Ukraine and Russian.
KEYWORDS: there, must, be, at least, 5 keywords

This is introduction section. This paper contains instructions for preparing the manuscripts. The text should be prepared in "**doc" or "docx"** format.

INSTRUCTIONS

The text should be typed as follows:
• **title**: Times New Roman, 12 pt, ALL CAPS, bold, 1 spacing, centred;
• **authors**: name, initials and family names; Times New Roman, 12 pt, bold, 1 spacing, centred;
• **affiliation(s)**: Times New Roman, 9 pt, italic, 1 spacing, centred;
• **abstract**: Times New Roman, 9 pt, 1 spacing, justified;
• **body text**: Times New Roman, 10 pt, 1 spacing, justified; paragraphs in sections should be indented right (tabulated) for 0.75 cm;
• **section titles**: Times New Roman, 10 pt, bold, 1 spacing, centred, without numbering, one line should be left, blank above section title;
• **subsection titles**: Times New Roman, 10 pt, bold, 1 spacing, centred, without numbering in accordance to the section (see below), one line should be left blank above subsection title;
• **figure captions**: width of the figure should be 85 or 170 mm, figures should be numbered (**Figure 1.**) and titled below figures using sentence format, Times New Roman, 9 pt, 1 spacing, centred (if one line) or justified (if more than one line); one line should be left blank below figure captions;
• **table captions**: width of the table should be 85 or 170 mm, tables should be numbered (**Table 1.**) and titled above tables using sentence format, Times New Roman, 10 pt, 1 spacing, justified, Tables should be formatted with a single-line box around the outside border and single ruling lines between rows and columns; one line should be left blank below tables;
• **equations**: place equations centred, numbered in Arabic (1), flush right, equations should be specially prepared in **MathType** or "**Microsoft Equation"** one line should be left blank below and above equation.

Additional instructions

Numerated figures and tables should be embedded in your text and placed after they are cited. Only sharp photographs and drawings are acceptable. Letters in the figures should be 3 mm high. The figures should be presented in one of the following graphic formats: jpg, gif, pcx, bmp, tif.

REFERENCES

Cite references in AIP style (https://guides.lib.monash.edu/citing-referencing/aip). Numbering in the order of referring in the text, e.g. [1], [2-5], etc. References should be listed in numerical order of citation in the text at the end of the paper (justified), Times New Roman, 9 pt, 1 spacing.

Journal Articles
[1] T. Mikolajick, C. Dehm, W. Hartner, I. Kasko, M. J. Kastner, N. Nagel, M. Moert, and C. Mazure, Microelectron. Reliab. **41**, 947-950 (2001), https://doi.org/10.1016/S0026-2714(01)00049-X.
[2] S. Bushkova, B.K. Ostafiychuk, and O.V. Copaiev, Physics and Chemistry of Solid State. **15**(1), 182-185 (2014), http://page.if.ua/uploads/pcss/vol15/!1501-27.pdf. (in Ukrainian)
[3] M. Yoshimura, E. Nakai, K. Tomioka and T. Fukui, Appl. Phys. Lett. **103**, 243111 (2013), http://dx.doi.org/10.7567/APEX.6.052301.

E-print Resourses with Collaboration Research or Preprint
[4] M. Aaboud et al. (ATLAS Collaboration), Eur. Phys. J. C, **77**, 531 (2017), http://dx.doi.org/10.1140/epjc/s10052-017-5061-9
[5] Sjöstrand et al., *Comput. Phys. Commun.* **191,** 159-177 (2015), https://doi.org/10.1016/j.cpc.2015.01.024.
[6] Boudreau, C. Escobar, J. Mueller, K. Sapp, and J. Su, (2013), http://arxiv.org/abs/1304.5639.

Books
[7] S. Inoue, and K.R. Spring, *Video Microscopy*: *The fundamentals*, 2nd ed. (Plenum, New York, 1997), pp. 19-24.
[8] I. Gonsky, T.P. Maksymchuk, and M.I. Kalinsky, *Біохімія Людини [Biochemistry of Man],* (Ukrmedknyga, Ternopil, 2002), p. 16. (in Ukrainian)

Edited Books
[9] Z.C. Feng, editor, *Handbook of Zinc Oxide and Related Materials: Devices and Nano Engineering, vol. 2*, (CRC Press/Taylor & Francis, Boca Raton, FL, 2012)

Book Chapters
[10] P. Blaha, K. Schwarz, G.K.H. Madsen, D. Kvasnicka, and J. Luitz, in: *WIEN2K, An Augmented Plane Wave Plus Local Orbitals Program for Calculating Crystal Properties,* edited by K. Schwarz (Techn. Universität Wien, Austria, 2001).
[11] M. Gonzalez-Leal, P. Krecmer, J. Prokop and S.R. Elliot, in: *Photo-Induced Metastability in Amorphous Semiconductors*, edited by A.V. Kolobov (Wiley-VCH, Weinheim, 2003), pp. 338-340.
[12] A. Kochelap and S.I. Pekar, in: *Теория Спонтанной и Стимулированной Хемилюминесценции Газов [Theory of Spontaneous and Stimulated Gas Chemiluminescence]* (Naukova dumka, Kyiv, 1986), pp. 16-29. (in Russian)

Conference or Symposium Proceedings
[13] C. Yaakov, and R. Huque, in: *Second International Telecommunications Energy Symposium Proceedings*, edited by E. Yow (IEEE, New York, 1996), pp. 17-27.
[14] V. Nikolsky, A.K. Sandler and M.S. Stetsenko, in: *Автоматика-2004: Матеріали 11 Міжнародної Конференції по Автоматичному Управлінню [Automation-2004: Materials of the 11th International Conference on Automated Management]* (NUHT, Kyiv, 2004), pp. 46-48. (in Ukrainian)

Patent
[15] I.M. Vikulin, V.I. Irha and M.I. Panfilov, Patent Ukraine No. 26020 (27 August 2007). (in Ukrainian)

Thesis / Dissertation
[16] R.E. Teodorescu, Ph.D. dissertation, The George Washington University, 2009.

Special Notes
1. Use International System of Units (SI system). 2. It is undesirable to use acronyms in the titles. Please define the acronym on its first use in the paper. 3. Refer to isotopes as ^{14}C, ^{3}H, ^{60}Co, etc.